TRANSACTIONS
OF THE ASME
Series D

Journal of BASIC ENGINEERING

September 1959

Divisions: LUBRICATION • HYDRAULIC • INSTRUMENTS AND REGULATORS
METALS ENGINEERING • Research Committees: AUTOMATIC REGULATION THEORY
EFFECT OF TEMPERATURE ON THE PROPERTIES OF METALS • FLUID METERS
PREVENTION OF FRACTURE IN METALS • MECHANICAL PRESSURE ELEMENTS
LUBRICATION • PLASTIC FLOW OF METALS

Published Quarterly by
THE AMERICAN SOCIETY OF MECHANICAL ENGINEERS

TRANSACTIONS OF THE ASME
Series D

Journal of
BASIC ENGINEERING

VOLUME 81 • SERIES D • NUMBER 3
September 1959

CONTENTS

275 **Static and Dynamic Control Characteristics of Flapper-Nozzle Valves**
T.-Y. Feng

285 **Some Measurements of Boundary-Layer Growth in a Two-Dimensional Diffuser**
J. F. Norbury

297 **The Skewed Boundary Layer**
E. S. Taylor

305 **On the Nature of Stall**
S. J. Kline

321 **Optimum Design of Straight-Walled Diffusers**
S. J. Kline, D. E. Abbott, and R. W. Fox

332 **Labyrinth-Seal Leakage Analysis**
W. Zabriskie and B. Sternlicht

341 **Centrifugal Manometer**
J. F. Kemp

349 **The Aerodynamic Design of Two-Dimensional Turbine Cascades for Incompressible Flow With a High-Speed Computer**
H. N. Cantrell and J. E. Fowler

362 **An Analysis of Axial Compressor Cascade Aerodynamics, Part I**
G. L. Mellor

379 **An Analysis of Axial Compressor Cascade Aerodynamics, Part II**
G. L. Mellor

387 **Loss and Stall Analysis of Compressor Cascades**
Seymour Lieblein

401 **Stall Prediction in Gas-Turbine Engines**
R. J. Lubick and L. E. Wallner

409 **A Survey of Stall Propagation—Experiment and Theory**
H. W. Emmons, R. E. Kronauer, and J. A. Rockett

417 **Modulation Phenomena in Stall Propagation**
J. A. Rockett

426 **Studies of Jet Compression—I, Apparatus and Methods. Results With Air at Room Temperature**
H. J. Hoge, S. S. Eichacker, and D. L. Fiske

EDITORIAL DEPARTMENT

Editor, J. J. JAKLITSCH, JR.
Consulting Editor, LEO BLODGETT
Production, JEAN NORTH
Art Editor, HENRY BALFOUR

OFFICERS OF THE ASME

President, G. B. WARREN
Secretary, C. B. SCHIER, II
Treasurer, E. J. KATES
Assistant Treasurer, H. J. BAUER

PUBLICATIONS COMMITTEE

Chairman, JOHN de S. COUTINHO
B. G. A. SKROTZKI
HENDLEY H. BLACKMON
R. D. MINDLIN
MARTIN GOLAND

Junior Representatives
A. T. WUSKA
A. S. GOLDSTEIN

REGIONAL ADVISORY BOARD

Region I, ROY L. PARSELL
Region II, GLENN R. FRYLING
Region III, F. J. HEINZE
Region IV, FRANCIS C. SMITH
Region V, H. M. CATHER
Region VI, C. R. EARLE
Region VII, M. POPOVICH
Region VIII, LINN HELANDER

Published quarterly by The American Society of Mechanical Engineers. Publication office at 20th and Northampton Streets, Easton, Pa. The editorial department is located at the headquarters of the Society, 29 West Thirty-Ninth Street, New York 18, N. Y. Cable address, "Mechaneer," New York. Price $3.00 a copy, $10.00 annually; to members, $1.50 a copy, $5.00 annually. Add 50 cents for postage to all countries outside the United States and Canada. Changes of address must be received at Society headquarters seven weeks before they are to be effective on the mailing list. Please send old as well as new address. . . . By-Law: The Society shall not be responsible for statements or opinions advanced in papers or . . . printed in its publications (B13, Par. 4). . . . Second-class mail privileges authorized at Easton, Penna. This publication is authorized to be mailed at the special rates of postage prescribed by Section 132.122 . . . © Copyrighted, 1959, by The American Society of Mechanical Engineers. Reprints from this publication may be made on condition that full credit be given the Transactions of the ASME, Series D—Journal of Basic Engineering, and the author, and that date of publication be stated.

TRANSACTIONS OF THE ASME
is indexed by the Engineering Index, Inc.

TRANSACTIONS OF THE ASME Series E

Journal of
APPLIED MECHANICS
Volume 81 • Series E • Number 3

CONTENTS FOR SEPTEMBER, 1959

TECHNICAL PAPERS

319 On Supersonic Wind Tunnels With Low Free-Stream Disturbances, M. V. Morkovin. (59—APM-10)
325 Velocity and Temperature Fluctuation Measurements in a Turbulent Boundary Layer, D. S. Johnson. (58—A-81)
337 Density Variation Effects in Stepped-Thrust Bearings, C. F. Kettleborough. (59—APM-19)
341 Response of a Nonlinear String to Random Loading, T. K. Caughey. (59—APMW-4)
345 Response to Van Der Pol's Oscillator to Random Excitation, T. K. Caughey. (59—APMW-5)
349 A Perturbation Solution of the Equations of Motion of a Gyroscope, Robert Goodstein. (59—A-5)
353 Vibration of Beam-Mass Systems With Time-Dependent Boundary Conditions, T. C. Yen and S. Kao. (59—APM-22)
357 Dynamic Loading Tests of an Aircraft-Type Beam, E. A. Ripperger and W. R. Barton.
367 Viscous Damping in Flexural Vibrations of Bars, M. K. Newman. (59—APMW-8)
377 Natural Modes and Their Stability in Two-Degree-of-Freedom Systems, R. M. Rosenberg and C. P. Atkinson. (58—A-57)
386 On Finite Bending of Pressurized Tubes, Eric Reissner. (59—APM-5)
393 Instability and Folding Deformation of a Viscoelastic Medium in Compression, M. A. Biot. (59—APMW-21)
401 Stress Distribution in Semi-Infinite Strip Subjected to Concentrated Load, P. S. Theocaris. (59—APM-17)
407 Postbuckling Behavior of Rectangular Plates With Small Initial Curvature, Noboru Yamaki. (58—A-59)
415 New Theory of Elastic Sandwich Plates—One-Dimensional Case, Yi-Yuan Yu. (59—APM-23)
422 On Invariant Perforation in an Infinite Strip, Chih-Bing Ling. (59—APM-20)
432 Thermal Stresses in Moderately Thick Elastic Plates, B. E. Gatewood. (59—APM-7)
437 Analysis of Plane Stress in Polar Co-ordinates, H. D. Conway. (59—APM-1)
440 The Stress Function of a Radial Strain, F. Goded. (59—APM-25)
442 Determination of Safe Loads of Beams Subjected to Twisting and Bending Moments, P. G. Hodge Jr., and R. Sankaranarayanan. (59—APM-26)

DESIGN DATA AND METHODS

448 Factors of Stress Concentration Due to Elliptical Fillets, M. M. Frocht and D. Landsberg.

BRIEF NOTES

451 Creep of Elastic Belt on a Pulley, G. V. Tordion. 452 Modification of Rayleigh's Principle for Calculating Beam Frequencies, F. M. Lewis. 454 Yield Point Load of an Annular Plate, P. G. Hodge, Jr. 455 Analysis of Indeterminate Structures by Displacement Method, P. H. Denke and C. K. Wang. 456 Internal Damping of Thermal Origin in Thin Wires, P. Srinivasan. 457 Lateral Buckling of Tapered Narrow Beam, L. H. N. Lee. 458 Stresses in Infinite Wedges Tapered in Width and Thickness, H. D. Conway. 460 Minimization of Spring Torque, T. Vreeland, Jr. 461 Steady-State Response of Linear Vibration Systems, M. E. Gurtin. 462 Further Understanding of Shakedown Theorems, Melvin Zaid. 462 Series Solution for Ellipsoidal Shells, Robert Schmidt.

DISCUSSION

465 Discussion of previously published papers by E. L. Reiss; G. N. Hatsopoulos and J. H. Keenan; F. A. McClintock; F. M. White, B. F. Barfield, and M. J. Goglia; M. M. Abbassi; Eli Sternberg and W. T. Koiter; M. J. Schilhansl

475 **BOOK REVIEWS**

TRANSACTIONS OF THE ASME Series B

Journal of
ENGINEERING FOR INDUSTRY
Volume 81 • Series B • Number 3

CONTENTS FOR AUGUST, 1959

187 Factors Influencing the Performance of Grinding Wheels, by E. J. Krabacher. (58—SA-40)
201 Vibrations of Flexible Precision Grinding Spindles, by R. S. Hahn. (58—A-97)
207 The Effect of Process Variables on Extrusion Pressures of Lead, by J. Frisch and E. G. Thomsen. (58—A-109)
217 Approximate Solutions to a Problem of Press Forging, by S. Kobayashi and E. G. Thomsen. (58—A-140)
228 Theory and Experiment of Press Forging Axisymmetric Parts of Aluminum and Lead, by S. Kobayashi, R. Herzog, J. T. Lapsley, Jr., and E. G. Thomsen. (58—A-154)
239 A Three-Dimensional, Tool-Life Equation—Machining Economics, by B. N. Colding. (58—A-123)
251 Some Observations on the Shearing Process in Metal Cutting, by S. Kobayashi and E. G. Thomsen. (58—A-139)
263 Observations on the Angle Relationships in Metal Cutting, by D. M. Eggleston, R. Herzog, and E. G. Thomsen. (58—A-138)

TRANSACTIONS
Series C

Journal of
HEAT TRANSFER
Vol. 81 • Series C • No. 3

CONTENTS FOR AUGUST, 1959

175 Heat Transfer Between Concentric Rotating Cylinders, by I. S. Bjorklund and W. M. Kays. (58—A-99)

187 Full-Scale Human-Body-Model Thermal Exchange Compared With Equational Condensation of Human Calorimetric Data, by L. P. Herrington. (58—A-181)

195 The Emissivity and Absorptivity of Parachute Fabrics, by J. P. Hartnett, E. R. G. Eckert, and R. Birkebak. (58—A-125)

202 An Experimental and Analytical Study of Vortex-Flow Temperature Separation by Superposition of Spiral and Axial Flows—Part 1, by J. E. Lay. (58—SA-71)

213 An Experimental and Analytical Study of Vortex-Flow Temperature Separation by Superposition of Spiral and Axial Flows—Part 2, by J. E. Lay. (58—A-90)

223 Analysis of the Aerodynamic Heating for a Re-Entrant Space Vehicle, by M. J. Brunner. (59—Av-5)

230 A Photographic Study of Boiling in the Absence of Gravity, by R. Siegel and C. Usiskin. (59—Av-37)

237 Some Radiator Design Criteria for Space Vehicles, by J. P. Callinan and W. P. Berggren. (59—Av-29)

245 Optimization of a Conventional-Fuel-Fired Thermoelectric Generator, by B. W. Swanson and E. V. Somers. (59—SA-14)

Technical Briefs

249 Heat Transfer From a Rotating Disk to Fluids of Any Prandtl Number, by E. M. Sparrow and J. L. Gregg.

251 An Approximate Treatment of Unsteady Heat Conduction in Semi-Infinite Solids With Variable Thermal Properties, by K.-T. Yang and Albin Szewczyk.

TRANSACTIONS
Series A

Journal of
ENGINEERING FOR POWER
Volume 81 • Series A • Number 3

CONTENTS FOR JULY, 1959

1958 Gas Turbine Progress Report

215 Introduction, by R. T. Sawyer. (58—A-46 A)

219 Materials, by A. W. Herbenar and G. R. Heckman. (58—A-46 B)

226 Turbine Cooling, by J. B. Esgar. (58—A-46 C)

234 Fuels, by A. D. Foster. (58—A-46 D)

244 Cycle Components, by P. F. Martinuzzi. (58—A-46 E)

259 Compound Piston-and-Turbine Engines, by A. L. London. (58—A-46 F)

265 Aviation, by O. E. Lancaster. (58—A-46 G)

280 Rocket Turbines, by O. E. Lancaster and C. J. Bates. (58—A-46 H)

290 Automotive, by F. L. Schwartz. (58—A-46 I)

298 Railroad, by P. R. Broadley, W. M. Meyer, D. S. Neuhart, E. L. Barlow, R. C. Bond, D. S. D. Williams, and B. W. C. Cooke. (58—A-46 J)

311 Marine, by J. W. Sawyer and H. M. Simpson. (58—A-46 K)

344 Industrial and Central Station, by B. G. A. Skrotzki. (58—A-46 L)

352 Nuclear, by R. P. Godwin and E. S. Dennison. (58—A-46 M)

TSUN-YING FENG[1]

Head, Power Control Systems Analysis Group, Flight Control Systems Analysis Section, Aircraft Division, Bell Aircraft Corporation, Buffalo, N. Y.

Static and Dynamic Control Characteristics of Flapper-Nozzle Valves

A basic study was conducted on a flapper-nozzle hydraulic control valve to explore in detail its static and dynamic control characteristics. These static and dynamic control characteristics are presented and both the theoretical and experimental results compared. Correlation between the theoretical and experimental results were found to be quite good.

THE FLAPPER-NOZZLE valve has been used extensively as a first-stage valve in many two-stage electrohydraulic servo valves. It is comparatively simple in construction and relatively reliable in operation. However, this type of valve has inherent drawbacks[2] because of metallurgical properties and flow characteristics. These drawbacks are tolerable to most present hydraulic servos. As the environmental conditions become increasingly severe, the effects may cause unacceptable servo performance. To improve or eliminate, if possible, these drawbacks, it is necessary to understand the basic characteristics of this type of control valve. With this objective, a basic study was made. This paper presents all important basic characteristics which are useful to future design of high-performance hydraulic servomechanisms, particularly those under severe environmental conditions.

Statics

Both the flapper and nozzle were made of cold-rolled steel and their physical dimensions are shown in Fig. 1. The flapper disk has a diameter of 1 in. which is large enough to avoid any edge effects on the fluid jet from the nozzle impinging on the flapper.

Fig. 2 shows the arrangement of the test apparatus. A traveling microscope is used to register the flapper position by aligning two marks—one on the microscope and the other on the flapper. The flapper is fastened to the force-sensing rod of a Statham Force Transducer (GI-80-1200) which is actuated by a differential screw. Three upstream orifice sizes with diameters of 0.0065, 0.004, and 0.002 in., were tested separately with the different size filters (0.5, 10 microns, and no filter). The supply pressure, ranging from 1000 to 3000 psig was kept constant by a pressure regulator for various flow rates under test.

Discharge Coefficients of Upstream Orifice and Curtain Area ($\pi d_N x$) of Flapper-Nozzle Valve. Both coefficients are plotted against their related pressure ratio and Reynolds number in Figs. 3, 4, 5, and 6. This information suggests that an average value of the discharge coefficient could be used for a given operating range of the pressure ratio or Reynolds number. The average value of C_u is 0.89 and C_c is 0.63 for all theoretical calculations in this paper. It has been found that the experimental result agrees quite well with the calculated values by means of this average method.

An abrupt change of C_u occurs at the pressure ratio 0.275 which corresponds to a Reynolds number of 2800, Figs. 3 and 4, and the variation of C_u with respect to RN is large for RN 2800 (discussion restricted to Fig. 4 only). Since RN changes as the fluid temperature fluctuates, C_u becomes very sensitive to temperature fluctuation for RN 2800, as shown in Fig. 4. This is likely

[1] Formerly Research Engineer, Aeronautical Division, Minneapolis-Honeywell Regulator Company, Minneapolis, Minn.

[2] Such as null shift.

Contributed by the Instruments and Regulators Division and presented at the Annual Meeting, New York, N. Y., November 30–December 5, 1958, of THE AMERICAN SOCIETY OF MECHANICAL ENGINEERS.

NOTE: Statements and opinions advanced in papers are to be understood as individual expressions of their authors and not those of the Society. Manuscript received at ASME Headquarters, August 28, 1958. Paper No. 58—A-160.

Nomenclature

A_c = curtain area of flapper-nozzle valve, sq in.
A_p = end area of second-stage spool, sq in.
A_n = nozzle area, sq in.
A_u = upstream orifice area, sq in.
B = viscous damping coefficient on flapper, lb-sec/in.
C_c = discharge coefficient of curtain area of flapper-nozzle valve
C_u = discharge coefficient of upstream orifice
D = differential operator d/dt, 1/sec
d = hydraulic diameter, in.
d_N = nozzle diameter, in.
d_u = diameter of upstream orifice, in.
$[E]\ \frac{\pi}{4} d_N^2$ = hydraulic spring rate, lb per in.
F = force, oz
i = initial condition
k_R = spring rate of flapper, lb per in.
k_s = spring rate of mechanical spring attached to second-stage spool, lb per in.
M = mass of flapper, lb-sec^2/in.
P_B = back pressure of exhaust chamber, psig
P_c = chamber pressure of nozzle, psig
P_s = supply pressure, psig
Q = volume rate of flow, cu in. per sec
RN = Reynolds number, $\rho V_{mean}\, d/\mu$
V_c = fluid volume between first and second-stage valves, cu in.
V_{mean} = mean velocity, ips
x = flapper displacement, in.
y = position of second stage spool, in.
ρ = fluid density, lb-sec^2/in.^{4}
μ = fluid viscosity, lb-sec/in.^{2}
Δ = small increment
ϕ = damping ratio
β = bulk modulus of hydraulic oil, psi
τ = time constant, sec
τ_1 = reciprocal of time constant, 1/sec
ω_r = frequency of damped oscillation, 1/sec
ω_N = undamped natural frequency, 1/sec

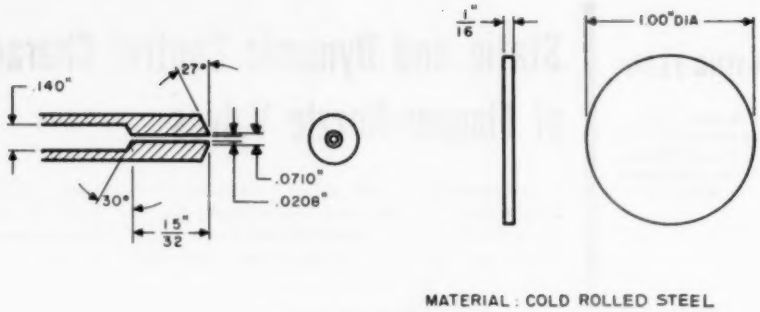

Fig. 1 Nozzle and flapper

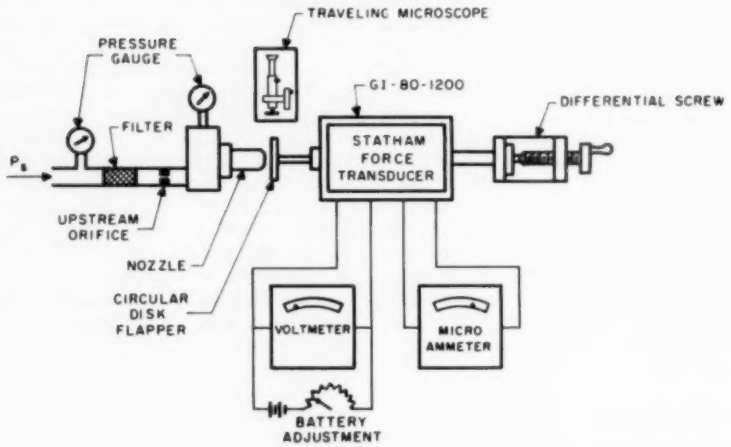

Fig. 2 Static test setup

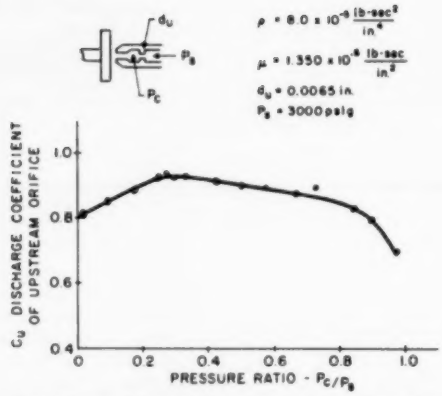

Fig. 3 Discharge coefficient of upstream orifice C_u versus pressure ratio P_c/P_s

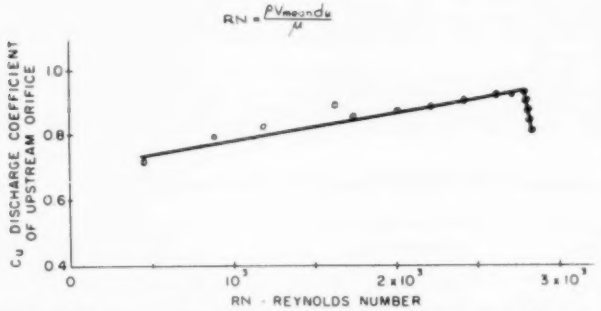

Fig. 4 Discharge coefficient of upstream orifice C_u versus Reynolds number, RN

to cause the null point of the chamber pressure to drift. Therefore, it is desirable to have the upstream orifice always operating at a Reynolds number less than 2800.

The discharge coefficient of the curtain area, C_c, was determined experimentally, only for low pressure ratios, Figs. 5 and 6, because it was intended primarily for the stability test.

Chamber Pressure Versus Flapper Position. The experimental results of the chamber pressure versus flapper position, shown nondimensionally in Fig. 7, are favorably compared with the calculated values. A slight discrepancy gradually showing up in the low values of x/d_n could be attributed to the irregularity of the nozzle tip or the misalignment between the flapper and the nozzle or the combination.

The favorable design point for maximum pressure sensitivity is the point of inflection on this curve. However, the neutral gap at this point is exceedingly small. If it is chosen to be the null point, then a close machining tolerance on the flapper and nozzle will be required and the valve may silt more easily.

Hydraulic Flow Forces on Flapper Versus Chamber Pressure and Flapper Position. The experimental results of flow forces on the flapper versus chamber pressure compare well with the calculated data in Figs. 8 and 9. Change in supply pressure, flapper-disk diame-

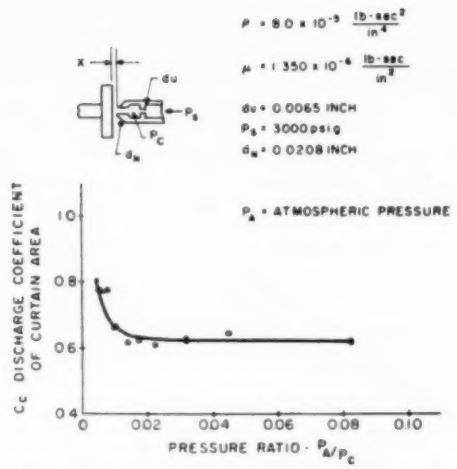
$\rho = 8.0 \times 10^{-5}$ lb·sec²/in⁴
$\mu = 1.350 \times 10^{-6}$ lb·sec/in²
$d_U = 0.0065$ INCH
$P_S = 3000$ psig
$d_N = 0.0208$ INCH
P_A = ATMOSPHERIC PRESSURE
C_c DISCHARGE COEFFICIENT OF CURTAIN AREA
PRESSURE RATIO - P_A/P_C

Fig. 5 Discharge coefficient of curtain area C_c versus pressure ratio P_A/P_c

ter, and upstream orifice indicate no effect on the flow forces. Fig. 10 shows the flow forces versus the flapper position. This is an inherent pressure feedback which can be used properly to stabilize a servo system.

Hydraulic Spring on Torque-Motor Armature. The hydraulic pressure acting on the flapper produces a force which varies with the flapper position. Its rate is a function of the initial setting of the neutral gap. Shown in Fig. 11 are the hydraulic spring characteristics for a single flapper-nozzle valve and in Fig. 12 for a dual nozzle-flapper valve. A linear hydraulic spring can be obtained by equating the neutral-gap area to the upstream-orifice area.

Silting. No significant silting has been obtained at either the upstream orifice (diameters 0.004 and 0.0065 in.) or the curtain area of the flapper-nozzle valve in the pressure range from 1000 to 3000 psig. No silting was reported even when the experiment was run without filters. Contamination report of the test stand indicated that the size distribution in a volume of 1 cu mm was as

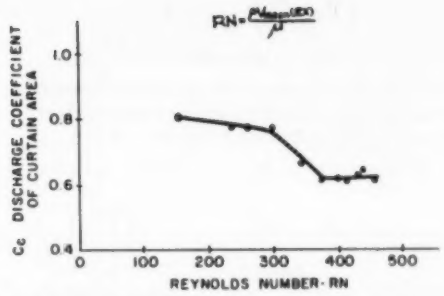

Fig. 6 Discharge coefficient of curtain area C_c versus Reynolds number, RN

follows: 5–10 micron 3 particles, 2.5–5 micron 5 particles, and 1–2.5 micron 47 particles.

Dynamics

Instrumentation. The test setup of the dynamic system is shown schematically in Fig. 13. A 2-gal accumulator located upstream helps eliminate all possible disturbances from the hydraulic pump. All pressure gages are shut off by means of the needle valves during the test. The variation of the chamber pressure is kept as small as possible so that the perturbation assumption is valid. An audio oscillator was used to provide the linearsyn with a carrier frequency of about 1000 cps which enables one to count the vibration frequency of the system.

Theory Versus Experiment. The dynamic equation (see Appendix) of the flapper-nozzle valve is:

$$\left(D^3 + \frac{M + B\tau}{M\tau} D^2 + \frac{\tau K_R + B}{M\tau} D + \frac{K_R + (|E|\pi/4)d_N^2}{M\tau}\right) \Delta x = 0 \quad (1)$$

The necessary condition for stability can easily be satisfied because all coefficients are positive. The sufficient condition requires

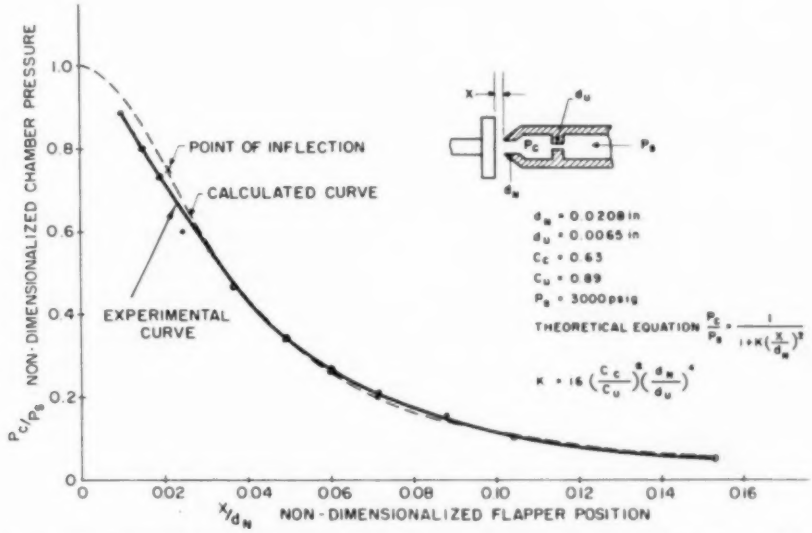

Fig. 7 Nondimensionalized chamber pressure P_c/P_s versus nondimensionalized flapper position X/d_N

$$\frac{\left(\frac{M + B\tau}{M\tau}\right)(\tau k_R + B)}{k_R + (|E|\pi/4)d_N^2} > 1.0 \qquad (2)$$

where B can be determined experimentally (Appendix). By comparing the order of magnitude term by term (Appendix), the expression (2) can be simplified as follows:

$$\frac{B/M(\tau k_R + B)}{k_R + (|E|\pi/4)d_N^2} > 1.0 \qquad (3)$$

The continuity equation is

$$x_i = 1/4\,\frac{C_d d_u^2}{C_c d_N}\left(\frac{P_s - P_{ci}}{P_{ci}}\right)^{1/2} \qquad (4)$$

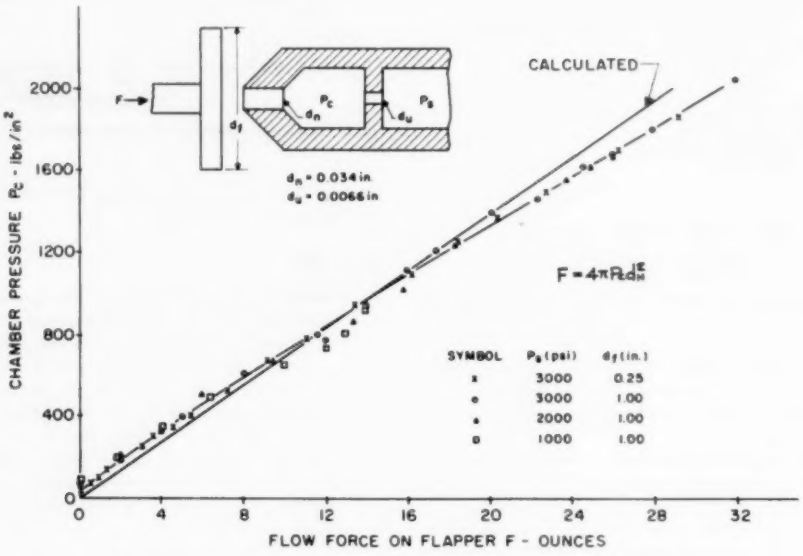

Fig. 8 Flow force on flapper versus chamber pressure for various P_s and d_f

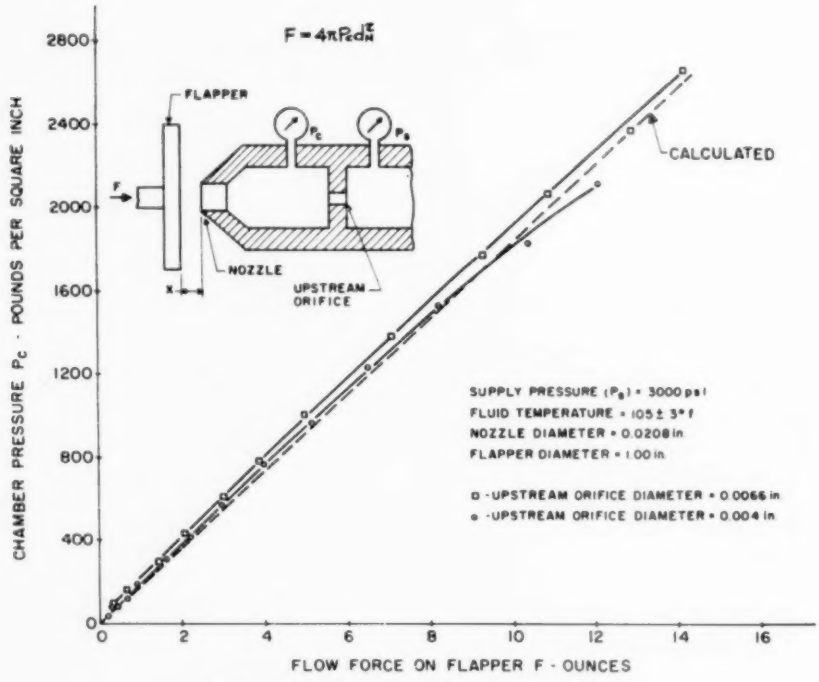

Fig. 9 Chamber pressure versus flow force on flapper

Substitution of (4) into (3) yields

$$\frac{B^2}{M}\frac{\dfrac{k_R}{B}\dfrac{4}{\pi}(2\rho)^{1/2}\left(\dfrac{A_p^2}{k_s}+\dfrac{V_{ci}}{\beta}\right)+\dfrac{C_w d_u^2}{(P_s-P_{ci})^{1/2}}\dfrac{P_s}{P_{ci}}}{k_R\dfrac{C_w d_u^2}{(P_s-P_{ci})^{1/2}}\left(\dfrac{P_s}{P_{ci}}\right)+C_c 2\pi d_N^3 (P_{ci})^{1/2}} > 1.0 \quad (5)$$

The term at the left of the inequality (5) gives the absolute stability characteristics of the flapper-nozzle valve. The summarized result is tabulated in Table 1.

Conclusion

The relationships developed among various physical parameters in this paper can be used to obtain quantitative or qualitative design information regarding static and dynamic performance of flapper-nozzle valves. The results presented here should be particularly useful in predicting the effects of changes in design parameters.

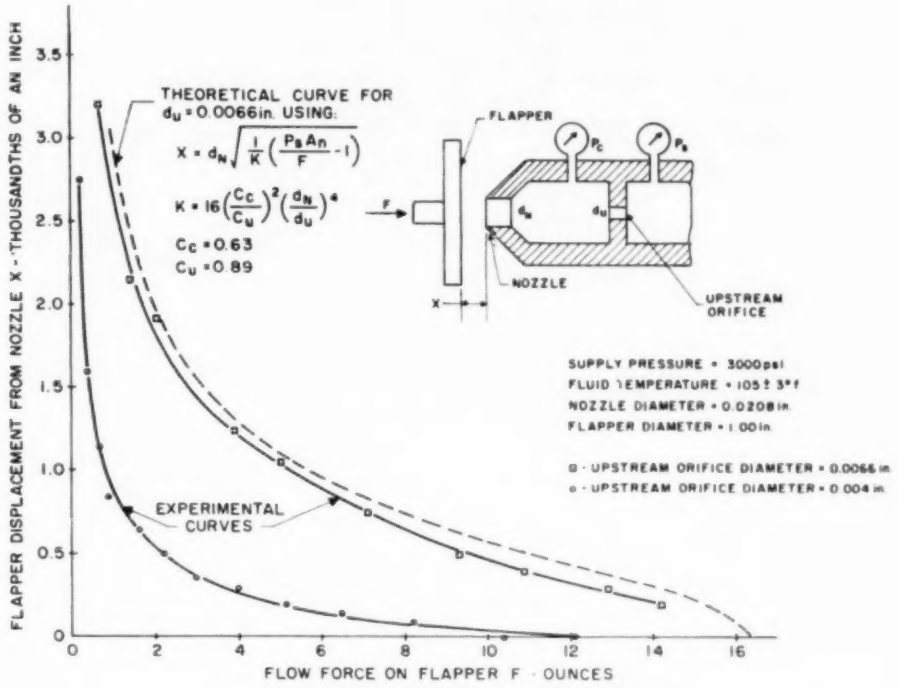
FLAPPER DISPLACEMENT FROM NOZZLE X - THOUSANDTHS OF AN INCH
THEORETICAL CURVE FOR
d_U = 0.0066in. USING:
$X = d_N\sqrt{\frac{1}{K}\left(\frac{P_S A_n}{F}-1\right)}$
$K = 16\left(\frac{C_C}{C_U}\right)^2\left(\frac{d_N}{d_U}\right)^4$
C_C = 0.63
C_U = 0.89
FLAPPER
NOZZLE
UPSTREAM ORIFICE
SUPPLY PRESSURE = 3000psi
FLUID TEMPERATURE = 105 ± 3°F
NOZZLE DIAMETER = 0.0208in.
FLAPPER DIAMETER = 1.00in.
□ - UPSTREAM ORIFICE DIAMETER = 0.0066 in.
○ - UPSTREAM ORIFICE DIAMETER = 0.004 in.
EXPERIMENTAL CURVES
FLOW FORCE ON FLAPPER F - OUNCES

Fig. 10 Flapper displacement versus flow force on flapper

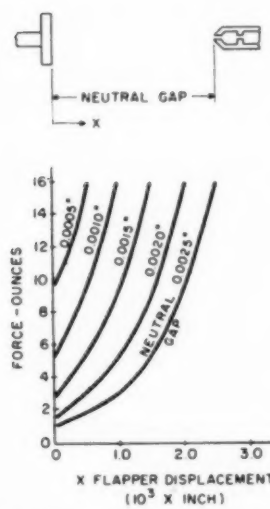

Fig. 11 Hydraulic-spring characteristics of a single flapper-nozzle valve for various neutral gaps

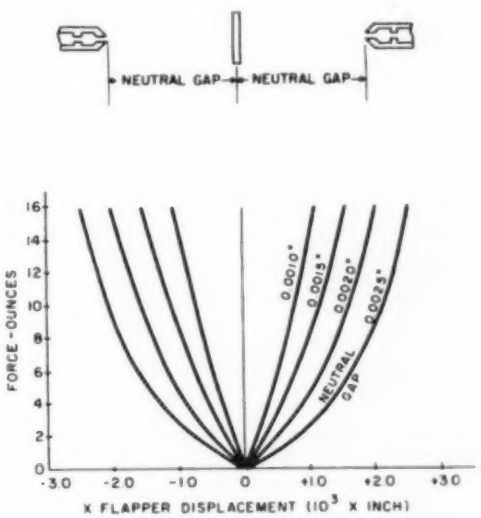

Fig. 12 Hydraulic-spring characteristics of a double nozzle-flapper valve for various neutral gaps

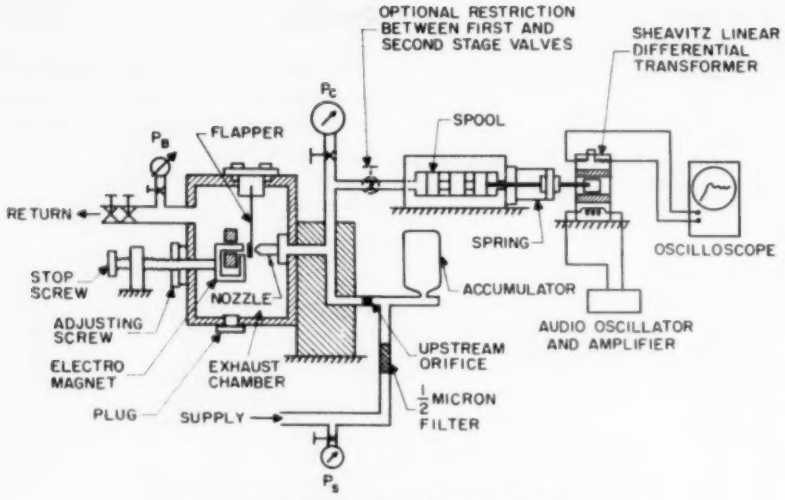

Fig. 13 Schematic drawing of dynamic test setup

P_s = 3000 psig P_{ci} = 500 psig
d_u = 0.0065 in. EXHAUST CHAMBER EMPTY

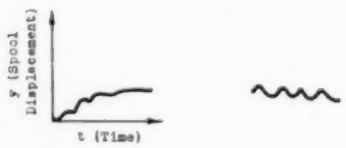

k_s = 2780 lbs/in k_s = 278 lbs/in

Fig. 14 Stability characteristics—decreasing stability with decreasing k_s

P_{ci} = 200 psig k_s = 2780 lbs/in
d_u = 0.0065 in. EXHAUST CHAMBER EMPTY

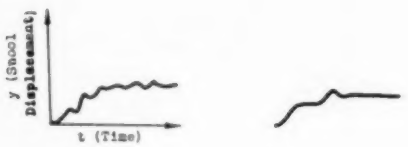

P_s = 3000 psig P_s = 1500 psig

Fig. 15 Stability characteristics—increasing stability with decreasing P_s

P_s = 3000 psig k_s = 2780 lbs/in
EXHAUST CHAMBER EMPTY

d_u = 0.0065 in d_u = 0.004 in
P_{ci} = 220 psig P_{ci} = 180 psig

Fig. 16 Stability characteristics—increasing stability with decreasing d_u

P_s = 3000 psig P_{ci} = 630 psig
P_B = 400 psig d_u = 0.0065 in
k_s = 278 lbs/in

WITHOUT RESTRICTION BETWEEN FIRST AND SECOND STAGE VALVES

WITH RESTRICTION BETWEEN FIRST AND SECOND STAGE VALVES

Fig. 17 Stability characteristics—increasing stability derived by introducing additional orifice between first and second-stage valves

Table 1 Stability of a flapper-nozzle valve

Significant parameters	Stability: Theory	Stability: Experiment
B = viscous damping on flapper	Increasing stability with increasing B	No test
M = flapper mass	Decreasing stability with increasing M	Theory verified by experiment but no photographs taken
k_R = mechanical spring rate of flapper	Increasing stability with increasing k_R if: $\frac{C_s S d_N^2 \left(\frac{A_p^2}{k_s} + \frac{V_{ci}}{\beta}\right)\left(2\rho P_{ci}\right)^{1/2}}{\frac{C_u^2 d_u^4}{P_s - P_{ci}}\left(\frac{P_s}{P_{ci}}\right)^2} > 1.0$	
	Decreasing stability with increasing k_R if: $\frac{C_s S d_N^2 \left(\frac{A_p^2}{k_s} + \frac{V_{ci}}{\beta}\right)\left(2\rho P_{ci}\right)^{1/2}}{\frac{C_u^2 d_u^4}{P_s - P_{ci}}\left(\frac{P_s}{P_{ci}}\right)^2} < 1.0$	No test
k_s = mechanical spring rate on second-stage spool	Decreasing stability with decreasing k_s	Fig. 14
A_p = end area of second-stage spool	Increasing stability with increasing A_p	No test
d_u = diameter of upstream orifice	Increasing stability with decreasing d_u	Fig. 16
P_s = supply pressure	Increasing stability with decreasing P_s	Fig. 15
Introducing additional orifice between first and second-stage valves	Increasing stability	Fig. 17
P_{ci} = initial chamber pressure	Increasing stability with increasing P_{ci} (possibly due to increasing viscous damping on the flapper)	Fig. 18
d_N = nozzle diameter	Increasing stability with decreasing nozzle diameter	No test
V_{ci} = initial chamber volume	Increasing stability with increasing V_{ci}	No test

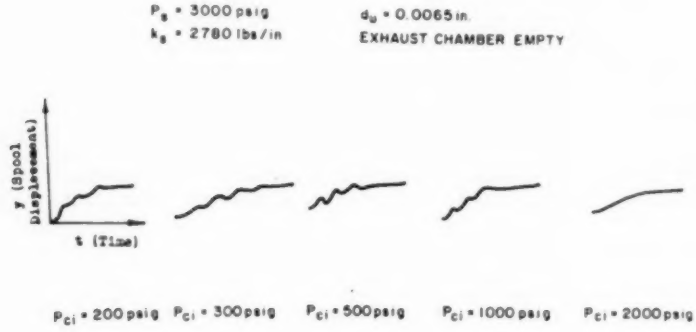

Fig. 18 Stability characteristics—increasing stability with increasing p_{ci}

Acknowledgment

The author wishes to express his sincere appreciation to Mr. O. H. Schuck, Director of Research, Aeronautical Division of Minneapolis-Honeywell Regulator Company, for his encouragement to write this paper. Most of the testing work of the nozzle-flapper valve was conducted by Mr. D. H. Anderson to whom the author is grateful.

Bibliography

J. F. Blackburn, "Contributions to Hydraulic Control—3, Pressure-Flow Relationships for Four-Way Valves," TRANS. ASME, vol. 75, 1953, pp. 1163–1170.

APPENDIX

Analysis of Flapper-Nozzle Valve

Consider that the spool, Fig. 19, is a spring-loaded bellows. The flow and force equations are:

Table 2 Order of magnitude of physical quantities of a typical control system

P_{ci}...0 (10^3) psi	M.....0 (10^{-6}) lb-sec^2/in
P_s...0 (10^3) psi	B.....0 (10^{-1}) lb-sec/in
d_N...0 (10^{-2}) in.	τ.....0 ($10^{-2} - 10^{-3}$) sec
k_s...0 (10^2–10^3) lb/in.	V_{ci}.....0 (10^{-1}) cu in.
k_R...0 (10) lb/in.	ρ.....0 (10^{-6}) lb-sec^2/in.^{4}
d_u...0 (10^{-3}) in.	$\lvert E \rvert \frac{\pi}{4} d_N^2$.0 ($10 - 10^2$) lb/in.

NOTE: 0 ( ) stands for order of magnitude.

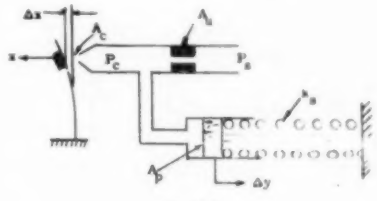

Fig. 19

$$\Delta Q_1 = A_p \frac{d\Delta y}{dt} \text{ (due to spool motion)} \quad (6)$$

$$k_s \Delta y = \Delta P_c A_p \quad (7)$$

$$\Delta Q_2 = \frac{V_{ci}}{\beta} \frac{d\Delta P_c}{dt} \text{ (due to oil compressibility)} \quad (8)$$

The continuity equation is

$$\Delta Q_{in} = \Delta Q_{out} + \left(\frac{A_p^2}{k_s} + \frac{V_{ci}}{\beta}\right) \frac{d\Delta P_c}{dt} \quad (9)$$

By linearization theory

$$\Delta Q_{in} = -C_u A_u \left[\frac{1}{2\rho(P_s - P_{ci})}\right]^{1/2} \Delta P_c \quad (10)$$

$$\Delta Q_{out} = +C_c \pi d_N x_i \left(\frac{1}{2\rho P_{ci}}\right)^{1/2} \Delta P_c + C_c \pi d_N \left(\frac{2P_{ci}}{\rho}\right)^{1/2} \Delta x \quad (11)$$

Combining (9), (10), and (11), write symbolically:

$$\Delta x = \frac{1 + \tau D}{E} \Delta P_c \quad (12)$$

where

$$\tau = \frac{\frac{A_p^2}{K_s} + \frac{V_{ci}}{\beta}}{C_u A_u \left[\frac{1}{2\rho(P_s - P_{ci})}\right]^{1/2} + C_c \pi d_N x_i \left(\frac{1}{2\rho P_{ci}}\right)^{1/2}} \quad (13)$$

$$E = -\frac{C_c \pi d_N \left(\frac{2P_{ci}}{\rho}\right)^{1/2}}{C_u A_u \left[\frac{1}{2\rho(P_s - P_{ci})}\right]^{1/2} + C_c \pi d_N x_i \left(\frac{1}{2\rho P_{ci}}\right)^{1/2}} \quad (14)$$

The force equation on the flapper is

$$MD^2 \Delta X + BD\Delta X + k_R \Delta X = \Delta P_c \frac{\pi}{4} d_N^2 \quad (15)$$

Solving simultaneously (12) and (15), the following is obtained:

$$\left(D^3 + \frac{M + B\tau}{M\tau} D^2 + \frac{\tau k_R + B}{M\tau} D + \frac{k_R - E\frac{\pi}{4} d_N^2}{M\tau}\right) \Delta x = 0 \quad (16)$$

Equation (16) can be represented by a functional diagram, Fig. 20, which delineates symbolically the significance of the system under study. It is clear from the block diagram that the force feedback on the flapper, by virtue of the variation of the chamber pressure, plays an important role in system stability.

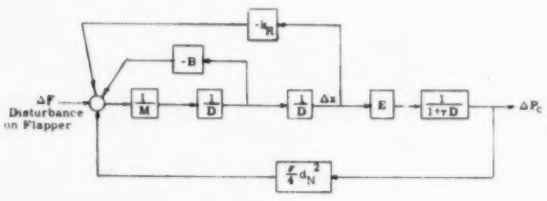

Fig. 20

Determining Viscous Damping Coefficient B on Flapper

If a third-order system is oscillatory, Equation (16) can be compared with the following:

$$(D + \tau_1)(D^2 + 2\phi\omega_r D + \omega_r^2)\Delta x = 0 \quad (17)$$

It is obvious:

$$\frac{M + B\tau}{M\tau} = \tau_1 + 2\phi\omega_r \quad (18)$$

$$\frac{\tau k_R + B}{M\tau} = \omega_r^2 + 2\tau_1\phi\omega_r \quad (19)$$

$$\frac{k_R + |E|\frac{\pi}{4} d_N^2}{M\tau} = \tau_1\omega_r^2 \quad (20)$$

For an oscillatory system ($\phi \ll 1$), $\omega_r \approx \omega_N$, τ_1 can be solved by Equation (20). Combining (18) and (19) yields

$$B = \frac{k_R\tau + M\tau\tau_1^2 - M\tau\omega_r^2 - \tau_1 M}{\tau_1\tau - 1} \quad (21)$$

DISCUSSION

S. Y. Lee[3]

No explanation was given for the behavior of C_u as shown in Figs. 3 and 4. The writer suspects that the shape of C_u versus Reynolds number curve depends greatly on the geometry of the upstream orifice which is not described in the paper. If this orifice is essentially a short tube, as suggested by some of the schematic drawings in the paper, then the C_u versus RN curve (Fig. 4) can perhaps be explained as follows: At low velocities (small RN), the fluid has the tendency to cling to the tube and the coefficient of contraction is close to unity. The velocity coefficient is relatively small because of the relatively large frictional effect. The discharge coefficient which is the product of coefficient of contraction and the velocity coefficient is approximately 0.70. As velocity increases, the velocity coefficient improves while the coefficient of contraction remains the same, resulting in higher coefficient of discharge. When the RN reaches 3×10^3, C_u reaches a maximum of 0.82. As the RN increases further, the jet begins to separate from the boundary of the tube and the coefficient of contraction approaches that of a sharp-edged orifice (0.62). This explains the sudden drop in C_u as shown in Fig 4. The author suggests that the RN be kept below 2800. This may be difficult in practice since the viscosity of the fluid can easily change by a factor of 10 due to temperature variations. The best solution seems to control the geometry of the upstream orifice (e.g., sharp-edged orifice or very short tube) so that the discharge coefficient remains constant over a wider range.

W. I. Mitchell[4]

This paper is interesting in that it represents a systematic study of flapper-nozzle valves, starting with theoretical and experimental descriptions of the characteristics of the basic elements of the flapper-nozzle valve. The experimental descriptions of orifice and nozzle-flapper discharge coefficients are particularly interesting in that they present some of the flow characteristics of these devices which are objectionable when occurring during operation of a flapper-nozzle valve. The dynamic analysis is enlightening as to the absolute stability of the flapper-nozzle valve driving a spring load.

[3] Massachusetts Institute of Technology, Cambridge, Mass.

[4] Research Specialist, Applied Physics Staff, Pilotless Aircraft Division, Boeing Airplane Company, Seattle, Wash.

With respect to the static characteristics discussed, there are several questions and comments which are pertinent:

A Do Figs. 3 and 4, upstream orifice coefficients versus pressure ratio, P_c/P_s, and Reynolds number, RN, respectively, represent single parameter relationships? In other words, was RN constant during the test giving the data in Fig. 3 and was P_c/P_s constant during the test giving the data in Fig. 4? Test data taken by both A. G. Gelalles[5] and by the writer indicate that the influence of RN on C_u is small compared to the influence of P_c/P_s, particularly in the range $0 \leq P_c/P_s \leq 0.3$. Since minute variations in geometry have a strong effect on the relationship between C_u and P_c/P_s, it would have been very helpful if a geometrical description of the orifice had been given by the author. It can only be assumed that the orifices used were of the conventional-drilled type which have the characteristics of a sharp-edged "short tube." It is of interest that there are two types of orifices designed for flapper-nozzle valve use which are available commercially,[6] which minimize the variations in C_u, and which give better quality control at lower cost than the usual drilled orifices.

B The geometrical design of the nozzle used by the author in his tests included a blunt tip such that the flat on the nozzle tip was several times larger than the nozzle-flapper clearances of interest. In the experience of the writer, and several electrohydraulic valve manufacturers, flat tipped nozzles will cause static flow discontinuities and dynamic instabilities, particularly in "open-loop" valves (no mechanical or electrical feedback from second-stage spool to first-stage flapper). Since no nozzle can be manufactured consistently with a perfect "sharp" tip and since large transients in the error signal to the flapper torquer will cause the flapper to strike and flat the nozzle (or indent the flapper), care must be taken in the hydraulic design to keep the nozzle pressure ratio $P_A/P_s > 0.3$ to minimize the effect of the nozzle flats. In Fig. 5, it would make the data more useful if the value of X at which the test was run were known, and if additional data showing the influence of X on C_c were included.

In conclusion, on the orifice and flapper-nozzle coefficients, it must be stated that they are extremely unpredictable, and any valve design which tends to minimize the coefficient variations and/or the effect of the variations is to be desired.

With respect to the dynamic analyses and experimental data presented by the author the following comments can be made:

A Frequency and transient response of valves is of interest as well as absolute stability. Presentation of the analytical and experimental results by the author in some form such as root loci which gives both response and stability information would be helpful. Equation (16) in this paper can be written in the transfer function form (with forcing function $\Delta F(t)$ applied to the flapper by the torquer):

$$\frac{\Delta X(S)}{\Delta F(S)} = \frac{\dfrac{1}{EA_N}(\tau S + 1)}{\dfrac{K_B}{EA_N}\left(\dfrac{S^2}{\omega_n^2} + \dfrac{2\zeta S}{\omega_n} + 1\right)(\tau S + 1) + 1}$$

where $\omega_n^2 = \dfrac{M}{K_B}$, $\dfrac{2\zeta}{\omega_n} = \dfrac{B}{K_B}$, and $A_N = \dfrac{\pi}{4} d_N^2$

S = Laplace operator

The transfer function for Y, which is the variable studied experimentally, can be written

$$\frac{Y(S)}{\Delta F(S)} = \frac{\dfrac{A_P}{A_N K_B}}{\dfrac{K_B}{EA_N}\left(\dfrac{S^2}{\omega_n^2} + \dfrac{2\zeta S}{\omega_n} + 1\right)(\tau S + 1) + 1}$$

Chu[7] shows typical root loci for this type of system.

The transfer function may be "optimized" for transient response with respect to open-loop gain $K(= K_B/EA_N)$, τ, ω_n, and ζ by the use of the "time-error integral" method.[8]

With respect to the absolute stability characteristics presented in the paper, it should be noted that it is possible for $K_B \leq 0$ in the case where the flapper is driven by an electromagnetic torquer. This will occur if the "negative" magnetic spring is greater than the "positive" mechanical spring. Thus, by Routh's criterion as used by the author, there is another condition for absolute stability which is that:

$$\frac{K_B + |E|A_N}{M\tau} > 0 \quad \text{or} \quad \frac{K_B}{|E|A_N} > -1.0$$

The stability trends given in tabular form by the author are not consistent. If stability increases with increasing A_P as stated, then it also *increases*, rather than "decreases," with decreasing K_B. Since P_{ci} has no influence on *viscous* damping, the statement as to why increasing P_{ci} increases stability is misleading.

B It may be of some interest in view of simplicity of algebraic manipulation to note that equations (10) and (11) may be rewritten utilizing expansion by Taylor's series:

$$\Delta Q_{in} = -\frac{Q_i}{2(P_S - P_{ci})}\Delta P_c \tag{10a}$$

$$\Delta Q_{out} = \frac{Q_i}{2P_{ci}}\Delta P_c + \frac{Q_i}{X_i}\Delta X \tag{11a}$$

This results in equations (13) and (14) being rewritten:

$$\tau = \frac{2P_{ci}(P_S - P_{ci})}{P_S Q_i}\left(\frac{A_P^2}{K_B} + \frac{V_{ci}}{\beta}\right) \tag{13a}$$

$$E = -\frac{2P_{ci}(P_S - P_{ci})}{X_i P_S} \tag{14a}$$

C The system analyzed and the system tested were not the same in that the load on the flapper-nozzle valve as analyzed was considered to be a pure spring-loaded bellows, whereas the load on the valve as tested was a "spool" of undefined mass and damping. It is conceivable, in fact probable, that the spool quadratic was comparable to the flapper quadratic. If this were true, as it is in some commercial valves, the test results would obviously be different from the theoretical results.

To summarize comments on this paper, it may be said that:

A Nonuniform orifice and nozzle-flapper coefficients are presented, but their effects on static and dynamic-valve characteristics are not discussed; nor are the methods of minimizing these effects discussed.

B The dynamic analysis, in being used only to indicate stability, loses much of the effectiveness it might have if used to indicate valve transient and frequency response as well as stability. Also the comparison between analysis and experiment is less convincing than if both had treated the same system.

[5] A. G. Gelalles, "Coefficients of Discharge of Fuel Injection Nozzles for Compression-Injection Engines," NACA Report No. 373, 1931.

[6] Information on the designs and sources for these commercially available orifices can be obtained from the discusser.

[7] Yaohan Chu, "Notes on Root-Locus Method for Automatic Control Systems," Brown Instrument Division, Minneapolis-Honeywell Regulator Co., June, 1952 (Fig. 11, p. 17).

[8] Greham and Rathrop, "The Synthesis of 'Optimum' Transient Response: Criterion and Standard Forms," AIEE Technical Paper 53-249, May, 1943.

D. E. Turnbull[9]

The author is to be congratulated on obtaining such interesting results since they provide a useful extension of the work by Sawaragi and Yonezawa.[10] It would be of particular interest to know if the author has examined the effects of loads on the second stage or spool valve and if so what these results have been. In addition, since much has been done with this type of valve with air or gas, has the author attempted to correlate his results with any of the earlier work?

Author's Closure

The author agrees with Prof. S. Y. Lee that his explanation given to the curve of C_u versus RN seems reasonable since the upstream orifice is a sharp-edged "short tube" which is about 0.042 in. long

Mr. Mitchell's remarks are very pertinent. The curves of C_u versus P_c/P_s and C_u versus RN are dependent on each other. The values of x and C_c are tabulated in Table 3. These values of x are not the experimental data[11] but are calculated based on a formula previously used for calculation of C_c. As a matter of fact, Fig. 5 has shown the influence of x on C_c implicitly since P_A is a constant.

Table 3

C_c	x (10^3 inch)
0.61	3.2
0.65	2.1
0.63	1.8
0.61	1.5
0.63	1.3
0.67	0.75
0.78	0.3

The natural frequency of the lumped mass (0.07 lb) consisting of spool, spring fixture, and transformer slug and the spring (K_s = 2780 lb/in.) was 624 cps which was well above the flapper quadratic of 377 cps. For K_s = 278 lb/in., the spool quadratic dropped to 197 cps. In both cases, the spool quadratic was not comparable to the flapper quadratic. However, the lower value of the spool quadratic was found comparable to the system frequency. This could have caused the system to be unstable and therefore a discrepancy in the prediction of K_s in Table 1.

In answer to Dr. Turnbull's questions, only the effects of the two spring loads on the second stage spool had been examined. No attempt was made to correlate the work reported in this paper with any of the early work in pneumatic flapper-nozzle valves

[9] The British Hydromechanics Research Association, Harlow, Essex, England. Assoc. Mem. ASME.

[10] Y. Sawaragi and Y. Yonezawa, "On the Flapper-Nozzle System Used for Pneumatic Controllers and Converters," Proceedings, Sixth Japan National Congress of Applied Mechanics, 1956.

[11] Experimental data were filed in Aeronautical Division of Minneapolis-Honeywell Regulator Company, Minneapolis, Minnesota.

Some Measurements of Boundary-Layer Growth in a Two-Dimensional Diffuser

J. F. NORBURY

Lecturer, Department of Fluid Mechanics, University of Liverpool, Liverpool, England

Low-speed experiments were carried out in a two-dimensional diffuser having a square throat and an area ratio of two to one. Measurements were made of static pressure distribution, velocity contours at throat and outlet, and boundary-layer growth along the four wall center lines. Visual flow experiments were performed using tufts and smoke filaments. Similar experiments were carried out with the throat boundary layers artificially thickened by means of round rods placed on the walls upstream. Disparities between the measured growth of momentum thickness and that predicted by the simple momentum equation are discussed, as well as the effect of the artificial thickening on diffuser efficiency.

Introduction

THE flow in a two-dimensional diffuser is not by any means two-dimensional, this term referring to the geometry rather than the fluid motion. In a diffuser having two plane and parallel walls and two divergent walls three-dimensional motion may arise in three ways:

(*a*) As a result of boundary-layer growth on the parallel walls.
(*b*) As a result of secondary flows.
(*c*) As an inherent property of an apparently two-dimensional boundary layer. (In this category are included turbulent velocity components, and the transitory stalls which have been described recently by Kline [1].[1])

The detailed nature of such diffuser flows is not by any means understood, but some previous work, e.g., Gibson [2], Reid [3], has given valuable data on the relation between diffuser form and over-all performance characteristics, while other investigators, e.g., Nikuradse [4], Vedernikoff [5], have been more exclusively concerned with boundary-layer phenomena. This work demonstrated the existence of a number of different flow regimes, and the relation between flow regime and diffuser geometry has been clarified recently by Kline, Moore, and Cochran [6].

The present work describes the results of an experimental investigation into the flow through a two-dimensional diffuser having a square throat and an area ratio of 2 to 1. The experiments lay in that flow regime described in reference [6] as "apparently well behaved." In particular, measurements were made of the growth of the boundary layers on both the divergent and parallel walls, and visual flow experiments were carried out to assist in the interpretation of results. The initial conditions were varied by fixing round rods upstream of the throat, and these were applied separately to the two pairs of opposite walls.

Nomenclature

x = axial distance along diffuser
y = distance from wall in plane normal to diffuser axis
u = velocity component in boundary layer in x-direction
U = main-stream velocity at edge of boundary layer
$\bar{U}$ = mean velocity
p = static pressure at distance x along diffuser
ρ, ν = density, kinematic viscosity
τ, τ_w = shear stress, shear stress at wall
A = area of cross section of diffuser
W = breadth of diffuser
d = depth of diffuser
L = length of diffuser
δ = thickness of boundary layer
δ_1 = displacement thickness of boundary layer $\left[\delta_1 = \int_0^\delta \left(1 - \frac{u}{U}\right) dy\right]$
δ_2 = momentum thickness of boundary layer $\left[\delta_2 = \int_0^\delta \frac{u}{U}\left(1 - \frac{u}{U}\right) dy\right]$
H = boundary-layer form parameter ($H = \delta_1/\delta_2$)
Δ = area of (three-dimensional) boundary layer
Δ_1 = displacement area of boundary layer $\left[\Delta_1 = \int_0^\Delta \left(1 - \frac{u}{U}\right) dA\right]$
$\mathbf{R}$ = Reynolds number $\left(\mathbf{R}_{W_i} = \frac{W_i \bar{U}_i}{\nu}, \quad \mathbf{R}_L = \frac{L\bar{U}_i}{\nu}\right)$
C_p = static pressure-rise coefficient, $\left[C_p = (p_e - p_i)/\frac{1}{2}\rho \bar{U}_i^2\right]$
C_p' = $(p_e - p_i)\Big/\frac{1}{2}\rho U_i^2$
C_{ps}' = local pressure-rise coefficient $\left[C_{ps}' = (p - p_i)\Big/\frac{1}{2}\rho U_i^2\right]$
η_p = static pressure efficiency $\left\{\eta_p = C_p \Big/ \left[1 - \left(\frac{A_i}{A_e}\right)^2\right]\right\}$
X = distance expressing boundary-layer divergence rate
I = interference factor, defined in equation (5)
Q = rate of volume flow

Subscripts

i = at throat
e = at outlet section

Apparatus

The experimental diffuser had a throat 6 in. square, an area ratio of 2 to 1, and a length of 4 ft. The roof and floor were plane and parallel, and the side walls were flared outward symmetrically according to the relation:

[1] Numbers in brackets designate References at end of paper.

Contributed by the Fluid Mechanics Subcommittee of the Hydraulic Division and presented at the Annual Meeting, New York, N. Y., November 30–December 5, 1958, of THE AMERICAN SOCIETY OF MECHANICAL ENGINEERS.

NOTE: Statements and opinions advanced in papers are to be understood as individual expressions of their authors and not those of the Society. Manuscript received at ASME Headquarters, September 8, 1958. Paper No. 58—A-196.

$$W = 6 + 0.01804x^{3/2} \quad (1)$$

the breadth, W, and length, x, being given in inches.

The use of this shape gave a smooth transition from the throat to the diverging passage, rapid changes of wall direction and curvature being avoided. The parallel throat preceding the diffuser was 6 in. long, and the air was brought to this throat from a centrifugal blower through a duct having the following components:

(*a*) A blower diffuser, 9 ft long, followed by a triple gauze.
(*b*) A settling length, 11 ft long, followed by a cloth gauze.
(*c*) A three-dimensional contraction, of area ratio 20.4, followed by a two-dimensional contraction, of area ratio 4/3. A plan view of the latter part of the system is shown in Fig. 1.

The roof of the diffuser consisted of reinforced strips of perspex, each 6 in. wide. A steel strip, carrying a pitot tube, could be placed between any pair of perspex strips to allow total pressure traverses across sections at 6-in. intervals between the throat and outlet planes. Measurements along the vertical center lines were made using a straight-stemmed vertical pitot tube. This instrument caused excessive interference effects when it was traversed into the side-wall boundary layers, and for horizontal center line traverses a tee-shaped pitot tube was used having a vertical stem with measuring heads at the extremities of the horizontal tee, 3 in. apart. It was estimated that the maximum error in locating the measuring heads was 0.003 in.

Static pressure holes of 0.032 in. diam were drilled at 6-in. intervals along the center lines of the side walls. Measurements of static pressure also could be made across the roof of the diffuser using a hole placed in the steel traversing strip which carried the pitot tubes.

Each pitot tube interfered slightly with the diffuser flow. To overcome this difficulty the throat static pressure was held constant during the taking of pitot-tube readings, and the effect of interference on the recorded velocity profiles was then negligible.

To allow for the influence of velocity gradients in displacing the effective center of the pitot tube a constant correction was applied to the readings. No measurements of turbulence were made but it was felt that the gauzes preceding the settling duct, and the large over-all area ratio (27.2:1) of the contraction would insure a low level of main-stream turbulence at the throat.

Experimental Conditions. Tests were carried out under four different sets of conditions and these will be referred to as Series A, B, C, and D. The conditions were as follows:

Series A: Clean diffuser
Series B: Boundary layers on roof and floor artificially thickened
Series C: Boundary layers on side walls artificially thickened
Series D: Boundary layers on all four walls artificially thickened

The artificial thickening of each layer was performed by a $^1/_4$-in-diam round rod placed on the wall 10 in. upstream of the throat.

The Reynolds numbers were substantially the same for each series (Table 1).

In Series D the flow was not examined in much detail, the only measurements being of the longitudinal static pressure distribution, and of the wall center-line boundary layers at throat and outlet.

Presentation of Results

Performance Characteristics. Table 1 gives the principal measured and derived quantities. In Fig. 2 the longitudinal variation in static pressure and main-stream velocity are plotted in nondimensional terms. The static pressure is expressed in terms of a local pressure coefficient, C_{px}', such that

$$C_{px}' = \frac{p - p_t}{\frac{1}{2}\rho U_t^2} \quad (2)$$

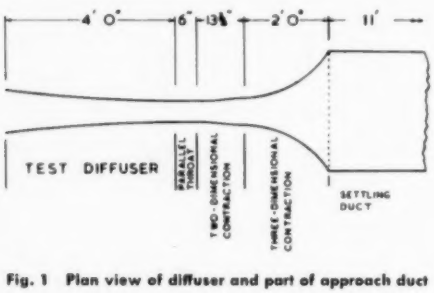

Fig. 1 Plan view of diffuser and part of approach duct

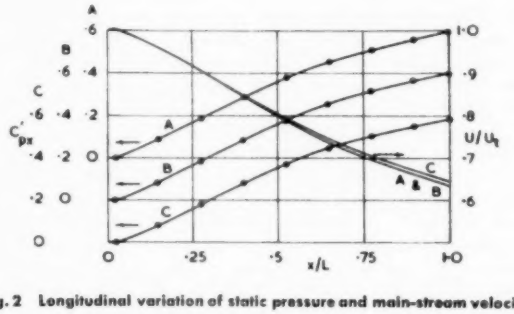

Fig. 2 Longitudinal variation of static pressure and main-stream velocity

Table 1 Principal measured and derived quantities

Quantity	Test series A	B	C	D
Reynolds number $R_{W_t} = U_t W_t/\nu$	5.35×10^5	5.29×10^5	5.31×10^5	5.22×10^5
Reynolds number $R_L = U_t L/\nu$	4.28×10^6	4.23×10^6	4.25×10^6	4.18×10^6
Throat static head	−0.327	−0.336	−0.327	−0.335
Throat main-stream total head	0.224	0.227	0.237	0.254
Throat main-stream velocity head	0.551	0.563	0.564	0.589
Δ_{1t}/A_t	0.0137	0.037	0.0305	0.068 (approx)
Δ_{1e}/A_e	0.232	0.242	0.258	0.294
U_t/U_e	0.986	0.963	0.970	0.932
Throat mean velocity head	0.536	0.522	0.530	0.511
C_p	0.610	0.643	0.617	0.655
η_p	0.814	0.857	0.823	0.873

NOTE: All pressure heads expressed in feet of water.

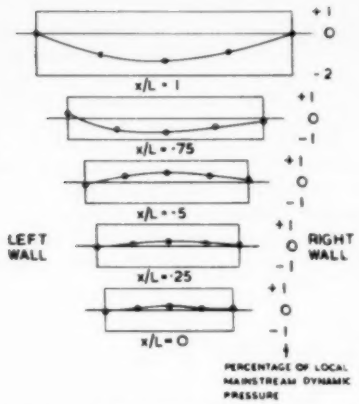

Fig. 3 Transverse variation of static pressure on roof, Series A

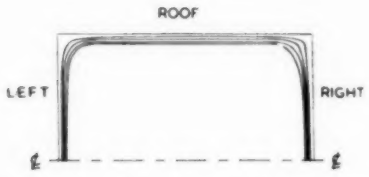

Fig. 4 Velocity contours in entry plane (upper half), Series A. Curves are u/U = 0.98, 0.95, 0.90, 0.85.

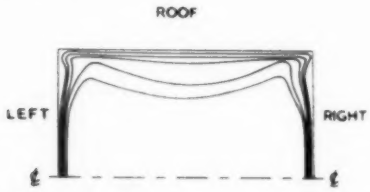

Fig. 5 Velocity contours in entry plane (upper half), Series B. Curves are u/U = 0.98, 0.95, 0.90, 0.85, 0.80.

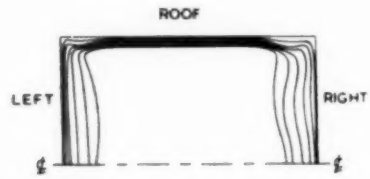

Fig. 6 Velocity contours in entry plane (upper half), Series C. Curves are u/U = 0.98, 0.95, 0.90, 0.85, 0.80, 0.70.

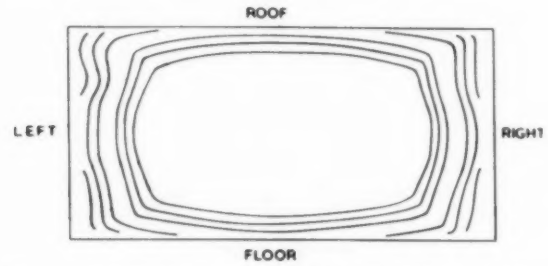

Fig. 7 Velocity contours in outlet plane, Series A. Curves are u/U = 0.9, 0.8, 0.7, 0.5, 0.4, 0.3.

The three curves are quite similar in both cases; in fact the curves for Series A and B are indistinguishable.

Transverse Variation of Static Pressure Across Roof. The results for Series A are plotted in Fig. 3, the variation being expressed as a percentage of the local main-stream dynamic pressure at the section concerned. The zero lines are mean values of end readings of the roof pressure tapping, since these agreed closely with the readings taken from pressure tappings on the side-wall center lines. The terms "right wall" and "left wall" refer to the right and left side walls as seen when looking downstream from the throat.

The transverse variation was less than 1 per cent of the local dynamic pressure, except at the outlet section. Nevertheless, systematic variations are clear, and the trend changed from higher center-line pressure to lower between $x/L = 0.5$ and 0.75.

The results for series B and C were entirely similar in character, showing only slight differences in magnitude from those for Series A.

Boundary-Layer Growth. Velocity contours for the upper half of the throat plane are shown in Figs. 4 to 6, and for the outlet plane in Figs. 7 to 9.

Figs. 10 to 12 show the variation of displacement thickness, δ_1, momentum thickness, δ_2, and form parameter, H, along the center lines of the four bounding surfaces in Series A. In Fig. 11 the broken lines indicate the growth of momentum thickness obtained by introducing experimentally measured values into the simple form of the momentum equation, which for two-dimensional layers is

$$\frac{d\delta_2}{dx} = -(H+2)\frac{\delta_2}{U}\frac{dU}{dx} + \frac{\tau_w}{\rho U^2} \tag{3}$$

A curve of $d\delta_2/dx$ was found for the boundary layers on the right side wall by combining measured values of

$$(H+2)\frac{\delta_2}{U}\frac{dU}{dx}$$

with values of $\tau_w/\rho U^2$ obtained from the Squire-Young relation

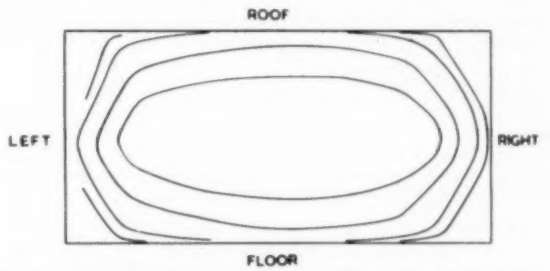

Fig. 8 Velocity contours in outlet plane, Series B. Curves are u/U = 0.9, 0.7, 0.5, 0.4.

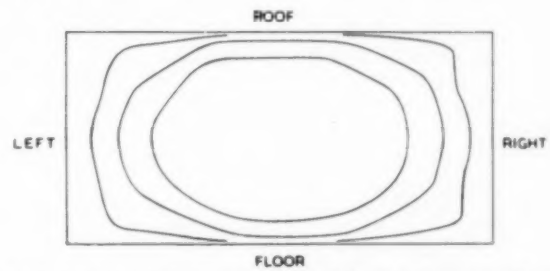

Fig. 9 Velocity contours in outlet plane, Series C. Curves are u/U = 0.9, 0.7, 0.5.

[7]. The broken curve of Fig. 11 was then obtained by graphical integration.

Similar calculations also were performed using the Ludwieg-Tillmann relation [8] for $\tau_w/\rho U^2$. However, the resulting curves are not shown in the figure since their gradients were not materially different from those of the curves obtained by use of the Squire-Young relation.

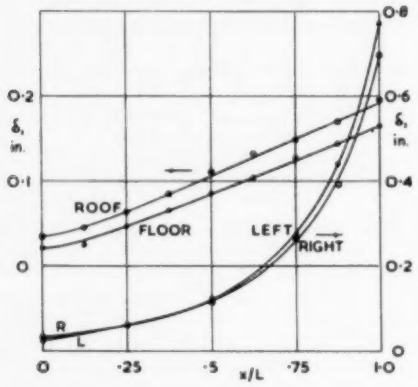

Fig. 10 Variation of displacement thickness, δ_1, Series A

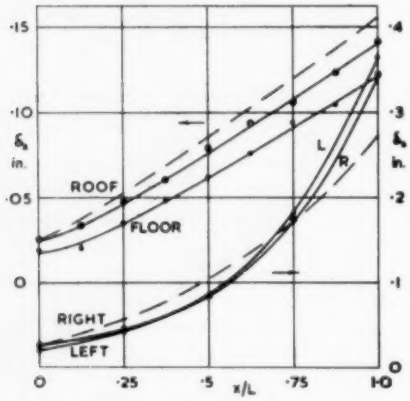

Fig. 11 Variation of momentum thickness, δ_2, Series A. Broken lines indicate curves obtained from momentum equation.

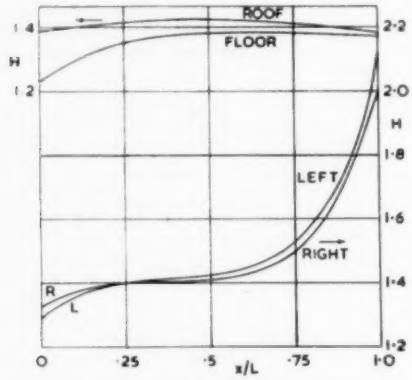

Fig. 12 Variation of form parameter, H, Series A

It should be remarked that the definitions of δ_1, δ_2, and H given in the nomenclature, and therefore the foregoing momentum equation, are slightly different from those normally employed, though formally the same. This is a consequence of the fact that the velocity measurements were made in planes normal to the diffuser axis, and therefore not normal to the side walls. The coordinate y used in the definition is thus taken as the distance from the wall in a plane normal to the diffuser axis.

In considering the diverging layer on the roof, a form of momentum equation was used which is strictly applicable only to wedge flows, in which the streamlines radiate from a line. Its simple form becomes

$$\frac{d\delta_2}{dx} = -(H+2)\frac{\delta_2}{U}\frac{dU}{dx} + \frac{\tau_w}{\rho U^2} - \frac{\delta_2}{X} \qquad (4)$$

where X is the distance from the section considered to the focal point of the streamlines. (The quantity X is described in more detail in reference [9].) For the outward curving diffuser flow, X varies along the diffuser and values of $X(x)$ were deduced from the streamline pattern for potential flow through the diffuser. The term δ_2/X could then be evaluated and the broken curve in Fig. 11 was obtained in a similar manner to that for the side-wall layer.

It is interesting to compare the variation of H for one of the side-wall layers of Series A with the variation predicted by methods of calculation applicable to two-dimensional flow. Results for the right-wall layer are shown in Fig. 13, the calculated curves having been obtained by the methods of Rubert and Persh [10] and Norbury [9]. The two calculations gave similar results, and it appears that over the last quarter of the diffuser the experimental value of H was rising more rapidly than would be expected in two-dimensional flow.

Figs. 16 to 21 show the growth of center-line boundary layers for Series B and C. Mean values of the principal center-line boundary-layer quantities are tabulated in Table 2.

Interference Factor. The main-stream velocity at any section of the diffuser depends on the total displacement area, Δ_1, of the boundary layers at the section, and this is different from that which would occur if each boundary layer had its center-line displacement thickness right across the wall. It is convenient to define an interference factor, I, such that

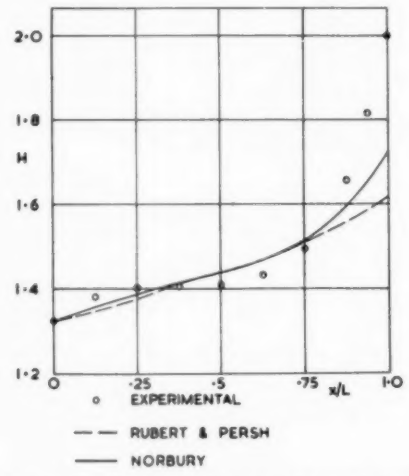

Fig. 13 Calculations of H for right-wall layer, Series A

Table 2 Principal center-line boundary-layer quantities; with interference factors at throat and outlet

Quantity		Test series A	B	C	D
Mean values for side-wall layers	δ_{1t}	0.030	0.027	0.094	0.099
	δ_{1e}	0.737	0.563	0.920	0.933
	δ_{2t}	0.022	0.023	0.079	0.082
	δ_{2e}	0.355	0.328	0.528	0.546
	H_t	1.31	1.23	1.18	1.20
	H_e	2.05	1.72	1.74	1.71
Mean values for roof and floor layers	δ_{1t}	0.027	0.098	0.033	0.104
	δ_{1e}	0.180	0.362	0.188	0.472
	δ_{2t}	0.020	0.084	0.026	0.092
	δ_{2e}	0.131	0.261	0.140	0.331
	H_t	1.31	1.17	1.31	1.13
	H_e	1.38	1.40	1.35	1.43
	I_t	1.11	0.91	1.11	...
	I_e	1.29	1.22	1.34	1.02 (approx.)

NOTE: All thicknesses expressed in inches.

$$I = \frac{\Delta_1}{d\Sigma\delta_{1-} + (W - \Sigma\delta_{1-})\Sigma\delta_{1<}} \tag{5}$$

where

δ_{1-} = displacement thickness of side-wall layer at center line
$\delta_{1<}$ = displacement thickness of diverging layer at center line

Values of Δ_1 were obtained using the continuity equation

$$Q = \int_A u dA = U(A - \Delta_1)$$

the volume flow, Q, being calculated from the throat velocity distribution.

Curves of I versus x/L are shown in Fig. 22.

Visual Flow Experiments. To visualize the flow, smoke was injected through the diffuser roof, using a hole in the steel strip normally used to mount the pitot tubes. By traversing the injection point tranversely the traces shown in Fig. 14 were obtained for Series A. The significance of the traces is better appreciated by looking at the figure obliquely rather than normally.

The flow along the side walls was examined using tufts about 2 in. long and disposed in vertical rows. The configurations on the right wall for Series A are shown in Fig. 15. Unlike the smoke traces the tuft directions could not be plotted but had to be estimated by eye. Thus the lines shown in the figure represent trends rather than exact locations.

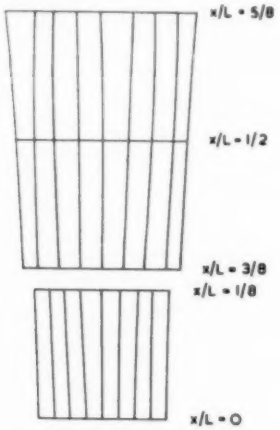

Fig. 14 Smoke traces on roof, Series A

Table 3 Figures demonstrating change of curvature of main-stream flow, Series A

x/L	W	$\Sigma\delta_{1-}$	$W - \Sigma\delta_{1-}$	First diff.	Second diff.
0	6.000	0.060	5.940		
				0.217	
1/8	6.264	0.087	6.157		0.252
				0.469	
1/4	6.748	0.122	6.626		0.114
				0.583	
3/8	7.376	0.167	7.209		0.087
				0.670	
1/2	8.120	0.241	7.879		0.055
				0.725	
5/8	8.964	0.360	8.604		0.034
				0.759	
3/4	9.900	0.537	9.363		−0.056
				0.703	
7/8	10.910	0.844	10.066		−0.243
				0.460	
1	12.000	1.474	10.526		

NOTE: Quantities expressed in inches.

Discussion of Results

General Remarks. Some features of the results obtained in Series A were reproduced in Series B and C. For example, the momentum thickness of the center-line boundary layers increased more slowly at first than would be expected from the momentum equations, Figs. 11, 17, and 20. Farther downstream, however, the layers on the side walls grew more rapidly than was expected, while the diverging layers thickened at approximately the rate suggested by the momentum equation.

Again, in the early part of the diffuser the static pressure was always greater on the vertical center line than at the side walls, while a reversal in transverse pressure gradient took place in each case just before $x/L = 3/4$. This reversal was due to the high rate of increase, over the last quarter of the diffuser, of the sum of the displacement thicknesses of the side-wall layers, which caused the initial outward curvature of the main stream to be changed to an inward curvature at about $x/L = 3/4$. This is demonstrated for Series A by the figures of $(W - \Sigma\delta_{1-})$ and their first and second differences, given in Table 3. The figures for Series B and C gave similar results.

Another common feature was the asymmetry displayed by the side-wall layers. In every case the layer on the left-hand wall thickened slightly more rapidly than that on the right.

The interference factor invariably increased to a maximum at some point along the diffuser, and then fell toward the outlet.

In the next four sections we seek an explanation of the nature of these results, and in particular of the disparities between the measured values of momentum thickness and the values calculated from the simple forms of the momentum equation. The problem is the more difficult because of the incompleteness of existing knowledge of turbulent boundary layers developing under more strictly controlled conditions. However, a qualitative in-

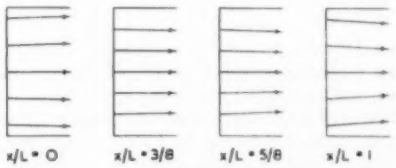

Fig. 15 Approximate tuft configurations on right wall, Series A

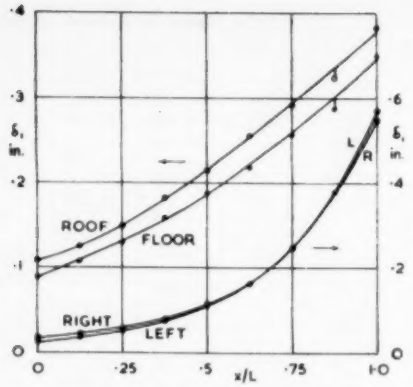

Fig. 16 Variation of displacement thickness, δ_1, Series B

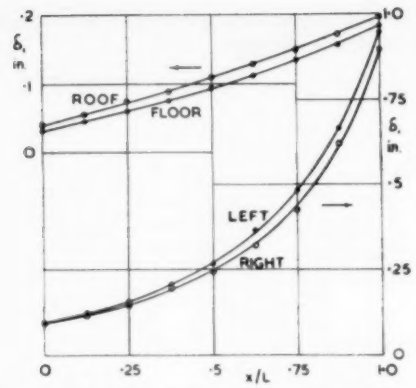

Fig. 19 Variation of displacement thickness, δ_1, Series C

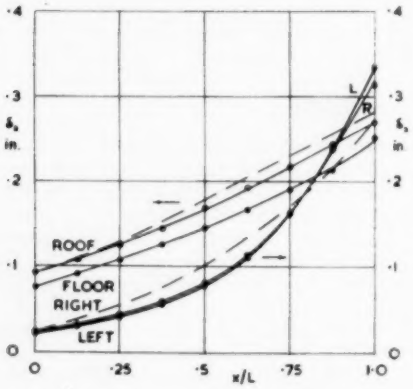

Fig. 17 Variation of momentum thickness, δ_2, Series B. Broken lines indicate curves obtained from momentum equation.

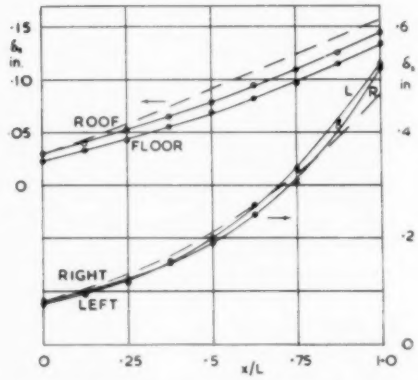

Fig. 20 Variation of momentum thickness, δ_2, Series C. Broken lines indicate curves obtained from momentum equation.

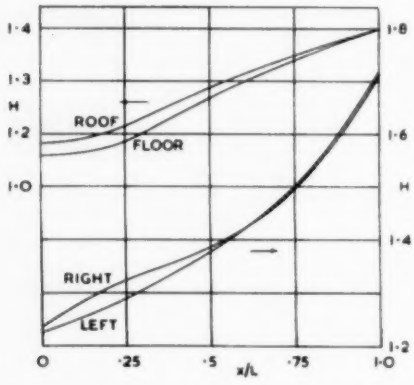

Fig. 18 Variation of form parameter, H, Series B

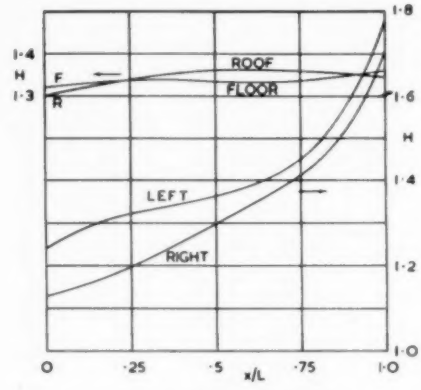

Fig. 21 Variation of form parameter, H, Series C

terpretation may be attempted, and to serve as a basis for the discussion we consider first a more general form of the momentum equation applicable to certain three-dimensional flows.

A More General Boundary-Layer Momentum Equation. We consider a boundary-layer flow bounded by the x-z plane, and moving generally in the direction of the x-axis. We assume that the velocity component, w, in the z-direction is not necessarily zero, imposing the condition that such lateral flow is symmetrical about the x-y plane. We also consider the effect of turbulent stresses, and we take into account the possibility that the static pressure varies with y across the depth of the layer, having the value P at $y = \delta$.

The momentum equation for the flow in the x-y plane then becomes

$$\frac{d\delta_2}{dx} + (H+2)\frac{\delta_2}{U}\frac{dU}{dx} = \frac{\tau_w}{\rho U^2} - \frac{1}{U^2}\int_0^\delta (U-u)\frac{\partial w}{\partial z}\,dy - \frac{1}{\rho U^2}\int_0^\delta \frac{\partial}{\partial x}(P-p)dy - \frac{1}{U^2}\left[\int_0^\delta \frac{\partial}{\partial x}\overline{u'^2}dy + \int_0^\delta \frac{\partial}{\partial z}\overline{u'w'}\,dy\right] \quad (6)$$

where u', w', are turbulent velocity components in the x,z-directions, respectively.

The term

$$\frac{1}{U^2}\int_0^\delta (U-u)\frac{\partial w}{\partial z}\,dy$$

signifies the effect of the lateral flow and, in fact, for "wedge" flows it becomes the term δ_2/X, which appeared in equation (4). For a two-dimensional mean flow in which conditions are independent of z, this term becomes zero, as does the term

$$\frac{1}{U^2}\int_0^\delta \frac{\partial}{\partial z}\overline{u'w'}\,dy$$

Equation (6) will be used in considering boundary layers on both the diverging and the parallel walls.

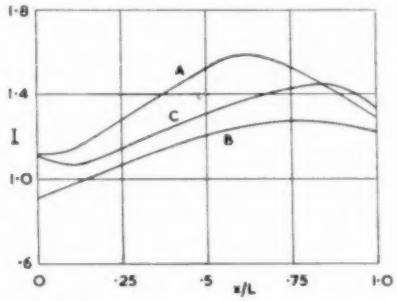

Fig. 22 Variation of interference factor, I

Boundary-Layer Development—Series A. The results of several investigators of two-dimensional turbulent boundary layers in adverse pressure gradients, e.g., Wieghardt [11], Schubauer and Klebanoff [12], have shown discrepancies between measured values of momentum thickness and values calculated from equation (3). The discrepancies occurred as separation was approached, the measured values rising above the calculated values. Such discrepancies have been attributed to the omission of the terms

$$\frac{1}{U^2}\int_0^\delta \frac{\partial}{\partial x}\overline{u'^2}dy \quad \text{and} \quad \frac{1}{\rho U^2}\int_0^\delta \frac{\partial}{\partial x}(P-p)dy$$

in the simple momentum equation, while it also has been pointed out, Clauser [13], that lack of strict two-dimensionality of the mean flow could be a contributory factor.

The discrepancy occurring in the first part of the right-wall layer of Series A was different from those mentioned in the foregoing, in that the measured values of δ_2 fell below the calculated values, and also in that the layer was far from separation, the value of H being less than 1.41 in the relevant region. Therefore it does not seem possible that the term

$$\frac{1}{U^2}\int_0^\delta \frac{\partial}{\partial x}\overline{u'^2}dy$$

could make a significant contribution to the disparity, while the static pressure measurements recorded in Fig. 3 show that the term

$$\frac{1}{\rho U^2}\int_0^\delta \frac{\partial}{\partial x}(P-p)dy$$

was negligible. Moreover, it is hardly conceivable that the term

$$\frac{1}{U^2}\int_0^\delta \frac{\partial}{\partial z}\overline{u'w'}\,dy$$

could have a significant positive value.

However, the disparity could be accounted for by a small divergence of the flow away from the wall center line. In fact, if the flow were a wedge-type flow, the required divergence angle at a point 1 in. from the wall center line would be less than 2 deg. A row of tufts placed on the wall at the throat gave definite evidence of such a divergence, Fig. 15.

Similar considerations apply to the flow in the early part of the roof boundary layer, in which the value of H was never greater than 1.43. The incorporation of the term δ_2/X in equation (4) allowed for the flow divergence which would occur in potential flow, and the disparity between measured and calculated values of $(d\delta_2/dx)$ may be attributed to an outward drift of the boundary-layer fluid across the potential-flow streamlines. The smoke traces, which could be plotted with some accuracy, gave evidence of a small but definite outward drift, Fig. 14.

It seems possible that the lateral drift of fluid in the boundary layers at the throat was part of a more complete system of secondary flows, but no measurements were made which would establish the form of this. The existence of such a system was not improbable since the boundary layers emerging from the settling duct were subjected to considerable curvatures in the contraction.

From about halfway along the diffuser the roof boundary layer thickened at approximately the rate suggested by equation (4). This was in contrast to the behavior of the right-wall layer, for which the gradient of measured values of δ_2 rose steadily to become about 1.7 times larger than that of the calculated curve at the outlet section. At this section the value of H for the layer was 2.0, and while the data recorded in Fig. 3 show that the value of the term

$$\frac{1}{\rho U^2}\int_0^\delta \frac{\partial}{\partial x}(P-p)dy$$

was very small, it must now be considered that the term

$$\frac{1}{U^2}\int_0^\delta \frac{\partial}{\partial x}\overline{u'^2}dy$$

had a significant value.

From the data available it is impossible to evaluate either this or the term

$$\frac{1}{U^2}\int_0^\delta \frac{\partial}{\partial z}\overline{u'w'}\,dy$$

However, if we take as a guide Bidwell's analysis [14] of the Schubauer-Klebanoff data [12] we find that at $H = 2.0$ the term

$$\frac{1}{U^2}\int_0^\delta \frac{\partial}{\partial x}\overline{u'^2}dy$$

was much less than the 40 per cent of the measured value of $d\delta_2/dx$ which represents the disparity in the present case. Further evidence may be obtained from the approximate expression for δ_2 due to Ross and Robertson [15], in which an empirical allowance is made for the terms omitted in the simple two-dimensional momentum equation. The expression is

$$\frac{\delta_2}{\delta_{2i}} = \left(\frac{U_i}{U}\right)^{3+G} \tag{7}$$

where subscript i indicates initial conditions, and G is slightly dependent on the initial boundary-layer Reynolds number. With initial conditions chosen anywhere between $x/L = 0$ and $x/L = 1/2$, this expression gives a value for $d\delta_2/dx$ at outlet rather lower than that obtained from equation (3). This rather unexpected result at least tends to confirm that the turbulent normal stress term could not wholly account for the observed disparity in gradients of δ_2.

The tufts placed on the wall near the outlet section were subject to considerable lateral fluctuations. This presumably was the result of a high level of turbulence relative to local velocity in the neighborhood of the wall, as indicated by the results of Schubauer and Klebanoff [12] and, for an axisymmetric layer, Robertson and Calehuff [16]. However, the mean directions of the tufts, depicted in Fig. 15, indicated a very marked convergence of the flow toward the wall center line. It thus appears that at the end of the right-wall layer the term

$$\frac{1}{U^2}\int_0^\delta (U - u)\frac{\partial w}{\partial z}\, dy$$

had a significant negative value and that the difference in gradients of δ_2 may be accounted to a combination of this with some effect of the turbulent stresses.

The convergence of the flow also would contribute to the rise in measured values of H above those predicted for two-dimensional flow, Fig. 13.

The velocity contours in the outlet plane, Fig. 7, are reminiscent, at least near the corners, of the velocity contours obtained by Nikuradse [17] in a straight pipe of rectangular section in which secondary flows were occurring. They give rise to the idea that the convergent flow in the boundary layers on the side walls might have been part of a system of secondary flows somewhat similar to that shown schematically in Fig. 23. Such a system would certainly tend to produce the considerable fall in interference factor which was observed near the end of the diffuser, Fig. 13.

Fig. 23 Schematic representation of possible secondary flows in outlet plane (upper half), Series A

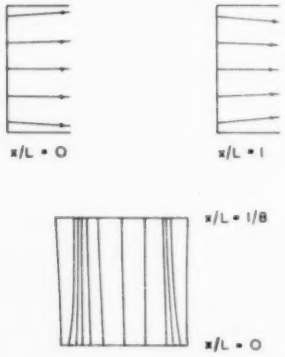

Fig. 24 Smoke traces and tuft configurations, Series C

One further point remains for mention. The slightly asymmetrical development of the boundary layers on opposite side walls may possibly be attributed to asymmetry of the initial lateral, or secondary, flows. The tuft configurations supported this view.

Boundary-Layer Development—Series C. The throat-velocity contours for Series B and C, Figs. 8 and 9, indicate that in both cases the initial flow was more complicated than in Series A. Series C is dealt with first because of the clearer evidence afforded by the smoke filaments of the nature of the flow.

The center-line boundary-layer development showed the same general features as in Series A, although the difference in gradient between measured and calculated values of δ_2 was everywhere smaller. Arguments similar to those propounded in the previous section would indicate a slight flow divergence near the center line of each wall at the throat, this view being supported by the evidence of the visual flow experiments, Fig. 24. However, in the roof layer smoke traces originating near the side walls were initially carried inward quite strongly toward the center line. Moreover, when the smoke filament was injected at points about 1 in. from the side walls it was carried downward away from the roof, rather than along the roof, indicating with some precision the meeting points of the oppositely directed lateral flows, and giving clear evidence of a strong vortex localized in each corner. Such vortexes could produce the distortion of the velocity contours apparent in Fig. 6.

These localized vortexes presumably originated upstream as a result of interaction between the boundary layers on the parallel walls and the thickening rods on the side walls. The rods would produce strong local curvature of the roof and floor layers in their own planes, with a consequent generation of secondary vorticity. The directions and approximate locations of the corner vortexes are shown in Fig. 25(*a*).

Over the downstream half of the diffuser, as in Series A, the thickening of the roof layer was quite closely in conformity with equation (4), while the measured gradient of δ_2 for the artificially thickened right-wall layer was greater than that indicated by equation (3), the ratio of the two at the outlet section being about 1.5. At this section the value of H for the layer was 1.71, considerably less than in Series A. Bidwell's analysis showed that in the Schubauer-Klebanoff layer at $H = 1.71$ the value of the term

$$\frac{1}{U^2}\int_0^\delta \frac{\partial}{\partial x}\overline{u'^2}\, dy$$

was quite small. As additional evidence, the relation of Robertson and Ross, equation (7), was used to calculate $d\delta_2/dx$ at the outlet

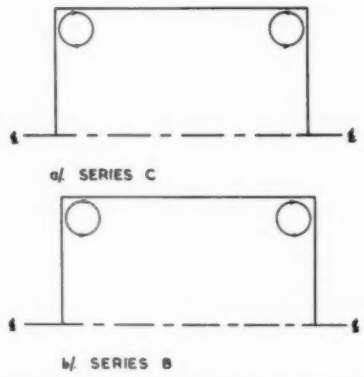

Fig. 25 Directions and approximate locations of corner vortexes, Series B and C

section, using initial values taken from $x/L = 1/2$ where the growth of δ_2 was approximately equal to the rate indicated by equation (3). The result lay between the measured gradient and that obtained from equation (3), being only slightly greater than the latter.

The behavior of the tufts was entirely similar to that in Series A, indicating a considerable flow convergence, and the disparity in gradients of δ_2 may again be attributed to a combination of effects.

The nature of the velocity contours at outlet, Fig. 9, again suggests the possibility that this flow convergence may be part of a secondary vortex system similar to that represented in Fig. 23 for Series A. As in Series A, the interference factor was falling at the outlet section.

Boundary-Layer Development—Series B. In this series the thickening rods were placed on the parallel walls rather than on the side walls as in Series C. Hence it might be expected that the pattern of vortexes emanating from the ends of the rods would be similar to that for Series C, but turned through a right angle, as shown in Fig. 25(*b*). The visual flow experiments, Fig. 26, and the velocity contours, Fig. 5, were consistent with this pattern.

The boundary-layer measurements showed the same characteristics as in the other series, though the initial rate of thickening of the artificially thickened roof layer was almost equal to the calculated rate. The smoke traces near the roof center line were initially less divergent than in the other cases, while the tufts confirmed a divergent flow at the center of the side-wall layers.

At the downstream end of the right-wall layer the ratio of measured gradient of δ_2 to that calculated was just under 1.4, while the value of H was 1.71. Thus Bidwell's analysis suggests a low value for the turbulent normal stress term, while the value of $d\delta_2/dx$ at outlet obtained from equation (7) was, as in Series A, rather lower than that obtained from equation (3). The behavior of the tufts was similar to that in the other series, indicating a significant value for the term

$$\frac{1}{U^2}\int_0^\delta (U-u)\frac{\partial w}{\partial z}\,dy$$

The effect of the term

$$\frac{1}{U^2}\int_0^\delta \frac{\partial}{\partial z}\,\overline{u'w'}\,dy$$

remains indeterminate.

Although it seems possible that the lateral flow in the side-wall boundary layers formed part of a secondary-flow system similar to that suggested for Series A and C, the evidence in the velocity contours was less marked. Also the rate of fall of the interference factor toward the outlet section was lower than in Series A and C.

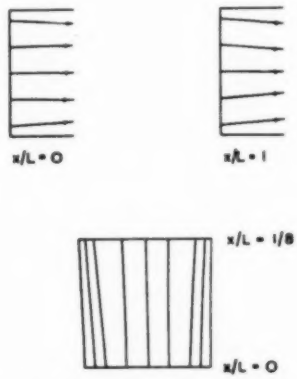

Fig. 26 Smoke traces and tuft configurations, Series B

Comparison of Diffuser Efficiencies. To compare the diffuser performance in the four test series the criterion used will be the static pressure efficiency

$$\eta_p = C_p \Big/ \left[1 - \left(\frac{A_t}{A_e}\right)^2\right]$$

values of which are given in Table 1.

Previous experiments by Peters [18], Robertson and Ross [19], and Winternitz and Ramsay [20], to investigate the effect of thickening the throat boundary layers were carried out on conical diffusers. They all obtained the same result, viz., that thickening produced a deterioration in performance. Thus, when we compare the figures for Series A and B of the present experiments, Table 1, it is surprising to find that thickening of the roof and floor layers produced an increase of about 4 per cent in the static pressure efficiency. It is possible that the local corner vortexes produced by the thickening rods caused this rise by their effect on the distribution of momentum loss in the boundary layers. It is noteworthy in this respect that the interference factor in Series B was lower than that in Series A all along the diffuser.

The initial thickening stimulated a greater increase in growth in the side-wall layers of Series C than in the diverging layers of Series B, and the efficiency in Series C was only 1 per cent higher than in Series A.

When all four layers were thickened (Series D) the efficiency was the highest of the four, being 6 per cent higher than for Series A. In this case the interference factor at outlet, estimated at 1.02, was considerably lower than the others.

The results are seen in a different light when values of the pressure coefficient, C_p, are compared with values of C_p', the denominator of the latter coefficient being the main-stream dynamic pressure at the throat, rather than the dynamic pressure, $\frac{1}{2}\rho\bar{U}_t^2$, based on mean velocity, Table 4.

Table 4 Comparison of values of C_p and C_p'

	A	*B*	*C*	*D*
C_p	0.610	0.643	0.617	0.655
C_p'	0.594	0.597	0.580	0.569

In terms of the throat main-stream dynamic pressure, the pressure rises in Series A and B were about equal, while those of C and D were lower. The differences between the two sets of figures arise because, for a given volume flow, thickening of the throat boundary layers increases the main-stream dynamic pressure and also the flux of kinetic energy past the throat. This would tend to increase the pressure rise, but in all the cases discussed by previous investigators [16, 17, 18] this tendency was more than offset by the increased rate of boundary-layer growth. In the present tests, by contrast, the increase in growth of boundary-layer displacement area caused by the artificial thickening was sufficiently small to result in a net gain in static-pressure efficiency.

Conclusions

Experiments carried out in a two-dimensional diffuser showed that the rate of increase of boundary-layer momentum thickness along the center lines of the divergent side walls was initially smaller than that calculated from the simple two-dimensional form of the momentum equation, becoming much greater than the calculated value near the diffuser outlet. On the parallel

walls the growth was at first smaller than that calculated from the simple momentum equation appropriate to diverging flow, but over the downstream part the measured rate of thickening was approximately equal to the calculated value.

The initial disparities may be explained by lateral flow in the boundary layers, divergent from the wall center line. The discrepancies for the side-wall layers near the outlet were partly due to convergent lateral flows in the layers, though the effect of turbulent stresses was probably also significant. The measurements did not admit a quantitative assessment of these effects.

When round rods, placed upstream of the throat, were used to thicken the boundary layers artificially there was evidence that they produced secondary vortexes localized in the corners of the duct. The artificial thickening led to increases in static-pressure efficiency instead of the expected fall.

Acknowledgments

The work was carried out in the Department of Mechanical Engineering at the University of Liverpool. The author is indebted to Profs. J. H. Preston and W. J. Kearton for their interest and help, and to the staff of the workshop for their painstaking craftsmanship.

References

1 S. J. Kline, "Some New Conceptions of the Mechanism of Stall in Turbulent Boundary Layers," *Journal of the Aeronautical Sciences*, vol. 24, 1957, p. 469.

2 A. H. Gibson, "On the Resistance to Flow of Water Through Pipes or Passages Having Divergent Boundaries," *Transactions of the Royal Society of Edinburgh*, vol. 48, part 1, 1913, p. 97.

3 E. G. Reid, "Performance Characteristics of Plane-Wall Two-Dimensional Diffusers," NACA Technical Note 2888, 1953.

4 J. Nikuradse, "Untersuchungen über die Strömungen des Wassers in Konvergenten und Divergenten Kanälen," *Forschungs Arbeiten Gebiet Ingenieur Wesens*, Heft 289, 1929.

5 A. M. Vedernikoff, "An Experimental Investigation of the Flow of Air in a Flat Broadening Channel," translated as NACA TM 1059, 1944, Central Aero-Hydrodynamical Institute, Moscow, Russia, Report No. 21, 1928.

6 S. J. Kline, C. A. Moore, and D. L. Cochran, "Wide-Angle Diffusers of High Performance and Diffuser Flow Mechanisms," *Journal of the Aeronautical Sciences*, vol. 24, 1957, p. 470.

7 H. B. Squire and A. D. Young, "The Calculation of the Profile Drag of Aerofoils," Aeronautical Research Council, Reports and Memoranda No. 1838, 1937.

8 H. Ludwieg and W. Tillmann, "Untersuchungen über die Wandschubspannung in Turbulenten Reibungsschichten," *Ingenieur-Archiv*, Heft 17, 1949 (translated as NACA TM 1285).

9 J. F. Norbury, "An Approximate Method for the Calculation of Turbulent Boundary Layers in Diffusers," *The Aeronautical Quarterly*, vol. 8, 1957, p. 58.

10 K. F. Rubert and J. Persh, "A Procedure for Calculating the Development of Turbulent Boundary Layers," NACA Technical Note 2478, 1951.

11 K. Wieghardt, "Über die Wandschubspannung in Turbulenten Reibungsschichten bei Veranderlichem Aussendruck," *ZWB Untersuchungen und Mitteilungen*, Nr. 6603, 1943.

12 G. B. Schubauer and P. S. Klebanoff, "Investigation of Separation of the Turbulent Boundary Layer," NACA Technical Note 2133, 1950.

13 F. Clauser, "Turbulent Boundary Layers in Adverse Pressure Gradients," *Journal of the Aeronautical Sciences*, vol. 21, 1954, p. 91.

14 Jerold M. Bidwell, "Application of the von Karman Momentum Theory to Turbulent Boundary Layers," NACA Technical Note 2571, 1951.

15 Donald Ross and J. M. Robertson, "An Empirical Method for Calculation of the Growth of a Turbulent Boundary Layer," *Journal of the Aeronautical Sciences*, Readers' Forum, vol. 21, 1954, p. 355.

16 J. M. Robertson and G. L. Calehuff, "Turbulence in a Diffuser Boundary Layer," *Proc. ASCE*, vol. 83, No. HY5, 1957, p. 1393.

17 J. Nikuradse, "Untersuchungen über Geschwindigkeitsverteilung in Turbulenten Stromungen," *Forschungs Arbeiten Gebiet Ingenieur Wesens*, Heft 281, 1926.

18 H. Peters, "Energieumsetzung in Querschnittserweiterungen bei Verschiedenen Zulaufbedingungen," *Ingenieur-Archiv*, Heft 1, 1931, p. 92 (translated as NACA TM 737, 1934).

19 J. M. Robertson and D. Ross, "Effect of Entrance Conditions on Diffuser Flow," *Proc. ASCE*, separate volume 78, No. 141, 1952.

20 F. A. L. Winternitz and W. J. Ramsay, "Effects of Inlet Boundary Layer on Pressure Recovery, Energy Conversion, and Losses in Conical Diffusers," *Journal of the Royal Aeronautical Society*, vol. 61, 1957, p. 116.

DISCUSSION

J. P. Johnston[2]

The author is to be congratulated for a lucid presentation of a very thorough piece of experimental work. It is not often that one is privileged to read such a well-presented description.

Unfortunately, the author fails to provide some of the data most often sought by other workers. For instance, in this case, it would have been most useful if measured velocity profiles (u versus y) had been presented in tabular form. As is usual, the author presents only enough of the experimental information to cover the points he wishes to make. This situation is often aggravated by the publication policies of the technical societies, which require a paper to be condensed to the greatest possible extent, thereby causing much valuable data to be lost forever from the public record.

In particular, we wish to comment on the interpretation of some terms appearing in the momentum-integral equations for boundary-layer flows which exhibit a plane of symmetry such as is the case here. As the author so clearly points out, an additional term,

$$\frac{1}{U^2}\int_0^\delta (U-u)\frac{\partial w}{\partial z}\,dy \tag{8}$$

must be added to the two-dimensional momentum-integral equation to account for divergence and skewing effects occurring on either side of the plane of symmetry (x-y plane where $z = 0$). It is instructive to break this term into two parts. One of which accounts for the fact that the main-flow steamlines may diverge or converge on either side of the plane of symmetry and the other accounts for the fact that the boundary-layer velocity profiles may not be collateral, but may be skewed, at points adjacent to the plane of symmetry.[3] Note that on the plane of symmetry the profiles must be collateral.

Fig. 27 illustrates a set of normal velocity components $\bar{u}$ and $\bar{w}$ associated with the main-flow direction and the main-flow velocity vector $\bar{U}$, together with the velocity components used in the paper. One may show, on the streamline of symmetry, that

$$\frac{1}{U^2}\int_0^\delta (U-u)\frac{\partial w}{\partial z}\,dy = \frac{1}{\bar{U}^2}\int_0^\delta (\bar{U}-\bar{u})\frac{\partial \bar{w}}{\partial z}\,dy + \frac{\partial \alpha}{\partial z}\frac{1}{\bar{U}^2}\int_0^\delta \bar{u}(\bar{U}-\bar{u})dy \tag{9}$$

With the convention that

$$\frac{1}{\bar{U}^2}\int_0^\delta (\bar{U}-\bar{u})\bar{w}dy = \theta_{zz} \tag{10}$$

Equation (9) reduces to

$$\frac{1}{U^2}\int_0^\delta (U-u)\frac{\partial w}{\partial z}\,dy = \delta_2\frac{\partial \alpha}{\partial z} + \frac{\partial \theta_{zz}}{\partial z} \tag{11}$$

In the case of "wedge flows" there is no skewing of the velocity profiles. θ_{zz} is zero everywhere and $\partial\alpha/\partial z = 1/X$ [see Equation

[2] Research Engineer, Condenser and Ejector Engineering Department, Ingersoll-Rand Company, Phillipsburg, N. J.

[3] E. S. Taylor, "The Skewed Boundary Layer," published in this issue, pp. 297–304.

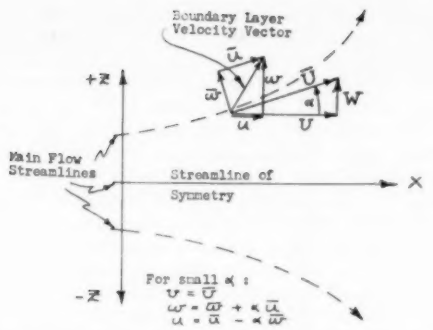

Fig. 27 Description of velocity-vector components near a plane of symmetry

(4) in the paper]. This illustrates the fact that the $\partial\theta_{zz}/\partial z$-term accounts for skewing effects which occur only when there is curvature in the main-flow streamlines off the plane of symmetry and the $\delta_2(\partial\alpha/\partial z)$-term accounts for the effect of divergence or convergence of the main flow.

Since $\partial\alpha/\partial z$ is a quantity of the main flow, it may be estimated to some degree of accuracy for calculation purposes. For instance, if the main flow is two-dimensional

$$\frac{\partial\alpha}{\partial z} = -\frac{1}{U}\frac{\partial U}{\partial x} \tag{12}$$

The estimation of the value of the skewing term, $\partial\theta_{zz}/\partial z$, is not so straightforward. Recent work[3] indicates that, through most of a turbulent boundary layer, one may assume

$$\bar{w} = A(\bar{U} - \bar{u}) \tag{13}$$

A is a constant (with respect to y) of proportionality. With this assumption it is found, on a plane of symmetry, that

$$\frac{\partial\theta_{zz}}{\partial z} = \frac{\partial A}{\partial z}(\delta_1 - \delta_2) \tag{14}$$

Inviscid analysis[4] allows one to say to a first approximation that $A \simeq 2\alpha$, so that

$$\frac{\partial\theta_{zz}}{\partial z} \simeq 2\frac{\partial\alpha}{\partial z}(\delta_1 - \delta_2) \tag{15}$$

Experiments by the writer[5] indicate that

$$\frac{\partial\theta_{zz}}{\partial z} \simeq \frac{\partial\alpha}{\partial z}(\delta_1 - \delta_2) \tag{16}$$

actually represented his data better than Equation (15).

It is unfortunate that the author took no measurements of the skewed profiles on either side of the wall center lines of his diffuser so that one could check the foregoing expressions against more data. However, it is suspected that the magnitude of the crossflows was so small as to defy measurement.

It is hoped that these comments, which are intended to amplify some of the author's work will assist the reader in understanding the effects of main-flow streamline divergence and boundary-layer skewing both of which modify the growth of momentum thickness along a plane of symmetry type of boundary-layer flow.

[4] H. B. Squire and K. G. Winter, "The Secondary Flow in a Cascade of Airfoils in a Non-Uniform Stream," *Journal of the Aeronautical Sciences*, vol. 18, 1951, pp. 271–277.

[5] J. P. Johnston, "Three-Dimensional Turbulent Boundary Layer," ScD thesis, Mechanical Engineering Department, Massachusetts Institute of Technology, Cambridge, Mass., June, 1957.

B. A. Waitman[6] and S. J. Kline[7]

The author's data are very interesting to anyone concerned with flow in diffusing passages. The strongly three-dimensional nature of the boundary-layer development is clearly evidenced by these data which are more complete in this sense than any previously published.

The most striking feature of these data is the great difference in the boundary-layer development and characteristics on the diverging walls as compared to the parallel walls. In the cases observed by the author, the diverging-wall boundary layers thicken and approach stall much more rapidly than those layers on the parallel walls. However, the secondary-flow patterns presented do not seem sufficient to explain this result since the secondary flows reverse direction and not only flow outward from the corners toward the center line of the diverging walls, but also toward the center line of the parallel walls. This would seem to imply similar behavior of the boundary-layer characteristics on the diverging and parallel walls when viewed from the secondary-flow behavior alone. Hence some part of the complete explanation still seems to be missing. Further investigations might include not only detailed measurements of the pressure field but also measurements of the corner boundary layers as the results of Moore and Kline,[8] and Cochran and Kline[9] show first stall almost always occurs in the corners despite the secondary-flow patterns observed by the author.

In the sense of shifting the major pattern from one regime to another on the flow-regime chart, reported by Moore and Kline,[8] the changes in flow patterns and recovery with altered secondary-flow conditions observed by the author are appreciable but not large.

Caution must be used in interpreting the changes caused by the insertion of rods in the inlet. The use of rods can alter performance not only by changing the secondary-flow patterns, but also by altering the mixing rate between main stream and the boundary layers over the whole cross section owing to increased turbulent fluctuations. During preliminary tests reported by Cochran and Kline,[9] the effect of a rod near the wall in the boundary layer was sufficient to change the entire flow pattern and cause an increase in performance. More detailed investigations of this mixing effect, reported by Moore and Kline,[10] show that almost any kind of large-scale mixing introduced with thin-inlet boundary layers will tend to raise recovery if the loss due to the mixer is not charged. This increase is strongly dependent on the regime of operation. In the regime investigated by the author, the effect experienced would be moderate as found. Whether an increase or decrease is found probably depends strongly on other boundary-layer parameters. Thus it is not clear whether or not all of the changes observed are directly attributable to secondary-flow effects.

Finally, secondary flows in plane-walled passages are different from those occurring in curved passages. Secondary flows in curved passages, such as cascades, are explicable in terms of pressure-gradient effects imposed on the boundary layer by the potential solution of the main flow. These pressure gradients do not exist in straight passages. Therefore the secondary flow

[6] Research Assistant, Stanford University, Stanford, Calif. Assoc. Mem. ASME.

[7] Associate Professor of Mechanical Engineering, Stanford University, Stanford, Calif. Mem. ASME.

[8] C. A. Moore and S. J. Kline, "Some Effects of Vanes and of Turbulence on Two-Dimensional Wide-Angle Subsonic Diffusers," NACA TN 4080, June, 1958.

[9] D. L. Cochran and S. J. Kline, "The Use of Short Flat Vanes for Producing Efficient Wide-Angle Two-Dimensional Subsonic Diffusers," final report on NACA Contract NAw-6500, April, 1957, to be published as NACA TN 4039.

[10] C. A. Moore and S. J. Kline, "Investigation of Airfoils, Plates, Grids and Rods for Boundary Layer Control in Subsonic Diffusers," Progress Report to NACA under Contract NAw-6317, August, 1954.

must originate from another source; at present, this source is unknown. Thus a fundamental a priori explanation for the patterns recorded by the author seems unavailable.

Author's Closure

The author is grateful to the discussers, whose remarks throw a fresh light on some of the results presented in the paper. Dr. Johnston's analysis of the term $\frac{1}{U^2}\int_0^\delta (U - u)\frac{\partial w}{\partial z} \cdot dy$ is very valuable in separating out the effects of divergence and skewing. While in the present case no measurements were made of the skewed velocity profiles on either side of the wall center lines, the velocity profiles along the center lines were analyzed in the light of Coles's[11] work on the "wake-law." Although the boundary layers were affected both by divergence and secondary flows the profiles obeyed the wake-law quite closely, except in those cases where they had been artificially thickened upstream of the throat.

Mr. Waitman and Professor Kline have pointed out the striking differences between the boundary-layer development on the diverging walls and on the parallel walls, remarking that these differences cannot be explained by secondary flow effects alone. In fact, the differences are essentially due to the divergence of the main stream outside the boundary layer on the roof and floor, this divergence being absent in the case of the layers on the side walls. The point may be clarified by reference to Dr. Johnston's equation (11). The term $\partial\theta_{zz}/\partial z$ arising from secondary flows may have a significant value for all four center line layers. The reduced rate of growth of the parallel wall layers by comparison with the diverging wall layers is essentially due to the large difference in values of the term $\delta_2.\partial\alpha/\partial z$.

Although the secondary flow patterns observed in the present case would tend to delay separation in the corners of the duct it is not surprising that the first signs of separation should almost invariably occur in the corners. Measurements of the outlet plane velocity distributions (Figs. 7 to 9) indicate that despite the secondary flows the boundary layers on the diverging walls tend to thicken toward the corners of the duct.

The comments on the effects of the thickening rods are of considerable interest and underline the necessity for a closer understanding of turbulence mixing processes in general.

The secondary flows occurring in the diffuser exemplify the two types described by Mr. Waitman and Professor Kline. The secondary flows entering the throat were principally due to boundary layer curvature in the contraction (similar to that occurring in cascades) while those predominating over the downstream part were of the type that occurs in plane walled ducts. The mechanism of this latter type remains a matter of conjecture.

[11] D. Coles, "The Law of the Wake in Turbulent Boundary Layers," *Journal of Fluid Mechanics*, vol. 1, pt. 2, 1956, pp. 191–226.

EDWARD S. TAYLOR

Professor of Aircraft Engines and Director of the Gas Turbine Laboratory, Massachusetts Institute of Technology, Cambridge, Mass. Mem. ASME

The Skewed Boundary Layer

The geometry of the skewed boundary layer is described, and two methods of producing it are discussed. Experimental results show that the form of the usual skewed boundary layer is a thin collateral sublayer under a quasi-collateral outer region. The geometry of separation of a skewed boundary layer is discussed. It is concluded that separation of a skewed boundary layer may differ radically from that of a collateral boundary layer and that separation criteria used for collateral boundary layers may give misleading results when applied to skewed boundary layers. It is concluded that the understanding of the skewed boundary layer can contribute to improved design of turbomachinery.

FOR SEVERAL years the Gas Turbine Laboratory at M.I.T. has been taking a special interest in the skewed boundary layer. The purpose of this paper is to present the state of our understanding of this phenomenon in the hope that it will stimulate others to think about this important problem and thus make progress toward its solution.

Geometry of the Skewed Boundary Layer

An idea of the geometry of a skewed boundary layer can be obtained by viewing an ordinary, or collateral boundary layer from a co-ordinate system moving parallel to the wall on which the boundary layer is formed.

Fig. 1(*a*) is the velocity profile of an ordinary boundary layer showing the variation of the velocity u, with distance from the wall y. Fig. 1(*b*) shows a polar plot which is this velocity profile when viewed along the y-axis. Fig. 1(*c*) shows the same profile viewed from the same direction but from a co-ordinate system moving with a velocity $-w$, parallel to the wall. It will be observed that the result of viewing in this manner is to make an originally collateral boundary layer appear skewed; that is, the velocity varies in *direction* as well as in magnitude as the wall is approached. A skewed boundary layer which can be resolved into a collateral boundary layer by viewing from a moving co-ordinate system will be called quasi-collateral.

If now the wall is presumed to *start* moving with the observer, shear forces cause a new boundary layer to be formed. In the early stages of formation the relative velocity in this new boundary layer will be in the same direction as w thus forming a typical skewed boundary layer as shown in Fig. 1(*d*). It is clear that the motion of the co-ordinate system could be in any relation to the direction of the original velocity.

A similar phenomenon occurs when flow along a stationary hub or casing encounters a rotating hub or shroud ring in a turbine or compressor. It also occurs when the flow over a rotating hub or shroud ring encounters a stationary hub or casing. In either of these cases, an initially collateral boundary layer will be skewed or an initially skewed boundary layer will have its skewing altered.

Another way of producing a skewed boundary layer is by causing a collateral boundary layer to turn a corner. The end wall boundary layer of a flow passing through a cascade of airfoils is such a case. In this case the boundary layer turns more

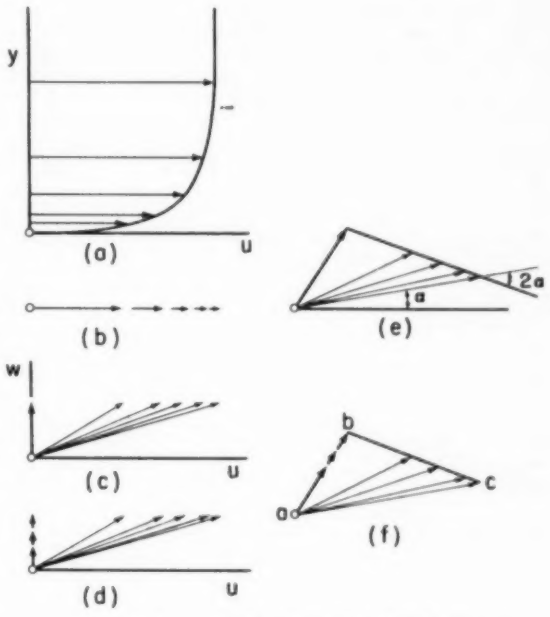

Fig. 1 Geometry of the skewed boundary layer

than the main flow. This is the well-known phenomenon of secondary flow. A linearized inviscid analysis of this problem proposed by Squire and Winter [1][1] and extended by Hawthorne [2] indicates that for small angles of turn α, skewing as shown in Fig. 1(*e*) results. According to this analysis, the tips of the vectors representing the velocity lie on a straight line which makes an angle 2α with the direction of the main flow. Thus the boundary layer predicted by the analysis of Hawthorne is quasi-collateral. The inviscid assumption is obviously untenable deep in the boundary layer (near the wall) since in this region shear forces can hardly be negligible. In addition, the linearizing assumptions are good only for small angles of turn, and in the inviscid analysis the angle of turn near the wall is never small. Thus the analysis of Squire and Winter and of Hawthorne cannot be expected to hold near the wall. Indeed, experimental results [3, 4] indicate that, near the wall, a collateral sublayer is formed as in Fig. 1(*f*).

In the case of a skewed boundary layer formed by turning a stream having a collateral boundary layer, there exists an appro-

Contributed by the Fluid Mechanics Subcommittee of the Hydraulics Division and presented at the Annual Meeting, November 30-December 5, 1958, New York, N. Y., of THE AMERICAN SOCIETY OF MECHANICAL ENGINEERS.

NOTE: Statements and opinions advanced in papers are to be understood as individual expressions of their authors and not those of the Society. Manuscript received at ASME Headquarters, August 5, 1958. Paper No. 58—A-113.

[1] Numbers in brackets designate References at end of paper.

priate moving co-ordinate system from which the outer portion of a skewed boundary layer will appear collateral; that is, the outer part of the boundary layer is quasi-collateral just as in the case of a skewed boundary layer generated by relative motion.

It is not implied here that the geometric form described in the foregoing is the only kind of skewed boundary layer. It is clear that starting with an already skewed boundary layer and subjecting it to either process a still different shape can be produced. With an appropriate mechanism any conceivable shape of boundary layer could be produced at a point. However, the shape just pictured seems to characterize nearly all of the skewed boundary layers on which measurements are available and therefore probably represents a large percentage of the boundary-layer population. (Reference [4] shows boundary layers from a number of sources compared in this way.) Perhaps this shape should more properly be said to characterize a newly formed skewed boundary layer since the following argument will show that if such a boundary layer is allowed to proceed over a flat plate in the absence of any pressure gradient, the result will be a decay of the skewing causing the boundary layer to approach a collateral boundary layer. This phenomenon is easily understood if we note that the direction of the shear stress within the fluid is the direction of the tangent to the curve representing the locus of the vector tip in the boundary-layer polar plot. Thus in the boundary layers just described, the shear stress at and near the wall is in the direction *a-b* in Fig. 1(*f*) while, in the outer part of the boundary layer, the shear stress is in the direction of the line *b-c*. This latter statement can be seen to be true since, if we view the boundary layer from an appropriate steadily moving co-ordinate system, it will appear to be a collateral boundary layer in the direction *b-c*.

If now we take a lamella of the boundary layer which includes the velocity vector which ends at *b*, we find that on the side nearer the wall the shear force on this layer is in the direction *b-a* while, on the side away from the wall, the shear force is in the direction *b-c*. Both of these forces have components perpendicular to *a-c* and in the same direction. Thus the fluid at this level will have its momentum altered in such a way as to reduce the component of velocity perpendicular to *a-c* ("cross-flow velocity") and thus progressively round out the angle *b* of the triangle, causing the boundary-layer profile to approach a collateral layer.

In one of the earliest skewed boundary-layer experiments done in the Gas Turbine Laboratory [5] the profile was generated by causing a collateral profile formed on a pipe wall to flow into a revolving section of pipe. Measurements taken at the exit of the revolving section, which was several diameters long, indicated that the profile had indeed decayed to one that was nearly collateral relative to the moving wall whereas the profile at the entrance to the revolving section (which was not measured) was skewed about 45 deg.

If we reflect that turbomachinery contains both of the skewing mechanisms referred to, it is clear that skewed boundary layers are prevalent in such machines. It is, in fact, evident that the ordinary or collateral boundary layer is the exception rather than the rule in these devices. It therefore becomes a matter of importance to inquire into the nature of the skewed boundary layer and the limitations thereby imposed on the operation and design of fluid machinery.

Separation of the Skewed Boundary Layer

The most important limitation imposed by the boundary layer is the high losses and unsteady flow which can result from separation at undesired locations. The geometry of steady separation of the collateral boundary layer is reasonably well understood and the condition for separation may be simply described as the condition where the wall shear stress vanishes. As will be shown, this criterion is not valid for the skewed boundary layer.

Separation of a collateral boundary layer is often defined as "the phenomenon which occurs at the point where the shear stress vanishes" or "that which occurs where the wall boundary layer reverses in direction." These definitions are of no value when the phenomenon under consideration is a skewed boundary layer. In this case there is no angle of skew[2] which can be associated with any phenomenon resembling separation and, furthermore, a phenomenon resembling separation can occur without the disappearance of the wall force and without anything which could be described as "backflow." It seems useful to define separation in a way which will include the familiar separation of a collateral layer and which will distinguish between separated and unseparated flow with any type of boundary layer.

As a step toward a definition,[3] we will define a limiting streamline. The direction of flow in a skewed boundary layer changes as the wall is approached. At the wall, the velocity is of course zero and the direction meaningless but at an infinitesimal distance from the wall there is an infinitesimal velocity and a definite direction. This direction defines (for steady flow) a set of limiting streamlines. In the case of the collateral boundary layer the limiting streamline direction is the same as the direction of the free stream and the concept is therefore unnecessary. On the other hand, the free-stream direction and the limiting streamline direction are, in general, different in the case of a skewed boundary layer.

Separation can now be defined as follows:

Separation occurs when a limiting streamline leaves the wall; i.e., becomes a finite distance from the wall.

This definition is essentially that of Maskell [6]. It includes the familiar separation of a collateral boundary layer. It also includes some phenomena which have not previously been associated with the word separation. For example, the phenomenon which occurs at the trailing edge of an airfoil is definitely separation in the foregoing sense. Separation as presently defined therefore does not necessarily connote any undesirable effect. For separation at an undesired location we may reserve the word "stall." This latter word is a description of a partly subjective phenomenon, since the words undesired or undesirable imply inquiry into the mind of the user or designer rather than into the phenomenon itself.

A useful method of visualizing separation of a skewed boundary layer is to imagine a collateral boundary layer steadily separating along a line perpendicular to the flow direction. Let us now imagine, as before, that the wall starts moving *along the line of separation*. It is herein assumed that such a wall motion will not essentially alter the flow previously existing at right angles to the motion. If we view the flow from the moving wall we will have a picture of separation of a skewed boundary layer. It is quite evident that the component of wall shear stress normal to the line of separation is still zero, but the shear stress now has a component parallel to the line of separation. In cases where the direction of the line of separation is unknown, the value or direction of the shear stress is evidently of no help as a criterion for separation.

Let us now look at the limiting streamlines of our model of a separated boundary layer. This model comprises a separating collateral boundary layer with a wall motion at right angles to it. It is assumed that the wall motion changes essentially only components of velocity in the direction of wall motion. If we examine the limiting streamlines, it is clear that the velocity

[2] Note 180-deg skew indicates separation only in the case of a collateral boundary layer.

[3] Note the following argument is essentially that of Maskell [6].

component in the direction of the original flow vanishes at the separation line and that therefore *limiting streamlines become tangent to the line of separation* when the boundary layer is skewed.

If we exclude cases where separation occurs at a discontinuity in slope of the wall such as a sharp trailing edge, it appears that separation of a skewed boundary layer always results in tangency of the limiting streamlines which characterize Maskell's [6] "ordinary separation point," while separation of a collateral boundary layer is from a "singular point" or a line composed of such points. Only in this latter case does the shear stress vanish at the separation point.

If we carry the model a little farther, it is clear that with a collateral boundary layer the separation line will be at right angles to the velocity vector while with a skewed boundary layer the separation line, in general, will be oblique to the free-stream direction, and tangent to the limiting streamline.

One of the properties of the collateral boundary layer is that separation can only occur in an "unfavorable" pressure gradient i.e., a static pressure which rises in the direction of flow of the main stream. In the case of the skewed boundary layer it is clear from the superposed model that the relation of the direction of the pressure gradient to the free-stream direction gives no information on the possibility of separation.

It also appears that the pressure gradient in the direction of the limiting streamlines is likewise of little value in predicting separation. The superposition model suggests that the direction in which pressure gradient is important is the direction perpendicular to the separation line. Since this latter direction is usually unknown, this information, even if the superposition model were valid, would be of doubtful value.

If we take a perpendicular to the surface at some point and trace streamlines backward from this line thereby generating a stream surface, it will be seen that the resulting surface for the collateral boundary layer will be plane and perpendicular to the wall. In fact any curvature of this surface would destroy the collateral nature of the boundary layer. Thus the collateral boundary layer is essentially two-dimensional, and derivatives of flow properties perpendicular to the stream surface must be small if not zero. A similar procedure for the skewed boundary layer will produce a twisted stream surface. It is clear that since this surface is not, in general, normal to the solid boundary, flow on this stream surface will be affected by shear forces from adjacent fluid. This reasoning suggests that the skewed boundary layer existing along a line perpendicular to the wall above a point on the wall is the result of actions which take place above a considerable area of the wall upstream of the point, while the collateral boundary layer at a point depends only on what happens to the flow immediately above a line on the wall upstream of the point.

Experimental Results

Experimental skewed boundary layers have been obtained in the Gas Turbine Laboratory with three different types of apparatus.

(*a*) A cascade of turbine nozzles Fig. 2 taken from reference [3]. This apparatus produced a skewed laminar boundary layer on the end wall. Fig. 3 is a sample polar plot.

(*b*) A free jet impinging on a wall, Fig. 4 taken from reference [4]. A sample polar diagram of the turbulent layer formed on the bottom wall of this apparatus is shown in Fig. 5.

(*c*) A vaneless diffuser, Fig. 6. The results of investigation by Gardow and others with this apparatus have not been published yet but a sample polar plot of the resulting turbulent boundary layer is presented in Fig. 7.

The following general conclusions can be drawn from this experimental work.

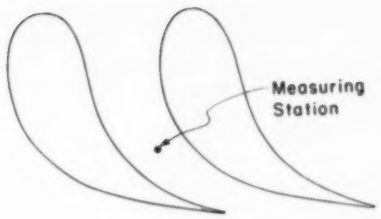

Fig. 2 Turbine cascade

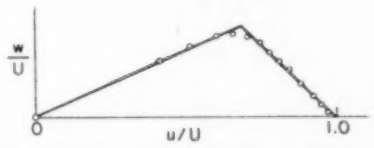

Fig. 3 Skewed laminar boundary layer from reference [3]

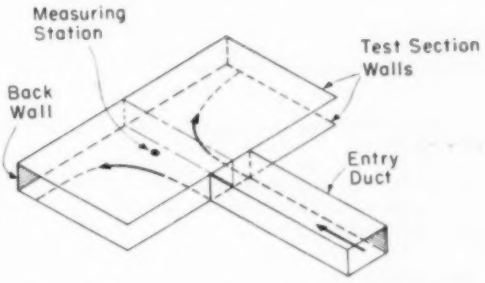

Fig. 4 Isometric view of test section of reference [4]

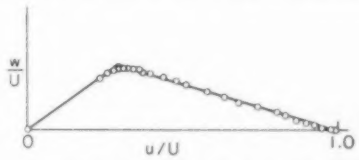

Fig. 5 Skewed turbulent boundary layer from reference [4]

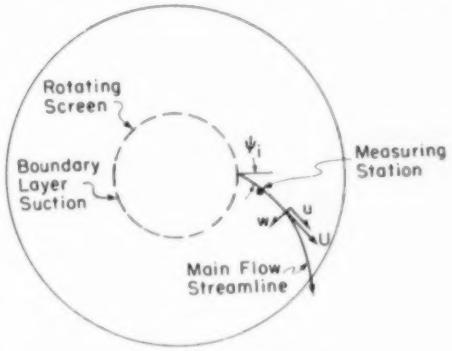

Fig. 6 Diagram of vaneless diffuser

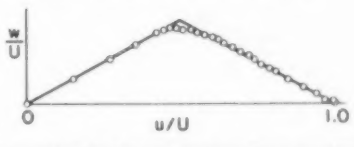

Fig. 7 Skewed turbulent boundary layer from vaneless diffuser

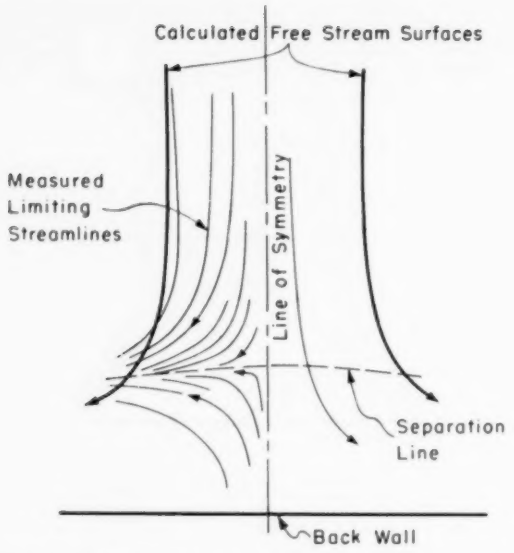

Fig. 8 Limiting streamlines and separation line from reference [4]

1 The polar plot appears to be almost always triangular, indicating a collateral boundary layer near the wall and a quasi-collateral region further from the wall joined by a transition region.

2 For cases where the skewed boundary layer is formed by turning a collateral boundary layer, the angle α in Fig. 1(*e*) is reasonably well predicted by inviscid analysis [4].

3 Pressure rise in the boundary layer expressed in terms of the maximum velocity head has often been used as a criterion for separation

$$\left(\Delta p \Big/ \frac{\rho v^2}{2g_0}\right)$$

This appears to be a very poor design parameter if the boundary layer is skewed. Fig. 8 taken from reference [4] shows limiting streamline directions with a line of separation to which all limiting streamlines become tangent. The pressure coefficient on the line of symmetry is about 0.5 but near the edge of the free jet the pressure coefficient must be close to zero. Unfortunately no measurements were made in this region.

4 The vortex sheet of reference [3] which is reproduced in Fig. 9 shows a phenomenon which according to our definition is a separation occurring in a nozzle where the pressure gradient is favorable. The resemblance to the "free vortex layer" of Maskell is striking. It is concluded that an "unfavorable pressure gradient" does not necessarily accompany separation of a skewed boundary layer.

Conclusion

The skewed boundary layer is seen to have interesting properties which differ in kind from those of the ordinary collateral layer. We believe that improved turbomachinery can result from a better understanding of these properties.

References

1 H. B. Squire and K. G. Winter, "The Secondary Flow in a Cascade of Airfoils in a Non-Uniform Stream," *Journal of the Aeronautical Sciences*, vol. 18, 1951, pp. 271–277.

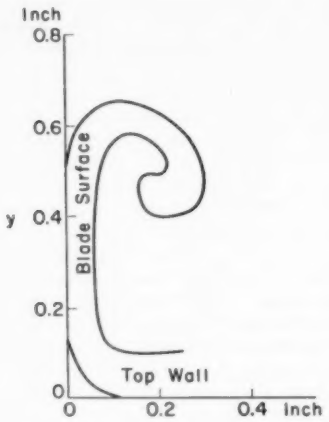

Fig. 9 Configuration of vortex sheet at corner

2 W. R. Hawthorne, "Secondary Circulation in Fluid Flow," *Proceedings of the Royal Society*, series A, vol. 206, 1951, pp. 374–387.

3 Y. Senoo, "The Boundary Layer on the End Wall of a Turbine Cascade," M.I.T. Gas Turbine Laboratory Report No. 35, October, 1956.

4 J. P. Johnston, "Three-Dimensional Turbulent Boundary Layer," M.I.T. Gas Turbine Laboratory Report No. 39, May, 1957.

5 A. H. Stenning, "The Turbulent Boundary Layer in Spiral Flow," SM thesis in Mechanical Engineering, M.I.T., 1951.

6 E. C. Maskell, "Flow Separation in Three-Dimensions," Report Aero 2565, Royal Aircraft Establishment, Farnboro, England, November, 1955.

7 Y. Senoo, "Three Dimensional Laminar Boundary Layer in Curved Channels With Acceleration," M.I.T. Gas Turbine Laboratory Report No. 37, November, 1956.

DISCUSSION

R. C. Dean, Jr.[4]

This discusser welcomes this contribution of important results from the Gas Turbine Laboratory's long-term project on three-dimensional flow in turbomachinery. He is pleased to comment on this work since he had a small part to play in it during its early days.

There is no doubt that this work has clarified our concepts of the skewed boundary layer, particularly, in view of the accumulating evidence reported in this paper and in more detail and extent by Johnston [4], that many skewed boundary layers fit the triangular polar-plot model surprisingly well. In most turbomachines, boundary layers lead quite short lives between great alteration and rebirth due to transit from a stationary to a rotating wall, or shedding from blades or vigorous stirring by moving blade tips. Thus, we can expect that the characteristics of "newly formed" skewed boundary layers reported in this paper will apply to almost all flow situations in fluid machines.

Accepting then the widespread occurrence of the triangular-polar-plot skewed boundary layer, we are quite curious to know why the boundary layer demonstrates two remarkably different regions joined so abruptly that only a small transition region has been observed. The quasi-collateral nature of the outer region is understandable in a boundary layer skewed by turning, but what is the mechanism that produces the collateral layer near the wall?

The inviscid secondary flow analyses of Squire and Winter and of Hawthorne lead to an increasing angle of skew as the wall is

[4] Head, Advanced Engineering Department, Ingersoll-Rand Company, Phillipsburg, N. J. Assoc. Mem. ASME.

approached. Surely viscous effects will attenuate this increase, but would they be expected to eliminate it entirely? The pressure forces that skew the outer region also act upon the inner region. How can this latter region sustain any pressure components normal to line *a-b* in Fig. 1(*f*), without immediately developing skew to produce a shear gradient at the wall which is necessary to balance the pressure-force component? Since such skew near the wall apparently has not been observed, perhaps the explanation is that the direction *a-b* is the direction of the pressure gradient in the main flow outside the boundary layer or at least close to the wall? These latter two directions are the same according to classical boundary-layer theory, but perhaps they are not the same in a skewed boundary layer. The discusser asks then whether the direction of line *a-b* has ever been compared to the direction of the pressure gradient *at the wall?* In any event, he suggests investigation of the causes of the collateral region near the wall as a fruitful task.

In addition, the sudden change in character at the polar triangle peak also requires further explanation. Even if line *a-b* does align with the pressure gradient at the wall, that coincidence still would not explain the rather sharp peak; one would still expect a gradual transition. Of course, it must be remembered that the polar plot is greatly misleading relative to distance from the wall since the peak usually lies in the lower 10 per cent of the total layer thickness. However, the writer does not think that this distortion alone can explain the apparent, near-singular region between the two types of flow.

On considering separation, the statement is made in the paper that, the separation line "in general will be oblique to the free-stream direction and tangent to the limiting streamline." Maskell [6] explains this matter in considerably more detail and defines two types of separation; "ordinary," where the limiting streamline is tangent to the solid surface and to the separation line at the point of separation, and "singular," where the limiting streamline need be tangent to neither the surface nor the separation line. With the former type, only the shear stress (or velocity gradient normal to the wall) component normal to the separation line vanishes at the separation point, while the component parallel to the separation line remains finite. In the latter case, the shear stress vanishes totally at the separation point. Maskell admits and illustrates cases where singular points of separation can exist on a line of ordinary separation, but does not consider lines of singular separation except in two-dimensional flow.

It is true by definition that a collateral (or two-dimensional) boundary layer must separate along a line normal to the flow composed of singular separation points. Such behavior appears to be achievable in careful experiments (for example, see Clauser[5]). On the other hand, it does not seem to be true, necessarily, that skewed boundary layers can separate only in the ordinary fashion or along a line of ordinary points containing discrete singular points. Is it not possible that a skewed boundary layer could also separate along a line of singular points as does the collateral boundary layer? In the skewed boundary layer, the limiting streamline could join a line of singular separation at any included angle between 0 and 90 deg with the only condition that the wall shear stress must vanish at juncture. This condition means that both orthogonal components of the shear stress must vanish at juncture and further, if the included angle is to be *between* 0 and 90 deg, the shear components must vanish at the same rate at juncture. We see then that the occurrence of a line of singular separation, particularly with oblique incidence of the limiting streamlines, requires very special, but, as far as we have been able to determine, physically possible conditions. The uniqueness of the required conditions explains, probably, why no one has yet reported a confirmed case of a singular separation line in a skewed flow.

Separation is well defined in the paper and includes stall as a sub-phenomenon. Stall is commonly considered to lead to detrimental results—high losses, unsteadiness, flutter, and so forth. As the author states, the definition of "detrimental results" requires inquiry into the mind of the user or designer rather than into the phenomenon itself. However, in practice, it is usually quite clear when "detrimental results" ensue, for the performance of the device then degenerates catastrophically. Of course, one can have a little bit of stall and it even may do some good to stir up and exercise a tired flow (see Kline, Abbott, and Fox[6]).

It does appear that there is a connection between the type of stall and the severity of its consequences. Ordinary separation in a skewed boundary layer usually appears to be stable and mild in consequences; stall bubbles are rarely associated with this type of flow. In contrast, singular separation of collateral boundary layers usually has eddies or stall bubbles in association. These accumulations may be stationary, quasi-stationary, or of the shedding variety. It is these eddies that commonly cause most of the detrimental results in fluid flow for they are composed of relatively slowly moving fluid which produces large-scale mixing and consequent losses in the bounding main flow. It is interesting to note that the cases where large losses and major unsteadiness occur appear to involve singular separation; these are two-dimensional flows and the presence of sharp edges on the solid boundary. As Maskell [6] points out, the latter case can easily exhibit singular separation. Kline's[7] investigations of diffuser stall can be explained likewise. In this case, as long as the stall bubbles or eddies remained smaller in transverse extent than the depth of the diffuser, no large-scale disturbance occurred; however, when the stall bubbles grew to the depth of the passage, by amalgamation or otherwise, then large-scale transitory stall commenced with a great depreciation of performance. It is suggested here that, when the stall eddy blocks the entire depth of the duct, perhaps the separation becomes singular and unsteady due to the loss of the governing action of shear at the separation point.

Perhaps the designer should always configure his passages to insure some skew in the boundary layer giving it an extra degree of freedom to avoid catastrophy. Certainly further clarification of separation in generalized flows will be an important contribution and likely will hold the key to many unresolved fluid-flow phenomena.

Finally, the author points out that the common separation criteria for two-dimensional flows are of little value in skewed flows. Since most flows of practical interest are skewed, this conclusion explains why conventional boundary-layer theory is of so little direct use to the applied fluid mechanic. The significant bastion of applied fluid mechanics is the three-dimensional, turbulent boundary layer; it still remains virtually unassaulted. For his widening of the small breach in this subject, the author is to be congratulated.

H. P. Eichenberger[8]

The author has presented a complicated topic in a very simple manner. The observation of the peculiar triangular relationship between crossflow and boundary-layer velocities is, at first, surprising and then, after second thought, one wonders that this has not been found earlier on purely theoretical grounds. This

[5] F. H. Clauser, "Turbulent Boundary Layers in Adverse Pressure Gradients," *Journal of the Aeronautical Sciences*, vol. 21, 1954, pp. 91–108.

[6] S. J. Kline, D. E. Abbott, and R. W. Fox, "Optimal Design of Straight-Walled Diffusers," published in this issue pp. 321–331.

[7] S. J. Kline and P. W. Runstadler, "Some Preliminary Results of Visual Studies of the Flow Model of the Wall Layers of Turbulent Boundary Layer," *Journal of Applied Mechanics*, vol. 26, TRANS. ASME, vol. 81, 1959, pp. 166–170.

[8] Chief System Engineering, Tapco, Thompson Ramo Wooldridge, Cleveland, Ohio.

impression of obviousness is, of course, the mark of great observations or ideas.

A few words will be said to explain qualitatively how such a velocity distribution can be expected on theoretical grounds:

Researchers in turbulent boundary layer have written the complete differential equations including the averaged turbulent-velocity products (e.g., Townsend[9]). These equations are so complicated that the tendency is very strong to neglect some terms on the grounds that they are small as compared to others.

Measurements have shown that a two-layer model represents the facts surprisingly well; in the layer near the wall viscous dissipation is very large and the boundary layer adjusts immediately to new conditions; i.e., main-flow inertia is negligible. In the outer layer the phenomena depend on the history of the flow as they do in inviscid flow.[9] In this region viscosity has no influence upon the secondary-flow velocity and therefore Hawthorne's inviscid secondary-flow theory can be applied which leads to the straight line in the outer region of the boundary layer. Surprising remains the short transition region; an indication that Townsend's two-layer, boundary-layer model applies also to three-dimensional boundary layers as well as it does to two-dimensional boundary layers.

A. G. Hansen[10]

This paper is interesting in that it provides another basis for understanding the behavior of the three-dimensional boundary layer. At present there is a need for simple representations such as afforded by the author's triangular polar plots. Hopefully such representations would be applicable to numerical or "approximate" methods of analyzing the boundary-layer equations.

The experimental data presented in this paper seem to support the "triangular-plot" concept quite well. In addition, it would be interesting to determine if the results of theoretical solutions of the boundary-layer equations give similar results. In order to investigate this matter (at least in a preliminary fashion) polar plots were made of several exact solutions based on the analysis presented by Hansen and Herzig.[11] The boundary-layer flows investigated[11] arise from main-stream flows over a flat plate such that the streamlines of the flow are translated. The orientation of the co-ordinate axes employed is shown in Fig. 10. The velocity components of the main stream are given by

$$U = \text{const} = U_0 \ (x\text{-component})$$
$$W = \text{const}\ x^n \ (z\text{-component})$$

If we designate by u, w, and v the boundary-layer velocity components in the x, z, and y-directions, respectively, the solution of the three-dimensional boundary-layer equations for this problem is given by

$$u = U_0 F'(\eta)$$
$$w = WP(\eta)$$
$$v = {}^1/_2(\eta F' - F)(\nu U_0/x)^{1/2}$$

where

$F(\eta)$ = Blasius function
$P(\eta)$ = function tabulated in Hansen and Herzig[11]
$\eta = y(U_0/\nu x)^{1/2}$

We now consider a flow defined by

$$U = 1$$
$$W = 2x$$

The streamlines of this flow are the family of parabolas

$$z = x^2 + \text{const}$$

Polar plots are now calculated at the positions $x = {}^1/_4$, $x = {}^1/_2$, and $x = 1$. The results are shown, respectively, in Figs. 11, 12, and 13, herewith. The small circles on each plot correspond to a point approximating one quarter of the boundary-layer thickness. The figures show that there is a transition from a smoothly curved plot, Fig. 11, to plots which correspond more closely to the triangular plots of the author. The changing shape of the patterns can be explained qualitatively as follows: Near the leading edge of the plate ($x = {}^1/_4$) the pressure gradient of the main stream acts in such a manner as to cause rapid overturning of the boundary layer. As the flow progresses farther downstream, the direction of the pressure gradient is such that the component causing overturning is decreased while the component causing acceleration of the boundary layer is increased.

[9] A. A. Townsend, "The Structure of Turbulent Shear Flow," Cambridge University Press, Cambridge, England, 1956, p. 232.

[10] Head, Nucleonics Section, Cornell Aeronautical Laboratory, Buffalo, N. Y.

[11] A. G. Hansen and H. Z. Herzig, "Cross Flows in Laminar Incompressible Boundary Layers," NACA TN 3651, February, 1956.

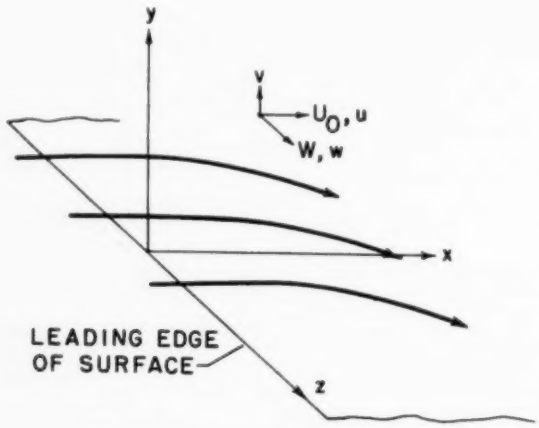

Fig. 10 Co-ordinate axes for flow over surface

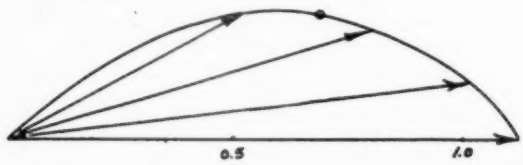

Fig. 11 Polar plot at $x = 1/4$ (streamlines: $z = x^2 + \text{const}$)

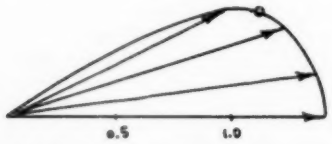

Fig. 12 Polar plot at $x = 1/2$ (streamlines: $z = x^2 + \text{const}$)

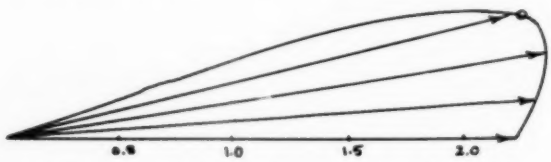

Fig. 13 Polar plot at $x = 1$ (streamlines: $z = x^2 + \text{const}$)

As another illustration, we choose a main-stream flow defined by

$$U = 1$$
$$W = 3x^2$$

The main-flow streamlines are given by

$$z = x^3 + \text{const}$$

The polar plot of the boundary-layer solution is evaluated a $x = 1$ and the result given in Fig. 14. The triangular nature of this plot is quite evident.

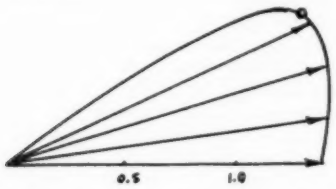

Fig. 14 Polar plot at $x = 1$ (streamlines: $z = x^3 + \text{const}$)

In conclusion, the theoretical solutions suggest that the triangularity of a polar plot may well depend on the position in the flow field at which the plot is made. Near the point of origination of the secondary flow, the results indicate a fairly pronounced deviation from this condition. At points farther downstream, the condition appears to be more closely realized.

J. P. Johnston[12]

In this paper, the author has presented a valuable contribution to the understanding of the complex field of three-dimensional, boundary-layer flows. Of particular interest is his discussion of separation of skewed boundary layers and the concept of the triangular polar plot which indicates the existence of a collateral region in the layer near the wall and a quasi-collateral region farther from the wall. With respect to the triangular-plot concept, we have a few comments.

It should be pointed out that the preponderance of the data used to show the generality of the triangular polar plot model is from experiments under conditions of turbulent flow. As a matter of fact, the only known measured skewed velocity profiles in laminar flow are those of Senoo,[13] one of which is shown in Fig. 3 of the paper. Of course, many theoretical laminar-flow solutions of skewed flows have been developed. A study of these theoretical solutions in the polar plot form gives no indication of simple triangular model.

Since Senoo's work is the only one available where laminar-flow theory and experiment can be compared, it is useful to present it in more detail. This is done in Fig. 15 which shows three polar plots taken along the center line of the turbine cascade passage (see Fig. 2 in paper). It is suspected that the data at station 4 are the same as those of Fig. 3 in the paper. Station 3 is about one third of the distance upstream from station 4 (measuring station in Fig. 2 of the paper) to the blade leading-edge plane, and station 5 is downstream of station 4 about halfway to the plane of the blade trailing edges.

Shown on the figure, in addition to the data, are lines indicating the best fit of the triangular model to the data, the linearized inviscid theory (references [1] and [2] in the paper) and Senoo's laminar boundary-layer solution. Note that Senoo's theory predicts the same polar plot at all three stations. At stations 3 and 4, Senoo's theory does not fit the data anywhere but near the wall

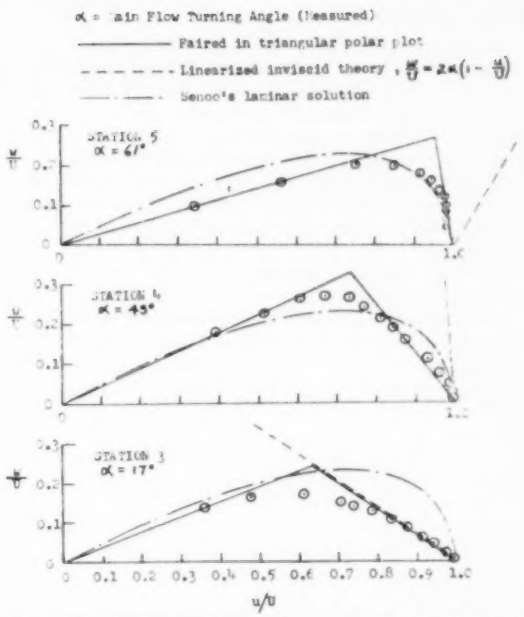

Fig. 15 Polar plots of data of Senoo along center line of end wall of a turbine cascade, Ref. [3] in paper

(i.e., where u/U is small). However, it does seem to fit the data fairly well downstream, station 5, except near the wall. Conversely, the linearized inviscid theory fits the data (in the outer part of the layer where it should be valid) quite well upstream at station 3, but not at all farther downstream. In all cases the simple triangular model fits the data fairly well.

The failure of Senoo's theory to fit the data at upstream locations can be explained by the fact that it gives a very poor representation of the real upstream boundary conditions in that it allows no upstream condition where the main flow is uniform and parallel and where the boundary layer is collateral. It should be noted that at station 5 where the theory seems to coincide with the data in the polar plot, it corresponds rather poorly with the cross-flow data when plotted against distance from the wall. Also note that, as pointed out in the foregoing, the shape of the laminar-flow solution of Senoo gives no hint of the triangular nature of the polar plot.

The failure of the linearized inviscid theory is correctly explained by the author where he states that this theory is only valid for small angles of turn. In the case of the experiment, the main flow angle of turn α was 17 deg at station 3, 43 deg at station 4, and 61 deg at station 5. All of which, except that at station 3, are much too large for the use of the inviscid theory.

In view of the points made here, one must come to the following conclusions:

1 In the case of laminar skewed boundary layers, there is not enough experimental evidence to justify the use of the triangular model nor is there basis in established laminar theory for such a model.

2 In laminar (or turbulent) skewed boundary layers the use of the linearized inviscid theory is invalid, except when the *main-flow* turning angle is small.

Despite these points of difference in detail, we feel that this paper captures the essence of a great amount of work and thinking on the problem of the skewed boundary layer in a form that should stimulate much thought. It is hoped that it will lead others to investigate this complex subject.

[12] Ingersoll-Rand Company, Phillipsburg, N. J.

[13] Reference [3] in the paper is now available as Y. Senoo, "The Boundary Layer on the End Wall of a Turbine Nozzle Cascade," TRANS. ASME, vol. 80, 1958, pp. 1711–1720.

Author's Closure

Our present knowledge is sufficient to answer some of the interesting questions raised by Dr. Dean. The line *a-b*, Fig. 1(*f*), is the direction of the limiting streamline. This direction differs, in general, from the direction of the pressure gradient at the wall. For example, the limiting streamlines in a vaneless diffuser are not radial. In fact, they tend to be more nearly tangential.

In speaking of the polar triangle, it must be remembered that this concept is not a physical fact but merely a convenient descriptive device. The small extent of the transition region remains a puzzle. The author agrees with Dr. Dean that the case of separation along a line of singular points oblique to the flow direction is very improbable.

In discussing the difference between ordinary separation of a skewed boundary layer and singular separation of a collateral layer, it must be remembered that the collateral layer is merely a special case of the skewed boundary layer and the distinction between the two in any practical case must be quantitative (how much skewing?) rather than qualitative. In the author's experience, highly skewed boundary layers do often separate without the catastrophic results which sometimes accompany the separation of a collateral layer. On the other hand, a collateral boundary layer may also separate without greatly altering the pressure distribution associated with potential flow.

The comments of Drs. Hansen and Johnston regarding the application of the polar triangle to laminar boundary layers are well taken. The author's experience with this subject is admittedly very limited. Moreover, the author finds it difficult to say which of Dr. Hansen's polar plots, Figs. 11, 12, 13, or 14, can be represented more closely by a triangle and therefore hesitates to agree with Dr. Hansen's conclusion. Perhaps a word or two is in order on the fitting process. Clearly *any* reasonable shape of polar plot can be approximated by two straight lines. The choice of two slopes gives quite a bit of latitude. If in addition we can arbitrarily choose a point on one of the straight lines as well as its slope, a still better fit is possible. This explains the difference between Dr. Johnston's Fig. 15 (station 4) and Fig. 3 which is indeed a representation of the same data. In the original reference [13] the co-ordinate system was taken along the center line of the passage, and crossflow measured with respect to the tangent to the center line at the point of measurement. Dr. Johnston evidently retained this co-ordinate system. The author assumed that the edge of the boundary layer was defined by the point at which the magnitude of the velocity became measurably smaller than that of the free stream and defined his co-ordinate system from the measured direction at the edge of the boundary layer. It is therefore not surprising that Fig. 3 shows a somewhat better fit than Fig. 15.

Dr. Johnston's remarks about the application of Senoo's theory to "data at upstream locations" deserves a word of comment. This theory is specifically designed to give information about boundary layers with reasonable length of approach. It would be fortuitous if this theory gave good predictions at "upstream locations" where the assumptions of the theory are far from valid.

STEPHEN J. KLINE

Associate Professor of Mechanical Engineering, Stanford University, Stanford, Calif. Mem. ASME

On the Nature of Stall[1]

The physical data available on the problem of stall are reviewed. The discussion is centered on the problem of flow in passages. The emphasis is placed on systematic visual data showing flow patterns as a function of geometrical parameters. These data lead to a view of stall as a spectrum including three or possibly four major types of flow patterns; these patterns involve both transient and steady elements. A qualitative parameter is formulated which provides a classification for the major types of stall. It is shown that this parameter and its underlying concepts are useful in rationalizing known but previously inexplicable results and in obtaining important qualitative predictions. Comparisons between the predictions of boundary-layer theory and the actual systematic stall data of passages are given.

THE PROBLEM of stall[2] is a very old but very important and definitely unsolved problem. In fact, a recent survey [1][3] has suggested that it is perhaps the most important single unsolved problem of fluid mechanics bearing on mechanical engineering design applications. This paper has a dual purpose: (*a*) To provide in so far as possible a comprehensive simple physical picture of what occurs in stalling flows; (*b*) to compare this physical picture with the various types of results and data from available approaches to this problem in an attempt to point up both the available correlations and the disparities between known results and available theory. The bulk of the discussion is centered on the flow in passages, and the related problems of external flow are discussed only briefly.

An attempt is made to discuss not only the question of whether stall will occur, but also what happens in a passage containing appreciable areas of stall. This latter matter has been little discussed and is very poorly understood.

Very good and reasonably recent summaries of the literature have been given on a number of separate but related topics. The data available on turbulent shear layers and turbulence have been admirably summarized by Townsend [2], the attempts at empirical correlations of turbulent boundary layers by Ross [3], and the concept of and data on "equilibrium" turbulent boundary layers by Coles [4] and Townsend [5, 2]. Older turbulent-boundary-layer methods and a large amount of correlated data are given by Schlichting [6], and an extensive compilation of data on airfoils is given by Abbott and Doenhoff [7].

The considerable implications of the following material in the design of diffusers are largely omitted from the present paper, and are treated instead in a companion paper [8] and its underlying references [9, 10]. The fundamental question, "Why do some of the strange flow patterns reported for apparently well behaved turbulent boundary layers occur?" is treated primarily in a separate paper by the author and P. W. Runstadler [11].

1 PHYSICAL DESCRIPTION OF STALL

Classical Pictures of Stall and Older Data

The modern description of the process of flow separation or stall stems directly from Prandtl's boundary-layer concept. The

[1] This work is currently continuing under the financial sponsorship of the Air Force Office of Scientific Research of the Air Research and Development Command, Contract AF49(638)-295. Reproduction in whole or part for any purposes of the United States Government is permitted. Support of earlier portions of the work relating to the underlying references was provided by the National Advisory Committee for Aeronautics and also the Small Aircraft Engine Department of the General Electric Company.

[2] The term stall in the present paper refers to any backflow at a wall whether small or large, transient or steady.

[3] Numbers in brackets designate References at end of paper.

Contributed by the Fluid Mechanics Subcommittee of the Hydraulics Division and presented at the Annual Meeting, New York, N. Y., November 30–December 5, 1958, of THE AMERICAN SOCIETY OF MECHANICAL ENGINEERS.

NOTE: Statements and opinions advanced in papers are to be understood as individual expressions of their authors and not those of the Society. Manuscript received at ASME Headquarters, September 28, 1958. Paper No. 58—A-170.

Nomenclature

e = total energy stored in a unit mass
e_i = internal thermal energy per unit mass
$\mathrm{Eu} = \dfrac{x}{\frac{1}{2}\rho V^2}\dfrac{\partial p}{\partial x}$
h = width of stall area at exit in fully developed stall
$h_p = e + p/\rho$
$H = \delta^*/\theta_1$, form parameter
L = length of diffuser walls
p = static pressure
Q = heat transfer
R_1 = radius of diffuser throat (conical)
R_w = Reynolds number based on throat velocity V_1 and width W_1
s = entropy per unit mass
T = temperature (absolute)
u = local velocity, $u = u(x, y)$
u' = rms value of fluctuations in u
U = free stream velocity, $U = U(x)$
v = local velocity normal to wall
v' = rms value of fluctuations in v
V = one-dimensional velocity in flow direction
x = distance along wall
w_b = backflow rate of stalled fluid
w_e = maximum possible rate of steady removal of stalled fluid by entrainment
W_1 = width of diffuser throat (two-dimensional)
W_x = thermodynamic work
2θ = total included angle of divergence between diffuser walls
δ^* = displacement thickness of boundary layer
θ_1 = momentum thickness of boundary layer
$\sigma = w_b/w_e$
ρ = density
τ = shear
δ = thickness of wall layers
$\beta = (2L/W_1)\sin\theta$
μ = viscosity
$( )_e$ = exit of diffuser
$( )_w$ = wall conditions
$( )_y$ = local conditions distance y from wall
$( )_1$ = inlet conditions at throat of diffuser

original derivation of the pertinent equations is available in English [12]. Prandtl's ideas are shown in Fig. 1, taken from the transcriptions of Prandtl's lectures by Tietjens [13].

Several ideas implicit in the model of stall shown in Fig. 1(*c*) are important to the present discussion: (*a*) It implies a steady, two-dimensional flow pattern. Of course, many workers have recognized that this is only an approximation, but for the most part the over-all model has been accepted without appreciable modification, and this acceptance inherently assumes that at least the major elements of the flow pattern are believed to be describable by a steady two-dimensional model. This assumption in turn has led to the formulation of the analytical criterion of stall as the point at which the derivative $(du/dy)_{y=0} = 0$; this of course is equivalent to zero wall shear since

$$\tau = \mu \left(\frac{\partial u}{\partial y}\right)_{y=0}$$

and μ is finite.

Proceeding on this basis a very large number of attempts have been made to predict the actual occurrence of stall from the boundary layer equations. In general, these attempts can be summarized in the following way: If the boundary layer is laminar, the prediction gives a reasonable result a satisfactory percentage of the time. However, it has long been known that even in this case a considerably more accurate result is achieved if the pressure distribution employed is that measured in the actual flow rather than that predicted from potential flow. The explanation for this rests in the fact that when a stall such as that shown in Fig. 1(*c*) occurs the entire flow pattern, including the pressure distribution, is usually greatly altered from that given by potential flow. For example, the wonderful movies taken by Allborn under Prandtl's direction at Göttingen years ago show very clearly that, on the airfoils pictured, the stall does not start near the same point where it finally comes to rest; instead the stall begins in these cases very near the tail of the airfoil section shown and builds up gradually. In this process the main stream is forced away from the wall, thereby altering the pressure distribution at the surface. The stalled area gradually moves forward on the airfoil as it increases in size until a new equilibrium of sorts is achieved with an entirely new flow pattern like that shown in Fig. 1(*c*). This pattern of Fig. 1(*c*) will be called the "classical stall model," and for reasons that will appear later, it also will be referred to in the following as "fully developed stall."

The situation in the case of the turbulent boundary layer however has been and remains quite different. In this case, it is safe to say that no adequate prediction method has been developed although a number of varying methods have been tried exhaustively. This conclusion is reiterated both by Clauser [14] and Robertson, et al. [15] in recent and extensive efforts using similarity and empirical methods, respectively. Still more recently Coles [4] and Townsend [5] have calculated the conditions for what Coles calls a "continuously separating" equilibrium layer and Townsend takes to be the upper limit of possible equilibrium profiles, but these ideas have not yet received empirical verification in so far as stall is concerned. They will be compared with over-all data in Section 3.

It is, of course, also well known that if a real fluid is made to flow past a sharp corner, as shown in Fig. 1(*d*), it will stall abruptly and a recirculation will be encountered very roughly as pictured. However, the details of the recirculating flow in the corner do not appear to have been studied carefully.

The study of stall on airfoils and in cascades also has shown that a stall can occur abruptly from a point at or near the leading edge at high angles of attack as shown in Fig. 1(*e*). Such stalls usually occur on thin plate-like airfoils while the type described in the foregoing and shown in Fig. 1(*c*), and in the Prandtl movies, normally occurs on thick airfoil sections. Usually, the sharp stall on thin airfoils occurs where the boundary layer is still laminar, and the type of stall that commences at the rear section of the airfoil begins in a turbulent layer.

A number of observers also have recorded laminar stall bubbles that are relatively stationary and occur near the leading edge of an airfoil or cascade blade. These usually lead to transition in less stable free shear layer, and then to reattachment of the turbulent layer so generated. In cascade practice this is known

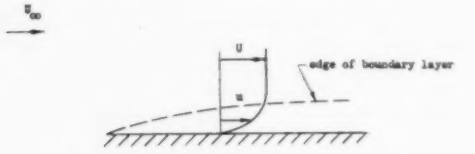

Fig. 1(*a*) Prandtl's boundary layer concept

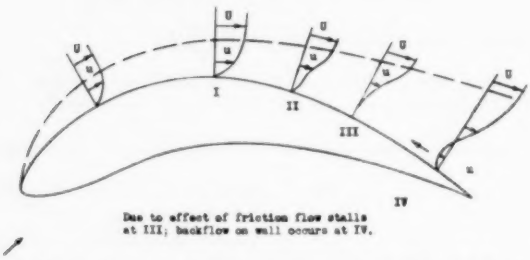

Fig. 1(*b*) Development of boundary-layer velocity profile in adverse pressure gradient (vertical scale exaggerated) due to effect of friction flow stalls at III; back flow on wall occurs at IV.

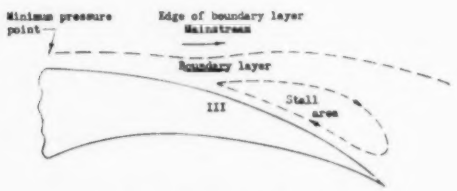

Fig. 1(*c*) Classical stall model

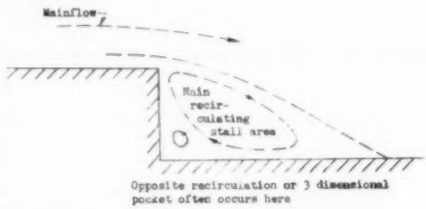

Fig. 1(*d*) Abrupt stall at a sudden expansion

Fig. 1(*e*) Stall near leading edge of thin airfoil at high angle of attack

as low Reynolds-number stall as opposed to high Reynolds-number stall that usually occurs in the turbulent portion of the layer farther downstream.

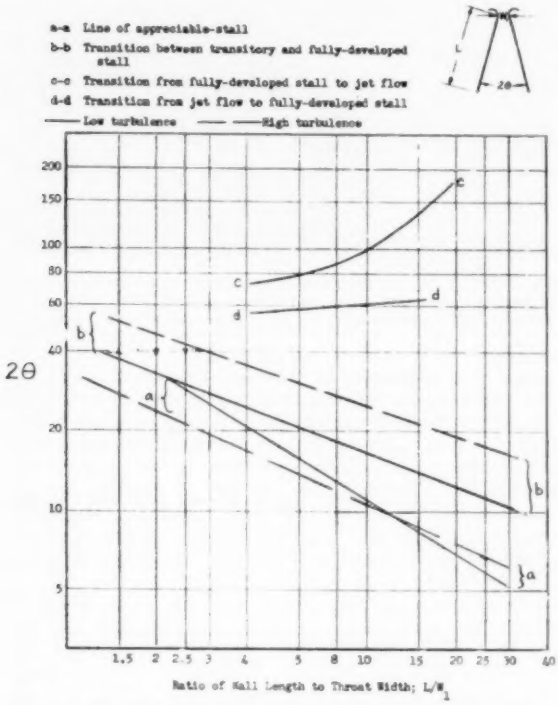
a-a Line of appreciable stall
b-b Transition between transitory and fully-developed stall
c-c Transition from fully-developed stall to jet flow
d-d Transition from jet flow to fully-developed stall
Low turbulence
High turbulence
2θ
Ratio of Wall Length to Throat Width; L/W1

Fig. 2(a) Regimes of flow two-dimensional plane-walled diffusers [8]

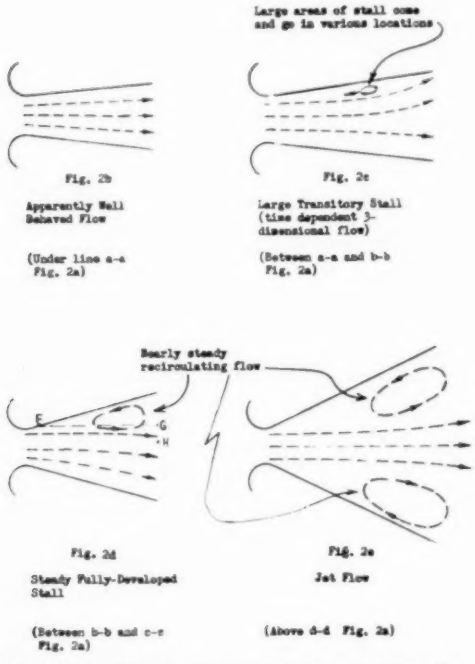
Large areas of stall come and go in various locations
Fig. 2b
Apparently Wall Behaved Flow
(Under line a-a Fig. 2a)
Fig. 2c
Large Transitory Stall (time dependent 3-dimensional flow)
(Between a-a and b-b Fig. 2a)
Nearly steady recirculating flow
Fig. 2d
Steady Fully-Developed Stall
(Between b-b and c-c Fig. 2a)
Fig. 2e
Jet Flow
(Above d-d Fig. 2a)

Fig. 2(b–e) Schematic diagrams of regimes of diffuser flow

Recent Results in Diffusing Passage Flows

In 1954, C. A. Moore and the author undertook systematic visualization studies of the flow patterns found in straight-walled diffusers as a means for learning more about the nature of the flows encountered and for developing good wide-angle subsonic diffusers. The latter result has been largely achieved, and the results are given in [8–10]. However, the studies of the nature of the flows found are still continuing. The history

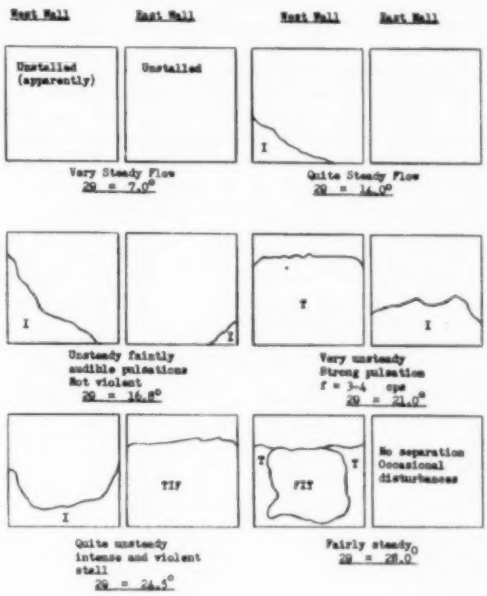
East Wall
West Wall
Unstalled (apparently)
Very Steady Flow 2θ = 7.0°
Quite Steady Flow 2θ = 14.0°
Unsteady faintly audible pulsations Not violent 2θ = 16.8°
Very unsteady Strong pulsation f = 3-4 cps 2θ = 21.0°
Quite unsteady intense and violent stall 2θ = 24.5°
No separation Occasional disturbances
Fairly steady 2θ = 28.0°

Each pair of squares represents the diverging walls as seen looking out from inside the diffuser. I = intermittent transitory stall; T = transitory stall; TIF = transitory stall with intermittent fixed stall; FIT = fixed stall with intermittent transitory stall; F = stable fixed stall. $R_{e_1} = 2.4 \times 10^5$, $L/W_1 = 8.0$, $W_1 = 3.00$ in.

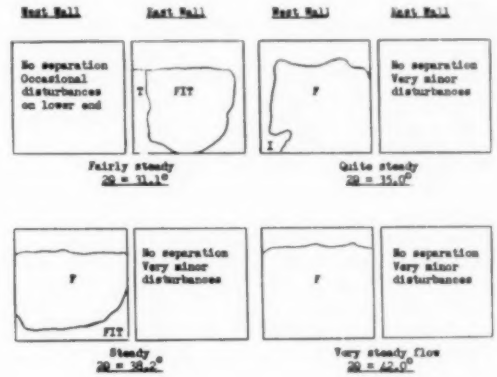
East Wall
West Wall
No separation Occasional disturbances on lower end
Fairly steady 2θ = 11.1°
No separation Very minor disturbances
Quite steady 2θ = 15.0°
Steady 2θ = 38.2°
Very steady flow 2θ = 42.0°

Each pair of squares represents the diverging walls as seen looking out from inside the diffuser. I = intermittent transitory stall; T = transitory stall; TIF = transitory stall with intermittent fixed stall; FIT = fixed stall with intermittent transitory stall; F = stable fixed stall. $R_{e_1} = 2.4 \times 10^5$, $L/W_1 = 8.0$, $W_1 = 3.00$ in.

Fig. 2(f) Sketches of successive flow patterns of stall as divergence angle is increased

of these studies is given in [16, 8, 9, 17, 18]; the major results are summarized in the following.

The flow-regime data found are shown on Fig. 2(*a*). This figure includes not only the data from a water table and a separate air unit [9, 10], but also more recent unpublished data taken on another water table by D. C. Briggs[4] and D. Gage[4] under the author's direction. Fig. 2(*a*) amounts to an allocation chart showing four major regimes of flow that occur in symmetric, plane-walled two-dimensional diffusers. Beginning from the bottom of the figure these are called, respectively: Apparently unstalled flow, Fig. 2(*b*); large transitory stall, Fig. 2(*c*); fully-developed stall, Fig. 2(*d*); and jet flow, Fig. 2(*e*).

The line *a-a* in Fig. 2(*a*) was located initially by use of movable dye injectors of roughly $^1/_8$ in. diam at some distance from the wall in low-speed water flow. Line *a-a* corresponds to the location where clearly distinguishable back-flows can first be found over such an injector in the boundary layer. Thus the line *a-a* marks the initial appearance of large stalls in the sense that one whole area of flow, of the order of magnitude of the boundary-layer thickness, reverses direction temporarily.

The region between lines *a-a* and *b-b* is called "large transitory stall" and the entire region is characterized by large, low frequency stalls that come and go in time. It is to be emphasized that this transitory pattern persists indefinitely when the geometry of the diffuser lies in the zone indicated.

Initially, the line *a-a* was called the line of "first stall," and it was also more or less accepted that the demarcation line between stall and no stall was relatively sharp and definite as suggested by the generally accepted model. However, further investigation revealed that neither of these conventional ideas corresponded with what was actually observed. In reality, some stalls do occur very near the wall far below line *a-a* in Fig. 2(*a*) and the change from a potential-flow, boundary-layer-type pattern to a transient-stall pattern is relatively gradual. However, the stalls[5] that occur below line *a-a* are of a different type; this type of stall involves only the wall layers of the boundary layer (sublayer and buffer layer), and is apparently an inherent part of the structure of the turbulent boundary layer with moderate and strong adverse pressure gradients. Under these conditions small "streaks of stall" occur regularly very near the wall, are caught up by the main stream, and are swept back downstream. The streaks form part of a regular but transient three-dimensional pattern that is repeated over the entire wall [11]. At about line *a-a* they are no longer swept away immediately, and they begin to accumulate into large areas of stall.

A typical pattern of flow including small streaks of stall in the wall layers is shown in Fig. 3. This is a photograph obtained by a visual method called the needle-trace technique. In this method[6] a line of dye is placed *on the wall* with a 6-in-long, 0.010-in-ID hypodermic needle attached to a standard medical syringe. The dye then follows the fluid motion making visible the layers very near the wall. Further discussion of these patterns and their implications are given in [11].

Between lines *b-b* and *c-c* of Fig. 2(*a*), the flow pattern is that of an asymmetric fully developed steady stall as shown in Fig. 2(*c*). The particular wall on which the stall appears is arbitrary, in symmetric configurations, and is due to some very small initial effect that is often extremely hard to trace. This implies that stability considerations are important in such a flow. The fully developed stall pattern corresponds to the classical stall

[4] Research Assistants, Department of Mechanical Engineering, Stanford University, Calif.

[5] The word stall is used here in the sense of any upstream motion at the wall.

[6] Developed by J. A. Miller, formerly Research Assistant, Stanford University, Stanford, Calif.

Fig. 3 Wall layers of turbulent boundary just downstream from a point of minimum pressure. Dye visualization of wall layers [11]. Flow direction right to left, original dye trace placed on wall normal to flow.

pattern first propounded by Prandtl and sketched in Fig. 1(*c*). It is emphasized that this pattern is relatively steady with far less flow fluctuation than occurs in the large transitory stall region or even in the upper part of the apparently unstalled regime. Some unsteadiness does occur in the mixing region between lines *F-G* and *F-H* in Fig. 2(*d*); it embodies the well-known features of discrete vortex roll up and break down, and some unsteadiness near the nose of the stall area occurs at angles just above line *b-b*. However, the major flow pattern is relatively steady.

The location of line *b-b* is affected materially by the amount of disturbances in the inlet. The available tests suggest that any type of large-scale fluctuations in the inlet flow is about equally effective in raising the line *b-b*. Line *a-a*, on the other hand, is much less affected by turbulence level except at very low L/W_1, and high 2θ.

The jet-flow pattern, Fig. 2(*e*), is also relatively steady. The slopes of the lines *a-a* and *b-b* in Fig. 2(*a*) are negative while the lines *c-c* and *d-d* are positive; this qualitative difference to the same parameters suggests the presence of some different kind of governing mechanisms. The zone between lines *c-c* and *d-d*, Fig. 2(*a*), is a hysteresis region; increasing angle at constant L/W_1 shows transition from fully developed stall to jet flow at line *c-c*, decreasing angles shows transition at line *d-d*. Such behavior again suggests the importance of stability considerations.

Summary of Physical Picture in Passage Flows

The flow patterns discussed in connection with Fig. 2(*a*) can best be described either as a spectrum or as a series of stages with continuously increasing amounts of stall occurring as either the divergence angle or the length-to-width ratio of the passage is increased. This spectrum begins at very low angles and continues to very high values; it encompasses major patterns that are steady and transient, symmetric and asymmetric, and two and three-dimensional. While the transitions from one pattern to another are relatively continuous, the lines *a-a* and *b-b* have considerable meaning for design purposes as is explained in detail in [8], and the difference in over-all flow pattern between the center of any two adjacent zones is quite significant. Systematic pictures of the flow patterns from wall-tuft observations in a two-dimensional air unit with a Reynolds number based on throat width of 240,000 are shown in Fig. 2(*f*). This figure is from the results of Cochran [10], and it shows quite clearly the continuous growth of stall and the large alteration in flow pattern as angle is increased at constant L/W_1.

Effects of Nongeometrical Parameters

The author's initial reaction to Fig. 2(*a*) was that the various lines on it would probably shift as a function of other variables. However, further tests revealed that the lines *a-a* and *b-b* were at most very weakly dependent on Reynolds number over the range from 6000 to at least 300,000 based on throat width and mean throat velocity. It also was found that it was essentially independent of the aspect ratio of the throat for flat diffusers with aspect ratios from 1:4 in one direction to 20:1 in the other.

It was still felt that the result of Fig. 2(*a*) would probably be grossly altered by changes in inlet boundary-layer conditions since all the tests by Moore [9] and Cochran [10] were run with thin turbulent inlet boundary layers. However, preliminary water-table investigations during late 1957 suggest that the flow regime is altered much less than might be expected due to relatively large changes in inlet boundary-layer conditions.[7] These results on inlet conditions are partially substantiated by the work of Copp [32], Uram [30], and Norbury (unpublished).

Data on the effect of Mach number are even more meager, amounting to only a few points; however, these data *suggest* that only a small lowering (5–10 per cent) in line *a-a* occurs due to increases in Mach number up to the condition where shock waves and choking effects are encountered.

Relation Between Flow Regimes and Performance

At this point the reader is cautioned that the preceding remarks apply only to flow regime and not to performance; that is, performance, as measured in terms of static pressure recovery or effectiveness, is dependent on Reynolds number, aspect ratio, inlet boundary-layer conditions, and Mach number. In other words, performance is a function of a larger number of variables than flow regime.

Comparison of Data With Classical Concepts Including Results in Vaned Passages

Most calculations of stall do not depend on the geometrical parameters shown in Fig. 2(*a*), but instead attempt to compute what happens to a given boundary layer as it proceeds down a wall under specified free-stream pressure variation and inlet boundary-layer conditions. In order to compare the concept of stall as a series of stages more directly with such calculations, a test was made employing a flexible lucite wall in a water table as shown in Fig. 4. By adjustment of the displacement at point *B* in Fig. 4, it is relatively easy to adjust the rate of development of stall to give a fully developed stall just upstream of point *B*. Using a needle-trace technique to examine the successive flow conditions found, it was observed that the boundary layer progressed from a normal turbulent boundary layer in a favorable pressure gradient at *A*, through the conditions seen for a turbulent layer in an adverse pressure gradient, *A-C*, where small local transitory streaks of stall occur, then to a condition where large fluctuating stalls occurred (in the floor corner in this case), and finally to a fully developed stall where the entire flow on the wall was reversed. This result shows that the same series of stages of stall development *can* occur as a function of downstream distance as those found by systematic geometrical variation of straight-walled channels.

Thus while it is possible to obtain a clear-cut stall at a given location, as for example in Figs. 1(*d*) and 2(*d*), this type of stall apparently occurs in internal flow only when wall curvature is extreme or a very high pressure gradient is suddenly encountered as in shock interactions. In cases where good aerodynamic design is employed in an attempt to avoid stall, it is more likely that the pattern of events will follow through a series of stages like those described in the foregoing.

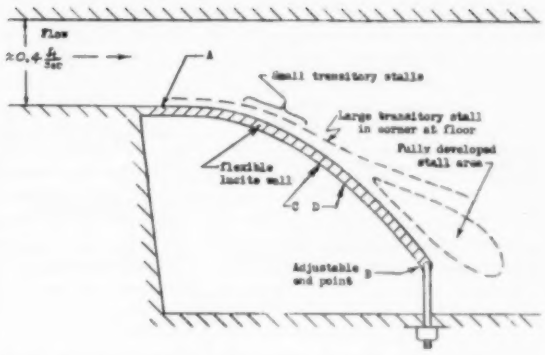

Fig. 4 Development of stall on a curved wall (plan view of water table)

In addition to the considerable differences between the classical models of stall and the flow patterns shown in Fig. 2(*a*), the early results of C. A. Moore [9] also showed that surprisingly good flow patterns could be achieved by use of short flat vanes in wide-angle diffusers. These results were verified quantitatively in considerable detail by Cochran [10]. Cochran's results showed that excellent recoveries, relatively even velocity profiles, and smooth flows could be achieved by these short-vane systems up to total included divergence angles of 42 deg for all L/W_1-values tested.[8] (The 42-deg upper limit is due to the limits of the apparatus, not apparently to the method.) In so far as the present paper is concerned, the important aspect of these vaned-diffuser results is not their obvious design significance, but is instead the fact that the vanes operate best when placed essentially on the streamlines of the potential flow as shown in Fig. 5(*a*). Since they are thin flat vanes, this implies that very little modification of the steady potential-flow pressure distribution can be created, but nevertheless a very large increase in performance and flow steadiness and a complete change in flow pattern are uniformly observed over a wide range of conditions.

This last point is a crucial one since the entire structure of boundary-layer theory rests on the assumption that the flow pattern is determined by the pressure distribution of the potential flow and the history of the boundary layer *alone*. Furthermore, in *any* boundary-layer theory now available, other things being equal, increased adverse-pressure gradient gives a prediction of increased stall. This matter of vaned units can therefore be singled out as a good means for pointing up the conflicts between theory and results.

Consider three diffusing passages; each has identically the same outside walls and identical inlet flows. For the present purposes it is useful to take these conditions to be: A bell-mouth entry from a large room with a fixed flow rate and high inlet turbulence, a total divergence angle of 28 deg and $L/W_1 = 8$. This is done to conform to conditions actually tested by Cochran [10].[9] If we make the first unit a simple plane-walled diffuser with no

[7] These results on inlet are definitely preliminary and should be regarded as such until systematic studies now in process are completed.

[8] For example, at $L/W_1 = 8$ the optimum recovery of the unvaned unit tested was 0.76 and occurs at $2\theta = 14$ deg. With vanes Cochran obtained recoveries of 0.78 at 30 deg and 0.70 at 42 deg with smooth symmetric flows.

[9] A perhaps more striking result occurs if one uses $L/W_1 = 8$, 20 deg divergence angle, and a low inlet turbulence with only one vane, since the only vane is then on the center line. However, Cochran did not test with these exact conditions.

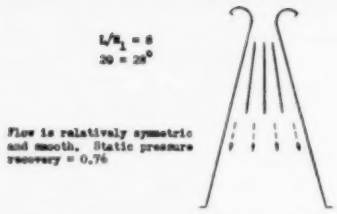

Fig. 5(a) Typical short-vane installation of type tested by Cochran and Kline [10]

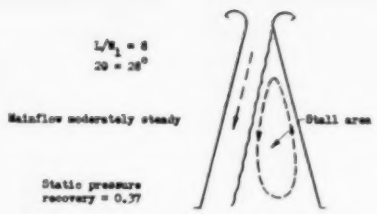

Fig. 5(b) Diffuser of Fig. 5(a) with no boundary-layer control

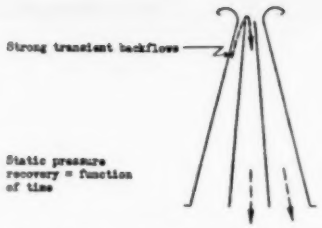

Fig. 5(c) Diffuser of Fig. 5(a) with two full length splitter vanes

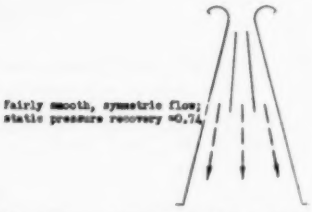

Fig. 5(d) Diffuser of Fig. 5(a) with two short vanes

boundary-layer control, Fig. 5(*b*), it will operate in the fully developed stall region with a recovery of about 37 per cent. If we then insert a vane cluster with two vanes each extending all the way from the throat to the exit, Fig. 5(*c*), three passages of $2\theta = 9^1/_3$ deg and $L/W_1 = 24$ are formed. The recovery will then increase a little, but will be very hard to measure accurately because the flow will be extremely unsteady with transient back flows up one wall that periodically spill over into the center passage; that is, large transitory stalls occur, as predicted by Fig. 2(*a*). We then insert two shorter vanes, still symmetrically placed, as shown in Fig. 5(*d*), but now each passage formed lies below line *a-a* in Fig. 2(*a*). The resulting flow is relatively smooth and symmetric, and the recovery achievable with careful vane adjustment is approximately 75 per cent. The only differences between the three units of Figs. 5(*b*), 5(*c*), and 5(*d*) are the vanes, and they are $^1/_{16}$-in. thick compared to the passage width of 3 to 5 inches.

These results are quite inexplicable in terms of boundary-layer theory and the classical steady-stall model of Fig. 1(*e*). Several able workers have suggested to the author that the function of the vanes arises from the change in pressure distribution due to the displacement thickness of the boundary layer that inevitably develops on both sides of each vane. However, this cannot be the case. In the first place, such an explanation fails entirely to account for the fact that a short vane will sometimes give better performance than a long one as found by Cochran [10]. Even more important is the fact that insertion of vanes actually *raises* the pressure recovery, with all other conditions held constant, by a factor of 2. In the example of Figs. 5, the three units compared were purposely chosen so that the history of the boundary layer on the side wall upstream from the throat, the condition of the side wall and its geometry, the entering velocity profile, and the entering free-stream turbulence were all identical in the three cases. Comparison of the unvaned unit with the short vane case then shows that the adverse pressure gradient on the side wall in the section covered by vanes in Fig. 5(*d*) is *more than doubled* by insertion of the short vanes. However, without the vanes a fully developed stall occurs, and with them no large stalls are found in the vane passages. *Thus the adverse pressure gradient applied to a given boundary layer under constant conditions has been more than doubled, and at the same time a fully developed stall has been entirely eliminated.*

The result just given is in such direct and violent contradiction to any normal conceptions of boundary-layer behavior or predictions of boundary-layer theory that one of two things must be the case: Either the data presented are wrong in some way, or the explanation lies in some phenomenon that is not explained by the boundary-layer concept alone. Some further comment on the validity of the data is therefore in order.

The data of Moore [9] were all obtained in a water table with Reynolds numbers varying from 6 to 20,000 based on throat width and mean velocity at the throat. The data taken by Cochran [10] were obtained in a separate air unit with a Reynolds number of 240,000 on the same basis. The over-all flow patterns carefully recorded in the two cases are in complete agreement in all major regards. In addition, the quantitative results quoted on recovery for the unvaned and short-vane units, in the foregoing comparison are from careful data taken by Cochran in which the 20 to 1 uncertainty interval was estimated at 1.2 per cent for the most steady flows and 9.2 per cent for very unsteady flows as with the long vanes mentioned. The data are consistent and repeatable and show that similar results can be obtained for all units tested, including a considerable variation in flow rate, divergence angle, and L/W_1. Also, more recently, several other observers have repeated and extended Moore's results as shown in Fig. 2(*a*). These data include utilization of an entirely separate water channel and inlet section including several variations

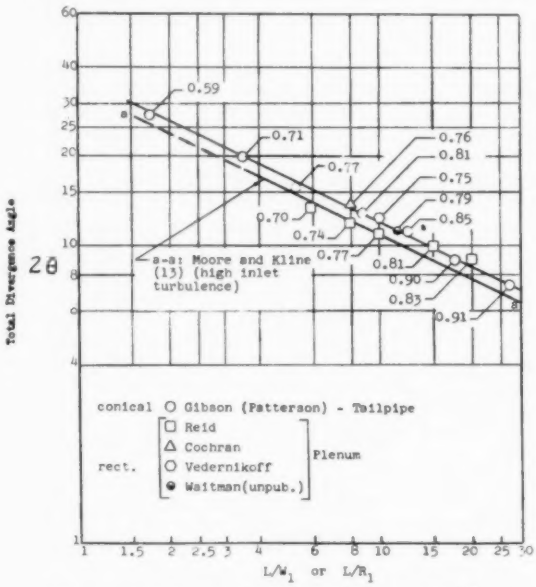

Fig. 6 Correlation of optimum recovery at constant L/W_1 (Numbers attached to points indicate observed value of peak recovery)

of both the old apparatus and the new one. The expected reproducibility of 1 or 2 deg in angle was obtained in the region studied by Moore. Thus there seems to be no internal reason to doubt the validity of the data.

To check the results still further an extensive study of the available literature on diffusers has been made. The bibliography of this study is given in [8] and includes some 39 references. The central correlation achieved is shown in Fig. 6. The explanation for the correlation of Fig. 6 is given in [8]; physical reasoning is presented in [8] to show that optimum recovery at constant L/W_1 is expected to lie a short distance above line a-a in Fig. 6, and that the minimum point in the recovery curve observed by Gibson [26] for conical units and Cochran [10] for two-dimensional units lies a little above line b-b of Fig. 2(a). (The reader is again cautioned that this correspondence does not extend to the value of recovery or effectiveness achieved at optimum or other locations.)

The pertinent point in the present discussion is that all of the known data for optimum recovery at constant L/W_1 in plane-walled diffusers are plotted in Fig. 6. They represent the work of six independent observers on an equal number of apparatus, and each point is an optimum from a series of runs. The plotted data include the results from both conical and flat units operating with inlet conditions varying from $\delta_1^*/W_1 = 0.003$ to ≈ 0.010, with Reynolds numbers based on throat width, and throat velocity varying from 6000 to 800,000, and with various downstream and upstream geometries. Despite this all of the plotted points lie within ± 5 per cent, and all but two points lie within ± 2 per cent of a single straight line. Using this fact to predict flow regime, a number of units have been successfully designed over the past two years encompassing several geometries, a large range of Renyolds numbers and throat widths from less than 1 in. to many feet.

Thus while one could wish that data were available over a wider range, particularly on inlet conditions, there seems to be little doubt that Fig. 6 contains at least much of the pertinent fundamental information on passage stall. It then remains to provide a better means for understanding the phenomena found. A beginning on this problem is given in the two following sections.

2 CLASSIFICATION OF STALLS AND RATIONALIZATION OF BEHAVIOR

Classification of Stalls by Use of Sigma Parameter

Consider a control surface including the boundary layer and a portion of the adjacent free stream on a wall in a diffuser as shown in Fig. 7. Take the definition of stall as any motion at the wall in the upstream direction. Since the observations discussed in Section 1 show that some stalled fluid is produced even at low values of adverse pressure gradient, it is appropriate to discuss the rate of production of stalled fluid. Define the rate of such actual backflows inside the control surface as w_b. If the flow in the entire diffuser is to be truly steady or periodically steady, then it is necessary that the backflow w_b must ultimately be removed and carried out of the diffusing passage: if this is not done, then more and more stalled fluid will accumulate in the diffusing passage, and the flow configuration by definition could not be steady or periodically steady. Since the observations show that such stalled fluid is removed by mixing with the main flow, it is appropriate to define another flow rate w_s as the *maximum rate* at which stalled fluid *can be removed steadily* by entrainment in the main flow under local conditions. This rate w_s need not actually be occurring since it is defined as a possible maximum. It is also understood that w_s represents a time average over at least one cycle if periodic events are occurring, and that it is a function of local flow conditions in the outer portions of the boundary layer and in the nearby free stream. We then form the qualitative parameter $\sigma = w_b/w_s$.[10] σ is called a qualitative parameter because at present there are usually no means available for calculating its numerical value accurately.

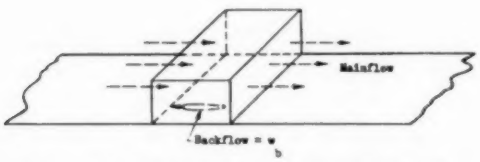

Fig. 7 Control surface for continuity analysis of stall

If we assume that $\sigma < 1$, then it follows that any stall which occurs must be transitory in nature since when w_s exceeds w_b, a given stall cannot exist 100 per cent of the time.

If we assume that $\sigma = 1$, then a steady-stall configuration occurs in which a finite area of the flow involves some kind of steady recirculation of fluid. This usually gives the classical or fully developed truly steady-stall model.

If we assume that $\sigma > 1$, then a shedding wake or periodic type large stall will occur. This is illustrated in Fig. 8(a). If w_b is temporarily greater than w_s, then the stalled area will increase in size by virtue of continuity as shown in Fig. 8(b). But such an increase in size cannot continue indefinitely. Ultimately, the stall

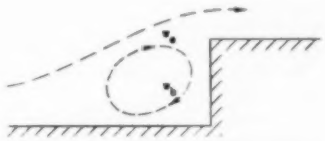

Fig. 8(a) Stall in a contraction corner

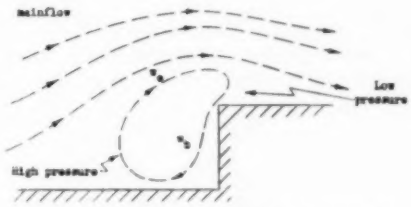

Fig. 8(b) Unstable growth of contraction corner stall

grows to the point where some portion of it becomes directly impinged upon by the momentum of the main stream as sketched in Fig. 8(b). When this occurs, a portion of the stall is torn away and moves downstream; the cycle then repeats itself. For reasons that will appear shortly, such stalls do not appear in diffusers, with faired walls, but do sometimes occur in sudden changes in cross section, as shown in Fig. 8, and behind bluff bodies in external flow.

Some Examples of Application of the σ Concept Including an Explanation for the Action of Vanes

Consider first a fully developed stall in a straight-walled diffuser. Application of a stability argument to the known flow

[10] This parameter was formulated independently by Chapman, et al. [19], but applied by them only to the truly steady stall. The ideas involved were also noted by Thomas [20] but do not seem to have been utilized in the present fashion prior to discussion by the author [17].

pattern, Fig. 9(*a*), shows the following: If in Fig. 9(*a*), w_b exceeds w_s, then the stalled area must grow in size. Application of Euler's *S*-equation between points *C* and *D* of Fig. 9(*a*) then shows that the pressure at the exit will decrease since:

Euler's equation:

$$p_2 - p_1 = \frac{\rho}{2}(V_1^2 - V_2^2)$$

Continuity yields $V_1W_1 = V_2b = V_2(W_2 - h)$, where h measures the distance from the wall to the dividing streamline of the mean flow, coming from the point of complete stall, *F*. Combining Euler's equation and continuity, gives:

$$p_2 - p_1 = \frac{\rho}{2} V_1^2 \left[1 - \left(\frac{W_1}{W_2 - h}\right)^2\right] \qquad (1)$$

And since h is increased, $p_2 - p_1$ decreases. But a decrease in p_2 reduces w_b, and increases w_s; it thus tends to equalize w_s and w_b and to create a steady flow or equilibrium configuration. Similarly, a deficit of w_b below w_s tends to shrink the size of the stall region, increase p_2, and finally to equalize w_b and w_s. Thus, if perturbed, the flow pattern of Fig. 9(*a*) tends to return to an equilibrium configuration in which steady flow occurs. Detailed observations, of course, show some periodic motions along the slipstream indicated by the lines *F-G* and *F-G'* in Fig. 9(*a*), but the major flow pattern is relatively steady.

This argument suggests that either a decrease in w_b or an increase in w_s can alter the flow pattern and the recovery measured. An increase in w_s will occur if large-scale fluctuations are present in the inlet. This probably explains, among other things, the large increase in the angle recorded for line *b-b* in Fig. 2(*a*) with increase in inlet turbulence. A more critical test of the argument can be realized by artificially decreasing w_b. Such an experiment has been carried out by D. E. Abbott at the author's suggestion. Mr. Abbott placed a small fence on the stalled wall as shown in Fig. 9(*b*). Despite the fact that this fence did not extend onto the side walls over the entire width of the stall, and that no attempt was made to optimize the size of the fence, a location was readily found where the recovery of the diffuser was increased approximately 10 per cent when no change was made except insertion of the fence.

The foregoing discussion introduced the notion of growth and decay of stalled areas of flow as a function of the value of σ at a given instant in time. This suggests that perhaps similar considerations can be used to account for the previously inexplicable results obtained with vanes and also for the observed shift of the point where complete stall begins to where it finally settles down on airfoils. To study the problems of stall inception and vane behavior, a diffuser was set up in a small water channel with a divergence angle of approximately 45 deg and an L/W_1 of 8 so that the flow pattern of the unmodified passage was a fully developed steady stall as shown in Fig. 2(*d*). A vane cluster of the type developed by Cochran [10] was then inserted; this blows out the stall quite rapidly (in approximately 5 to 10 sec for the flow rate employed). In order to insure a stall on a predetermined wall, the vane cluster was then cocked at a small angle to the center line of the unit. After a minute or so in this position, the vane cluster was removed and the build-up of the fully developed stall was observed.

This sequence of events was repeated a large number of times both with and without the introduction of various disturbances upstream. The flow patterns were studied by injecting dyes, and from these repeated observations a composite picture of stall inception as a function of time was achieved and checked. These studies indicated that stall is a growth phenomenon, that is, it begins with a local area in which w_b exceeds w_s. The growth of the stall area in this regime then pushes the main flow away from the wall which apparently decreases w_s locally and results in further stall growth until the stable flow pattern of Fig. 9(*a*) is reached. In the particular geometry employed, the stall starts in the corner just downstream from the throat, grows down the corner, then up the wall, and finally pushes its way out into the main stream. The successive pictures of the transient-stall growth are shown in the sketches of Figs. 10(*a*) through 10(*d*). The time required for these events is remarkably long (a minute or more compared to the 5 to 10 sec for removal by the vanes).

This growth explanation relies on the assumption that the initial stall acts in such a way that w_s is decreased locally or at

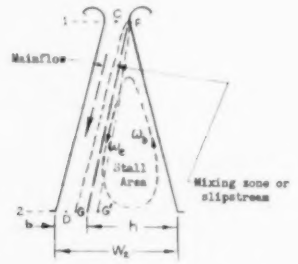

Fig. 9(*a*) Stability of fully developed stall in plane-walled diffuser

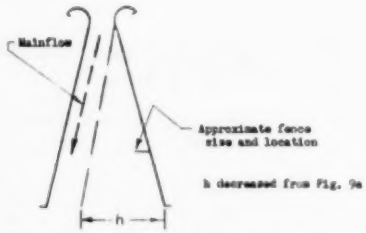

Fig. 9(*b*) Fully developed stall with blocking fence

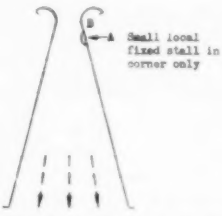

Fig. 10(*a*) Just after vanes removed (essentially unstalled flow; small stall begins at A)

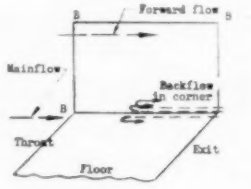

Fig. 10(*b*) About 20 sec after Fig. 10(*a*) (stall on wall B-B covers whole wall corner)

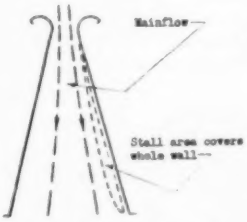

Fig. 10(*c*) About 40 sec after Fig. 10(*a*) (stall is now a slice covering whole channel depth)

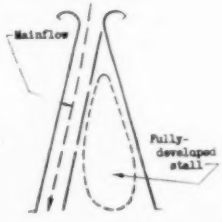

Fig. 10(*d*) 60–90 sec after Fig. 10(*a*) (stall is now fully developed)

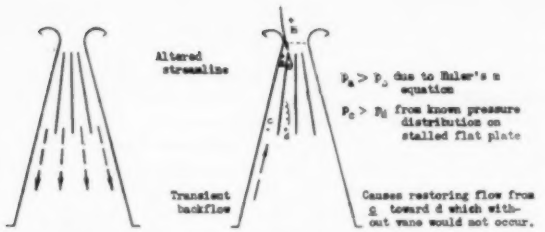
Altered streamline
Transient backflow
$P_a > P_c$ due to Euler's n equation
$P_c > P_d$ from known pressure distribution on stalled flat plate
Causes restoring flow from c toward d which without vane would not occur.

Fig. 11(a) Steady-flow pattern with short vanes. $2\theta = 28$ deg, $L/W_1 = 8$.

Fig. 11(b) Action of vanes under transient-flow conditions

least is not increased by the ensuing gradual change in flow pattern. This fact can be used to explain the success of the vane systems tested by Cochran [10]. In Fig. 11(*a*) is sketched the vane geometry illustrated previously with streamlines representing a steady flow. In Fig. 11(*b*) the same unit is shown with the streamlines that would occur if a stall area began to grow in the way shown in Fig. 10(*c*). Under the flow conditions of Fig. 11(*b*), the vanes take on a loading due to the angle of attack generated by the altered streamlines. The net effect of this loading is to direct more main-stream flow toward the area that has begun to stall and thus to raise w_c in the critical region.

The same result is obtained by considering each vane as an airfoil, and hence subject to the Kutta condition over some finite range of angle of attack near zero. This suggests that the real function of the vanes in these configurations is stabilization of the flow pattern by alteration of transient response. In the symmetric flow the vanes do very little, if anything, but, if a stall commences to build up, the action of the vanes causes a local increase in w_c where required; this provides a restoring action that is not present in the otherwise equivalent unvaned channel. This concept has been checked further by observations of the wall layers in the vaned passages; small transitory stalls are regularly observed, but these stalls do not build up and alter the entire flow pattern as they do when no vanes are present.

Consider again the flow past a step as shown in Fig. 1(*d*). Normally such flows are shedding wakes in incompressible flows although the data are very limited. It is quite possible that, by bleeding a small amount of flow from the corner, in order to achieve a balance between w_b and w_c, a stable flow without shedding can be achieved. Such a configuration would be very useful in many design situations provided that the amount of bleeding required is not too large. This suggestion is verified to some degree by the results found by Hazen[11] in vortex-trap diffusers. Hazen's experiments in one case showed that a shedding wake from a recirculating vortex-trap region could be stabilized by a small amount of bleed.

Comparison of Internal and External Flow in Terms of the σ Concept

Inherent in the stability argument introduced in the preceding section as an explanation for the excellent results achieved by use of flat-vane systems in diffusers is the conception that the stall characteristics of a given surface can be modified by the presence of another nearby solid surface even though the pressure gradients of the steady flow are unaltered. If this is true, then it must imply that the stall characteristics of narrow passages are different, at least in part, from those of airfoils and other bodies in external flow. This is, in fact, apparently correct inasmuch as the data presented by Abbott and Doenhoff [7] show that the typical airfoil exhibits a sharp break in performance very soon after the onset of large stalls while the data of Gibson [26] on conical diffusers and Cochran [10] on two-dimensional diffusers show in both instances a very much slower drop in performance after the beginning of stall.

Apparently, then a nearby solid wall can exert a restraining action on the free stream which tends to deter the growth of large stall areas. This restraining action operates both due to continuity, for fixed flow rate, and also due to the close coupling between the pressure rise in the diffuser passage and the exit width of the main stream exhibited by equation (1). If this is true, it also should follow that a passage with large L/W_1 should be more affected by this restraining action than a passage with low L/W_1. This is substantiated by considering the limit, $L/W_1 \to 0$, and the data of Fig. 2(*a*). The case $L/W_1 \to 0$ corresponds to external flow ($W_1 \to \infty$) and also to a sudden expansion ($L \to 0$). In both these cases, the stall characteristics are relatively abrupt, and the flow can be described fairly appropriately as either stalled or unstalled. This does not imply that stall on an airfoil need occur abruptly in time or that a stall region is entirely steady near its nose.

As noted previously, the stall usually starts in some small areas and grows, and there is usually a definite area just upstream of the nose of the stall area in turbulent boundary-layer stall where considerable unsteadiness occurs. The difference is that in external flow when a large stall begins to develop, it grows to some finite size so that some appreciable area of the wall is fully stalled all the time in the steady state, and the complete stall then begins at a *relatively* fixed location in space. In passages of large L/W_1 a finite and important regime exists in which large stalls grow and wash out over large distances in an apparently periodic fashion. The data for airfoils showing abrupt stall characteristics is of course well known, and was the source of the description of stall as a steady flow initially, but it must be remembered that these data are the steady-state patterns that result after the stalled flow has reached some equilibrium configuration.

An abrupt stall in a passage requires that the lines *a-a* and *b-b* approach each other. Fig. 2(*a*) shows that this is precisely what happens as $L/W_1 \to 0$. The curves indicate that the lines *a-a* and *b-b* intersect in the region $1/2 < L/W_1 < 2$; at lower L/W_1 the onset of stall is then relatively sudden changing from a largely unstalled configuration to a fully developed stall without the intermediate stage of large transitory stall. The exact value of the intersection depends strongly on both the free-stream turbulence level and the downstream geometric configuration. The value of $L/W_1 \simeq 1$ corresponds to the case of low inlet turbulence level and a long pipe of constant area downstream; however, the data in this region are at present very limited.

Since the relative size of the large transitory-stall region in passages as measured by the ratio of the angle at line *b-b* to that at line *a-a* increases uniformly as L/W_1 increases, the tendency of the flow pattern to break down to a fully developed stall is apparently more and more inhibited as L/W_1 increases. This is shown by the fact that in Fig. 6 the actual value of pressure rise achieved increases as L/W_1 increases in any one set of homologous data prior to the onset of large transitory stall.

The explanation of the previous paragraph also suggests at least something about the question, "Why does the irregular large fluctuating flow region called large transitory stall occur at all?" The answer apparently lies in the fact that, while the large pressure recoveries in this region create a w_b too large to permit a stable flow pattern of the potential-flow, boundary-layer type, at the same time the restraining influence of each wall on the other is large enough so that a complete flow breakdown cannot occur. That is, the fully developed stall pattern is also unstable between lines *a-a* and *b-b* because the opposite wall will not physically allow the main stream to deviate a sufficient distance from the wall on which the stall commences. Apparently a time fluctuation in

[11] By private communication from Mr. T. Sweeney.

the value of σ thereby results so that the large stalls appear and disappear. Such a time fluctuation in σ could be generated either by time variation in the upstream disturbances entering the diffuser, or by the sequence of flow patterns that inherently occur during the growth of stall on one wall. The relative importance of these two effects has not been studied at the present time.

Losses and Transient Effects Including a Thermodynamic Analysis

For many years it has been known that the losses in diffusing passages are very high. This fact led some early observers to conclude that the friction factors increased in adverse pressure gradients. However, the careful work of Ludwieg and Tillmann [21], Clauser [14], and many others has clearly shown that the wall shear drops sharply in adverse pressure gradients as would be expected from consideration of the mean velocity profiles of the boundary layer. Despite this, typical diffuser efficiencies are far below comparable nozzle efficiencies. In addition to this result many observers have noted that fluctuations occur in diffusers of even very small divergence angle.

Both of the previous results are inexplicable in terms of the velocity gradients of the mean flow, but if one admits the picture of small stalls very near the wall that arise from the inherent flow model of the wall layers of the turbulent-shear layer in adverse pressure gradients, as described in [11], then an explanation can be provided. As noted in Section 1, increases in the value of adverse pressure gradient increase the transverse size, decrease the length of the small streaks of stall, and increase the number of such streaks occurring. As reported in [11] each such streak is associated with the production and break up into eddying fluctuations of a longitudinal vortex system arising from the wall layers. Thus the increased number and transverse size of the streaks of stall imply the generation and breakdown of an increased number of longitudinal vortex systems of increased size as well as increased mixing due to the streaks of stall. These facts, taken together, imply increased losses, increased pressure pulsations, and increased Reynolds stresses at greater distances from the wall.

It is also instructive to analyze the thermodynamics of the flow in an adverse pressure gradient. Consider a particle in a diffuser, for example near the wall just downstream of the throat in Fig. 10(*a*). Any such particle of fluid in the diffuser, which has a total pressure less than the exit pressure, cannot move out the end of the diffuser unless a certain minimum amount of work is done upon it. This follows from the fact that, if the particle is decelerated to zero velocity, it still will not have a pressure as great as the exit pressure. An explicit proof of this fact is now given. We begin with the energy equation for the steady motion of a particle through the control surface in the form:

$$dQ = dh_F + dW_x \tag{2}$$

By definition $h_F = e + p/\rho$, and dW_x is the work done by the particle exclusive of flow work. In the present case we are considering adiabatic flow, and hence dQ is zero. Noting that the only internal energies stored in the particle are the internal thermal energy e_i and the kinetic energy $V^2/2$ we can then write Equation (2) as

$$dh_F = de_i + pd\left(\frac{1}{\rho}\right) + \frac{1}{\rho}dp + VdV = -dW_x \tag{3}$$

where the minus sign denotes work input. Furthermore, for one pure substance in the absence of effects of fluid shear, capillarity, and external fields, and for the observer who rides on the particle, the first law, second law, and state principle of thermodynamics require that:

$$Tds = pd\left(\frac{1}{\rho}\right) + de_i \tag{4}$$

For a particle undergoing an adiabatic process the second law of thermodynamics also dictates that the entropy of the particle may not decrease. Consequently, the sum $de_i + pd(1/\rho)$ must be greater than or equal to zero; the greater than applies to any irreversible and the equality to any reversible process. Under the best possible conditions, that is, for a reversible process, a given particle must therefore obey the equation

$$\frac{1}{\rho}dp + VdV = -dW_x \tag{5}$$

If the work input is zero, the maximum possible pressure rise is then

$$p_0 - p = \int_V^0 -\rho V\, dV \tag{6}$$

Equation (6) is, of course, nothing but Euler's equation and could have been used at the outset. However, if the more general form, equation (3), is also used, the minimum quantitative amount of work required for a given pressure rise can be expressed.

Suppose that the following process is carried out. Let the particle move downstream reversibly, adiabatically, and without work interchange until its velocity is zero. The pressure rise created is then given by equation (6) and the final pressure achieved is stagnation pressure by definition. However, it was assumed initially that the particle has a stagnation pressure less than the exit pressure of the diffuser. Since the velocity V of the particle is now zero, equation (5) dictates that any further pressure rise can only occur if

$$-dW_x > 0 \tag{7}$$

that is, a certain minimum work input is required. The value of this minimum work input is the same for any reversible path between given end states, and it may thus be found for the process just discussed by equation (5). It is consequently

$$-(W_x)_{\min} = \int_{p_0}^{p_{exit}} \frac{1}{\rho}\, dp \tag{8}$$

For an incompressible flow, equation (8) integrates immediately to give

$$-(W)_x = \frac{1}{\rho}(p_{exit} - p_0) \tag{9}$$

or more generally, we can write by use of the mean value theorem

$$-(W_x) = \frac{1}{\bar{\rho}}(p_{exit} - p_0) \tag{10}$$

where $\bar{\rho}$ is a suitable average density which will always lie between the extreme values of ρ involved in the integration. Since ρ is always greater than zero by definition, no ambiguity of sign can occur in either equation (9) or equation (10). It therefore follows that the requirement of a work input exists only for particles that have a deficiency in total pressure. Furthermore, the minimum work requirement is, at least to a first approximation, proportional to the difference between total pressure and exit pressure. It is also evident that it is impossible for such a work requirement to exist in a favorable pressure gradient zone since by definition if $\partial p/\partial x < 0$ then

$$p_{exit} < p < p_0$$

In simple diffusers, where the only possible source of the work required on the particles with deficient stagnation pressure is the

kinetic energy of the main stream, a large fraction of the work required for low-speed particles will necessarily be accomplished by shear effects and will thereby increase the total losses. Despite this, no present-day analysis of diffusers accounts for losses of this type. Since equation (10) shows that the work required is very sensitive not only to the character of the inlet boundary layer but also to the excess of leaving pressure over stagnation pressure of the low-energy particles, it follows that in units operating with high recovery it is to be expected that the amount of transient effects will increase as one progresses down the wall toward the exit. The analysis also suggests that such units probably will have some local transient backflows of appreciable size even though the mean flow velocity is forward at all points. In addition, other things being equal, the effect of inlet conditions will be more pronounced in a unit with higher recovery and hence more noticeable as one moves down the wall of a given diffuser toward higher area ratios in an apparently unstalled flow. The observations of Moore [9] and the results of Chapman, et al. [19], also show that inlet conditions have a very strong influence when large areas of stall occur. Thus there is a general tendency for the effect of inlet conditions to become more important as the geometry is altered in the direction of movement upward or to the right on Fig. 2(*a*).

Verification of the increased effect of inlet conditions at higher recoveries is shown in the data of Uram [30]. Increased losses due to increased thickness of inlet boundary layer are visible in the results of Uram [30] and Copp [32]. Excellent quantitative verification of the increase in transient effects appears in the recent paper by Robertson and Calehuff [22]. They report detailed measurements of mean velocity profile, shear and of u' and v' rms fluctuations at several stations in a conical diffuser with a total divergence angle of 7.5 deg and an L/R_1 of 15.6. This geometry lies only slightly below line *a-a* in Fig. 6, and thus we would anticipate that strong fluctuations involving streaks of reverse flow near the walls would occur, but that a complete reversal of the main flow would not. If the succession of states described in Section 1 in connection with Fig. 4 is appropriate, then in addition it would be expected that the magnitude of these reverse flows would increase in the downstream direction as also suggested from the thermodynamic analysis just given. These predictions are substantiated by Robertson and Calehuff's data. The mean velocity profile nowhere reverses, but the rms magnitude of the u' fluctuations increases steadily in the downstream direction; the rms value of u'/U near the wall reaches 70 per cent just before the exit. Since the mean velocity in this same region does not exceed 10 per cent of U, it is clear that very strong backflows must occur locally despite the forward mean flow.

Conclusions Regarding the σ Concept

The great disadvantage of the σ concept is the present inability to calculate its value quantitatively. Despite this it appears to be at least an important missing part of the problem of stall since it is sufficient to rationalize all known forms of boundary-layer control and also to rationalize a number of otherwise inexplicable results.

The σ concept is based on the observation that production of stalled fluid arises primarily from regular three-dimensional, transient backflows very near the walls. This idea seems central to a full understanding of stall processes, and further discussion of it is given in the final section.

3 RELATION BETWEEN DIFFUSER PERFORMANCE AND BOUNDARY-LAYER THEORY

Preliminary Remarks

In Sections 1 and 2 a number of results have been given which demonstrate that classical steady boundary-layer theory alone is not sufficient to explain the observed stall performance of passages. In addition to boundary-layer concepts the stability of the over-all flow pattern, particularly as affected by mixing between the main stream and the wall layers apparently is important in determining the stall characteristics of passage flows. The purpose of the present section is to assess further the meaning of these results and thus hopefully to suggest approaches by which an adequate solution to the problem of stall in passages may possibly be achieved.

In order to avoid any misunderstanding, it is stated at the outset that the utility and validity of boundary-layer theory as a whole are not subject to question. What is under question is the limit of validity of such theories in two specific ways: (*a*) Is classical boundary-layer theory alone adequate for dealing with flows at or very near stall and at very high values of adverse pressure gradients? (*b*) Can the same correlation, boundary layer or otherwise, be used to describe the stall characteristics of both external flow and passages of moderate and high L/W_1? The discussion of these questions is preliminary and suggestive rather than final or definitive; while it hopefully clarifies some aspects of the problem, further data and study definitely will be required before final conclusions can be given with adequate assurance.

A Simple Force Analysis

To make clearer the nature of the physical processes occurring near stall, and hence to suggest what must be looked for, it is useful to make a simple force balance on an element of the wall layers of the flow. The wall layers are in general the source of production of stalled fluid, and are thus the crucial layers. The intent of this analysis is to find what forces act, not to examine their nature in detail; it is thus appropriate to use the simplest possible momentum analysis. Such an analysis is constructed on the basis of the control volume of Fig. 12.

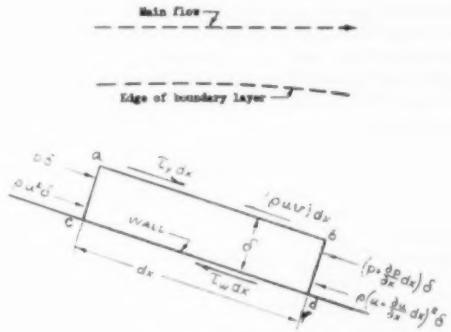

Fig. 12 Control surface for force analysis of wall layers

Fig. 12 shows a control surface including a small section of the wall layers with the outer surface taken parallel to the wall. In Fig. 12 we define τ_y as the average shear, laminar and turbulent, on the outer surface *ab*. The control surface is drawn so that the surface *ab* is parallel to the wall at a distance δ. The dimension δ approximates the total thickness of the so-called laminar sublayer and buffer layer. We adopt the point of view that a steady flow does exist with a *mean* motion of the wall layers in the forward or downstream direction, and we then look for the equilibrium of forces in the x-direction required to fulfill this assumption. In this point of view it is justifiable to assume that $\delta(\partial p/\partial y) = 0$. The momentum theorem then yields for incompressible steady flow

$$p\delta + \tau_y dx + \rho u^2 \delta =$$

$$\left(p + \frac{\partial p}{\partial x}\,dx\right)\delta + \tau_w dx + \rho\left(u + \frac{\partial u}{\partial x}\,dx\right)^2 \delta + \rho u v\,dx$$

Cancelling first-order terms, dividing by dx, expanding

$$\left(u + \frac{\partial u}{\partial x}\,dx\right)^2$$

and rearranging gives

$$(\tau_y - \tau_w) = \delta\frac{\partial p}{\partial x} + 2\rho u\frac{\partial u}{\partial x}\delta + \rho u v \tag{11}$$

Also continuity requires

$$\rho u\delta = \rho\left(u + \frac{\partial u}{\partial x}\,dx\right)\delta + \rho v\,dx$$

or

$$\delta\frac{\partial u}{\partial x} + v = 0 \tag{12}$$

Inserting Equation (12) into Equation (11) provides a cancellation of terms which gives

$$\tau_y - \tau_w = \delta\left(\frac{\partial p}{\partial x} + \rho u\frac{\partial u}{\partial x}\right) \tag{13}$$

Dividing Equation (13) by $\delta(\partial p/\partial x)$ to normalize yields

$$\frac{(\tau_y - \tau_w)}{\delta\dfrac{\partial p}{\partial x}} = 1 + \frac{\rho u\dfrac{\partial u}{\partial x}}{\dfrac{\partial p}{\partial x}} \tag{14}$$

If U is the free-stream velocity, then by definition $u \ll U$. Furthermore, if we demand that the *mean* flow of the wall layers be forward over an appreciable distance on the wall of a diffuser then $\partial u/\partial x < U/x$; since $u/U < 0.2$ and if U decreases by as much as 20 per cent, then $\partial u/\partial x > U/x$ would require a *mean* flow upstream near the wall after a short distance. Finally, to at least a first approximation

$$\frac{\partial p}{\partial x} = -\rho U\frac{\partial U}{\partial x}$$

and therefore

$$\frac{\rho u\dfrac{\partial u}{\partial x}}{\dfrac{\partial p}{\partial x}} \simeq \frac{\rho u\dfrac{u}{x}}{\rho U\dfrac{U}{x}} = \left|\frac{u^2}{U^2}\right| \ll 1$$

This argument merely states that the mean momentum of the wall layers is of the order of u^2 and thus in the absence of back flows in mean velocity the steady forces arising from changes in the momentum flux of these layers is small compared to the pressure change for large changes in U since Δp is of the order of ΔU^2.

Thus the force equilibrium of the wall layers for *mean* forward flow contains only two significant terms; namely, a retarding force $\delta(\partial p/\partial x)dx$ and a balancing forward force $(\tau_y - \tau_w)dx$. Accordingly, the necessary condition to maintain a steady mean forward flow of the wall layers is that these two forces balance, that is

$$\frac{\delta}{\tau_y - \tau_w}\frac{\partial p}{\partial x} \cong 1 \tag{15}$$

Equation (15) has a number of important implications. It is clear that so far as the crucial wall layers are concerned the pertinent nondimensional parameter has nothing to do with either length in the flow direction or the dynamic pressure of the free stream since both of these parameters cancel out in the appropriate normalization. This same conclusion was emphasized by Clauser [14]. Despite this a number of workers still utilize the conventional Euler number $(x/q)\partial p/\partial x$ in attempts to correlate results on stalls. Such a correlation can be expected to work only if there is a unique relation between the shear and the mean velocity distribution such that

$$\delta/(\tau_y - \tau_w) \approx x/q \tag{16}$$

Apparently such a relation does exist for certain cases of families of equilibrium flows. However, there is no immediately obvious reason why Equation (16) should be generally true. A similar comment relates to normalization based on wall shear τ_w alone; Equation (15) shows that it is the excess of τ_y over τ_w that is crucial, and thus normalization on wall shear values taken from zero pressure-gradient flows is certain to provide misleading results. What is more, it is questionable whether a correlation parameter employing only wall shear as suggested by Clauser [14] is sufficient. This follows from the fact that the two parameters

$$\frac{\delta}{\tau_w}\frac{\partial p}{\partial x} \text{ and } \frac{\delta}{(\tau_w - \tau_y)}\frac{\partial p}{\partial x}$$

will be the same only if there is a unique relation between τ_w and τ_y.

Finally, and most important, the force analysis shows clearly that the crucial quantity in preventing stall is the shear stress τ_y since it gives rise to the only force of appreciable magnitude acting on the wall layers of the flow in the direction needed to prevent complete stall.

In a turbulent boundary layer the dominant term in the shear τ_y arises from momentum transport effects, that is, from a Reynolds stress rather than from laminar shear. As shown in [11] the pertinent stress appears to be due to the mixing arising from a transient three-dimensional instability in the wall layers which gives rise to streaks of back flow even at relatively mild adverse pressure gradients.

At present not enough is known about these instabilities in a turbulent shear layer to make meaningful detailed calculations concerning the term τ_y; however, the foregoing remarks make clear that the transient mixing effects are crucial in determining stall onset and behavior since they give rise to the dominant part of the critical τ_y term. It must therefore follow that complete understanding of the problem of stall of turbulent shear layers must encompass more than merely description of the mean velocity profiles unless there is an entirely unique relation between the mean profile and the fluctuating terms for all possible turbulent shear layers.

The inherently three-dimensional nature of the motions of the wall layers reported recently by a number of observers [11] do not necessarily prohibit the use of a two-dimensional boundary-layer theory so long as one remains in the *small* transitory stall region; in that region, the three-dimensional aspects of the flow are repeated a sufficient number of times, even on relatively small walls, so that it may be possible to represent the shear stress τ_y quite adequately by a suitably defined two-dimensional average.

The foregoing remarks about possible two-dimensional averages should not be construed as implying that such methods can be extended to include the prediction of the onset of large stalls in passages of high L/W_1. Since the stall inception in that case involves large three-dimensional transient flows of the same order of size as the passage, it is quite unlikely that any purely two-dimensional, steady theory will be successful in predicting the

behavior of such a flow regime. Furthermore, the observations of Robertson and Calehuff [22] and the visual studies reported in [11] both show quite clearly that τ_y does increase strongly as the flow goes toward separation. The values of u'/U measured in a 7.5-deg diffuser by Robertson and Calehuff reach 5–10 times the maximum values found in typical zero pressure-gradient layers before the occurrence of any large-scale stalls were found. This makes clear the risk inherent in using intensity, mixing length, or "eddy" viscosity values taken from zero pressure gradient or pipe flows as a means for determining the constants required for calculation of the turbulent layer in adverse pressure gradients.

Perhaps even more important than the preceding remarks in so far as stall in passages is concerned is the relation between the shear τ_y and the σ-concept discussed in Section 2. This relation can be used to clarify somewhat further the possible reasons for the considerably different stall behavior of internal and external flow reported in the foregoing. Consider what happens if at some section of the wall the shear term τ_y is not large enough to balance the pressure forces; that is, Equation (15) is not satisfied. Then a mean forward flow of the wall layers cannot occur, and the unbalanced forces will cause accelerations in the wall layers in the upstream direction resulting in the piling up of stalled fluid near the wall. If this process results in pushing the main stream away from the wall, as is apparently the case in external flow and in the fully developed stall regime in passages, then no compensating rise in τ_y need occur; it is then easy to visualize a breakdown of the entire flow pattern until some new, relatively steady equilibrium condition is achieved. On the other hand, in a narrow passage with constant through-flow, if stalled fluid begins to pile up on the wall, the main flow is constrained by the opposite wall to remain in close proximity to the growing stall region. Under these conditions, the observations of [11] suggest, but definitely do not prove, that the mixing would be increased, and hence τ_y would increase. This increase in τ_y, if taken together with a temporary alteration in the pressure forces due to the brief existence of the finite stalled region in the channel, might well be sufficient to provide the periodic increases in σ that are necessary to maintain the large transitory stall pattern. If these remarks are correct, then it should follow that stall prediction based on data taken in external flow would predict stall in passages far sooner than it actually occurs.

Use of Classical Boundary-Layer Theory to Predict Stall

Perhaps the most thorough study of the applicability of boundary-layer theory to the fluid motions all the way to and including stall is that of Hewson [23]. Unfortunately, this work is not generally available; however, it shows that in the region approaching a fully developed stall the Karman boundary-layer integral equation is not obeyed. Hewson reports that the flow in this region is quite unsteady. However, by making rough measurements of the pressures he found that large values of dp/dy did occur, and that if these measured dp/dy-values were used to compute a correction to classical boundary-layer theory in a form suggested by Squire, then about two thirds of the 100 per cent discrepancy between the data and the predictions of the Karman integral equation could be eliminated. It is not clear whether the remaining third arises from Reynolds' stress or uncertainty in the data. Hewson's view of the problem is that incorporated in the classical stall model, but his remarks suggest that transitory stalls did occur in his experiments before the point of full stall more or less as described in connection with Fig. 4 in Section 1. Consideration of the sharp curvature which occurs as a streak of stall turns back downstream near the wall, Fig. 3, makes it relatively easy to understand how such dp/dy-terms could be generated on the average well upstream from the point where fully developed stall occurs. If this view is correct, then Hewson's results can be interpreted as the average or steady-state manifestations of the remarks made, in the foregoing discussion, on the importance of the mixing between the free stream and the wall layers.

However, Hewson's result also demonstrates a discrepancy from classical theory quantitatively in another sense since a necessary condition for use of the normal boundary layer equations is that dp/dy is small. If this condition is not obeyed, and Hewson's work shows clearly that it is not for some distance upstream from the point where fully developed stall commences, then for this reason alone it is not to be expected that classical boundary-layer theory will be sufficient to predict separation. From this same point of view, it is quite apparent that boundary-layer theory cannot really be sufficient to predict what occurs exactly at a point of complete separation since Fig. 1(*c*), showing the classical stall model, demonstrates that strong streamline curvature must occur in the main flow, and hence large dp/dy-terms must occur near the nose of the separated region.

In assessing the possible utility of boundary-layer methods for practical calculations of flows with adverse pressure gradients, one other result due to Coles [24] is very important. Coles has made extremely careful comparisons of the data from the best available observations by a number of workers on the applicability of the Karman integral equation of the boundary layer. In all cases Coles finds excellent agreement for flows with negative, zero, and very slightly positive pressure gradients. On the other hand, for flows with moderately strong adverse pressure gradients and near full stall no agreement at all is found. The complete reason for this disagreement is not understood by Coles (or anyone else apparently) at the present time. It may well be due to any or some combination of dp/dy-effects, transient effects, or lack of two-dimensionality in the flow. The foregoing discussion concerning streaks of stall at least suggests that the transient effects and the dp/dy-effects are closely related, and it could probably be tentatively concluded that the difficulty arises from neglect of these terms were it not for the fact that the tremendous sensitivity of the boundary-layer velocity profile to remarkably small three-dimensional components in the main flow has been demonstrated by a number of workers. Since the stall data reported here include large-scale three-dimensional effects in some instances, it is clear that the problem will require further study before a final conclusion on the complete reasons for the discrepancy between the Karman integral equation and the measured data can be made clear.

In the meantime, it is also clear that any prediction of stall which assumes that dp/dy is small, or relies on the Karman integral equation for the basic computation method must be viewed as a dubious procedure.

However, this definitely does not rule out the possibility of some form of velocity-profile similarity up to, including, and past full stall, since such correlations are empirical and do not rely on the assumptions of boundary-layer theory. Such a result for separated flows has been achieved in fact by Coles [24] for at least a few cases of external flow in the form of a remarkable correlation which he has called the "law of the wake."

Comparison of Predictions From Internal and External Flow

The direct observations and the over-all data both indicate that the growth of stall in passages of high L/W_1 and in external flow are quite different. The more detailed force analysis also suggests that the stall should occur later in passages of high L/W_1 than in external flow. If this is true then, even if a definite similarity of mixing effects and velocity profile exists for external flow all the way to stall, L/W_1 is a parameter that is out of control for the case of passage flows, and it may be necessary to make a sharp distinction between passage flows and external flows in

order to achieve uniformly correct predictions of stall by any means. This idea of a missing parameter is certainly in keeping with the one fact that is common to the many methods of stall prediction, that is, they all work in some cases but not in others.

A recent survey of the empirical data has been given by Bam-Zeilovitch He determines a stall parameter from normalization of the Navier-Stokes equations; this parameter he expresses as $(\delta/q)(\partial p/\partial x)$. He then shows that there is a reasonably constant value of this parameter for the data from external flow. Using this same value for diffusers he then ventures a prediction that a conical diffuser with a total included angle of 6 deg will stall completely, essentially at the throat, if it is preceded by two or more diameters of straight pipe just upstream from the entrance. However, this result is totally at variance with the data of Gibson [26] as shown in Fig. 6. Gibson has a longer entrance pipe than that assumed by Bam-Zeilovitch, but nevertheless the data show no large stalls will occur until an L/R_1 of 30 to 40 is reached. This result is characteristic of the difficulty encountered in using external flow correlations in passages of high L/W_1.

In Fig. 13 results of a portion of calculations performed by members of a graduate class at Stanford University[12] are compared with the line a-a from Fig. 6. The methods of computation suggested by Doenhoff and Tetervin [33] and Ross [3] are presented. The inlet conditions and Reynolds numbers used were taken to correspond to the data of Cochran [10]. It is interesting to observe that the methods of Ross and Doenhoff and Tetervin give equivalent results for the whole range of interest at least with these inlet conditions. It is also clear that, while both methods give a reasonable result for low values of L/W_1, they predict stall at values farther and farther below the observed inception of large transitory stall as L/W_1 increases. Thus at 7 deg both calculations predict stall at L/W_1 of 9, but in reality no large stalls are observed until L/W_1 reaches 25. Since W_1 in these computations was 3 in., this corresponds to an error of some 48 in. in wall length.

In 1954, Clauser [14] introduced a more rational method for correlation of turbulent boundary-layer characteristics based on the concept of "equilibrium" flows. This work has been considerably extended by Coles [4] and Townsend [5, 2]. Both Townsend and Coles have shown that an equilibrium turbulent layer is characterized by a constant value of Euler's number in the form $(x/q)(\partial p/\partial x)$, and that a limiting value for this parameter exists. Coles suggests that this limit represents a continuously separating layer and Townsend remarks that it probably represents an upper limit of "equilibrium" boundary-layer theory. It is useful to compare these results with those obtained from the data of Fig. 6 and the empirical methods of Ross and of Doenhoff and Tetervin. These comparisons must be interpreted with caution since the results of Townsend and Coles apply strictly only to equilibrium flows coming from upstream infinity with a constant Euler number everywhere, but in a straight-walled diffuser the ideal Euler number constantly increases. Nevertheless, it is clear from Fig. 13 that the results of Coles for equilibrium boundary-layer theory do not provide a means for prediction of stall. The results of Townsend [5] have not been plotted since Coles' result appears to be in better agreement with the available data from external flow. However, it is worth noting that Townsend's result would have precisely the same slope in Fig. 13 as that of Coles but would lie a factor of two higher at all points. Thus while it would be closer to agreement it would still fall below the results found from the semiempirical methods plotted and would thus also fail to predict the diffuser results.

In Fig. 13, the results from equilibrium theory appear as a line of constant slope minus 1, the results from the semiempirical methods are represented by a line of slope approximately minus

[12] Thanks are due to Messrs. R. W. Fox, R. E. Lundberg, R. A. Storholm, D. P. Jordan, and M. E. Davenport for these results.

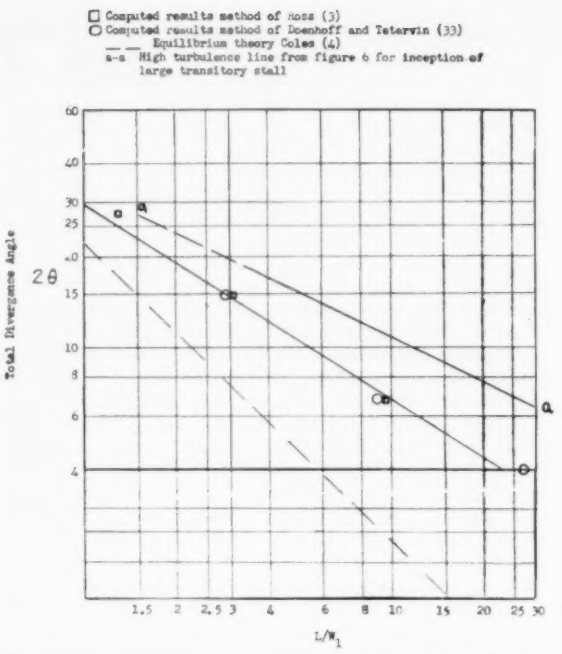

Fig. 13 Comparison of line a-a with computed results of empirical methods and equilibrium theory

0.62, and the line a-a has a slope of approximately minus 1/2. Furthermore, as anticipated in the discussion of the effect of L/W_1 on stall, the actual stall inception diverges systematically from the results of the predictions, as L/W_1 increases. At low L/W_1 the predictions of the semiempirical methods, the results of equilibrium boundary-layer theory and the data at least approach order of magnitude agreement, but at high L/W_1 all prediction methods indicate stall far too soon. This result definitely tends to confirm the suggestion made in the foregoing that the stalls in passages of high L/W_1 are affected by nearby walls in such a way that the onset of large stalls is delayed. In comparing these various results, it must be remembered that the boundary-layer methods all predict a two-dimensional, steady, complete stall. Thus in one sense they should be compared with the fully developed stall model shown as line b-b in Fig. 2(a). Despite this considerable "benefit of doubt" given the prediction methods they still all predict stall far too soon in passages of high L/W_1. This again emphasizes the need for inclusion of stability considerations and of transient elements in the flow models for predicting the onset and behavior of stall in passage flows. These remarks suggest that the answer to both of the questions raised concerning use of boundary-layer theory at the beginning of this section are negative. It also follows from the foregoing remarks on transient mixing effects that the underlying but unstated problem still remains the construction of an adequate method for prediction of the behavior of turbulent shear layers. Further careful experimental work should make clear the physical facts involved, but whether or not a theory can be formulated that is adequate but is still sufficiently simple for engineering purposes cannot yet be foreseen.

Conclusions

The major conclusions of the three sections of the paper taken together appear to be as follows:

1 Stall in passages is a spectrum or series of stages of condi-

tions including transient and three-dimensional, as well as steady and two-dimensional, effects.

2 In a turbulent boundary layer, small streaks of stall occur very near the wall even for relatively modest values of adverse pressure gradient; consequently, the use of a parameter expressing the ratio of the rate of production of stalled fluid to the steady maximum possible rate of removal by main-stream forces provides a more adequate and useful description of stall than the conventional stall or no-stall description.

3 The data on vaned diffusers and the correlation of optimum recovery data from all known results, suggest that the stall characteristics of passages with high values of length-to-width ratio are not the same as the stall characteristics of airfoils and other objects in external flow. In passage flows, the stall characteristics are greatly influenced by the stabilizing effect of nearby walls. This conclusion is substantiated by preliminary comparison of the available prediction methods with diffuser-performance data.

4 The considerable preponderance of evidence available, including particularly the results of Hewson and the vaned-diffuser data, suggested that boundary-layer theory alone is not sufficient to predict the onset or the behavior of stall. This remark applies primarily to calculations based on the assumption that dp/dy is zero across the shear layer inasmuch as direct correlations of velocity profile including stalled and reattaching flows have already been achieved for some cases.

5 Complete analysis of either the losses inherent in adverse pressure-gradient flows containing boundary layers or the prediction of the onset and behavior of stalls apparently requires knowledge of inlet conditions and must involve analysis of the transient as well as the steady behavior of the flow.

6 Further correlations of the type shown in Fig. 6, careful study of the various stall data to account for the L/W_1 effect, additional studies of not only the mean flow but also the transient characteristics of both boundary layers and of stalled flows, and more fundamental studies on the basic flow models of the turbulent shear layer are probably all needed in order to achieve a complete and reliable means for understanding and predicting stall behavior. Until at least considerably more data of these types are available, it is questionable whether any theoretical method can be firmly enough grounded in physical fact to insure a much more successful solution to the stall problem than those already achieved by the extremely numerous methods now available. In the meantime, it is likely that predictions of stall based on correlations of the type shown in Fig. 6 will supply not only simpler but also more reliable results for passage flows than any available theoretical method.

References

1 S. J. Kline and R. C. Dean, Jr., "Unresolved Problems of Fluid Mechanics," *Mechanical Engineering*, vol. 80, December, 1958, pp. 54–55.

2 A. A. Townsend, "The Structure of Turbulent Shear Flow," The University Press, Cambridge, 1956.

3 D. Ross, "A New Approach to Turbulent Boundary Layer Problems," *Proceedings ASCE*, vol. 81, 1955, Separate No. 604.

4 D. Coles, "Remarks on the Equilibrium Turbulent Boundary Layer," *Journal of the Aeronautical Sciences*, vol. 24, 1957, pp. 495–506.

5 A. A. Townsend, "The Properties of Equilibrium Boundary Layers," *Journal of Fluid Mechanics*, vol. 1, 1956, pp. 561–573.

6 H. Schlichting, "Boundary Layer Theory," McGraw-Hill Book Company, Inc., New York, N. Y., 1955.

7 I. H. Abbott and A. E. Doenhoff, "Theory of Wing Section," McGraw-Hill Book Company, Inc., New York, N. Y., 1949.

8 S. J. Kline, D. E. Abbott, and R. W. Fox, "Optimum Design of Straight Walled Diffusers," Stanford University, Report PD4, April, 1958, published in this issue, pp. 321–331.

9 C. A. Moore, Jr., and S. J. Kline, "Some Effects of Vanes and of Turbulence in Two-Dimensional Wide-Angle Subsonic Diffusers," U. S. NACA TN 4080, June, 1958.

10 D. L. Cochran and S. J. Kline, "The Use of Short Flat Vanes for Producing Efficient Wide-Angle Two-Dimensional Subsonic Diffusers," NACA TN 4309, September, 1958.

11 S. J. Kline and P. W. Runstadler, "Some Preliminary Results of Visual Studies of the Flow Models of the Wall Layers of the Turbulent Boundary Layer," *Journal of Applied Mechanics*, vol. 26, TRANS. ASME, vol. 81, 1959, pp. 166–170.

12 W. F. Durand, "Aerodynamic Theory," Springer, Berlin, Germany, vol. 3, 1935.

13 L. Prandtl and O. Tietjens, "Fundamentals of Hydro- and Aero Mechanics," McGraw-Hill Book Company, Inc., New York, N. Y., 1934.

14 F. H. Clauser, "Turbulent Boundary Layers in Adverse Pressure Gradients," *Journal of the Aeronautical Sciences*, vol. 21, 1954, pp. 91–108.

15 J. M. Robertson and J. W. Holl, "Effect of Adverse Pressure Gradients on Turbulent Boundary Layers in Axisymmetric Conduits," *Journal of Applied Mechanics*, vol. 24, TRANS. ASME, vol. 79, 1957, pp. 191–196.

16 C. A. Moore and S. J. Kline, "Investigation of Airfoils, Plates, Grids, and Rods for Boundary Layer Control in Subsonic Diffusers," Progress Report to NACA under Contract NAw-6317, August, 1954.

17 S. J. Kline, "Some New Conceptions of Stall Including the Behavior of Vaned and Unvaned Diffusers," Progress Report to NACA under contract NAw-6500, March, 1957.

18 S. J. Kline, "Some New Conceptions of the Mechanism of Stall in Turbulent Boundary Layers," *Journal of the Aeronautical Sciences*, vol. 24, 1957, pp. 470–471.

19 D. R. Chapman, D. M. Kuehn, and H. K. Larson, "Analysis of and Experiments on Separated Flows in Supersonic and Subsonic Streams," Ninth International Congress of Applied Mechanics, Brussels, 1956, *Actes*, vol. 2, pp. 156–157.

20 A. R. Thomas, discussion to A. A. Kalinske, "Conversion of Kinetic to Potential Energy in Flow Expansions," *Trans. ASCE*, vol. 111, 1946, pp. 388–389.

21 H. Ludwieg and W. Tillmann, "Investigations of the Wall-Shearing Stress in Turbulent Boundary Layers," NACA TM 1285, 1950.

22 J. M. Robertson and G. L. Calehuff, "Turbulence in a Diffuser Boundary Layer," *Proceedings, ASCE*, vol. 83, 1957, Paper No. 1393.

23 C. T. Hewson, "The Growth and Separation of a Turbulent Boundary Layer," Diss. Cambridge University, 1949.

24 D. Coles, "The Law of the Wake in the Turbulent Boundary Layer," *Journal of Fluid Mechanics*, vol. 1, 1956, pp. 191–226.

25 E. G. Reid, "Performance Characteristics of Plane-Wall Two-Dimensional Diffusers," NACA TN 2888, February, 1953.

26 A. H. Gibson, "On the Flow of Water Through Pipes and Passages Having Converging or Diverging Boundaries," *Proceedings of the Royal Society (London)*, series A, vol. 83, 1910, pp. 366–378.

27 A. A. Kalinske, "Conversion of Kinetic to Potential Energy in Flow Expansions," *Trans. ASCE*, vol. 3, 1946, pp. 355–374.

28 A. Roshko, "On the Development of Turbulent Wakes From Vortex Streets," NACA TN 2913, March, 1953.

29 G. M. Bam-Zeilovitch, "The Computation of the Separation Point of the Boundary Layer," *Izv. Akad. Nauk, SSR, Otd. Tech. Nau.*, 12, December, 1954 (in Russian).

30 E. M. Uram, "The Growth of an Axisymmetric Turbulent Boundary Layer in an Adverse Pressure Gradient," Proceedings of the Second U. S. Congress of Applied Mechanics, 1954.

31 J. F. Norbury, "An Approximate Method for the Calculation of Turbulent Boundary Layers in Diffusers," *Aeronautical Quarterly*, vol. VIII, February, 1957.

32 M. R. Copp and P. L. Klevatt, "Investigations of High Subsonic Performance Characteristics of a 12-Deg 21-In. Conical Diffuser Including Effect of Change in Inlet Boundary Layer Thickness," WACA RM L9H10, 1950.

33 A. Doenhoff and N. Tetervin, "Determination of General Relations for the Behavior of Turbulent Boundary Layers," NACA Rept. 772.

DISCUSSION

Jules L. Dussourd[13]

In Reference [10] of the paper (as a Stanford University report rather than NACA TN), Cochran and Kline have formulated (pages 70 and 71) design criteria for straight-walled, wide-angle diffusers with vanes. Of these, Criterion 4 sets the optimum

[13] AiResearch Manufacturing Company of Arizona, Phoenix, Ariz.

length for the vanes. Application of this criterion yields vanes of considerable length; in fact, nearly equal to the over-all diffuser length, for a diffuser designed for optimum pressure recovery. This may be shown as follows, using the symbols of Cochran and Kline:

f = vane length
a = upstream vane spacing
W_1 = diffuser inlet width
W_2 = diffuser exit width
2θ = diffuser divergence angle
n = number of vanes
L = diffuser wall length
$W_1 = a(n + 1)$
$\frac{W_2}{W_1}$ = 4 for near optimum recovery
$\frac{W_2 - W_1}{2L} = \tan\theta \cong \theta$
$\frac{2\theta}{n+1}$ = 7 deg

Combining this yields:

$$\frac{L}{a} = 24.5$$

whereas, Criterion 4 calls for:

$$\frac{f}{a} = 20$$

Examination of the test data contained in the same reference, however, indicates that optimum recovery is achieved when the length of the unit vanes is approximately equal to *one half* of the over-all diffuser length. It would be of considerable usefulness to have the author express his most up-to-date thinking on this subject.

Author's Closure

In answer to the question raised by Dr. Dussourd, the following may be of assistance. The result of vanes nearly as long as the passage stems directly from Dr. Dussourd's assumption that $W_1/W_2 = 4$. As shown in reference [8], there are several different optimums of technical significance, and $W_1/W_2 = 4$ will not correspond to all of them; it is a special case. Moreover, in design practice one must deal frequently with situations which cannot be made optimum and the question of best vane length under nonoptimum conditions required by initial passage shape is therefore of significance. In both instances, that is, for optimum and nonoptimum outer passage shapes, best performance may occur with vanes running the full length of the outer passage or with far shorter vanes depending upon the shape of the original unvaned passage. Actually, as can be seen from a cross plot of Figs. 20 or 26 of the report to which Dr. Dussourd refers, performance is relatively insensitive to vane length provided the vanes are reasonably long but not so long that any individual passage has a geometry lying above the line of appreciable stall, line a-a of Fig. 6. Maintaining individual angles near seven degrees, on the other hand, is important in performance. These design matters are discussed in more detail than is possible here in references [8 and 10].

Since preparation of this manuscript, several additional relevant reports have been called to the author's attention or have appeared in print. These will be cited briefly for completeness.

First, recent papers by Stratford, [34, 35] have independently verified the existence of transitory stall in a boundary layer before full stall. In studies of a layer which was almost but not quite entirely separated, Stratford observes, "a special region of flow with very high turbulence level close to the wall." This is consistent with the remarks in connection with Fig. 4. It is also consistent with the description of the behavior of the basic unstable model of turbulence as a turbulent boundary nears complete stall given by the author and P. W. Runstadler in [11].

Second, some comment should be made on the validity of the results obtained by Hewson [23]. As noted by the writer, and as re-emphasized by Prof. F. H. Clauser in oral discussion at the ASME stall symposium in December, 1958, there is some doubt regarding the results arising from lack of a check on the two-dimensionality of the flow by Hewson. Much of this doubt is removed by the work of Newman [36], which was called to the author's attention by Prof. C. Nicholl. Newman independently found that the Karman equation did not hold near a stall region. The discrepancy was composed of two terms, one representing dp/dy forces (see discussion above), and one representing apparent shear terms which were much larger than found in boundary layers far from separation. The magnitude of the dp/dy term is in general agreement with Hewson's result. Newman did check the two-dimensionality of his flow with care.

Third, the suggestion advanced by the author that velocity profile correlations might hold up to full stall and that turbulent boundary-layer separation should be correlated on the basis of intermittent separation (short of the section where the wall shear vanishes) have been verified by a remarkable correlation due to Sandborn [37]. These results are too lengthy for complete discussion here, but it should be noted that this correlation shows the profiles at stall are a two-parameter family rather than a one-parameter family and hence explains the inconsistent results obtained by several earlier attempts involving one-parameter velocity profiles. The turbulent correlation achieved is not found by setting $C_f = 0$ and indeed shows a small but finite value of C_f at stall inception. Those results, taken together with the physical observations of the author and a reanalysis of the data of Stratford [35], will be the subject of a further paper by Sandborn and the author shortly. It is hoped that this work will shed further light on both the correlation and the physical picture of stall.

Finally, the author would like to reiterate that, while this discussion hopefully adds to the physical insight on the problem of stall, the story is by no means yet complete and will not be until we are able to give a mathematical theory which will describe the phenomena observed and give consistently reliable predictions. The author hopes that continuing studies on these problems now in process will in some measure contribute toward such a result.

Additional References

34 B. S. Stratford, "The Prediction of Separation of the Turbulent Boundary Layer," *Journal of Fluid Mechanics* vol. 5, no. 1, (1959), pp. 1–16.

35 B. S. Stratford, "An Experimental Flow With Zero Skin Friction Throughout Its Region of Pressure Rise," *Journal of Fluid Mechanics*, vol. 5, no. 1, 1959, pp. 17–35.

36 B. G. Newman, "Some Contributions to the Study of the Turbulent Boundary Layer Near Separation," Rep. ACA-53, Aero Res. Council (Australia) 1951.

37 V. A. Sandborn, "An Equation for the Mean Velocity Distribution of Boundary Layers," NASA Memo 2-5-59E, February, 1959.

S. J. KLINE

Associate Professor, Department of Mechanical Engineering, Stanford University, Stanford, Calif. Mem. ASME

D. E. ABBOTT

Research Assistant, Department of Mechanical Engineering, Stanford University, Stanford, Calif.

R. W. FOX

Research Assistant, Department of Mechanical Engineering, Stanford University, Stanford, Calif.

Optimum Design of Straight-Walled Diffusers[1]

The four common optimum problems in diffuser design are defined. These optima are located in relation to the over-all flow regimes in terms of geometrical parameters for straight-walled units. Using an empirically derived transformation of variables between the conical and two-dimensional geometries, all available data for optimum recovery at constant ratio of wall length to throat width are correlated by a single straight line. This line lies slightly above and parallel to the line of onset of large transitory stall on the chart of over-all flow regimes. The correlated results are based on a literature survey. The range of conditions for each investigation is tabulated for convenient future reference.

THE EMPHASIS of this paper is on design considerations; references to underlying fluid mechanical considerations are given where pertinent. The methods used and the data covered have definite limitations and blank spots; however, the suggestions given represent the best solutions available in terms of present data.

The two basic problems encountered in the design of straight-walled diffusers discussed in this paper are:

(*a*) Prediction of over-all flow regime.
(*b*) Design of optimum straight-walled diffusers.

All available studies show that adequate theoretical methods, either exact or approximate, do not exist for the solution to either problem (*a*) or (*b*). Detailed reasons for this are given in [2, 11];[2] subsequent studies have reinforced this conclusion.

It is therefore appropriate to formulate an empirical scheme using the existing data for the predictions desired. The amount of data is scant, and hence it is very useful to employ a correlation method between the data for various geometries in order to make the best use of what few data are available and to generalize the results. An extensive literature survey has shown that the following two types of data are available:

1 Performance data on recovery and effectiveness.
2 Maps of flow regime to be expected.

The first type of data is available primarily for conical diffusers and two-dimensional flat diffusers. The second is available only for two-dimensional flat diffusers. It is therefore desirable to relate the flow regimes to the performance curves and to associate the parameters of the flat units with those of the conical units.

Two pitfalls exist in this work: (*a*) There are several different kinds of optima for which performance data may be given. (*b*) There is not a complete correspondence between flow regime found and a particular value of recovery; that is, even though the same values of certain parameters may locate the optimum recovery for two units, the value of recovery at the optimum in general will differ between the units. The same remark applies to the value of recovery found at other points along the performance curves.

In this paper four different types of optimal problems are defined, and methods of prediction are given for each type. The flow-regime charts given, together with the method developed for correlating the various geometries, should allow good prediction of the location of optimum conditions and/or the general type of flow to be expected, assuming reasonable inlet conditions, straight walls, and low Mach numbers. Some tentative remarks also are made about possible application when these conditions are not satisfied.

Flow Patterns in Flat Two-Dimensional Diffusers

Effects of Geometrical Parameters. The flow patterns in flat two-

[1] This work was commenced under financial support from the National Advisory Committee for Aeronautics and is continuing under the financial sponsorship of the Air Force Office of Scientific Research, Contract AF 49(638)-295. Reproduction in whole or in part for any purposes of the United States Government is authorized.

[2] Numbers in brackets designate References at end of paper.

Contributed by the Fluid Mechanics Subcommittee of the Hydraulic Division and presented at the Annual Meeting, New York, N. Y., November 30-December 5, 1958, of THE AMERICAN SOCIETY OF MECHANICAL ENGINEERS.

NOTE: Statements and opinions advanced in papers are to be understood as individual expressions of their authors and not those of the Society. Manuscript received at ASME Headquarters, August 1, 1958. Paper No. 58—A-137.

Nomenclature

A_R = area ratio (A_2/A_1)

C_{PR} = actual pressure recovery $\dfrac{\dfrac{1}{A_2}\displaystyle\int_{A_2} P_2 dA_2 - \dfrac{1}{A_1}\int_{A_1} P_1 dA_1}{\dfrac{1}{A_1}\displaystyle\int_{A_1} q_1 dA_1}$

= $(P_2 - P_1)/q_1$ (one-dimensional)

$C_{PR_{ideal}}$ = ideal pressure recovery $(1 - 1/A_R^2)$

H_L = head loss due to dissipation

$\bar{H}_L$ = nondimensional head loss (H_L/q_1)

P = static pressure

q = dynamic pressure ($\rho V^2/2g_c$)

V = one-dimensional velocity of flow

W_1 = throat width

δ^* = boundary-layer displacement thickness

η_p = pressure effectiveness ($C_{PR}/C_{PR_{ideal}}$)

ρ = density

$( )_1$ = inlet to diffuser

$( )_2$ = exit of diffuser

δ = 99 per cent boundary-layer thickness

δ^{**} = boundary-layer momentum thickness

dimensional units have been studied in detail and are reported in references [13] and [2].[3] Reference [11] discusses some additional implications of these results. It is noted that, while it is convenient to divide the flow patterns found into distinct regimes, in reality they represent an essentially continuous spectrum, with lower pressure gradients and shorter diffusers giving less stall and smoother flow (other things being equal).

If the diffuser-divergence angle is continuously increased from zero degrees while the inlet-flow conditions, the wall length, and the throat width are held constant, the following regimes of flow are found:

1 A region of no "appreciable" stall in which the main flow is well behaved and apparently unseparated.

2 A region of large transitory stall in which the separation varies in position, size, and intensity with time. This is a regime of highly pulsating flows.

3 A region of fully developed stall in which the major portion of the diffuser is filled with a large triangular shaped turbulent recirculation region extending from the diffuser exit to a position close to the diffuser throat. The main flow follows along one wall continuously, and relatively smoothly.

4 A jet-flow region in which the main flow is separated from both walls. The separation begins slightly downstream from the throat, and the flow does not reattach until well downstream from the diffuser. This occurs only at quite high angles of divergence.

For a more detailed description of these flow regimes and the nature of the transitions between them, the reader is referred to [13], [2], and [11].

These flow regimes are reproduced for convenience in Fig. 1. It is to be noted that this figure applies to the following conditions: (*a*) Thin inlet boundary layer compared to passage width, (*b*) flat velocity profile outside boundary layer at inlet, (*c*) low Mach number and high Reynolds number, (*d*) flat, straight-walled passages, and (*e*) downstream tailpipe or partially blocked exit. Also, the jet-flow regime lies at still higher angles of divergence than shown in Fig. 1, see [11] or [13], but is omitted here since the lower angle region is that of interest in most diffuser design.

Effects of Nongeometrical Parameters. The effect of entering turbulence level is shown in Fig. 1. For internal flow the curves marked high turbulence level will normally apply. What tests are available indicate that the source of the turbulence is not of critical importance; so long as it is high and of relatively large scale, more or less the same over-all effects are observed.

It is believed that the geometry of the passage downstream from the diffuser may have an effect on the location of the lines *a-a* and *b-b;* particularly *b-b* at high angles and low L/W_1-values. This effect and the downstream blockage effect in general are definitely in need of further study. At present there is no rational means for predicting the importance of such effects. Small effects of this kind also have been reported by Robertson and Holl [20] in a unit operating just below line *a-a*.

Data relating other types of effects to the flow regime to be anticipated are either few or nonexistent. The following remarks are made, therefore, purely as the best available "guestimate," and not as final conclusions.

In regard to the effect of inlet boundary layer, preliminary visualization studies of alteration of inlet profile completed at Stanford University in 1957, in which both laminar inlet layers and fully established turbulent profiles were employed, suggest that inlet boundary-layer profile apparently has relatively little effect on flow regime. This quite surprising result has also been verified to some extent both by Norbury[4] and by Uram [25]. Uram varied his inlet boundary-layer thickness by a factor of 3,

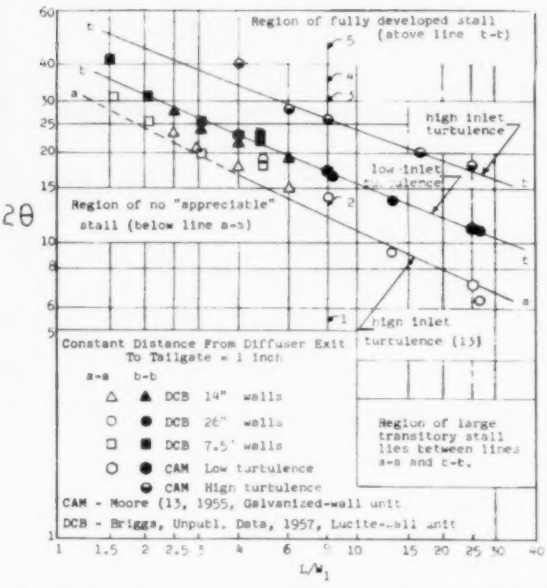
Region of fully developed stall (above line t-t)
high inlet turbulence
low inlet turbulence
Region of no "appreciable" stall (below line a-a)
2θ
high inlet turbulence (15)
Constant Distance From Diffuser Exit To Tailgate = 1 inch
a-a b-b
DCB 14" walls
DCB 26" walls
DCB 7.5° walls
CAM Low turbulence
CAM High turbulence
Region of large transitory stall lies between lines a-a and t-t.
CAM - Moore (13, 1955, Galvanized-wall unit
DCB - Briggs, Unpubl. Data, 1957, Lucite-wall unit
L/W1

Fig. 1 Flow regimes in plane-wall two-dimensional subsonic diffusers

but found that his shape parameters (δ^*/δ,** etc.) in the downstream flow were still essentially unaltered. Since the shape parameters correlate fairly well with stall conditions, this tends to verify the lack of sensitivity of flow regime to inlet boundary-layer conditions.

The explanation for this strange result apparently lies in the fact that increased mixing effects generated by relatively large adverse pressure gradients as discussed in [21] markedly decrease the history effect of the boundary layer as compared to events in zero or negative pressure gradients.

The reader is cautioned that inlet boundary layer does have a large effect on losses and recovery. Furthermore, if a large area of the whole inlet flow which is deficient in stagnation pressure occurs near one wall, stall definitely will occur sooner than shown in Fig. 1 or 2; that is, lines *a-a* and *b-b* are markedly lowered.

The whole problem of inlet conditions needs systematic study. Such an investigation is currently under way at Stanford University under sponsorship of the General Electric Company and hopefully will be the subject of a later paper.

The effect of throat-aspect ratio on flow regime is entirely negligible as shown by data of [13] covering the range from 20:1 to 1:4. The effect of Reynolds number on the flow regime within the range of available data is slight or small. The effect of Mach number is unknown but is probably small up to the occurrence of local choking.

Thus, while the data of Fig. 1 are subject to the restrictions given in the preceding section, some of these restrictions can be relaxed enabling the data to be used over a considerably wider range of conditions as discussed in the foregoing. Such extrapolations are currently necessary and useful even if not totally reliable.

In Fig. 1, line *a-a* is drawn for the condition of high inlet turbulence since the usual mechanical-engineering system has a high turbulence level. Actually, reference [13] shows that there is some small effect of turbulence level on line *a-a*. However, the uncertainty in the data is relatively large and the amount of data is relatively small at high values of 2θ where the change in turbulence level has the greatest effect. The line shown can be considered relatively well established for $L/W_1 > 4$, but for a number

[3] Some recent unreported additional data are also included herein.
[4] By private communication.

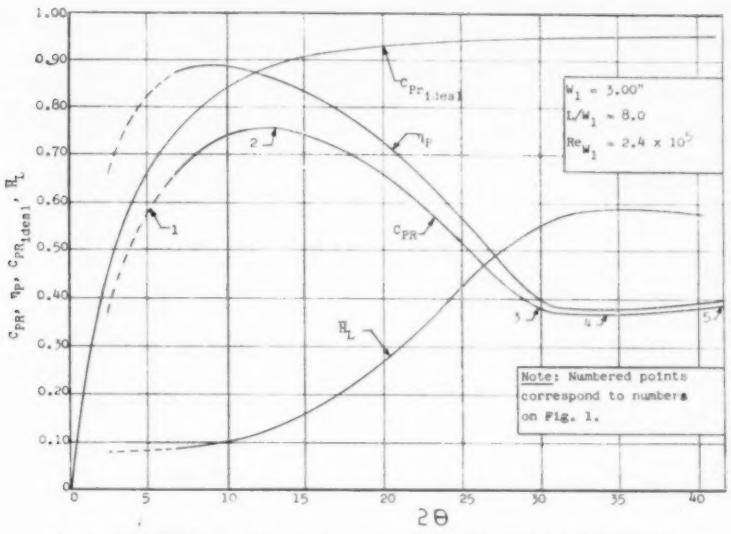

Fig. 2 Typical diffuser performance curves. Rectangular diffuser, Cochran [2].

of reasons, some of which will appear later, should be used with caution for $L/W_1 < 4$.

Correlations of Two-Dimensional, Conical, and Annular Geometries

In order to make the best use of the existing data it is advantageous to employ a correlation method between the data for various geometries.

Fig. 3 shows the curves for conical and two-dimensional flat units superimposed. It is noted that the correlation is based on the following association of variables:

Flat		Conical
2θ	$\longrightarrow$	2θ
L/W_1	$\longrightarrow$	L/R_1

Use of equivalent cone angles or L/D_1 for the conical units does not appear to correlate the results even though superficially it might appear more logical. The association given is based on the idea that the area ratio be made the same at least up to first order in terms of the variables employed, and at the same time the expansion angle should be preserved. This is suggested by the data.

For flat units

$$\frac{A_2}{A_1} = A_R = 1 + 2\frac{L}{W_1}\sin\theta$$

For conical units

$$A_R = 1 + 2\frac{L}{R_1}\sin\theta + \left(\frac{L}{R_1}\right)^2 \sin^2\theta$$

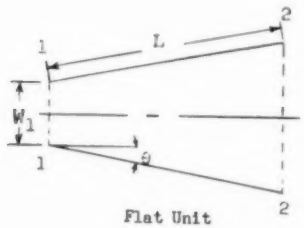

Flat Unit

Comparison of the two expressions for A_R shows the basis of the relation. However, the second-order terms in these expressions are not small at the higher angles and L/W_1-values. Despite this, the correlations work well, in so far as flow regime is concerned, for all comparable data thus far available even at large L/W_1 and 2θ-values. It is noted that this correspondence does *not* extend to the value of recovery, but it does seem to work well for location of flow regime. This is further substantiated in the section on optimum designs.

Following this scheme for annular units, either of two expressions can be used. The first is

Flat		Annular
2θ	$\longrightarrow$	2θ
L/W_1	$\longrightarrow$	L/R_1

This association is also derived by comparing the area-ratio expressions. For an annular unit the area ratio can be written as

$$A_R = \frac{1 + 2\frac{L}{R_1}\sin\theta + \left(\frac{L}{R_1}\right)^2 \sin^2\theta - \left(\frac{B_2}{R_1}\right)^2}{1 - \left(\frac{B_1}{R_1}\right)^2}$$

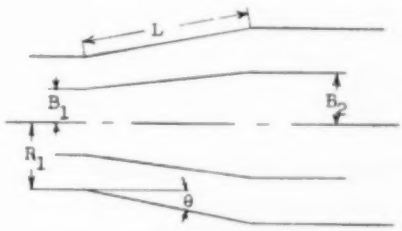

Annular Unit

If $B_1 = 0$, then the denominator becomes unity. In this case the correspondence of area ratios will in general be better than for conical units since the two terms involving squares tend to cancel. An even better correspondence can be found in the case where the two walls of the annular diffuser are parallel. In this case the area ratio becomes

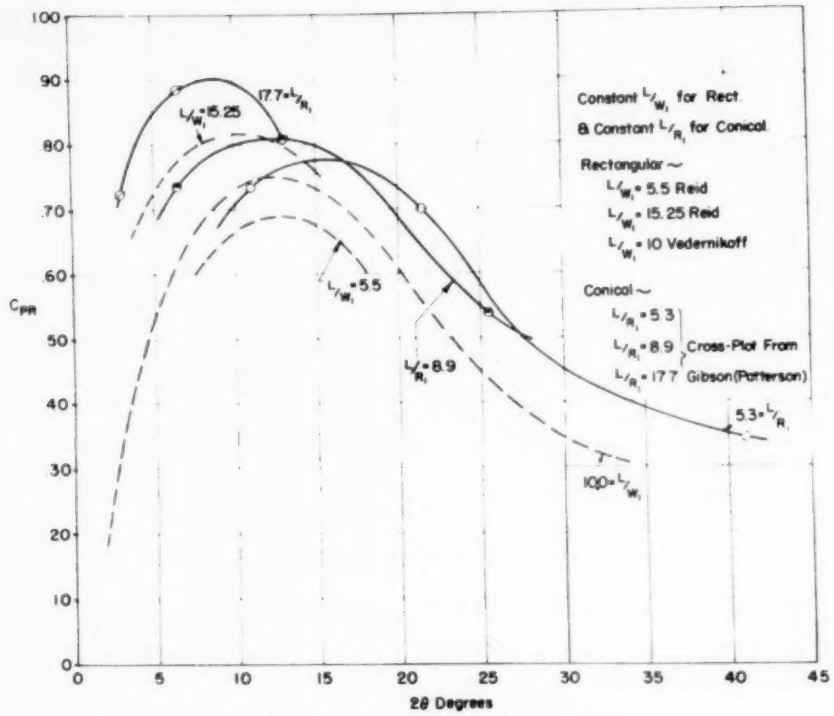

Fig. 3 Comparison of conical and rectangular diffusers

$$A_R = 1 + 2\frac{L}{(R_1 + B_1)}\sin\theta$$

and the appropriate association of variables is

Flat		Annular
2θ	$\longrightarrow$	2θ
L/W_1	$\longrightarrow$	$L/(R_1 + B_1)$

(Note that the + sign is correct even though $R_1 - B_1 = W_1$.)

The association of variables given is surprisingly good for correlating conical and flat units regarding flow regime. Not enough annular data exist to provide any real check on the correlation suggested for flat and annular units. However, the method has been applied successfully in two cases.

It is believed that the vane systems described in [2] also should be applicable to conical and annular units using the correlation of variables given in the foregoing and the same criteria given in [2] for flat units. At least one instance of such a design also has been carried out successfully. Where possible, some radial spacers also should be employed as stabilizers in such round geometries to prevent a spiraling form of transitory stall.

Optimal Design and Diffuser Performance

Relation Between Flow Regime and Performance. In Fig. 2 the correlation of flow regime with location on the performance curve developed in references [2, 11] is reproduced. It shows that optimum recovery at constant length occurs at or slightly above the line a-a which marks the border between no appreciable stall and large transitory stall. From the design point of view it should be noted that the regions between points 2 and 3 in Fig. 2 represent a region of large pulsations and very unsteady flow. It also should be noted that the flows found at angles above point 4 are much steadier although not without some fluctuations. Furthermore, since the recovery curve passes through a minimum near point 4, in some instances a larger divergence angle may be better than an intermediate value. It can be seen from Figs. 1 and 2 that this minimum point on the C_{PR} curve lies slightly above the line b-b in the regime of fully developed stall. In such instances, the use of flat vanes designed according to the procedures suggested in [2][6] often can be employed to advantage. These short-vane systems, if properly designed, can give good recovery, smooth flow, and uniform exit-velocity profiles up to divergence angles of at least 45 deg.

Diffuser Losses. In discussing performance it is very useful to derive an explicit relation between head loss, ideal recovery, and actual recovery. This is readily done as follows:

By definition, for steady one-dimensional incompressible flow,

$$\bar{H}_L = \frac{H_L}{q_1} = \frac{\left(\frac{P_1}{\rho_1} + \frac{V_1^2}{2g_c}\right) - \left(\frac{P_2}{\rho_2} + \frac{V_2^2}{2g_c}\right)}{\frac{V_1^2}{2g_c}} = \frac{(P_1 + q_1) - (P_2 + q_2)}{q_1} \quad (1)$$

Rearranging Equation (1) yields

$$\bar{H}_L = \frac{q_1 - q_2}{q_1} - \frac{P_2 - P_1}{q_1} \quad (1a)$$

Using the equation of continuity, the definition of $C_{PR_{ideal}}$, and Equation (1a), it can be shown readily that this is equivalent to the following:

[6] Reference [2], pp. 69–71 and 80–81. Several other means of boundary-layer control are also known to be effective alone or in combinations. Discussion of these effects is beyond the scope of this paper.

$$\Pi_L = C_{PR_{ideal}} - C_{PR} \quad (2)^6$$

This function is plotted in Fig. 2 from the data in reference [2]. It is seen that Π_L is a monotonically increasing function with increasing divergence angle. This is quite meaningful up to the angle that corresponds to that for optimum recovery (slightly above the line *a-a*) and in this region it needs no special interpretation. However, for the region beyond optimum recovery, it must be interpreted with caution for the following reason: The loss of head, Π_L, is a measure not only of dissipation in the flow but also of the leaving loss; that is, Π_L charges the diffuser not only with the head loss due to dissipation but also with the excess of kinetic energy leaving the unit above that which would occur with a one-dimensional exit-velocity profile. For some purposes this is a measure of loss desired, but for other purposes it is not. In particular, if a tailpipe or downstream duct is added to the diffuser, some of the leaving loss arising from nonuniformity of velocity profile at the exit of the diffuser usually will be recovered downstream.

Optimal Design of Simple Passages. Four important optimum problems are commonly encountered as follows:

1 Minimum loss of total pressure is desired for a given pressure rise.

2 Maximum recovery for a given area ratio is desired regardless of length in the flow direction.

3 It is desired to design for optimum recovery within a given length in the direction of flow.

4 Optimum recovery for any possible geometry is desired for the given inlet conditions; this can be called the best optimum.

Other optimum problems can be formed, but these four are believed to be the most common and important. It is reiterated that the location of these optima *are all different*. This can be demonstrated in part as follows:

The curve of pressure effectiveness, η_P, given in Fig. 2, illustrates the fact that the maximum of η_P occurs at an appreciably smaller 2θ than does the maximum of C_{PR}. (This phenomenon also was noted by Reid [19].) Using the definition of η_P and $C_{PR_{ideal}}$, it can be shown readily that this must be so. Consider a diffuser having W_1, L/W_1, and all inlet conditions held constant as the included angle is increased continuously from zero degrees. At $2\theta = 0$, the diffuser is simply a pipe in which a decrease in static pressure occurs due to losses; thus $C_{PR} < 0$ and $\eta_P = -\infty$. At some small positive value of 2θ the momentum conversion will just offset the frictional static pressure loss; therefore both C_{PR} and η_P will be zero. As 2θ is increased, the rate of increase of C_{PR} is reduced by the additional losses and by the production of a less uniform exit-velocity profile. It can be seen from the definition of η_P that the logarithmic increase of η_P is equal to the difference of the logarithmic increases of C_{PR} and $C_{PR_{ideal}}$; i.e.,

$$\eta_P = C_{PR}/C_{PR_{ideal}}$$

and

$$\ln \eta_P = \ln C_{PR} - \ln C_{PR_{ideal}}$$

To find the maximum of η_P as a function of 2θ, we differentiate and equate to zero. This yields

$$\frac{\partial}{\partial\theta}(\ln \eta_P) = \frac{\partial}{\partial\theta}(\ln C_{PR}) - \frac{\partial}{\partial\theta}(\ln C_{PR_{ideal}}) = 0$$

or

$$\frac{1}{C_{PR}}\frac{\partial C_{PR}}{\partial\theta} = \frac{1}{C_{PR_{ideal}}}\frac{\partial C_{PR_{ideal}}}{\partial\theta} \quad (3)$$

Equation (3) shows that when η_P is a maximum the fractional rate of increase with angle of C_{PR} and $C_{PR_{ideal}}$ are identical. Further, since C_{PR} at this point is positive and since by definition both $C_{PR_{ideal}}$ and $\partial C_{PR_{ideal}}/\partial\theta$ are positive, Equation (3) shows that the rate of increase of C_{PR} with angle, at the point of maximum effectiveness, η_{P_1} is always greater than zero. In other words, the maximum of C_{PR} *cannot* occur at the angle of maximum η_P. For any divergence angle greater than that required to obtain maximum effectiveness, the ideal pressure recovery increases proportionately faster than the actual pressure recovery and hence η_P decreases with further increase in 2θ, but C_{PR} will continue to increase so long as $\partial(C_{PR})/\partial\theta > 0$.

In fact, by employing Equation (2), it can be shown that the rate of increase of losses equals the rate of increase of $C_{PR_{ideal}}$ at the point of maximum C_{PR}.

$$\Pi_L = C_{PR_{ideal}} - C_{PR} \quad (2)$$

Differentiating and equating $\partial C_{PR}/\partial\theta$ to zero yields

$$\frac{\partial \Pi_L}{\partial\theta} = \frac{\partial C_{PR_{ideal}}}{\partial\theta} - \underbrace{\frac{\partial C_{PR}}{\partial\theta}}_{0}$$

Therefore, when C_{PR} is a maximum,

$$\frac{\partial \Pi_L}{\partial\theta} = \frac{\partial C_{PR_{ideal}}}{\partial\theta} \quad (4)$$

Thus, as 2θ is increased above the angle which gives maximum effectiveness, the actual pressure recovery will continue to rise with increase in angle until the added losses and increased rate of momentum efflux (brought about by the increase in angle) balance the theoretical gain in recovery made possible by the increased angle and the concomitant increase in area ratio.

It is also instructive to examine under what conditions we would expect this balance to occur in terms of the flow regimes plotted in Fig. 1. The nondimensional loss term, Π_L, is composed of two parts: (*a*) Dissipation due to wall shear and mixing; (*b*) leaving momentum loss.

As mentioned in the previous discussion, the angle at which the pressure increase due to increasing area is just offset by the sum of wall friction and mixing losses in an apparently unstalled flow pattern is of the order of 1 deg total divergence. Consequently, it is unlikely that wall friction and mixing effects will be sufficient to cause a reversal of the trend of the C_{PR} curve so long as the flow pattern contains no appreciable stalls. Similarly, the leaving loss will increase smoothly and slowly as a function of angle so long as the exit-velocity profile corresponds to an essentially unstalled flow pattern. Thus the maximum recovery is not likely to occur so long as the major flow pattern contains no appreciable stalls.

On the other hand, as soon as large stalls begin to appear, whether transient or steady, both the mixing loss and the leaving loss will rise sharply; mixing losses due to bluff drag are known to be an order of magnitude higher than those due to skin friction alone, and any stall which occupies an appreciable area of the exit plane (on the average over both time and space) will increase the leaving loss inversely as the square of the effective exit area. Thus a relatively small amount of stall can cause a downward trend in the recovery curve, and hence we should expect to find the point of maximum recovery as a function of angle very soon after we are first able to discern large transitory stalls as shown by line *a-a* in Fig. 1. As will be shown later, this is indeed the case.

With the aid of Equations (2), (3), and (4) and the available data we are now in a position to find the location of the four different optima enumerated in the foregoing:

[6] This relation can be extended readily to two or three-dimensional flows, but the extension merely complicates Equation (2) without adding to the physics.

Minimum Total Head Loss Per Unit Actual Pressure Rise. Minimum total head loss per unit actual pressure rise is coincident with optimum effectiveness. This is easily demonstrated as follows:

From Equation (2),

$$\frac{H_L}{C_{PR}} = \frac{C_{PR_{ideal}} - C_{PR}}{C_{PR}} = \frac{1}{\eta_p} - 1 = \frac{1 - \eta_p}{\eta_p}$$

Since $\eta_p \leq 1$ this function is a minimum when η_p is a maximum inasmuch as this gives both the largest denominator and the smallest numerator.

Gibson [5] and Reid [19] show that optimum effectiveness occurs at an angle of approximately 7 deg for all but very short diffusers. This value of 7 deg is total included angle of diffusion, and it is the same for both the conical and flat units despite the fact that the pressure gradients differ in the two cases. Thus, to design for minimum loss, it is only necessary to use a total divergence angle of 7 deg, and the length required to provide the necessary area ratio. The only precaution to be observed is that L/W_1 or L/R_1 should not exceed about 25 if large fluctuations are to be avoided, Fig. 1.

Optimum Recovery for Given Area Ratio. Examination of the data of Reid [19] also shows that the optimum of this type (optimum recovery at constant area ratio) is very flat in the zone of steady flows. Thus, so long as the design is such that it falls below line *a-a* in Fig. 1 which shows the flow regimes, almost any convenient length of diffuser can be selected without appreciable penalty. In fact, the curves are so flat that the gains to be realized by altering length to the optimum value are probably more apparent than real owing to the uncertainty in the data. This remark holds only for the region below line *a-a*. Above line *a-a*, geometrical area ratio rapidly loses design significance as noted in the following.

Optimum Recovery for Given Length. As explained previously, maximum C_{PR} as a function of angle will occur only when the rate of increase of losses become large, i.e., after the average amount of stall in the diffuser begins to increase rapidly. Thus we would expect to find optimum recovery, as angle is increased at constant L/W_1, at a point slightly above line *a-a*. This conclusion is entirely in agreement with Fig. 4, which shows that optimum recovery at constant L/W_1 lies very close to a fixed 10 per cent above line *a-a*.

Fig. 4 shows the correlation of all the data on optimum recovery for a given length, available to the authors, and a summary of the ranges, conditions, and so on, of the data is given in detail in Table 1. The lack of scatter is remarkable, but despite this, the curve must be used with some caution due to the large number of parameters noted previously. No data for high Mach

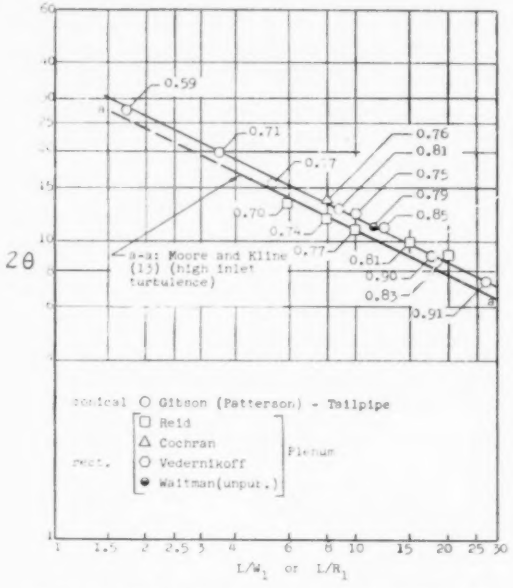

Fig. 4 Correlation of optimum recovery at constant L/W_1

Table 1 Diffuser data—Literature survey

Reference	2θ	A_R	δ_1^*/W_1	δ_1^*/δ_1^{**}	$Re_1 \times 10^{-6}$	L/W_1	M_1	δ_1	W_1	δ/W_1	Config. and control
Peters [18][a]	var	2.33	var	1.2–1.3	0.2	...	0.13	...	...	...	Cone[c]
Little and Wilbur [12][a]	var	2.00	var	1.2–1.3	1.2	...	var	...	...	...	Cone
Squire [24]	var	4.00	~0.006	..	0.5	5.7 to 14.3	<0.45	~0.1	1.75	...	Cone
Copp [3]	10	2.00	var	1.45	1.2	4.74	var	...	...	...	Cone
Valentine and Carroll [26]	23	2.00	var	1.28	2.8	...	var	...	...	...	Cone VG
Gratzer and Smith, [38]	var	4.00	var	1.6–1.2	0.7	...	0.18	...	...	...	Cone
Gibson [5][a, b]	var	var	~0.01	...	0.2	...	<0.2	...	...	...	Cone
Squire and Carter, [39]	var	var	0.08	1.3	0.45	...	0.45	...	...	...	Cone
Cochran [2][a]	var	var	0.003	1.82	0.43	8	0.2	0.06	3	0.02	Rect vane
Verdernikoff [27][a]	var	var	~0.006	...	0.1–0.2	10	0.1	~0.1	3.94	~0.03	Rect
Young and Green [34][a]	var	4.0	...	...	var	var	var	0.25	2	0.125	Rect vane
Reid [19][a]	var	var	~0.006	...	0.8	var	0.1	0.08–0.12	4	0.025	Rect
Gibson [5][b]	var	var	~0.01	...	0.2	...	<0.2	...	...	...	Rect

[a] Used in correlation; considered at least reasonably adequate and of wide enough scope to establish a curve and optimum value of recovery.

[b] Often attributed to Patterson, but apparently taken by Gibson and replotted by Patterson. Gibson's upstream and downstream geometries were poor, but the results appear consistent.

[c] In this table W_1 represents channel width for two-dimensional units, and in conical units represents R_1 to agree with correlation of Fig. 4.

LEGEND: cone = conical; rect = rectangular; VG = vortex generators; var = variable vane = vaned configuration; Re_1 = Reynold's number based on W_1 and inlet conditions; M_1 = Mach number at inlet.

numbers or badly distorted inlet profiles are available. Nor are optimum data available on performance with plenum-chamber exit conditions at high divergence angles. Conservatism in design is desirable in the region of high angles until the further data, referred to previously in connection with downstream geometry effects, are available.[7]

Best Optimum for Any Geometry. The best of all such optima, that is, the best recovery possible for given inlet conditions with any geometry of diffuser is not clearly established; a trend is visible, however. Noting just the conical data in Fig. 4, it can be seen that the value of recovery increases uniformly as L/W_1 increases and 2θ decreases. However, the rate of increase is slowing rapidly and probably ceases near or not far beyond the last point at $2\theta = 7$ deg in Gibson's data. The only sufficient data for the flat case are Reid's and they show a similar trend. *Thus it is probably a good guess to take $2\theta = 7$ deg and L/W_1 of 25 to 30 as the general neighborhood of the best optimum.* This choice is further substantiated by the data of Cochran [2]. In all tests run by Cochran, which include a considerable range of variables, the best recovery was achieved when the vanes were designed in such a way that each individual passage lies in the region just delineated. Still further evidence for this choice lies in the fact that it represents the intersection of the line of minimum loss per unit actual pressure rise (7 deg) with the line of maximum length possible without large stalls. Thus it represents the largest area ratio achievable along the line of minimum loss without the appearance of large stalls. A design for lower area ratios in the segment between the line a-a and a 2θ of 7 deg will decrease recovery as shown by the data in Fig. 4. Design into the region to the right of or above line a-a will of course bring on large stalls. Design in the region below 7 deg and line a-a will increase losses for a given actual pressure rise. This suggests that the losses may rise faster than the increase in recovery due to increased area ratio on line a-a below 7 deg and hence that 7 deg may represent a balance between wall friction loss and mixing loss such that their sum is minimized. This last conclusion cannot be checked due to lack of sufficient data at very high L/W_1 and low angles.

[7] Reid's data seem to check this idea. Also Reid's unit had a thicker inlet boundary layer and lower inlet turbulence which may affect his results. The uncertainty in locating optima in Reid's data is also high due to the few points taken near the maximum of the curves.

Diffuser Performance. Fig. 5 shows the curves of recovery plotted in design-chart form for the two-dimensional data of references [2, 19, 27, and 34]. All the known data are given. A bibliography of all pertinent references is included. Despite the length of this bibliography, the available data are not nearly adequate since many of the references contain little information of use to the designer.

Since the available data are not nearly as extensive as might be desired, some remarks of use in applying judgment are pertinent. With thin inlet boundary layers, both the conical and flat data tend to follow the curve of ideal recovery fairly closely up to somewhat beyond the angle of optimum effectiveness. This implies that the performance at low angles of divergence is primarily a function of area ratio, and hence that the flow is nearly one-dimensional as is assumed in the simple theory. Thus in this region design is relatively straightforward. Predictions that will be reasonably close can be made on the basis of the one-dimensional theory. For first estimates frictionless flow is probably sufficient in many cases. For close estimates a suitable effectiveness factor must be applied. This is more difficult since all factors influencing effectiveness are not really known. It can be stated that conical units will give higher recoveries by a few points than flat or square units if other conditions are equal (Fig. 3). The data show that performance is also affected by inlet boundary layer and Reynolds number.

In regard to the effect of inlet boundary layer, the data contained in Fig. 4 include a threefold variation in δ_1^*/W_1 without

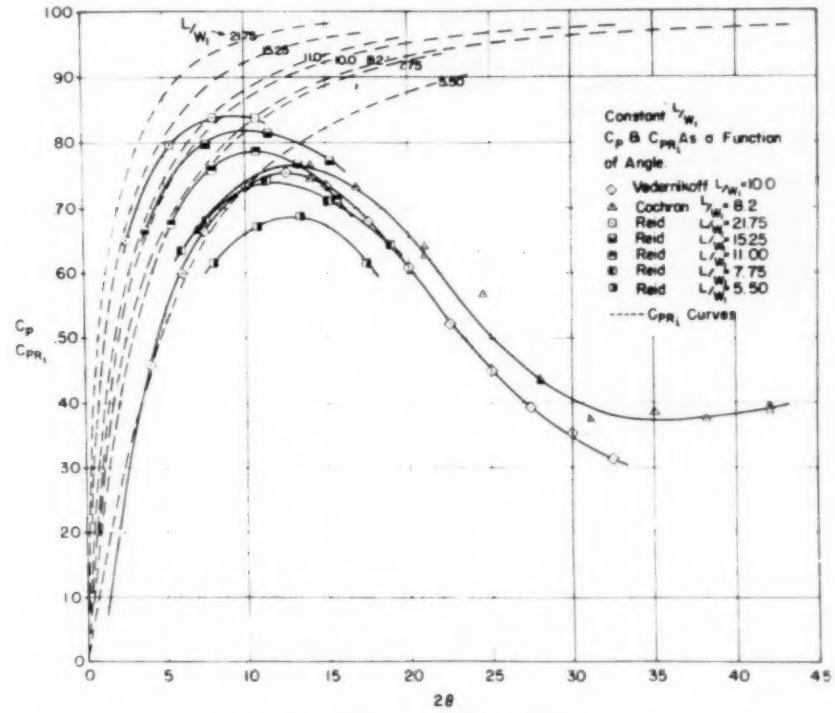

Fig. 5 Two-dimensional diffuser performance

any perceptible alteration in the location of optimum recovery. It is to be expected that thicker inlet boundary layers and lower Reynolds numbers will give poorer performance, but the amount of such effects is unknown. It is also believed that higher aspect ratios in flat units will give lower recoveries, but no data on this point are available.

The few available points suggest that increase in inlet Mach number up to 0.5 or somewhat higher does not appear to alter the losses and hence the performance, provided the design point is as much as 5 or 6 deg below line *a-a* at constant L/W_1. However, if the design is close to line *a-a*, then the losses appear to increase steadily with Mach number. This conclusion is based on the data of Little and Wilbur [12] and Copp [3]. It consists of only a few curves, but they all agree with the conclusion stated. The conservative units show flat performance up to choking followed by a sharp rise; the units designed near what would be optimum for low Mach numbers show increasing losses as Mach number is increased over the whole range of Mach number. Since the rate of increase of losses in the units increases with increasing Mach number, and since transitory stalls actually commence before line *a-a*, the probable explanation for this behavior is that the transitory stalls initiate some choking effects by flow blockage before line *a-a* is reached. This implies that optimum diffusers for high subsonic inlet Mach numbers probably lie a few degrees below rather than a few degrees above the line *a-a*. Sufficient data to substantiate this conclusion are not available. However, some degree of conservatism in design would appear warranted.

Again it is emphasized that correlation of flow regime does not imply correlation of recovery value. More variables enter into determining recovery than into determining flow regime. Thus Reynolds number, aspect ratio, and inlet boundary layer (within limits) do not appreciably affect flow regime, but they do affect recovery and losses.

In the region of optimum recovery and at still higher angles the situation is unfortunately even more complex than at lower angles, and is even less understood. The following remarks may be of some aid to the designer who must sometimes use passages in this region without any means for stall prevention. At quite high angles, in particular above line *b-b* of Fig. 1, area ratio of the diffuser is no longer significant since the flow does not follow the walls. This effect actually begins below line *a-a*, but does not become large until line *a-a* is approached. Thus area ratio becomes less and less significant as a variable as the angle increases. At very high angles the important parameters governing recovery are believed to be L/W_1, inlet conditions (including boundary-layer thickness and turbulence), and downstream geometry, but these remarks cannot be verified at present. The scatter in the region above line *b-b* is enormous, with recoveries ranging from 5 per cent to 50 per cent reported in what superficially appear to be comparable data. For good recovery, high L/W_1, high inlet turbulence, and thin inlet boundary layers are desirable. A partially blocked exit or tailpipe is also preferable to a plenum discharge in this region. Beyond these admittedly inadequate remarks, judgment is the only recourse at the present time.

In applying such judgment, the concepts of stall developed in [11] should be of assistance. In particular, it is pertinent to note that the losses due to wall shear can be estimated from available data, but these are not sufficient and generally give an estimate of losses that is far too low (often by a factor of 10 or more). The reason for this is that the primary losses are due to mixing of stalled fluid with oncoming flow, and no means for estimating this loss is now known. In addition, the recovery is reduced still further by distortions of the exit-velocity profile, and at present this effect cannot be predicted either. For these reasons, predictions of performance can now be made reliably in the region above line *a-a* only when entirely comparable data exist, and this almost never occurs unless specific flow tests of the system under design are made. In general, the discrepancy between predictable effects based on one-dimensional flow and wall-shear losses becomes larger and larger as the divergence angle of the passage increases.

Conclusion

Under many conditions a fairly reliable prediction of the location of optimum performance and/or of flow regime to be anticipated can be made for various geometries based on the correlations presented. The value of losses and recovery to be found at these conditions cannot yet in general be predicted.

Although the correlations given have little rational and no theoretical foundation at the present time, they nevertheless appear to give correct predictions for a greater percentage of the time for straight-walled passages than any known method based on boundary-layer theory alone. In addition, they are extremely simple and rapid in use.

References

1 A. J. Acosta and R. D. Bowerman, "An Experimental Study of Centrifugal-Pump Impellers," TRANS. ASME, vol. 79, 1957, pp. 1821–1839.

2 D. L. Cochran and S. J. Kline, "The Use of Short Flat Vanes for Producing Efficient Wide-Angle Two-Dimensional Subsonic Diffusers," NACA Final Report on Contract NAw-6404 and Progress Report PD-3 on Contract NAw-6500, April, 1957. To be published as NACA TN 4309.

3 Martin R. Copp, "Effects of Inlet Wall Contour on the Pressure Recovery of a 10° 10-Inch-Inlet-Diameter Conical Diffuser," NACA RM L51E11a, September 5, 1951.

4 C. R. Faulders, "Aerodynamic Design of Vaned Diffusers for Centrifugal Compressors," ASME Paper No. 56—A-213, 1956.

5 A. H. Gibson, "On the Flow of Water Through Pipes and Passages Having Converging or Diverging Boundaries," *Proceedings of the Royal Society, London*, series A, vol. 83, 1910, pp. 366–378.

6 A. H. Gibson, "On the Resistance to Flow of Water Through Pipes or Passages Having Divergent Boundaries," *Trans. Royal Society of Edinburgh*, vol. 48, part 1, 1913, pp. 97–116.

7 G. A. Gourzhienko, "Turbulent Flow in Diffusers of Small Divergence Angle," NACA TM No. 1137, October, 1947.

8 John R. Henry and Stafford W. Wilbur, "Preliminary Investigation of the Flow in an Annular-Diffuser-Tailpipe Combination With an Abrupt Area Expansion and Suction, Injection, and Vortex-Generator Flow Controls," NACA RM L53k30, 1954.

9 J. Herzog, "Investigation of Annular Diffusers," *Maschinenbau und Wärmewirtschaft*, Sonderabdruck aus 11. Jarhgang, Heft 7, 1956 (in German).

10 Curt A. Halzhauser and Leo P. Hall, "Exploratory Investigation of the Use of Area Suction to Eliminate Air Flow Separation in Diffusers Having Large Expansion Angles," NACA TN 3793, October, 1956.

11 S. J. Kline, "On the Nature of Stall," published in this issue, pp. 305–320.

12 B. H. Little, Jr., and Stafford W. Wilbur, "Performance and Boundary-Layer Data From 12° and 23° Conical Diffusers of Area Ratio 2.0 at Mach Numbers up to Choking and Reynolds Numbers up to 7.5×10^6," NACA Report 1201, 1954.

13 Carl A. Moore, Jr., and S. J. Kline, "Some Effects of Vanes and of Turbulence on Two-Dimensional Wide-Angle Subsonic Diffusers," NACA Final Rpt. on Contract NAw-6317 and Progress Report on Contract NAw-6404, September, 1955, NACA TN 4080, June, 1958.

14 William J. Nelson and Eileen G. Popp, "Performance Characteristics of Two 6° and Two 12° Diffusers at High Flow Rates," NACA RM L9H09, October 19, 1949.

15 Jerome Persh, "The Effect of Surface Roughness on the Performance of a 23° Conical Diffuser at Subsonic Mach Numbers," NACA RM L51K09, January 16, 1952.

16 G. N. Patterson, "Modern Diffuser Design," *Aircraft Engineering*, vol. 10, 1938, pp. 267–273.

17 Jerome Persh and Bruce M. Bailey, "Effect of Various Arrangements of Triangular Ledges on the Performance of a 23° Conical Diffuser at Subsonic Mach Numbers," NACA TN 3123, January, 1954.

18 H. Peters, "Conversion of Energy in Cross-Sectional Diver-

gences Under Different Conditions of Inflow," NACA TM No. 737, March, 1934.

19 Elliott G. Reid, "Performance Characteristics of Plane-Wall Two-Dimensional Diffusers," NACA TN 2888, February, 1953.

20 J. M. Robertson and J. W. Holl, "Effect of Adverse Pressure Gradients on Turbulent Boundary Layers in Axisymmetric Conduits," *Journal of Applied Mechanics*, vol. 24, TRANS. ASME, vol. 79, 1957, pp. 191–196.

21 S. J. Kline and P. W. Runstadler, "Some Preliminary Results of Visual Studies on the Flow Model of the Wall Layers of the Turbulent Boundary Layer," *Journal of Applied Mechanics*, vol. 26, TRANS. ASME, vol. 81, 1959, pp. 166–170.

22 J. B. Scott-Wilson and D. I. T. P. Llewelyn-Davies, "The Development of an Improved Diffuser for the 3 Ft × 3 Ft Tunnel, Royal Aircraft Establishment, Bedford," Royal Aircraft Establishment Technical Notes No: Aero. 2446, July, 1956.

23 Richard Scherrer and Warren E. Anderson, "Preliminary Investigation of a Family of Diffusers Designed for Near Sonic Inlet Velocities," NACA TN 3668, February, 1956.

24 H. B. Squire, "Experiments on Conical Diffusers," Ministry of Supply, Aeronautical Research Council Reports and Memoranda, No. 2751, A.R.C. Technical Report, 1953.

25 E. M. Uram, "The Growth of an Axisymmetric Turbulent Boundary Layer in an Adverse Pressure Gradient," Proceedings of the Second U. S. National Congress of Applied Mechanics, Ann Arbor, Michigan, 1954.

26 E. Floyd Valentine and Raymond B. Carroll, "Effects of Some Primary Variables of Rectangular Vortex Generators on the Static-Pressure Rise Through a Short Diffuser," NACA RM L52B13, May 22, 1952.

27 A. N. Verdernikoff, "An Experimental Investigation of the Flow of Air in a Flat Broadening Channel," NACA TM No. 1059, January, 1944.

28 Stafford W. Wilbur and James T. Higginbotham, "Investigation of Two Short Annular Diffuser Configurations Utilizing Suction and Injection as a Means of Boundary-Layer Control," NACA RM L54K18, January 25, 1955.

29 F. A. L. Winternitz and W. J. Ramsay, "Effects of Inlet Boundary Layer on Pressure Recovery, Energy Conversion, and Losses in Conical Diffusers," *Journal of the Royal Aeronautical Society*, February, 1957, pp. 116–124. Obtainable: loan or photocopy: IAS Library, New York, N. Y.

30 Charles C. Wood, "Preliminary Investigation of the Effects of Rectangular Vortex Generators on the Performance of a Short 1.9:1 Straight-Wall Annular Diffuser," NACA RM L51G09, October 10, 1951.

31 Charles C. Wood and James T. Higginbotham, "Effects of Diffuser and Center-Body Length on Performance of Annular Diffusers With Constant-Diameter Outer Walls and With Vortex-Generator Flow Controls," NACA RM L54G21, September 14, 1954.

32 Charles C. Wood and James T. Higginbotham, "The Influence of Vortex Generators on the Performance of a Short 1.9:1 Straight-Wall Annular Diffuser With a Whirling Inlet Flow," NACA RM L52L01a, February 9, 1953.

33 Richard R. Woollett, "Preliminary Investigation of Short Two-Dimensional Subsonic Diffusers," NACA RM E56C02, May 25, 1956.

34 A. D. Young and G. L. Green, "Test of High-Speed Flow in Diffusers of Rectangular Cross-Section," Ministry of Supply, Aeronautical Research Council Reports and Memoranda No. 2201, A.R.C. Technical Report, July 1944.

Additional References

35 G. M. Bam-Zeilovich, "Calculation of Boundary-Layer Separation," *Izvestiya Akademiya Nauk*, SSSR Otd. Tekh. Nauk no. 12, 1954, pp. 68–85 (in Russian).

36 J. P. Milliat, "Turbulent Air Flow in a Pipe With Diffusing Section," *La Houille Blanche*, vol. 11, 1956 (in French).

37 Von O Ruchti, "Research on Radial Diffusers," *Bericht der Deutschen Forschungsanstalt für Segelflug*, Ernst Udet, Institut für Aerodynamik und Flugmechanik Technische Berichte, Bd. 11, 1944 (in German).

38 L. B. Gratzer and R. H. Smith, "Boundary Layer Control for Wide Angle Diffusers," Rep. No. 300, University of Washington Aeronautical Laboratory, November 22, 1948.

39 H. B. Squire and P. Carter, "Further Experiments on Conical Diffusers," A. R. C. Rep. No. 13,499 (British N. P. L. Rep. No. T. P. 320), November 6, 1950.

DISCUSSION

Robert C. Dean, Jr.[8]

The authors and the others who have contributed to the diffuser research program at Stanford are to be congratulated for bringing order to an important subject over which there has been considerable confusion for many years. The discovery and classification by these investigators of the various regimes of flow occurring in diffusers was the key of their success. This break-through was achieved primarily by visualization studies with simple test apparatus. The success of this attack where many others utilizing elaborate probing techniques have failed is an important lesson in fluid mechanics research. It points out clearly that, in problems where the flow is unstable or may be unstable, point by point methods are often so difficult to correlate in time and space that they cannot be used to reveal the over-all flow pattern. Because instabilities, particularly stalling, must be suspected in all unknown flows, visualization should be prescribed as the first exploratory step. Of course, in cases where the over-all flow characteristics are well understood, point by point probing is a valuable technique. However, many of our most common flow configurations still lack today this over-all picture of the flow pattern to be expected. Professor Kline and his co-workers have demonstrated again the great power of enlightened observation.

The discusser has employed the results of the Stanford program several times in the design and development of diffusing systems. These results verify and even suggest broader applicability of the authors' results. Only at high subsonic Mach numbers was a divergence of results discovered. However, the authors now tell us that one should not design on line a-a, Fig. 1, in such cases, as we did, so that even our discrepancies may now be resolved in a qualitative manner.

As a contribution to the little evidence available on engineering application of the authors' results to diffusers of significantly altered form, two actual cases will now be presented.

The first is a diffusing elbow of area ratio 4.8 converting from an annular passage to a rectangular passage. The ratio of the length of the sharply-curved centerline to the outer radius at inlet was about 3. The inside radius of curvature in meridional plan was 68 per cent of the annulus outer radius at inlet. This elbow is sketched in Fig. 6. It represents a short diffuser of large divergence angle and very sharp turn.

Since one would expect virtually zero recovery in such a passage, a set of turning vanes was designed to split the flow into ten diffusing channels each of which was designed according to the authors' results. The only cognizance given to the curvature of each passage was to design its outer wall by streamline curvature methods in order to produce a variation of velocity over the inner wall which matched the computed one-dimensional velocity variation associated with the authors' two-dimensional diffuser of the same 2θ and L/W_1. The potential effect of curvature upon the location of line a-a in the authors' Fig. 1 was ignored. Several other approximations were made to account for sidewise divergence, the Kutta condition at vane trailing edges, and so forth, but they are not important to this discussion.

The authors' results, with our approximations, indicated that we should achieve a pressure recovery effectiveness η of 75 per cent. The measured value based on bulk mean velocities and averaged static pressures at inlet and exhaust was close to 100 per

[8] Head, Advanced Engineering Department, Ingersoll-Rand Company, Phillipsburg, N. J. Assoc. Mem. ASME.

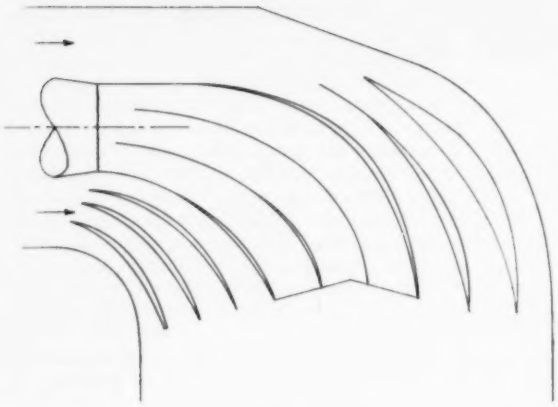

Fig. 6

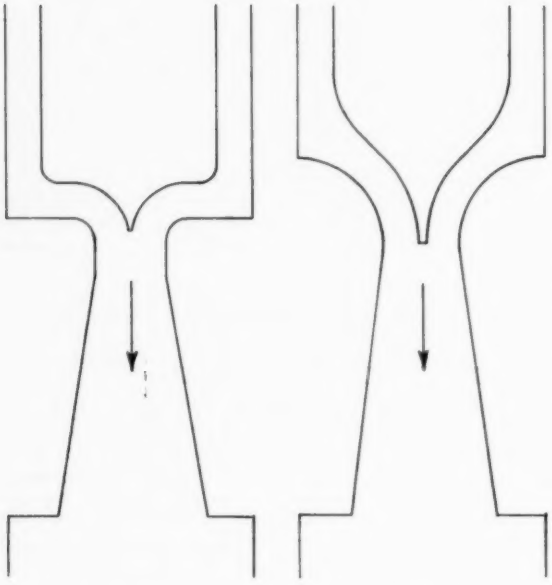

Fig. 7(a) Fig. 7(b)

cent at a bulk mean Mach number of 0.5 and similar Reynolds number of 2×10^6. We know, however, that strong wakes of upstream struts distorted the inlet velocity profile without, however, leading to gross asymmetry of the inlet flow. These distortions were responsible for the unusually high value of recovery based on bulk mean conditions. The distortions were measured without the elbow attached to the upstream pipe, but could not be measured in the diffusion tests. If they were similar in both cases and if momentum flux integrals were used for recovery calculations, the recovery effectiveness is estimated to have been 75 per cent or higher, but certainly no lower. These details should not obscure the fact that the authors' criteria applied approximately to a grossly different diffusing passage yielded excellent results. The significant lesson, we believe, is that for optimum performance one must avoid the severe stalling and instability that often occurs in fluid handling devices. The authors' criteria apparently allowed us to circumnavigate this pitfall and still load the diffuser sufficiently to produce high recovery in a tight space.

The second example shows the effects of a large alteration of inlet geometry from that used by the authors. This flow passage was tested in many forms, two of which are shown in Fig. 7(*a* and *b*). The diffuser was developed using water at a Reynolds number based on throat width of about 100,000. The L/W_1 of these diffusers was about 3.5; the total divergence angle was varied from about 5 to 30 deg. In every case, no matter what the inlet configuration, we found that the onset of large transitory stall occurred close to the authors' line *a-a* and that the pressure recovery was maximum there. The value of maximum pressure recovery did depend, however, on the inlet configuration. We were not able to produce a fully developed stall at $2\theta = 30$ deg which implies, according to Fig. 6, that our inlet turbulence level was high. This was to be expected in the wake of the upstream center body.

It is hoped that this evidence of the success of the authors' criteria in actual applications will encourage others to use this method. The discusser hopes that the authors and others will build upon this excellent base by exploring the many secondary variables such as passage curvature, inlet flow configuration, Reynolds number, Mach number, and so on. He urges serious attention to the problem of the design of arbitrary diffusing passages, for it is turning, twisting passages of varying sectional shape that are the common lot of the fluid machinery designer. Of first importance is the influence of passage centerline curvature upon the flow regime chart, Fig. 1, and upon the location of maximum recovery, Fig. 4.

Authors' Closure

The authors would like to express their thanks to Dr. Dean for his excellent illustration of the methods suggested, for encouragement during the past course of the work, and for his suggestions on future efforts. In regard to future work, additional studies are under way at Stanford University on two aspects mentioned by Dr. Dean; (i) effect of inlet conditions on flow regime and performance, (ii) effect of wall curvature on flow regime and performance. It is hoped that useful results from these works can be reported at a later date.

Since preparation of the original paper, one other reference has also been called to the authors' attention, an abstract of work by

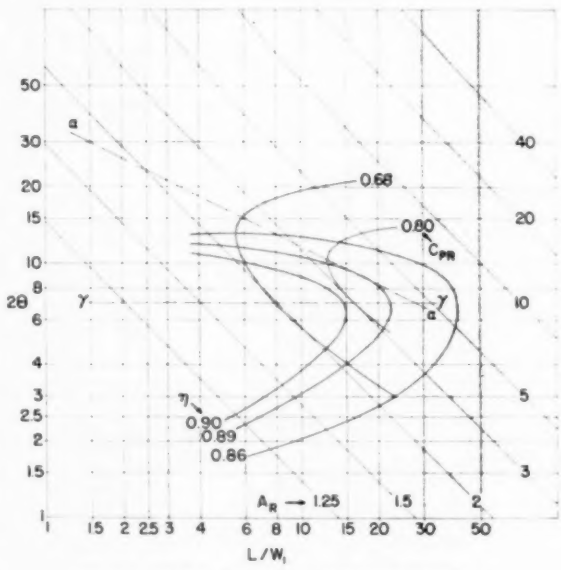

Fig. 8 Typical design curve, straight-walled diffusers

Rippl [40]. This work contains additional data on conical units. Although it is difficult to be certain from a translated abstract (complete original work not currently available to authors), it would appear that Rippl's observations concerning stall onset and trends of data are consistent with the discussion of the present paper. However, the location of optimum recovery at constant L/R_1 lies consistently 30 per cent below line a-a on Fig. 4 and is thus in disagreement with the data of Gibson. Although the uncertainty in location of optima in Rippl's data are large, it does not appear sufficient to explain this entire deviation. Rippl's results are in disagreement not only with Gibson but also with a number of design applications checked in this country in conical units. The preponderance of evidence thus suggests some type of difficulty in Rippl's results; the authors plan to check this further as soon as the complete work of Rippl can be obtained.

In the oral discussion on the present paper a question was raised concerning design charts prepared from the data of Fig. 5. Such a chart cannot be prepared in universal form since the recovery is a function not only of flow regime but also of Reynolds number, aspect ratio, inlet conditions, and Mach number. However, a chart can be prepared readily from any given set of data showing both isoplots and optimums. Such a figure has been prepared from the data of Reid [19] and is shown in Fig. 8. On this figure the line of optimum effectiveness, γ-γ, and optimum recovery at constant L/W_1, α-α, are shown; the penalty for deviation in a given design is also readily seen from the lines of constant effectiveness and recovery. However, it must be remembered that these numbers apply only to the particular conditions studied by Reid.

Finally the authors would like to add that while the information given does appear to represent some progress in means for design, it is not yet totally satisfactory since it does not supply an analytical basis nor a means for calculating performance.

Additional Reference

40 E. Rippl, "Experimental Investigations Concerning the Efficiency of Slim Conical Diffusers and Their Behavior With Regard to Flow Separation," *Monthly Technical Review*, vol. 2, March, 1958, p. 3.

W. ZABRISKIE

General Engineering Laboratory,
General Electric Company,
Schenectady, N. Y. Assoc. Mem. ASME

B. STERNLICHT

General Engineering Laboratory,
General Electric Company,
Schenectady, N. Y. Assoc. Mem. ASME

Labyrinth-Seal Leakage Analysis

The leakage flow through labyrinth seals in turbomachinery has been the subject of increasing concern as refinements and advances in design are made. Accurate knowledge of seal leakage is necessary in at least three areas of design: (a) Estimating the effect of seal leakage on performance; (b) regulating the leakage flow required for cooling purposes; (c) determining the thrust-bearing load which is a function of the pressure drop through the seal. This paper is concerned primarily with the fluid-flow aspect of gas leakage through labyrinth seals of the types commonly used in gas and steam turbines. This includes staggered and unstaggered seals of the axial type, which are most commonly used in turbomachinery. The attention to fluid-flow considerations does not imply that material compatibility and operating problems of expansion, deformation, and rub-in are unimportant. In fact, these mechanical considerations may overrule the fluid-flow considerations. For the foregoing reasons, it is desirable to be able to predict seal leakage flows, and thus this aspect of seal design has been singled out for consideration here.

THE AVAILABLE methods for estimating labyrinth seal leakage are numerous. Each method is based on certain simplifying assumptions which necessarily restrict the areas of applicability of the method. Thus 200 per cent differences are possible when using the different methods in calculation. The authors have reviewed the literature so that the state of the art could be evaluated. Information from the most pertinent references has been extracted and appears throughout the paper.

A method is developed in the paper for predicting leakage past the most commonly used seal, the straight-through labyrinth. The method is general in application, easy to use, and yields results accurate within 20 per cent of available test data.

No tests have been made in conjunction with this analysis. However, the available test data have been used to illustrate the correlation between theory and experiment.

Seal effectiveness is defined so that it may be used by design engineers in determining seal performance. It also can be employed as a relative measure for seal improvement.

Contributed by the Fluid Mechanics Subcommittee of the Hydraulics Division and presented at a joint session with the Instruments and Regulators Division at the Annual Meeting, New York, N. Y., November 30–December 5, 1958, of THE AMERICAN SOCIETY OF MECHANICAL ENGINEERS.

NOTE: Statements and opinions advanced in papers are to be understood as individual expressions of their authors and not those of the Society. Manuscript received at ASME Headquarters, August 8, 1958. Paper No. 58—A-118.

Geometrical Considerations in Seal Leakage

The leakage through any given seal is, of course, primarily dependent upon the clearance, over-all pressure ratio, and entrance pressure and temperature of the gas. In the design of the seal itself, the two most important variables are:

1 The shape of the teeth.
2 The size and shape of the chamber between teeth.

The effect of the tooth shape results from two factors:

(*a*) Ratio of tooth-tip thickness to clearance, b/h.
(*b*) Angle the front face of the tooth makes with the flow, θ.

The ratio of tooth-tip thickness to clearance, or relative sharpness of the tooth, has a significant effect on the coefficient of discharge. Fig. 1 shows that for a constant pressure ratio the discharge coefficient, and consequently the flow, will vary as much as 20 per cent. The effect of tooth-tip sharpness is marked at small clearances. Here a slight rounding of the edges will cause the tooth to perform as a nozzle.

The flow across a relatively broad tooth is described in a paper by Kearton [1][1] as being composed of three stages. In the first stage, there is a sudden contraction of the stream accompanied by a fall in pressure to a value less than the discharge pressure. In the second stage of the process, the stream probably enlarges so as to fill the constriction completely and there is a recovery of pres-

[1] Numbers in brackets designate References at end of paper.

Nomenclature

A = area, sq in.
B = chamber width, in.
b = tooth-tip width, in.
C = coefficient of discharge
E = seal effectiveness
f = friction factor
f = function of
g = gravitational constant, ft/sec^2
H = chamber depth, in.
h = clearance, in.
L = seal length, in.
l = pitch, in.
$\mathbf{M}$ = Mach number
m = hydraulic radius, in.
n = number of restrictions
P = total absolute pressure, psia
p = static absolute pressure, psia
R = gas constant, ft/deg F
N_{Re} = Reynolds number
T = total absolute temperature, deg R
V = velocity, ips
W = weight rate flow, lb per sec
x = distance along seal, in.
γ = ratio of specific heats
Δ = difference
θ = angle subtended by tooth face, angular deg
μ = absolute viscosity, lb-sec/sq in.
ρ = gas density, lb/ft^3

Subscripts

0 = upstream or initial condition
n = downstream or outlet condition
1, 2 = intermediate seal conditions

Superscripts

$\alpha = \dfrac{\gamma - 1}{\gamma}$

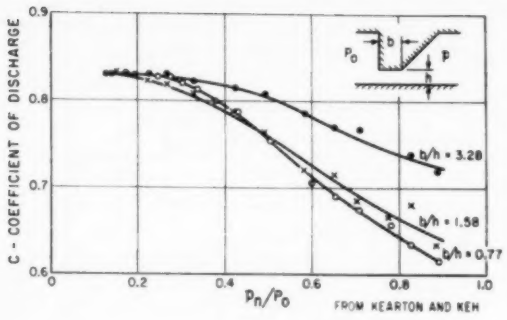

Fig. 1

sure. The subsequent flow, forming the third stage of the flow process, takes place in what is practically a very short channel of constant area, and the pressure will fall steadily owing to surface friction. The flow across relatively sharper teeth will consist of only the first, or first and second stages.

The angle which the front face of the tooth makes with the flow can have an appreciable influence on flow resistance. Data from Trutnovsky [2] on the resistance to flow of fins at various angles of attack indicates optimum resistance for a tooth angle of 40 deg. Data on discharge coefficients for various shapes of teeth are not available to any great extent. The most useful of the available data are shown in Fig. 1, where the discharge coefficient is shown to increase as the pressure ratio p_n/P_0 decreases. For this reason, a seal does not actually "choke" at the critical pressure ratio. The weight flow will increase by more than the increase in upstream pressure because the effective area increases with pressure ratio.

The size and shape of the chamber between teeth affect the strength of the vortex and eddies which convert the kinetic energy issuing from each tooth into internal energy. The chamber geometry has two important variables; the chamber width B and the chamber depth H. The literature considers each of these variables independently and often presents the data in nondimensional form with the carry-over or resistance plotted against B/h or H/h. The depth of the teeth does not have as great an effect on limiting leakage as does the chamber width. Work by Jerie [3] in flow visualization and experimentation on leakage through low-pressure seals indicates that the optimum tooth depth is equal to or slightly less than the pitch. Work by Trutnovsky [2] confirms the existence of optimum depth.

Optimizing the pitch of the teeth to secure minimum leakage in a given length seal deserves more attention than has been accorded to it in the literature. In optimizing the number of teeth in a given length seal, it is necessary to secure the proper balance between making the pitch as large as possible to reduce carry-over of kinetic energy and making the pitch as small as possible in order to get the greatest number of throttlings per unit length. The effect of tooth spacing on discharge coefficient is an additional consideration. It is well known that upstream or downstream disturbances tend to increase the discharge coefficient of an orifice. Thus there is further reason to increase the pitch in an effort to reduce the effective leakage area. Several sources present experimental data which suggest that an optimum pitch does exist. The data do not correlate too well, unfortunately, and indicate that this is an area where further experimentation would fill a gap in the fund of knowledge.

Data by Jerie [3] indicate that close spacing of the teeth can lead to a diffusing action of the seal with the resultant leakage higher than that passed by a single tooth. These test data may seem incredible at first, but one must consider the conditions under which the tests were conducted. The pressure ratio was very close to unity resulting in a single tooth-discharge coefficient of approximately 0.61. In the case of a two-tooth seal, the presence of another tooth apparently upset the contraction of the stream and resulted in higher discharge coefficients for the teeth. The increase in discharge coefficient caused the leakage flow to be greater than for the single tooth, despite the additional pressure loss from the second throttling. Work by Egli [4] and Trutnovsky [2] also indicates that the pitch/clearance ratio can be optimized for minimum leakage.

Method for Estimating Leakage in a Straight-Through or Unstaggered Labyrinth Seal. The straight-through labyrinth seal is most commonly used in present-day turbomachinery. Several different methods for estimating leakage have appeared in the literature. These include Martin's formula [5], procedure followed by Egli [4], procedure followed by Jerie [3], and others. Each of these methods is limited by the assumptions made in its derivation and will yield correct estimates only when the assumptions apply. The methods are characterized by the analysis of the problem as a series of orifices with corrections for tooth shape and geometry. An exception to this approach is that by Trutnovsky [2] who in 1943 wrote a treatise on the subject of labyrinth-seal leakage. Trutnovsky looked at seal leakage from an over-all standpoint and treated it as flow in a rough pipe. His solution of the basic equations describing the flow is quite complicated and difficult to use.

This paper presents a method which is outlined later and is an extension and simplification of the method used by Trutnovsky. The flow through an annulus is comparable to Fanno line flow; i.e., flow in a constant-area channel with friction but without heat loss or addition. In a labyrinth seal the roughness is very large compared to the hydraulic radius, but the mechanism of pressure loss is still the same as that of the smooth-wall tube.

The equations describing Fanno line flow are derived in several references on compressible fluid flow, e.g., Bailey [6] and Shapiro [7]. In brief, the equations are developed so that the friction parameter, $f\gamma x/2m$, relates the change in Mach number from inlet $\mathbf{M}_0$ to outlet $\mathbf{M}_n$ with the distance x across which the gas must flow in the constant-area annulus of hydraulic radius m and flow friction f to bring about this Mach-number change.

The total pressure at the seal inlet must be known as well as the static pressure at the outlet. With this information, it is possible to determine the relationship between the weight-flow parameter at the inlet, $W_0(T_0R)^{1/2}/CA_0P_0$, and at the outlet, $W_n(T_nR)^{1/2}/CA_np_n$.

Since $W_0 = W_n$, $A_0 = A_n$, and $T_0 = T_n$

then
$$\frac{W(T_0R)^{1/2}}{CAP_0}\frac{P_0}{\rho_n} = \frac{W(T_0R)^{1/2}}{CAp_n}$$

Now
$$\frac{W(T_0R)^{1/2}}{CAP_0} = f(\mathbf{M}_0)$$

and
$$\frac{W(T_nR)^{1/2}}{CAp_n} = f(\mathbf{M}_n)$$

Therefore $\mathbf{M}_0$ and $\mathbf{M}_n$ are related by the pressure ratio across the seal. The friction parameters are also a function of Mach number.

$$\left(\frac{f\gamma x}{2m}\right)_n + \left(\frac{f\gamma x}{2m}\right)_{0-n} = \left(\frac{f\gamma x}{2m}\right)_0$$

where
$$\left(\frac{f\gamma x}{2m}\right)_0 = f(\mathbf{M}_0), \quad \left(\frac{f\gamma x}{2m}\right)_n = f(\mathbf{M}_n)$$

and $(f\gamma x/2m)_{0-n}$ can be calculated for a given seal.

When both the friction parameter and weight-flow parameter

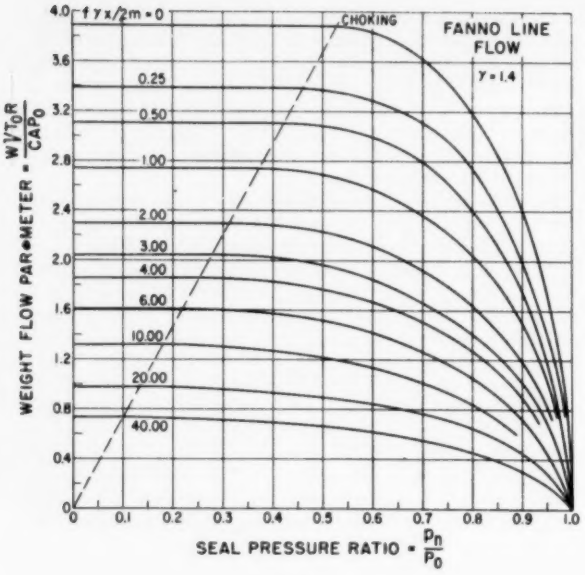

Fig. 2

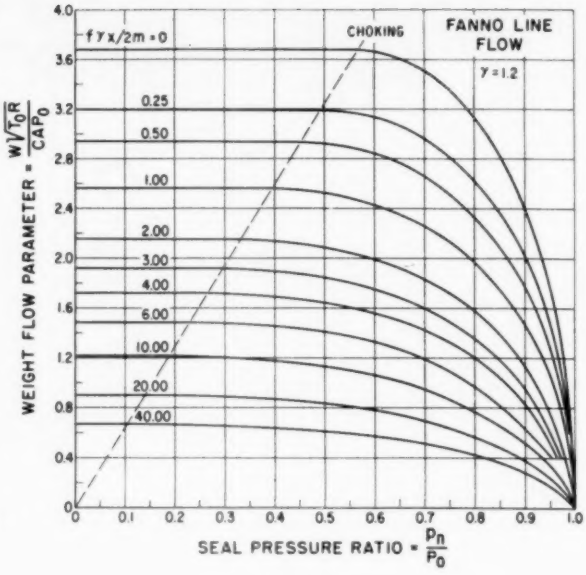

Fig. 3

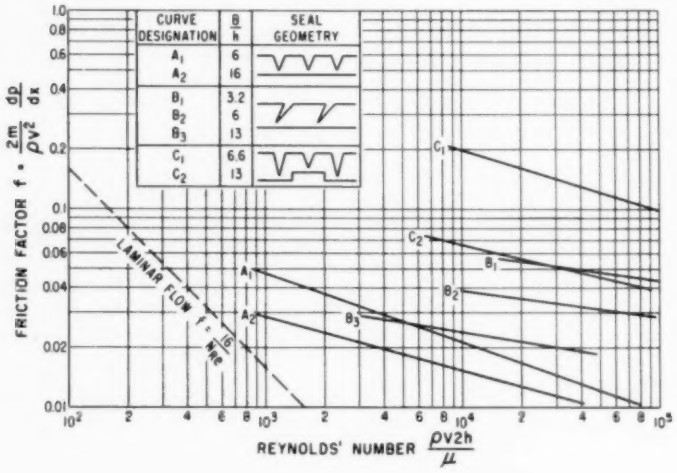

Fig. 4

are satisfied by the same values of M_0 and M_n, the leakage flow can be calculated since

$$\frac{W(T_0R)^{1/2}}{CAP_0} = f(M_0)$$

The Fanno line-flow relationships have been plotted in Fig. 2 for $\gamma = 1.4$ and in Fig. 3 for $\gamma = 1.2$. In estimating leakage the curves are entered at the pressure ratio of interest. At the calculated value of $(f\gamma x/2m)$ for the seal the weight-flow parameter is read. For known operating conditions the weight flow can be calculated. The value for the discharge coefficient is read from Fig. 1 at an average value for the pressure ratio per tooth. It should be recognized that this procedure for selecting the discharge coefficient may be in error because of two factors. The first factor is that the pressure ratio is not the same across each tooth of the seal. In reality the pressure drop per tooth increases in the direction of flow. Hence, basing the discharge coefficient on an average pressure ratio is not strictly correct. The other factor regarding the discharge coefficient is that the data in Fig. 1 were obtained for a single tooth with entrance and exit free from disturbances. Use of these values ignores the effects of upstream and downstream disturbances. When experimental data on these effects are obtained, the calculations will have increased accuracy. At present the estimates of discharge coefficient are considered accurate within ±10 per cent.

In cases where the friction factor varies significantly with Reynolds number, a trial-and-error solution is required. A Reynolds number must be assumed. For the specific seal geometry and assumed Reynolds number, a friction factor is obtained from Fig. 4. Using this friction factor the seal-leakage flow is calculated. Next, the Reynolds number based on this flow can be calculated directly and compared to the original estimate. If the resulting friction factors are significantly different, the weight flow should be recalculated.

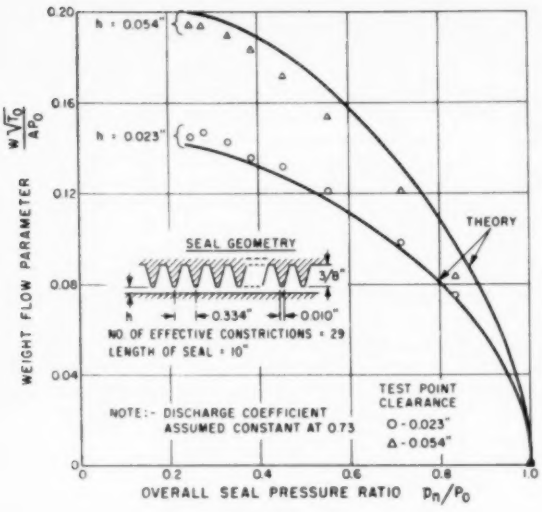

Fig. 5

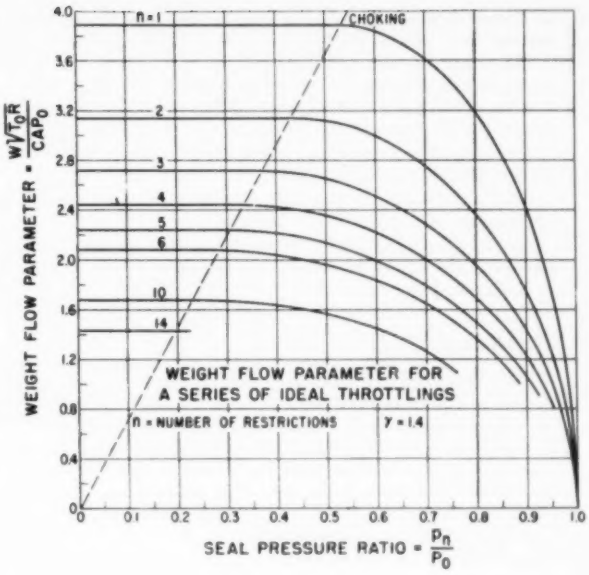

Fig. 6

A change in discharge coefficient will bring about a directly proportionate change in leakage flow. This is not true in the case of changes in the friction factor or length of seal. As an example, suppose that a seal is operating at a pressure ratio of 0.5 and the value of the friction parameter is 1.00. If the length of the seal or the friction factor is increased to double the friction parameter, only a 17 per cent reduction in leakage will be achieved.

Figs. 2 and 3 can be used for estimating flow in a smooth-wall annulus where a friction factor of 0.005 is commonly used. The line for ($f\gamma x/2m = 0$) is also the curve for a single restriction and represents the upper limit for leakage flow.

In looking at the data on friction factor and discharge coefficient several trends are evident. For a fixed pitch the friction factor decreases with decreasing clearance, thereby somewhat offsetting the benefits of a decreased flow area. In addition, for a fixed-tooth shape the discharge coefficient increases for a decreasing clearance, again tending to offset the decreased flow area.

Comparison Between Theory and Test. The Fanno line-flow theory has been correlated to test data for several different configurations over a wide range of operating conditions. The readily obtained results, a sample of which is shown in Fig. 5, show that the theory yields estimates within 20 per cent of actual test data. This represents a considerable improvement over previous methods where estimates up to 200 per cent in error could be calculated. In the calculations of Fig. 5, the discharge coefficient was assumed constant at 0.73. This is a somewhat arbitrary value based on the data in Fig. 1 with a nominal allowance for increase in discharge coefficient because of the influence of adjacent teeth. If the seal teeth are expected to rub in, leaving rough or rounded edges, a discharge coefficient of 0.85 would be more appropriate.

Leakage Through Seals in Series. To determine the loads on thrust bearings, the pressure between seals must be known. The interseal pressure must be assumed and then the weight flow through each seal calculated. If the weight flows are not the same, then a new pressure must be assumed and the solution repeated.

Staggered or Hi-Low Labyrinth Seal. The flow through a staggered seal can be analyzed quite easily if the assumption is made that all the kinetic energy developed at each restriction is transformed into internal energy in the chamber following the restriction. With this assumption, it is possible to write for each restriction the Saint Venant-Wantzel equation governing flow through a nozzle or orifice

$$\frac{W}{A} = C\left\{\frac{2g\gamma}{\gamma-1}\frac{P_0^2}{RT_0}\left(\frac{p_1}{P_0}\right)^{2/\gamma}\left[1-\left(\frac{p_1}{P_0}\right)^{\frac{\gamma-1}{\gamma}}\right]\right\}^{1/2}$$

letting

$$\alpha = \frac{\gamma-1}{\gamma}$$

For the first restriction

$$\frac{WT_0^{1/2}}{AP_0}\left(\frac{R\alpha}{2g}\right)^{1/2} = C_{0\text{-}1}\frac{p_1/p_0}{(p_1/p_0)^\alpha}\left[1-\left(\frac{p_1}{p_0}\right)^\alpha\right]^{1/2}$$

For the second restriction

$$\frac{WT_0^{1/2}}{AP_0}\left(\frac{R\alpha}{2g}\right)^{1/2}\frac{P_0}{p_1} = C_{1\text{-}2}\frac{p_2/p_1}{(p_2/p_1)^\alpha}\left[1-\left(\frac{p_2}{p_1}\right)^\alpha\right]^{1/2}$$

and for the nth restriction

$$\frac{WT_0^{1/2}}{AP_0}\left(\frac{R\alpha}{2g}\right)^{1/2}\left(\frac{P_0}{p_1}\right)\left(\frac{p_1}{p_2}\right)\cdots\cdots\frac{p_{n-1}}{p_n} = C_{(n-1)\text{-}n}\frac{p_n/p_{n-1}}{(p_n/p_{n-1})^\alpha}\left[1-\left(\frac{p_n}{p_{n-1}}\right)^\alpha\right]^{1/2}$$

where

$$\left(\frac{P_0}{p_1}\right)\left(\frac{p_1}{p_2}\right)\left(\frac{p_2}{p_3}\right)\cdots\cdots\frac{p_{n-1}}{p_n} = \frac{P_0}{p_n}$$

The functions

$$\frac{1}{(p_n/p_{n-1})^\alpha}\left[1-\left(\frac{p_n}{p_{n-1}}\right)^\alpha\right]^{1/2}$$

and

$$\frac{p_n}{p_{n-1}}\frac{1}{(p_n/p_{n-1})^\alpha}\left[1-\left(\frac{p_n}{p_{n-1}}\right)^\alpha\right]^{1/2}$$

can be plotted as functions of pressure ratio. These curves are

then used in the construction of Fig. 6, where the discharge coefficient was assumed constant from restriction to restriction.

The actual leakage in a staggered seal will differ from these theoretical results because of carry-over of kinetic energy and an increase in discharge coefficient at the last tooth as the seal approaches a choked condition. Kearton and Keh [8] show that a discharge coefficient of 0.67 is appropriate for a low-pressure ratio seal of the staggered-tooth type.

Results obtained from Fig. 6 will give minimum values of leakage for a given number of restrictions.

The equations derived in the foregoing can also be used to determine the pressure distribution in the gland. This was done by Robinson [9].

Evaluation of Seal Effectiveness

The effectiveness of a seal may be judged by comparing its leakage to that of two extreme cases: (*a*) The minimum possible leakage through a seal of a given number of teeth occurs when perfect throttling exists between the teeth; (*b*) the maximum possible leakage for a seal with a given tooth design occurs when the number of teeth is reduced to one. This comparison is shown in Fig. 7.

The definition of seal effectiveness as proposed herein is illustrated in Fig. 7. It is the ratio of the actual decrease in leakage from the single-tooth case to the maximum theoretically attainable decrease in leakage.

The data for a single tooth may be obtained from the ($f\gamma x/2m = 0$) line on Fig. 2 or 3 and discharge-coefficient data for the particular tooth shape. Representative data which are available on specific tooth forms are shown in Fig. 1.

The leakage through a seal in which ideal throttling occurs between teeth has been analyzed in several sources; viz., Kearton [8]. These data are presented in Fig. 6. Again, the discharge coefficient must be known. The pressure ratio across each tooth in a seal is usually not constant. Since the discharge coefficient is a function of pressure ratio, there will be a different C for each tooth. A mean discharge coefficient can be selected if the pressure distribution is known accurately. From the paper by Robinson [9], the pressure-ratio relationship between any two consecutive orifices may be obtained when ideal throttling is assumed. This enables the pressure distribution in a seal of any number of restrictions to be determined by a trial-and-error solution. A mean pressure ratio for the restriction may then be calculated and a mean value for C selected if the pressure distribution is known accurately.

By plotting actual test results or seal-leakage estimates on the same graph, it is possible to determine seal efficiency. This graphical comparison permits the designer to see readily what a given design has accomplished and to determine the maximum possible improvement.

Conclusion

This paper presents methods for calculation of labyrinth-seal leakage in which theory and practice are within 20 per cent accuracy. This yields considerable improvement in accuracy over other existing methods for calculation of labyrinth-seal leakage. Furthermore, the method presented is easy to use and time for computation is very short. A definition of seal effectiveness is presented which enables one to evaluate the efficiency of a seal. This is valuable in checking test data and also in seal design. The experimentalist can easily determine whether his test data fall within the theoretical limits. The design engineer can calculate

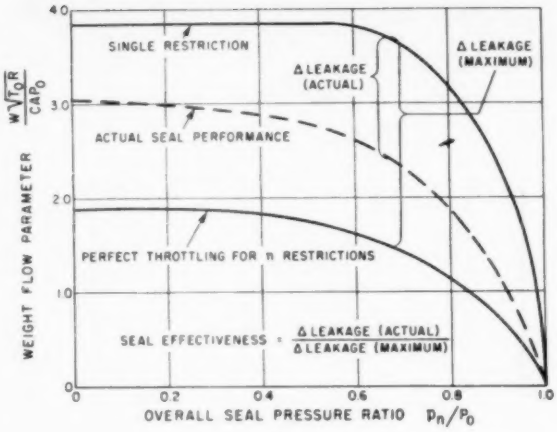

Fig. 7

readily the gain or loss in seal efficiency as he varies the seal parameters.

The main areas which need additional work are the estimates of discharge coefficient and friction factor. There is little information available on the effect of adjacent teeth and tooth geometry on discharge coefficient. Friction data for various tooth configurations are very limited and further investigation is needed. As these data become available, Figs. 1 and 4 can be drawn more completely. The characteristics of Fig. 4 may act as a guide for test on other seal geometries. Thus, with a limited number of tests, it is possible to span the field.

Acknowledgment

The authors wish to express their grateful appreciation to Mr. J. Fowler of the Large Steam Turbine-Generator Department and Messrs. F. A. Schweiger and W. P. Foster of the Aircraft Gas Turbine Division for their test data which were used to obtain data on friction factor versus Reynolds number.

References

1 W. J. Kearton, "The Flow of Air Through Radial Labyrinth Glands," *The Chartered Mechanical Engineer*, February, 1955, p. 109; see also *Proceedings of The Institution of Mechanical Engineers*, vol. 169, 1955.

2 K. Trutnovsky, "Beruehrungsfreie Dichtungen," Berlin, Germany, 1943 (available Library of Congress, call no. TJ529 T78).

3 J. Jerie, "Flow Through Straight-Through Labyrinth Seals," *Proceedings of the Seventh International Congress for Applied Mechanics*, vol. 2, 1948, pp. 70–82.

4 A. Egli, "The Leakage of Steam Through Labyrinth Glands," TRANS. ASME, vol. 57, 1935, pp. 115–122.

5 H. M. Martin, "Labyrinth Packings," *Engineering*, January 10, 1908, pp. 35–36.

6 N. P. Bailey, "The Thermodynamics of Air at High Velocities," *Journal of the Aeronautical Sciences*, vol. 2, 1944, pp. 227–238.

7 A. H. Shapiro, "Thermodynamics of Compressible Fluid Flow," Ronald Press, New York, N. Y., vol. 1, 1953.

8 W. J. Kearton and T. H. Keh, "Leakage of Air Through Labyrinth Glands of Staggered Type," *Proceedings of The Institution of Mechanical Engineers*, series A, vol. 166, 1952, pp. 180–188, and discussion, pp. 189–195.

9 C. S. L. Robinson, "Flow of a Compressible Fluid Through a Series of Identical Orifices," *Journal of Applied Mechanics*, vol 15, TRANS. ASME, vol. 70, 1948, pp. 308–310.

DISCUSSION

W. G. Cornell[2]

The authors are to be congratulated on an excellent and interesting contribution to seal technology. The use of an over-all, compressible flow model based on modern, one-dimensional gas-dynamics techniques is quite different from the detailed, sometimes incompressible, tooth-by-tooth models of earlier investigators. Like earlier models, empirical data on average tooth-discharge-coefficient are required. Unlike such models, a second parameter proportional to pressure gradient along the seal—the authors' "friction factor"—is introduced. Care must be taken to avoid confusion resulting from literal interpretation of the friction factor as physically equivalent to the effect of fluid friction at the walls of a pipe. In usual seals, the effect of wall friction is much smaller than the effect of fluid mixing. Thus, as shown in Fig. 4, geometric parameters have a considerable effect on the friction factor.

Consequently, it seems physically more reasonable to consider the authors' model as that of flow through a tortuous passage characterized by a "pressure drop coefficient" $dp/(1/2)\rho v^2 = f(dx)/m$ rather than that of flow through a rough pipe characterized by a friction factor, f.

J. L. Dussourd[3]

The problem of designing a labyrinth seal capable of holding the leakage flow below a specified amount is an old one for the mechanical designer. Because treatises on this subject, in general, have been complex to apply, the designer more often than not finds himself in need of assistance from his more aerodynamically minded colleagues. In this respect, it is welcome news that a procedure be made available that is practical and easy to use by a mechanical designer. The authors are to be congratulated for their simplified presentation which concerns itself with over-all effects, rather than the internal details of the flow process.

In any scientific effort such as this, it is always highly desirable to document the theory with substantial amounts of test results when available. Not only is this essential for the sake of good scientific practice, but also is this a necessity if one is to "sell" the procedure and stimulate confidence in its use. It is disappointing that only a few sparse test results have been included in the paper, especially in view of the fact that the authors had access to test data of their own in addition to the already appreciable amounts available in the literature. Curves of the type shown in Figs. 1 and 4 would be ideal for the presentation of large volumes of adequately reduced test information from various sources. It is realized that careful analysis, and perhaps additional systematic tests, would be required to separate the frictional effects from those of the vena contracta at the throat; but such facts must be established if the proposed method of solution is to be accepted generally as something better than just a quick approximation.

A. S. Gertz[4]

The problem of labyrinth leakage is, of course, important to all manufacturers of turbomachinery. It becomes even more important in the case of centrifugal compressors designed for low inlet volumes of approximately 1000 cfm. The labyrinth clearances for large-flow machines cannot be reduced proportionally for small-flow machines owing to mechanical reasons; hence the percentage leakage flow in small-flow machines becomes large and has a significant effect on performance calculations.

This paper, therefore, becomes very valuable from two aspects: (*a*) It summarizes previous literature, pointing out the divergence in correlation among the various methods and presenting the most pertinent information from each. (*b*) It presents a method of calculation which correlates with General Electric test data within 20 per cent.

To become more familiar with this method of calculation, three hypothetical labyrinth configurations were selected and the leakage was calculated for each configuration by both the Egli method and the method presented in this paper, using air as the gas. A tabulation of the various seal parameters follows:

Configuration	A	B	C
Upstream pressure, psia	30	30	80
Downstream pressure, psia	15	15	64
Temperature, deg R	625	625	625
Radial clearance, in.	0.010	0.020	0.020
Tooth-tip width, in.	0.0625	0.020	0.020
Diameter, in.	5	5	10
Pitch, in.	0.375	0.375	0.34
Number of teeth	4	4	20
Seal length, in.	1.1875	1.145	6.48

NOTE: All configurations were of the A type shown in Fig. 4 of the paper.

There was relatively good correlation between the two methods. In all cases the leakage flow by the Egli method was the larger of the two. Configurations A and B both gave approximately 17–20 per cent less flow using the method described in this paper. Configuration C gave approximately 34 per cent less flow than the Egli method.

The ease of calculation was about the same for both methods. The basic calculation outlined in the paper is simpler but requires a friction-factor check owing to the steepness of the friction-factor curves, which tends to even out the time required.

Since, as mentioned in the paper, the roughness in a labyrinth seal is very large compared to the hydraulic radius, the friction factor differs in concept from the usual pipe friction factor. This would indicate that a large number of checks must be made of friction factor versus Reynolds-number curves for various seal configurations.

It would be interesting to know whether any of the other labyrinth-leakage calculation methods indicated a satisfactory correlation with the test data in the authors' analysis.

The method of analysis presented in the paper appears sound and provides a good correlation with both test data and the Egli method as described in the foregoing. The authors are to be commended for re-examining the problems associated with labyrinth leakage and for the presentation of a new method of solution.

Erik Vohtz[5]

The authors have given a most valuable review of the available methods of analysis in a field of increasing concern in turbomachinery design and have developed a useful and simple method for estimating the leakage past straight-through seals.

It might be of interest to raise one point with regard to the authors' remarks on staggered seals.

A series of tests of various labyrinth seal arrangements has been conducted in the Stationary Air Test facility of the Large Steam Turbine-Generator Department of the writer's company. Fig. 8 shows the results of a test of a high-low, staggered-type seal. The calculation of this graph was made as follows: Seal

[2] Jet Engine Department, General Electric Company, Evendale, Ohio. Mem. ASME.

[3] AiResearch Manufacturing Company of Arizona, Phoenix, Ariz.

[4] Compressor Engineering Department, De Laval Steam Turbine Company, Trenton, N. J. Assoc. Mem. ASME.

[5] Turbine Fluid Mechanics Research, Large Steam Turbine-Generator Department, General Electric Company, Schenectady, N. Y.

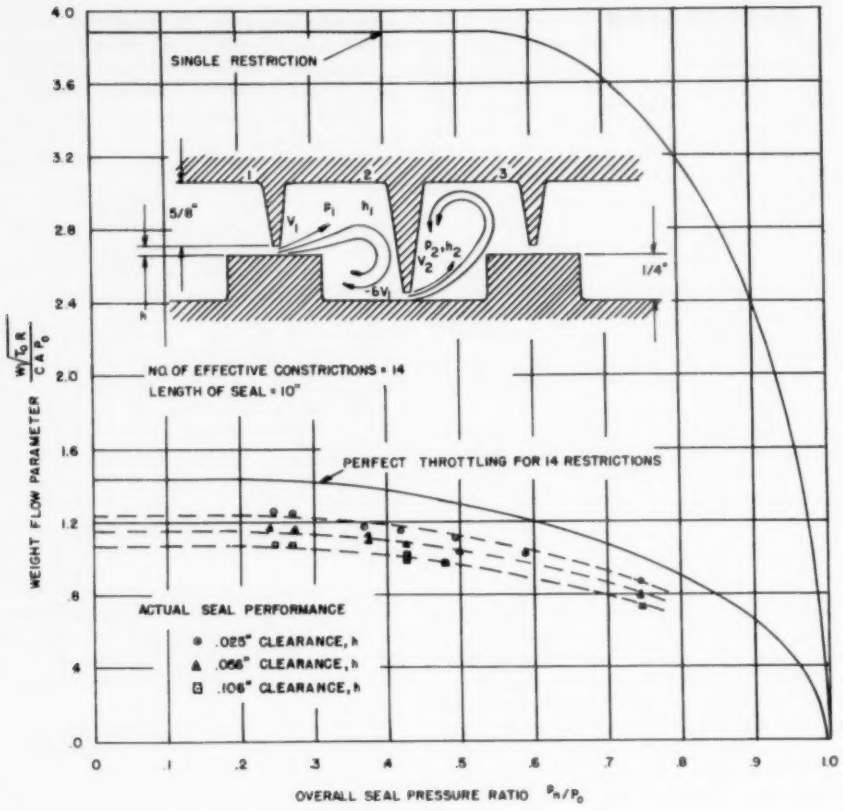

Fig. 8

leakage was measured by calibrated orifices; single throttling discharge coefficients were established by tests and range from 0.70 to 0.73, according to the particular average pressure ratio and clearance.

It will be noticed that the leakage through this seal is less than the minimum leakage indicated for this type of seal in Fig. 6 of the paper.

This fact may be explained by the formation of vortexes in the chambers between the teeth. These vortexes will make part of the velocity from one constriction effective as negative approach velocity for the following constriction. Consider the flow through constriction 2 in Fig. 8. The residual velocity from constriction 1, effective as negative velocity of approach for constriction 2 is $(-\delta V_1)$, p_1 is the static pressure in the outer filament of the vortex, equal to the throat pressure in constriction 1, and h_1 is the enthalpy in the chamber. Characters with subscript 2 refer to the same properties after constriction 2.

For adiabatic expansion through constriction 2 we have

$$h_1 - \frac{(\delta V_1)^2}{2Jg} = h_2 + \frac{V_2^2}{2Jg}$$

By assuming that the change in throat velocity from one constriction to the next is small, we may substitute V_1 by V_2 and write

$$V_2 = \left(\frac{1}{1+\delta^2}\right)^{1/2} [2Jg(h_1 - h_2)]^{1/2}$$

The last term in this equation will be recognized as the term

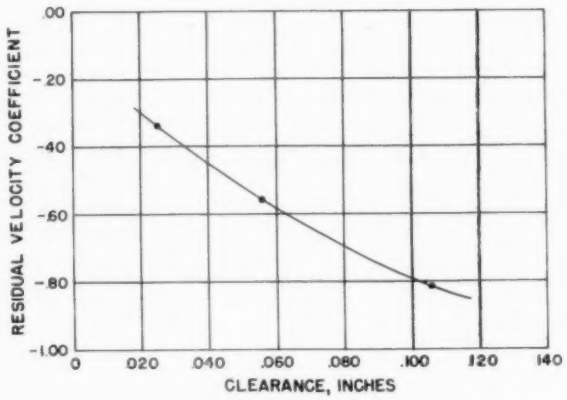

Fig. 9

that leads to the Saint Venant-Wantzel equation by the assumption of perfect fluid and by use of the continuity equation.

Thus

$$\frac{W}{A} = \left(\frac{1}{1+\delta^2}\right)^{1/2} C \left\{\frac{2g\gamma}{\gamma-1}\frac{p_1^2}{RT_1}\left(\frac{p_2}{p_1}\right)^{2/\gamma}\left[1-\left(\frac{p_2}{p_1}\right)^{\frac{\gamma-1}{\gamma}}\right]\right\}^{1/2}$$

This way, we are led to apply the factor $(1 + \delta^2)^{1/2}$ to the weight-flow parameter. The minimum leakage past a staggered seal would occur if the velocity from one constriction was 100 per cent available as negative velocity of approach for the following constriction. Thus the minimum leakage is $1/\sqrt{2}$ of that indicated in the paper.

Fig. 9 gives the residual velocity coefficient for the high-low seal in Fig. 8.

Authors' Closure

The authors are pleased to see the extent of interest in the subject of labyrinth-seal leakage and wish to thank the discussers for their questions and stimulating comments.

In reply to Mr. Cornell, we agree that the concept of the pressure drop coefficient is more reasonable from a physical standpoint than the interpretation of the friction factor f. Mr. Dussourd's disappointment with respect to the limited publication of experimental data is understandable. His own closing sentence, however, supplies the reason for our inability to supply substantial amounts of consistent test data to substantiate the theory. Few experiments in labyrinth-seal leakage have determined the single tooth-discharge coefficient, let alone the effect of upstream and downstream teeth on this coefficient. To accurately determine the so-called friction factor from the leakage flow data requires an accurate knowledge of the tooth-discharge coefficient. When these data are not available, an estimate for the discharge coefficient must be made. Where judgment is involved, it is extremely difficult to present a rigorous, conclusive correlation of theory and experiment. Improvement in the accuracy of estimating from 200 to 20 per cent was felt to be sufficient advancement without waiting for the availability of carefully performed experiments where the afore-mentioned factors are separable. The authors have made several other comparisons between controlled experiment and theory and in each case good accuracy resulted. Figs. 10 and 11 show two additional such

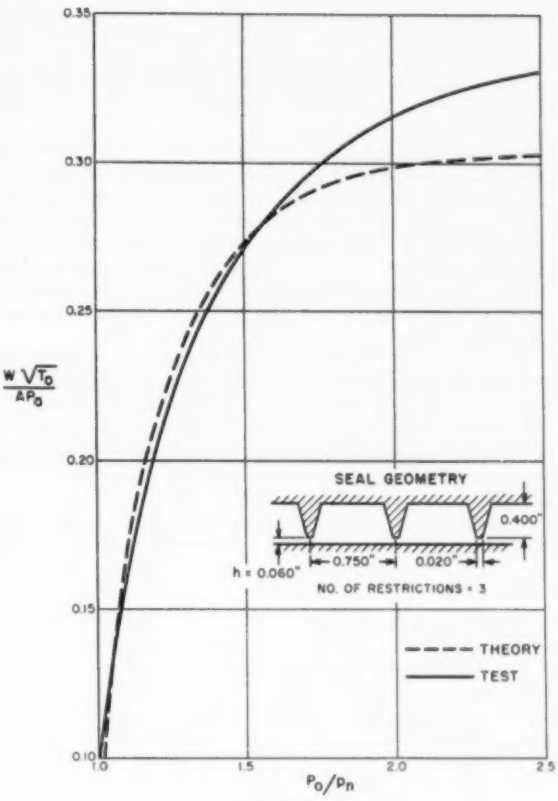

Fig. 11

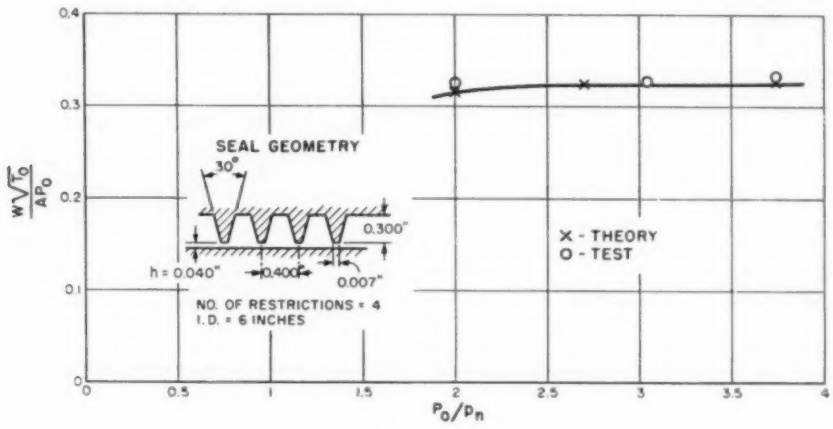

Fig. 10

comparisons. Credit for experimental data of Fig. 10 should be given to Mr. F. Schweiger and of Fig. 11 to Mr. P. W. Bauer, both of General Electric Co. Mr. Dussourd is referred to the discussion by Mr. Gertz if he needs to be further "sold" on this method of calculation.

Mr. Gertz's correlation with the Egli method represents a valuable addition to the paper. The methods of Kearton, Jerie, and Martin were examined by the authors. As long as the limitation of these methods in respect to geometry and pressure ratio were observed, general agreement was obtained. The difficulty for the average seal designer is that these limitations are not readily referenced and one method is generally used for all cases whether it applies or not. The advantage to the method described in this paper is that it can be applied to a wide variety of seal geometries over the incompressible and compressible flow ranges. Mr. Gertz states that this method of calculation and that by Mr. Egli requires approximately the same time. Yet Mr. Gertz has been familiar with Egli's method and not with

this. Thus, it may be concluded that once experience is gained this method will be faster. We find it considerably faster and applicable over a wider range of conditions.

The analysis and concepts employed by Mr. Vohtz are quite provoking. The fact that the actual leakage data lie below the perfect throttling line could be explained by the fact that the discharge coefficient for the tooth was probably measured for the case of the tooth against a flat seat with the flow impinging directly in the leakage direction. In the actual leakage test the flow approaches the tooth more or less perpendicularly to the leakage direction. The discharge coefficient, therefore, is likely to be less than that experimentally determined. It is not unreasonable to expect the discharge coefficient to be as low as 0.5, causing a replot of the test data to fall above the theoretical minimum leakage.

The use of a residual velocity coefficient should be a useful parameter for comparing relative performance of various seal geometries. In the derivation of the correction factor suggested by Mr. Vohtz, there seems to be an inconsistency in the use of symbols for enthalpy. If one interprets h to be the static enthalpy, then it appears to be a contradiction to write:

$$h_1 - \frac{(\delta V_1)^2}{2Jg} = h_2 + \frac{V_2^2}{2Jg} = \text{total enthalpy},$$

since this implies that the static enthalpy at 1 is less than the total enthalpy. Acknowledging the existence of the vortex with its associated reverse flow in each chamber, it is none the less mandatory that at some point near the seal tooth a stagnation point exists. The flow on one side of this point is part of the vortex while on the other side is the leakage flow past the subsequent tooth. At the stagnation point, the static enthalpy is equal to the total enthalpy. Thus, it seems more rigorous to write:

$$h_1 + \frac{\delta V_1^2}{2Jg} = h_2 + \frac{V_2^2}{2Jg}$$

The correction factor to the theoretical minimum leakage then becomes $\sqrt{\frac{1}{1-\delta^2}}$. When $\delta \to 0$, as for a staggered seal, the correction factor is unity. This result then agrees with the theoretical minimum leakage as given in the paper.

Centrifugal Manometer

J. F. KEMP

Senior Research Officer,
National Mechanical Engineering Research Institute,
South African Council for Scientific and Industrial Research,
Pretoria, South Africa

The operating principles and mechanical construction of a micromanometer, which utilizes air in lieu of a liquid as working fluid, are described. Some of the noteworthy features of the instrument include its high sensitivity and accuracy, quick response, wide range, and ease of manipulation. Differential pressures of the order of 5×10^{-3} mm water gage can be measured with an error of 1 per cent under normal laboratory conditions. The maximum range of the prototype described is 25 mm water gage, and the corresponding error at this value amounts to about 0.25 per cent.

Introduction

In LOW-SPEED aerodynamic research and in ventilation studies, it is often required to measure small pressure differences with high precision. The air flow in these studies is generally of such a nature that pressure differences vary with the square of the flow speeds, the pressure differences thus becoming extremely small when the flow speeds are very low.

Several extremely sensitive liquid manometers have been developed for the measurement of very small pressure differences [1, 2, 3],[1] but the use of a liquid in itself introduces sources of error, which have an increasingly detrimental effect on the accuracy of measurement as the flow speeds decrease. Evaporation, capillary action, wetting of the walls of containers or tubes, and differential expansion between the liquid and the metal components of the manometer are some of the sources of error associated with the use of a liquid in a manometer.

Reichardt [4], Simmons [5], and Nickel [6] have devised differential pressure gages in which air displaces the liquid as working fluid. The centrifugal manometer described in this paper is essentially an improved version of the Nickel type, although it can be claimed that the development of the new instrument was carried out independently of the work by Nickel. Improvements associated with the new manometer include a more refined and accurate working formula, a more effective pressure-balancing technique, a lower internal-flow resistance, and a more accurate method of determining rotational speeds. Each of these improvements in turn enhances the over-all accuracy of measurement that can be achieved under practical conditions.

[1] Numbers in brackets designate References at end of paper.

Contributed by the Hydraulic Division and presented at a joint session with the Instruments and Regulators Division at the Annual Meeting, New York, N. Y., November 30–December 5, 1958, of THE AMERICAN SOCIETY OF MECHANICAL ENGINEERS.

NOTE: Statements and opinions advanced in papers are to be understood as individual expressions of their authors and not those of the Society. Manuscript received at ASME Headquarters, April 25 1958. Paper No. 58—A-111.

Operating Principles and Basic Considerations

The operation of the centrifugal manometer may be explained with the aid of the schematic drawing in Fig. 1, where the instrument is shown connected to the two pressure tappings of a pitot-

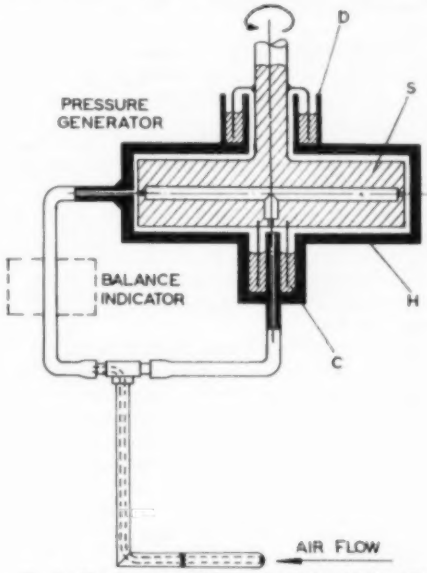

Fig. 1 The Centrifugal Manometer System (Schematic)

Nomenclature

a = sonic velocity
c = annulus width in the pressure generator
D = inner diameter of tube
e = base of Napierian logarithm
h = differential pressure in water gage
Δh = error in the measurement of h
L = length of tube
n = rotational speed of disk, rps
P = differential pressure of the generator
P_a = pressure rise in the annulus of the generator
P_d = pressure rise in the disk of the generator
ΔP = error in the measurement of P
p = static pressure at r
R = radius of disk
R_a = inner radius of housing
r = radial distance from axis of rotation
v = tangential speed of air at r, or alternately, mean flow speed in tube
z = axial distances (in cylindrical coordinates)
γ = specific heat ratio for air
μ = air viscosity
ρ = air density
ω = rotational speed of disk, rad/sec

Subscripts

1 = axis of rotation
e = the equivalent tube
i = the indicator tube
k, l, m = components in the pressure circuit

static tube for the purpose of measuring local velocity heads in an air stream.

The manometer comprises two essential components, viz., a differential-pressure generator and a balance indicator. The generated pressure is applied to oppose and balance the unknown pressure head, and the condition of balance is shown by the indicator. When balance obtains, no flow occurs in the connecting tubes between the generator and the source of the unknown differential pressure—in this case the pitot-static tube. Hence the balance indicator can be made in the form of a "stagnation" or "no-flow" indicator.

The accuracy of the system will depend to a large extent on the indicator's sensitivity, which may be defined in terms of the smallest flow speed that can be detected by means of this device. Since, in practice, the indicator can never have an infinitely high sensitivity, a small flow will take place, even under balanced conditions, and a correspondingly small pressure drop, associated with laminar flow in the connecting tubes and other components of the pressure circuit, will appear as an error in the measurement. It is clear that, for an indicator of given sensitivity, this error will increase linearly with the effective internal resistance of the circuit to laminar flow.

The development of a suitable balance indicator of high sensitivity is discussed under "The Balance Indicator" and the implications regarding circuit resistance are here analyzed on a quantitative basis.

The pressure generator in Fig. 1 operates by virtue of the centrifugal forces acting on a number of radial air columns in a rotating disk S. The disk is enclosed in a stationary, air-tight housing H, and a mercury seal D is provided where the driving shaft of the disk enters the housing. A similar seal C serves to transmit the static pressure at the center of the disk to a suitable tapping on the housing. Seal C also prevents internal circulation of air between the periphery and the center of the disk in the spaces between the disk and the housing.

The static pressure at the terminations of the air columns on the periphery of the disk is transmitted across the annular space between the rim of the disk and the housing by means of small static-pressure holes.

The pressure difference between the axis of rotation and the periphery of the disk can be calculated exactly from first principles, and is a function of the rotational speed and diameter of the disk and of the density of the air. Transmission of the pressure radially across the annular space between disk and housing is accompanied by a slight increase of pressure, since centrifugal forces are also encountered in the annulus. This pressure rise calls for the application of an "annulus correction," which can be calculated with good accuracy by means of the Navier-Stokes equations for fluid flow.

In the following section a suitable working formula will be derived for the differential pressure generator.

Differential Pressure Generation

Pressure Rise in the Rotating Disk. Under conditions of perfect pressure balance, there is no flow in the radial holes of the rotating disk. At any radius r from the axis of rotation, a positive static-pressure gradient exists which balances the centrifugal air forces so that

$$\frac{dp}{dr} = \rho\omega^2 r \tag{1}$$

where

p = static pressure at r
ρ = air density at r
ω = rotational speed of disk

For low rotational speeds ω, the density ρ of air in the disk can be assumed constant. By integrating equation (1), it is then easily found that

$$P_d = {}^1/_2\rho\omega^2R^2 \tag{2}$$

where

P_d = pressure rise in disk
R = radius of disk

At higher values of rotational speed ω, the compressibility of air in the disk has to be taken into account. For this purpose, isothermal conditions may be assumed to prevail in the disk.

According to the gas laws

$$p = \frac{\rho a^2}{\gamma} \tag{3}$$

where

a = sonic speed relating to the temperature in the disk
γ = specific heat ratio for air

Dividing equation (1) by equation (3) yields the differential equation

$$\frac{dp}{p} = \frac{\gamma\omega^2 r\, dr}{a^2} \tag{4}$$

the solution of which is

$$p = p_1 e^{\frac{\gamma\omega^2 r^2}{2a^2}} \tag{5}$$

where p_1 relates to the pressure on the axis of rotation.

Since $e^x = 1 + x + \frac{x^2}{2!} + \frac{x^3}{3!} + \ldots . \infty$, equation (5) can be applied to yield the pressure rise P_d in the disk in the form of a series:

$$P_d = \rho_1 \frac{\omega^2R^2}{2}\left[1 + \frac{\gamma}{4}\left(\frac{\omega R}{a}\right)^2 + \frac{\gamma^2}{24}\left(\frac{\omega R}{a}\right)^4 + \ldots . \infty\right] \tag{6}$$

where ρ_1 = air density at the axis of rotation.

If the peripheral speed ωR of the disk is small in comparison with sonic velocity a, equation (6) reduces to the same form as equation (2), where compressibility of the air is neglected. With the aid of equation (6) it can be shown that, under normal atmospheric conditions, the error incurred in the calculation of P_d when compressibility effects are neglected, will be less than 0.25 per cent if the peripheral speed of the disk is lower than about 90 ft per sec.

The Pressure Rise in the Annulus. The Navier-Stokes equations in cylindrical co-ordinates (r, z, ϕ) [7] can be applied to assess the pressure rise P_a in the annulus between the pressure transmission holes on the periphery of the disk and the collecting hole in the wall of the housing (Fig. 1). If the radial depth of the annulus is assumed to be small compared with the rim width of the disk, the flow in the vicinity of the pressure transmission holes will be essentially two-dimensional in nature. Axial and radial flow will be absent, while tangential flow speeds v (say), as well as the static pressure p in the annulus, will be functions of the radial distance r only, and not of axial and azimuthal positions z and ϕ respectively.

If incompressible flow is furthermore assumed, the otherwise complicated Navier-Stokes equations reduce to the following simple equations:

$$\frac{dp}{dr} = \rho\frac{v^2}{r} \tag{7}$$

and

$$\frac{d^2v}{dr^2} + \frac{1}{r}\frac{dv}{dr} - \frac{v}{r^2} = 0 \tag{8}$$

where

r = radial distance from axis of rotation
p = static pressure at r
ρ = air density in the annulus
v = tangential speed at r

The boundary conditions are the following:

$v = R\omega$ if $r = R$,

and

$v = 0$ if $r = R_a$.

As before, R and ω denote the radius and the rotational speed of the disk, respectively, while R_a is defined by the expression

$$R_a = R + c \tag{9}$$

where c = radial width of the annulus.

The solution of equation (8) is

$$v = \frac{\omega R^2}{(R_a - R)(R_a + R)}\left(\frac{R_a^2}{r} - r\right) \tag{10}$$

According to equation (7), the pressure rise P_a in the annulus is given by the expression

$$P_a = \int_R^{R_a} \rho \frac{v^2 dr}{r} \tag{11}$$

The value for v in Equation (10) can be substituted into equation (11), and by integrating between the limits R and R_a, the following expression is derived for P_a:

$$P_a = \rho \frac{\omega^2 R^2}{2}\left[\frac{R_a^2 + R^2}{R_a^2 - R^2} - \frac{4R^2R_a^2}{(R_a - R)^2(R_a + R)^2}\log_e \frac{R_a}{R}\right] \tag{12}$$

If the annulus width c is assumed to be small compared to the radius R of the disk, equation (12) can be simplified appreciably. For this purpose the log term is developed into an infinite series by substituting $(1 + c/R)$ for the term R_a/R. If those terms of c/R which contain powers higher than the second are neglected in relation to unity, equation (12) then becomes

$$P_a = {}^1/_3\rho\omega^2R^2\left(\frac{2c}{3R}\right) \tag{13}$$

The Working Formula for the Pressure Generator. Equations (2) and (13) combined yield the working formula for the pressure generator:

$$P = P_d + P_a = {}^1/_3\rho\omega^2R^2\left(1 + \frac{2c}{3R}\right) \tag{14}$$

In the prototype generator, the radius of the disk was made 114 mm, and the radial width of the annulus 1 mm. With these values the pressure rise in the annulus amounts to about 0.6 per cent of the total pressure rise, so that the annulus correction can by no means be neglected if accurate measurements are envisaged.

The most convenient practical form of equation (14), as applied to the prototype generator, was found to be the following

$$h = 13.58\rho n^2 \tag{15}$$

where

h = differential pressure in terms of mm water gage
ρ = air density, slugs per ft^3
n = rotational speed of the disk, rps

In order to determine an unknown differential pressure with the aid of the centrifugal manometer, it is only necessary to measure the rotational speed n, and to calculate the density of

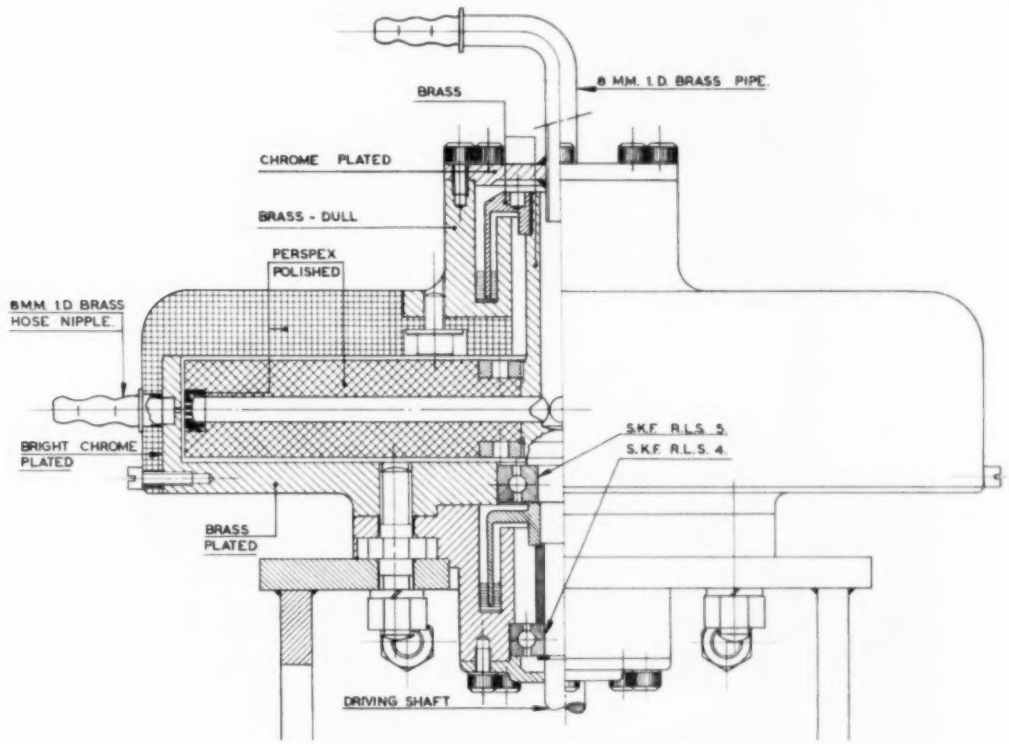

Fig. 2 Construction of the rotating disk and its housing

air under ambient atmospheric conditions from measurements of barometric pressure, and of dry and wet-bulb temperatures [8].

Mechanical Construction of the Prototype Pressure Generator

The mechanical construction of the prototype pressure generator is depicted in the drawing of Fig. 2 and in the photograph of Fig. 3.

In Fig. 2 a half-sectional view of the disk and its housing is presented. As the arrangement is similar to that in the schematic drawing of Fig. 1, only a few constructional features need to be explained.

In the design, a special attempt was made to limit the internal flow resistance of the apparatus, since this has an important bearing on the performance of the manometer system. Eight equally spaced radial holes, having a bore of 8 mm, are provided in the disk. Each hole is plugged with a perspex cap, which is machined simultaneously with the rim in order to obtain a smooth termination. Each cap contains eight 1-mm-diam pressure-transmission holes, approximately 1 mm in length.

The pressure is collected, via 64 evenly spaced 1-mm × 1-mm transmission holes, in an 8-mm × 3-mm annular cavity in the wall of the housing, whence it is transmitted to a single connecting nipple on the side of the housing. The pressure at the center of the disk is transmitted via the hollow driving shaft to a second nipple which is located on top of the housing.

The two mercury seals were designed to function effectively at rotational speeds of up to about 2000 rpm.

Provision was made to center all relevant components accurately, lest any pumping action should originate in the annular space between the disk and housing or at the mercury seals. It will be clear, from the description of the balance indicator, that any such pumping action would cause pulsations in the air column at the indicator, and would therefore have a detrimental effect on the operation of this device.

The complete assembly of the pressure generator can be studied

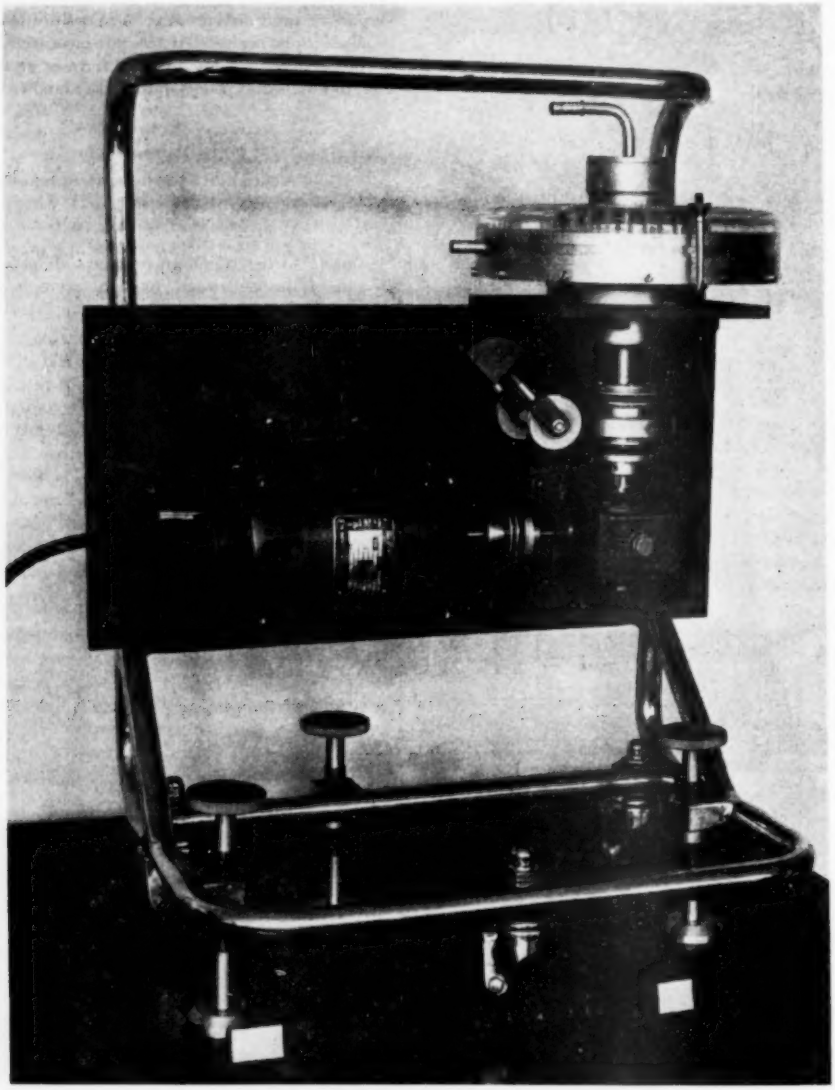

Fig. 3 The prototype differential pressure generator

with the aid of the photograph in Fig. 3. The disk is driven by a 1/6-hp, dc variable-speed motor, either directly by means of a belt drive (high speed range), or through a 1:20 worm reduction gearbox (low speed range). A dual clutch is incorporated and is designed in such a way that the switch over from one range to the other is effected by the throw of a lever.

Rotational speeds of the pressure generator are measured with high precision by means of a tachoscope, i.e., a combined revolution counter and stop watch. Each measurement is taken over a period of approximately one minute, during which time the rotational speed is continuously controlled to maintain pressure-balancing conditions.

The components comprising the variable speed drive are mounted on a duralumin plate, which in turn is bolted to a light tubular framework. The apparatus can be wheeled on the three rubber castors, or, if so required, can be carried by the upper part of the tubular frame which serves as a handle.

The prototype was designed to have a maximum pressure range of 25-mm water gage.

The Balance Indicator

Operation and Construction. Of the several devices which were evolved and tested as possible balance indicators for the centrifugal manometer, the one depicted in Fig. 4 proved to be the most effective.

The indicator tube is made of glass and is connected in series with one of the pressure leads from the generator. A fine mist of "atomized" oil is pumped into this tube and, by virtue of correct illumination, the movement of the minute oil droplets can be observed under a low-power microscope.

In the process of balancing the unknown differential pressure against that developed by the generator, the rotational speed of the manometer disk is adjusted until the oil droplets in the indicator tube become stationary.

The oil atomizer consists of a container C, a short open tube B, and a second tube A, which is connected to the rubber bellows. The air jet issuing from A is directed on to the open end of B where it creates a suction. The liquid is caused to overflow at the open end of B, and is broken up into a fine spray by the turbulent action of the jet.

Any light oil, such as instrument oil, is suitable for use in the indicator. Water or paraffin cannot be used, as these liquids have too high a rate of evaporation. If tubes A and B are made to have a bore of 1 mm, the size of oil droplets obtained is of the order of 1 micron. These droplets will remain suspended for minutes on end, and will react to the slightest movements of the air column in the tube.

A Zeiss Stereo microscope [9], having a magnification of 32, is used to observe the droplets, which have to be illuminated according to the scheme illustrated in Fig. 4, if the most effective visualization is required. A 15-w projection lamp is used as light source. If this lamp is set up in the same plane as the microscope, and on the opposite side of the indicator tube, as shown, the resultant intensity of reflected and refracted light from the oil droplets has a near maximum value in the direction toward the microscope. Provided that the two light spots X on the walls of the glass indicator tube do not overlap, as seen through the microscope, a good contrast is obtained between the illuminated droplets and their background.

Sensitivity of the Balance Indicator. A simple flow apparatus was constructed for determining the performance of balance indicators.

Water, flowing from an aspirator through a tall outlet pipe equipped with a suitable control valve, was used to draw air through the indicator tube. Mean flow speeds in the tube could be deduced from a knowledge of the flow rate and of the bore of the tube.

Tests repeatedly indicated that mean flow speeds of 0.01 mm per sec or less could be detected by means of the atomized-oil indicator described.

The sensitivity of this type of indicator is perhaps best demonstrated by the results of a velocity distribution test that was performed with an 8-mm-bore tube. Since the Stereo microscope has a very shallow focal depth, it can be focused on droplets moving along various streamlines in the tube. Flow speeds of individual droplets can be measured with the aid of the graduated eyepiece of the microscope and a stop watch. By applying this technique, the velocity distribution curve A in Fig. 5 was obtained. The dotted curve B depicts the ideal parabolic distri-

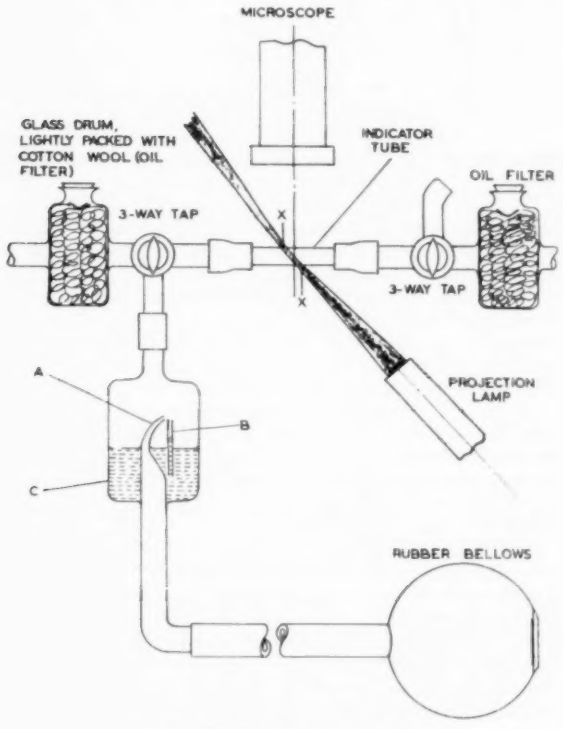

Fig. 4 Atomized-oil balance indicator

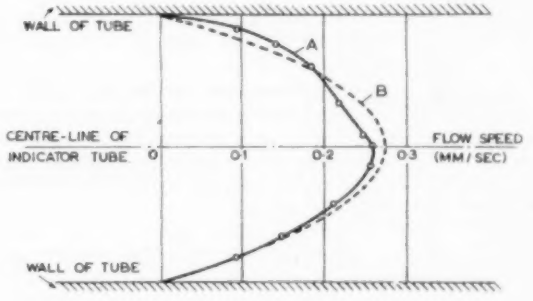

NOTATION:
A. DISTRIBUTION AS MEASURED.
B. IDEAL (PARABOLIC) DISTRIBUTION.

Fig. 5 Velocity distribution in the indicator tube

bution for laminar flow. By graphical integration, the mean flow velocity derived from curve A amounts to 0.142 mm per sec, while the measurement of water flow rate from the aspirator yields a value of 0.137 mm per sec. The difference between the two values of mean flow speed is therefore less than 4 per cent.

In the following analysis, the somewhat conservative value of 0.01 mm per sec will be used as sensitivity for the indicator.

The Optimum Dimensions of the Indicator Tube. The problem to be considered is the following: For a given setup of the centrifugal manometer, and for a given sensitivity of its balance indicator, what are the optimum dimensions of the indicator tube with regard to the accuracy of measurement of an unknown differential pressure?

The pressure circuit of the manometer system consists essentially of a number of tubes k, l, m, etc., connected in series. For the purpose of the analysis, all components of the circuit, with the exception of the indicator tube, will be represented by a single "equivalent" tube, which, under laminar flow conditions, will yield the same volumetric flow rate as the circuit for a given pressure difference.

The relative dimensions of the equivalent tube are given by the equation

$$\frac{L_e}{D_e^4} = \frac{L_k}{D_k^4} + \frac{L_l}{D_l^4} + \frac{L_m}{D_m^4} + \dots \tag{16}$$

where L and D denote lengths and diameters of tubes, and subscripts e, k, l, m, etc., relate to the equivalent tube and to the components k, l, m, etc., in the pressure circuit.

Due to the limited sensitivity v_i of the balance indicator, a pressure drop ΔP will exist across the circuit, and this pressure drop will represent the error of measurement. For laminar flow, ΔP is given by the equation

$$\Delta P = \frac{32\mu v_e L_e}{D_e^2} + \frac{32\mu v_i L_i}{D_i^2} \tag{17}$$

where

μ = viscosity of air
v = mean flow speed in the relevant tube

Subscripts e and i refer to the equivalent tube and to the indicator tube, respectively.

From continuity, however,

$$v_e = v_i D_i^2 / D_e^2 \tag{18}$$

so that equation (17) can be written as follows

$$\Delta P = 32\mu v_i \left[\frac{L_e D_i^2}{D_e^4} + \frac{L_i}{D_i^2} \right] \tag{19}$$

According to this equation the error ΔP becomes smaller as the length L_i of the indicator tube is decreased. For given values of L_e, L_i, and D_e and for a given sensitivity v_i, the optimum diameter D_i of the indicator tube is obtained by differentiating equation (19) and equating to zero, and is given by the following formula

$$\frac{L_i}{D_i^4} = \frac{L_e}{D_e^4} \tag{20}$$

In practice it was found that the dimensions D_i and L_i should not be made smaller than about 4 mm and 20 mm, respectively, if illumination and visualization of the oil droplets were to be performed successfully according to the technique illustrated in Fig. 4. Bearing these limitations in mind, equations (19) and (20) can be applied to investigate the effect of circuit resistance on the accuracy of the manometer when the optimum indicator tube is used. The results of an analysis carried out along these lines are presented by the graph in Fig. 6.

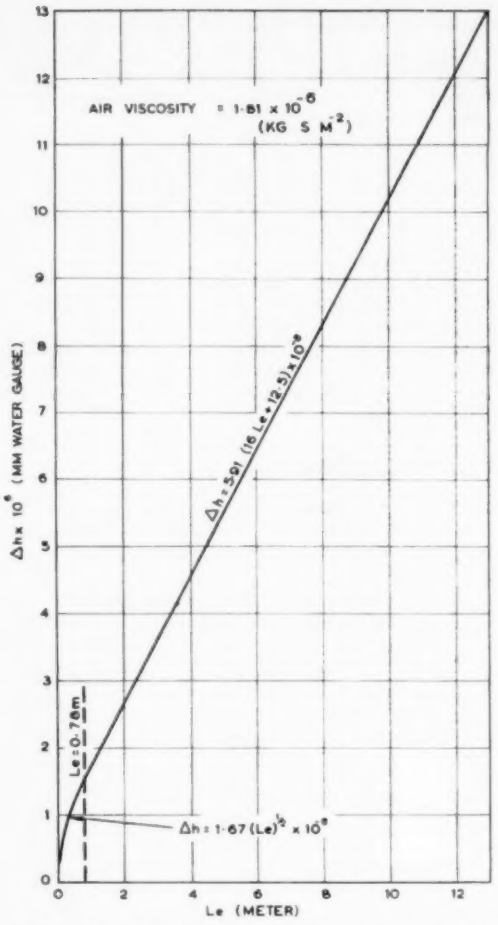

Fig. 6 The effect of circuit resistance on the accuracy of balance indication

The circuit resistance is represented in terms of the length L_e of the equivalent tube, whose diameter D_e has been arbitrarily selected as 10 mm for the present purpose. The ordinates Δh represent the error, in terms of mm water gage, that arises as a result of the limited indicator sensitivity of 0.01 mm per sec.

For $L_e < 0.78$ meter, the optimum diameter D_i of the indicator tube is greater than the minimum practical value of 4 mm, but for $L_e > 0.78$ meter, the value of 4 mm has to be used in order to obtain maximum accuracy. The optimum length L_i of the tube is equal to the minimum practical value of 20 mm, whatever the resistance of the circuit may be.

The lower part of the curve is of little practical value, since the internal flow resistance of the pressure generator, as illustrated in Fig. 2, already amounts to about 2 meters when expressed in terms of length L_e of the 10-mm-diam equivalent tube.

The curve indicates that the accuracy of the centrifugal manometer decreases with increasing resistance of the pressure circuit. Provided, however, that the manometer is used in conjunction with pressure probes or static pressure tappings designed to have a low internal resistance, the balance indicator functions with extreme accuracy.

Performance of the Centrifugal Manometer

The Manometer as Calibrator. A most useful application of the centrifugal manometer is that of calibrator for other manometers, such as those of the capacitance type [10]. For this purpose the balance indicator is not utilized, and the instrument under test is connected directly to the differential pressure generator. Differential pressures indicated by the instrument under test can then be compared with the corresponding values as supplied by the generator, and a suitable calibration curve can be prepared.

The performance of the centrifugal manometer when used in this role was investigated by connecting the generator in turn to a Betz projection manometer [11], a 13-in. Chattock-Fry Manometer [12], and a very sensitive electromagnetic micromanometer [13]. The results of these investigations are presented in Table 1, where h_G and h_T denote, respectively, the readings of the generator and the "test" instrument. The excellent agreement obtained in all instances serves as an indication of the accuracy of the calibrating technique.

Calibration of micromanometers according to this technique requires considerably less time and effort than in the case of existing methods [14, 15].

Accuracy of the Manometer Under Laboratory Conditions. Two series of tests were conducted in order to determine the performance characteristics of the centrifugal manometer, as used with the atomized-oil balance indicator.

In the first series, a flow apparatus similar to the one used for the tests on balance indicators was constructed. Air was drawn through a steel tube, by the action of the water flowing from the apparatus, and the manometer was connected to two static pressure tappings of low resistance on the tube. The bore of the tube and the distance between the pressure tappings were carefully measured.

By determining flow rates from the apparatus, and by applying the Hagen-Poiseuille formula for laminar flow in a pipe, static pressure differences between the tappings could be calculated and compared with the values as measured by the manometer. The results are summarized in Table 2, where h_G and h_F denote the readings of the manometer and of the flow apparatus, respectively.

Table 1

Test instrument	h_T (mm water gage)	h_G (mm water gage)
Betz projection manometer	25.00	25.02
	20.00	19.98
	10.00	10.06
	5.00	5.03
	2.00	2.00
	1.00	1.01
13-in. Chattock-Fry manometer	3.324	3.319
	2.493	2.491
	1.662	1.672
	1.329	1.333
	0.997	0.995
	0.665	0.662
	0.332	0.330
Electromagnetic micromanometer	1.966	1.968
	0.983	0.981
	0.492	0.494
	0.197	0.198
	0.098	0.099
	0.049	0.050
	0.0098	0.0097

Table 2

h_F	50.0	39.6	5.28	4.76
h_G	49.9	39.1	5.33	4.83

h_F and h_G in thousandths of mm water gage.

The results indicate that the accuracy of the manometer at 5×10^{-3} mm water gage is of the order of 5×10^{-3} mm water gage (2×10^{-4} in water gage), or better, since the flow apparatus itself is subject to inherent inaccuracies.

In the second series of tests, the manometer was connected to a low-resistance, Prandtl-type pitot-static tube which was set up in the working section of a small wind tunnel. At each of several constant air speeds in the tunnel, a large number of readings of velocity head, as measured by the manometer, were recorded. From these sets of readings, the repeatability (or inherent accuracy) of the manometer could be assessed. The repeatability was based on standard deviation as criterion.

At a nominal velocity head of 1.54×10^{-3} mm water gage, which corresponded to a flow speed of about 0.5 ft per sec, the standard deviation amounted to 1.38 per cent, so that the inherent accuracy of the manometer is of the order of 4×10^{-5} mm water gage.

Similarly, at a nominal velocity head of 1 mm water gage, the standard deviation was found to be 0.076 per cent so that the corresponding value of inherent accuracy amounted to approximately 1.7×10^{-3} mm water gage.

Conclusions

From these results it is evident that the centrifugal manometer is capable of measuring with an accuracy and repeatability beyond the scope of manometers of liquid type.

Apart from its high sensitivity and accuracy, the instrument has several other noteworthy features, of which some may be attributed to the fact that air is utilized as working fluid.

By virtue of its small air capacity and the operation of its balance indicator, the apparatus reacts almost instantaneously to pressure changes, so that little time is wasted before a measurement can commence.

In spite of its high sensitivity, the manometer is no delicate instrument that needs to be handled with particular caution. It is robustly constructed, easily transportable, and requires a minimum of maintenance. It can be used immediately after being moved and set up and can measure extremely small and relatively large differential pressures alternately and in quick succession without any loss in accuracy.

The wide effective range of the manometer deserves comment. The prototype is capable of measuring, with errors of less than 1 per cent, pressure differences ranging from 25 mm water gage to 5×10^{-3} mm water gage. This represents an effective range of 5000:1.

The instrument has been applied to measure mean air speeds in moderately unsteady flow, for instance, at the outlet of a diffuser in which the flow had partially separated from the walls.

Finally, the differential pressure generator can be used to advantage as a standard of calibration for other manometers.

Acknowledgments

The work described in this paper was performed in the National Mechanical Engineering Research Institute. It forms part of a thesis which is to be submitted to the University of Stellenbosch, Prof. R. L. Straszacker being the promotor. The paper is published by permission of the University and of the South African Council for Scientific and Industrial Research.

The author gratefully acknowledges the assistance of Dr. M. D. Kranz and Mr. M. L. Strydom during the development of the instrument.

References

1 V. M. Falkner, "A Modified Chattock Gauge of High Sensitivity," Reports and Memoranda of the Aeronautical Research Committee, No. 1589, 1934.

2 E. Ower, "A Micromanometer of High Sensitivity," Reports and Memoranda of the Aeronautical Research Committee, No. 1308, 1930.

3 F. A. MacMillan, "Liquid Manometer With High Sensitivity and Small Time Lag," *Journal of Scientific Instruments*, vol. 31, 1954, pp. 17–20.

4 H. Reichardt, "Die Torsionswaage als Mikromanometer," *Zeitschrift für Instrumentenkunde*, vol. 55, 1935, pp. 24–25.

5 L. F. G. Simmons, "A Sensitive Air Manometer," *Journal of Scientific Instruments*, vol. 31, 1954, pp. 195–196.

6 E. Nickel, "Messung von Druck, Geschwindigkeit, Dichte und Drehzahl," *Archiv für Technisches Messen*, Report V 1343-12, 1951.

7 H. Schlichting, "Grenzschicht Theorie," G. Braun, Karlsruhe, Germany, first edition, 1951, pp. 47–48.

8 J. F. Kemp and J. A. Uyterlinden, "The Density of Moist Air," *Journal of the Institution of Heating and Ventilating Engineers*, vol. 25, 1957, pp. 137–138.

9 "Das Stereo-Mikroskop" (Anon.), *Zeitschrift für Instrumentenkunde*, vol. 5, 1957, p. 98.

10 "A Capacity-Type Micromanometer for Measuring Very Low Differential Pressures" (Anon.), *Instrument Practice*, vol. 10, no. 11, 1956, pp. 1026–1027.

11 R. C. Pankhurst and D. W. Holder, "Wind-Tunnel Technique," Pitman, London, England, first edition, 1952, pp. 303–304.

12 E. Ower, "The Measurement of Air flow," Chapman and Hall, London, England, third edition, 1949, pp. 209–216.

13 J. F. Kemp, "A Liquid Manometer With Electro-Magnetic Balance Indicator," to be published.

14 E. Ower, "The Measurement of Air Flow," Chapman and Hall, London, England, third edition, 1949, pp. 233–235.

15 R. A. Gross, "Calibration of Sensitive Differential Pressure Devices," *Review of Scientific Instruments*, vol. 25, no. 3, 1954, pp. 218–220.

16 H. Schlichting, "Grenzschicht Theorie," G. Braun, Karlsruhe, Germany, first edition, 1951, pp. 61–62.

H. N. CANTRELL

Manager, Computational Research, Large Steam Turbine-Generator Department, General Electric Company, Schenectady, N. Y. Mem. ASME

J. E. FOWLER

Supervisor, Turbine Fluid Mechanics Research, Large Steam Turbine-Generator Department, General Electric Company, Schenectady, N. Y. Mem. ASME

The Aerodynamic Design of Two-Dimensional Turbine Cascades for Incompressible Flow With a High-Speed Computer

A method for the design of large turning angle, turbine bucket cascades is given. The method, based on conformal mapping from the logarithmic hodograph, is well adapted for use with high-speed computing machinery. Examples are given of bucket shapes designed by this method. A comparison is presented between design and test-measured pressure distribution for two cascades.

THE PRODUCTION of large steam turbines for power generation calls for the design and manufacture of machines which will meet the thermodynamic cycle and power output required by the customer. The particular cycle chosen in each case is determined on the basis of fuel costs, capital charges, available cooling-water temperature, power output desired, and other factors. As a consequence, it is found necessary by steam-turbine builders to maintain flexibility in design to meet the individual needs of different customers. Thus many individual stage designs must be made for differing pressure levels, stage loadings, diameters, and so on. Such a situation requires that a flexible design method for bucket sections be used for optimum performance. This paper describes such a blade-design method which is in use in the company with which the authors are associated.

General Approach

The problem of blade design for turbines has been treated by many writers. In some cases the three-dimensional problem has been attacked, but the greatest amount of work has been devoted to cascades. The cascade approach was adopted in this case.

In selecting a design method for impulse-type steam-turbine buckets certain special characteristics of such blading must be kept in mind. In particular, it must be noted that these buckets have large deflection angles, as great as 130 deg. Blades must have mechanically strong cross sections to permit long life under heavy loading. In the design of such high-deflection, heavily loaded cascades, with the necessity of high efficiency, it becomes essential that the pressure distribution on the blade surface be controlled. Control of the pressure distribution enables the designer to avoid boundary-layer separation with the accompanying losses in performance.

The requirement of control over the pressure distribution on the blade surface rules out the use of the many approximate methods of blade design and imposes the necessity for a mathematically rigorous system. However, due to the lack of manageable rigorous methods for cascade design with compressible flow, it was necessary, for the time being, to base the approach on incompressible-flow methods.

It is well known that the irrotational, plane flow of an incompressible fluid can be represented by an analytic function of a complex variable. The use of the complex variable then permits one to utilize the powerful methods of conformal mapping in the solution of the design problem. One such method, due to Weinig,[1] makes use of a mapping of the flow about a circular

Contributed by the Fluid Mechanics Subcommittee of the Hydraulic Division and presented at the Annual Meeting, New York, N. Y., November 30–December 5, 1958, of THE AMERICAN SOCIETY OF MECHANICAL ENGINEERS.

NOTE: Statements and opinions advanced in papers are to be understood as individual expressions of their authors and not those of the Society. Manuscript received at ASME Headquarters, August 28, 1958. Paper No. 58—A-141.

[1] F. Weinig, "Die Strömung um die Schaufeln von Turbomaschinen," J. A. Barth, Leipzig, Germany, 1935.

Nomenclature

a, b, c = dimensions in logarithmic hodograph plane
C = a constant
$d\bar{s}$ = vector line element
e = 2.173 = base of natural logarithms
i = $\sqrt{-1}$
I_1, I_2, I_3 = integrals defined in text
j = trailing-edge wedge angle
k = dimension in logarithmic hodograph plane
K_1, K_2 = constants described in text
l = leading-edge wedge angle
ln = logarithm to base e
$P_1, P_2, \ldots P_{10}$ = co-ordinates of points on real axis of R-plane
$R = p + iq$, $R = re^{i\delta}$ = complex variable of auxiliary R-plane
r = radius in R-plane
$r_1, r_2, \ldots r_n$ = co-ordinates of points on real axis of R-plane, or radii in R-plane
s = radius in S-plane
$S = f + ig$, $S = se^{i\nu}$ = complex variable of auxiliary S-plane
$\bar{S} = f - ig$ = complex conjugate of S
$T = 1/S$
t = blade pitch
u = velocity component in x-direction
v = velocity component in y-direction
$\bar{V}$ = vector velocity

(*continued on next page*)

obstacle in a picture plane into the flow about a cascade. The mapping function is determined by imposing on the picture-plane flow field an analytic function which describes the complex conjugate velocity, $u - iv$, of the flow about the cascade. The shape of the cascade profiles is then determined by a numerical integration of the function

$$dz = \frac{dW(\tau)}{u(\tau) - iv(\tau)}$$

around the circumference of the circular obstacle in the picture plane.

The method of Weinig permits one to design blades with rounded leading edges, and finite wedge angles, and thickness at the trailing edge. Further, Weinig's method permits a study of the behavior of the flow under off-design conditions. It is found, however, that a satisfactory velocity distribution cannot be prescribed in advance, particularly for impulse buckets. Also, numerical difficulties may be encountered in designing impulse buckets. This difficulty is due to the mapping of a large portion of the blade surface into two very small regions of the picture plane circle. These regions are near the points representing the leading and trailing-edge stagnation points.

An alternative approach, which was used in this case, is to utilize a mapping from the logarithmic hodograph plane to the physical plane. The co-ordinates of the logarithmic hodograph plane are related to the physical flow by the expression

$$\zeta = \xi + i\eta = \ln(u - iv) = (\ln w) - i\theta \tag{1}$$

if the physical flow is described by an analytic function

$$W(z) = \varphi + i\psi \tag{2}$$

one then has

$$\zeta = \ln(u - iv) = \ln\left[\frac{\partial\varphi}{\partial x} + i\,\frac{\partial\psi}{\partial x}\right] = \ln\frac{dW}{dz} \tag{3}$$

and a conformal mapping exists between the two planes.

For a hodograph solution

$$W(\zeta) = \varphi(\xi, \eta) + i\psi(\xi, \eta)$$

the transformation from the log-hodograph plane to the physical plane is given by the inverse of equation (3) as

$$dz = e^{-\zeta}\frac{dW}{d\zeta}\,d\zeta \tag{4}$$

The use of the logarithmic hodograph mapping permits rather precise control over the suction-side velocity, and allows one to specify the leading and trailing-edge wedge angles. Further, in view of the work published on hodograph methods in compressible flow, it gives promise of extension to a compressible flow design method in the future. The method as presently constituted is limited to the design of blades with sharp edges at the leading and trailing edges, and cannot handle the general case of a rounded entrance. This limitation is not considered to be serious for turbine-bucket design, and may be eliminated by future studies.

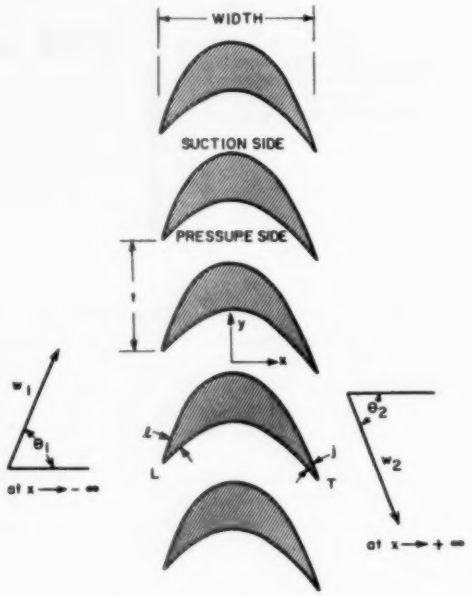

Fig. 1 Cascade nomenclature

Properties of Conformal Mappings of Bucket Cascades

In establishing a conformal mapping for the flow about an infinite cascade of blades it is desirable to map to a single flow field. The mapping is thus made in such a manner that one of the infinite number of identical strips of the flow field, say that between the streamlines ψ_{a1} in Fig. 2, is mapped upon one sheet of an infinity of identical Riemann surfaces. It can easily be shown that in such a mapping the flow at an infinite distance upstream from the cascade must map into a logarithmic singular point, which for incompressible flow has the form

Nomenclature

w = velocity magnitude
$W = \varphi + i\psi$ = analytic function of a complex variable
$z = x + iy$ = complex variable describing position in the physical plane
Re = real part
Im = imaginary part
α_n = direction change at nth corner of a polygon
β = auxiliary angle in R-plane
Γ = circulation about a blade
δ = angle in R-plane
δ_0, δ_∞ = specific angles in R-plane
$\zeta = \xi + i\eta$ = complex variable of logarithmic hodograph plane
ζ_0 = complex constant of integration
$\eta = -\theta$ = co-ordinate in logarithmic hodograph
$\xi = \ln w$ = co-ordinate in logarithmic hodograph
θ = flow direction in z-plane, measured from x-axis
$\lambda = \ln s$ = variable of integration
ν = angle in S-plane
ρ = auxiliary radius in R-plane
τ = complex variable describing position in Weinig picture plane
φ = velocity potential described by $u = \dfrac{\partial\varphi}{\partial x}$, $v = \dfrac{\partial\varphi}{\partial y}$
ψ = stream function described by $u = \dfrac{\partial\psi}{\partial y}$, $v = -\dfrac{\partial\psi}{\partial x}$

$$W_1 = \frac{w_1 l}{2\pi} e^{-i\theta_1} \ln(\zeta - \zeta_1)$$

$$= \frac{w_1 l}{2\pi} [\cos\theta_1 \ln(\zeta - \zeta_1) - i \sin\theta_1 \ln(\zeta - \zeta_1)] \quad (5)$$

The term $\cos\theta_1 \ln(\zeta - \zeta_1)$ in equation (5) represents a symbolic source from which the streamlines emanate. The necessity for the streamlines to diverge from a point in the log hodograph follows from the uniform velocity and angle of the upstream flow, represented by a single point in the log hodograph. The term $i \sin\theta_1 \ln(\zeta - \zeta_1)$ similarly represents a symbolic vortex, and results from the requirement that the flow, at an angle to the real axis, be infinitely repeating in y.

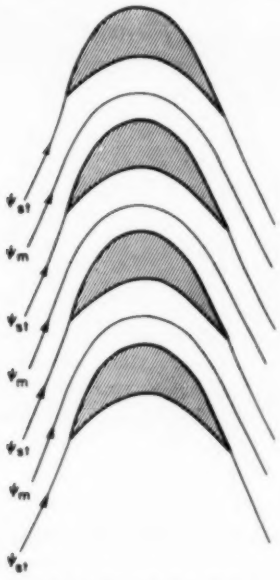

Fig. 2 Cascade flow field

Similarly, the downstream flow maps into a singular point of the form

$$W_2 = -\frac{w_2 l}{2\pi} e^{-i\theta_2} \ln(\zeta - \zeta_2) \quad (6)$$

ζ_1 and ζ_2 in equations (5) and (6) are the locations of each singular point in the picture plane, and the nomenclature is that of Fig. 1.

With these requirements in mind we indicate the form of the logarithmic hodograph of the flow through a cascade of buckets, Fig. 3.

The stagnation streamline ψ_{st}, emanates from the symbolic source-vortex at ζ_1 and flows to the leading-edge stagnation point L. The point L, because of the zero velocity, maps into $\xi = -\infty$. At L the streamline ψ_{st} branches along the blade corresponding to the two lines labelled "suction side" and "pressure side" in Fig. 3. At $\xi \to -\infty$ these branches are spaced apart vertically by l, the leading-edge wedge angle. The bifurcated streamline closes at T, the trailing-edge stagnation point with the wedge angle j. The pressure-side velocity being lower than that on the suction side causes the pressure-side streamline to map to the left of the suction-side streamline. The other streamlines map in the manner shown, with the streamline ψ_{st} representing

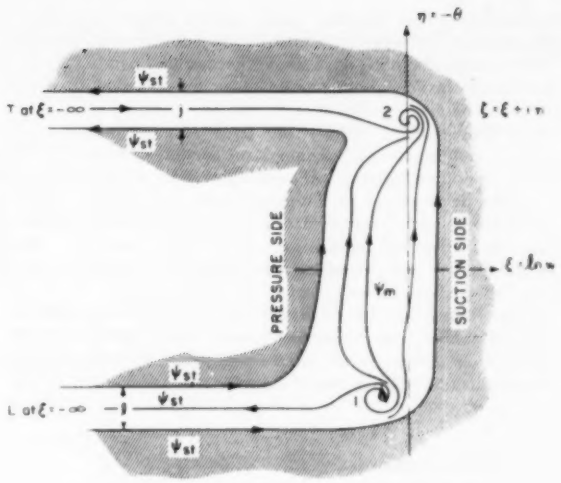

Fig. 3 Logarithmic hodograph of a bucket cascade flow

the branch cut along which the Riemann surfaces are joined. It should be noted that this form of mapping applies to a cascade with sharp wedges at the leading and trailing edges, and with monotonic change in angle along the two surfaces. A nonmonotonic angle change or a rounded leading edge will, in general, lead to a multiple-valued function $W(\zeta)$ in the hodograph, and will not be considered here.

The circulation about a blade in the cascade is given by the counterclockwise line integral

$$-\Gamma = \oint \bar{V} \cdot d\bar{s} = -w_1 l \sin\theta_1 + w_2 l \sin\theta_2 \quad (7)$$

where $\bar{V}$ and $d\bar{s}$ are the vector velocity and line element, respectively. The line integral also can be written as

$$-\Gamma = \oint \bar{V} \cdot d\bar{s} = \oint (u\,dx + v\,dy) = \mathrm{Re} \oint (u - iv)(dx + i\,dy)$$

or

$$-\Gamma = \mathrm{Re} \oint \frac{dW}{dz} dz = \mathrm{Re} \oint dW \quad (8)$$

A path about a blade in the cascade is equivalent to a path in the hodograph enclosing the two singularities but in the clockwise direction. An evaluation of the change in W for such a contour gives, for the function

$$W = \frac{w_1 l}{2\pi} e^{-i\theta_1} \ln(\zeta - \zeta_1) - \frac{w_2 l}{2\pi} e^{-i\theta_2} \ln(\zeta - \zeta_2)$$

$$\oint dW = \frac{w_1 l}{2\pi} e^{-i\theta_1}(-2\pi i) - \frac{w_2 l}{2\pi} e^{-i\theta_2}(-2\pi i)$$

$$= -w_1 l \sin\theta_1 + w_2 l \sin\theta_2 - i[w_1 l \cos\theta_1 - w_2 l \cos\theta_2]$$

But continuity requires that $w_1 l \cos\theta_1 = w_2 l \cos\theta_2$ hence one arrives at

$$-\Gamma = \oint dW = -w_1 l \sin\theta_1 + w_2 l \sin\theta_2 \quad (9)$$

and can conclude that the hodograph mapping yields the correct blade circulation.

Development of Design Method

The basic problem to be solved in the design method is now seen as that of finding an analytic function $W(\zeta)$ in the log

hodograph. This function must possess proper logarithmic singularities to represent the upstream and downstream infinities. The function also must have stagnation (saddle) points at points L and T in the hodograph, and its imaginary part must take on a constant value along the curves chosen to represent the mapping of the blade surface. Thus within the log-hodograph plane it is then possible to specify the important suction-side velocity distribution and consequently the behavior of the boundary layer.

In the development of the design method given here, many principles of applied mathematics, computing-machine application, and practical engineering design were involved. The authors believe that it is of interest to show the manner in which these affected the development of the final method. To do so it seems desirable to describe briefly the evolution of the method from an original idea to the final system. Since the method depends upon the use of the Schwarz-Christoffel transformation, the properties of this conformal mapping will be reviewed briefly.

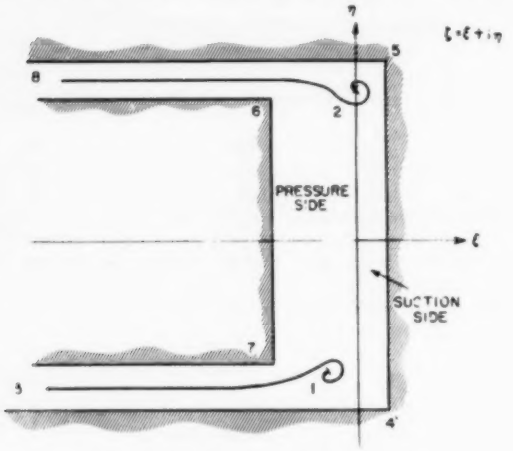

Fig. 4 Idealized logarithmic hodograph

The Schwarz-Christoffel transformation is defined by the relationship

$$\zeta = \int C(R - r_1)^{-\alpha_1/\pi}(R - r_2)^{-\alpha_2/\pi} \cdots \cdots (R - r_n)^{-\alpha_n/\pi} dR + \zeta_0,$$

where $r_1 < r_2 < \ldots < r_n$. It serves to map the interior of a closed polygon with $n + 1$ corners in the ζ-plane onto the upper half of the R-plane. The boundaries of the polygon in the ζ-plane map along the real axis of the R-plane. Any corner of the polygon may be mapped into the point at infinity in the R-plane. The constants $r_1, r_2, \ldots r_n$ are the co-ordinates of points on the real axis of the R-plane, and correspond to the corners of the polygon taken in counterclockwise order from that corner which maps into $R \to \infty$.

The value of α_n in the exponent is the change in the direction of the polygon boundary as one passes through the corresponding corner. The sign of α_n is positive for counterclockwise and negative for clockwise changes in direction.

It is permissible to consider the polygon to be closed at infinity in the ζ-plane. At such a point, the angle α is taken as equal in value to π for parallel boundaries.

One r-value may be assigned arbitrarily. The remaining r-values, the complex constant C, and an additive constant of integration ζ_0 must then take on values which result in the correct polygon geometry and orientation in the ζ-plane.

In applying this transformation, as a first step, the log-hodograph representation of a bucket, Fig. 3, was idealized by a polygon as in Fig. 4. The interior of this polygon (the flow field) was transformed to the upper half of the $R = p + iq$ plane, Fig. 5, by the Schwarz-Christoffel transformation

$$\zeta = \int C \frac{[(R - P_6)(R - P_7)]^{1/2}}{[(R - P_4)(R - P_5)]^{1/2}} \frac{dR}{R} + \zeta_0 \qquad (10)$$

which locates corner 3 at the origin and corner 8 at infinity, with the singularities mapping into points R_1 and R_2. Conjugate image singularities were then located in the lower half plane making the real axis a streamline. The parameters C, P_4, P_5, P_6, P_7, and ζ_0 were adjusted to give saddle points at the origin and at infinity in the R-plane and the correct geometry in the hodograph. Both ζ and W were then known as functions of R. The bucket in the z-plane was found by integrating

$$\int dZ = \int e^{-\zeta(R)} \frac{dW}{dR} dR$$

along the real axis of the R-plane.

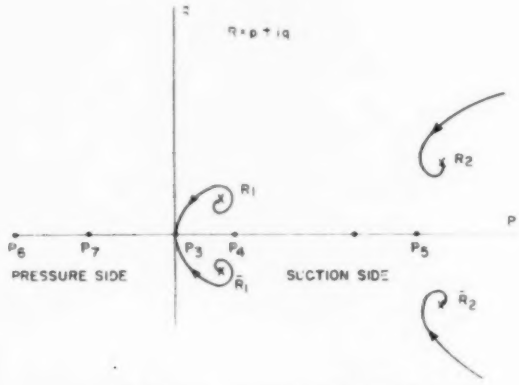

Fig. 5 R-plane representation of log-hodograph flow

This appeared quite simple and straightforward, but proved rather difficult to carry out. The transformation (10) involves elliptic integrals and must be integrated numerically. This can be done with acceptable accuracy everywhere except near the singularities at the vertexes 4, 5, 6, and 7. To get the bucket shape we must integrate through all of these points. This also can be done, but not easily, since for each corner a different and fairly complex transformation of the independent variable of numerical integration must be made. Such transformations are difficult to program for a digital computer, and are well beyond hand calculation in a practical design system.

This problem was solved by realizing that the sharp corners of the idealized polygon are neither necessary nor particularly desirable. The corners can be rounded by mapping two radial lines in the R-plate into the ζ-plane as shown in Fig. 6. Then another Schwarz-Christoffel transformation can be used to map the part of the R-plane included between these lines into the upper half of the S-plane, Fig. 6. This transformation is simply:

$$R = \frac{e^{i\delta_0} S^{\left[1 - \frac{(\delta_0 + \delta_\pi)}{\pi}\right]}}{1 - \frac{\delta_0 + \delta_\pi}{\pi}} \qquad (11)$$

The conjugate image singularities are then located in the lower half of the S-plane. The remainder of the method is the same as that previously described using the S-plane rather than the R-plane.

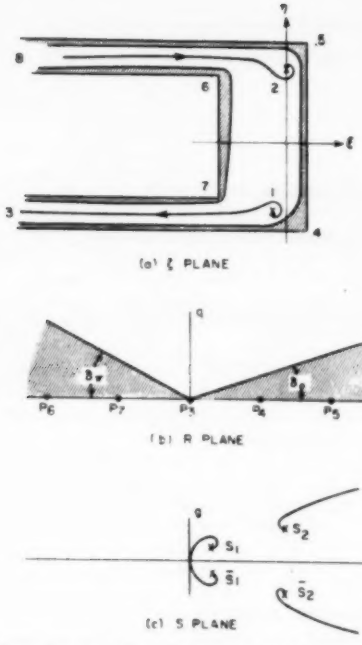

Fig. 6 Introduction of S-plane; (a) ζ-plane, (b) R-plane, (c) S-plane

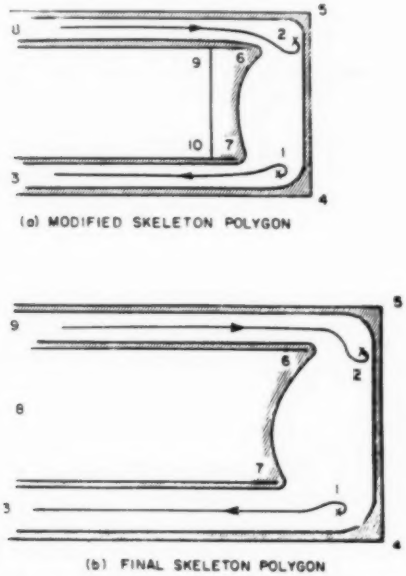

Fig. 7 Skeleton polygon revisions; (a) modified skeleton polygon, (b) final skeleton polygon

With this method equation (10) still has to be integrated numerically but now the singularities can be avoided. A single numerical integration program can be used on the computer, provided that the computer automatically changes its increment size to satisfy a given maximum allowable error. This can be programmed easily.

One bucket, designed with this method, was fairly satisfactory to the eye. It was immediately apparent, however, that the constant velocity on the pressure side resulted in too much load on the trailing edge of the profile. Since with the then-existing numerical and analytical methods almost any Schwarz-Christoffel transformation could be integrated, the skeleton polygon and rounded flow field shown in Fig. 7(*a*) were proposed. The transformation for this skeleton polygon is

$$\zeta = \int C \frac{(R - P_8)(R - P_7)}{(R - P_9)[(R - P_4)(R - P_5)(R - P_6)(R - P_{10})]^{1/2}} \frac{dR}{R} + \zeta_0 \quad (12)$$

Upon further thought, however, it appeared that the vertical portion of the skeleton polygon between vertexes 9 and 10 was not essential. Its removal resulted in the skeleton polygon and flow field shown in Fig. 7(*b*), with point 8 as an infinite point in the log-hodograph. The transformation for this skeleton polygon is

$$\zeta = \int C \frac{(R - P_6)(R - P_7)}{(R - P_9)[(R - P_4)(R - P_5)]^{1/2}} \frac{dR}{R} + \zeta_0 \quad (13)$$

But *this* transformation can be integrated analytically in closed form. The need for the troublesome numerical integration has been eliminated completely and we now have a more flexible method.

Design Method

The four planes of the final method are shown in Fig. 8. The transformations from one to the other are given by

From	*to*	*Equation*	
z	ζ	$\zeta = \ln \frac{dW}{dz}$	(3)
ζ	R	$\zeta = \int C \frac{(R - P_6)(R - P_7)}{(R - P_9)[(R - P_4)(R - P_5)]^{1/2}} \frac{dR}{R} + \zeta_0$	(13)
R	S	$R = \frac{e^{i\delta_0 S}\left[1 - \frac{\delta_0 + \delta_w}{\pi}\right]}{1 - \frac{\delta_0 + \delta_w}{\pi}}$	(11)
S	z	$dz = e^{-f(S)} \frac{dW}{dS} dS$	(14)

It will be noted that the dimensions j and l in Fig. 8(*b*) specify the blade-wedge angles, while k defines the angle of turn on the pressure side of the bucket. Similarly a, b, and c, through their control of ratio of suction-side to pressure-side velocity, specify the bucket loading, and therefore the pitch-to-width ratio. Thus the values of these six parameters have considerable effect upon the final bucket geometry.

Polygon Determination. Equation (13) gives the transformation of the skeleton polygon from the ζ-plane to the R-plane in terms of the parameters: C, P_4, P_5, P_6, P_7, P_9, and the constant of integration ζ_0.

In accordance with the requirements of the Schwarz-Christoffel transformation one of these parameters may be chosen arbitrarily. The others must take on values that give the correct geometry and location of the skeleton polygon in the logarithmic-hodograph plane. The flow field is further defined by the parameters δ_0 and δ_w.

What is really desired, however, is not the skeleton polygon, but a satisfactory flow field in the log-hodograph plane. Such a satisfactory flow field must have a desirable velocity distribution

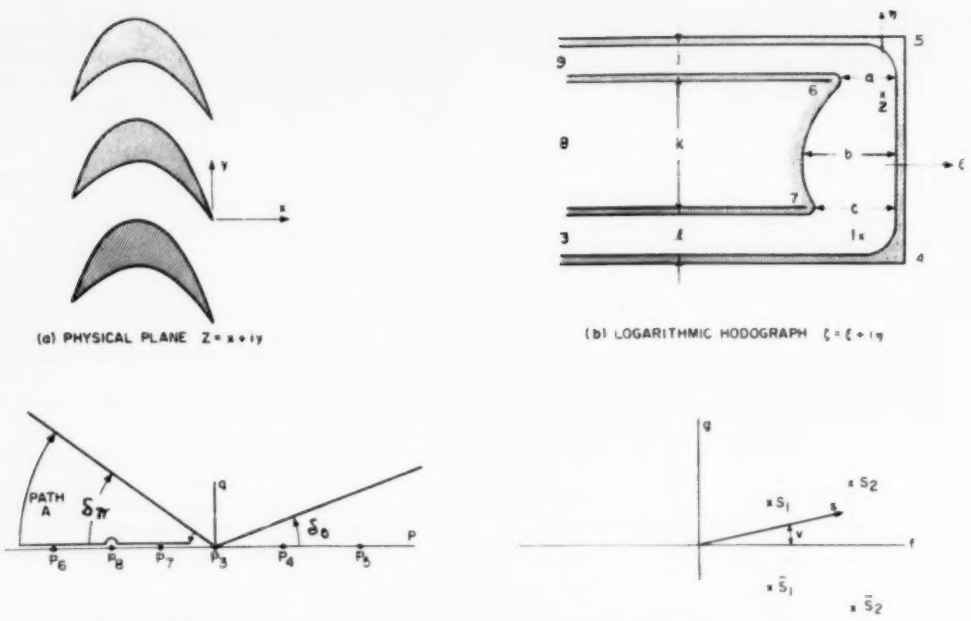

Fig. 8 Conformally related planes of final method

on the suction side of the blade, and the correct values of the dimensions a, b, c, j, k, and l of Fig. 8(b).

We now have nine parameters, six of which may be defined by the six geometric conditions on the log-hodograph flow field, and one of which locates the flow singularities in the log-hodograph plane. The other two parameters may have arbitrarily assigned values. The effect of δ_0 on the polygon is easy to visualize; i.e., δ_0 specifies how closely the suction-side velocity will approach a constant value. Therefore we will choose to specify its value. For the remaining conditions we will arbitrarily specify P_4, and ζ_0 will be adjusted to properly relate the locations of the singularities in the ζ and S-planes.

We now must evaluate the remaining parameters in terms of the chosen dimensions, which will be done in the following manner: The dimensions j, k, and l in the ζ-plane apply at $\xi \to -\infty$. It is thus possible, by limiting processes on line integrals in the R-plane, to relate these distances to the six parameters of the transformation. The lengths a, b, and c may then be approximated by line integrals along certain arcs in the R-plane between the radii at δ_0 and δ_π. Six equations between the parameters and the six geometric requirements will result. These equations can then be solved to evaluate the parameters.

Proceeding to introduce j, we set

$$R = re^{i\delta} \tag{15}$$

Equation (13) can then be written in differential form as

$$d\zeta = C\,\frac{(re^{i\delta} - P_6)(re^{i\delta} - P_7)}{(re^{i\delta} - P_3)[(re^{i\delta} - P_4)(re^{i\delta} - P_5)]^{1/2}}\,\frac{re^{i\delta}id\delta + e^{i\delta}dr}{re^{i\delta}} \tag{16}$$

We now divide both the numerator and denominator of (16) by r^2 and permit r to become very large. The fraction then approaches unity as a limit and with an integration path at constant radius (16) becomes

$$d\zeta = C\,id\delta \tag{17}$$

An integration of $d\delta$ from $\delta = \delta_0$ to $\delta = \pi - \delta_\pi$ corresponds to an integration of $d\zeta$ from the suction to the pressure side at point 9, giving

$$-i(j) = Ci(\pi - \delta_0 - \delta_\pi) \tag{18}$$

Thus the constant in (13) is

$$C = \frac{-j}{\pi - (\delta_0 + \delta_\pi)} \tag{19}$$

and (13) becomes

$$d\zeta = \frac{-j}{\pi - (\delta_0 + \delta_\pi)}\,\frac{(R - P_6)(R - P_7)}{(R - P_3)[(R - P_4)(R - P_5)]^{1/2}}\,\frac{dR}{R} \tag{20}$$

In much the same manner we evaluate the dimension l by an integral from $\delta = \delta_0$ to $\delta = \pi - \delta_\pi$ about point P_3.

Here we set $R = re^{i\delta}$ in (20) and let r become vanishingly small. Equation (20) then reduces to

$$d\zeta = \frac{-j}{\pi - (\delta_0 + \delta_\pi)}\left[\frac{P_6P_7}{P_5(P_4P_5)^{1/2}}\right]\left[id\delta + \frac{dr}{r}\right] \tag{21}$$

where use has been made of the relationship

$$\lim_{R \to 0}\left\{[(R - P_4)(R - P_5)]^{1/2}\right\} = (P_4e^{i\pi}P_5e^{i\pi})^{1/2} = -(P_4P_5)^{1/2} \tag{22}$$

Upon integrating $d\delta$ at constant radius from $\delta = \delta_0$ to $\delta = \pi - \delta_\pi$, we find the corresponding integral in ζ to be from the suction to the pressure side at point 3. This gives an evaluation of equation (21) as

$$l = \frac{-j}{\pi - (\delta_0 + \delta_\pi)} \frac{P_6 P_7}{P_8 (P_4 P_5)^{1/2}} (\pi - \delta_\pi - \delta_0) \tag{23}$$

or

$$l = -j \frac{P_6 P_7}{P_8 (P_4 P_5)^{1/2}} \tag{24}$$

The dimension k is introduced by means of a line integral along the path A of Fig. 8(c). The corresponding path of integration in ζ extends from the pressure side at point 3 around the skeleton at point 7 to point 8, vertically at point 8 to the upper leg of the skeleton, and around point 6 to the pressure side at point 9. The imaginary part of the integration in the ζ-plane is thus seen to be equal to k.

In performing the integral along the path A we note that in equation (20) the integral has only real values for values of R on the real axis. The parts of the line integral along the real axis in R from P_2 to P_3 and from P_8 to $-\infty$ will therefore make no contribution to the imaginary part of the integral and may be ignored. There then remain integrals about P_2, P_3, and at $r \to \infty$.

The integral about P_2 is evaluated from equation (21) as

$$\int_{\pi - \delta_\pi}^{\pi} \frac{-j}{\pi - (\delta_0 + \delta_\pi)} \frac{P_6 P_7}{P_8 (P_4 P_5)^{1/2}} i d\delta = -\frac{i\delta_\pi j}{\pi - (\delta_0 + \delta_\pi)} \frac{P_6 P_7}{P_8 (P_4 P_5)^{1/2}} = \frac{i\delta_\pi l}{\pi - (\delta_0 + \delta_\pi)} \tag{25}$$

The integral at $r \to \infty$ is given from equation (17) as

$$\int_{\pi}^{\pi - \delta_\pi} \frac{-j}{\pi - (\delta_0 + \delta_\pi)} i d\delta = \frac{i\delta_\pi j}{\pi - (\delta_0 + \delta_\pi)} \tag{26}$$

In order to evaluate the integral about P_3 we set

$$R - P_3 = \rho e^{i\beta}$$

and let ρ become very small. Equation (20) then gives, for ρ held constant,

$$\int_0^{\pi} \frac{-j}{\pi - (\delta_0 + \delta_\pi)} \frac{(P_3 - P_6)(P_3 - P_7)}{[(P_3 - P_4)(P_3 - P_5)]^{1/2}} \frac{i d\beta}{P_3} = \frac{-ij\pi}{\pi - (\delta_0 + \delta_\pi)} \frac{(P_3 - P_6)(P_3 - P_7)}{P_3 [(P_3 - P_4)(P_3 - P_5)]^{1/2}} \tag{27}$$

Summing the results of equations (25), (26), and (27) and equating to ik gives the desired relation

$$k = \frac{\delta_\pi (j + l)}{\pi - (\delta_0 + \delta_\pi)} - \frac{\pi j}{\pi - (\delta_0 + \delta_\pi)} \frac{(P_3 - P_6)(P_3 - P_7)}{P_3 [(P_3 - P_4)(P_3 - P_5)]^{1/2}} \tag{28}$$

To help solve for the remaining parameters we specify two additional quantities

$$K_1 = \frac{(P_6 P_7)^{1/2}}{P_3} \tag{29}$$

and

$$K_2 = (P_6 / P_7)^{1/2} \tag{30}$$

where K_1 and K_2 are restricted by

$$K_1 K_2 = \frac{P_6}{P_3} > 1 \tag{31}$$

since P_6 is greater than P_3 from Fig. 8(c)

$$\frac{K_1}{K_2} = \frac{P_7}{P_3} < 1 \tag{32}$$

We then solve for P_5, P_6, P_7, and P_8 explicitly in terms of δ_π, K_1, and K_2 from equations (24), (28), (29), and (30).

$$P_5 = \frac{1}{4} \left\{ \frac{C}{B^2} - C - \frac{P_4}{C} + \left[\left(\frac{P_4}{C} + C - \frac{C}{B^2} \right)^2 - 4P_4 \right]^{1/2} \right\}^2 \tag{33}$$

where

$$B = \frac{\frac{k}{j} \left[1 - \frac{(\delta_0 + \delta_\pi)}{\pi} \right] - \frac{\delta_\pi}{\pi} \left[1 + \frac{l}{j} \right]}{(1 - K_1 K_2) \left[1 - \frac{K_1}{K_2} \right]} \tag{34}$$

and

$$C = \frac{l}{j} \frac{\sqrt{P_4}}{K_1^2} \tag{35}$$

$$P_8 = -C \sqrt{P_5} \tag{36}$$

$$P_6 = K_1 K_2 P_8 \tag{37}$$

$$P_7 = \frac{K_1}{K_2} P_8 \tag{38}$$

The parameters of the transformation are now known in terms of the dimensions j, k, and l, and the parameters δ, K_1 and K_2. There remain the dimensions a, b, and c of the log hodograph for the evaluation of δ_π, K_1, and K_2. Unfortunately, no direct method exists for incorporating the remaining dimensions, so an approximate method must be used.

The properties of the transformation between the R and ζ-planes are such that, if a circle of radius P_7 is centered at P_2 the arc between δ_π and δ_0 very nearly maps into the line c. Similarly arcs of radii P_3 and P_6 very nearly map into b and a. We thus set $R = re^{i\delta}$ and evaluate

$$a = \mathrm{Re} \int_{\pi - \delta_\pi}^{\delta_0} \frac{-j}{\pi - (\delta_0 + \delta_\pi)} \frac{(r_6 e^{i\delta} - P_6)(r_6 e^{i\delta} - P_7)}{(r_6 e^{i\delta} - P_8)[(r_6 e^{i\delta} - P_4)(r_6 e^{i\delta} - P_5)]^{1/2}} i d\delta \tag{39}$$

with similar expressions for b and c involving r_8 and r_7.

These equations contain δ_π, K_1, and K_2 implicitly and must be solved by a trial-and-error iterative technique. The process followed is to first assign two sets of trial values to δ_π, K_1, and K_2. The equations for a, b, and c are evaluated numerically by the computer for each set. The computer then selects new trial values, based on the previous results. The process is continued until satisfactory convergence is attained.

With the parameters of the transformation known, equation (20) can be expanded into partial fractions as

$$\zeta = \frac{-j}{\pi - (\delta_0 + \delta_\pi)} \left\{ \int \frac{dR}{[(R - P_4)(R - P_5)]^{1/2}} - \frac{P_6 P_7}{P_8} \int \frac{dR}{R[(R - P_4)(R - P_5)]^{1/2}} + \left[P_8 - P_6 - P_7 + \frac{P_6 P_7}{P_8} \right] \int \frac{dR}{(R - P_8)[(R - P_4)(R - P_5)]^{1/2}} \right\}$$

$$+ \zeta_6 = \frac{-j}{\pi - (\delta_0 + \delta_\pi)} \{ I_1 + I_2 + I_3 \} + \zeta_6 \tag{40}$$

Evaluation of the integrals in equation (40) gives

$$I_1 = 2 \ln \left[(R - P_4)^{1/2} + (R - P_5)^{1/2}\right] \tag{41}$$

$$I_2 = \frac{-P_6P_7}{P_5(P_4P_5)^{1/2}} \ln \left\{ \frac{[(R - P_4)(R - P_5)]^{1/2} - (P_4P_5)^{1/2}}{R} + \frac{(P_4 + P_5)}{2(P_4P_5)^{1/2}} \right\} \tag{42}$$

and

$$I_3 = \frac{P_8 - P_6 - P_7 + \dfrac{P_6P_7}{P_8}}{[(P_8 - P_4)(P_8 - P_5)]^{1/2}} \times \ln \left\{ \frac{2(P_8 - P_4)(P_8 - P_5) + [2P_8 - (P_4 + P_5)](R - P_8) - 2[(P_8 - P_4)(P_8 - P_5)(R - P_4)(R - P_5)]^{1/2}}{R - P_8} \right\} \tag{43}$$

We thus have an explicit expression for ζ as a function of R. Since R is known as an explicit function of S from equation (11) we can calculate ζ directly for any given value of S.

Singularity Locations and Stagnation Points. The complex potential function for the singularities in the S-plane, Fig. 8, is

$$W = \frac{w_1 l}{2\pi} e^{-i\theta_1} \ln(S - S_1) - \frac{w_2 l}{2\pi} e^{-i\theta_2} \ln(S - S_2) + \frac{w_1 l}{2\pi} e^{-i\theta_1} \ln(S - \bar{S}_1) - \frac{w_2 l}{2\pi} e^{-i\theta_2} \ln(S - \bar{S}_2)$$

By setting $(w_1 l)/(2\pi) \cos \theta_1 = 1$, noting that continuity requires $w_1 l \cos \theta_1 = w_2 l \cos \theta_2$, and recalling that $\theta = -\eta$, this becomes

$$W = (1 + i \tan \eta_1) \ln(S - S_1) - (1 + i \tan \eta_2) \ln(S - S_2) + (1 - i \tan \eta_1) \ln(S - \bar{S}_1) - (1 - i \tan \eta_2) \ln(S - \bar{S}_2) \tag{44}$$

where

$$\left.\begin{aligned} S_1 &= s_1 e^{i\nu_1} \\ \bar{S}_1 &= s_1 e^{-i\nu_1} \\ S_2 &= s_2 e^{i\nu_2} \\ \bar{S}_2 &= s_2 e^{-i\nu_2} \end{aligned}\right\} \tag{45}$$

The flow in the S-plane must have stagnation points at $S = 0$ and $S = \infty$; that is, we must have

$$\frac{dW}{dS} = 0 \quad \text{at} \quad S = 0 \tag{46}$$

The condition at infinity is met by requiring that

$$\frac{dW(T)}{dT} = 0 \quad \text{at} \quad T = 0$$

where $T = 1/S$.

This leads to

$$\frac{dW}{dS} = \frac{dW}{dT} \frac{dT}{dS} = -\frac{1}{S^2} \frac{dW}{dT}$$

and the condition is therefore

$$S^2 \frac{dW}{dS} = 0 \quad \text{at} \quad S \to \infty \tag{47}$$

If we now differentiate equation (44), express the result as a single fraction with a common denominator, separate the numerator into real and imaginary parts, and apply conditions (46) and (47) we obtain

$$\nu_1 = \frac{\pi}{2} + \eta_1 - \sin^{-1}\left[\frac{s_1}{s_2} (\cos \nu_2 + \sin \nu_2 \tan \eta_2) \cos \eta_1\right] \tag{48}$$

$$\nu_2 = \frac{\pi}{2} - \eta_2 - \sin^{-1}\left[\frac{s_1}{s_2} (\cos \nu_1 - \sin \nu_1 \tan \eta_1) \cos \eta_2\right] \tag{49}$$

Usually $s_2 \gg s_1$ so these equations are very nearly independent.

We also obtain an expression for $(dW)/(dS)$ to be used in computing

$$\frac{dW}{dS} = \frac{2[s_2^2 - s_1^2 + 2s_1s_2(\tan \eta_1 \sin \nu_1 \cos \nu_2 - \tan \eta_2 \sin \nu_2 \cos \nu_1)]S}{(S - S_1)(S - \bar{S}_1)(S - S_2)(S - \bar{S}_2)} \tag{50}$$

Equations (48) and (49) may be solved for ν_1 and ν_2 if s_1 and s_2 are known. Thus the solution will be completely defined when s_1, s_2, and the real and imaginary parts of ζ_0 are determined. These constants are evaluated by relating the positions of the two singularities in the log-hodograph to their positions in the S-plane.

Equations (11) and (40) define the relationship between these two planes as

$$\zeta = \zeta(s, \nu) + \zeta_0 \tag{51}$$

The co-ordinates of the singularities in the ζ and S-planes may be substituted into equation (51) to give

$$\xi_1 + i\eta_1 = \zeta(s_1, \nu_1) + \zeta_0 \tag{52}$$

and

$$\xi_2 + i\eta_2 = \zeta(s_2, \nu_2) + \zeta_0 \tag{53}$$

Upon eliminating ζ_0 from these equations and separating into their real and imaginary parts there results

$$\xi_1 - \xi_2 = \mathrm{Re}[\zeta(s_1, \nu_1) - \zeta(s_2, \nu_2)] \tag{54}$$

$$\eta_1 - \eta_2 = \mathrm{Im}[\zeta(s_1, \nu_1) - \zeta(s_2, \nu_2)] \tag{55}$$

Equations (54) and (55) are solved with equations (48) and (49) by iteration to determine s_1, s_2, ν_1, and ν_2 from the known values of ξ_1, ξ, η_1, and η_2. The constant ζ_0 is then determined from equation (52).

Physical Plane Integration. The transformation from the S-plane to the physical plane is accomplished by integrating—from equation (14)

$$dz = e^{-i\zeta} \frac{dW}{dS} dS \tag{14}$$

where ζ is given as a function of S by equations (11) and (40) and $(dW)/(ds)$ is given by equation (50). The numerical integration of (14) is facilitated by integrating in terms of the variables

$$\lambda + i\nu = \ln S \tag{56}$$

where

$$\lambda = \ln s \tag{57}$$

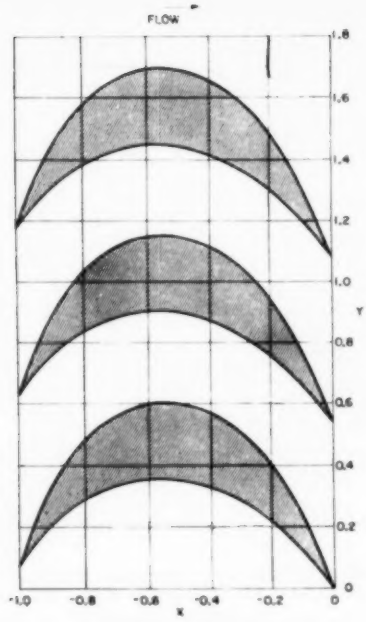

Fig. 9(a) Typical impulse bucket

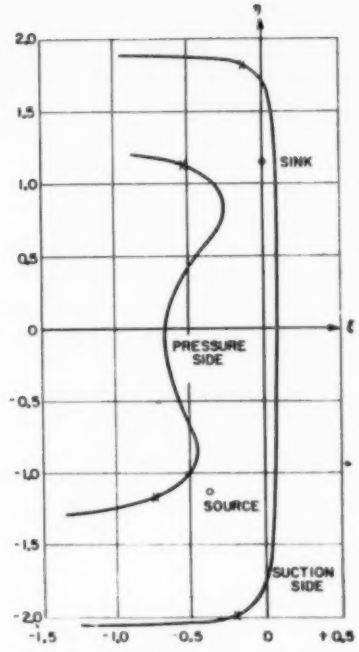

Fig. 9(b) Logarithmic hodograph of impulse bucket

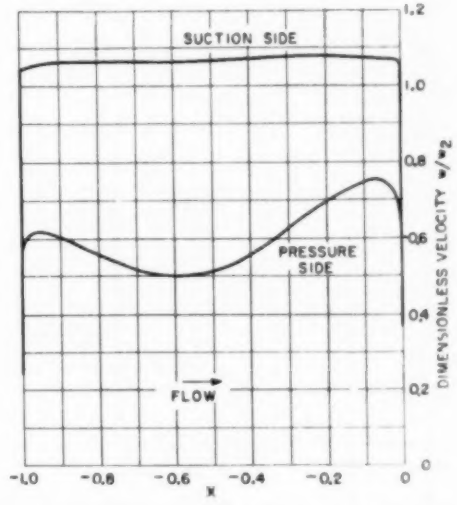

Fig. 9(c) Calculated velocity distribution for impulse bucket

and

$$dz = e^{-\bar{s}} \frac{dW}{dS} S(d\lambda + i d\nu) \tag{58}$$

With the help of this transformation we can traverse very large ranges in S numerically while keeping reasonable values of λ. We also can approach as near to $S = 0$ as desired without having to integrate numerically across the $S = 0$ point.

In practice it is found that we need not integrate to or from the exact leading and trailing-edge stagnation points on a typical bucket. An approach to within 10^{-6} blade widths of these points is possible with quite moderate ranges of λ, such as ± 10.

The suction and pressure sides are integrated independently from a common point. The closure of the resulting profile at the other point provides an excellent check on the numerical accuracy of the over-all calculation, but has never been a problem. Integration error tolerances are normally set to give closure errors less than 0.1 per cent of the bucket width.

Typical Blade Designs

Figs. 9 and 10 illustrate typical cascades designed by the method. In Fig. 9, (*a*) represents an impulse-type bucket, with the log hodograph given in (*b*) and the velocity distribution in (*c*). The points marked *x* in the log hodograph represent points on the blade surface not more than 0.001 of the blade width from the leading and trailing edges. Thus it can be seen that only a limited portion of the log hodograph is mapped into the actual blade surface.

The velocity distribution, Fig. 9(*c*), illustrates the ease with which it is possible to approach a desirable uniform suction-side velocity on the blade, and also, how the maximum suction-side velocity may be held to a value only moderately higher than the discharge velocity. This close control of the maximum suction-side velocity permits the designer to eliminate the possibility of flow separation due to adverse pressure gradients. It is of particular interest in this case to note how well the velocity distribution can be estimated from the shape of the boundary streamlines in the log-hodograph plane.

Fig. 10 illustrates the blade section, log hodograph, and velocity distribution for a blade designed for a moderate reaction level. Here it will again be noted that excellent control over the suction-side velocity distribution has been attained.

Several cascade models have been built with the blade shapes designed by this system. These cascade tests are carried out to determine the behavior of the designs with real fluids.

Fig. 11 compares the theoretical with the measured pressure distribution for an impulse cascade of 128-deg turning angle, tested at two different discharge Mach numbers in air. The

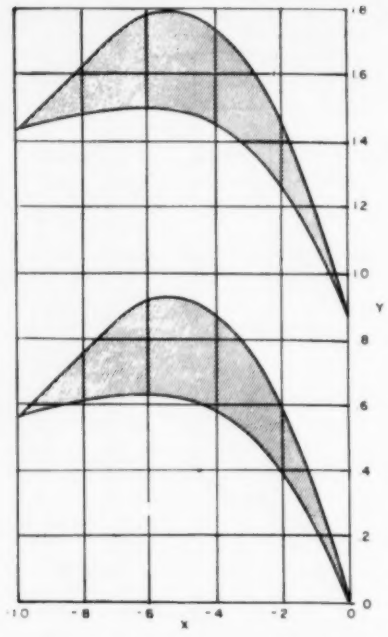

Fig. 10(a) Typical moderate reaction bucket

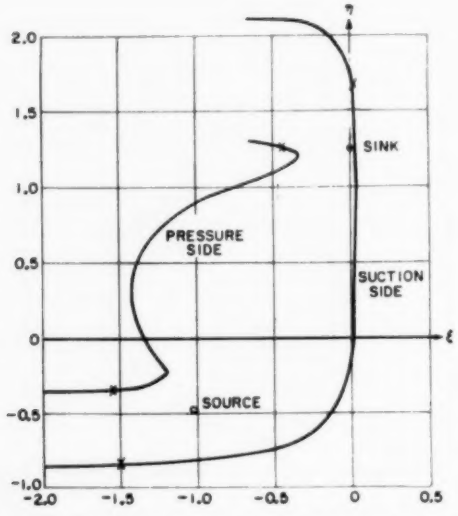

Fig. 10(b) Logarithmic hodograph of moderate-reaction bucket

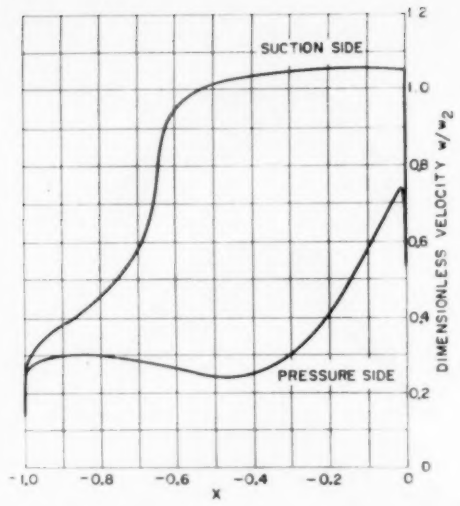

Fig. 10(c) Calculated velocity distribution for moderate reaction bucket

correspondence of the actual and theoretical pressures is gratifyingly close, particularly on the pressure side. The suction-side pressure deviates from the theoretical value due to the effect of the boundary layer and the compressibility of the air.

Fig. 12 is a similar comparison of theoretical and measured pressure distributions for a cascade designed for moderate reaction; i.e., 120-deg turning angle. Here the effect of compressibility at the higher Mach number is somewhat more marked than in the impulse case. However, the correspondence between the theoretical and measured pressure distributions is still satisfactory.

Conclusions

The authors believe that the method given here not only presents an interesting approach to the design problem for impulse-type turbine buckets, but also illustrates a general method of attack when using large computing machines in such problems. Further experimental work is being carried on with buckets designed by this method. It is planned to make a report on the experimental results when sufficient information on the actual performance is available.

Acknowledgments

The authors wish to express their appreciation to Mr. Hans Kraft for his enthusiastic support and many helpful suggestions during the development of this method, to Mr. B. K. Genetti for his capable work in planning the machine computations, to Miss J. A. Brucker for the programming involved, and to the Large Steam Turbine-Generator Department of the General Electric Company for permission to publish this work.

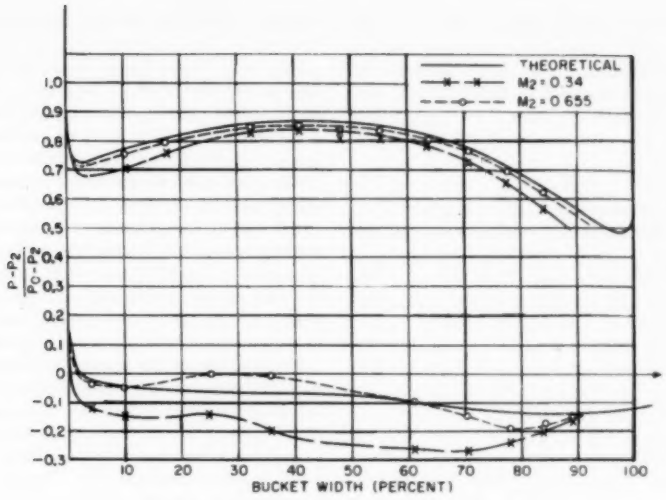

Fig. 11 Pressure distribution on an impulse bucket

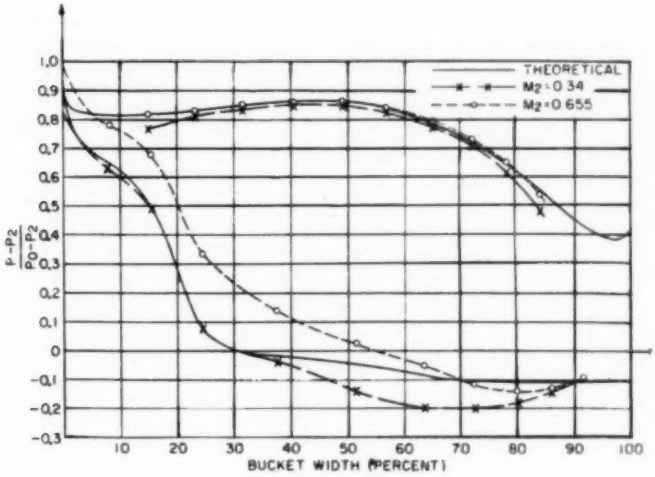

Fig. 12 Pressure distribution on a low-reaction bucket

DISCUSSION

W. G. Cornell[2]

Congratulations are due to the authors for an excellent contribution to the state of the art of turbomachinery design. It is refreshing to see a very practical and modern application of the classical potential flow theory to the difficult configuration of highly cambered cascades. The authors are careful to point out the limitation of their analysis to incompressible flow. This limitation is not severe for the problem at hand, however. Just as the single "laminar flow" wing had superior performance at high subsonic Mach numbers, although designed for essentially incompressible flow, the present buckets should be good high speed buckets since the flat suction-side velocity distribution designed for low speeds will be gradually modified by compressibility effects at higher speeds and sharp suction-side velocity peaks will be avoided.

[2] Jet Engine Department, General Electric Company, Evendale, Ohio. Mem. ASME.

Coda H. T. Pan[3]

The authors deserve much credit for combining the skills of numerical computation and mathematical theories of conformal mapping to establish a useful procedure for designing turbine cascades.

In comparing this method with the picture-plane method, the authors mentioned that the latter has the advantages of permitting a study of the off-design flow conditions and of permitting more flexibility in edge configurations. Extension of the present method to include both of these features is more or less straightforward. This may be accomplished if we recognize that $S = f + ig$, Fig. 8(d), is really a convenient picture plane; which is

[3] Engineering Training and Education, General Electric Company, Schenectady, N. Y.

transformed into the turbine cascade with sharp edges by equation (14).

To study the off-design conditions of the sharp edged profile, one may retain the transformation relation, equation (14), and describe the off-design conditions in the plane $S = f + ig$. For an entrance angle

$$\eta_1' = \eta_1 + \epsilon_1 \tag{59}$$

where $\epsilon_1 \neq 0$, one can no longer prescribe the vanishing of dW/dS at $S = 0$. Kutta-tail condition, which is presumed to remain valid, still requires vanishing of $S^2 \dfrac{dW}{dS}$ at $S \to \infty$. The latter condition is given by equation (49) provided one substitutes η_1' for η_1 and

$$\eta_2' = \eta_2 + \epsilon_2 \tag{60}$$

for η_2. After a straightforward rearrangement one obtains an explicit expression of η_2'.

$$\tan(\eta_2 + \epsilon_2) = \operatorname{ctn} \nu_2 - \frac{s_1}{s_2}\left[\frac{\cos \nu_1}{\cos \nu_2} - \frac{\sin \nu_1}{\sin \nu_2}\tan(\eta_1 + \epsilon_1)\right] \tag{61}$$

When ϵ_1 is very small one obtains approximately

$$\epsilon_2 = \frac{s_1}{s_2}\frac{\sin \nu_1}{\sin \nu_2}\left(\frac{\cos \eta_2}{\cos \eta_1}\right)^2 \epsilon_1 \quad \text{for small } \epsilon_1 \tag{62}$$

which reveals that the exit direction is insensitive to the entrance direction when s_1/s_2 is small. When the transformation relation, equation (14), is held invariant, the velocity magnitude at off-design is related to the velocity magnitude at design for any point either on or off the cascade surfaces is given by

$$\frac{w(\epsilon_1)}{w(\epsilon_1 = 0)} = \left|\frac{\dfrac{dW}{dS}(\epsilon_1)}{\dfrac{dW}{dS}(\epsilon_1 = 0)}\right|$$

$$= \left|1 + \frac{2\dfrac{s_1}{s_2}\sin \nu_1\left\{\left(\cos \nu_2 - \dfrac{s_1}{s_2}\cos \nu_1\right)\sin \nu_1 + \dfrac{s_2}{S}\left[1 - \left(\dfrac{s_1}{s_2}\right)^2\right]\right\}\dfrac{\sin \epsilon_1}{\cos(\eta_1 + \epsilon_1)}}{\left[1 - \left(\dfrac{s_1}{s_2}\right)^2 + 2\left(\dfrac{s_1}{s_2}\right)(\tan \eta_1 \sin \nu_1 \cos \nu_2 - \tan \eta_2 \sin \nu_2 \cos \nu_1)\right]\cos \eta_1}\right| \tag{63}$$

When ϵ_1 is very small, one obtains

$$\frac{w(\epsilon_1)}{w(\epsilon_1 = 0)} = \left|1 + \frac{2\dfrac{s_1}{s_2}\sin \nu_1\left\{\left(\cos \nu_2 - \dfrac{s_1}{s_2}\cos \nu_1\right)\sin \nu_1 + \dfrac{s_2}{S}\left[1 - \left(\dfrac{s_1}{s_2}\right)^2\right]\right\}\epsilon_1}{\left[1 - \left(\dfrac{s_1}{s_2}\right)^2 + 2\left(\dfrac{s_1}{s_2}\right)(\tan \eta_1 \sin \nu_1 \cos \nu_2 - \tan \eta_2 \sin \nu_2 \cos \nu_1)\right]\cos^2 \eta_1}\right| \tag{64}$$

When s_1/s_2 is a small number, the effect of off-design is confined in the vicinity

$$\frac{|S|}{s_2} \approx 0\left(\frac{s_1}{s_2}\right)$$

or,

$$|S| \approx 0(s_1) \quad \text{for small } \frac{s_1}{s_2} \tag{65}$$

Strictly speaking, equations (63) and (64) depict the off-design conditions with the same flow rate. For small s_1/s_2, since the exit direction does not change appreciably, this off-design condition is approximately the same if the exit velocity were kept invariant. Note that equations (63) and (64) blow up at $S = 0$. This is expected and is a necessary evil when one performs off-design analysis of a sharp leading edge cascade with potential theory.

In practice, a bucket designed by the present method would have to be rounded off at the leading edge in some arbitrary manner in order to minimize leading edge loss which is associated with the violent flow field indicated in the off-design analysis just given. At an off-design condition, the stagnation point shifts a distance which is usually very small in the case of a large turning-angle cascade. So long as this distance is not very large compared with the leading edge radius, as in the case of a large turning-angle cascade, it is usually satisfactory to round off the leading edge more or less arbitrarily. For a small turning-angle cascade, arbitrary rounding off of the leading edge may produce surprising results. It is important for such cases that a rational procedure to design a round leading edge be established.

Modification of the present method in order to specify more desirable edge configurations entails quite a bit of mathematical and computational difficulties. One may again treat $S = f + ig$ as the appropriate picture plane; however, equation (14) can no longer be used for obtaining the cascade shape since the hodograph information is not available. To establish the transformation from S to z in order to achieve the desired edge configurations, it is necessary to specify $\ln w$ on the real axis of S such that in the neighborhood of $S = 0$ it corresponds to the flow at the blunt nose of a profile. And if the trailing edge is to be closed, zero thickness, the following property of $\ln w$ is required.

$$\ln \frac{w_2}{w_1} + i(\eta_2 - \eta_1) = \frac{1}{\pi i}\int_{-\infty}^{\infty} \frac{\xi(f)(s_2 e^{i\nu_2} - s_1 e^{i\nu_1})df}{(f - s_2 e^{i\nu_2})(f - s_1 e^{i\nu_1})} \tag{66}$$

When a finite trailing edge is desired, equation (66) should be violated by a prescribed amount. Then the inclination angle of a tangent to the profile surface is calculated from

$$\theta(s) = -\eta(s) = \theta_T + \frac{1}{\pi}\int_{-\infty}^{\infty} \frac{\xi(f)df}{f - s} \qquad s \text{ is real} \tag{67}$$

where the subscript T refers to the trailing edge. And to define θ_T, one has

$$\theta_1 = \theta_T + \frac{1}{\pi}\int_{-\infty}^{\infty} \frac{\xi(f)(f - s_1 \cos \nu_1)df}{f^2 + s_1^2 - 2s_1 \cos \nu_1} \tag{68}$$

Equations (66), (67), and (68) are results of applying Cauchy's theorem to the analytic function $\ln (dW/dz)$ in the S plane. Success or failure to adapt the proposed extension of the present method in order to specify desired edge conditions may well hinge on skillful computation technique to evaluate the improper integrals in the last three equations.

Warner L. Stewart[4]

In general, I found the approach described in this paper very interesting and was impressed by the agreement between specified

[4] NASA, Lewis Research Center, Cleveland, Ohio.

velocity distribution and that obtained experimentally with the blades predicted to yield this velocity distribution.

I have only two general comments, each of which is primarily a desire for additional effort along the lines described in this paper. First, since the method, as it was presented, represents the two-dimensional incompressible flow case with no boundary layer or loss effects, the usefulness of it in turbomachine blade designs is somewhat limited. Most turbine design procedures allow for the compressibility effect and include a loss estimate either by an assumed boundary layer build-up or total pressure loss. They also should be three-dimensional in nature, i.e., the effect of the streamline variations that occur as the result of radial equilibrium on the blade surface velocity distribution should also be included. These additional factors have a considerable effect on the velocity distribution through turbine blading and, therefore, must be considered in order to impose controls on the blade surface velocity distribution. It is hoped that extensions of the method described in the paper into these other areas will be forthcoming in order to improve its usefulness as a design tool.

With respect to velocity limits imposed on the blade design, it appears that the method can be used to quickly evolve blading that can be investigated experimentally in two-dimensional cascades to study the influence of velocity distribution on blade loss and, hence, performance. Design controls used at Lewis currently consist of placing a minimum distribution on the suction surface without allowing the total of that on both surfaces to exceed a certain limiting value. Appropriate assignment of constants in the method could evolve groups of blading that could be used to further establish these limits or to perhaps obtain a better criteria for design. It is hoped that in the future additional uses of this method will involve effort such as this.

Authors' Closure

The authors wish to thank the discussers for their comments.

Mr. Cornell points out that the high-speed performance of these buckets should be good due to the flat suction side velocity distribution. Cascade tests on buckets designed by this method verify his opinion. In general, it has been found that the performance level is retained into the transonic regime. The suction side velocity distribution retains its favorable characteristics up to discharge Mach numbers at which strong trailing edge shocks begin to impinge on the suction surface.

Mr. Pan shows that the discharge conditions from the cascade with large deflections is virtually independent of small changes of the inlet angle. This agrees with the authors' experience in developmental work as well as that found using another type of cascade analysis. His prediction that the off design effects are confined to a small region near the leading edge are also confirmed by test. Mr. Pan's extension of the method to produce rounded leading edges is of interest. However, the authors have found that judicious rounding of the leading edge leads to very satisfactory results and are thus somewhat reluctant to undertake the large additional effort involved in this extension to the theory.

In response to Mr. Stewart, the authors wish to point out that they are very cognizant of compressibility, viscous, and three-dimensional effects. The steam turbine designer, however, finds that most of his stages operate at quite low Mach numbers and have little sidewall divergence. These characteristics make a two-dimensional, incompressible design system more acceptable to the steam turbine engineer. The extension of the system to account for compressibility, however, is under study. The addition of three-dimensional effects due to radial equilibrium phenomena is a difficult problem and will require rather extensive research.

Methods for predicting the boundary layer behavior on high deflection cascades such as these are being explored by the authors' company, but as yet no sufficiently reliable methods have been found. For this reason the authors place much more reliance on the results of cascade and running stage tests than on analytical predictions of the blading performance. Such testing work is a part of the continuous program carried out by the authors' company for the improvement of steam turbine performance.

PART I

An Analysis of Axial Compressor Cascade Aerodynamics[1]

A method is presented whereby complete potential flow solutions for any cascade geometry may be obtained with comparatively great rapidity on desk calculators. This solution is carried out for the case of symmetrically cambered airfoils such as the 65-series compressor and circular arc airfoils and the results presented in a compact graphical form completely account for the potential flow effects of camber, profile thickness, stagger, solidity, and angle of attack. Real fluid effects will be assessed and correlated in Part II using the present results as a supporting theory.

Potential Flow Analysis With Complete Solutions for Symmetrically Cambered Airfoil Families

G. L. MELLOR

Assistant Professor of Mechanical Engineering, Princeton University, Princeton, N. J.

1 Introduction

CASCADE information to assist in the design of axial compressors and fans today exists mainly in the form of a comparatively sketchy number of experimental data and some empirical rules which have limited ranges of application. The job of correlating data to correctly include the effect of the various cascade variables is frustrating and perhaps impossible in the absence of a supporting theory. As Carter [1][2] pointed out in 1950, the then existing methods of conformal transformation or extensions of thin airfoil theory often involved several weeks of calculations. He also correctly noted that, for the designer of multistage axial compressors who may have to consider the performance of a wide variety of cascade geometries before the design is finalized, such a procedure is out of the question. In 1955 Schlichting [2, 3] reported that he had reduced the time requirement to obtain the potential flow performance for one cascade geometry from 20 days (he referred to [4 and 5]) to 20 hours on a

[1] The work on which this paper is based was done at the Gas Turbine Laboratory, Massachusetts Institute of Technology, Cambridge, Mass., under the joint sponsorship of Allison Division of the General Motors Corporation, Curtiss-Wright Corporation, General Electric Company, Office of Naval Research, and Westinghouse Electric Company. The author wishes to thank Prof. E. S. Taylor and Mr. Kurt Schneider for their encouragement and assistance.

[2] Numbers in brackets designate References at end of paper.

Contributed by the Hydraulic Division and presented at the Annual Meeting, New York, N. Y., November 30–December 5, 1958, of THE AMERICAN SOCIETY OF MECHANICAL ENGINEERS.

NOTE: Statements and opinions advanced in papers are to be understood as individual expressions of their authors and not those of the Society. Manuscript received at ASME Headquarters, August 5, 1958. Paper No. 58—A-83.

Nomenclature

θ, z = co-ordinates normal and parallel to the cascade axis

x, y = co-ordinates parallel and normal to the blade chord

θ = also used as transformed chord co-ordinate; $x/c = (1 - \cos\theta)/2$

c = blade chord

s = blade gap

t = maximum blade thickness

Cb = blade camber (defined by Equation (2*a*) in the text)

Θ = circular arc camber (the included angle between tangents to the camber line extremities)

λ = stagger angle

β = air angles relative to the cascade axis

α = air angles relative to the blade chord

δ = air deviation angle relative to blade trailing edge angle, $\beta_2 - \lambda$

V = air velocity

u, v = induced velocities in x and y direction

F_x, F_θ = blade force in axial and tangential direction/chord · span

L = lift force/chord · span

D = drag force/chord · span

p = static pressure

p_0 = stagnation pressure

C_L, C_{p_0}, etc. = lift, pressure coefficient, etc. (nondimensionalized on $\rho V_m^2/2$)

γ = vorticity distribution

q = source and sink distribution

Γ = (with subscripts given in text) normalized blade surface velocity function; induced by distributed vorticity

Q = (with subscripts given in text) normalized blade surface velocity function; induced by distributed sources and sinks

A = (with subscripts given in text) cascade coefficients

ξ = ratio of pressure rise on blade surface to over-all cascade pressure rise

Subscripts

id = an ideal or lossless flow

1 = plane far upstream

2 = plane far downstream

m = the mean velocity or angle

c = camber terms

t = thickness terms

α = angle of attack terms

s, p = suction and pressure blade surface, respectively

desk calculator. This was an order of magnitude improvement. What is offered here is several more orders of magnitude improvement while at the same time increasing the degree of accuracy. Furthermore, complete solutions are presented for circular arc, 65-series compressor blade camber lines, and other similar symmetrically cambered airfoils in a form which is convenient to apply and which separately demonstrates the effect on the pressure distribution and lift coefficient of each cascade variable.

Airfoil Geometric Parameters. The airfoil itself may be described by a camber distribution $y_c(x)$ and a thickness distribution $y_t(x)$. An airfoil family may be described by $f_c\,(x/c)$ and $f_t(x/c)$ which are scaled up or down by the constants Cb and t/c, so that,

$$\frac{y_c}{c} \equiv \mathrm{Cb}\, f_c\left(\frac{x}{c}\right) \tag{1a}$$

$$\frac{y_t}{c} \equiv \frac{t}{c}\, f_t\left(\frac{x}{c}\right) \tag{1b}$$

t is the maximum thickness of the airfoil and f_t therefore reaches a maximum value of one. Cb is defined by the equation

$$\mathrm{Cb} \equiv 2\int_0^\pi \frac{dy_c}{dx}\cos\theta\, d\theta \tag{2a}$$

and by substituting (1a) in (2a) we obtain

$$2\int_0^\pi f_c'\cos\theta\, d\theta = 1 \tag{2b}$$

where θ is the transformed chord position, $x/c = \dfrac{1-\cos\theta}{2}$. Cb is often written as C_{L_i} or C_{L_o} and, as will be seen later, is theoretically the lift coefficient for an isolated airfoil at the design angle of attack. However, the use of these symbols gives rise to confusion between an actual geometric parameter and a resulting aerodynamic parameter. In a cascade, the lift coefficient is not, in general, equal to the value Cb at the design angle of attack. For some airfoils, such as the 65-series airfoil, the value of Cb is given directly as the means of identifying the airfoil. For a circular arc the camber is given by the arc angle Θ. If the equation for an arc is substituted in (2b) Cb and Θ may be related

$$\mathrm{Cb} = \frac{\pi}{2}\,\Theta(1 - 0.05\Theta^2) \quad [\Theta \text{ is given in radians}] \tag{3}$$

(3) contains only the first two terms in the series relationship.

Cascade Geometric Parameters. The cascade geometric parameters may be specified by c/s, the solidity, and λ, the stagger angle.

Aerodynamic Parameters. Fig. 1, which may be derived easily from momentum and continuity considerations and from the definition of stagnation pressure loss, describes the relationships between the cascade geometry, the velocity vectors, and the resulting aerodynamic force vectors. In this presentation the velocities V_1 and V_2 are, respectively, reckoned at stations far upstream and far downstream where the wake has fully mixed out. This also applies to the static pressure rise, $\Delta p = p_2 - p_1$, and the stagnation pressure loss, $\Delta p_0 = p_{01} - p_{02}$. $\bar{V}_m$ is defined as the vector mean velocity with components $V_{xm} = V_{x1} = V_{x2}$, and $V_{\theta m} = (V_{\theta 1} + V_{\theta 2})/2$. The ideal lift force L_{id} and pressure force $F_{xid} = \dfrac{s}{c}\,\Delta p_{id}$ are the hypothetical lift and pressure forces that one would obtain for the actual velocity vectors and for $D = \Delta p_0 = 0$. These forces may be related to the vector geometry according to the following equations:

$$F_\theta = \frac{s}{c}\,\rho V_x \Delta V_\theta \tag{4a}$$

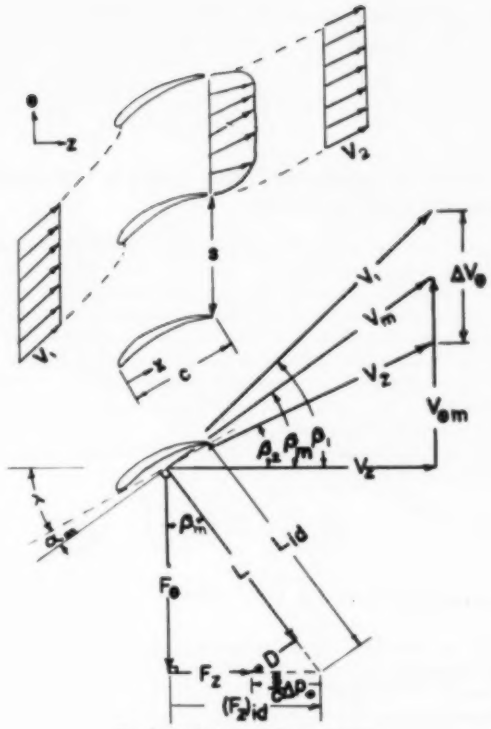

Fig. 1 Velocity and force diagram

$$(F)_{xid} = \frac{s}{c}\,\rho V_{\theta m}\Delta V_\theta \tag{4b}$$

$$L_{id} = \frac{s}{c}\,\rho V_m \Delta V_\theta \tag{4c}$$

$$D = 0 \tag{4d}$$

The relationships among the forces when $D \neq 0$ may be obtained directly from Fig. 1. There is no need to append the subscript id to F_θ since $F_\theta = (F_\theta)_{id}$. L_{id} is the total resultant force for this ideal case, which may be written in nondimensional form

$$(C_L)_{id} = \frac{L_{id}/c}{\dfrac{\rho}{2}V_m^2} = 2\,\frac{s}{c}\,\frac{\Delta V_\theta}{V_m} \tag{5}$$

For the remainder of this paper we will deal only with an ideal or inviscid flow and we therefore take the liberty of leaving off the subscript id. Now the circulation about one airfoil may be simply determined by taking the line integral $\oint \bar{V}\cdot d\bar{r}$ on a closed path comprising two streamlines s distance apart and joined by two lines parallel to the cascade (θ-direction) one far upstream and the other far downstream. The result is $\oint \bar{V}\cdot d\bar{r} = s\Delta V_\theta$. When inserted into (5) we obtain:

$$C_L = \frac{2}{cV_m}\oint \bar{V}\cdot d\bar{r} \tag{6}$$

which, of course, is the Kutta-Joukowski law.

The strength of the vortex sheet comprising the airfoil camber line is defined according to the relation

$$\gamma \equiv V_s - V_p \tag{7}$$

where $V_s(x)$ and $V_p(x)$ are, respectively, the velocity on the suc-

tion and pressure surface of the airfoil. By Stokes' law the total circulation equals $\int_0^c \gamma dx$ and therefore

$$C_L = 2 \int_0^1 \frac{\gamma}{V_m} d\left(\frac{x}{c}\right). \tag{8}$$

2 Results of Applying the Present Theory to Symmetrically Cambered Airfoils in Cascade

A complete derivation of the theory and method of calculation will be presented in Section 3. However, since calculations for airfoils cambered symmetrically about their midchords have been completed, it has been decided to first present these results as they are fairly general and usable without recourse to the details of the theory. It should be understood that it is only the results of the present section that are restricted to symmetrically cambered airfoils and the methods of Section 3 may in the future be applied to the nonsymmetrical cases.

The derivative of an airfoil camber distribution symmetrical about $x = c/2$ is antisymmetrical

$$f_c\left(\frac{x}{c}\right) = f_c\left(1 - \frac{x}{c}\right) \tag{9a}$$

$$f_c'\left(\frac{x}{c}\right) = f_c'\left(1 - \frac{x}{c}\right) \tag{9b}$$

One result of this is that the design angle of attack is zero for a single airfoil and we can therefore say that Cb is equal to the theoretical lift coefficient at zero angle of attack.

Velocity Distribution. With the understanding that a full derivation will be given in Section 3 we can write down the result for the blade surface velocity distribution

$$\frac{V}{V_m} = 1 \pm 2\pi A_0 \cdot \Gamma_{00} \pm 2\pi A_1 \cdot \Gamma_{01} \pm \mathrm{Cb} \cdot \Gamma_{0\Sigma} + 2\pi A_0 \frac{c}{s} \sin\lambda \cdot \Gamma_{\Sigma 0} + 2\pi A_1 \frac{c}{s} \sin\lambda \cdot \Gamma_{\Sigma 1} + \frac{t}{c} \cdot Q_0 + \frac{t}{c} \frac{c}{s} \cdot Q_\Sigma \tag{10}$$[1]

(+ suction surface; − pressure surface)

where the terms Γ and Q are normalized functions of x/c and are plotted in Figs. 2, 3, and 4. The values of A_0 and A_1 are obtained according to the following equations:

$$A_0 = A_{0c} \cdot \frac{\mathrm{Cb}}{2\pi} + A_{0\alpha} \cdot \sin\alpha_m + A_{0i} \cdot \frac{i}{c} \tag{11a}$$

$$A_1 = A_{1c} \cdot \frac{\mathrm{Cb}}{2\pi} + A_{1\alpha} \cdot \sin\alpha_m + A_{1i} \cdot \frac{i}{c} \tag{11b}$$

where the cascade coefficients, A_{0c}, $A_{0\alpha}$, A_{0i}, A_{1c}, $A_{1\alpha}$, A_{1i} are plotted in Figs. 5 and 6 as functions of c/s, λ, and Cb. In Section 3 the general method of approach is to imagine vortexes and source and sinks to be distributed along all the blade camber lines in the cascade which induce velocities everywhere in the flow field according to the Biot-Savart law. One can then determine the distribution which correctly satisfies the blade boundary conditions. As a result of this, it will be seen in Section 3 that the functions Γ_{00}, Γ_{01}, and $\Gamma_{0\Sigma}$ are the components of the blade surface velocity induced by the blade's own vorticity whereas $\Gamma_{\Sigma 0}$ and $\Gamma_{\Sigma 1}$ are induced by the vorticity on the remainder cascade. Q_0 and Q_Σ are source-induced component functions due to the blade itself and the remainder cascade, respectively. Q_0 and Q_Σ directly reflect the effect of blade thickness.

Lift Coefficient. The three Γ_0 terms, because they are preceded by a plus sign for the suction surface velocity and a minus sign for the pressure surface velocity, are the only terms that contribute

[1] A more exact expression may be obtained by substituting cos α_m for 1 and by multiplying cos α_m and the last four terms by $1 + (dy_c/dx)^2$. For the angles of attack where there is any physical validity to potential flow solutions and for the low cambered airfoils used in compressors, these are negligible corrections.

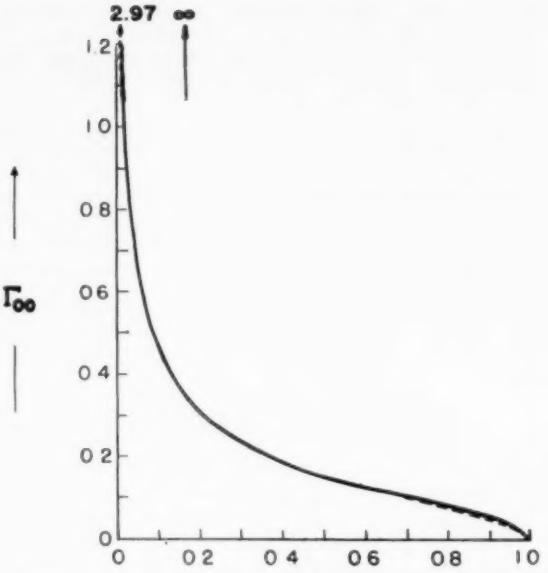

(a) $\Gamma_{00} = (1 + \cos\theta)/2\pi \sin\theta$ (solid line); (dashed line obtained in reference [6], page 82, for $t/c = 0.10$)

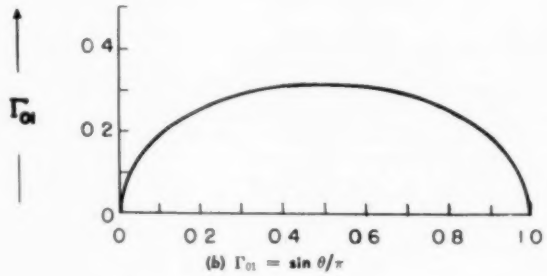

(b) $\Gamma_{01} = \sin\theta/\pi$

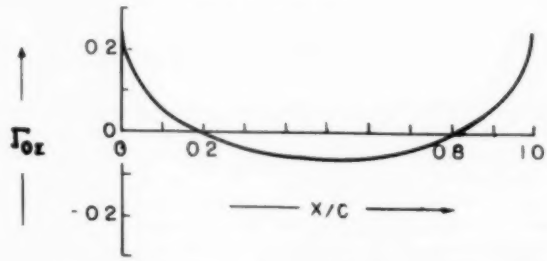

(c) $\Gamma_{0\Sigma} = \sum_{n=1}^{\infty} \sin(2n + 1)\theta/(2n + 1)\pi$ (for 65-series compressor blade camber line or NACA $a = 1.0$ mean line); $\Gamma_{0\Sigma} = 0$ (for circular arc air-foils)

Fig. 2 Self-induced velocity functions due to vorticity distribution

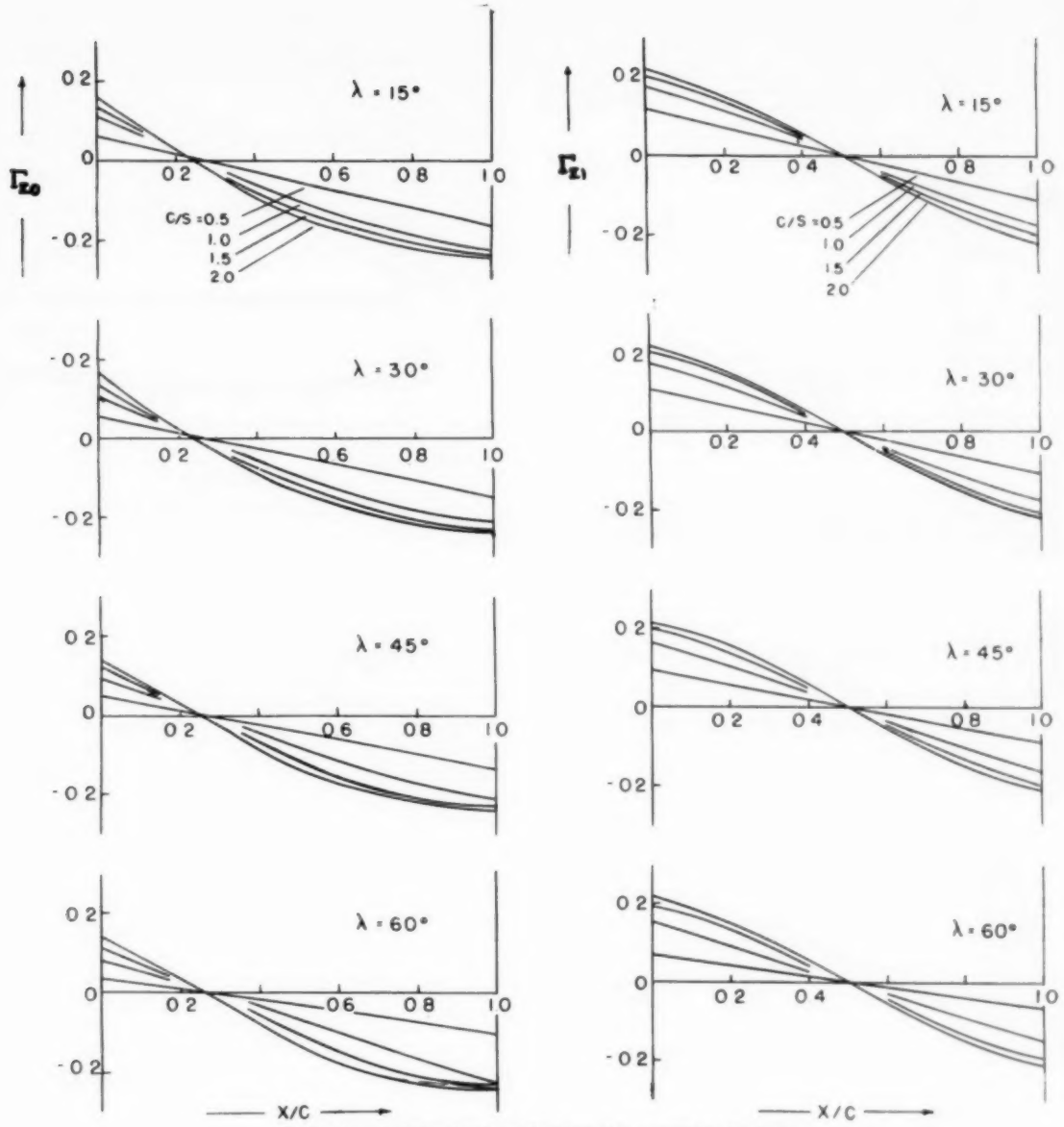

Fig. 3 Cascade-induced velocity functions due to vorticity distribution

directly to the airfoil lift. Since $\gamma = V_s - V_p$ we see that the absolute value of the sum of the three Γ_0 terms is equal to γ/V_m and if this is inserted into (8) we obtain

$$C_L = 2\pi A_0 + 2\pi A_1 \tag{12}$$

Therefore it is seen that Γ_{00} and Γ_{01} as plotted in Figs. 2(*a*) and 2(*b*) have been normalized so as to produce a unit contribution to the lift coefficient. $\Gamma_{0\Sigma}$ represents the details of the velocity (or vorticity) distribution and integrates to zero.

By inserting (11) into (12) we obtain

$$C_L = 2\pi A_s \cdot \frac{Cb}{2\pi} + 2\pi A_\alpha \cdot \sin\,\alpha_m + 2\pi A_t \cdot \frac{t}{c} \tag{13}$$

where the coefficients A_s, A_α, A_t simply represent the combination of terms, $A_{0s} + A_{1s}$, $A_{0\alpha} + A_{1\alpha}$, $A_{0t} + A_{1t}$, respectively, and are plotted in Fig. 7.

In Fig. 8 a comparison of the relative effects of camber, angle of attack, and thickness on the lift coefficient is shown for a particular case. Although a full comparison of theory and data is postponed until Part II, the data for this particular case are also plotted in Fig. 8 where it may be seen that agreement between theory and experiment is very good.

The Pressure Rise Through a Compressor Cascade. In Appendix 2 and later in Part II we will use an approximation for $\Gamma_{\Sigma 0}$ and $\Gamma_{\Sigma 1}$, namely,

$$\Gamma_{\Sigma 0} \cong \frac{\xi_0}{2}\left(\frac{1}{2} - \frac{x}{c}\right); \quad \Gamma_{\Sigma 1} \cong \frac{\xi_1}{2}\left(\frac{1}{2} - \frac{x}{c}\right)$$

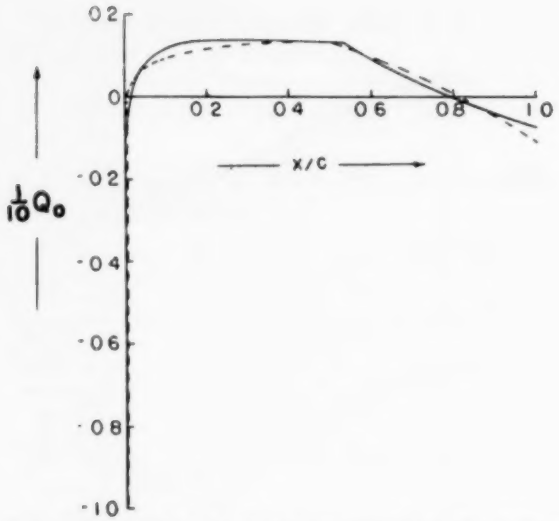

(a) Self-induced (for the 65-series compressor blade profile; solid calculated here, dashed line is more accurate solution from reference [6], page 82)

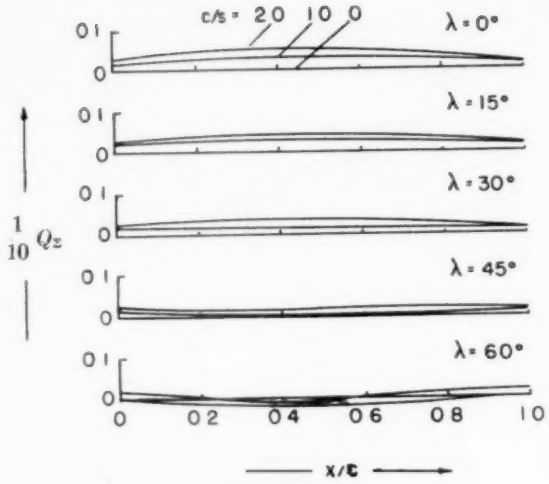

(b) Cascade-induced

Fig. 4 Velocity functions due to source distribution

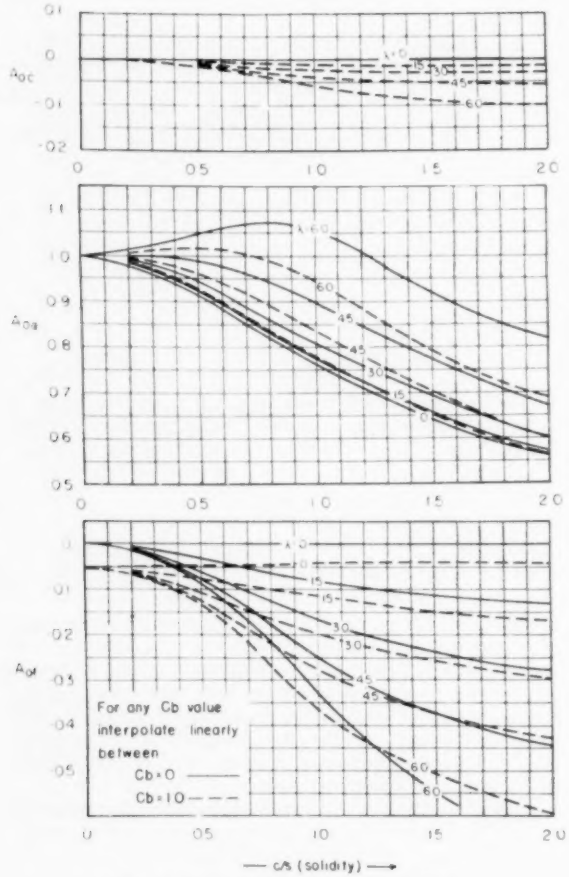

Fig. 5 Cascade coefficients in the equation
$A_0 = A_{0c}(Cb/2\pi) + A_{0a}(\sin \alpha_m) + A_{0t}(t/c)$

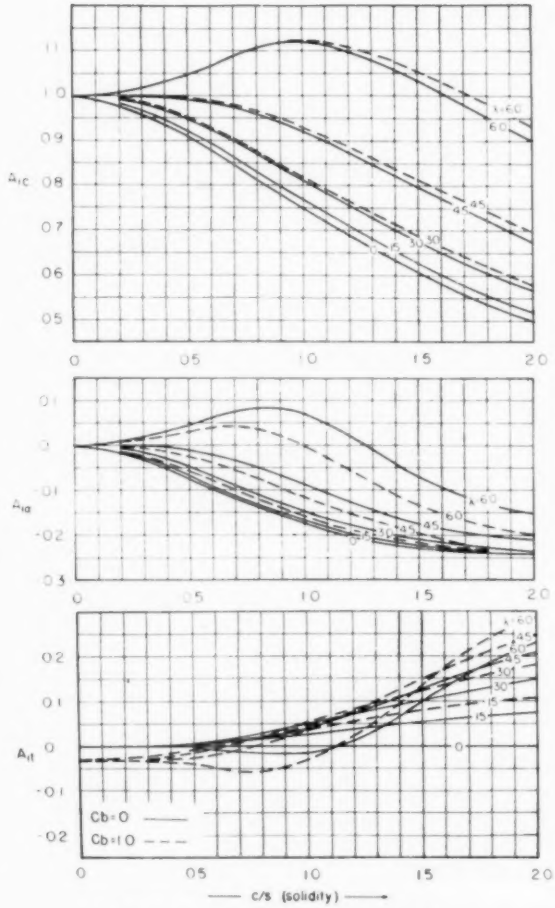

Fig. 6 Cascade coefficients in the equation
$A_1 = A_{1c}(Cb/2\pi) + A_{1a}(\sin \alpha_m) + A_{1t}(t/c)$

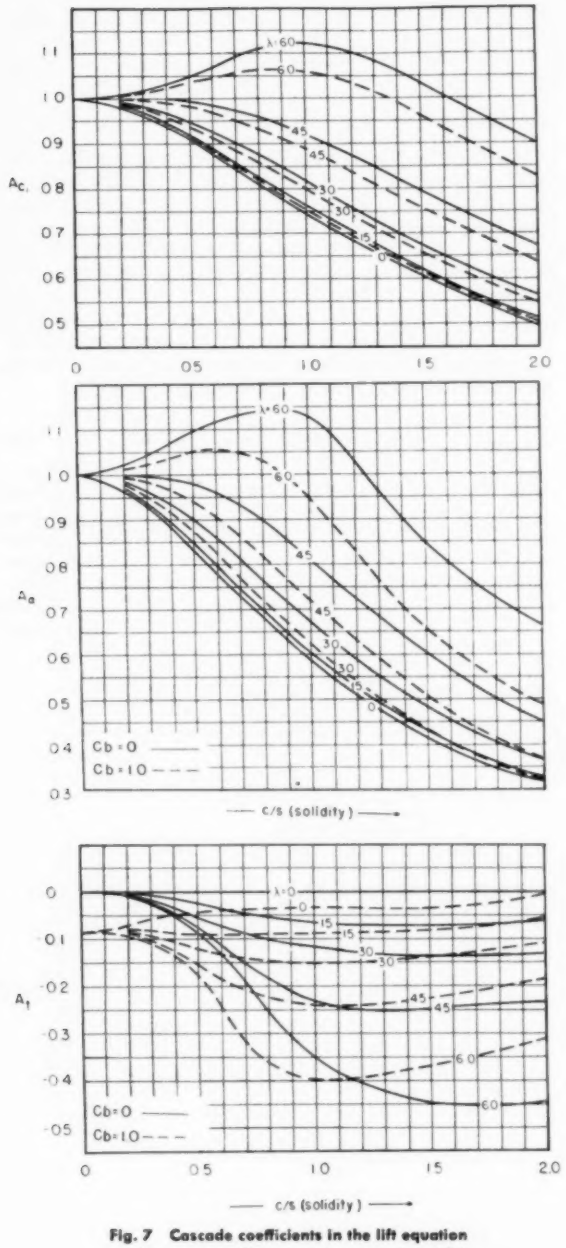

Fig. 7 Cascade coefficients in the lift equation
$C_L/2\pi = A_c(Cb/2\pi) + A_\alpha(\sin \alpha_m) + A_t(t/c)$

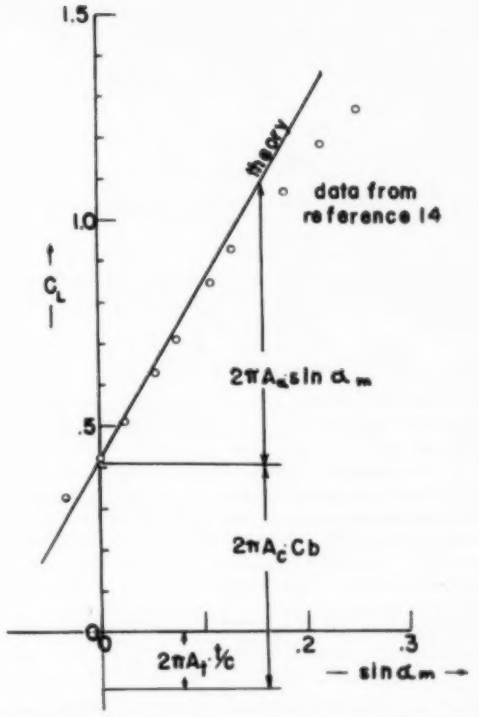

Fig. 8 Illustration of the relative importance of angle of attack, camber, and thickness and a comparison of theory and data for the 10C4/25/50 airfoil (10 per cent C4 profile, $\Theta = 25°$, circular arc) $\lambda = 42.5°$, $c/s = 1.333$

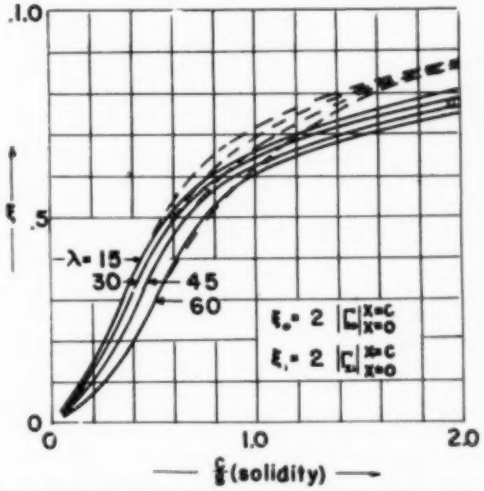

Fig. 9 Ratio of pressure rise on blade surface to over-all cascade pressure rise

where ξ_0 and ξ_1 are obtained from Fig. 3 according to the relation $\xi = 2\left|\Gamma_\Sigma\right|_{x=0}^{x=c}$. Thus, although the approximation for Γ_{Σ_1} is better than it is for Γ_{Σ_0}, the slopes of both Γ_{Σ_0} and Γ_{Σ_1} are sufficiently accurate for our latter needs since the average slopes are exactly equal to $\xi_0/2$ and $\xi_1/2$. Now ξ_0 and ξ_1 are plotted in Fig. 9 and it is also sufficiently accurate to say

$$\Gamma_{\Sigma_0} \cong \Gamma_{\Sigma_1} \cong \frac{\xi}{2}\left(\frac{1}{2} - \frac{x}{c}\right) \tag{14}$$

where $\xi \cong \xi_0 \cong \xi_1$.

Some significance may be attached to ξ by considering that the difference between the trailing edge pressure and the leading edge pressure may be written from Bernoulli's equation

$$\frac{p_{t.e.} - p_{l.e.}}{\frac{\rho}{2} V_m^2} = \left|\left(\frac{V}{V_m}\right)^2\right|_{x=c}^{x=0}$$

If, for our purpose here, we disregard the thickness function Q_0

and Q_Σ in Equation (10), we obtain by substituting (10), (12), and (14) into the Bernoulli equation

$$\frac{p_{1.e.} - p_{1.e.}}{\frac{\rho}{2} V_m^2} = \xi \frac{c}{s} \sin \lambda C_L \tag{15}$$

From Fig. 1 it can be seen that

$$\frac{c}{s} F_s = \frac{p_{d\infty} - p_{u\infty}}{\frac{\rho}{2} V_m^2} = \frac{c}{s} \sin \beta_m C_L \tag{16}$$

where $p_{d\infty} - p_{u\infty}$ is the difference in pressure between downstream infinity and upstream infinity. Dividing (15) by (16) we obtain

$$\frac{p_{1.e.} - p_{1.e.}}{p_{d\infty} - p_{u\infty}} = \frac{\sin \lambda}{\sin \beta_m} \xi \tag{17}$$

Thus the blade surface does not "feel" the entire pressure rise and the ratio of blade "effective" pressure rise to over-all pressure is given by (17).

Range of Application, Approximation, Corrections. The approximations will be mentioned specifically in Section 3, but a brief discussion may be in order at this point. An exact determination of errors is impossible, but it may be stated that errors exist (because of basic approximations in the analysis) which are proportional to Cb^2 and $(t/c)^2$ and which are about 1 per cent for Cb = 1.0 ($\Theta = 36°$) or for $t/c = 0.10$. Truncation errors in the infinite series solution appear to be negligible with an exception noted later in connection with Weinig's solution. $\Gamma_\infty = (1 + \cos\theta)/2\pi \sin\theta$ in Fig. 2(a) which is exact in the $t/c \to 0$ limit may be replaced by the isolated airfoil solution (such as given in [6]) for finite thicknesses. Notably, the leading edge velocity in the finite thickness case is not infinite as given by the analytical expression and as seen in Fig. 2.

Q_0 may also be replaced by a more exact solution of the isolated airfoil case as shown in Fig. 4(a).

It should be noted that the second harmonic $\Gamma_{02} = \sin 2\theta/2\pi$ can be included in (10) if it is felt that a higher degree of accuracy is required. Its coefficient A_2 has been calculated in Section 3, but it will be seen to be fairly small (it is zero for the isolated airfoil case) and has been neglected in (10). It would not be small in the case of nonsymmetrically cambered airfoils. A major simplifying result of the calculations is that the coefficients of the higher harmonics, $\sin n\theta$ ($n > 2$), are to a very good approximation determined independent of c/s and λ then lumped into the single function $\Gamma_{0\Sigma}$. Physically speaking, small details of the airfoil camber line slope result in a detailed velocity distribution, $\Gamma_{0\Sigma}$, which is negligibly affected by blade to blade interference.

Weinig's Solution. In 1935 Dr. F. Weinig [7], using methods of conformal transformation, solved the flat-plate problem which, when Cb = t/c = 0, reduces to determining a value K or "lattice coefficient" in the equation $C_L = 2\pi K \sin \alpha_m$. The values given by Weinig's theory as seen in reference [8] check exactly with the present author's A_α (Cb = 0) with the exception that at the extreme condition $c/s = 2.0$ and $\lambda = 60°$ there is a 5 per cent discrepancy which entirely disappears when either $c/s \leq 1.50$ or $\lambda \leq 45°$. The error probably would have been entirely eliminated by carrying more terms in the infinite series solution, but since it is so small (at least below $c/s = 2.0$) there is no need to lengthen the calculation procedure.

Weinig's solution, therefore, serves as a check on the solution given here, and adds confidence to the further predicted effects of camber and thickness.

The Limiting Case of the Isolated ($c/s \to 0$) Thin ($t/c \to 0$) Airfoil. For the symmetrically cambered thin airfoil at $c/s = 0$, it can be seen from Fig. 7 that

$$A_0 = \sin \alpha_m \tag{18a}$$

$$A_1 = \frac{\text{Cb}}{2\pi} \tag{18b}$$

and therefore $$C_L = 2\pi \sin \alpha_m + \text{Cb} \tag{19}$$

It is therefore seen that one of the features of this solution is that it reduces exactly to the classical isolated airfoil equation as $c/s \to 0$.

The Limiting Case of Closely Packed ($c/s \to \infty$) thin ($t/c \to 0$) Airfoils in Cascade. For circular arc blades it is possible to say that the trailing edge angle relative to the chord line is $-\Theta/2$ where Θ is also related to Cb in Equation (3).

The limiting case of closely packed airfoils is presumed to be the case where the air leaves the airfoil in a direction parallel to the trailing edge. Values of A_s and A_α may be obtained for this case by writing (5) in terms of the flow angles (see Fig. 1)

$$C_L = 2 \frac{s}{c} \cos \beta_m (\tan \beta_1 - \tan \beta_2) \tag{20}$$

We now perform the following steps:

a) Substitute $\tan \beta_1 = 2 \tan \beta_m - \tan \beta_2$ (see Fig. 1).

b) Set $\beta_2 = \lambda - \Theta/2$.

c) Expand $\cos \beta_m = \cos (\lambda + \alpha_m)$ and $\tan \beta_m = \tan (\lambda + \alpha_m)$ according to trigonometric indentities.

d) Set $\tan \frac{\Theta}{2} \cong \frac{\Theta}{2}$ and $\cos a_m \cong 1.0$

The result after rearranging terms is:

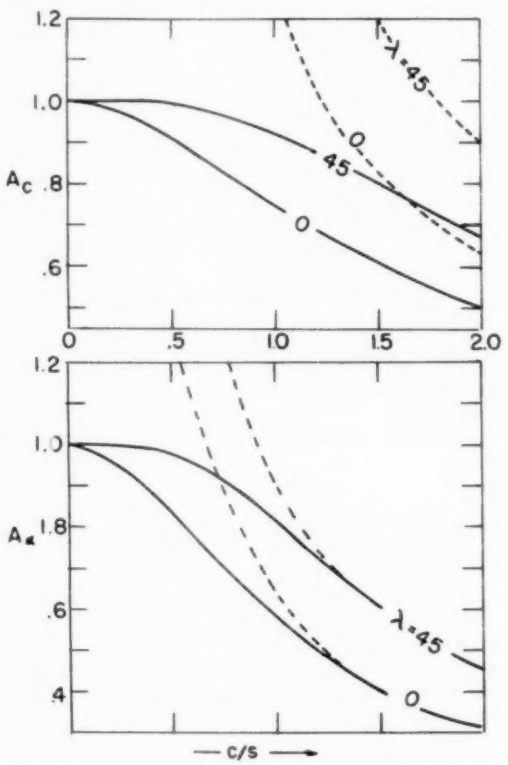

Fig. 10 Comparison of potential flow solution and result obtained by assuming zero deviation angle (the second-order effect of Cb is not considered)

$$C_L\left(\frac{c}{s} \to \infty\right) = \frac{4s/c}{\cos\lambda + \sin\lambda \dfrac{\Theta}{2}}\left[\frac{\Theta}{2}\right] + \frac{4s/c}{\cos\lambda + \sin\lambda \dfrac{\Theta}{2}}\,[\sin\alpha_m]. \quad (21)$$

Noting again that $\mathrm{Cb} = \frac{\pi}{2}\Theta$, we obtain the coefficients A_s and A_α by comparing (21) to (13),

$$A_s(c/s \to \infty) = \frac{\frac{4}{\pi}\, s/c}{\cos\lambda + \sin\lambda\Theta/2} \quad (22a)$$

$$A_\alpha(c/s \to \infty) = \frac{\frac{2}{\pi}\, s/c}{\cos\lambda + \sin\lambda\Theta/2}. \quad (22b)$$

In Fig. 10 we compare the values of $A_s(\mathrm{Cb} = 0)$, $A_\alpha(\mathrm{Cb} = 0)$ from Fig. 7 and Equation (22). If we think in terms of deviation angle $\delta = \beta_2 - \beta_{1,s}$, we see that deviation angle due to angle of attack is effectively zero when $c/s \geq 1.3$, but that the deviation angle due to camber is quite large even at $c/s = 2.0$.

The Deviation Angle and Constant's Rule for Thin (t/c = 0) Circular Arc Blades. We first set $\beta_2 = \lambda - \Theta/2 + \delta$ in step b above and obtain,

$$A_s = \frac{\frac{4}{\pi}\frac{s}{c}\,[1 - \delta/\Theta/2]}{\cos\lambda + \sin\lambda\left(\frac{\Theta}{2} - \delta\right)} \quad (23)$$

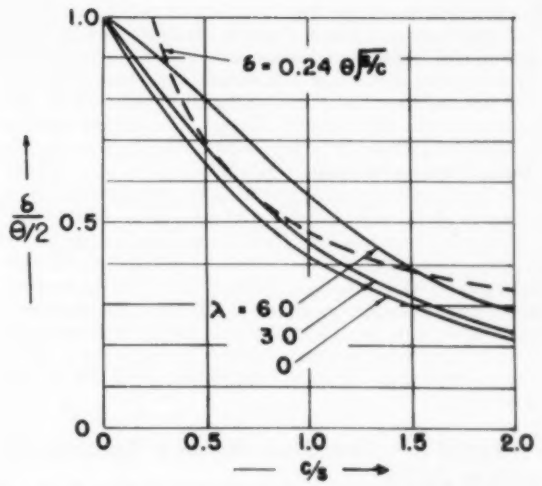

Fig. 11 Comparison of circular arc deviation angle obtained from potential flow solution and Constant's rule (the second-order effect of Cb and cases other than $\alpha_m = t/c = 0$ are not considered)

where both sides of the equation should now represent true values of A_s.

Rearranging, we obtain

$$\frac{\delta}{\Theta/2} = 1 - \frac{\frac{\pi}{4}\cdot\frac{c}{s}\cdot\cos\lambda\cdot A_s}{1 - \frac{\pi}{4}\frac{c}{s}\sin\lambda A_s\frac{\Theta}{2}}. \quad (24)$$

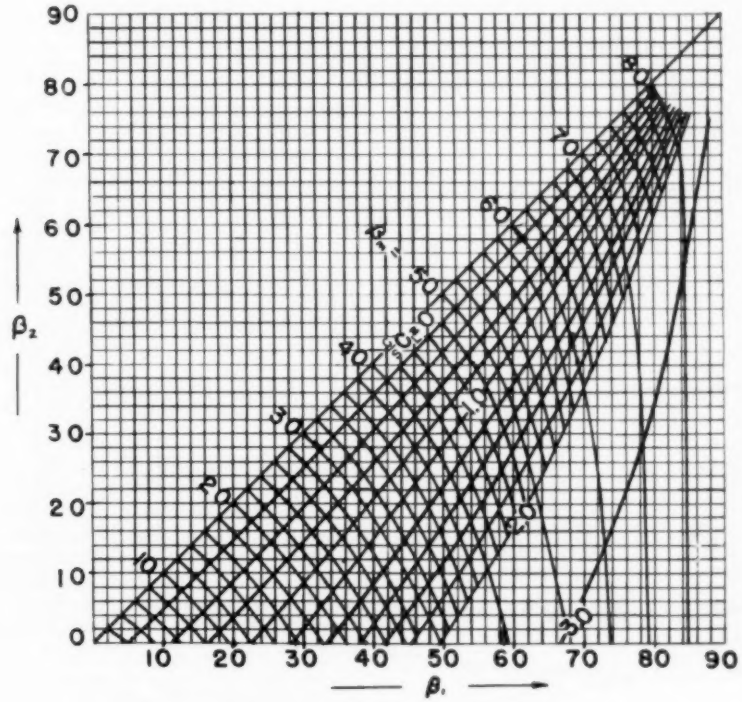

Fig. 12 An aid to transform from the variables, $\frac{c}{s}$ C_L, β_m to β_1, β_2

A_s is now determined from Fig. 7. In Fig. 11 we compare the results with Constant's rule $\delta = m\Theta\sqrt{s/c}$ where m has been set equal to 0.24 [reference [1] gives $m = m(\lambda)$] and where $\delta = \delta(\Theta = 0)$; $A_s = A_s(\mathrm{Cb} = 0)$. It is seen that the simple rule does show some agreement with the comparatively exact results presented here in the middle solidity range. It should be noted that Equation (24) applies only to circular arc blades where $t/c = \alpha_m = 0$.

Choice of Working Parameters. As will be seen in Part II, this author likes to work directly in terms of α_m (or some function of α_m such as $\tan\beta_m$) and $C_L = 2(s/c)\,\Delta V_\theta/V_m$ [or $\Delta V_\theta/V_{\theta m} = (c/s)\,C_L/2\sin\beta_m$] even when applying the cascade information to the compressor design problem since it is felt that this reduces computational labor and, in fact, expresses some of the interesting compressor parameters directly. However, for those who like to think in terms of inlet and exit angles, more inclusive determinations of the deviation angle $\delta(c/s, \lambda, \mathrm{Cb}, t/c)$ can be obtained by straight forward computation using Fig. 12 and Equation (13).

3 Potential Flow Analysis and Method of Calculation for Airfoils in Cascade

The reader who is familiar with classical isolated thin airfoil theory[4] will have no difficulty understanding this extension to a cascade of airfoils since the basic theoretical structure is essentially the same. Of course, aside from the terms in the isolated airfoil problem, the cascade equations are cluttered with a good many others, and we are faced with the difficult numerical solution of those terms which cannot be integrated analytically. The main contribution here is that the method of numerical analysis combined with the theoretical approach yields results in the form (10), (11), and (13) which are fairly accurate and which require comparatively little computational labor. We therefore cease to solve for a cascade case (specified by c/s, λ, Cb, t/c); we solve for all cases. As previously mentioned, Schlichting reports that he has reduced the time requirement for one cascade geometry from 20 days to 20 hours on a desk calculator. Corresponding to his calculation for one cascade geometry 40 geometrical solutions have been calculated in this paper in 40 hours; but the forms (10), (11), (13) allow for an infinite number of combinations among the variables c/s, λ, Cb, and t/c and therefore plots such as Fig. 7 can be made which tell the whole story about the variation of $C_L\,(c/s, \lambda, \mathrm{Cb}, t/c, \alpha_m)$.

[4] Originally developed by H. Glauert. The author referred primarily to reference [9] where a concise derivation is presented.

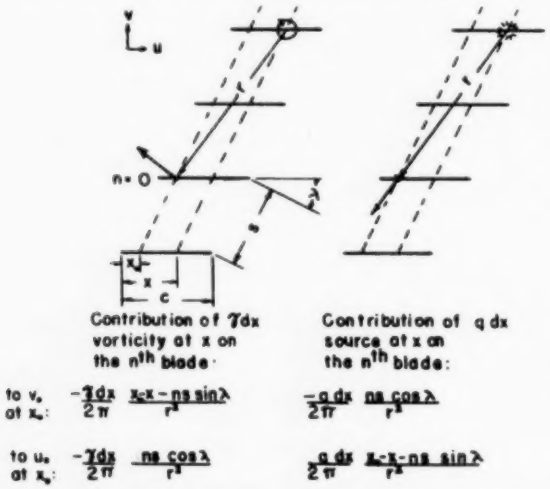

Fig. 13 Contribution of a dx segment of the distributed singularity at any point x on any blade to the velocity at a point x_0 on the $n = 0$ blade

Induced Velocity Equations. In Fig. 13 the contribution of $\gamma\,dx$ vorticity and $q dx$ source at x on the nth blade to the velocity at x_0 on the 0th blade is shown according to the Biot-Savart law. Summing up all the blades from $-\infty$ to $+\infty$ and integrating them all at once from $x/c = 0$ to $x/c = 1$ yields

$$\frac{v_0}{V_m} = -\frac{1}{2\pi}\int_0^1 \frac{\gamma}{V_m}\frac{dx}{x_0 - x} - \frac{c/s}{2}\int_0^1 \frac{\gamma}{V_m} R\left(\frac{x_0 - x}{c}, \frac{c}{s}, \lambda\right) d\left(\frac{x}{c}\right) - \frac{c/s}{2}\int_0^1 \frac{q}{V_m} I\left(\frac{x_0 - x}{c}, \frac{c}{s}, \lambda\right) d\left(\frac{x}{c}\right) \quad (25a)$$

$$\frac{u_0}{V_m} = \frac{-c/s}{2}\int_0^1 \frac{\gamma}{V_m} I\left(\frac{x_0 - x}{c}, \frac{c}{s}, \lambda\right) d\left(\frac{x}{c}\right) + \frac{1}{2\pi} \times \int_0^1 \frac{q}{V_m}\frac{dx}{x_0 - x} + \frac{c/s}{2}\int_0^1 \frac{q}{V_m} R\left(\frac{x_0 - x}{c}, \frac{c}{s}, \lambda\right) d\left(\frac{x}{c}\right) \quad (25b)$$

where

$$R\left(\frac{x_0 - x}{c}, \frac{c}{s}, \lambda\right) = \frac{1}{\pi}\left[\sum_1^\infty + \sum_{-\infty}^{-1}\right] \frac{\frac{x_0 - x}{c}\cdot\frac{c}{s} - n\sin\lambda}{\left(\frac{x_0 - x}{c}\cdot\frac{c}{s} - n\sin\lambda\right)^2 + n^2\cos^2\lambda}$$

$$I\left(\frac{x_0 - x}{c}, \frac{c}{s}, \lambda\right) = \frac{1}{\pi}\left[\sum_1^\infty + \sum_{-\infty}^{-1}\right] \frac{n\cos\lambda}{\left(\frac{x_0 - x}{c}\cdot\frac{c}{s} - n\sin\lambda\right)^2 + n^2\cos^2\lambda}$$

Pistolesi [10] has found that R and I, which can be called the cascade influence functions, may be expressed in closed form. His derivation is repeated in Appendix 1 where it is shown that R and I are actually the real and imaginary parts of a complex function.[5] Scholz [11] has already tabulated these numbers and we have merely reproduced Table 1 from his work.

It will be seen that in determining distances in (25a, b) we have ignored the effect of camber displacement. Thus the first term on the right side of (25a) (which by the way is the only term remaining for the thin isolated airfoil case) should be exactly written

$$\frac{1}{2\pi}\int_0^c \frac{\gamma}{V_m}\frac{dx}{x_0 - x}\left[\frac{1}{1 + \left(\frac{y_0 - y}{x_0 - x}\right)^2}\right]$$

It has been assumed that $\left(\frac{y_0 - y}{x_0 - x}\right)^2 \ll 1.0$.

In Equation (25a, b) and in the future development of the theory it is assumed that the difference between the induced velocity on the blade surface and on the camber line are negligible. Inspection of this assumption discloses errors proportional to Cb^2 and $(t/c)^2$ as discussed in Section 2.

Profile Thickness. The addition of profile thickness to the

[5] Scholz [11] and Schlichting [3] originally derived the basic equations entirely in terms of complex numbers, e.g., $w(z) = u - iv$ which eliminated for a time the necessity of carrying separate equations for u and v. However, they must be subsequently separated to obtain numerical solutions.

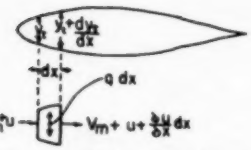

Fig. 14 The profile thickness boundary condition

camber line is accomplished by superimposing sources and sinks on the camber line.

If we consider a segment of the profile (Fig. 14) dx in length, the condition that no fluid crosses the blade surface is obtained from the equation of continuity:

$$(V_m + u)y_t + q dx = \left(V_m + u + \frac{du}{dx}\,dx\right)\left(y_t + \frac{dy_t}{dx}\,dx\right)$$

or

$$q = V_m \frac{dy_t}{dx} + \frac{d(uy_t)}{dx} \tag{26}$$

q representing the strength of the source distribution at x is the amount of imaginary fluid injected at the camber line.

It may be shown that the variation of u/V_m in the y direction within the profile is of the order $(t/c)^2$. It therefore has been considered constant.

If we assume that $\dfrac{d(uy_t)}{dx}$ is small, (26) becomes simply

$$\frac{q}{V_m} = \frac{dy_t}{dx} = \frac{t}{c} f_t'(x/c) \tag{27}$$

which, in fact, represents the solution of q since $\dfrac{dy_t}{dx}$ is known. We will later determine in Appendix 2 the correction resulting from the inclusion of the term $\dfrac{1}{V_m}\dfrac{d(uy)}{dx}$. It is quite small and may, in fact, be neglected entirely except where extreme accuracy is required.

The condition that the integrated source and sink distribution be zero for a closed body is automatically satisfied.

$$\frac{Q}{V_m} = \int_0^c \frac{q}{V_m}\,dx = \int_0^c \frac{dy_t}{dx}\,dx = 0$$

It should be mentioned that although the profile shape $f_t(x/c)$ used in the previous solutions was the 65-series compressor blade [12] the results should apply generally to other airfoil-like shapes since again the effects of the details of one blade's profile (or source distribution details) on adjacent blades are attenuated. It is only necessary to substitute the correct isolated airfoil solution in Q_0 [Fig. 4(a)].

Solution for the Vortex Sheet Distribution Which Satisfies the Boundary Conditions

The cambered airfoil is built up by superimposing a distribution of sources and sinks, the determination of which has been given, and vortexes on the camber line. The airfoil is approached by a velocity V_m at an angle α_m. The object of the problem is to find the correct distribution of vorticity which, together with the source and sink distribution, will induce the amount of velocity, u_0 and v_0 (in the x and y direction), which just cancels out the component of V_m normal to the blade camber at x_0. This condition of flow tangency may be written,

$$\frac{V_m \sin \alpha_m + v_0}{V_m \cos \alpha_m + u_0} = \left(\frac{dy_c}{dx}\right)_0 = \mathrm{Cb}\, f_c'\left(\frac{x_0}{c}\right) \tag{28}$$

where y_c is the camber distribution.

The Kutta-Joukowski condition which states that the flow must leave the blade at an angle parallel to blade trailing edge is automatically satisfied by stating that any solution we obtain for the vorticity distribution must have the value zero at the trailing edge.

$$[\gamma]_{x=c} = 0 \tag{29}$$

If it were not zero, the flow would skirt around the trailing edge with zero radius of curvature and with an infinite velocity. However, it should be noted that the flow will, in theory, have a zero radius of curvature and an infinite velocity at the *leading edge* which is alleviated in a real flow by separation at the leading edge of an infinitely thin airfoil and in conventional airfoils by the finite nose radius of a thickened blade profile.

We next assume a Fourier expansion as a solution for $\dfrac{\gamma}{V_m}$ in the form

$$\frac{\gamma}{V_m} = 2A_0 \frac{1 + \cos\theta}{\sin\theta} + 4\sum_{n=1}^{\infty} A_n \sin n\theta \tag{30}$$

All terms satisfy the Kutta condition $[\gamma]_{\theta=\pi} = 0$.

Now (30) and (27) may be substituted into (25a, b) and (25a, b) may be substituted into (28) yielding

$$\sum_0^{\infty} A_n g_n = \sin\alpha_m - \mathrm{Cb}\, f_c'(\theta_0) + \mathrm{Cb}\sum_0^{\infty} A_n h_n - \frac{t}{c}\,\mathrm{Cb}\,B - \frac{t}{c}\,T \tag{31}$$

where

$$g_0\left(\theta_0, \frac{c}{s}, \lambda\right) = 1 + \frac{1}{2}\frac{c}{s}\int_0^{\pi} R[1 + \cos\theta]d\theta$$

$$g_n\left(\theta_0, \frac{c}{s}, \lambda\right) = -2\cos n\theta + \frac{1}{2}\frac{c}{s}\int_0^{\pi} 2R\sin n\theta \sin\theta\, d\theta; \qquad n > 0$$

$$h_0\left(\theta_0, \frac{c}{s}, \lambda\right) = \frac{1}{2}\frac{c}{s}\int_0^{\pi} f_c'(\theta_0) I(1 + \cos\theta)d\theta$$

$$h_n\left(\theta_0, \frac{c}{s}, \lambda\right) = \frac{1}{2}\frac{c}{s}\int_0^{\pi} 2f_c'(\theta_0) I \sin n\theta \sin\theta\, d\theta; \qquad n > 0$$

$$B\left(\theta_0, \frac{c}{s}, \lambda\right) = \frac{1}{2}\int_0^{\pi} f_c'(\theta_0) f_t'(\theta) \times \left[\frac{1/\pi}{\cos\theta - \cos\theta_0} + \frac{c}{s}\,\frac{R}{2}\right]\sin\theta\, d\theta$$

$$T\left(\theta_0, \frac{c}{s}, \lambda\right) = \frac{c/s}{2}\int_0^{\pi} f_t'(\theta_0) I \frac{\sin\theta}{2}\,d\theta$$

where we have omitted the functional dependency of R and I in the notation, i.e.,

$$R, I = R\left(\frac{x_0 - x}{c}, \frac{c}{s}, \lambda\right), I\left(\frac{x_0 - x}{c}, \frac{c}{s}, \lambda\right) = R\left(\theta, \theta_0, \frac{c}{s}, \lambda\right), I\left(\theta, \theta_0, \frac{c}{2}, \lambda\right)$$

and where we have utilized two well-known equations which are derived in many textbooks (the present author referred to [13]):

$$\int_0^\pi \frac{(1-\cos\theta)d\theta}{\cos\theta-\cos\theta_0} = \pi$$

$$\int_0^\pi \sum_{n=1}^{\infty} \frac{A_n \sin n\theta \sin\theta\, d\theta}{\cos\theta-\cos\theta_0} = -\pi \sum_{n=1}^{\infty} A_n \cos n\theta_0.$$

Essentially, the basis of the analysis by Schlichting was to calculate numerically and tabulate functions similar to g, h, B, and T for every c/s, λ and at many chord intervals θ_0 (or x_0/c). He then fitted Equation (31) to the boundary condition (28) at three of the chord positions to give three simultaneous equations which may be solved for A_0, A_1, and A_2.

In this report, we proceed with a Fourier analysis analogous to that performed in thin airfoil theory. If we now multiply every term of Equation (31) by $\cos k\theta_0$ and integrate from 0 to π, we have

$$\sum_{n=0}^{\infty} A_n g_{nk} = \sin\alpha_m \delta_{0k} - \mathrm{Cb}\,\frac{1}{\pi}\int_0^\pi f_c'(\theta_0)\cos k\theta_0 d\theta_0 + \mathrm{Cb}\sum_{n=0}^{\infty} A_n h_{nk} - \frac{t}{c}\,\mathrm{Cb}\,B_k - \frac{t}{c}\,T_k \quad (32)$$

$$g_{0k}\left(\frac{c}{s},\lambda\right) = \delta_{0k} + \frac{c/s}{2\pi}\int_0^\pi\int_0^\pi R(1+\cos\theta)\cos k\theta_0\, d\theta\, d\theta_0$$

$$g_{nk}\left(\frac{c}{s},\lambda\right) = -\delta_{nk} + \frac{c/s}{2\pi}\int_0^\pi\int_0^\pi 2R\sin n\theta\sin\theta\cos k\theta_0\, d\theta\, d\theta_0; \quad n>0$$

$$h_{0k}\left(\frac{c}{s},\lambda\right) = \frac{c/s}{2\pi}\int_0^\pi\int_0^\pi f_c'(\theta_0)I(1+\cos\theta)\cos k\theta_0\, d\theta\, d\theta_0$$

$$h_{nk}\left(\frac{c}{s},\lambda\right) = \frac{c/s}{2\pi}\int_0^\pi\int_0^\pi f_c'(\theta_0)2I\sin n\theta\sin\theta\cos k\theta_0\, d\theta\, d\theta_0; \quad n>0$$

$$B_k\left(\frac{c}{s},\lambda\right) = \frac{1}{2\pi}\int_0^\pi\int_0^\pi f_c'(\theta)\, f_t'(\theta_0) \times\left[\frac{1/\pi}{\cos\theta-\cos\theta_0}+\frac{c}{s}\,\frac{R}{2}\right]\sin\theta\cos k\theta_0\, d\theta\, d\theta_0$$

$$T_k\left(\frac{c}{s},\lambda\right) = \frac{c/s}{2\pi}\int_0^\pi\int_0^\pi f_t'(\theta)I\cos k\theta_0\,\frac{\sin\theta}{2}\,d\theta\, d\theta_0$$

where

$$\delta_{nk} = \begin{cases} 1.0 & \text{when } n=k \\ 0 & \text{when } n\neq k \end{cases}$$

If we set $c/s = t/c = 0$ in (33) we would obtain exactly the relations that one obtains in isolated airfoil theory.

$$A_0 = \sin\alpha_m - \frac{\mathrm{Cb}}{\pi}\int_0^\pi f_c'\, d\theta$$

$$A_n = -\frac{\mathrm{Cb}}{\pi}\int_0^\pi f_c'\cos n\theta\, d\theta$$

Determination of the Double Fourier Integrals

It is now necessary to solve numerically the double integrals of

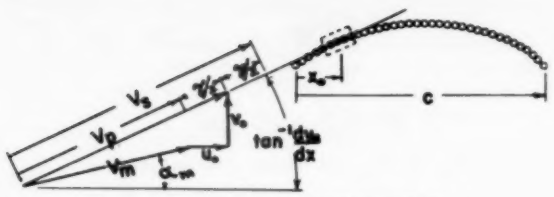

Fig. 15 The camber line boundary condition

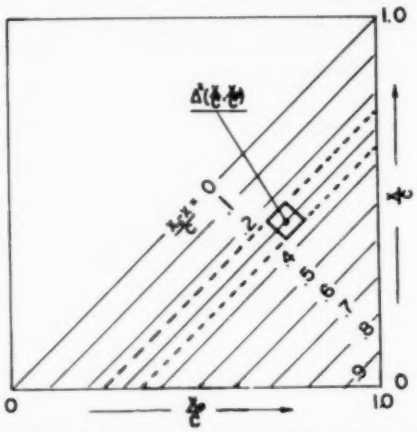

Fig. 16 Illustrating the method of obtaining the double Fourier integrals of Equation (32)

Equation (32) for any c/s or λ. These integrals are in the form

$$g(c/s,\lambda) = \int_0^\pi\int_0^\pi R\left(\frac{x_0-x}{c},\frac{c}{s},\lambda\right)F(\theta,\theta_0)d\theta\, d\theta_0 \quad (33)$$

Using the Equations $\frac{x}{c} = \frac{1-\cos\theta}{2}$; $d\left(\frac{x}{c}\right) = \frac{1}{2}\sin\theta\, d\theta$, (33) may be transformed back to x and x_0,

$$g(c/s,\lambda) = \int_0^1\int_0^1 R\left(\frac{x_0-x}{c},\frac{c}{s},\lambda\right) F\left(\frac{x}{c},\frac{x_0}{c}\right) d\left(\frac{x}{c}\right) d\left(\frac{x_0}{c}\right)$$

where the g used here could be g_{nk}, h_{nk}, B_k, T_k of Equation (32) and R could be either R or I. $F(\theta,\theta_0)$ could be sine, cosine, basic thickness, or basic camber functions of the variables θ and θ_0. A straightforward way of evaluating the integral would be to numerically integrate through x/c holding x_0/c constant. Many integrations would be necessary so that a second numerical integration through x_0/c could be performed. This process would have to be performed again every time new values of λ and c/s were chosen.

We will now present a method which will greatly reduce the calculation labor when it is necessary to calculate the double integrals for many values of c/s and λ.

Let us look at an x/c versus x_0/c plot in Fig. 16 upon which lines of constant $\frac{x_0-x}{c}$ have been drawn. Of course, R is also constant on these lines. The integral of Equation (33) may be imagined to be a solid whose base is 1×1 and whose height at any x_0/c, x/c point is $R\left(\frac{x_0-x}{c}\right)F\left(\frac{x}{c},\frac{x_0}{c}\right)$. If we can find the volume of the solid we will have evaluated the integral.

The first step in the numerical process is to determine the

value of a particular *section* of the solid exclusive of the value R. That section is bounded by lines of constant $\left(\frac{x_0 - x}{c}\right)_n + \frac{1}{2}\Delta\left(\frac{x_0 - x}{c}\right)$, $\left(\frac{x_0 - x}{c}\right)_n - \frac{1}{2}\Delta\left(\frac{x_0 - x}{c}\right)$ and the edges $x_0/c = 1$ (or 0) and $x/c = 0$ (or 1).

Now Fig. 16 shows such a section which is further broken up into smaller *segments*. We can therefore find the volume of each section by adding up the areas $\Delta^2(x/c, x_0/c)$ of each segment which has been multiplied by the appropriate value of $F(x/c, x_0/c)$. Let us denote this by

$$\Delta g\left[\left(\frac{x_0 - x}{c}\right)_n\right] = \sum F\left[\left(\frac{x_0 - x}{c}\right)_n, \frac{x_0}{c} \text{ or } \frac{x}{c}\right] \times \Delta^2\left(\frac{x}{c}, \frac{x_0}{c}\right) \quad (34)$$

Since R is constant in the section the value g may be determined by adding up all the sections after multiplication by the appropriate R. Therefore,

$$g(\lambda, c/s) = \sum R\left[\left(\frac{x_0 - x}{c}\right)_n, c/s, \lambda\right] \Delta g\left[\left(\frac{x_0 - x}{c}\right)_n\right] \quad (35)$$

The point is that once the Δg's have been determined and tabulated once and for all, it is only necessary to perform the simple numerical integration of Equation (35) for each $R\left(\frac{x_0 - x}{c}\right)$ function given in Table 1 and corresponding to the various values of c/s and λ.

Actually, it is necessary to operate on only half of the square of Fig. 16 since $R\left(\frac{x_0 - x}{c}\right)$ is antisymmetric about $\frac{x_0 - x}{c} = 0$. Therefore

$$R\left(\frac{x_0 - x}{c}\right) = -R\left(-\frac{x_0 - x}{c}\right) \quad (36)$$

or

$$R(\theta, \theta_0) = -R(\pi - \theta, \pi - \theta_0)$$

Now Equation (33) could just as easily be written

$$g\left(\lambda, \frac{c}{s}\right) = \int_0^\pi \int_0^\pi R(\pi - \theta, \pi - \theta_0) \times F(\pi - \theta, \pi - \theta_0) d(\pi - \theta) d(\pi - \theta_0) \quad (37)$$

Combining (33) and (37) and making the substitution (36) yields

$$g\left(\lambda, \frac{c}{s}\right) = \int_0^\pi \int_0^\pi R(\theta, \theta_0) \frac{F(\theta, \theta_0) - F(\pi - \theta, \pi - \theta_0)}{2} d\theta\, d\theta_0 \quad (38)$$

The interesting thing about Equation (38) is that if the integration is carried over half of Fig. 16 divided by the line $(x_0 - x)/c = 0$ the result is equal to the result of integrating over the other half.

Furthermore, if $F(\theta, \theta_0)$ is symmetric or if

$$F(\theta, \theta_0) = F(\pi - \theta, \pi - \theta_0)$$

$g(\lambda, c/s)$ is then zero. This happened to a number of the integrals of Equation (32). For example, g_{10} would give $\frac{\sin^2\theta - \sin^2(\pi - \theta)}{2} = 0$ in the integrand making the whole integral equal to 0 while, on the other hand, $g_{11} - 1$ would give $\frac{\sin^2\theta\cos\theta_0 - \sin^2(\pi - \theta)\cos(\pi - \theta_0)}{2} = \sin^2\theta\cos\theta$. In the case of the function f_s' and f_1' we simply evaluate the integral based on a "new" function $[f'(\theta) - f'(\pi - \theta)]/2$.

In Table 2 we show the Δg's that were obtained from Equation (34), where Fig. 16 had been broken up into $\Delta\left(\frac{x_0 - x}{c}\right) = 0.1$ sections. Actually, it was found to be accurate enough to use an increment $\Delta\left(\frac{x_0 - x}{c}\right)$ corresponding to $\Delta\left(\frac{x_0 - x}{c}\right) = 0.2$ which simply means that the rows of numbers in Table 2 may be

Table 1 Cascade influence functions (from Reference [11])

λ	0°		15°		30°		45°		60°		75°		90°	
$\frac{x_0 - x}{c}$	R	I	R	I	R	I	R	I	R	I	R	I	R	I
0	0	0	0	0	0	0	0	0	0	0	0	0	0	0
0.05	0.052	0	0.050	0.026	0.027	0.046	0.002	0.053	-0.023	0.047	-0.045	0.026	-0.052	0
0.1	0.106	0	0.090	0.052	0.055	0.089	0.003	0.103	-0.049	0.092	-0.091	0.053	-0.104	0
0.15	0.153	0	0.135	0.076	0.079	0.134	0.004	0.158	-0.078	0.141	-0.137	0.081	-0.159	0
0.2	0.204	0	0.179	0.101	0.107	0.172	0.006	0.210	-0.102	0.186	-0.184	0.110	-0.217	0
0.25	0.249	0	0.222	0.122	0.135	0.217	0.009	0.264	-0.126	0.237	-0.233	0.140	-0.274	0
0.3	0.296	0	0.263	0.142	0.164	0.256	0.018	0.313	-0.147	0.291	-0.282	0.171	-0.337	0
0.35	0.341	0	0.303	0.161	0.196	0.292	0.028	0.363	-0.165	0.343	-0.332	0.213	-0.401	0
0.4	0.300	0	0.343	0.177	0.226	0.325	0.043	0.413	-0.181	0.401	-0.384	0.255	-0.473	0
0.45	0.419	0	0.378	0.191	0.257	0.356	0.060	0.460	-0.191	0.460	-0.438	0.304	-0.550	0
0.5	0.454	0	0.412	0.204	0.287	0.382	0.082	0.504	-0.196	0.523	-0.491	0.361	-0.636	0
0.6	0.517	0	0.475	0.223	0.349	0.426	0.133	0.583	-0.186	0.652	-0.604	0.511	-0.853	0
0.7	0.571	0	0.529	0.236	0.407	0.456	0.197	0.647	-0.158	0.779	-0.688	0.731	-1.180	0
0.8	0.617	0	0.576	0.245	0.459	0.477	0.259	0.686	-0.052	0.880	-0.680	1.037	-1.771	0
0.9	0.654	0	0.615	0.251	0.504	0.489	0.318	0.709	+0.052	0.939	-0.468	1.357	-3.420	0
1.0	0.685	0	0.649	0.254	0.540	0.495	0.368	0.718	0 .150	0.948	-0.061	1.453	-----	0
1.1	0.711	0	0.677	0.256	0.572	0.499	0.410	0.719	0.224	0.930	+0.252	1.260	-----	0
1.2	0.737	0	0.701	0.257	0.598	0.500	0.441	0.716	0.268	0.901	0.294	1.021	-----	0
1.3	0.754	0	0.721	0.258	0.620	0.500	0.464	0.714	0.288	0.875	0.232	0.869	-----	0
1.4	0.774	0	0.738	0.258	0.636	-----	0.483	0.710	0.296	0.857	0.139	0.806	-----	0
1.5	0.787	0	0.754	0.259	0.655	-----	0.496	0.709	0.300	0.852	0.052	0.805	-----	0
1.6	0.801	0	0.767	0.259	0.666	-----	0.508	0.709	0.308	0.854	-0.010	0.846	-----	0
1.7	0.814	0	0.779	-----	0.678	-----	0.520	0.708	0.309	0.857	-0.037	0.911	-----	0
1.8	0.823	0	0.789	-----	0.688	-----	0.530	0.707	0.317	0.862	-0.024	0.980	-----	0
1.9	0.833	0	0.798	-----	0.699	-----	0.539	0.707	0.328	0.865	+0.024	1.030	-----	0
2.0	0.841	0	0.807	0.259	0.707	0.500	0.548	0.707	0.338	0.868	0.085	1.045	-----	0
2.1	-----	0	-----	-----	-----	-----	-----	-----	-----	-----	0.137	1.027	-----	0
2.2	-----	0	-----	-----	-----	-----	-----	-----	-----	-----	0.149	0.993	-----	0
2.3	-----	0	-----	-----	-----	-----	-----	-----	-----	-----	0.168	0.961	-----	0
2.4	-----	0	-----	-----	-----	-----	-----	-----	-----	-----	0.157	0.940	-----	0
2.5	0.873	0	0.842	0.259	0.729	0.500	0.580	0.707	0.374	0.867	0.140	0.933	-----	0
∞	1.000	0	0.966	0.259	0.866	0.500	0.707	0.707	0.500	0.866	0.259	0.966	-∞	0

Table 2 Intermediate calculation in determining the double Fourier integral solution

$\frac{x_0 - x}{c}$	$\Delta(g_{00}\cdot 1)$	$\Delta(g_{02})$	$\Delta(g_{11}\cdot 1)$	$\Delta(g_{20})$	$\Delta(g_{22}\cdot 1)$	$\Delta(h_{00})$	$\Delta(h_{01})$	$\Delta(h_{10})$	ΔB_0	ΔB_1	ΔT_0	ΔT_1
.05	1.569	-3.895	-4.175	-5.725	-8.375	-.479	-.259	-.601	.586	-.600	-.640	1.525
.15	3.182	-5.636	-8.731	-2.738	-12.262	-1.114	-.555	-1.105	.574	-.777	-.030	2.849
.25	4.465	-3.224	-10.812	-0.359	-1.165	-1.384	-.394	-1.436	.793	-.885	1.939	3.353
.35	5.559	-5.040	-12.098	5.183	-4.813	-1.473	.181	-1.529	.754	-.486	3.815	2.996
.45	6.240	-5.586	-11.846	8.836	-6.897	-1.652	.017	-1.606	.724	-.039	5.890	2.657
.55	7.274	-4.333	-11.603	11.266	-2.387	-1.825	.345	-1.495	.552	.689	8.066	2.096
.65	7.880	-2.153	-10.096	12.844	1.730	-1.849	.664	-1.340	.382	1.036	8.290	1.200
.75	8.474	.374	-8.101	10.783	6.087	-2.144	1.109	-1.174	.141	1.418	7.785	-.062
.85	9.164	3.883	-5.282	9.034	6.009	-2.339	1.663	-.751	-.438	1.454	7.087	-2.039
.95	9.821	7.905	-1.916	3.830	3.083	-3.307	2.984	-.323	-1.174	1.520	5.012	-3.486

Table 3 Double Fourier integral solutions

	x/c	g_{00}	g_{02}	g_{11}	g_{20}	g_{22}	h_{00}	h_{01}	h_{10}	Z_0	B_1	T_0	T_1
	0	1.000	0	-1.000	0	-1.000	0	0	0	.052	-.033	0	0
0°	0.5	1.093	.001	-1.096	.094	-0.989	0	0	0	.053	-.024	0	0
	1.0	1.314	-.013	-1.339	.317	-0.978	0	0	0	.056	-.003	0	0
	1.5	1.583	-.046	-1.646	.589	-0.982	0	0	0	.062	.021	0	0
	2.0	1.872	-.084	-2.011	.876	-1.002	0	0	0	.072	.043	0	0
15°	0.5	1.084	.001	-1.087	.084	-0.990	-.012	.006	-.006	.052	-.024	.035	.002
	1.0	1.290	-.008	-1.309	.284	-0.975	-.036	.016	-.020	.055	-.004	.105	.010
	1.5	1.550	-.037	-1.610	.551	-0.975	-.059	.024	-.034	.061	.019	.172	.022
	2.0	1.828	-.082	-1.950	.836	-0.992	-.084	.032	-.050	.069	.041	.240	.036
30°	0.5	1.054	.002	-1.054	.054	-0.996	-.022	.011	-.011	.052	-.027	.064	.002
	1.0	1.220	.005	-1.222	.223	-0.970	-.068	.031	-.037	.053	-.009	.200	.023
	1.5	1.447	-.011	-1.476	.460	-0.951	-.115	.048	-.067	.057	.013	.338	.043
	2.0	1.696	-.046	-1.772	.714	-0.962	-.160	.062	-.096	.064	.033	.462	.072
45°	0.5	1.009	.003	-1.006	.008	-0.991	-.026	.014	-.014	.052	-.032	.080	.002
	1.0	1.106	.024	-1.070	.105	-0.965	-.094	.045	-.050	.049	-.019	.218	.016
	1.5	1.264	.033	-1.255	.299	-0.927	-.162	.069	-.093	.049	.003	.480	.055
	2.0	1.486	.012	-1.468	.524	-0.914	-.226	.090	-.136	.054	.023	.664	.098
60°	0.5	.955	.001	-0.953	-.046	-1.005	-.026	.014	-.013	.052	-.037	.076	0
	1.0	.944	.045	-0.893	-.069	-0.969	-.112	.058	-.056	.045	-.033	.328	.004
	1.5	1.076	.096	-0.968	.088	-0.884	-.196	.087	-.111	.039	-.009	.597	.057
	2.0	1.210	.042	-1.112	.278	-0.860	-.276	.112	-.164	.040	.011	.822	.114

$$g_{10} = g_{21} = g_{12} = h_{11} = 0$$

$$g_{01} = 1 - g_{00}$$

paired off and combined. Table 3 contains the final g values according to (38).

Particular Solutions for Symmetrically Cambered Airfoils. As mentioned before, the values of f_e' and f_i' were actually taken for the 65-series compressor blade [12] in computing h, B, and T. However, it was readily apparent that the final results would apply with excellent accuracy to other similar (symmetrically cambered) blades as long as Cb is correctly calculated from Equation (2) and the correct velocity distribution for the isolated case is used for Γ_{02} and Q_0 in (10).

Now several simplifications may be made to Equation (32). They are:

a) The diagonal terms g_{nn} are very nearly equal to 1.0 for $n > 2$ and may be given that quantity.

b) Nondiagonal terms of g_{nk} may be neglected for $n > 2$ and $k > 2$.

c) h_{nk} terms may be neglected for $n > 1$ and $k > 1$.

d) $g_{10} = g_{21} = g_{12} = h_{11} = 0$; $g_{01} = 1 - g_{00}$.

e) Since $f_e'(x) = -f_e'(c - x)$, $\int_0^\pi f_e'(\theta) \cos k\theta \, d\theta$ is zero for even values of k.

The result is,

$$\left.\begin{aligned} A_0 g_{00} + A_2 g_{20} &= \sin \alpha_{z_0} + \mathrm{Cb}\,(A_0 h_{00} + A_1 h_{10}) \\ &\quad - \frac{t}{c}\,(\mathrm{Cb}\,B_0 - T_0) \end{aligned}\right\} \quad (39)$$

$$\left.\begin{aligned} A_1(1 - g_{00}) + A_1 g_{11} &= \frac{\mathrm{Cb}}{2\pi} \\ &\quad + \mathrm{Cb}\,(A_0 h_{01}) - \frac{t}{c}\,(\mathrm{Cb}B_1 + T_1) \end{aligned}\right\} \quad (39)\ (cont.)$$

$$A_0 g_{02} + A_2 g_{22} = 0$$

for all symmetrically cambered blades $\Big\}$ $A_n = 0$; $\quad n > 2 =$ even

for 65-series compressor blade ($a = 1.0$ camber line) $\Big\}$ $A_n = \dfrac{\mathrm{Cb}}{2\pi}\,\dfrac{1}{n}$; $\quad n > 2 =$ odd

for circular arc camber line $\Big\}$ $A_n = 0$; $\quad n > 2 =$ odd

The fact that $A_{n>2}$ does not feed back appreciably into the first three sets of (39) is merely an expression of the physical fact that, while $A_{n>2}$ results in local induced velocities on a given blade, its effect is washed out by the time it is propagated to adjacent blades. This is understandable since the integrated vorticity of $A_{n>2}$ (and also A_2) is zero and exerts no effect on the airfoil lift. A_2 is equal to $-(g_{02}/g_{22})A_0$ and from Table 3 is seen to be fairly small. A_2 would take on considerable importance in the case of nonsymmetrically cambered airfoils

Now (39) may be solved for the A's and these in turn may be partitioned according to (11*a*, *b*). The result is

Table 4 Cascade coefficients

i	Cb	c/s	$A_{0\alpha}$	A_{0cb}	A_{0t}	$A_{1\alpha}$	A_{1cb}	A_{1t}	A_{α}	A_{cb}	A_{t}
	0	0	1.000	0	0	0	1.000	0	1.000	1.000	0
	1	0	1.000	0	-.052	0	1.000	-.033	1.000	1.000	-.085
0°	0	0.5	.915	0	0	-.078	.912	0	.837	.912	0
		1.0	.765	0	0	-.175	.747	0	.588	.730	0
		1.5	.643	0	0	-.228	.608	0	.415	.608	0
		2.0	.559	0	0	-.243	.497	0	.316	.497	0
	1	0.5	.915	0	-.048	-.078	.912	.004	.837	.912	-.044
		1.0	.765	0	-.043	-.175	.747	.010	.588	.730	-.033
		1.5	.643	0	-.040	-.228	.608	.004	.415	.608	-.036
		2.0	.559	0	-.040	-.243	.497	.497	.038	.316	-.002
15°	0	0.5	.915	0	-.032	-.070	.920	.005	.845	.920	-.027
		1.0	.777	0	-.082	-.172	.764	.026	.605	.764	-.056
		1.5	.654	0	-.112	-.224	.621	.052	.430	.621	-.060
		2.0	.569	0	-.137	-.242	.513	.077	.327	.513	-.060
	1	0.5	.905	-.002	-.079	-.075	.920	-.011	.830	.915	-.090
		1.0	.758	-.012	-.121	-.177	.767	.035	.581	.755	-.088
		1.5	.634	-.013	-.148	-.226	.626	.079	.408	.613	-.069
		2.0	.549	-.014	-.170	-.242	.519	.115	.307	.505	-.055
30°	0	0.5	.949	0	-.061	-.048	.949	.005	.901	.949	-.056
		1.0	.819	0	-.164	-.147	.818	.049	.672	.818	-.115
		1.5	.694	0	-.235	-.210	.678	.100	.484	.678	-.135
		2.0	.602	0	-.278	-.237	.564	.150	.365	.564	-.128
	1	0.5	.930	-.010	-.108	-.058	.950	-.017	.872	.940	-.125
		1.0	.780	-.024	-.197	-.160	.823	.052	.620	.799	-.145
		1.5	.652	-.030	-.257	-.218	.688	.124	.454	.658	-.133
		2.0	.561	-.030	-.295	-.240	.577	.186	.321	.547	-.109
45°	0	0.5	.991	0	-.079	-.009	.994	.005	.982	.994	-.076
		1.0	.902	0	-.251	-.069	.925	.040	.814	.925	-.211
		1.5	.778	0	-.373	-.176	.797	.128	.602	.797	-.245
		2.0	.670	0	-.445	-.219	.672	.212	.451	.672	-.233
	1	0.5	.964	-.013	-.127	-.022	.994	-.027	.942	.981	-.154
		1.0	.856	-.039	-.278	-.116	.928	.036	.720	.889	-.242
		1.5	.704	-.052	-.372	-.198	.812	.150	.506	.760	-.222
		2.0	.598	-.055	-.429	-.251	.695	.247	.367	.638	-.182
60°	0	0.5	1.047	0	-.080	.049	1.049	-.004	1.096	1.049	-.084
		1.0	1.063	0	-.334	.067	1.120	-.017	1.130	1.120	-.351
		1.5	.921	0	-.550	-.072	1.033	.102	.849	1.033	-.448
		2.0	.817	0	-.672	-.154	.899	.229	.665	.899	-.443
	1	0.5	1.019	-.014	-.130	.033	1.049	-.045	1.052	1.035	-.175
		1.0	.950	-.060	-.367	-.002	1.120	-.032	.948	1.060	-.399
		1.5	.792	-.091	-.505	-.135	1.053	.135	.657	.962	-.368
		2.0	.689	-.102	-.594	-.200	.929	.294	.489	.827	-.310

$$A_{0\alpha} = \frac{1}{P_0 + \text{Cb}\, h_{10} \dfrac{P_1}{g_{11}}} \tag{40}$$

$$A_{0c} = -\frac{h_{10}}{g_{11}} \frac{1}{P_0 + \text{Cb}\, h_{10} \dfrac{P_1}{g_{11}}}$$

$$A_{0t} = -\frac{\text{Cb}\, B_0 + T_0}{P_0 + \text{Cb}\, h_{10} \dfrac{P_1}{g_{11}}}$$

$$A_{1\alpha} = -\frac{P_1}{g_{11}} A_{0\alpha}$$

$$A_{1c} = \frac{-1}{g_{11}} - \text{Cb}\, \frac{P_1}{g_{11}} A_{0cb}$$

$$A_{1t} = \frac{-T - \text{Cb}\, B_1}{g_{11}} - \frac{P_1}{g_{11}} A_{0t}$$

where we have set $P_0 = g_{00} - \dfrac{g_{02} g_{01}}{g_{22}} - \text{Cb}\, h_{00}$

$$P_1 = 1 - g_{01} - \text{Cb}\, h_{01}$$

Table 4 was computed using these equations and the values from Table 3. It will be seen that the A coefficients contain the camber term Cb. Because they are invariably multiplied by small coefficients it is valid to interpolate linearly between the A's computed for Cb = 0 and those computed for Cb = 1.0 in Table 4 and Figs. 5, 6, and 7.

Blade Surface Velocity Distributions

From Fig. 15 it may be seen that

$$\frac{V_0}{V_\infty} = \left(\cos \alpha_\infty + \frac{u_0}{V_\infty}\right) \sqrt{1 + \overline{y_c'}^2} \pm \frac{\gamma/2}{V_\infty} \tag{41}$$

Now the values of u_0/V_∞ and γ/V_∞ are determined from Equations (25*b*) and (30). (41) then takes the form of Equation (10) if

$$\Gamma_{0c} = \frac{1 + \cos \theta}{2\pi \sin \theta} \tag{42a}$$

$$\Gamma_{0t} = \frac{\sin \theta}{\pi} \tag{42b}$$

$$\Gamma_{0\Sigma} = \sum_{n=2}^{\infty} \frac{2}{\pi} \int_0^\pi f_c'(\theta_0) \cos n\theta_0 \, d\theta_0 \sin n\theta^6 \tag{42c}$$

$$\Gamma_{\Sigma 0} = \frac{1}{4\pi \sin \lambda} \int_0^\pi I(1 + \cos \theta) d\theta \tag{42d}$$

$$\Gamma_{\Sigma 1} = \frac{1}{2\pi \sin \lambda} \int_0^\pi I \sin^2 \theta \, d\theta \tag{42e}$$

$$Q_0 = \frac{1}{2\pi} \int_0^\pi \frac{f_c' dx}{x_0 - x} \tag{42f}$$

$$Q_\Sigma = \frac{1}{2} \int_0^\pi R f_t' d\left(\frac{x}{c}\right) \tag{42g}$$

[6] For the 65-series camber line ($a = 1.0$) $2 \int_0^\pi f_c'(\theta_0) \cos n\theta_0 \, d\theta_0$ equals $1/n$ when n is odd and zero when n is even.

Table 5 Blade surface velocity functions

		Γ_{z0}						Γ_{z1}					
λ	x/c	0	.2	.4	.6	.8	.10	0	.2	.4	.6	.8	.10
	c/s												
	0	0	0	0	0	0	0	0	0	0	0	0	0
0	0.5	0	0	0	0	0	0	0	0	0	0	0	0
	1.0	0	0	0	0	0	0	0	0	0	0	0	0
	1.5	0	0	0	0	0	0	0	0	0	0	0	0
	2.0	0	0	0	0	0	0	0	0	0	0	0	0
15	0.5	.065	.017	-.031	-.078	-.120	-.155	.113	.070	.024	-.024	-.070	-.113
	1.0	.110	.026	-.059	-.132	-.194	-.218	.176	.117	.041	-.041	-.117	-.176
	1.5	.137	.027	-.082	-.155	-.207	-.234	.202	.140	.050	-.050	-.140	-.202
	2.0	.160	.025	-.097	-.173	-.218	-.241	.219	.156	.056	-.056	-.156	-.219
30	0.5	.060	.016	-.028	-.071	-.111	-.147	.105	.065	.022	-.022	-.065	-.105
	1.0	.104	.027	-.055	-.127	-.191	-.217	.171	.113	.039	-.039	-.113	-.171
	1.5	.134	.030	-.078	-.159	-.209	-.235	.203	.140	.050	-.050	-.140	-.203
	2.0	.152	.028	-.094	-.173	-.213	-.239	.215	.153	.056	-.056	-.153	-.215
45	0.5	.051	.014	-.025	-.061	-.097	-.132	.092	.056	.019	-.019	-.056	-.092
	1.0	.094	.026	-.046	-.116	-.167	-.216	.164	.105	.036	-.036	-.105	-.164
	1.5	.125	.032	-.069	-.157	-.209	-.234	.200	.137	.049	-.049	-.137	-.200
	2.0	.145	.032	-.090	-.174	-.217	-.239	.216	.153	.056	-.056	-.153	-.216
60	0.5	.038	.010	-.017	-.045	-.074	-.106	.070	.041	.014	-.014	-.041	-.070
	1.0	.081	.024	-.035	-.097	-.166	-.222	.152	.091	.030	-.030	-.091	-.152
	1.5	.113	.035	-.055	-.154	-.216	-.256	.196	.132	.047	-.047	-.132	-.196
	2.0	.134	.039	-.080	-.183	-.217	-.240	.213	.151	.057	-.057	-.151	-.213

Table 5 (continued)

		Q_z					
λ	x/c	0	.2	.4	.6	.8	1.0
	c/s						
	0	0	0	0	0	0	0
0	0.5	.120	.166	.172	.167	.144	.119
	1.0	.224	.273	.296	.259	.247	.195
	1.5	.256	.356	.410	.385	.299	.202
	2.0	.265	.417	.500	.456	.328	.193
15	0.5	.127	.136	.136	.137	.132	.134
	1.0	.213	.247	.263	.257	.230	.189
	1.5	.249	.330	.372	.354	.286	.201
	2.0	.259	.393	.461	.427	.315	.194
30	0.5	.087	.084	.081	.082	.086	.089
	1.0	.176	.175	.170	.173	.178	.173
	1.5	.229	.253	.261	.263	.244	.199
	2.0	.248	.310	.346	.337	.277	.195
45	0.5	.017	.008	.005	.005	.012	.026
	1.0	.104	.046	.017	.017	.064	.144
	1.5	.190	.129	.081	.104	.177	.198
	2.0	.229	.198	.156	.192	.222	.199
60	0.5	-.068	-.074	-.078	-.077	-.072	-.061
	1.0	-.007	-.101	-.141	-.129	-.059	.071
	1.5	.137	-.031	-.156	-.102	+.092	.206
	2.0	.199	.056	-.111	-.001	.159	.207

The last five equations must be solved numerically. (42*c, f*) are independent of solidity and are easily determined. (42*d, e, g*) are of the form

$$\Gamma(x_0) = \int_0^1 R\left(\frac{x_0 - x}{c}\ \frac{c}{s}, \lambda\right) F\left(\frac{x}{c}\right) d\left(\frac{x}{c}\right) \qquad (43)$$

where Γ implies either Γ or Q and where we have converted back to the x/c system with the equation $x/c = (1 - \cos\theta)/2$.

Equation (43) may be written numerically

$$\Gamma(x_0) = \sum R\left(\frac{x_0 - x_n}{c}\ \frac{c}{s}, \lambda\right) F\left(\frac{x_n}{c}\right) \Delta\left(\frac{x}{c}\right) \qquad (44)$$

Fig. 17 will serve to illustrate the method of computation. As an example, the velocity at $x_0/c = 0.4$ may be written

$$\Gamma(0.4) = \left[R\left(0.3, \frac{c}{s}, \lambda\right) F(0.1) + R\left(0.1, \frac{c}{s}, \lambda\right) F(0.3) + R\left(-0.1\,\frac{c}{s}, \lambda\right) F(0.7) + R\left(-0.5\,\frac{c}{s}, \lambda\right) F(0.9)\right] (0.2)$$

for $\Delta\,(x/c) = 0.2$.

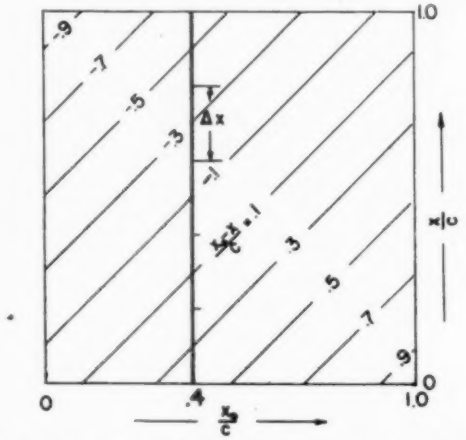

Fig. 17 Illustrating the method of obtaining the velocity functions Γ and Q

Γ may be rapidly obtained at any other x_0/c simply by cyclic permutations of the terms R and F in Equation (44) as can be seen in Fig. 17. The results are recorded in Table 5.

APPENDIX 1

Cascade Influence Functions

The cascade influence functions R and I which are responsible for converting the single airfoil equations to cascade equations may be written

$$R\left(\frac{x_0 - x}{c}, \frac{c}{s}, \lambda\right) = \frac{1}{\pi} \sum_{-\infty}^{\infty} \frac{\dfrac{x_0 - x}{s} - n \sin\lambda}{\left(\dfrac{x_0 - x}{s} - n \sin\lambda\right)^2 + n^2 \cos^2\lambda} - \frac{1}{\pi} \frac{s}{x_0 - x}$$

$$I\left(\frac{x_0 - x}{c}, \frac{c}{s}, \lambda\right) = \frac{1}{\pi} \sum_{-\infty}^{\infty} \frac{n \cos\lambda}{\left(\dfrac{x_0 - x}{s} - n \sin\lambda\right)^2 + n^2 \cos^2\lambda}$$

R and I may be combined to give a single complex number.

$$R + iI = \frac{1}{\pi} \sum_{-\infty}^{\infty} \frac{\frac{x_0 - x}{s} - n \sin \lambda + in \cos \lambda}{\left(\frac{x_0 - x}{s} - n \sin \lambda\right)^2 + n^2 \cos^2 \lambda} - \frac{1}{\pi} \frac{s}{x_0 - x}$$

$$= \frac{1}{\pi} \sum_{-\infty}^{\infty} \frac{1}{\left(\frac{x_0 - x}{s} - n \sin \lambda\right) - in \cos \lambda} - \frac{1}{\pi} \frac{s}{x_0 - x}$$

$$= \frac{1}{e^{-\Omega}} \sum_{-\infty}^{\infty} \frac{1}{\frac{\pi}{e^{-\Omega}}\left(\frac{x_0 - x}{s}\right) - in\,\pi} - \frac{1}{\pi} \frac{s}{x_0 - x}$$

Now this series is exactly the expansion for the closed form

$$R + iI = e^{\Omega} \coth\left(\pi \frac{x_0 - x}{s} e^{\Omega}\right) - \frac{1}{\pi} \frac{s}{x_0 - x}$$

The real and imaginary parts of this expression may be separated using common trigonometric identities. The result is

$$R = \frac{\cos \lambda \sinh\left[2\pi \frac{x_0 - x}{s} \cos \lambda\right] + \sin \lambda \sin\left[2\pi \frac{x_0 - x}{s} \sin \lambda\right]}{\cosh\left[2\pi \frac{x_0 - x}{s} \cos \lambda\right] - \cos\left[2\pi \frac{x_0 - x}{s} \sin \lambda\right]} - \frac{1}{\pi} \frac{s}{x_0 - x}$$

$$I = \frac{\sin \lambda \sinh\left[2\pi \frac{x_0 - x}{s} \cos \lambda\right] - \cos \lambda \sin\left[2\pi \frac{x_c - x}{s} \sin \lambda\right]}{\cosh\left[2\pi \frac{x_0 - x}{s} \cos \lambda\right] - \cos\left[2\pi \frac{x_0 - x}{s} \sin \lambda\right]}$$

which Scholz has tabulated and which is reproduced in Table 1.

APPENDIX 2

Correction for Neglecting the $\frac{d}{dx}\left[\frac{u}{V_m} y_t\right]$ Term in Equation (26)

The greatest contribution to u/V_m is found in the terms

$$2\pi A_0 \frac{c}{s} \sin \lambda \, \Gamma_{0\Sigma} \tag{45a}$$

$$2\pi A_1 \frac{c}{s} \sin \lambda \, \Gamma_{\Sigma 1} \tag{45b}$$

from Equation (10).

In Equation (17) we noted that a linear approximation to the functions in Fig. 3 may be made.

If (17) is substituted into (45*a*, *b*) and (45*a*, *b*) into $d/dx\left(\frac{u}{V_m} y_t\right)$ we have

$$(2\pi A_0 + 2\pi A_1)\xi \frac{c}{s} \frac{t}{c} \sin \lambda \frac{d}{dx}\left[\left(\frac{1}{2} - \frac{x}{c}\right) f_t\right] \tag{46}$$

where $2\pi A_0 + 2\pi A_1 = C_L$ and $y_t = \frac{t}{c} f_t$. It is further assumed that $\xi = \xi_0 = \xi_1$. Now this term is carried all the way through the analysis in the same manner as $\frac{t}{c} f_t'\left(\frac{x}{c}\right)$ in Equation (27). After performing the calculations for every c/s and λ, it was discovered that the main contribution was to increase T_0 and T_1 of Table 3 by an amount δT_0 and δT_1, respectively, in such a manner that $\delta T_0/T_0$ and $\delta T_1/T_1$ could be written

$$\frac{\delta T_0}{T_0} = 0.07 C_L \xi \frac{c}{s} \frac{t}{c} \sin \lambda \tag{47a}$$

$$\frac{\delta T_1}{T_1} = 0.30 C_L \xi \frac{c}{s} \frac{t}{c} \sin \lambda \tag{47b}$$

If (47) is put into the Equations (40) we find that

$$\frac{\delta C_L}{C_L} = 2\pi\xi \frac{c}{s} \frac{t}{c} \sin \lambda \left[0.07 \frac{T_0}{g_{00}}\left(\frac{1 - g_{00}}{g_{11}} - 1\right) + 0.30 \frac{T_1}{g_{11}}\right] \tag{48}$$

which with Table 3 shows that the effect of including $\frac{d}{dx}\left[\frac{u}{V_m} y_t\right]$ in Equation (26) is indeed small for airfoils in the order of $t/c = 0.1$ or less.

References

1 A. D. S. Carter, "The Low Speed Performance of Related Airfoils in Cascades," ARC Current Paper No. 29, 1950.

2 H. Schlichting, "Problems and Results of Investigations on Cascade Flow," *Journal of the Aeronautical Sciences*, vol. 21, no. 3, 1954, pp. 163–178.

3 H. Schlichting, "Berechnung der reibungslosen inkompressiblen Strömung für ein vorgegebenes ebenes Schaufelgitter," VDI Forschungsheft 447, 1955.

4 J. R. Garrick, "On the Plane Potential Flow Past a Lattice of Arbitrary Airfoils," NACA T.R. 788, 1944.

5 W. Traupel, "Die Berechnung der Potentialströmung durch Schaufelgitter," *Sulzer Techn. Rdsch.*, 1945, Nr. 1, s. 25/42.

6 I H. Abbot, A. E. von Doenhoff, and L. S. Stivers, "Summary of Airfoil Data," NACA Report Number 824, 1945.

7 F. Weinig, "Die Strömung um die Schaufeln von Turbomaschinen," J. A. Barth, 1935.

8 G. F. Wislicenus, "Fluid Mechanics of Turbomachinery," McGraw-Hill Book Company, Inc., New York, N. Y., 1947.

9 A. M. Kuethe and J. P. Schetzer, "Foundations of Aerodynamics," John Wiley & Sons, Inc., New York, N. Y., Chapman and Hall, Limited, London, England, 1950.

10 E. Pistolesi, "Sul calcolo di schiere infinite di ali sottili," *L'Aerotechnica*, vol. 17, 1937, pp. 484–506.

11 N. Scholz, "Ein Berechnungsverfahren zum Entwurf von Schaufelgitterprofilen," VDI Forschungsheft 442, 1954.

12 L. J. Herrig, J. C. Emery, and J. R. Erwin, "Systematic Two-Dimensional Cascade Tests of NACA 65-Series Compressor Blades at Low Speeds," NACA RM L51G31, 1951.

13 L. M. Milne-Thomson, "Theoretical Aerodynamics," D. Van Nostrand Company, Inc., New York, N. Y., 1952.

14 S. J. Andrews, "Tests Related to the Effect of Profile Shape and Camber-Line on Compressor Cascade Performance," ARC R. and M. No. 2743, 1955.

DISCUSSION[7]

N. K. H. Scholz[8]

The author's cascade analysis represents, in the writer's opinion,

[7] Also, discussion of G. L. Mellor, "An Analysis of Axial Compressor Cascade Aerodynamics, Part 2—Comparison of Potential Flow Results With Experimental Data," published in this issue, pp. 379–386.

[8] Aerodynamics Specialist, MAN-Turbomotoren GmbH, Munich, Germany.

an excellent contribution to the aerodynamical theory of cascades. He consequently extends the well-established, thin, single-airfoil theory established by H. Glauert to airfoils in cascades. The computational methods of N. Scholz (direct problem) and H. Schlichting (indirect problem) (author's [11] and [3]) are based on the same background. The remarkable improvement for the direct problem against Schlichting's method would seem to be that the kinematic flow condition at the profile contour is now satisfied in integral form so that the entire profile shape enters into the equation. In this connection the attention of the reader is drawn to the fact that, according to Schlichting, this flow condition can only be satisfied for three profile co-ordinates, each selected at random of the camber line and the base profile. However, there seems to be scarcely any improvement as regards time consumption against Schlichting's method, in so far as possible cascade and profile geometry is concerned. The time requirement of 20 hr indicated in Schlichting's paper refers to a cascade profile with six different inflow angles; that is, to the computation of six different pressure distributions.

As also is mentioned by the author, equation (10) gives infinite velocities for the velocity distribution for $A_0 \neq 0$ on the profile shape. In the actual flow, however, the height of the suction peak depends largely on the shape of the profile nose and the latter in turn is decisive for the separation characteristic of the cascade. On the basis of the single-airfoil theory of F. Riegels, however, the suction peak can be computed by multiplying the velocity of equation (10) with the factor $1/[1 + (dy_t/dx)^2]^{1/2}$ (see author's reference [3]). This is absolutely necessary for a boundary-layer analysis.[9] Against that, the factor $1 + (dy_c/dx)^2$ indicated in the footnote to equation (10) is not intelligible.

Appendix 2 shows that the neglect of term $d(uy_t/V_\infty)/dx$ in equation (26) is negligibly small for $t/c < 0.1$. Although the writer does not wish to doubt this, the author's proof is incorrect since equation (26) already neglects $u \neq f(y)$, which is actually not true. In the author's reference [11] the writer has shown how this point can be treated more correctly by developing $u(y)$ into a Taylor series.

The author's statements on the application of the parameters c_L and α_∞, and ϕ and ψ, respectively, agree widely with the opinion expressed by the writer.[9, 10] The only difference is that the writer suggests the value $\Delta V_\theta/V_e = \psi\phi$ instead of the variable ψ. It is noticeable that the simple relation can be proved

$$\psi = A\phi + B$$

with A and B as constants, which depend only on the cascade geometry. Similar suggestions also are contained in a paper by W. Albring.[11]

To this meritorious effort to predetermine the separation characteristic of a cascade, the writer wishes to add: Attempts made hitherto to determine the optimum loading of the cascade (A. R. Howell [16] of Part II, O. Zweifel,[12] and K. Wichert[13]) contain only c_L, s/c, and β_∞ as parameters, and no indication as to the influence of the angle of incidence α_∞ and the profile camber Cb. A decisive improvement of the present analysis lies in the addition of the two latter parameters, the influence of which on the separation is doubtless very important. In spite of this, the reliability of all these tests must not be overestimated. The occurrence of separation is a very complex problem, a satisfactory solution to which can only be obtained by a boundary-layer analysis. Recently a material contribution to this has been given by L. Speidel and N. Scholz.[9]

Author's Closure

The author wishes to thank Dr. Scholz for his penetrating observations. In particular, his mention of F. Riegels' thickness correction provides a simple way to account for the thickness singularity at the leading edge. For example, the correction $1/[1 + (dy_t/dx)^2]^{1/2}$ which approaches zero at the leading edge when combined with $\Gamma_\infty = (1 + \cos\theta)/2\pi \sin\theta$ [see Fig. 2(*a*)] which approaches infinity at the leading edge yields the finite value $(\Gamma_\infty)_{corr.} = 1/\pi \sqrt{2R/c}$ at the leading edge. Here R is the leading edge radius. For the 65-series blade this gives the value 2.74 which is close to the value 2.97 from reference [6].

The author agrees with all of Dr. Scholz's other comments except that concerning computational time requirements and this is important. The fact is that compared to Schlicting's method (and apparently all other previous methods) the time improvement is tremendous. The time of 40 hours refers in this paper to the entire calculation. And this represents all possible cascade solutions with only the restriction of low camber and thickness (but high enough to include all compressor airfoils of interest) and airfoils with symmetrical camber distributions (which are currently in use probably 90 per cent or more of the time). Actually, then, in so far as most current design is concerned there is no need to talk further of computational time requirements since the job is done once and forever.

[9] L. Speidel and N. Scholz, "Untersuchungen über die Strömungsverluste in ebenen Schaufelgittern," *VDI-Forschungsheft*, 464, 1957.

[10] N. Scholz, "Über die Durchführung systematischer Messungen an ebenen Schaufelgittern," *Zeitschrift für Flugwissenschaften*, vol. 4, 1956, pp. 313–333.

[11] W. Albring, "Das Eulerdiagramm zur Auslegung von axialen Schaufelrädern," *Wissenschaftliche Zeitschrift der Technischen Hochschule*, Dresden, vol. 7, 1957–1958, pp. 67–78.

[12] O. Zweifel, "Die Frage der optimalen Schaufelteilung bei Beschaufelungen von Turbomaschinen, insbesondere bei grosser Umlenkung in den Schaufelreihen," *BBC-Mitteilungen*, vol. 32, 1945, pp. 436–444.

[13] K. Wichert, "Beitrag zur optimalen Schaufelbelastung in axial durchströmten Turbomaschinen," *Zeitschrift Maschinenmarkt*, vol. 62, 1956, pp. 11–15.

PART II

An Analysis of Axial Compressor Cascade Aerodynamics[1]

The theoretical potential flow results of Part I are compared with the large number of NACA 65-series compressor blade data. It is found that a single empirical constant used to modify the theory permits reasonable predictions of turning or lift coefficient to be made for any cascade geometry in the unstalled regions of flow. Furthermore, it is demonstrated that the theory allows a considerable number of plus and minus stalling angle of attack data to be collapsed to a single empirical curve. Conversely such a curve, once established, allows stalling predictions to be made for any cascade geometry. One interesting point on this curve is the loading limit above which the cascade is always stalled.

Comparison of Potential Flow Results With Experimental Data

G. L. MELLOR

Assistant Professor of Mechanical Engineering, Princeton University, Princeton, N. J.

Introduction

In the past, potential flow solutions have been an extremely useful tool in conjunction with experimental investigations and the design application of single airfoils or wings. The need for such solutions for cascades has actually been greater in view of the fact that there are more variables involved. To test enough geometrical configurations to explore all areas of possible benefit to designers is a task of gigantic proportions.

The author has briefly indicated in the introduction to Part I the great computational difficulties of obtaining cascade solutions. It is his claim that these difficulties have largely been surmounted in the subsequent development of Part I. The effort here is, first, to demonstrate the usefulness of the theory and, second, to produce design information beyond that given explicitly by the data.

The only data available, which cover the geometric variables to any great extent, are the 10 per cent thick 65-series compressor blade data presented in NACA Research Memorandum L 51G31 by Herrig, Emery, and Erwin [12].[2] A full description of these airfoil shapes is given in reference [12]. The attempt is made to predict the lift coefficient data and also bring together the large number of stall data to form a single empirical statement of when a cascade stalls.

In this paper the turning data of reference [12] will be converted to the lift coefficient form,

$$(C_L)_{id} = \frac{L_{id}/c}{\frac{\rho}{2} V_m^2} = 2 \frac{s}{c} \frac{\Delta V_\theta}{V_m} \tag{5}$$

described in Part I. It is probably best to think of $(C_L)_{id}$ in terms of the right-hand term since $\Delta V_\theta / V_m$ is exactly related to the actual air geometry where $\Delta V_\theta = V_{\theta 1} - V_{\theta 2}$. $V_{\theta 1}$ is the upstream tangential velocity component and $V_{\theta 2}$ is the mixed-out, downstream tangential velocity component.

As in Part I, we will henceforth drop the subscript id, since we will only refer to the ideal lift coefficient and never to the actual lift coefficient.

For the most part, the theory-data comparisons will be plotted as C_L versus sin α_m curves for constant inlet angle β_1. Because of the construction of the NACA cascade test apparatus (see reference [15]) the inlet air angle was held fixed for a given blade camber and solidity while the angle of attack was varied by changing the stagger angle λ. Later we will present constant λ-information which is more suitable for the compressor design process.

[1] The work on which this paper is based was done at the Gas Turbine Laboratory, Massachusetts Institute of Technology, Cambridge, Mass., under the joint sponsorship of Allison Division of the General Motors Corporation, Curtiss-Wright Corporation, General Electric Company, Office of Naval Research, and Westinghouse Electric Company. The author wishes to thank Prof. E. S. Taylor and Mr. Kurt Schneider for their encouragement and assistance.

Contributed by the Hydraulic Division and presented at the Annual Meeting, New York, N. Y., November 30–December 5, 1958, of The American Society of Mechanical Engineers.

Note: Statements and opinions advanced in papers are to be understood as individual expressions of their authors and not those of the Society. Manuscript received at ASME Headquarters, August 8, 1958. Paper No. 58—A-84.

[2] Numbers in brackets refer to the References at the end of either Part I or Part II.

Nomenclature

(In addition to those given in Part I)

I. L. F. = Impulse Loading Factor
S. L. F. = Smooth Loading Factor
ϕ = cascade "flow coefficient"
Φ = stage flow coefficient
ψ = cascade "work coefficient"
Ψ = stage work coefficient
η = cascade and stage efficiency
s = cascade characteristic slope
$\Delta\phi$ = range
ψ^*, ϕ^* = nominal value of ψ and ϕ, located midway between plus and minus stall

Analysis

An Empirical Camber Correction Term. In Fig. 18 a sample velocity distribution and lift coefficient from reference [12] is compared with the potential flow solution computed according to Equation (10). To force agreement between theory and data the following steps were taken:

(a) Correct the theoretical camber term Cb used in the computation of A_0, A_1, and C_L in Equations (11a, b) and (13) of Part I by the value

$$\text{Cb}_{\text{effective}} = 0.725\ \text{Cb}_{\text{theoretical}} \qquad (49)^3$$

(b) Set the $\Gamma_{0\Sigma}$ normalized velocity distribution of Equation (10) and Fig. 2(c) equal to zero. As indicated in Fig. 2(c) this function integrates to zero and therefore has no direct bearing on the lift coefficient. We are here simply eliminating the abrupt velocity changes at the leading and trailing edges.

The result of performing these steps is shown in Fig. 18 where fairly good agreement is shown for both corrected lift coefficent and corrected velocity distribution. It is perhaps propitious to point out here that the camber correction agrees not only with the lift coefficient data of reference [12], but also with isolated airfoil data as discussed in pages 30–31 of reference [6]. All of these data will be presented and discussed in more detail below.

The slope of the 65-series camber line (or $a = 1.0$ mean line) theoretically approaches infinity at the leading and trailing edges and therefore the blade edges contribute greatly to the Cb as defined by the integral $2\int_0^\pi (dy_c/dx)\cos\theta\, d\theta$ [Equation (2a) of Part I]. One could therefore achieve the same result in step (a) by reducing the camber-line slopes at the blade's extremities in such a way that the slopes are maintained constant from approximately $x/c = 0.05$ and 0.95 out to 0 and 1.00, respectively. Step (b) would then more or less follow automatically through Equation (42c) of Part I since $\Gamma_{0\Sigma}$ is composed of the higher harmonics whose coefficients would be small if it were not for the high blade extremity slopes.

At the moment the author has no clear-cut explanation of the camber correction given in Equation (49). Discussion on this point can be focused on the case of a single airfoil at zero angle of attack. Since, from reference [6], the correction is apparently independent of thickness, one can further restrict attention to the infinitely thin airfoil. In this case, one can rule out the possibility that the correction is due to assumptions made in the theory. Since the correction can be rationalized by mathematically reducing the camber slope effectiveness in the small region, 0.05 c, at the chord extremities either local separation or just local boundary layer thickening might be the proper physical rationalization. This explanation provides little comfort when discussing events at the leading edge however.

[3] Equations are numbered continuously from Part I.

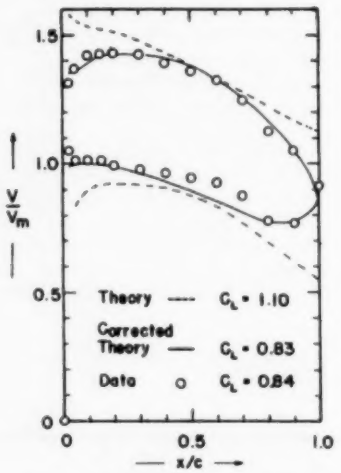

Fig. 18 Comparison of velocity distribution and lift coefficient of data, theory, and corrected theory. Data are for the 65-(12) 10, $c/s = 1.0$, $\beta_1 = 45°$, $\alpha_1 = 12.1°$ ($\lambda = 32.9$, $\sin\alpha_m = 0.060$) cascade geometry. Local velocities are determined from pressure measurements and Bernoulli's equation.

Determination of Stall Loading Factors. In Fig. 19 a typical plot of C_L and C_D versus $\sin\alpha_m$ ($\cong\alpha_m$) is shown. One point on this plot corresponds to the data given in Fig. 18.

In the future we will not consider the whole C_D variation, but will instead define an approximate middle range drag coefficient $C_D{}^*$ and also define as stall points those values of α_m where C_D exceeds $C_D{}^*$ by the value 0.01. This definition is simply an analytical convenience. Whether $(C_D)_{\text{stall}}$ is defined as $C_D{}^* + 0.01$ or as $2\,C_D{}^*$ as Howell [16] did, the stall values of α_m will be nearly the same since the slope of C_D versus α_m is very high in the stalling region.

The two stall points will individually be termed the plus and minus stall points; the minus stall point referring to the lowest stall in α_m regardless of whether it is actually a plus or minus numerical value.

In this section the effort is made to determine some pertinent loading factors which will correlate the plus and minus stall data of reference [12].

Now, the point where the blade stalls or separates must be some function of the blade pressure distribution or velocity distribution. As seen in Equation (10) and in Figs. 2, 3, and 4, the main contribution to this velocity distribution for a symmetrically cambered airfoil is given by the terms

$$\pm 2\pi A_0 \cdot \Gamma_{00}; \quad \pm 2\pi A_1 \cdot \Gamma_{01}$$

and

$$(2\pi A_0 + 2\pi A_1)\,\frac{c}{s}\sin\lambda \cdot \Gamma_\Sigma$$

where we have incorporated the approximation of (14) for both $\Gamma_{\Sigma 0}$ and $\Gamma_{\Sigma 1}$, namely that,

$$\Gamma_{\Sigma 0} \cong \Gamma_{\Sigma 1} \cong \frac{\xi}{2}\left(\frac{1}{2} - \frac{x}{c}\right) \equiv \Gamma_\Sigma \qquad (14)$$

We have also excluded consideration of the $t/c \cdot Q_0$ function since it is constant in the present discussion where we are considering airfoils of a given profile thickness and $\frac{t}{c}\,\frac{c}{s}\,Q_\Sigma$ because it

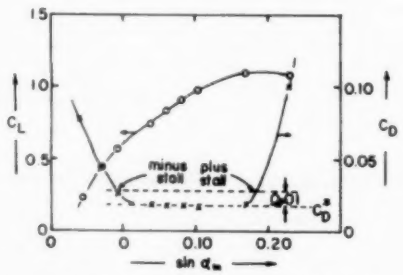

Fig. 19 Illustration of the middle range drag $C_D{}^*$ and the plus and minus stall definition

is a small effect as seen in Fig. 4(*b*). The term $\pm$Cb Γ_{02} represents the details of the camber shape and integrates to zero. It, of course, leads to the squared-off velocity distributions which, as we have seen, are not actually present in a real flow. It has therefore been excluded in the present discussion.

First, we will call the term Γ_{00} [see Fig. 2(*a*)] the impulse loading function and its multiplier $2\pi A_0$, the Impulse Loading Factor. Therefore,

$$\text{I. L. F.} = \text{Impulse Loading Factor} = 2\pi A_0 \qquad (50)$$

Thick airfoils do not have the infinite velocity at the leading edge given by $\Gamma_{00} = (1 + \cos\theta)/2\pi \sin\theta$. However, the velocities are indeed large and we simply say that the Impulse Loading Factor represents a nose loading which is more or less sharp depending primarily on the nose radius and to a lesser extent on the entire thickness distribution. When $A_0 = 0$ we have what is essentially a smoothly entering flow with the stagnation point at $x/c = 0$.

Secondly, we can build up the remaining part of the velocity distribution as illustrated in Fig. 20 which is essentially a smooth or slow velocity (or pressure) change. It is seen that the localities of deceleration near the blade suction (convex) trailing edge and near the blade pressure (concave) leading edge due to the smooth lift term $2\pi\ A_1\ \Gamma_{01}$ [see Fig. 2(*b*)] are simultaneously aggravated by the over-all deceleration term given by $2\pi\ (A_0 + A_1)\xi(c/s)$ sin $\lambda(1/2)(1/2 - x/c)$ which is, of course, inherently associated with a diffusing cascade. It therefore should be possible to form an approximate smooth loading term as follows:

$$\text{S. L. F.} = \text{Smooth Loading Factor} = 2\pi A_1 + K2\pi(A_0 + A_1)\xi(c/s) \sin\lambda \qquad (51)$$

where we have assumed that the blade's tendency to stall due to a smooth velocity or pressure changes is made up of a linear combination of the lift term and the over-all deceleration term. The constant K may be considered a weighting factor accounting for the relative ability of the two terms Γ_{01} and $1/2(1/2 - x/c)$ to contribute to airfoil stall. If we say that the important quantity is the decrease in velocity between the mid-chord position and the trailing edge on the suction surface of the airfoil we would find that

$$K = \frac{1/4}{\Gamma_{01}(x/c = 1/2) - \Gamma_{01}(x/c = 1)} = 0.78 \qquad (52)$$

The exact same value of K is obtained between the leading edge and the mid-chord position on the pressure surface. This value of K can only be considered a rough estimate since Γ_{01} gives a locally sharper slope than $1/2(1/2 - x/c)$ and should therefore be more heavily weighted than is indicated by the value of 0.78. We will in fact allow K to be determined empirically, expecting, however, that the empirically determined value should not differ greatly from 0.78.

Theory—Data Correlation and Comparison. What we do now is simply ask the data for the *functional relationship* between the Impulse Loading Factor $2\pi A_0$ and the Smooth Loading Factor $2\pi A_1 + K2\pi(A_0 + A_1)\xi(c/s)$ sin λ to give stall. The results are plotted in Fig. 21. K was determined by trial and error as equal

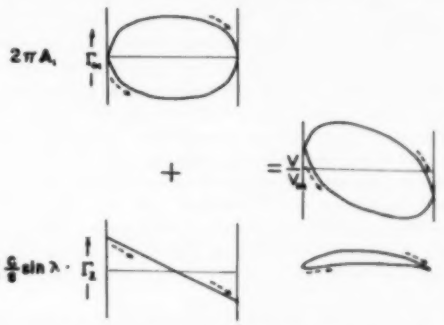

Fig. 20 Illustration of the smooth velocity distribution composed of a part due to lift and a part due to cascade flow deceleration. The dashed arrows mark the two regions of strong local deceleration.

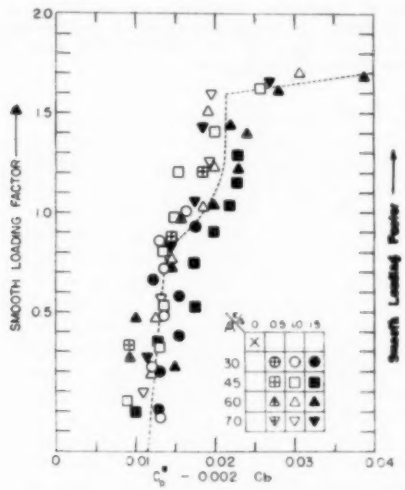

Fig. 21(*a*) C_D^* versus the smooth loading factor. C_D^* has previously been corrected by 0.002 Cb which presumably is necessitated by the sharp trailing edge slope of the 65-series (a = 1.0 mean line) airfoil. Note: The value given by the turbulent flat plate equation $C_D = 0.144\ R_N^{-1/5}$ at the test Reynold's Number of 245,000 is 0.012.

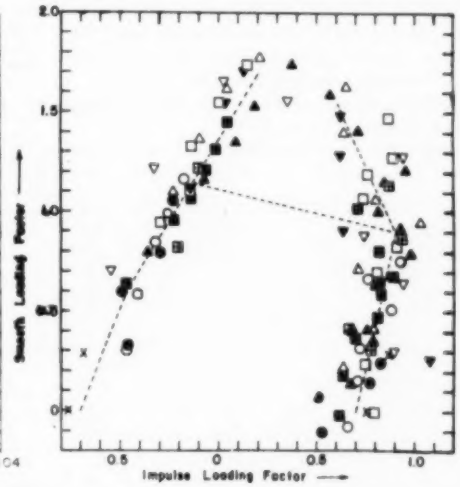

Fig. 21(*b*) The locus of plus and minus stall (or where $C_D = C_D^* + 0.01$) as a function of the Smooth Loading Factor and the Impulse Loading Factor. The dotted line running between the plus and minus stall line is the limit loading line as described in Fig. 22.

to 0.55. In other words, for trials using $K = 0.50$ or 0.60 it was apparent that the points began to drift away from the mean value line and continued to do so the more K departed from 0.55.

In Fig. 21(*a*) the middle range drag C_D^* midway between plus and minus stall is plotted against the S. L. F. Here C_D^* has been empirically corrected by the value 0.002 Cb which in effect acknowledges the fact that that part of the velocity distribution Cb Γ_{0Z} which theoretically results in abrupt velocity changes at the blade's extremities does, by virtue of the flow's propensity to separate locally and thereby eliminate this condition, contribute directly to C_D^*. The remaining and much larger variation of C_D^* (at the mid-range value of I. L. F.) is seen to be a function of the S. L. F.

In Fig. 21(*b*), the locus of stall, or where $C_D = C_D^* + 0.01$, is plotted as a function of the S. L. F. and the I. L. F. Conversely the dashed line gives the functional relationship between the I. L. F. and the S. L. F. for both plus and minus stall.

It is helpful to note that for an isolated airfoil ($c/s = 0$) I. L. F. $= 2\pi A_0 = 2\pi \sin \alpha_m$ and S. L. F. $= 2\pi A_1 =$ Cb. Thus since $C_L = 2\pi A_0 + 2\pi A_1$, the I. L. F. and the S. L. F. become equal to the components of the lift coefficient due to angle of attack and camber, respectively. The single airfoil data used in Fig. 21 were the NACA 65-009 (page 205 of reference [6]) and the NACA 65-410 (page 209) airfoils. It was assumed that the difference between a 9 and 10 per cent thick airfoil is negligible. Also the cases used were those with roughened leading edges. The roughened leading edge insures early boundary layer transition where otherwise the blade would be largely laminar when tested in the Langley, low-turbulence wind tunnel. It is presumed that the cascade tunnel of reference [12] had reasonably high, free-stream turbulence, since the resulting drag data do not exhibit the characteristic "laminar bucket" of an airfoil with a large laminar boundary layer as observed in the single airfoil data of reference [6].

In Fig. 22 the dashed stall line has been computed for each individual cascade geometry and compared again with the stall data on an individual basis. Also in Fig. 22 a full comparison is finally made between the lift coefficient theory and data. The dashed line running between the plus and minus stall lines is defined as the line of limit loading above which

(*a*) the lift coefficient does not increase with an increase in Cb at the rate predicted by theory. In fact, a maximum lift coefficient is encountered a little bit above the limit loading line.

(*b*) the drag begins to increase rapidly. (The peculiar shape of the C_D^* curve will be discussed later.)

(*c*) the range between plus and minus stall begins to decrease markedly.

Although there are some discrepancies in general, the theory checks quite well with the data. The discrepancies that do exist can, by direct observation or by a mental crossplot, be seen to be completely random. The fact that all of the C_L data at $c/s = 0.5$ are lower than the predicted values is disturbing. However, by crossplotting the data against c/s, the reader can verify the fact that these particular data must be defective. In reference [12] it is stated that a smaller set of blades ($c = 2.5$ in.) was used for the $c/s = 0.5$ case than was used in $c/s = 1.0$ and $c/s = 1.5$ case ($c = 5.0$ in.) which leads one to think that the defect might be in the actual blade construction. Of course, in the isolated airfoil case, $c/s = 0$, the airfoils tested were much larger ($c = 2$ ft) and fairly accurate airfoil construction and data collection could be accomplished.

In general, it may be happily concluded that the corrected theory can provide a useful analytical tool and, in fact, provides information which in certain spots is better than the data. Furthermore, as seen in Fig. 22, it allows for a clear-cut specification of stall for every geometry. This could never be achieved by

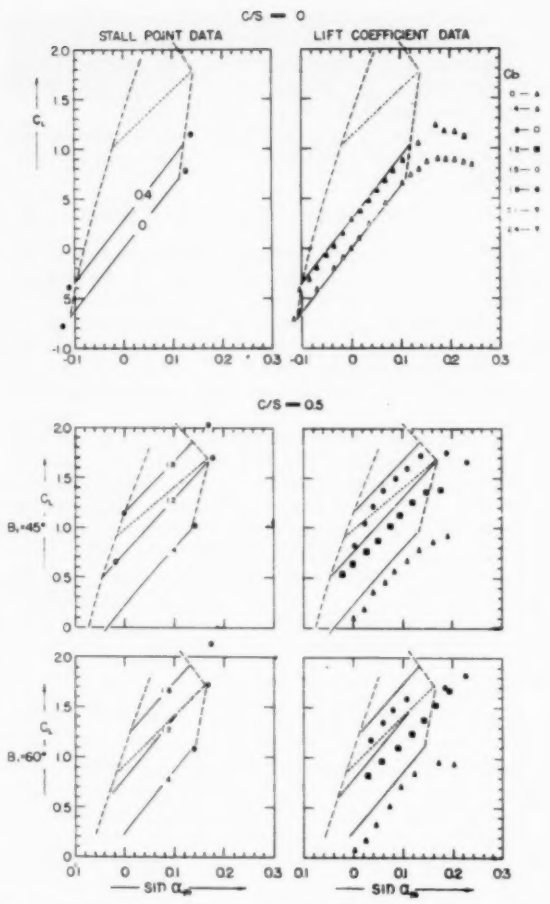

Fig. 22 Comparison of experimental and theoretical lift coefficient and stall points. At the limit loading line, running between the plus and minus stall lines, the lift coefficient data begin to fall below the theoretically predicted values.

directly crossplotting and interpolating the data. Some years back, the author tried this with discouraging results.

Some explanation is necessary with regard to the apparently peculiar shape of Fig. 21(*a*) where the C_D^* values begin to rise perceptibly near the loading limit and then flat off until C_D^* suddenly increases in quite a dramatic way. In a sense, this somewhat distorts the true picture since the S. L. F. is computed from theory [and Equation (49)] and, as can be seen in Fig. 22, above the limit loading line the lift coefficient does not actually increase with increases in Cb as predicted by the theory. Therefore, if one were to construct a loading factor which was more closely related to the actual velocity or pressure distribution on the airfoil, the flattened region just before the sudden C_D^* increase would not appear.

Before leaving this subject, it would be well to point out that if we take the loading factor values at the mid-range limit loading point in Fig. 21(*b*), namely, I. L. F. = 0.43 and S. L. F. = 1.10, and combine them, we obtain

$$C_L + 0.55\,\xi \frac{\sin \lambda}{\sin \beta_m} C_p = 1.53 \tag{53}$$

since $C_L = 2\pi A_0 + 2\pi A_1$ and $C_p = c/s \sin \beta C_L$ where the over-

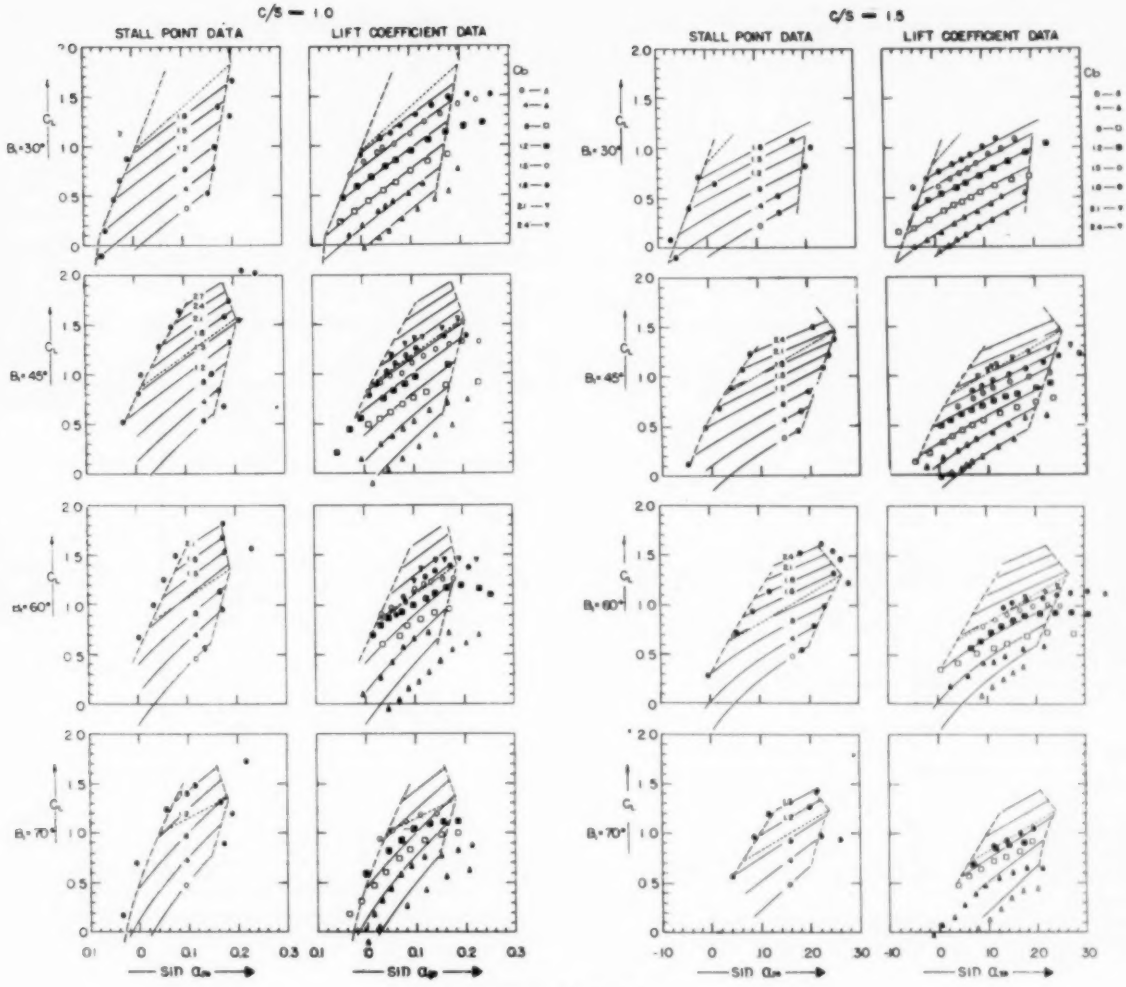

Fig. 22 *(continued)*

all pressure coefficient $C_p = (V_1^2 - V_2^2)/V_m^2$ as described in Part I. With ξ (sin λ)/sin β_m set equal to 1.00, this form conforms to the limit loading parameter proposed by Wislicenus [8] where the value given here as 0.55 was stipulated by him to lie between the limits 0.50 and 1.00 and the value given here as 1.53 was stipulated to lie between the limits 1.00 and 1.70.

Other Airfoil Shapes. C_L versus sin α_m curves may be drawn for any blade from the solutions of Part I, if the camber line is symmetrical, or from further numerical calculations using the theory of Part I if nonsymmetrical. However, it is necessary to know the camber correction value which from our experience here may be determined from isolated airfoil experiments. Thus from reference [6] one can see, for instance, that for the NACA four digit series, $Cb_{eff.} = 0.92\ Cb_{theor.}$. It is also shown that the corrections are very nearly independent of profile thickness. From the single piece of circular arc datum shown in Fig. 8 of Part I it may be deduced that no correction is necessary, i.e., $Cb_{eff.} = 1.00\ Cb_{theor.}$. This is reasonable when one considers our hypothesis explaining the necessity of such a correction, since the circular arc camber does not produce theoretical velocity discontinuities at the blade's extremities.

It is not expected that the stall curve of Fig. 21 will be accurate for any blade whose basic camber line and actual thickness distribution differ appreciably from the 65-series 10 per cent thickness blade family. Of course, if it is assumed that the constant $K = 0.55$ is reasonably universal, then the stall curve may be established for a given blade family from data at any value of c/s or λ or in particular from isolated airfoil data. The low camber isolated airfoil data of reference [6] will at least establish the stall curve for low values of S. L. F. where the effect on operating range of such variables as blade thickness, for example, may immediately be evaluated.

From the present results, it would appear that increased attention should be given to high, as well as low, camber single airfoil experiments. Such experiments transcribed to any cascade geometry would, of course, require only a very small fraction of the cost of the wide range of cascade experiments necessary to obtain the equivalent, completely empirical information.

Design Information. In Fig. 23 C_L versus sin α_m curves are worked out as functions of Cb, c/s, and constant stagger angle λ, which is the form directly applicable to the compressor design process. It should be recalled that the theoretical predictions above the loading limit are bad, but they have nevertheless been drawn in up to the point where C_D^* increases drastically [see Fig.

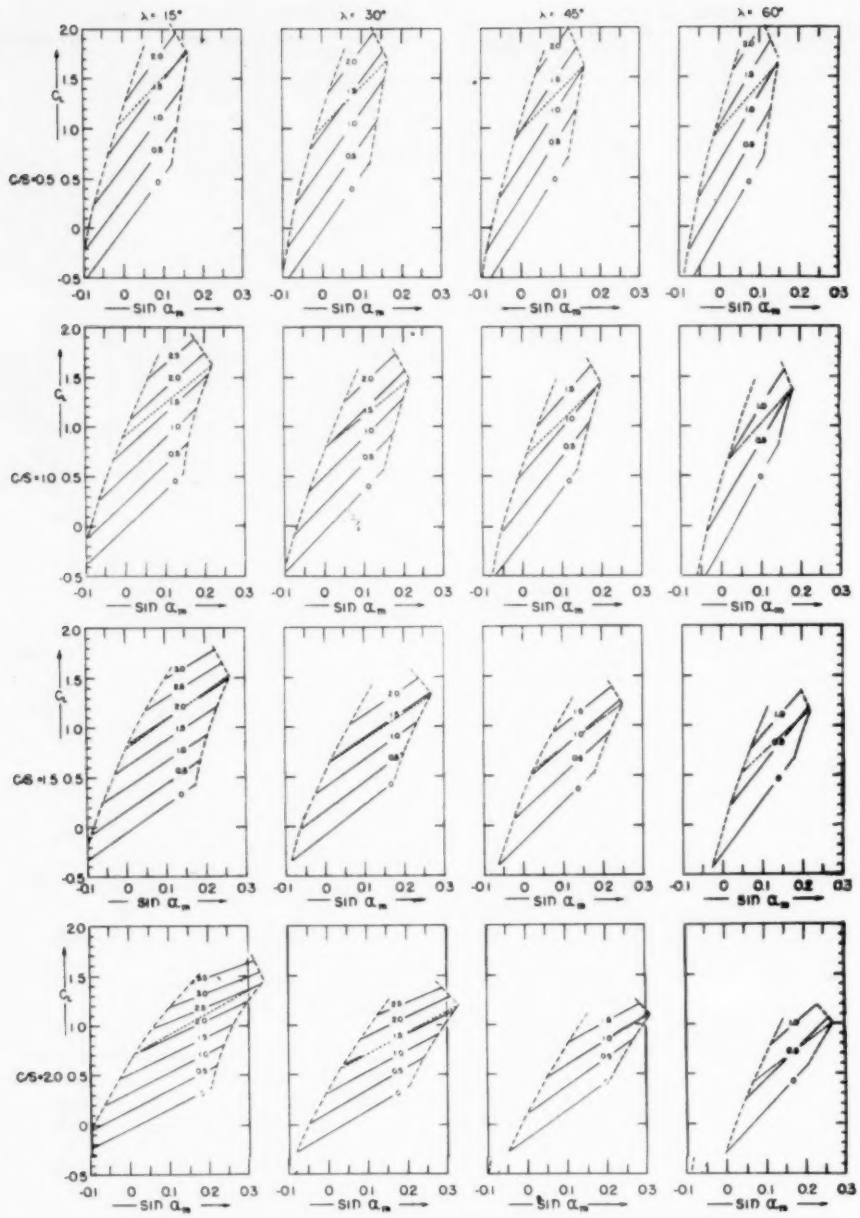

Fig. 23 Theoretically predicted cascade performance for constant stagger angle λ

21(*a*)]. It is expected, however, that the loading limit will also correspond to the limit of design.

While the airfoil parameters are most useful for the initial collection of cascade information, they are not too convenient for direct application to the design problem. The author has found the variables ϕ, ψ, η defined according to the relation

$$\phi = \frac{V_z}{V_{\theta_m}} = \cot \beta_m = \cot (\lambda + \alpha_m) \tag{54}$$

$$\psi = \frac{\Delta V_\theta}{V_{\theta_m}} = \frac{c/sC_L}{2 \sin \beta_m} \tag{55}$$

$$\eta = \frac{(\Delta p)_{\text{actual}}}{(\Delta p)_{\text{ideal}}} = 1 - \frac{C_D}{C_L} \frac{1}{\sin \beta_m \cos \beta_m} \tag{56}$$

to be a most useful choice of cascade parameter to insert directly into a machine design system. The relations just given may be easily derived by recourse to Fig. 1 and Equations (4*b*) and (5) of Part I.

If we examine the symmetrical stage diagram in Fig. 24 we see that $\vec{W}_1 - \vec{W}_2 = \vec{V}_1 - \vec{V}_2 = \vec{\Delta} V_\theta$ and $\vec{V}_1 - \vec{W}_1 = \vec{V}_2 - \vec{W}_2 = \vec{U}$. Furthermore, for a *symmetrical* stage it is seen that $V_{\theta_m} = -W_{\theta_m}$

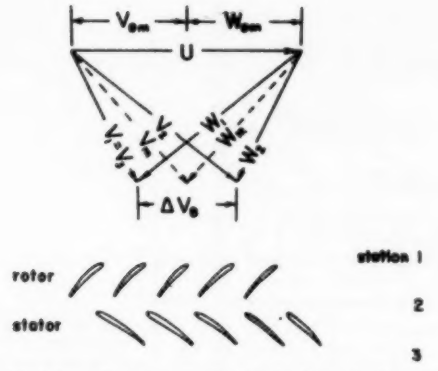

Fig. 24 Symmetrical stage diagram. *V* refers to absolute velocities, *W* to velocities relative to the rotor whose velocity is *U*.

$= U/2$. Now from the definition of the stage work coefficient

$$\Psi = \frac{U\Delta V_\theta}{U^2} = \frac{\Delta V_\theta}{U}$$

and the stage flow coefficient

$$\Phi = \frac{V_a}{U}$$

it can be seen that

$$\Psi_{\text{sym. stage}} = \frac{1}{2}\,\psi \tag{57a}$$

$$\Phi_{\text{sym. stage}} = \frac{1}{2}\,\phi \tag{57b}$$

For symmetrical stages the stage efficiency is identically equal to η as just defined.

In other words, the cascade variables ϕ, ψ, and η bear a direct relationship to the actual stage characteristics. They are, in part, the values which must be optimized in a good compressor design.

For nonsymmetrical repeating stages, Ψ and Φ must be related to an average of the rotor and stator ψ and ϕ, and value according to the relations,

$$\Psi = \frac{\psi_s\psi_r}{\psi_s + \psi_r} \tag{58a}$$

$$\Phi = \frac{\phi_s\phi_r}{\phi_s + \phi_r} \tag{58b}$$

$$\eta = \eta_s\left(\frac{V_{\theta m}}{U}\right) + \eta_r\left(\frac{W_{\theta m}}{U}\right) \tag{58c}$$

where the subscripts, s and r, refer to stator and rotor, respectively. The derivation of Equations (58*a*, *b*, *c*) may be easily derived by the interested reader.

Nominal values of ψ^*, ϕ^*, and η^* are herewith defined (corresponding to nominal values of $C_L{}^*$, $\alpha_m{}^*$, and $C_D{}^*$) as the point midway between plus and minus stall. No particular qualities are ascribed to the nominal values, and it is not necessarily true that the nominal values pertain to a compressor design point. They are simply a convenient point of reference.

The next important quantity to obtain is the range $\Delta\phi = \phi_{-\text{stall}} - \phi_{+\text{stall}}$ corresponding to $\Delta\alpha_m = (\alpha_m)_{+\text{stall}} - (\alpha_m)_{-\text{stall}}$. This can be written,

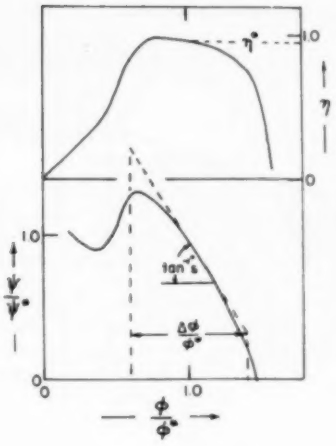

Fig. 25 Stage characteristic illustrating the variables ψ^*, ϕ^*, the operating range $\Delta\phi/\phi^*$ and η^*

$$\Delta\phi = \cot\left(\beta_m{}^* - \frac{\Delta\alpha}{2}\right) - \cot\left(\beta_m{}^* + \frac{\Delta\alpha}{2}\right)$$

Now, by expanding the cotangent according to trigonometric identities and since $\Delta\alpha/2$ is small we can set

$$\sin\frac{\Delta\alpha_m}{2} \cong \frac{\Delta\alpha_m}{2} \quad \text{and} \quad \cos\frac{\Delta\alpha_m}{2} \cong 1 - \frac{1}{2}\left(\frac{\Delta\alpha_m}{2}\right)^2$$

The previous equation then simplifies considerably after rearranging terms to

$$\Delta\phi = \frac{\Delta\alpha}{\sin^2\beta_m{}^* - \left(\frac{\Delta\alpha}{2}\right)^2} \tag{59}$$

If we recall that $\phi = V_a/V_{\theta m}$ bears a close relationship to the machine flow coefficient, we can consider $\Delta\phi$ as the change in flow between positive and negative stall. However, it is not the absolute range in mass flow that is significant for any machine. A percentage range such as $\Delta\phi/\phi^*$ is the only sensible number to ascribe to a stage before actual machine dimensions are specified. Therefore,

$$\frac{\Delta\phi}{\phi^*} = \frac{\Delta\alpha}{\cos\beta_m{}^*\sin\beta_m{}^* - \cot\beta_m{}^*\left(\frac{\Delta\alpha}{2}\right)^2} \tag{60}$$

obtained from Equations (54) and (59) will, in the future, be used to denote the *range*.

It is convenient to define a slope s which is

$$-s = \frac{d\psi/\psi^*}{d\phi/\phi^*} = \frac{C_L'}{C_L{}^*}\sin\beta_m{}^*\cos\beta_m{}^* - \cos^2\beta_m{}^* \tag{61}$$

where $C_L' = dC_L/d\alpha_m$. The pertinent variables are pictured in Fig. 25 where it may be noted that the straight line performance characteristic equation in the unstalled region is given by

$$\frac{\psi}{\psi^*} = (1 - s) + s\frac{\phi}{\phi^*} \tag{62}$$

In Fig. 26 plots of $\frac{\Delta\phi}{\phi^*}$ and η^* as functions of ϕ^* and ψ^* have been computed from the C_L versus α_m curves of Fig. 23. For each solidity the limit loading computed at the nominal mid-range point provides the upper limit to these curves and thus it is presumed to be a design limit. From Fig. 23 it can be seen that this

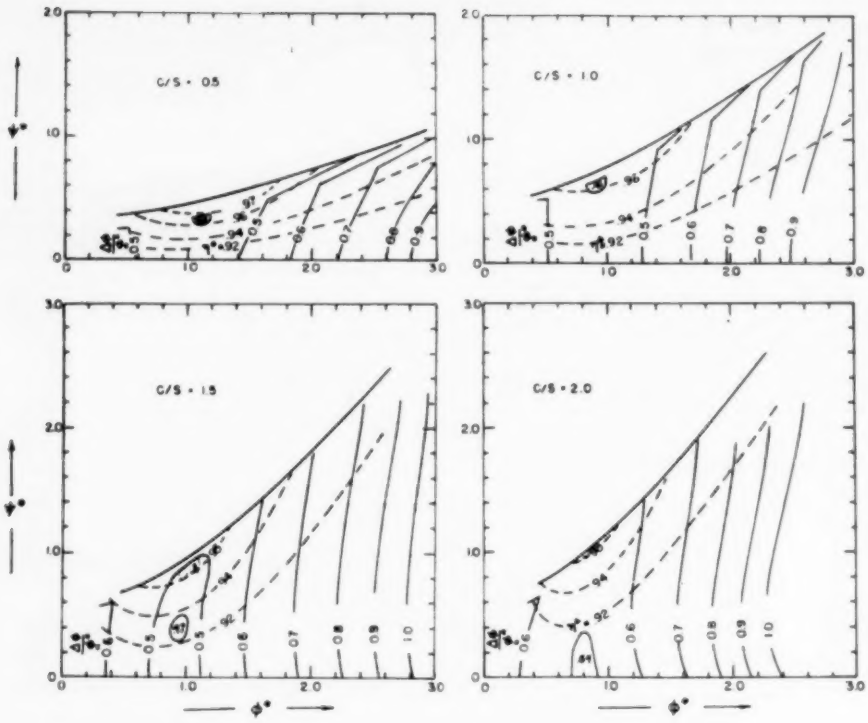

Fig. 26 Plot of $\Delta\phi/\phi^*$ and η^* as functions of ψ^* and ϕ^*. The plots are bounded by the limit loading line.

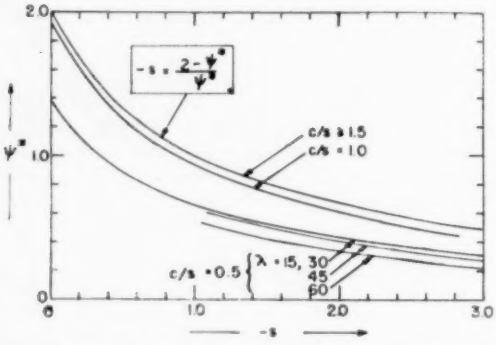

Fig. 27 s versus ψ^*. s is the ordinate emphasizing that lines of constant s in Fig. 26 would be nearly horizontal lines.

mid-range point does not always coincide with the blade geometry giving an abrupt change in range and this fact may be noted in Fig. 26 where the $\frac{\Delta\phi}{\phi^*}$ values sometimes decrease sharply before the upper loading limit is attained.

In Fig. 27 the value of s is plotted as a function of ψ^* and λ, and c/s since s is a strong function of ψ^*, a weak function of c/s, and a very weak function of λ (or $\beta_m{}^*$). A limiting expression may be obtained by assuming that the exit air angle β_2 is held constant while β_1 is varied. Therefore from Fig. 1 of Part I

$$\frac{\Delta V_\theta}{V_z} = \tan\beta_1 - k$$

and

$$\frac{V_{\theta m}}{V_z} = \frac{\tan\beta_1 + k}{2}$$

where $k = \tan\beta_2$. By combining these relations, we obtain

$$\psi = 2(1 - k\phi) \tag{63}$$

By starring ψ and ϕ and using the starred expression to remove k from (63) it may be rearranged in the form of equation (62) where

$$-s_{(\text{constant exit angle})} = \frac{2 - \psi^*}{\psi^*} \tag{64}$$

Thus we see in Fig. 27 that the values of s obtained from the potential flow calculations quickly converge to the limiting expression for constant exit angle. This conforms with the results shown in Fig. 10 of Part I. It is felt by the author that the characteristic slope s is an important design parameter having a strong effect on the off-design performance of multistage compressors.

The use of the parameters ψ and ϕ have been found by the author to be a great convenience. They are cascade parameters and are functions of the cascade variables only, but they are related directly to the significant stage parameters. The necessity of numerous little investigations to assess the effect of this or that variable on Ψ, Φ, or η is eliminated and the choice of a design for any given application is greatly facilitated. It should be noted that lines of constant $\tan\beta_1$ and $\tan\beta_2$ appear as straight lines on the $\psi - \phi$ chart and this is a convenience in later design calculations. After an aerodynamic design has been specified, it is easy to determine the actual blade geometry by working back to Fig. 23 through Equations (54) and (55).

References

15 J. R. Erwin and J. C. Emery, "Effect of Tunnel Configuration and Testing Technique on Cascade Performance," NACA Report No. 1016, 1951.

16 A. R. Howell, "The Present Basis of Axial-Flow Compressor Design," ARC, R + M 2095, *Proceedings, I. Mech. E.*, published in U. S. by ASME

SEYMOUR LIEBLEIN

Aeronautical Research Engineer,
Lewis Research Center,
National Aeronautics and
Space Administration,
Cleveland, Ohio

Loss and Stall Analysis of Compressor Cascades

A simple equation expressing the wake momentum thickness as a primary function of the suction-surface diffusion ratio (ratio of maximum surface velocity to outlet velocity) of conventional low-speed cascade blades is derived from boundary-layer theory in conjunction with simplifying approximations. The derived equation is utilized to gain an insight into qualitative effects on stalling diffusion ratio of such factors as Reynolds number, transition location, and extent of local laminar separation. Use of parameters suggested by the analysis is shown to result in generalized experimental loss and stall correlations and in means for estimating total-pressure loss and unstalled range of operation for commonly used blades.

Introduction

Because of the complexity and three-dimensional character of the flow in multistage axial-flow compressors, it has been necessary to adopt various simplified means for obtaining blade-design data. In particular, experimental investigations of low-speed two-dimensional cascade blades have been utilized in axial-flow compressor research to determine the aerodynamic performance of compressor blade elements. Considerable cascade data have appeared in the literature [1],[1] for example, and many successful compressor designs have been realized based on the use of these data.

A schematic diagram of a conventional low-speed two-dimensional cascade tunnel is shown in Fig. 1 to illustrate the principal components of the setup. The test section contains the row or cascade of blades set in a mounting device such that various cascade air inlet angles and blade angles of attack can be obtained. Measurements of the outlet flow (air angle, static pressure, loss in total pressure) are obtained from a traverse along the cascade a short distance downstream of the blades.

Since the aerodynamic performance of cascade blades is largely governed by the growth and separation of the boundary layers on the blade surfaces, the determination of generalized loss and stall limit characteristics of conventional blades is an important aspect of cascade research. The problem of loss and stall prediction in cascades is made difficult by the large number of factors that influence the growth of the boundary layers, that is, surface velocity distribution, blade Reynolds number, free-stream turbulence, and surface roughness. However, it has been possible through analysis of experimental data to gain an insight into the gross or first-order behavior of blade losses and stall in limited cases through the use of various empirical stall coefficients and diffusion factors [2, 3, 4, 5]. These correlations were based primarily on the experimental observation that blade-surface velocity distributions that result in large amounts of deceleration or diffusion in velocity along the surfaces tend to produce relatively thick boundary layers and eventual separation or stall.

In the present paper, the diffusion concept is expanded and

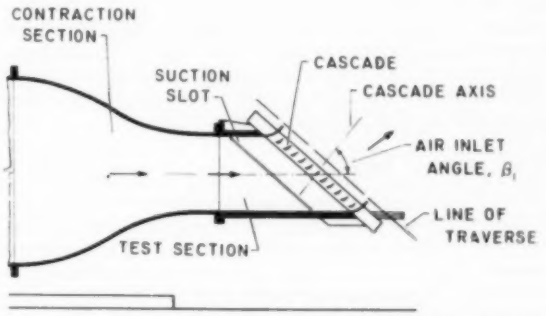

Fig. 1 Schematic layout of conventional low-speed cascade tunnel

[1] Numbers in brackets designate References at end of paper.

Contributed by the Hydraulic Division and presented at the Annual Meeting, New York, N. Y., November 30–December 5, 1958, of The American Society of Mechanical Engineers.

Note: Statements and opinions advanced in papers are to be understood as individual expressions of their authors and not those of the Society. Manuscript received at ASME Headquarters, August 4, 1958. Paper No. 58—A-91.

Nomenclature

a = factor in equation for equivalent diffusion ratio
C_D = drag coefficient
C_f = total skin-friction coefficient
C_f' = total skin-friction coefficient for flat-plate flow (based on chord-length Reynolds number)
C_f^{**} = total skin-friction coefficient for flat-plate flow (based on transition-distance Reynolds number)
c = chord length
c_f = local skin-friction coefficient $\left(\text{wall shear stress} \Big/ \frac{1}{2}\rho V^2\right)$
D_{eq} = equivalent diffusion ratio
f_θ = averaging factor for momentum-thickness variation in momentum-thickness equation
H = form factor of wake or boundary layer (δ^*/θ)
j = factor in momentum-thickness equation
k = factor in momentum-thickness equation
l = length of flow surface
P = total pressure
Re_c = blade-chord Reynolds number
s = blade spacing
V = free-stream velocity
v = local velocity in wake
x = distance along outlet flow direction or along flow surface

(Continued on next page)

placed on a firmer basis through an "engineering" application of the boundary-layer momentum equation to cascade blade surfaces. By means of simplifying approximations, a simple relation is investigated for the variation of blade-wake momentum thickness with blade-surface diffusion for conventional blades. Experimental verification of the derived equation over a wide range of cascade configurations (i.e., solidity, stagger angle, and camber) is conducted from available data from typical low-speed blade sections.

The results of the development are utilized for blade-loss analysis in two ways. First, the derived relation between wake momentum thickness and surface diffusion is examined in order to obtain a qualitative indication of the fundamental effects on loss and limiting diffusion (stall limit) of such secondary factors as blade-chord Reynolds number and the location and nature of the transition from laminar to turbulent flow. Second, the derived concepts are utilized to analyze the available experimental data in an effort to explain the observed behavior and to establish generalized loss and stall correlations. The established experimental correlations and stall limits are then applied to design use by expressing the variables involved in equivalent parameters readily obtained from design quantities. Sample calculations are provided to illustrate how values of design-point total-pressure loss and unstalled range of operation can be predicted as functions of the design parameters of solidity, stagger angle, and blade loading for conventional blades.

Development of Equation

The objective of the mathematical analysis is to develop a simple analytical relation between the blade-wake momentum thickness and the blade-surface velocity diffusion for conventional cascade blades. The development treats incompressible two-dimensional flow, and considers that the blade peak suction-surface velocity occurs close to the leading edge and that the boundary layer of the suction surface contributes the major portion of the wake. These conditions are generally observed for conventional blade sections in the range of operation from minimum-loss to high-angle-of-attack stall (which is the region of interest in blade design). Typical surface velocity distributions are shown in Fig. 2, a schematic representation of the blade wake development is given in Fig. 3, and the definitions of wake properties are presented in Fig. 4.

Basic Relations. In the plane of the blade trailing edge, the momentum thickness of the wake can be expressed as the sum of the momentum thicknesses of the pressure and suction-surface boundary layers at the trailing edge. Theoretically, the growth of the boundary-layer momentum thickness θ on a blade surface can be described by the von Karman momentum equation as a function of the local-skin-friction coefficient c_f and the velocity gradient along the surface dV/dx as

$$\frac{d\theta}{dx} = \frac{c_f}{2} - (H + 2)\frac{\theta}{V}\frac{dV}{dx} \tag{1}$$

where V is the local free-stream velocity outside the boundary layer. Integration of Equation (1) from $x = 0$ to $x = x_{te}$ can be conducted by assuming for simplicity that the maximum free-stream surface velocity V_{max} occurs at the leading edge and that a mean value of $(H + 2)(\theta/c)$ can be taken so that

$$\left(\frac{\theta}{c}\right)_{te} = \left(\frac{C_f}{2}\right) + j \log_e\left(\frac{V_{max}}{V_{te}}\right) \tag{2}$$

where

$$j = \overline{(H + 2)(\theta/c)} \tag{3}$$

C_f is the conventional total skin-friction coefficient,[2] and the velocity V_{te} is the free-stream surface velocity at the trailing edge. In the ensuing analysis, however, since there is generally little change in wake momentum thickness and free-stream velocity between blade trailing edge and measuring station location [6], trailing-edge values will be taken to be those at the measuring station (station 2).

Examination of surface-velocity distributions of conventional cascade blades (as illustrated in Fig. 2) indicates that, as blade camber or blade angle of attack is increased, large changes in velocity gradient occur on the blade suction surface, but comparatively small changes occur on the pressure surface. Furthermore, changes in surface friction coefficients will be small compared to the changes in the suction-surface diffusion term. Thus, changes in total wake momentum thickness will result primarily from the diffusion contribution of the suction-surface boundary layer. Accordingly, for the complete wake (both surfaces), the momentum thickness can then be expressed as

$$\left(\frac{\theta}{c}\right)_2 = \epsilon + j_s \log_e\left(\frac{V_{max,s}}{V_2}\right) \tag{4}$$

where

$$\epsilon = \frac{1}{2}(C_{f,p} + C_{f,s}) + j_p \log_e\left(\frac{V_{max,p}}{V_2}\right) \tag{5}$$

The ratio at maximum surface velocity to outlet velocity V_{max}/V_2 will hereafter be called the surface diffusion ratio.

It can be shown from calculations of several common averaging processes, that for the range of values of H and θ/c normally encountered for conventional blades, it is sufficiently accurate to

[2] It is assumed for simplicity in the integration of the local friction term in Equation (1) that the blade-surface length is effectively equal to the chord length.

Nomenclature

α = angle of attack, angle between inlet-air direction and blade chord
β = air angle, angle between airflow and axial direction
Δ = change in quantity
$\Delta\beta$ = air turning angle ($\beta_1 - \beta_2$)
ϵ = factor in momentum-thickness equation
δ^* = displacement thickness of wake or boundary layer
θ = momentum thickness of wake or boundary layer
σ = solidity (chord/spacing)
$\bar{\omega}$ = total-pressure loss coefficient, $(\Delta\bar{P})_2 \Big/ \frac{1}{2}\rho V_1^2$

Subscripts

lm = laminar
ls = laminar separation
max = maximum
p = pressure surface
s = suction surface
st = stall condition
tb = turbulent
te = trailing edge
tr = transition
x = outlet flow direction or direction along flow surface
y = normal to axial direction
1 = cascade inlet station
2 = cascade outlet measuring station

Superscripts

— = average value of quantity
* = reference minimum-loss condition

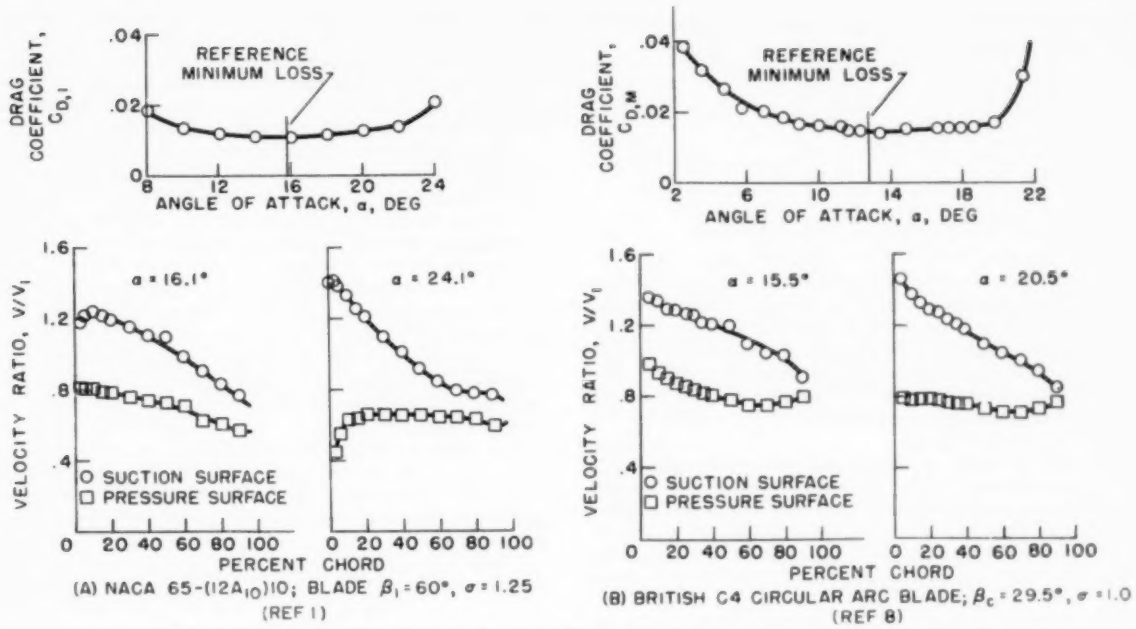

Fig. 2 Typical surface velocity distributions in region from minimum loss to positive stall for conventional cascade blades

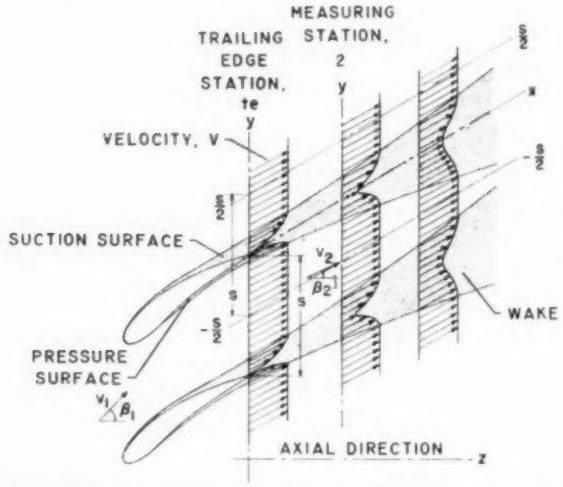

Fig. 3 Schematic representation of wake development in flow across cascade blades

express j_s in Equation (4) in terms of the individual chordwise average values of H and θ/c such that

$$j_s = \overline{(H_s + 2)(\theta/c)_s} = (\overline{H}_s + 2)(\overline{\theta/c})_s \qquad (6)$$

Now the average momentum thickness in Equation (6) can be expressed as some factor times the momentum thickness at the measuring station, such that

$$\left(\frac{\bar{\theta}}{c}\right)_s = f_\theta \left(\frac{\theta}{c}\right)_{2,s} = f_\theta \left(\frac{\theta_s}{\theta}\right)_2 \left(\frac{\theta}{c}\right)_2 \qquad (7)$$

where f_θ is some averaging factor that satisfies the equality.

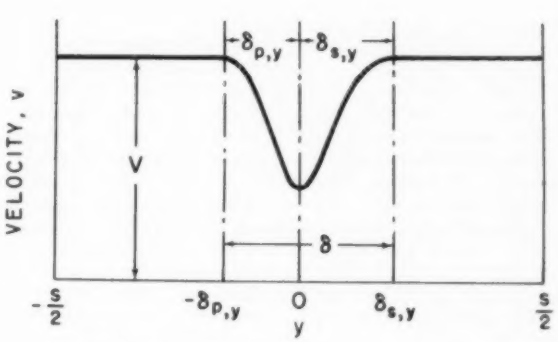

DISPLACEMENT THICKNESS:

$$\delta_y^* = \delta_{s,y}^* + \delta_{p,y}^* = \int_{\delta_{p,y}}^{\delta_{s,y}} \left(1 - \frac{v}{V}\right) dy$$

$$\delta^* = \delta_s^* + \delta_p^* = \delta_y^* \cos\beta$$

MOMENTUM THICKNESS:

$$\theta_y = \theta_{s,y} + \theta_{p,y} = \int_{\delta_{p,y}}^{\delta_{s,y}} \frac{v}{V}\left(1 - \frac{v}{V}\right) dy$$

$$\theta = \theta_s + \theta_p = \theta_y \cos\beta$$

$$H = \frac{\delta^*}{\theta} = \frac{\delta_y^*}{\theta_y} \qquad \delta = \delta_s + \delta_p = \delta_y \cos\beta$$

Fig. 4 Model variation of velocity in plane normal to axial direction, and definitions of wake properties

Substitution for $(\overline{\theta/c})_2$ according to Equation (7) into Equations (6) and (4) then gives for the wake momentum thickness

$$\left(\frac{\theta}{c}\right)_2 = \frac{\epsilon}{1 - k_s \log_e \left(\frac{V_{\max,s}}{V_2}\right)} \tag{8}$$

where

$$k_s = (2 + \bar{H}_s) f_\theta \left(\frac{\theta_s}{\theta}\right)_2 \tag{9}$$

An analytical equation for the variation of wake momentum thickness with suction-surface diffusion ratio is thus obtained in terms of a factor ϵ, which is a function primarily of the skin-friction coefficients, and a factor k_s, which involves some mean values of H and θ along the surface. It now remains to analyze the ϵ and k_s factors over the range of diffusions encountered in cascades, in order to obtain an indication of their magnitude and possible relation to $V_{\max,s}/V_2$.

Evaluation of Terms. A direct evaluation of the various terms in Equations (5) and (9) cannot be made because of the general absence of experimental data for the development of the boundary layer along the surfaces of compressor cascade blades. However, a preliminary indication of the approximate magnitude of the ϵ and k_s terms can be obtained from an examination of available boundary-layer data from similar flow surfaces.

Theoretically, the case of zero diffusion ($V_{\max}/V_2 = 1$) is represented by a constant velocity on the blade surfaces, as would be obtained on very thin uncambered blades set at zero angle of attack. The boundary-layer development will therefore be similar to that of the flat plate, so that

$$\epsilon = \frac{1}{2} C_{f,p}' + \frac{1}{2} C_{f,s}' = C_f'$$

where C_f' is the conventional total skin-friction coefficient for the flat plate. A zero diffusion on both blade surfaces, however, cannot be attained with conventional blades of thicknesses of about 10 per cent, inasmuch as some variation in velocity will always occur on one or both of the surfaces. Since negative velocity gradients and average free-stream velocities greater than inlet velocity occur for conventional blades at low diffusion, it is expected that the total skin-friction coefficient will be somewhat lower than the conventional flat-plate value based on inlet-velocity Reynolds number.

As suction-surface diffusion is increased, the cascade data show that the negative velocity gradients on the suction surface increase markedly, while the negative velocity gradients on the pressure surface generally decrease by a comparatively small amount. A further net reduction in total friction coefficient is therefore likely as diffusion ratio is increased to the separation value. The third term in the ϵ factor involving the pressure-surface diffusion ratio [Equation (5)] will also generally tend to decrease slightly with increasing suction-surface diffusion ratio. The resulting change in the value of ϵ, however, is expected to be quite small, since the values of pressure-surface diffusion ratio involved are close to unity. Thus, on the basis of these considerations, the value of ϵ is expected to be generally somewhat smaller than the total flat-plate friction coefficient and to tend to decrease slightly with increasing suction-surface diffusion ratio. For the range of blade-chord Reynolds numbers normally encountered in cascade tests ($\mathrm{Re}_c = 2.0 \times 10^5$ to 2.5×10^5), the flat-plate friction coefficient C_f' is about 0.0060 for turbulent flow and about 0.0028 for laminar flow [6, p. 439]. The factor ϵ in the momentum-thickness equation should therefore have a value somewhere between these limits.

In evaluating the magnitude of the k_s term in Equation (9), recourse was made to data from isolated airfoil sections. Experimental variations of boundary-layer momentum thickness and form factor in predominantly turbulent boundary layers are shown in Fig. 5 for the flat plate (constant free-stream velocity) and for the upper surface of several isolated airfoils for which flow separation has occurred near the trailing edge (at $x = l$).

Although the specific averaging processes required to make the values of f_θ and $\bar{H}_s$ in Equation (9) satisfy Equations (6) and (7) are not known, it will be assumed for simplicity that the magnitude of these terms can be obtained from the experimental data by considering the mean values for f_θ and $\bar{H}$ as

$$\bar{H} = \int_0^1 H d(x/l)$$

and

$$f_\theta = \int_0^1 \frac{\theta}{\theta_{(x/l)=1}} d(x/l)$$

For zero diffusion, from the flat-plate data of Fig. 5, $\bar{H} = 1.33$ and $f_\theta = 0.57$. (For the classical flat-plate boundary-layer theory with $\theta \propto x^{4/5}$, $f_\theta = 0.556$.) Thus, with essentially symmetrical boundary layers on both surfaces, $(\theta_s/\theta)_2 = 0.5$, and the factor

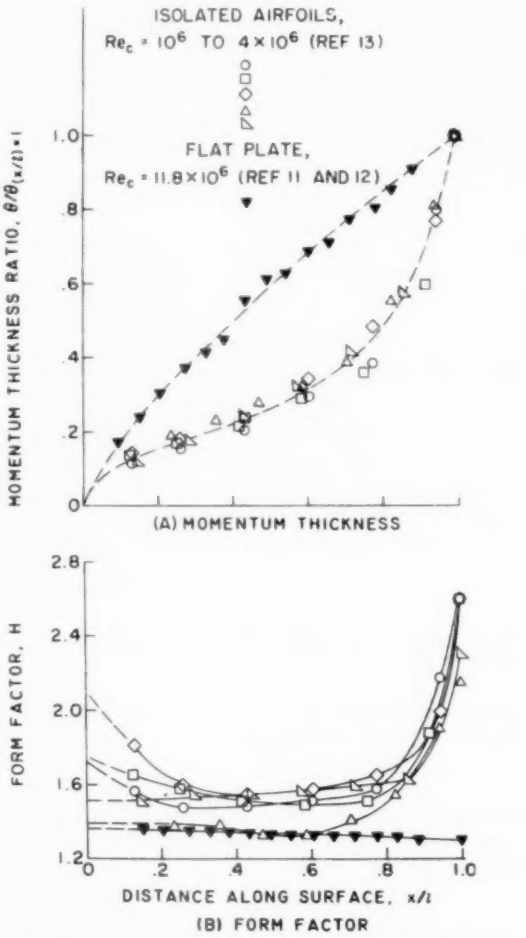

Fig. 5 Experimental variation of boundary-layer momentum thickness and form factor along several flow surfaces for turbulent flow

k_s, from Equation (9), will be about 0.95 for the case of zero diffusion.

For the case of diffusion resulting in separation (isolated airfoil data in Fig. 5), an essentially constant value of $f_\theta = 0.33$ was computed for all airfoils, while an average value of $\overline{H}_s = 1.60$ was obtained. If similar values of $\overline{H}_s$ and f_θ occur for cascade blades (as is most likely, since the suction-surface velocity distributions of isolated and cascade airfoils are generally similar), then, since (θ_s/θ_2) may be about 0.90 for the stalled condition,[3] k_s values of about 1.07 may be obtained. Thus, it appears reasonable to conjecture that k_s might tend to increase somewhat with $V_{\max,s}/V_2$ or possibly be essentially constant for conventional cascade blades with turbulent boundary layers.

On the basis of these considerations, it is now possible to obtain a rough indication of the expected variation of wake momentum thickness with diffusion ratio by assuming representative constant values of ϵ and k_s (say, by taking $\epsilon = 0.005$ and $k_s = 1.0$). As might be anticipated, an essentially exponential variation of momentum thickness with diffusion ratio is indicated in this case.

Comparison With Experiment. Experimental values of wake momentum thickness $(\theta/c)_2$ and diffusion ratio $V_{\max,s}/V_2$ were determined for the commonly used NACA 65(A_{10})-series blades [1] and the British C.4 circular-arc blades [7, 8]. Both blades are low-speed thick-nose profiles of 10 per cent maximum thickness and symmetrical mean-camber lines. The data used for these sections were obtained from tunnels in which good two dimensionality control was exercised by means of tunnel-wall boundary-layer suction. Some of the important characteristics of the blade configurations used for the correlation are listed in Table 1.

Since the loss data in the references were reported in terms of various drag coefficients, it was necessary to convert the data to values of $(\theta/c)_2$ by means of the conversion equations derived in [5]. The suction-surface diffusion ratio was computed according to the relation

$$\frac{V_{\max,s}}{V_2} = \left(\frac{V_{\max,s}}{V_1}\right)\frac{V_1}{V_2} = \left(\frac{V_{\max,s}}{V_1}\right)\frac{\cos\beta_2}{\cos\beta_1}\left[1 - \left(\frac{\theta}{c}\right)_2 \frac{H_2\sigma}{\cos\beta_2}\right] \quad (10)$$

where $V_{\max,s}/V_1$, β_1, and β_2 are obtained from the measured blade performance and surface velocity distributions, and $(\theta/c)_2$ is determined as has been indicated. (A constant value of $H_2 = 1.08$ was used, as suggested in [5, 9].)

The correlation is presented for the reference condition of minimum-loss angle of attack, defined as the midpoint of the range extending between the values of angle of attack at twice minimum loss (see Fig. 2). Values of $(\theta/c)_2$ and $V_{\max,s}/V_2$ at minimum loss were obtained from faired curves of these quantities against angle of attack for each configuration.[4]

The results of the experimental correlation for the NACA 65-(A_{10}) and C.4 circular-arc blades are shown in Fig. 6. The effectiveness of the use of the parameters of wake momentum thickness and diffusion ratio in producing a generalized loss correlation over the range of solidities, cambers, and air inlet angles covered is quite marked. It is noted that a good fit of the experimental data can be obtained from Equation (8) with $\epsilon = 0.004$ and $k_s = 1.17$, as shown by the dashed curve in Fig. 6. (Apparently, for these data, the speculated reduction in ϵ with $V_{\max,s}/V_2$ is not significant, or perhaps there is a compensating effect between a decreasing ϵ and an increasing k_s.)

Since the boundary-layer flow for the blades of Fig. 6 is predominantly turbulent, the flat-plate friction coefficient at the Reynolds number of the data should be somewhat less than 0.006. The experimentally determined value of $\epsilon = 0.004$ therefore appears reasonable, since, according to the previous considerations, it should be smaller than the flat-plate friction coefficient. It is also noted that the value of $k_s = 1.17$ obtained from the data of Fig. 6, although somewhat larger, is fairly close to the values deduced previously from the predominantly turbulent boundary-layer data on isolated airfoils. Actually, a higher value of k_s for the cascade compared with the isolated airfoil case may be expected, since higher average values of H_s will occur due to the lower Reynolds numbers and the existence of local laminar separation in the cascade. The empirical ϵ and k_s values therefore appear entirely reasonable, and the derived momentum-thickness equation can be considered as a satisfactory approxi-

[3] According to the results of [5], $(\theta/c)_2$ for conventional blades is about 0.004 at zero suction-surface diffusion and about 0.02 at stall. Since the pressure-surface velocity distributions change very little with increasing suction-surface diffusion, the pressure-surface momentum-thickness contribution should also change little, and tend to remain of the order of 0.002 at stall.

[4] In so doing, an attempt was made to eliminate some of the obvious increases in momentum thickness that appear in the data due to local laminar separations. The data thus tend to approach the variation for a predominantly turbulent flow without laminar separation bubbles.

Table 1

BLADE NUMBER	1		2	3
BLADE	NACA 65($C_{1,0}A_{10}$)10		10C4/30C50	10C4/31C50
REFERENCE	1		7	8
AIR INLET ANGLE, β_1, DEG	30, 45, 60, 70		30, 45, 60	VARIABLE
BLADE CHORD ANGLE, DEG	VARIABLE		VARIABLE	29.5
CAMBER	0, 4, 8, 12, 15, 18, 21, 24, 27[a]		[b]30	[b]51
SOLIDITY	0.5,0.75	1.0,1.25,1.5	1.0	1.0
CHORD LENGTH, IN.	2.5	5	5	4
ASPECT RATIO	2	1	1	6
REYNOLDS NUMBER	2×10^5	2.5×10^5	2.5×10^5	2.2×10^5
INLET MACH NUMBER	0.14	0.09	0.09	0.09
TUNNEL	NACA 5-INCH LOW SPEED			AUSTRALIAN LOW SPEED
BOUNDARY LAYER CONTROL	END AND SIDE POROUS WALL SUCTION. SIDE WALL SLOT SUCTION.			SIDE WALL SLOT SUCTION
TURBULENCE FACTOR	1.2		1.2	1.12
MEASURING STATION, x/c	1		1	$1\frac{1}{2}$

[a] VALUES OF ISOLATED LIFT COEFFICIENT, $C_{1,0}$

[b] VALUES OF CAMBER ANGLE, DEGREES

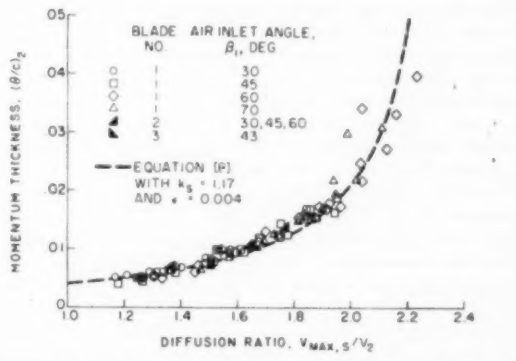

Fig. 6 Experimental variation of wake momentum thickness with suction-surface diffusion ratio at minimum-loss angle of attack for NACA 65($C_{10}A_{10}$)10 blades and C.4 circular-arc blades.

mate representation of the wake thickness of conventional cascade blades.

Application of Results. Although the derived equation is an approximate and nonrigorous development,[5] and therefore incapable of yielding accurate quantitative results, it can be utilized to provide qualitative insights into the principal factors affecting the variation of wake momentum thickness with diffusion ratio. This is made possible through the effective use of the flat-plate friction coefficient in the evaluation of the ϵ term and of mean chordwise values of boundary-layer form factor and momentum thickness in the evaluation of the k_s term in Equation (8). Thus, if the effects on ϵ and k_s of such secondary factors as chord Reynolds number, surface roughness, turbulence, and so forth, can be determined, then the resultant effects on limiting diffusion ratio can be estimated.

The concepts of the diffusion analysis can also be used to interpret available experimental loss data and to establish correlations in more generalized forms for purposes of design studies. Examples of the application of the results to qualitative evaluations of secondary factors and to analysis of experimental data will now be given.

Qualitative Evaluations

According to the formulation of Equation (8), a limiting value of suction-surface diffusion rate is reached for each value of k_s when $(\theta/c)_2$ approaches infinity, as given by

$$\left(\frac{V_{\max,s}}{V_2}\right)_{\lim} = e^{1/k_s}$$

The prime importance of the state of the surface boundary layer in determining the allowable diffusion ratio is thus clearly indicated. It was found previously that k_s may be about unity (limit. $V_{\max,s}/V_2 = 2.73$) for isolated airfoils with turbulent boundary-layer flow at high Reynolds number (order of 10^6 or greater), and about 1.17 (limit. $V_{\max,s}/V_2 = 2.35$) for the conventional cascade blades [1] at a Reynolds number of about 2.5×10^5 (predominately turbulent flow.)

Variations in ϵ in Equation (8) will be reflected as direct variations in the magnitude of the momentum thickness and will affect only the rate at which the limiting diffusion ratio is approached. Since the value of ϵ is approximately equal to or at least proportional to the flat-plate friction coefficient C_f', it will be a direct function of the blade-chord Reynolds number and the surface roughness of the blade, values of which can be obtained, for example, from [6, p. 439] and from [6, chap. XXI], respectively. For the case of partly laminar and partly turbulent flow, the friction coefficient can be calculated as indicated in the appendix. Although the proper relation between ϵ and C_f' cannot be accurately determined from the correlation of Fig. 6, it appears that for practical purposes, values between $\epsilon = 0.8\,C_f'$ and $\epsilon = C_f'$ should be satisfactory.

Calculated Variations. An indication of the possible variation in k_s and ϵ with varying boundary-layer state was obtained from consideration of hypothetical form-factor profiles representative of cascade flow with varying transition location and local laminar separation (transition occurs after separation of the laminar boundary layer). Fig. 7 shows highly idealized variation of H_s with chord-length distance along the surface for various locations of laminar separation and turbulent reattachment. In the figure, laminar separation is shown to occur at the 0, 0.2, and 0.4 chord points followed by a turbulent reattachment either immediately [$(\Delta x/c)_{ls} = 0$, solid line], or after 0.1 chord length [$(\Delta x/c)_{ls} = 0.1$, dashed line]. Turbulent separation is assumed to occur at the trailing edge, as is likely to occur for a heavily loaded blade.

[5] Principal reservation lies in the use of mean values of H and θ in the integration of the momentum equation and in the validity of the von Karman equation in regions of separation where the normal pressure gradients and turbulent stresses may not be negligible.

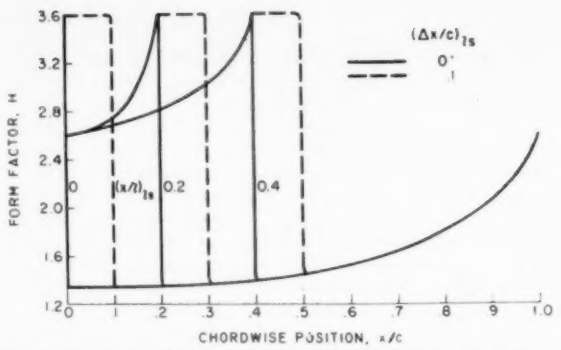

Fig. 7 Idealized variations of boundary-layer form factor along blade surface for various degrees of local laminar flow. Transition and turbulent reattachment after laminar separation, and turbulent separation at trailing edge.

Average values of form factor $\bar{H}_s$ were determined by integration for each curve in Fig. 7, and corresponding values of f_θ determined from the simplifying assumption that

$$f_\theta = \left(\frac{x}{c}\right)_{tr} f_{\theta,\,lm} + \left[1 - \left(\frac{x}{c}\right)_{tr}\right] f_{\theta,\,tb}$$

where $f_{\theta,\,lm}$ is taken as 0.63[6] and $f_{\theta,\,tb}$ is 0.33. Values of k_s were then determined for each transition location according to Equation (9) by assuming $\theta_s/\theta_2 = 0.90$. Values of flat-plate friction coefficient C_f' for each case were determined from Equation (19) in the appendix for $\mathrm{Re}_c = 2.5 \times 10^5$. The results of the calculations for k_s and C_f' for the illustrative cases of Fig. 7 are listed in Table 2.

Table 2 Calculated values of boundary-layer factors

$(x/c)_{ls}$	$(\Delta x/c)_{ls}$	$\bar{H}_s$	f_θ	k_s	C_f'
0	0	1.58	0.33	1.06	0.0059
	0.1	1.80	0.36	1.23	0.0058
0.2	0	1.88	0.39	1.36	0.0055
	0.1	2.10	0.41	1.51	0.0051
0.4	0	2.19	0.44	1.66	0.0047
	0.1	2.41	0.47	1.86	0.0044

Calculated variations of $(\theta/c)_2$ with $V_{\max,s}/V_2$ for the transition configurations of Fig. 7 assuming that k_s and ϵ are constant over the entire range of $V_{\max,s}/V_2$ (with $\epsilon = C_f'$) are shown in Fig. 8 for illustrative purposes. (In an actual flow, of course, it is recognized that k_s and ϵ might not be constant, since transition and separation characteristics will vary with the diffusion ratio.) Thus, a wide range of values of momentum thickness and limiting diffusion ratio may theoretically be obtained for a given cascade, depending on the location of the transition and the behavior of the surface boundary layer in the transition region.

Design Considerations. According to the preceding analysis, for a given application in cascade design, the stalling diffusion ratio can be increased by designing the blade and cascade in order to tend to reduce the total friction coefficient and the extent of laminar flow. These objectives can be accomplished in several ways: By utilizing a large value of blade-chord Reynolds number and high free-stream turbulence level; by maintaining smooth

[6] Obtained from integrations of theoretical variations of laminar boundary-layer momentum thickness for the flat plate ($f_\theta = 0.66$) and for a linearly decreasing velocity resulting in separation ($f_\theta = 0.61$).

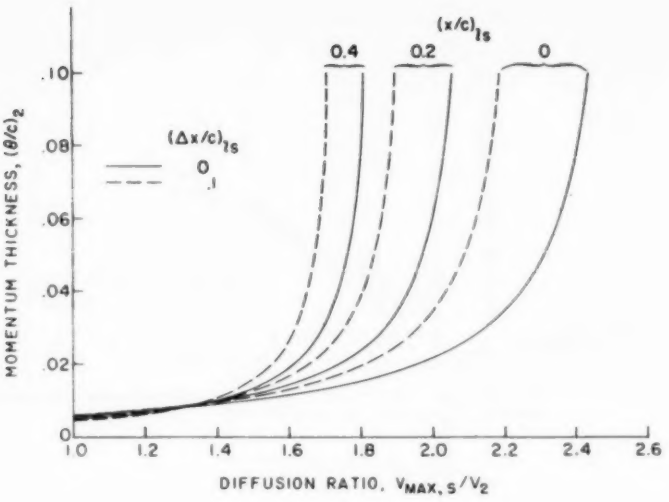

Fig. 8 Calculated variation of wake momentum thickness with suction-surface diffusion ratio for case of transition after laminar separation with turbulent reattachment as indicated in Fig. 7

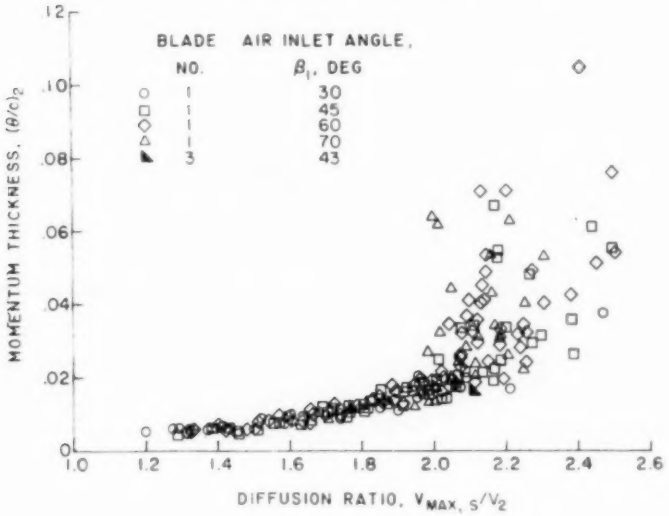

Fig. 9 Experimental variation of wake momentum thickness with suction-surface diffusion ratio at angles of attack greater than minimum loss

blade surfaces; and by designing for peak surface velocity near the leading edge so that the initial boundary layer at the start of diffusion is small.

In axial-flow compressor design, the situation is more favorable in some respects than in the cascade. For the same Reynolds numbers, the turbulence levels are generally greater in the compressor due to the wakes and disturbances of preceding blade rows. On the other hand, the use of high peak velocities at the blade leading edge may not be consistent with good high Mach number performance. The maintenance of high Reynolds number and low relative surface roughness, however, should likewise be effective in increasing the stalling diffusion ratios of compressor blade sections.

The analysis also indicates the desirability of carefully qualifying indicated values of stalling diffusion ratio derived from experimental data for the blade-chord Reynolds number and turbulence levels of the tests.

Analysis of Experimental Data

According to the derived equation, fundamental parameters for the correlation of cascade loss data should be the wake momentum thickness and the suction-surface diffusion ratio. The effectiveness of these parameters in producing a generalized correlation for the 10-per cent thick NACA 65(A_{10})-series blades and the C.4 circular-arc blade at minimum-loss angle of attack has already been shown in Fig. 6. A corresponding plot of $(\theta/c)_2$ against $V_{\max,s}/V_2$ for these blades at angles of attack greater than minimum loss is shown in Fig. 9, revealing a wide spread of the data at large values of diffusion ratio. Inasmuch as these cascade data were obtained at values of Reynolds number and free-stream turbulence for which local laminar separations were present [1], it is reasonable to conjecture that the data spread at high values of diffusion ratio may be due in large measure to the effects of variations in the nature and location of these separations (as illustrated in Fig. 8). Furthermore, the data indicate that a significant margin of improvement in the general $(\theta/c)_2$ against $V_{\max,s}/V_2$ variation exists for these blades if the factors influencing the data spread can be controlled.

For cascade design use, prediction is desired of the loss in total pressure and the stall limit over a wide range of blade solidities, air inlet angles, and air-turning angles. Such predictions are now

possible for the NACA 65(A_{10})-series blades and C.4 circular-arc blade considered herein. For example, according to the correlations of Fig. 6, once the suction-surface diffusion ratio is known, a value of wake momentum thickness can be estimated for the minimum-loss condition. The corresponding loss in total pressure at the cascade measuring station can then be computed from the relation [10].

$$\bar{\omega} = 2\left(\frac{\theta}{c}\right)_2 \frac{\sigma}{\cos\beta_2}\left(\frac{\cos\beta_1}{\cos\beta_2}\right)^2\left(\frac{2H_2}{3H_2-1}\right)\left[1-\left(\frac{\theta}{c}\right)_2\frac{\sigma H_2}{\cos\beta_2}\right]^{-2} \quad (11)$$

where $\bar{\omega}$ is the total-pressure loss coefficient $\Delta\bar{P}_2 \Big/ \frac{1}{2}\rho V_1^2$ and H_2 is the wake form factor at the measuring station. (According to [5, 9], a constant value of $H_2 = 1.08$ can be used for conventional configurations.)

In the study of blade stall, various concepts and definitions of blade stall have been used in cascade practice. In general, blade stall refers to the condition where a marked deterioration of the flow occurs as a result of the growth or separation of the boundary layer on the blade surface. Specifically, blade stall has been defined to occur, for example, when the loss attains twice its minimum value, when a relatively marked decrease in turning angle is observed, or when a certain rate of increase in loss is attained. The correlations of Figs. 6 and 9, however, suggests that perhaps a more universal criterion of stall might be adopted in terms of the diffusion ratio $V_{\max,s}/V_2$. From these data at both minimum-loss and greater angles of attack, it appears that the rate of increase of wake momentum thickness may become marked for values of $V_{\max,s}/V_2$ greater than about 1.9. Thus, a stalling diffusion ratio for design use can be defined as the value above which a large rise in wake thickness, and therefore in loss, is possible.

Equivalent Diffusion Ratio. The preceding section indicated that the total-pressure loss and the stall margin can be estimated once the design suction-surface diffusion ratio $V_{\max,s}/V_2$ is known. For design purposes, however, since surface velocity data may be unavailable, it is desirable to establish an equivalent diffusion ratio approximately equal to $V_{\max,s}/V_2$ that is based on readily calculated inlet and outlet conditions. Such an equivalent diffusion ratio can be established for the NACA 65(A_{10}) and C.4 circular-arc blades on the basis of Equation (10).

In Equation (10), it is first noted that for simplicity the bracket term involving $(\theta/c)_2$ is sufficiently small to be neglected. An empirical correlation could be established between $V_{\max,s}/V_1$ and the circulation parameter $(\cos^2\beta_1/\sigma)(\tan\beta_1 - \tan\beta_2)$ at minimum-loss angle of attack as shown in Fig. 10. An empirical equation for $V_{\max,s}/V_1$ is readily derived as

$$\frac{V_{\max,s}}{V_1} = 1.12 + 0.61\frac{\cos^2\beta_1}{\sigma}(\tan\beta_1 - \tan\beta_2) \quad (12)$$

so that an equivalent diffusion ratio at minimum loss designated by the symbol D_{eq}^* is obtained in terms of inlet and outlet conditions as

$$D_{eq}^* = \frac{\cos\beta_2}{\cos\beta_1}\left[1.12 + 0.61\frac{\cos^2\beta_1}{\sigma}(\tan\beta_1 - \tan\beta_2)\right] \approx \left(\frac{V_{\max,s}}{V_2}\right)^* \quad (13)$$

The corresponding plot of $(\theta/c)_2$ against D_{eq}^* at minimum loss is shown in Fig. 11.

An empirical correlation for $V_{\max,s}/V_1$ was also obtained for angles of attack greater than minimum loss as a function of the angle difference $\alpha - \alpha^*$. The corresponding equivalent diffusion ratio is

$$D_{eq} = \frac{\cos\beta_2}{\cos\beta_1}\left[1.12 + a(\alpha-\alpha^*)^{1.43} + 0.61\frac{\cos^2\beta_1}{\sigma}(\tan\beta_1 - \tan\beta_2)\right] \quad (14)$$

where $a = 0.0117$ for the NACA 65(A_{10}) blades and $a = 0.007$ for the C.4 circular-arc blade.

According to Equation (14), the equivalent diffusion ratio of a blade section at any angle $(\alpha - \alpha^*)$ can be determined for a given solidity and air inlet angle, if the air outlet angle β_2 is known. Therefore, let β_2 be determined in the following manner: If it is assumed that the air turning angle $(\Delta\beta = \beta_2 - \beta_1)$ varies essentially linearly with α in the region from minimum loss to positive stall, then

$$\beta_2 = \beta_1 - \Delta\beta = \beta_1 - \Delta\beta^* - \frac{d(\Delta\beta^*)}{d\alpha}(\alpha - \alpha^*) \quad (15)$$

where $\Delta\beta^*$ is the turning angle and $d(\Delta\beta^*)/d\alpha$ is the slope of the turning-angle variation at minimum loss. Representative values of $d(\Delta\beta^*)/d\alpha$ as a function of σ and β_1 derived from examination of available cascade data and values of α^* and $\Delta\beta^*$ are given in [5].

The plot of $(\theta/c)_2$ against D_{eq} given by Equations (14) and (15) shown in Fig. 12 is similar to the corresponding plot against $V_{\max,s}/V_2$ at angles of attack greater than minimum loss given in Fig. 9. When plotted against equivalent diffusion factor, how-

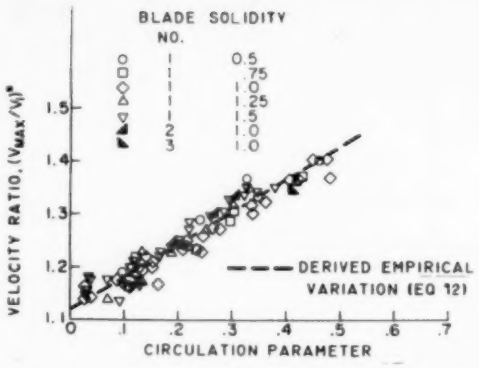

Fig. 10 Correlation of suction-surface velocity ratio with circulation parameter at minimum-loss angle of attack

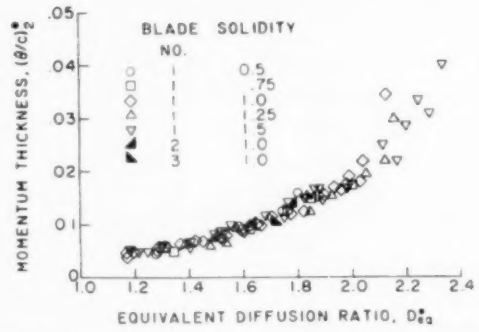

Fig. 11 Correlation of wake momentum thickness with equivalent diffusion ratio at minimum-loss angle of attack

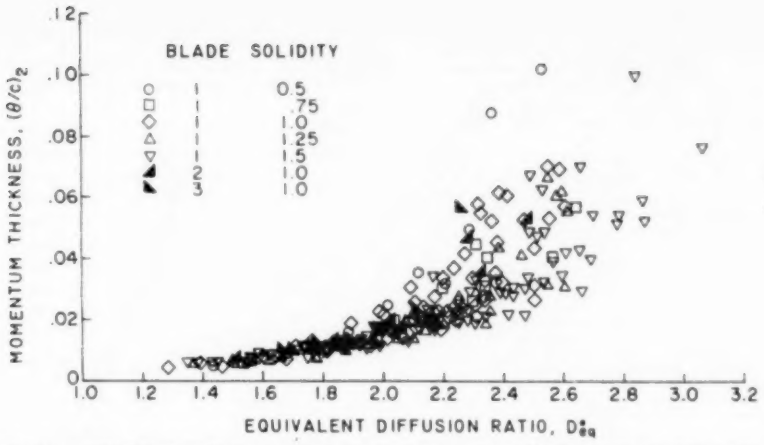

Fig. 12 Correlation of wake momentum thickness with equivalent diffusion ratio for data points at angles of attack greater than minimum loss

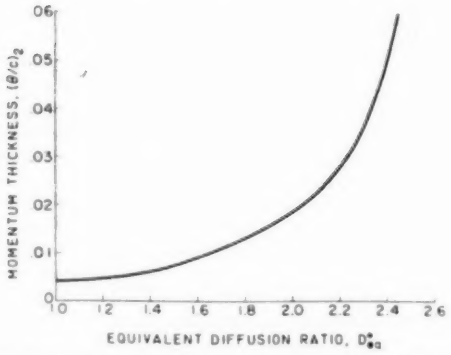

Fig. 13 Representative variation of wake momentum thickness with equivalent diffusion ratio at minimum-loss angle of attack used in calculations of cascade loss variations

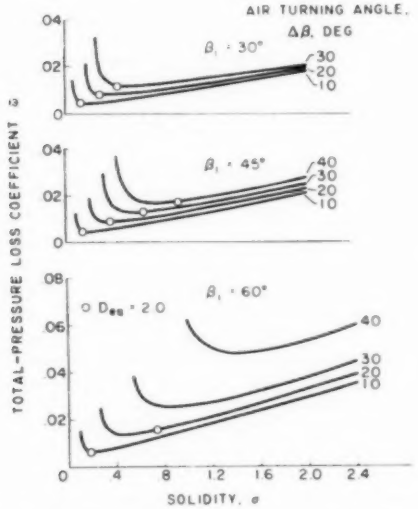

Fig. 14 Calculated variation with solidity of low-speed total-pressure loss coefficient at minimum-loss angle of attack for conventional cascade blades of 0.10 maximum thickness ratio

ever, the correlations at both minimum-loss and greater angles of attack indicated that blade stall can occur for values of equivalent diffusion factor greater than about 2.

Sample Calculations. The loss in total pressure of a given blade design at minimum loss can be computed from Equation (11) if a representative variation of $(\theta/c)_2$ with $D_{eq}{}^*$ is established as in Fig. 13 (obtained as representative variation of Fig. 11). Illustrative calculations of the variation of minimum-loss total-pressure-loss coefficient $\bar{\omega}$ with blade solidity σ obtained from this curve are shown in Fig. 14 for a range of values of air inlet angle β_1 and air turning angle $\Delta\beta^*$. The sharp rise in loss coefficient at the lower solidity values in Fig. 14 is a result of the rapid increase in diffusion ratio as solidity is reduced. The circles on the curves indicate the points at which the equivalent diffusion ratio is equal to 2. (At $\beta_1 = 60$ deg, $D_{eq}{}^*$ is greater than 2 at all solidities for $\Delta\beta$ values of 30 and 40 deg.)

The equations developed for equivalent diffusion ratio can also be used to obtain an estimate of the low-speed unstalled range of operation of conventional cascade blades. At the stalled condition, from Equation (14)

$$D_{eq,\,st} = \frac{\cos\beta_{2,\,st}}{\cos\beta_{1,\,st}}\left[1.12 + a(\alpha_{st} - \alpha^*)^{1.43} + 0.61\,\frac{\cos^2\beta_{1,\,st}}{\sigma}\,(\tan\beta_{1,\,st} - \tan\beta_{2,\,st})\right] \quad (16)$$

where $(\alpha_{st} - \alpha^*)$ is the angle of attack range from reference minimum loss to positive stall, hereinafter called the half range. For cascade operation at fixed air inlet angle, the equivalent diffusion ratio at stall can be expressed in terms of conditions at minimum loss [from Equation (15)] as

$$D_{eq,\,st} = \frac{\cos\left[\beta_2{}^* - \dfrac{d(\Delta\beta^*)}{d\alpha}\,(\alpha_{st} - \alpha^*)\right]}{\cos\beta_1{}^*}\left\{1.12 + a(\alpha_{st} - \alpha^*)^{1.43} + 0.61\,\frac{\cos^2\beta_1{}^*}{\sigma}\left[\tan\beta_1{}^* - \tan\left(\beta_2{}^* - \frac{d(\Delta\beta^*)}{d\alpha}\,(\alpha_{st} - \alpha^*)\right)\right]\right\} \quad (17)$$

Thus, for a fixed value of $D_{eq,\,st}$ and given values of $\beta_1{}^*$ and σ, the half range $(\alpha_{st} - \alpha^*)$ can be computed as a function of $\beta_2{}^*$, and consequently $\Delta\beta^*$. Calculated variations of half range with

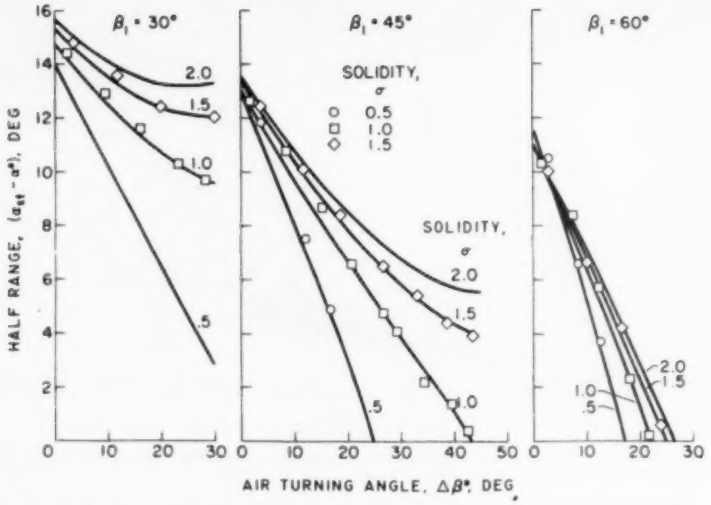

Fig. 15 Calculated variation with minimum-loss air turning angle of low-speed half range from minimum loss to positive stall for conventional cascade blades of 0.10 maximum thickness ratio. Data points for NACA 65(A_{10}) blades.

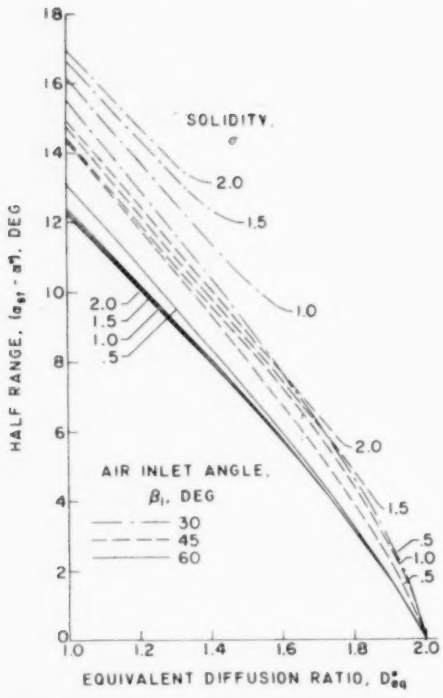

Fig. 16 Calculated variation of half range from minimum loss to positive stall with equivalent diffusion ratio at minimum loss for conventional cascade blades of 0.10 maximum thickness ratio

$\Delta\beta^*$ and σ are shown in Fig. 15 for $D_{eq,st} = 2$ and $a = 0.0117$. Also shown in the figure for comparison are values of half range determined from calculations of D_{eq} against α for individual blades from [1].

The unstalled half range can also be determined as a function of the diffusion level at minimum loss, since D_{eq}^* [Equation (13)] can be computed from the quantities in Equation (17). Plots of $(\alpha_{st} - \alpha^*)$ against D_{eq}^* for $D_{eq,st} = 2$ and $a = 0.0117$ are shown in Fig. 16 to illustrate the effect of minimum-loss or "design" diffusion on unstalled range at fixed air inlet angle.

It is thus seen that, when the correlation parameters of wake momentum thickness and diffusion ratio are used as suggested by the derived equation, a significant prediction of the loss and stall characteristics of conventional blade section can be obtained. These correlations can be used for generalized studies for design optimization and initial blade selection. However, when specific data exist, it would be well to recheck the resulting design in terms of the actual data for the section.

Summary

Application of the boundary-layer momentum equation to conventional cascade blades has shown, through several simplifying approximations, that the blade wake momentum thickness can be expressed as a primary function of the ratio of maximum surface velocity to outlet velocity (diffusion ratio). Analysis of available experimental data for the NACA 65-series and British C.4 circular-arc blades in terms of measuring-station wake momentum thickness $(\theta/c)_2$ and suction-surface diffusion ratio $V_{max.s}/V_2$, as suggested by the derivation, produced a significant loss correlation at minimum-loss angle of attack that was essentially independent of solidity, air inlet angle, and blade camber. It was further shown that the experimental data variation can be reasonably described by the derived approximate relation between momentum thickness and diffusion ratio.

Inasmuch as the two secondary factors derived in the momentum thickness equation were determined by the blade friction coefficient and the type of boundary-layer flow, it was possible to gain an insight into the qualitative effects on the momentum-thickness diffusion-ratio variation of such factors as blade-chord Reynolds number, transition location, and extent of local laminar separation. Illustrative calculations made for ranges of values of friction coefficient and transition behavior showed that a wide range of curves of momentum thickness against diffusion ratio can be obtained for different boundary-layer histories. These results indicated that for maximum allowable values of suction-

surface diffusion ratio (value above which $(\theta/c)_2$ becomes excessive), blades should be designed for low friction coefficient (high Reynolds number and low relative surface roughness) and minimum laminar flow (high Reynolds number and high free-stream turbulence).

The experimental correlation between wake momentum thickness and suction-surface diffusion ratio was made applicable for conventional blade-design use by empirically establishing an equivalent diffusion ratio expressible in terms of only the design velocity triangle and the blade solidity. The possibility of blade stall at minimum loss and greater angles of attack, as evidenced by a sharp rise in wake momentum thickness, occurred when the equivalent diffusion ratio attained a value of about 2. With the use of the equivalent diffusion ratio, calculations were made of the total-pressure loss and unstalled range of operation of conventional cascade sections as functions of solidity, air inlet angle, and air turning angle.

APPENDIX

For partly laminar and partly turbulent flow, the flat-plate friction coefficient is given by [from 6, p. 434],

$$C_f' = C_{f,\,\mathrm{tb}}' - \left(\frac{x}{c}\right)_{\mathrm{tr}} (C_{f,\,\mathrm{tb}}^{**} - C_{f,\,\mathrm{lm}}^{**}) \qquad (18)$$

where $(x/c)_{\mathrm{tr}}$ is the extent of the laminar region, $C_{f,\,\mathrm{tb}}'$ is the turbulent total friction coefficient based on the chord-length Reynolds number, and $C_{f,\,\mathrm{lm}}^{**}$ and $C_{f,\,\mathrm{tb}}^{**}$ are the laminar and turbulent total friction coefficients, respectively, based on the Reynolds number at $(x/c)_{\mathrm{tr}}$.

In order to obtain an equation in which all friction coefficients are based on blade-chord Reynolds number, use is made of the general relations [6, pp. 108 and 433]

$$C_{f,\,\mathrm{lm},\,x}' = \frac{1.328}{\sqrt{\mathrm{Re}_{c\cdot x}}} \quad \text{and} \quad C_{f,\,\mathrm{tb},\,x}' = \frac{0.074}{\sqrt[5]{\mathrm{Re}_{x\cdot x}}}$$

to give

$$C_{f,\,\mathrm{lm}}^{**} = \frac{C_{f,\,\mathrm{lm}}'}{\sqrt{\left(\frac{x}{c}\right)_{\mathrm{tr}}}} \quad \text{and} \quad C_{f,\,\mathrm{tb}}^{**} = \frac{C_{f,\,\mathrm{tb}}'}{\sqrt[5]{\left(\frac{x}{c}\right)_{\mathrm{tr}}}}$$

Substitution in Equation (18) then yields, for partly laminar and partly turbulent flow

$$C_f' = C_{f,\,\mathrm{tb}}'\left[1 - \left(\frac{x}{c}\right)_{\mathrm{tr}}^{4/5}\right] + C_{f,\,\mathrm{lm}}'\left(\frac{x}{c}\right)_{\mathrm{tr}}^{1/2} \qquad (19)$$

where $C_{f,\,\mathrm{tb}}'$ and $C_{f,\,\mathrm{lm}}'$ are obtained for the blade-chord Reynolds number in question.

References

1 L. J. Herrig, J. C. Emery, and J. R. Erwin, "Systematic Two-Dimensional Cascade Tests of NACA 65-Series Compressor Blades at Low Speeds," NACA TN 3916, 1957. (Supersedes NACA RM L51G31.)

2 G. F. Wislicenus, "Fluid Mechanics of Turbomachinery," McGraw-Hill Book Co., Inc., New York, N. Y., 1947, p. 345.

3 S. Lieblein, F. C. Schwenk, and R. L. Broderick, "Diffusion Factor for Estimating Losses and Limiting Blade Loadings in Axial-Flow Compressor Blade Elements," NACA RM E53D01, 1953.

4 M. Savage, "Analysis of Aerodynamic Blade-Loading Limit Parameters for NACA 65($C_{10}A_{10}$)10 Compressor-Blade Sections at Low Speeds," NACA RM L54L02a, 1955.

5 S. Lieblein, "Analysis of Experimental Low-Speed Loss and Stall Characteristics of Two-Dimensional Compressor Blade Cascades," NACA RM E57A28, 1957.

6 H. Schlichting, "Boundary-Layer Theory," McGraw-Hill Book Co., Inc., New York, N. Y., 1955.

7 A. R. Felix and J. C. Emery, "A Comparison of Typical National Gas Turbine Establishment and NACA Axial-Flow Compressor Blade Sections in Cascade at Low Speed," NACA TN 3937, 1957. (Supersedes NACA RM L53B26a.)

8 F. G. Blight and W. Howard, "Tests on Four Aerofoil Cascades. Pt. I—Deflection, Drag, and Velocity Distribution," Rep. E.74, Aero. Res. Labs., Dept. Supply, Melbourne (Australia), July, 1952.

9 S Lieblein and W. H. Roudebush, "Low-Speed Wake Characteristics of Two-Dimensional Cascade and Isolated Airfoil Sections," NACA TN 3771, 1956.

10 S. Lieblein and W. H. Roudebush, "Theoretical Loss Relations for Low-Speed Two-Dimensional-Cascade Flow," NACA TN 3662, 1956.

11 W. Tillman, "Investigation of Some Particularities of Turbulent Boundary Layers on Plates," British Reps. and Translations No. 45, March, 1946.

12 K. F. Rubert and J. Persh, "A Procedure for Calculating the Development of Turbulent Boundary Layers Under the Influence of Adverse Pressure Gradients," NACA TN 2478, 1951.

13 A. E. von Doenhoff and N. Tetervin, "Determination of General Relations for the Behavior of Turbulent Boundary Layers," NACA Rep. 772, 1943. (Supersedes NACA WR L-382.)

DISCUSSION

H. C. Eatock[7]

The author is to be congratulated on his ingenious and useful work. He has had to make a number of simplifying assumptions while carrying his calculations through quite a few steps. His work is very well repaid by the excellent experimental agreement he has achieved!

For designers working with a body of experimental cascade results this paper will be useful in confirming observed trends and in extrapolating beyond the test limits. The curves of unstalled-incidence range against blade loading, Fig. 16, are immediately useful. They show at once that, even for low-speed compressors, the operating range narrows as the design is changed to higher work per stage.

The writer's company has been collecting cascade data since 1948.[8] Most of our results have been on basic C7, C4, or two-arc compressor cascades, and on T6 turbine cascades. Our aim has been to cover the entire operating field including inlet Mach number up to about 1. We have tested literally hundreds of configurations on a fairly high-speed basis. Inlet conditions are controlled by upstream air injection and a large number of blades are tested in each cascade. No suction is applied on the walls of the blade passage so that boundary-layer build-up on these walls causes the axial velocity to increase through the cascade in a similar manner to the early stages of a compressor. Thus we are quite interested in comparing our results with NASA data deduced using fully two-dimensional tests.

The loss curves of Fig. 14 check well with the analysis of our data. We have covered solidities from 2.0 to 0.5 so we cannot check the stalls occurring at very low solidities. All the other trends were checked and with absolute values of loss coefficient usually within ±0.005 of the author's predicted values.

The limit $D_{eq}^* = 2.0$ is of particular interest to the writer. This can be taken as a load function which, if exceeded, predicts a bad cascade. During our early testing we found some of these bad cascades. The writer developed several loading functions which distinguished the bad cascades from their brothers. One of these was

$$C_{l_{\mathrm{rms}}}\sqrt{\sigma} \leq 2.0$$

where

[7] Preliminary Aerodynamics Analyst, Orenda Engines Limited, Malton, Ontario, Canada.

[8] F. H. Keast, "High-Speed Cascade Testing Techniques," TRANS. ASME, vol. 74, 1952, p. 685.

$$C_{l_{2m}} = \frac{2}{\sigma} (\tan \beta_{1m} - \tan \beta_2) \frac{\cos^2 \beta_2}{\cos \beta_{2m}}$$

and the vector mean angle, β_{2m} is from

$$\tan \beta_{2m} = {}^1/_2(\tan \beta_1 + \tan \beta_2)$$

$C_{l_{2m}}$ is the lift coefficient based on vector mean direction and outlet velocity and is borrowed from Howell.[9] $C_{l_{2m}}$ is taken at that incidence which gives the maximum limiting (stalling) Mach number. This incidence is reasonably close to the author's minimum-loss incidence except at very low staggers. It was found, entirely empirically, that, if this loading function was greater than 2, the cascade would be marginal and, if it was greater than 2.2, it would be bad. The intriguing thing is that $C_{l_{2m}}\sqrt{\sigma} = 2.0$ gives limits very close to $D_{eq}^* = 2.0$. The author's loading function thus agrees very well with our test results. This function was developed in early 1953 and covered blades up to 50 deg camber over solidities from 2.0 to 0.5. Our testing since then has not shown up any cascade which violates this rule. The agreement between the author's rule, solidly based on theory, and this purely empirical one is remarkable in that it extends to solidities well beyond those tested.

A brief check of the author's theory with our test results has shown excellent agreement. This is a further check on his results and also shows that the NACA 65 series and the C7 profile are comparable as far as minimum loss and ultimate loading are concerned.

J. F. Klapproth[10]

The author is to be commended on this extension and improvement of his original diffusion parameter. The paper is clearly written and well organized, characteristic of the high standards the author has established in all of his reports.

The use of a diffusion parameter to evaluate proposed compressor designs and assist in the analysis of performance is, of course, common practice. The earlier diffusion parameter or *D*-factor of the author was quickly accepted and very widely used among all designers as a primary design and analysis tool. We can anticipate that this latest contribution will be as quickly and as widely used.

Most useful applications of the diffusion-parameter concept are concerned with the compressor rather than the cascade. Reference [5] of the paper, also by the author, contains a brief consideration of the deviations from the cascade that will exist in the compressor. He lists these as compressibility, changes in axial velocity across the blade row, change in radius across the blade, secondary flows, spanwise boundary-layer flows, end effects, and so on. These, of course, should be considered whenever possible. The writer's comments are concerned primarily with accounting in an approximate manner for the effects of changes in axial velocity and radius through the blade row, in an effort to make the proposed diffusion parameter more directly applicable to compressors.

As reference [5] points out, the change in outlet velocity for a change in axial velocity can be corrected by

$$\frac{V_1}{V_2} = \frac{\cos \beta_2 V_{x1}}{\cos \beta_1 V_{x2}}$$

However, for a given inflow and outflow angle, a change in axial velocity also results in a change in circulation. Similarly, a change in radius through the blade row will change the circulation. By following the suggestion of reference [5], the circulation parameter is written as:

$$\frac{\cos^2 \beta_1}{\sigma} (\tan \beta_1 - \tan \beta_2) \equiv \frac{\cos^2 \beta_1}{r_1 \sigma V_{x1}} (r_1 V_{u1} - r_2 V_{u2})$$

where V_u is the absolute tangential component. When a change in axial velocity or radius is assumed, the equation takes the following form:

For stators,

$$\frac{\cos^2 \beta_1}{\sigma} (\tan \beta_1 - \tan \beta_2) \equiv \frac{\cos^2 \beta_1}{\sigma} \left(\tan \beta_1 - \frac{r_2}{r_1} \frac{V_{x2}}{V_{x1}} \tan \beta_2 \right)$$

For rotors,

$$\frac{\cos^2 \beta_1}{\sigma} (\tan \beta_1 - \tan \beta_2) \equiv \frac{\cos^2 \beta_1}{\sigma} \left[\tan \beta_1 - \frac{r_2}{r_1} \frac{V_{x2}}{V_{x1}} \tan \beta_2 - \frac{\omega r_1}{V_{x1}} \left(1 - \frac{r_2^2}{r_1^2} \right) \right] \quad (20)$$

The effect of the change in circulation caused by changes in axial velocity and radius will result, of course, in a change in the velocity around the airfoil. If it is assumed that the resultant velocity distribution is similar to that for an airfoil with an increased camber to produce the same absolute circulation, then Equation (20) can be used to express the circulation parameter. The expression for equivalent diffusion ratio corresponding to Equation (13) of the paper, but accounting for changes in axial velocity and radius in an approximate manner, would then be

$$D_{eq}^* = \frac{\cos \beta_2}{\cos \beta_1} \frac{V_{x1}}{V_{x2}} \left[1.12 + 0.61 \frac{\cos^2 \beta_1}{\sigma} K \right]$$

where

$$K = \tan \beta_1 - \frac{r_2}{r_1} \frac{V_{x2}}{V_{x1}} \tan \beta_2 - \frac{\omega r_1}{V_{x1}} \left(1 - \frac{r_2^2}{r_1^2} \right)$$

For stators, ωr is, of course, zero.

In view of the undoubtedly wide application that this latest work of the author will find, it is hoped that it will soon be extended to account for compressibility effects.

L. H. Smith, Jr.[11]

The author is to be commended for an excellent application of basic scientific principles to a down-to-earth engineering problem.

In this discussion the writer will use the results found by the author to calculate the efficiency of certain ideal compressor stages. All of the stages considered here are so-called repeating stages, made up of one rotor and one stator with stator-discharge conditions the same as rotor-inlet conditions. All blade rows operate at the reference minimum-loss condition. The blade rows are spaced far enough apart axially so that there is no unsteady interference between them, but the loss assigned to each row is taken as only that which has occurred up to the cascade-outlet measuring station so that Equation (11) can be used. Equation (13) and Fig. 13 are then used with Equation (11) to relate the blade-row losses to the stage-velocity-diagram properties and the solidities. The stage efficiency is defined here as

$$\eta = \frac{(\text{work input}) - (\text{rotor loss}) - (\text{stator loss})}{\text{work input}}$$

The work input is taken as proportional to the product of rotor-blade speed and change across the rotor of tangential velocity, according to the Euler equation of turbomachinery.

Since the author has shown that the equivalent diffusion ratio

[9] A. R. Howell and A. D. S. Carter, "Fluid Flow Through Cascades of Aerofoils," NGTE, R6, 1946.

[10] Supervisor, Compressor Development Unit, General Electric Company, Cincinnati, Ohio.

[11] Compressor Aerodynamicist, General Electric Company, Cincinnati, Ohio. Assoc. Mem. ASME.

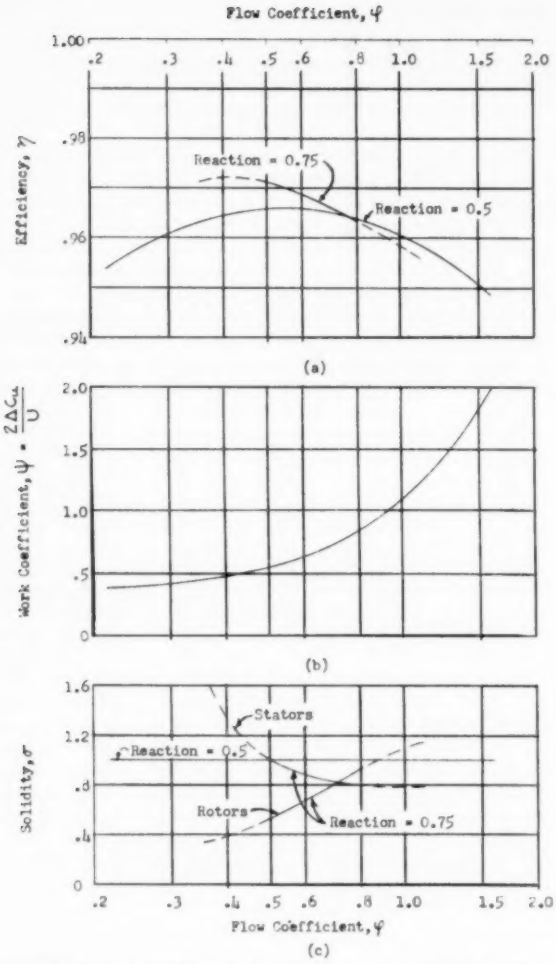

Fig. 17 Properties of stages having $D_{eq}^* = 1.64$. Dashed lines are extrapolations into regions not completely covered by cascade tests.

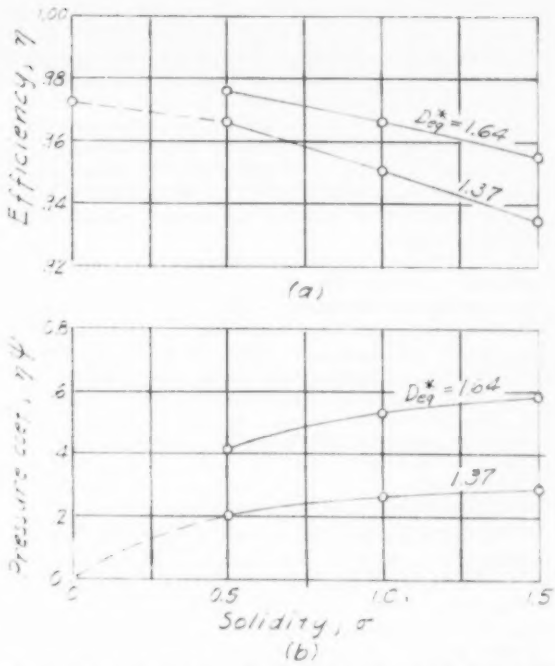

Fig. 18 Effect of solidity on efficiency and pressure coefficient. Reaction ratio = 0.5 and flow coefficient = 0.5.

is a good measure of the aerodynamic loading and range capabilities of a cascade, it is of interest to compare different stages while holding this parameter fixed. We then have three further independent quantities that can be varied; e.g., flow coefficient (ratio of axial velocity to blade speed), reaction ratio (ratio of static pressure rise in the rotor to that in the whole stage), and either rotor or stator solidity.

In the first study that was made the equivalent diffusion was fixed at a moderate value, $D_{eq}^* = 1.64$. A reaction ratio of 0.5 (symmetrical stages) was chosen and a solidity of unity was used for both rotors and stators. The resulting variation of efficiency with flow coefficient is shown in Fig. 17(a), herewith. It is seen that the efficiency is maximum at a flow coefficient of about 0.55. This is in surprisingly good agreement with the classical method of C. Keller which predicts, based on the assumption of constant drag/lift ratio, that the optimum flow coefficient is just under 0.5. In Fig. 17(b), the work coefficient (the ratio of twice the work input to the squared blade speed) that results from these assumptions is shown.

The effect of reaction ratio was studied by designing stages with 75 per cent reaction to have the same work coefficients as the 50 per cent reaction stages for the same flow coefficients. Since the same D_{eq}^* was maintained also, the rotor and stator solidities were no longer unity. The values of these solidities are shown in Fig. 17(c) and the derived efficiency variation is given in Fig. 17(a). It is interesting to note that for the lower flow coefficients the 75 per cent reaction blading is more efficient than the symmetrical blading. This occurs because the solidity has been significantly reduced in the rotor, and the consequent reduction in drag/lift ratio overshadows the effect of the less-favorable skewed velocity diagram.

In order to investigate separately the effect of solidity on efficiency, 50 per cent reaction stages having a flow coefficient of 0.5, $D_{eq}^* = 1.64$, and solidities of 0.5 and 1.5, were examined for comparison with the previously discussed stages with unity solidity. The result is a plot of efficiency versus solidity, Fig. 18(a). The drop-off in efficiency with increasing solidity is seen to be quite significant (the 100 per cent efficiency line is a pertinent reference). Also shown in Fig. 18(a) is a line for stages designed to have $D_{eq}^* = 1.37$. These stages have about 50 per cent more angle-of-attack range than the others.

The point at zero solidity requires further explanation. It was determined that the author's Equation (12), giving the ratio of maximum surface velocity to inlet velocity, was not applicable at solidities near zero. This was determined by expressing the author's circulation parameter in terms of lift and drag coefficients in order to remove the solidity, and then noting that the flow angle β continued to exert a significant influence on the expression. Since at zero solidity the result obviously must be independent of flow angle, it was concluded that it would be dangerous to use Equation (12), and hence Equation (13), when the solidity was lower than 0.5, the lowest value used in the correlation. Instead, the Bogdonoff measurements[12] were used to determine a relationship between lift coefficient and diffusion

[12] S. M. Bogdonoff and H. E. Bogdonoff, "Blade Design Data for Axial-Flow Fans and Compressors," NACA ACRL5F07a, L-635, July, 1945.

ratio. (In that memorandum[12] tests of isolated airfoils of high camber are reported.) For a diffusion ratio of 1.37, a lift coefficient of 0.81 was found, and use of Fig. 13 led to a drag coefficient of 0.0116. The resulting efficiency of 97.22 per cent is plotted in Fig. 18(*a*) and is connected to the rest of the points with a broken line. This efficiency is seen to be lower than an extrapolation of the solid curve would indicate. The zero-solidity point was not calculated for $D_{eq}^* = 1.64$ because the highest camber tested by the Bogdonoffs[12] ($C_{L\,0} = 1.8$) was not sufficiently high to reach that diffusion value at the (estimated) reference minimum loss condition.

Fig. 18(*b*) displays the pressure coefficients for the stages whose efficiencies are shown in Fig. 18(*a*). The conclusion to be drawn from these figures is that the use of solidities much above unity is difficult to justify because only slightly higher pressure coefficients are obtained, but significantly lower efficiencies are suffered. It also appears that range comes at a high price; the 50 per cent increase in range obtained by decreasing the equivalent diffusion ratio from 1.64 to 1.37 caused the loss, i.e., $1 - \eta$, to increase by 45 per cent and the pressure coefficient to decrease by 50 per cent.

Walter C. Swan[13]

I wish to congratulate the author for the outstanding contribution this paper constitutes in the area of axial flow compressor design and performance analysis. This new technique of correlating blade element loading with viscous and wake mixing losses offers the compressor designer an extremely practical tool for achieving approximate complete radial equilibrium solutions for real flows in both the direct and inverse problems.

This writer has applied Mr. Lieblein's wake momentum thickness-equivalent diffusion concept to statistical correlations of both rotor and stator row element data and achieved similar characteristic curves to those discussed by Mr. Lieblein in the two-dimensional cascade case. It was found possible to obtain modifications to these curves for such items as compressibility and position along the blade span. Applying these results to a single stage design, using iterative techniques in a digital computer, yielded results which were very accurately reproduced on actual test. Off design performance was also found to be closely predictable, when applying the author's techniques to a stream filament performance method. Rotating stall was observed by hot wire on test when the calculated equivalent diffusion reached a magnitude of approximately 2.20.

I am sure that those who are involved with the task of designing axial flow compressors which must accurately achieve both a specified design condition and a required range will find this paper to be a real milestone toward the practical design of turbomachines.

[13] Supervisor, Staff Engineering, Transport Division, Boeing Aircraft Corpo ration, Renton, Wash.

Author's Closure

It is indeed gratifying for a researcher to learn of the corroboration of his theory or of the application of his results to practical design studies. In this respect, the comments of Messrs. Eatock, Klapproth, Smith, and Swan are received with sincere appreciation.

The agreement found with the extensive cascade investigations mentioned by Mr. Eatock is considered quite significant in that it reveals an essential similarity in the minimum loss and loading limit characteristics of conventional cascade sections. It is intriguing indeed that the magnitude of the loading parameter $C_{L\,\text{lim}}$ used by Mr. Eatock is very nearly the same as the derived stalling equivalent diffusion ratio, D_{eq}^*. Although the theoretical equivalence of the two parameters is not immediately obvious, their numerical near equivalence can readily be illustrated by sample calculations of limiting cascade velocity triangles as indicated in the following table:

β_1	σ	$\Delta\beta$	D_{eq}^*	$C_{L\,\text{lim}}$
45	0.5	24.77	2.00	1.91
45	1.0	43.18	2.00	2.17
60	0.5	17.14	2.00	2.03
60	1.0	22.14	2.00	1.91

The extension of the equivalent diffusion ratio to include changes in radius and axial velocity across the blade row derived by Mr. Klapproth is most welcome, and the author shares his hope for the ultimate inclusion of compressibility and other compressor effects. In this respect, it is interesting to find, from Mr. Swan's comment, that such an application of the diffusion ratio in the prediction of test results from an actual compressor single stage has proved useful.

The results achieved by Mr. Smith in his evaluations of compressor stage performance based on the diffusion ratio are indeed enlightening, and the author is in agreement with the derived conclusions. In particular, attention is called to his result showing high efficiencies for the higher design D_{eq}^*, since it demonstrates that higher blade loading in itself does not necessarily mean lower efficiency. The crux of the matter is the comparative rates of increase of work input and losses as diffusion ratio is increased.

The author is grateful to Mr. Smith for the caution concerning the extension of the equivalent diffusion ratio to solidities lower than 0.5. The reason for the difficulty here is that the circulation parameter in the expression for equivalent diffusion ratio is in reality the circulation multiplied by $\cos\beta_1$. Thus the β dependence will remain when the circulation is converted to lift and drag coefficients. The need for the additional β_1 term, as established empirically, is not clear from the physics of the situation. However, the extension to zero solidity devised by Mr. Smith should be entirely adequate.

ROBERT J. LUBICK
LEWIS E. WALLNER
NASA, Lewis Research Center, Cleveland, Ohio

Stall Prediction in Gas-Turbine Engines

From a study of multistage compressors operating in gas-turbine engines the sequence of events which occur during the stall process was determined. By using this information and stage-characteristic curves, it is shown that the compressor stall limit may be computed for any disturbance.

DURING the past several years, an intensive study of gas-turbine engines for aircraft propulsion has been conducted by the NACA at the Lewis Flight Propulsion Laboratory, now the Lewis Research Center of the NASA. One of the most important operating limits, which has been ever present in the running of these machines, is the phenomenon commonly referred to as compressor stall. This general phenomenon of compressor stall produces a host of problems, many of which have busied researchers at several different laboratories in a search for solutions or what we applied research people are prone to term "fixes." For clarification, let us define the compressor stall in which we are most interested as Mr. Stodola did some 30 years ago; that is, "a sudden sending back of the compressed fluid through the compressor and into the atmosphere" [1].[1] By this definition we mean to infer that in this particular paper we are most concerned with the compressor stall that results in surging and thus represents a positive operating limit for the machine. This does not mean that some of the other varieties of stall, such as the rotating type in the low-speed regime, are not important, but rather that the scope of the work presented in this paper is limited to the higher compressor speeds where stall generally results in the violent flow oscillations called compressor surge. Some of the low-speed stall problems are discussed in references [2–5].

Compressor stall that results in surge has been accepted generally as a simultaneous breakdown of flow in all the stages of a multistage compressor. The over-all compressor stall-limit line determined by fuel-flow accelerations of a complete engine has been found to be the same as the stall-limit line obtained on a compressor test rig where the back pressure was slowly increased. However, recently it was discovered that, for very rapid disturbances such as might occur from diffuser buzz or armament firing, the compressor was not stalling on the conventional stall-limit line as obtained on the compressor rig. When the compressor was overloaded very quickly, stalls were obtained both above and below the stall-limit line that had been defined by making slow transients to the stall condition. It was apparent then that the rate of disturbing transient on the sequence of events occurring prior to stall was important to the definition of the compressor stall limit. Newly developed instrumentation and recording techniques made it possible to study transient-stage performance during rapid changes in compressor loading on full-scale gas-turbine engines.

The object of this work then is to obtain a better understanding of the manner in which stall is propagated through the compressor by means of a close study of individual stage action during transients to the compressor stall limit. The knowledge of compressor dynamics is then used to describe an engine model that lends itself to analytical study from which the compressor stall limit can be predicted.

Method

The principal means of obtaining multistage-compressor performance was by a series of altitude chamber tests of full-scale turbojet engines. The installation of a typical engine in a test facility of the Lewis Laboratory is shown in Fig. 1. An engine is pictured in a test chamber where atmospheric and engine operating conditions could be simulated with a high degree of freedom. At each of the instrumentation locations indicated in Fig. 2 comprehensive pressure and temperature measurements were taken and recorded on a high-speed recording oscillograph. Instrumentation technique is of utmost importance to the understanding of the flow phenomena involved during the approach to compressor stall. For a study of the flow process, high-response measurements significant to 0.001 sec must be made not only at the entrance and exit of the machine, but at several intermediate stations.

Fig. 1 Turbojet installation in altitude wind tunnel

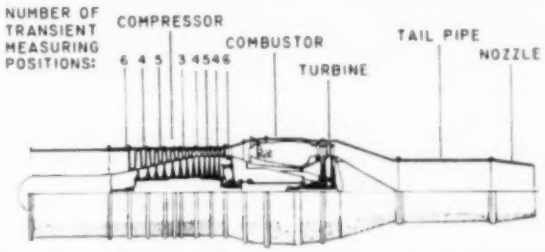

Fig. 2 Engine schematic showing location of transient compressor instrumentation

[1] Numbers in brackets designate References at end of paper.

Contributed by the Fluid Mechanics Subcommittee of the Hydraulics Division and presented at the Annual Meeting, New York, N. Y., November 30–December 5, 1958, of THE AMERICAN SOCIETY OF MECHANICAL ENGINEERS.

NOTE: Statements and opinions advanced in papers are to be understood as individual expressions of their authors and not those of the Society. Manuscript received at ASME Headquarters, August 1, 1958. Paper No. 58—A-133.

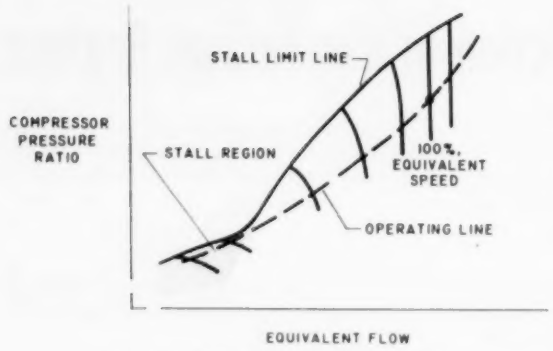

Fig. 3 Typical compressor operating map

The experimental program usually started with mapping the region of "safe operation" of the compressor. This consisted of locating the steady-state operating line in terms of pressure ratio and flow or speed, and then loading the compressor, for instance, by closing the exhaust nozzle slowly, to determine where the compressor was stall limited. The result of such experiments would be a map, such as is shown in Fig. 3, where stall-limit and steady-state compressor pressure ratios are plotted as a function of flow with lines of constant speed. The stall line thus obtained by making slow changes in loading will hereafter be referred to as the quasi-steady-state stall limit. Test experience has shown this stall-limit line to be the same whether obtained on a compressor test rig by making small discharge throttle changes or on a turbojet engine where the loading is increased by making small changes in exhaust-nozzle area.

Compressor Stall Process

Compressor Stall Limit. As a start toward understanding the process occurring during the approach to compressor stall, the quasi-steady-state stall line for a multistage axial-flow compressor is compared with stall points obtained by making fuel-flow throttle bursts in Fig. 4. The time involved from the increase in fuel flow to the point where compressor surging commenced is on the order of 0.2 sec. For changes in compressor loading requiring tenths of seconds, these data indicate the quasi-steady-state stall line to be a good description of the compressor operating limit.

Now let us consider a type of transient that is different from the foregoing in one important respect; namely, instead of requiring several tenths of a second, let us impose inlet pressure or temperature disturbances that can change compressor loading in but a few hundredths of a second. Compressor stalls obtained by such transients are shown in Fig. 5 where compressor operation is again shown in terms of pressure ratio and equivalent speed. From these data it is apparent that, when the approach to stall is rapid, that is, measured in hundredths instead of tenths of a second, the compressor stalls at pressure ratios that do not fall on the quasi-steady-state stall line.

To understand why the rate of loading change affects compressor performance let us examine slow and rapid temperature transients in greater detail. For the slow transient, the inlet and outlet conditions of the compressor can be related to each other by the usual steady-state equations. However, where the transient occurs in a few hundredths of a second, changes occur at the inlet so fast that the usual steady-state relations are no longer valid. This can be better understood by considering the fluid transport time from the front to the rear of the compressor. It takes about 0.02 sec for a change in inlet conditions to be felt at the outlet stage. If the inlet transient then is rapid compared to this time, the first few stages of a compressor may change radically in operating condition, with little or no change at the outlet.

Stage Mismatch. The stage mismatch that can take place in a multi-stage compressor is illustrated by the engine sketch and the experimental compressor temperature curves shown in Fig. 6. This shows a turbojet engine being exposed to an inlet-temperature transient. The temperature-rise rate is 10,000 deg per sec (which incidentally is not unusually high for aircraft flying in the vicinity of armament exhaust gases), and the time for the heated gases to move from the front to the rear of the compressor is 0.02 sec. As a result, in 0.02 sec after the initiation of the transient, the inlet temperature will have changed from 500 to 700 R. However, since the heated gases have not reached the outlet, the discharge temperature has remained constant, as indicated on the curves at 960 R. It is apparent then that, during the initial phase of a temperature transient, the design relation between the compressor stages is altered considerably, and thus it would be reasonable to expect characteristics different from those obtained when the machine is operating "on-design."

Stage Loading. For a further insight into the stage performance obtained during the approach to stall in a multistage compressor, let us first consider the transients pictured by the oscillograph traces of fuel flow, engine speed, and compressor-discharge pressure in Fig. 7. For the smaller transient (shown on the left of the figure) the engine fuel flow increased from the initial to the final value in about 0.1 sec, after which there was an orderly increase in compressor-discharge pressure and an accompanying rise in engine speed. For the larger increase in fuel flow pictured on the right of Fig. 7, the compressor-discharge pressure rises to a maximum, then suddenly drops off sharply. The decrease in pressure signals a flow breakdown somewhere within the compressor and thus the beginning of the stalling process. This point is called the compressor stall limit and represents a point on the compressor stall-limit line. After the pressure has dropped to a low enough value, flow is re-established and the pressure rises again. At this time, if the fuel flow is not reduced, the compressor again builds up in pressure to the stall point, and the cycle repeats itself in an action commonly referred to as compressor surge.

During the approach to compressor stall, interstage pressure measurements on an expanded time scale are shown in Fig. 8. The traces were obtained at the inlet, 5th, 10th, and exit stages with high-response pressure instrumentation. The pressure probe at the exit indicates the largest increase in pressure prior to the stall. Stall in the figure has been labeled "region of stall inception" because of the greatly expanded time scale; that is, it would be difficult to select a single point on the time scale as being the compressor stall point. It is interesting to observe the steady and rapid increase in pressure in the exit stage up to a maximum where it "tops out" (see point A). As this pressure starts to drop, there is a rapid build-up in pressure measured in stator stage 10. A similar action can then be observed in the upstream stages. This action may be explained as follows: At high rotor speeds a sufficiently large fuel input will load the rear stages until one stage stalls. At this instant there is a rapid drop in airflow through the stalled stage, and, therefore, the airflow through the remaining stages must decrease to readjust to the new operating condition. As the flow is reduced at essentially constant speed, the angle of attack increases until other stages stall. The time required for a given stage to stall will depend on the flow margin between the operating point and the stall point.

Significant changes in stage loading can be determined most readily by evaluating the pressure ratio across individual stage groups during the time stalling progresses through the machine. Histories of the stage-pressure ratios were therefore constructed for several stage groups during the entire acceleration to stall. In Fig. 9 are plotted stage-group pressure ratios as functions of

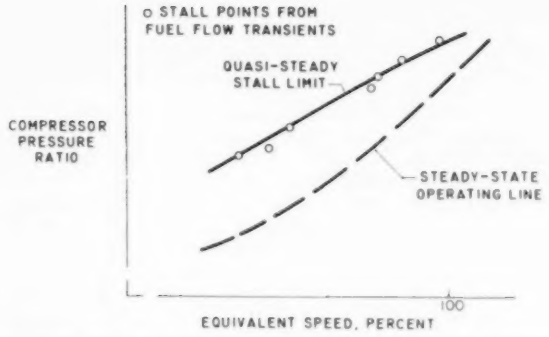

Fig. 4 Comparison of compressor stall points obtained from fuel flow transients with quasi-steady stall limits

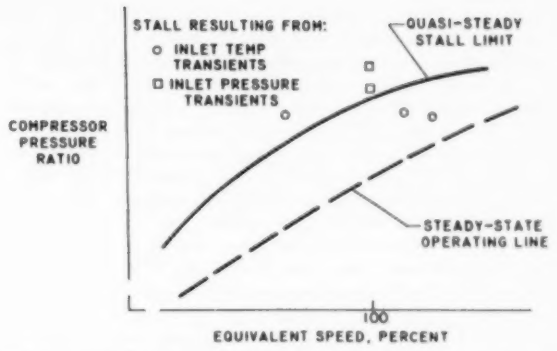

Fig. 5 Comparison of compressor stall points obtained for rapid inlet transients with quasi-steady stall limits

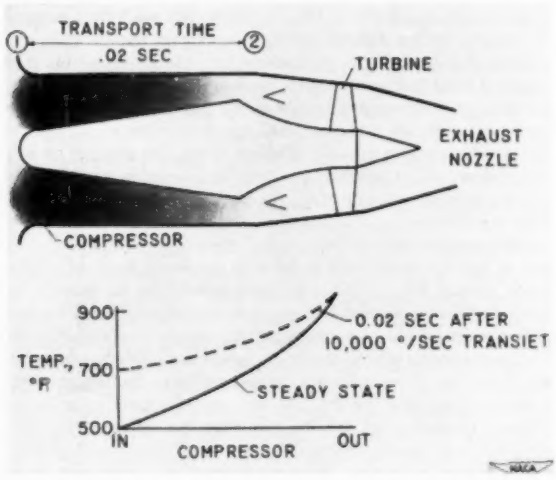

Fig. 6 Effect of rapid inlet-temperature transients on compressor temperatures

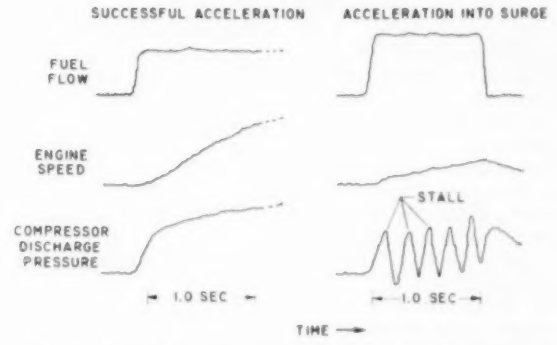

Fig. 7 Variation of engine parameters for fuel-flow accelerations

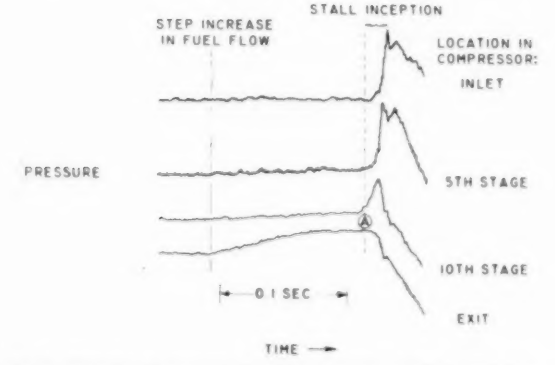

Fig. 8 Behavior of pressures throughout compressor during acceleration into surge

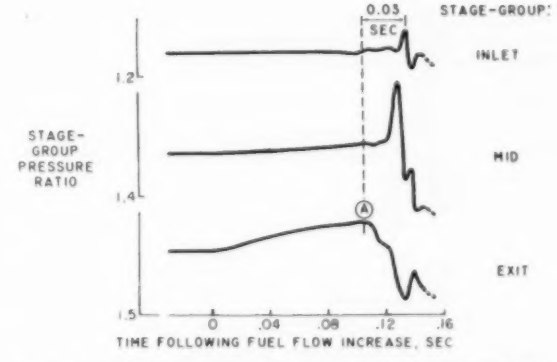

Fig. 9 Variation of stage-group pressure ratio during acceleration into surge

time during the stall process. Prior to the critical point, A in Fig. 9, the maximum loading change takes place in the exit-stage group. It is this group that stalls first, followed in succession by the upstream stages to the inlet. Progression of the stalling process through the compressor requires between 0.02 and 0.03 sec. It is interesting to note that the loading or pressure ratio of the upstream stages does not change materially during the approach to stall of the exit-stage group. Although the stalling of the stage groups is shown here to occur in an orderly fashion, this sequence need not always be consistent. As was pointed out previously, the time required for a given stage to stall will depend on where the stage is operating before the stalling cycle begins. For example, if when a rear stage stalled (causing a flow readjustment through the machine) stage 9 were operating much closer to its critical flow than stage 13, for instance, then stage 9 may stall prior to stage 13. Therefore some stall sequences were observed that were not in the geometric order shown in Fig. 9.

Stage Stall Lines. The stage-group stall points as obtained in Fig. 9 are for a fuel-flow transient initiated at one particular value of engine speed. The stall points resulting from several fuel-flow accelerations initiated over a range of engine speeds were collected and are shown in Fig. 10 as a function of speed. These stall points do not occur simultaneously, but rather in a time sequence as was demonstrated in Fig. 9. For a given stage group, the stall points correlate to a single line in an orderly fashion. The fact that the stage pressure ratio, during an acceleration to the compressor stall limit, rises to a unique value at a given speed and then drops off confirms that this peak pressure ratio is a stall point for that particular stage group. The locus of these peak pressure ratios obtained during the stall process then represents the stall line for that particular stage group.

Also shown in Fig. 10 are the respective stage-group, steady-state operating lines. The difference in pressure ratio between the steady-state operating line and the stall-limit line, commonly referred to as the stall margin, can be noted readily in Fig. 10. At high speeds the exit-stage group has the smallest stall margin, while at low speeds it is the inlet group that has the smallest margin, which is typical of multistage, axial-flow compressors. It is apparent then that the exit stages will stall first at high rotating speeds and that the large stall margin available in the upstream stages suggests the plausibility of a transfer of loading to these earlier stages. At speeds below those shown in Fig. 10, the problem of rotating stall enters the picture, and the analysis of the stage stalling process becomes clouded by strong interaction effects. As mentioned earlier, this paper will not deal with that problem but will be concerned mainly with the higher speed range.

Some of the trends obtained during transient operation can now be explained by reference to the steady-state stage-characteristic curves. Typical characteristic curves plotted in terms of the commonly used pressure and flow coefficients for inlet and exit-stage groups are shown in Fig. 11. The data are from a number of engines having different stage designs and matching to emphasize the similarity in characteristics. As is typical for inlet stages of axial-flow compressors, the loading (pressure coefficient) increases with decreasing engine speed, Fig. 11(A), which is consistent with the decreased stall margin for the inlet group at low speeds shown in Fig. 10. Stalling of the inlet group is usually not violent but is followed by some quasi-steady type of stall pattern such as rotating stall, tip stall, hub stall, and so forth. This is indicated by the fact that the characteristic curves are continuous from normal into stalled operation. Detailed discussion of the low-speed stall problem is presented in [2–5]. Exit-stage groups, Fig. 11(B), are characterized by an increase in loading with increasing speed, again consistent with the decreased stall margin for the exit group at high speeds shown in Fig. 10. The engine-speed effects shown on these characteristic curves result from the flow-continuity requirements in multistage compressors as explained in [6]. At any rate, the peak pressure coefficient, or stall point, for the exit stage is a definite operating limit for it is usually followed by a violent breakdown in flow, which generally signals the beginning of a compressor surge cycle.

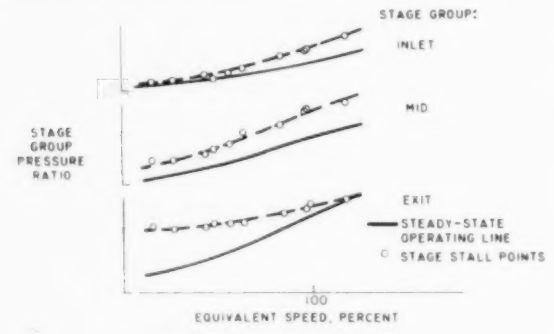

Fig. 10 Stage-group stall limits

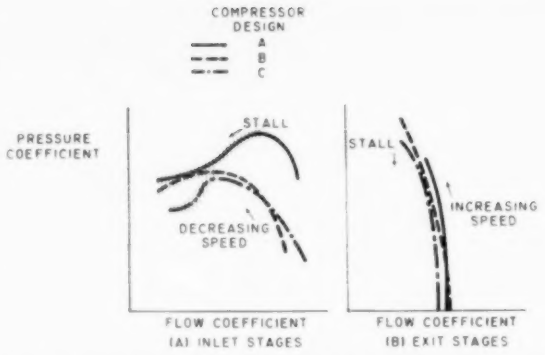

Fig. 11 Typical stage characteristics for inlet and exit-stage groups

Stall Prediction

Stall From Characteristic Curves. The stall point of a stage is a unique value when expressed in terms of pressure coefficient—a nondimensional parameter. That is, a given stage has a single value of pressure coefficient at stall regardless of operating conditions such as rotating speed, inlet pressure, and so forth. By using this singular value of pressure coefficient at the stall point, the variation of stall pressure ratio as a function of speed can be calculated. This relation can be seen by reference to the equation of pressure coefficient:

$$\psi = \frac{3600 g J c_p}{n(\pi d_m)^2} \frac{T_1}{N^2} \left[\left(\frac{P_2}{P_1} \right)^{\frac{\gamma-1}{\gamma}} - 1 \right]$$

where

c_p = specific heat at constant pressure, Btu/lb-deg R
d_m = mean diameter, ft
g = acceleration due to gravity, ft per sec²
J = mechanical equivalent of heat, 778 ft-lb/Btu
N = rotor speed, rpm
n = number of stages in group
P = total pressure, psfa
T = stagnation temperature, deg R
γ = ratio of specific heat
ψ = pressure coefficient

Subscripts:

i = inlet of group of stages
o = outlet of group of stages

For a known value of pressure coefficient ψ and a known variation of stage-inlet temperature T_i, the stage pressure ratio P_o/P_i therefore becomes a function only of engine speed N. Hence from the peak pressure coefficient on a stage-characteristic curve, the stage-stall-pressure-ratio curve can be calculated over the desired speed range. The important question then reduces to whether or not a stage or group of stages stalls at the same pressure ratio when the loading is imposed transiently as compared to the quasi-steady-state condition. To answer this question, the stall line for the exit-stage group was computed from the stage-characteristic curve for a range of speeds and is shown in Fig. 12. Superimposed on this curve are stage stall points obtained during accelerations of the compressor by means of transient increases in fuel flow. During fuel-flow transients, the initial change in compressor loading requires a few tenths of a second because of the inherent lag in the combustion process. However, when one of the stages has been loaded to the stall point, the stage-stalling sequence thereafter is very rapid—requiring but a few hundredths of a second to complete, as was demonstrated by the data in Fig. 8. Stage-stall data obtained in this manner are therefore representative of rapid transients. The good agreement between calculated and experimental stall points indicates that the steady-state characteristic curve for a group of stages is indicative of stage performance during transient engine operation.

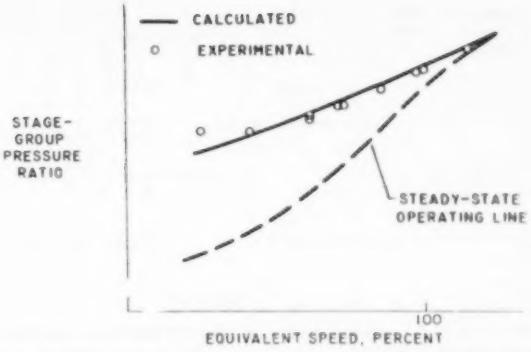

Fig. 12 Comparison of calculated and experimental stage-group stall limits

Concept for Analogy. To construct a practical picture of dynamic compressor operation then, the following observations should be reviewed: That during rapid transients a significant stage mismatch is set up within a multistage compressor, and that the steady-state characteristic curves constitute a usable description of stage performance during transient operation. It is apparent then that it becomes impractical to consider a multistage compressor as a single unit when flow conditions are changing so rapidly within the machine. To handle this component in any engine calculations requires that it be considered in smaller parts, such as single stages, where the entering and leaving conditions are more closely related.

A new picture was conceived for this stage analysis. Ordinarily, if we know the entering conditions to a compressor stage, the leaving conditions can be predicted by means of the stage-characteristic curve that relates the exit pressure and temperature to the inlet pressure, temperature, and flow. For any steady-state or slowly changing transient, the outlet flow can be assumed equal to the inlet flow. However, in the case of a rapid transient, the effect of time on the weight flow must be accounted for. The important thing here is the time required for the fluid to move through the stage. Compressor performance was computed then by selecting the model indicated in Fig. 13, which is a sketch of a single compressor stage followed by a volume. Knowing the stage-entrance conditions, the leaving temperature and pressure can be computed from the design curve. The time lag as a result of fluid transport may be computed by introducing an equivalent stage volume and a mean velocity in series with the stage. If conditions at station 2 are considered to be the stage outlet, the time variation of flow may now be computed. By using this picture, the gas-turbine engine was represented on an analog computer in the form sketched in Fig. 14. The compressor was considered in four parts; the steady-state performance of each part was represented by a stage-characteristic curve, and the dynamic behavior by a suitable volume. The combustor was represented by an equivalent volume, and the turbine by a pressure-flow relation. The details of this calculation method are explained in [7]. Before considering the results of transient performance as obtained by the use of this model and an electronic

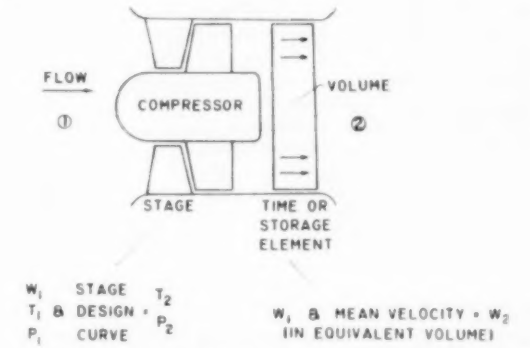

Fig. 13 Concept used for compressor simulation

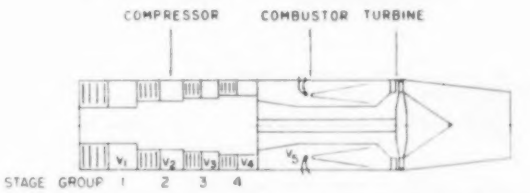

Fig. 14 Engine model used in analog simulation for stall study

analog computer, the response of a multistage compressor to a pressure disturbance should be considered.

Response Characteristics. Pressures measured at the exit of a multistage compressor when the inlet pressure was being varied in a sinusoidal fashion are shown in Fig. 15. When the oscillation frequency is low, Fig. 15(*a*), the pressure measured at the compressor exit is a good facsimile of the inlet pressure, both in frequency and amplitude as shown. The phase shift is small, and the period at the inlet is about the same as at the exit. It is evident then that the lag in the compressor is low during such low-frequency oscillations. Where the inlet pressure frequency is raised to a substantial value, the outlet-pressure oscillations no longer follow the inlet pressure in either phase or amplitude, Fig. 15(*b*). The complete description of the dynamic characteristics of a compressor is defined in what is commonly termed the frequency-response curves, which are simply plots of the pressure-amplitude reproduction and phase shift as a function of inlet-pressure frequency of oscillation. In addition, these curves are a convenient method of comparing the experimental and analytical compressor performance during changes in loading.

The response characteristics of an experimental engine are

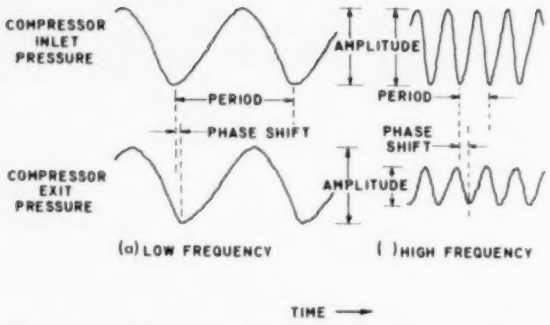

Fig. 15 Relation between compressor inlet and outlet pressure during inlet-pressure oscillations

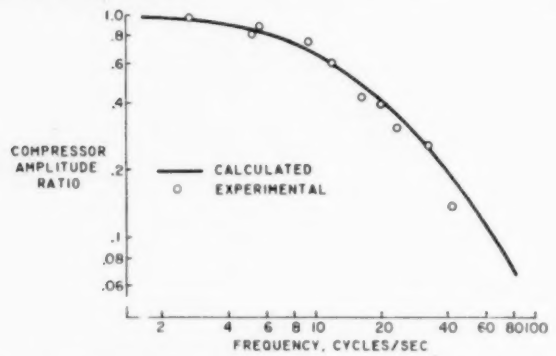

Fig. 16 Compressor frequency response for inlet-pressure oscillations; amplitude ratio

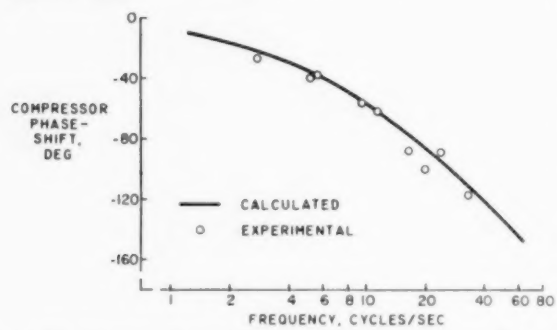

Fig. 17 Compressor frequency response for inlet-pressure oscillations; phase shift

compared with those obtained on an analog computer, with the engine representation previously described, by the curves in Figs. 16 and 17. It can be seen that both the phase-shift and amplitude-ratio data obtained on the test engine were reproduced accurately on the computer for inlet pressure oscillations over a wide frequency range. The variation of amplitude ratio with frequency, Fig. 16, indicates the attenuation in pressure as frequency increases. At a frequency of 60 cycles per sec (cps), the amplitude of exit-pressure oscillations is only 10 per cent of the amplitude obtained at low frequencies. This implies that at high frequencies there is essentially little variation in pressure at the compressor exit. Similarly, the phase shift, Fig. 17, increases markedly at higher frequencies and is also indicative of the lag within the compressor. The combination of pressure attenuation and phase shift across the compressor can result in stall. At any

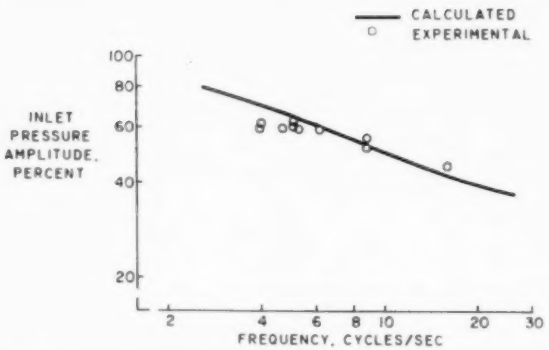

Fig. 18 Comparison of experimental and calculated stall limits for inlet-pressure oscillations

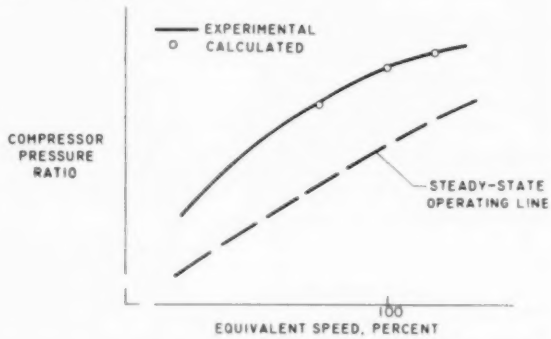

Fig. 19 Comparison of experimental and calculated stall limits for fuel flow transients

rate, the agreement of the calculated and experimental data indicates that engine transients actually can be simulated by means of an analog computer having a suitable description of the engine geometry and the compressor stage-characteristic curves.

Compressor Stall Prediction. Use of this engine-model concept to reproduce transient behavior of the compressor-engine combination for a very practical problem makes itself manifest in the prediction of the compressor stall limit. Two experiments were performed involving the compressor stall limit as obtained by distinctly different approaches. In the first experiment, the pressure at the compressor inlet was oscillated with sufficient amplitude until the stall limit was reached. Stalls were obtained in this manner over a frequency range from 4 to about 17 cps. This problem was then duplicated on the analog computer where the inlet pressure to the simulated engine also was varied up to the point where some stage group was stall limited. The results of these studies are compared in Fig. 18, where inlet-pressure amplitude required for stall is plotted as a function of pressure-oscillation frequency. The calculated inlet-pressure amplitude required for stall agrees reasonably well with the experimental measurements. This is especially apparent when the attainable degree of accuracy of transient-pressure measurements of this type is considered.

The second experiment performed to check the ability to predict the stall limit of the compressor consisted of making transient increases in loading by means of fuel-flow accelerations; that is, the compressor stall limit was established by making numerous increases in fuel flow sufficiently large to stall the compressor over a range of rotating speeds. The process was then duplicated on the simulated engine by introducing temperature increases at the rear of the compressor. It was found that stall points obtained

in this fashion checked the experimental data at several speeds as indicated by the results shown in Fig. 19.

From these experiments then it is apparent that, with a proper description of the engine geometry together with the compressor stage-characteristic curves, it is possible to predict the compressor stall limits. The stall may be computed for disturbances at the front or at the rear of the compressor, whether the rate of loading change is slow or rapid.

Conclusions

In conclusion, it is apparent that the surge process in a multistage compressor is in reality a step-by-step stalling of the individual compressor stages. These stages are stalled at the same critical pressure ratios during quasi-static increases in loading as during very rapid transients in inlet flow. Pressure-ratio limit of the entire compressor is only realistic for relatively slow changes in loading, where the steady-state stage matching is not upset. For rapid transients where a large stage mismatch is set up within the machine, no single compressor stall line is a good description of the operating limit. The transient operation of a multistage compressor operating in a turbojet engine can be simulated accurately by means of a description of the engine geometry and the compressor stage-characteristic curves. Stall may be predicted for disturbances at the front or at the rear of the compressor regardless of the rate of loading change.

Acknowledgment

The efforts of many of the Lewis Laboratory mechanics, computers, and engineers contributed to this paper. In particular the authors are grateful for the guidance received from Messrs. M. J. Saari, W. A. Fleming, D. S. Gabriel, and B. T. Lundin.

References

1 A. Stodola, "Steam and Gas Turbines, vol. II," McGraw-Hill Book Company, Inc., New York, N. Y., 1927, pp. 1265–1266.

2 T. Iura and W. D. Rannie, "Observations of Propagating Stall in Axial-Flow Compressors," Report No. 4, Mechanical Engineering Laboratories, C. I. T., Navy Contract N6-ORI-102, April, 1953.

3 Merle L. Huppert and William A. Benser, "Some Stall and Surge Phenomena in Axial Flow Compressors," *Journal of the Aeronautical Sciences*, vol. 20, 1953, pp. 835–845.

4 H. W. Emmons, C. E. Pearson, and H. P. Grant, "Compressor Surge and Stall Propagation," TRANS. ASME, vol. 77, 1955, pp. 455–467; discussion, pp. 467–469.

5 A. G. Smith and P. J. Fletcher, "Observations on the Surging of Various Low-Speed Fans and Compressors," Memorandum No. M. 219, British NGTE, July, 1954.

6 W. A. Benser and H. B. Finger, "Compressor Stall Problems in Gas Turbine Type Aircraft Engines," Preprint No. 751, SAE, 1956.

7 David S. Gabriel, Lewis E. Wallner, Robert J. Lubick, and George Vasu, "Some Effects of Inlet Pressure and Temperature Transients on Turbojet Engines," *Aeronautical Engineering Review*, vol. 16, September, 1957, pp. 54–59.

DISCUSSION

R. C. Dean, Jr.[2]

The material presented in this paper greatly clarifies the process of complete stall of an axial compressor. The authors are to be complimented for a lucid presentation of a synthesis of results from a long NACA program of axial-compressor research.

The great simplicity and general usefulness of this method depends critically upon the statement that the performance of each stage in the compressor can be reduced to a single universal curve of pressure coefficient versus flow coefficient. This curve is implied to be characteristic irrespective of rotative speed, pressure level, and the rate of change of flow conditions.

Since this generality is so critical to the usefulness of the method offered, it is regrettable that the authors have not documented it with test data or references to test data. Definitions of the expressions used for flow and pressure coefficients are not included in the paper which omission hampers the reader in testing the stated generality against test data available to him. Only after a diligent search was the writer able to find definitions of these terms.[3] Even then the coefficients were not defined in algebraic terms. While the definitions of these coefficients may be commonplace to the authors, they are not to the general reader, particularly since several different definitions are in widespread usage.

The authors do not mention whether the characteristic stage curve is affected by variation of Reynolds number. It is also not clear whether these curves can be measured only in a complete compressor or whether they may be secured from single-stage tests. The writer would presume that single-stage tests would not give the required information as a result of significant interference effects from upstream and downstream stages. One is also tempted to ask whether these interference effects are independent of rotative speed, Mach number, and Reynolds number.

The writer hopes that the authors will clarify and carefully document this important point in their closure of this discussion.

The discussion throughout the paper until the very end is concerned with the *approach* of a compressor to complete stall. No consideration is undertaken of the behavior of the machine when the flow actually reverses during surging. Thus Stodola's definition of stall, which the authors have adopted, is not really applicable to their treatment. Neither will this treatment serve as an analysis of surge with flow reversal. To extend the method to full surge would require performance data for reversed flow through the stage. When such data are required, can they be obtained from a multistage compressor? Do such data also form a single characteristic curve for each stage independent of rotative speed, Mach number, Reynolds number, and so forth?

J. L. Dussourd[4]

The authors are to be congratulated for their detailed analysis of the less obvious aspects of the surge phenomenon in a multistage compressor. They describe and illustrate the process of stall propagation across the stages, helping to create a "feel" for the relative magnitude of the controlling quantities. They also demonstrate that, even with approximate representation of the individual stage performance and individual stall limits, reasonably accurate representation of the transient compressor behavior can be made by means of a simple analog.

The general concepts formulated in this paper lead to various applications beyond those expressed in the paper. They provide, for example, the means for establishing experimentally which stage or which aerodynamic component reaches a surging condition prematurely or belatedly. This can be done by studying the stall sequence, taking due note of the stages that surge out of turn. Proper corrective measures will then increase the compressor operating range. The compressor may thus be "tuned" by readjusting those components which are either under or overloaded.

The writer wishes to raise the question as to whether the data shown in Fig. 10 truly represent stall points for the individual stages or groups of stages. As surge is reached and the exit stages are stalled out one after another, the peak pressures recorded at some intermediate stage may correspond either to the true stage-stall pressure ratio or to some higher pressure present because of the arrival of a strong pressure pulse initiated at the exit of the compressor.

[2] Head, Advanced Engineering Department, Ingersoll-Rand Company, Phillipsburg, N. J. Assoc. Mem. ASME.

[3] NACA RM 56B06, p. 82.

[4] AiResearch Manufacturing Company of Arizona, Phoenix, Ariz.

H. P. Grant[5]

The experimental results presented by the authors answer some fundamental qualitative questions about transient response of gas-turbine engines that have bothered engine designers for some time, and the demonstration of a logical model that generates the same kind of results is helpful. It would appear that the model could be simplified further to eliminate the need for machine computation without sacrificing essential features by substituting for the detailed characteristic curves of compressor-stage groups and turbine a small number of shape parameters that would describe the steady-state characteristic curves in the small region of interest bounded by normal operating line and stall line. If this is the case then the analysis could be more easily applied to such problems as predicting whether a proposed change in design would adversely affect transient response.

Authors' Closure

The authors wish to express their appreciation for the interest, questions, and comments of the discussers.

As Mr. Dean points out, the analysis of compressor behavior after surging has begun is absent from the paper. As implied in the title, it is the approach to and the prediction of stall in compressors operating in gas-turbine engines that interests the authors; the mechanism of flow conditions within the machine after surging and flow reversal has commenced is another problem. The scope of work involved, however, was concentrated in the region of compressor operation where the stall of a stage group inevitably resulted in surging of the compressor with attendant flow reversal.

Although the definitions of pressure coefficient and flow coefficient vary somewhat to suit individual applications, the terms are generally used by researchers in the compressor field (References [2, 5, 8, 9]). As used in this paper, the pressure coefficient (ψ) is defined as the ratio of useful work input to the square of the mean-radius wheel speed. The equation of pressure coefficient, in terms that are readily measurable, is stated in the section entitled, Stall From Characteristic Curves, in the body of the paper. The flow coefficient (ϕ) is defined as the ratio of the inlet axial velocity to the mean-radius wheel speed and can be calculated from

$$\phi = \frac{60R}{\pi d_m A} \frac{W_a T_i}{N P_i}$$

where A = stage-inlet flow area, sq ft
d_m = stage mean diameter, ft
N = rotor speed rpm
P_i = stage-inlet total pressure, lb/sq ft abs
T_i = stage-inlet stagnation temperature, deg R
R = gas constant, 53.3 ft-lb/(lb) (deg R)
W_a = air weight flow lb/sec

[5] Manager, Flow Corporation, Arlington, Mass.

These coefficients are useful as descriptions of stage performance, and for the practical range of compressor operation in gas-turbine engines they are largely independent of Reynolds number, rotative speed, or Mach number variations. This is especially true in the region near the design speed, which was of greatest interest to the authors (Reference [9] page 105).

There are generous amounts of experimental data in the literature on single-stage performance and on multistage compressors. Little information is available, however, on the comparison of the performance of a single isolated stage with the performance of the same stage as part of a compressor. More data of this type are needed before single-stage data can be used to predict the stall conditions of a multistage compressor.

The question raised by Mr. Dussourd is very appropriate. The proof of whether the peak pressure ratio points obtained transiently (Fig. 10) are really the stall points requires comparison with the stage stall point as obtained in a quasi-static fashion. This type of comparison was made for the exit stage group (Fig. 12), which showed agreement, over the speed range covered, between the transient peak-pressure ratios and the quasi-steady stall point of the stage-group characteristic curve. Unfortunately, the quasi-steady stall points of the inlet and midstage groups shown in Fig. 10 were not available. However, calculation of the stage-group pressure coefficient (ψ) from the peak pressure ratio points of Fig. 10 resulted in a single maximum value for a given stage group. This appears to be further evidence that the locus of peak pressure ratio points does represent the stage-group stall line.

The authors appreciate Mr. Grant's concern of simplifying the analytical model in order to reduce machine computation time. It should be stressed here that all the analytical solutions presented in the paper were performed on an electronic analog computer (Reference [7]) and not a digital-type computer. The electronic analog computer is ideal for problems involving a time-dependent solution, such as our case. The nature of the analog computer allowed changes, such as altered stage characteristic curves, relatively easily and gave direct time-dependent results of simulated engine operation.

The stage characteristic curve can be simplified by some linear approximation only if small transient excursions about the operating point are desired. For the solutions of problems up to the stage stall point, however, the location of the initial operating point, the stall point, and the shape of the connecting characteristic curve are all important.

References

8 Frank E. Marble, "Propagation of Stall in a Compressor Blade Row," Technical Report No. 4, GALCIT, January, 1954. (Office Sci. Res., Air Res. and Dev. Command Contract AF 18(600)-178).

9 Members of the Compressor and Turbine Research Division, "Aerodynamic Design of Axial-Flow Compressors, Volume III," Chapter XIII. NACA RM E56B03b, August, 1956. Declassified by authority of Research Abstract, dated September 3, 1958.

H. W. EMMONS

Gordon McKay Professor of Mechanical Engineering, Harvard University, Cambridge, Mass. Mem. ASME.

R. E. KRONAUER

Associate Professor of Mechanical Engineering, Harvard University, Cambridge, Mass.

J. A. ROCKETT

Post-Doctoral Research Assistant, Harvard University; now Assistant Project Engineer, Pratt and Whitney Aircraft, E. Hartford Conn.

A Survey of Stall Propagation—Experiment and Theory

The experimental literature on stall propagation is summarized in terms of an idealized compressor which possesses properties typical of the bulk of published data. The published analyses are examined and all are shown to have one fundamental restriction or another which makes them unable to predict all of the relevant features of stall propagation—most notably the number of stall cells. A relatively simple mathematical model is constructed which offers the possibility of a complete prediction.

DURING the winter of 1949–1950, while working with a single-stage axial compressor at Harvard University, H. P. Grant [1][1] observed a regular, periodic, and relatively simple type of flow pulsation. This particular disturbance, which is now called "stall propagation," had not been reported previously; its importance was recognized immediately. The work which followed this discovery was described by H. W. Emmons at a meeting of the NACA Compressor Subcommittee in the spring of 1951 and, at about the same time, the same type of disturbance was independently recognized by W. D. Rannie at the California Institute of Technology. In September, 1952, W. R. Sears of Cornell University, presented this phenomenon to the scientific public in a paper [17] presented to this Society.[2]

In the 9 years since H. P. Grant first recognized stall propagation, a fairly sizable effort has been made to understand this type of compressor surge. In the following review paper we will summarize the experimental work which has been done by describing the behavior of a hypothetical compressor whose surge characteristics are a composite of the various machines which have been tested. The theoretical work which has been done on stall propagation will be summarized as special cases of a general theoretical formulation. One important feature of stall propagation, the disturbance wave length, cannot be predicted by any of the theories published to date. The general formulation used here, while relatively simple, offers the possibility of determining all of the important features of stall.

Experimental Observations

A number of people working in various parts of the world have studied stall propagation in a variety of machines [1–16]. Rather than reciting here what each experimenter has done, we will describe the stall behavior of a hypothetical research compressor, using a composite of all their experience as a basis for the description. Let us imagine our hypothetical compressor casing as a smooth, annular volume formed by a pair of concentric surfaces of revolution, Fig. 1. At one end the two surfaces flare out and roll back on themselves to form an annular inlet; at the other end the gap between them is covered by an axisymmetric, adjustable throttle. There are no support struts or vanes of any kind inside the annulus between the inlet and throttle nor are there any obstructions outside the casing near enough to its ends to cause any significant disturbance inside the casing. In a constant-diameter section near the inlet, provision has been made for installing in various combinations (*a*) an axial-flow-fan rotor, (*b*) a stator at any of several distances downstream of the rotor, (*c*) inlet guide vanes at any of several stations ahead of the rotor, and (*d*) at various adjustable spacings additional rotors and stators, with accompanying fairings on the inner and/or outer casings to vary the flow area.

As the first experimental configuration let us imagine only a single rotor installed in the casing; there is neither a stator nor an inlet guide-vane assembly. This configuration reproduces as closely as possible the one assumed by all the existing cascade-stall theories. Strictly speaking, such an arrangement has been tested only by Grant [1], Stenning [9], and Kriebel [16]. However, other single-stage tests have approximated this geometry. As a reference for correlating the stall performance of the rotor we choose the conventional performance map; curves of total pressure rise as a function of mass flow for various constant rpm, Fig. 2(*a*). For convenience we also plot a second set of curves on the map—total pressure rise as a function of mass flow for constant throttle setting. If the map were replotted giving the total pressure coefficient

$$C_p = \frac{\text{Total pressure rise across rotor}}{\text{Dynamic pressure corresponding to rotor-tip speed}}$$

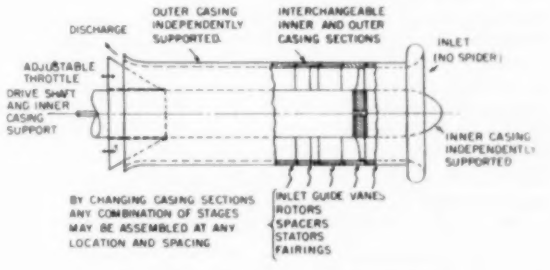

Fig. 1 Hypothetical research compressor

[1] Numbers in brackets indicate References at end of paper.

[2] A chronology of the early work on rotating stall is given in [7].

Contributed by the Fluid Mechanics Subcommittee of the Hydraulics Division and presented at the Annual Meeting, New York, N. Y., November 30–December 5, 1958, of THE AMERICAN SOCIETY OF MECHANICAL ENGINEERS.

NOTE: Statements and opinions advanced in papers are to be understood as individual expressions of their authors and not those of the Society. Manuscript received at ASME Headquarters, September 10, 1958. Paper No. 58—A-150.

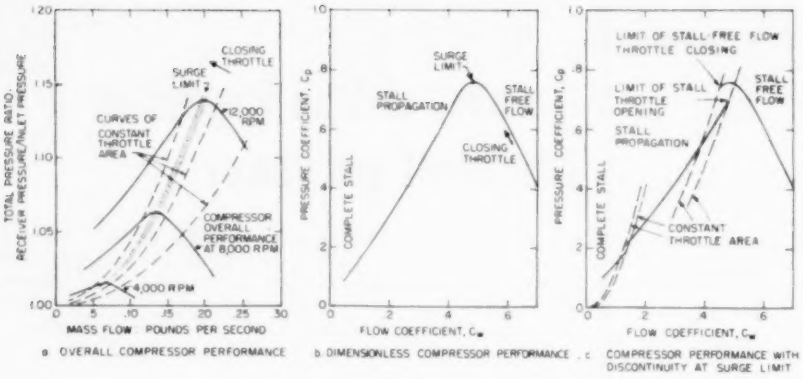

Fig. 2

as a function of the flow coefficient

$$C_w = \frac{\text{Mass flow}}{\text{Flow when mean axial velocity equals tip speed}}$$

constant rpm data for Mach numbers below about 0.4 would collapse approximately to a single curve, and data for any one constant throttle setting to a single point, Fig. 2(*b*). If quite precise measurements were made we probably would find a slight Reynolds-number effect on the surge limit together with some unavoidable data scatter since the pressures throughout the range of surge flows vary irregularly.[3]

The pressure-rise curve at the surge limit might take either of two forms; we could not predict which in advance. In one case the onset of surge is marked by a significant, discontinuous drop in both C_p and C_w, the discontinuity in C_p perhaps exceeding 20 per cent of the peak pressure coefficient, Fig. 2(*c*). The discontinuous drop in pressure at surge inception would occur at a smaller throttle opening than the discontinuous rise in pressure at surge cessation. The $C_p - C_w$ characteristic shows a "hysteresis loop" at the surge limit. The discontinuity in C_w is related to that in C_p since the change in the mode of operation—stable to surge—occurs at constant throttle. In the other case the onset of surge is marked by no significant discontinuity in the pressure rise—mass-flow curve, Fig. 2(*b*). The pressure coefficient reaches a maximum at the surge limit and then falls steadily as the flow is reduced. If there is any discontinuity at all in this case it is very small and has gone undetected.

When a compressor goes into surge the effects can be quite dramatic. The drop in pressure is accompanied by an increase in noise indicative of pulsating air flow and mechanical vibration. Commonly, only a small number of predominant frequencies is superimposed on a high background noise. The lowest frequency components are usually associated with a Helmholtz-type resonance of the machine with its inlet and/or outlet volumes. These may or may not be measurable with conventional pressure probes depending upon the frequency. The higher frequencies, of the order of the rpm, associated with stall propagation, cannot be measured with conventional probes. Thus, until the adaptation of the hot-wire technique to compressor testing, little of a quantitative nature could be learned about the stall operation of rotating machines. When hot-wire anemometer probes and rapid-response pressure transducers are installed at various locations ahead of and behind the rotor, the general flow patterns existing during surge operation can be inferred from their outputs.

The details of the flow below the surge limit are strongly connected with the gross behavior indicated by the pressure-rise curve. They will be considerably different for a blade row which has the performance shown in Fig. 2(*b*) than for one which has the performance shown in Fig. 2(*c*). For the present we will consider the former case. First setting the throttle for operation just on the high flow side of the surge limit, the hot wires indicate a regular pattern of alternating high-velocity jets separated by uniformly narrow blade wakes. In the blade wakes the minimum velocity observed is of the order of half that in the jets. The pressure transducers indicate a nearly constant static pressure rise across the rotor, although there are small amplitude pressure fluctuations at the blade frequency. If the throttle is now closed slightly, putting the compressor into surge, the hot-wire outputs reveal that, although most of the blades, to judge from the shape of their wakes, are operating normally, there are periodic disturbances during which the mean flow through one or more blade passages is very strongly retarded, the minimum velocity occasionally going to zero. The retarded flow is quite turbulent with a strong component at the blade frequency. There may be several retarded-flow "stall cells" on the wheel at any instant. These cells are more or less uniformly spaced around the rotor and move relative to the rotor and also relative to the casing at approximately constant speed. The static pressure rise across the rotor at a cell is much reduced. However, the regions of static pressure fluctuation are not as sharply localized as those of velocity fluctuation. This is stall propagation.

One of the most important unsolved problems of propagating stall research is that of predicting the number of stall cells which will be found at a given flow. After the stall-initiating transient has died out we would find several stall cells on our hypothetical rotor. By opening the throttle carefully after stall propagation has been established, the number of cells can be reduced. Continuing to open the throttle eventually will give a single, small cell. Although the machine can be run indefinitely at this throttle setting with one-cell stall it will, in the absence of stall, run equally indefinitely at the same throttle without stalling. By closing the throttle after stall propagation has been established the number of cells can be increased. The maximum number of cells a given rotor can support is a moot question of propagating-stall research but, with the smooth, unobstructed casing we have postulated, the rotor might exhibit as many as one cell for every three blades.[4] Further throttling after the maximum number of cells has been attained results in an amalgamation of the stall into fewer, larger cells. This amalgamation may occur in gradual stages or quite abruptly, but eventually a very large single cell

[3] Since Reynolds number based on blade chord is typically in excess of 10^5 and Reynolds number based on blade thickness in excess of 10^4 the effect of Reynolds number is slight.

[4] In this connection see the tests of Stenning in a radial-flow circular cascade [13]. At low solidities only 1½ blades were associated with each cell.

is observed. This may extend over more than half the rotor. Within the large stall cells, reverse flow is found; air passes upstream through some of the stalled-blade passages. Across these blades there is a static pressure drop; i.e., the static pressure upstream exceeds that downstream.[5] At the same instant, across the unstalled blades the pressure rise is observed to be that associated with steady, unstalled operation near the surge limit. At extremely low net flows, the regular, periodic, propagating-stall pattern gives way to completely turbulent flow.

In general, a stall cell can be lost by decay, i.e., weakening in intensity and decreasing in width, or by amalgamation with an adjacent cell. Similarly, a cell can be added by the nucleation and growth of a new cell between existing cells or by the splitting of an existing cell. All of these processes occur singly and in various, sometimes quite complicated, combinations with a particular rotor. The only detailed data on the cell number changing process is reported by Rockett in a companion paper [10]. Two of the most interesting features of a cell number change are (*a*) changes in the number of cells occur at constant rpm and constant throttle, and (*b*) under certain operating conditions the spacing between cells oscillates steadily with a definite frequency. Both of these features suggest that, at certain fixed operating points, the mechanism determining stall wave length is weak.

Many of the actual configurations tested are sufficiently close to the isolated rotor to make a correlation of the data reasonable. One of the fundamental quantities is the velocity of stall propagation, and its dependence on wave length. To nondimensionalize the propagation velocity, we use the inlet tangential velocity (wheel speed for no inlet guide vanes). For any particular geometry this has been universally found to give a constant dimensionless quantity. To nondimensionalize the wave length, we have chosen the axial projection of the chord. All quantities are taken at the mid-span of the blades. The data for six comparable blade rows is given in Fig. 3. The correlation is only fair, but this is understandable, since none of the geometric nondimensional variables (thickness ratio, camber, stagger, and solidity) has been included. As the table in Fig. 3 indicates, these variables cover a considerable range in the cases reported; thus one may conclude that their influence on the propagation velocity is relatively weak. Note that the minimum wave length, measured in projected chords, is remarkably uniform for this assortment of blade rows. On the other hand, the maximum wave length varies greatly, for in every case (except the radial cascade) this corresponds to the one-cell pattern and the wave length is set by the circumferential length of the blade row. Probably two different mechanisms predominate in setting minimum and maximum wave lengths; in the first case the mechanism is linked to blade-chord length and in the second case to circumference length.

Throughout the range of mass flows where stall propagation is observed, the fraction of the annulus area covered by the stall cells varies almost linearly with mass flow.[6] Extending the line to zero flow gives 100 per cent coverage, Fig. 4. This has led to the conjecture [15] that the unstalled blades are operating at the flow associated with the surge limit point while the stalled blades are operating blocked (zero flow). While this conjecture is an oversimplification, it is a reasonable first approximation to conditions in the multicell regime. At high stalling flows, close to the surge limit, there appears to be a significant flow through the stall cells while at low stalling flows (the large single-cell regime) there is undoubtedly reverse flow in the cells.[7] These

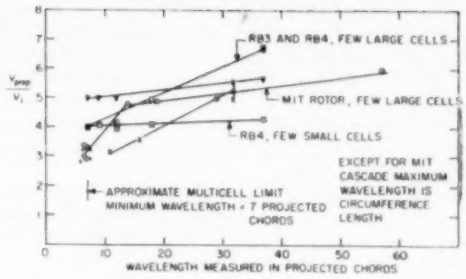
RB3 AND RB4, FEW LARGE CELLS
MIT ROTOR, FEW LARGE CELLS
RB4, FEW SMALL CELLS
EXCEPT FOR MIT CASCADE MAXIMUM WAVELENGTH IS CIRCUMFERENCE LENGTH
APPROXIMATE MULTICELL LIMIT MINIMUM WAVELENGTH = 7 PROJECTED CHORDS
WAVELENGTH MEASURED IN PROJECTED CHORDS

	GAP / PROJECTED CHORD	INLET ANGLE	EXIT ANGLE (APPROX.)
○ M.I.T. ROTOR [4]	1.3	67° - 84.5°	22°
▲ HARVARD RB3 [1]	2.2	66° - 68.4°	21°
▼ HARVARD RB3 SLOTTED [1]	2.2	62° - 68.4°	21°
■ HARVARD RB4 [10]	1.1	63.5° - 81.5°	36°
◆ M.I.T. RADIAL FLOW CASCADE [13]	1.2	63.5° - 68.5°	38°
× NACA ROTOR [5]	1.0	55° - 64°	22.5°

Fig. 3 Stall-propagation data

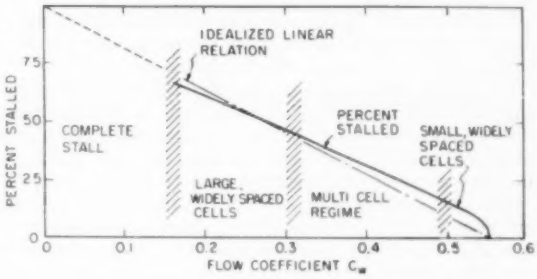

Fig. 4 Per cent of rotor annulus stalled versus mass flow

remarks are supported by deviation of the actual data for fraction covered from the simple linear relation, Fig. 4. At very high stalling flows there is also a tendency for the cells to be more intense at one end of the blade span than at the other. The details of this three dimensionality (i.e., radial variation) of course will depend on the particular rotor design; we probably may ignore it in evaluating a two-dimensional stall theory. On the other hand, the reverse flow in the large cells is a fact with which almost certainly we will have to reckon in any adequate theory for that regime.

Thus far we have been considering a rotor with the pressure rise-flow curve of Fig. 2(*b*). A rotor which behaves as in Fig. 2(*c*) in general will show practically none of the small cell and multicell behavior. When such a rotor is throttled beyond the surge limit it will pass abruptly to the large-cell regime, exhibiting typically one, or perhaps two large cells covering close to one third of the annulus area. The propagation velocities correspond roughly to the data of Fig. 3 when nondimensionalized in the same way. Because the flow coefficient is not far below the surge limit the implication is that the stall cell may pass a significant through flow. However, there may be regions of reverse flow within the cell itself.

The addition of stationary blading can cause major alterations in the stall behavior. For a rotor with the characteristic of Fig. 2(*b*), the addition of a stator a few chords downstream has two effects: (*a*) The maximum number of cells is decreased; (*b*) the amalgamation of cells into larger units begins at a higher flow coefficient. Decreasing the distance between rotor and stator strengthens the effects, and if the coupling is very strong all multicell patterns may be suppressed. At the same time the pressure-rise curve has come to be more like Fig. 2(*c*), but the actual changes may be slight.

[5] For details see [5, 6, 10].

[6] Rockett [10] and Fabri [15] found a linear relation but Iura and Rannie [2] did not.

[7] At Harvard, hydrogen-sulfide tracer gas injected downstream of a stator which was itself six chords downstream of the rotor was clearly detected a chord length ahead of the rotor. The cell wave length was in excess of 35 chords; see also [8].

From these remarks one might conclude that for an isolated rotor which possesses no small multicell behavior the addition of a stator would produce no significant change in stall behavior. For at least one such rotor tested at Harvard, this is not the case. The addition of the stator at a moderate (six chord) spacing served to produce a multicell regime where none had existed for the rotor alone. Moving the stator close to the rotor suppressed the multicell regime [1, 10].

Placing inlet guide vanes upstream of the rotor has no marked effect on the small multicell behavior. However, as would be expected, if the stall disturbance is large enough to be felt a considerable distance from the rotor, then its behavior is influenced strongly by the adjacent vanes. Fixed blading decreases the stall-propagation velocity relative to the fixed blades and increases the cell size, the extent of these effects increasing with the relative amount of fixed to rotating blades and their proximity.

Adding more stages to a rotor-stator pair produces a complex variety of behaviors that cannot be assessed systematically with our present limited knowledge. One principle seems to apply when downstream stages have a favorable stall margin compared to a leading stage. In this case a high flow stall disturbance in the head stage may damp out in the subsequent stages, giving a satisfactory over-all performance for the machine [14].

To conclude this section some mention should be made of true surge as distinguished from stall propagation. One characteristic of stall propagation is that the flow passing through the annulus, integrated over the entire area, is steady in time; that is, the propagating disturbances merely serve to redistribute the flow over the area. Surge is an oscillation of the total (integrated) flow through the annulus. Surge frequencies are typically lower than stall-propagation frequencies by more than an order of magnitude so that during a surge cycle the compressor will travel up and down the performance curve in quasi-steady state. The inception of surge and its frequency are set by the shape of the performance curve (including reverse-flow performance which is usually not measured) and the volumes in the flow ducting to which the compressor is connected [12]. Thus there is no fundamental connection between stall propagation and surge except that the falling pressure characteristic which is necessary for surge excitation may originate in the stall-propagation regime. A hot-wire record of a surge cycle shows that, as the flow oscillates between its maximum forward and maximum reverse limits, stall propagation occurs at the appropriate flow values. Historically, "surge limit" has been the term used to denote the transition from regular to disturbed (noisy) flow. Usually the disturbance so observed will be stall propagation rather than true surge, but the common acceptance of the term has led to its retention here.

Fundamental Blade-Row Theory

The study of the flow through an axial-flow blade row, steady or nonsteady, may be approached at several different levels of detail. In the most complex evaluation one must consider the individual blades with their individual boundary layers, spanwise velocities, secondary flows in the end-wall boundary layers, and so on. Because of the alternation between moving and stationary blade rows in a turbomachine it has been found convenient and sufficiently accurate for many purposes to replace the detailed inlet and exit flows by mean conditions, defined generally as circumferential averages. With mean velocity, flow angle, and pressure[8] so defined, the steady blade-row performance can be expressed in terms of two nondimensional coefficients. One set of coefficients commonly employed consists of the turning angle and loss coefficient. Sometimes loss coefficient is replaced by pressure coefficient and turning angle by deviation angle; i.e., exit flow angle. In either case a condition of mass conservation through the blade row is required to complete the specification of exit quantities in terms of inlet quantities.

Through the device of circumferential averages the blade row in imagination can be replaced by a plane across which the coefficients apply (the "actuator disk"). This technique has been proved through satisfactory quantitative prediction of multistage performance from experimental data taken on cascade or single-blade rows. If this were not the case, the problems of axial-flow design would indeed be horrible. It is not now possible to predict with acceptable accuracy the detailed performance of a single-blade row from fundamental fluid equations, and the interactions between blade rows with relative motion are even more difficult.

When performance at low flow rates (stall regime) is considered, the same coefficients used in the same way are still reasonably successful as a basis for multistage design. However, the blades are now subjected to periodic excitation from the moving stall cells; the exciting forces are an order of magnitude larger than the forces due to impinging wakes from the upstream row and fall in an entirely different frequency zone. The structural integrity of the blade row is jeopardized and it becomes important for the design analyst to know the number of stall cells, their size, shape, and the speed with which they move. Implicit in the numerous analyses which have been offered to date [11–21] is the hope that a suitable correlation of these important quantities can be based upon the coefficients which describe the mean performance of a blade row; augmented perhaps by some additional geometric parameters (such as blade chord, camber, solidity) and possibly by some simple parameters peculiar to unsteady motion (such as a phase lag or time delay associated with stall). As yet no entirely suitable correlation has been found, but the hope still flourishes. Considering the analyses as a whole, it appears that almost any reasonable physical model predicts the occurrence of stall propagation and gives a value of propagation velocity (in terms of average coefficients) of correct general magnitude. A few analyses [15, 18] give an explanation of the shape of the small multicells, and one [13] offers a prediction of the wave length first observed when the flow is throttled. It appears to the present authors that a fusion of suitable features of this previous work can lead to a model which has the capability of describing all the relevant properties of stall propagation, although complete success cannot yet be reported.

Generating a Stall Model

A model of stall performance must contain three parts: (*a*) An upstream flow field (perhaps including an upstream blade row); (*b*) a downstream flow field (or blade row); (*c*) a set of conditions relating upstream and downstream properties at the row under investigation. All previous analyses have treated an infinitely long two-dimensional airfoil cascade between upstream and downstream fields which extend to infinity.[9] Mean rotor (or stator) circumference is introduced later as a constraint on allowable wave lengths. For reasons described previously the blade row is generally treated as an actuator disk and we will continue this practice.[10] For some experimental observations, notably those of Stenning [13] in a very low-solidity cascade this approximation is highly suspect, but for the bulk of the reported

[8] For a compressible fluid, density or some other thermodynamic variable also would be required. We consider the incompressible case for simplicity, both here and in what follows.

[9] Special assumptions sometimes replace the downstream field [11, 13].

[10] This assumption does not eliminate the influence of blading dimensions. Their effects will enter through the cascade characteristics.

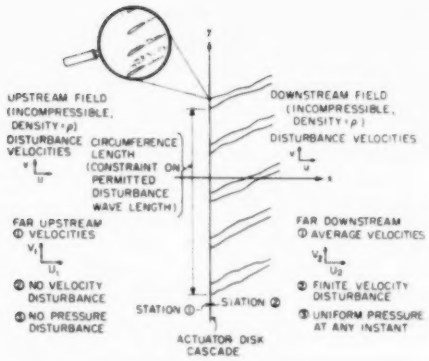

Fig. 5 Representation of stall flow in a cascade

data it is probably quite reasonable. Finally, the flow is assumed incompressible, an entirely reasonable assumption since most of the observations which require explanation were obtained at low to moderate Mach number. In all of these features we will follow previous practice.

Fig. 5 pictures the cascade stall flow just described with the addition of appropriate conditions far upstream and far downstream. Neglecting any reverse flow in large stall cells, the fluid approaching from far upstream is irrotational and remains so (by Helmholtz theorem). Thus upstream disturbance velocities can be derived from a potential at every instant of time,

$$u = \phi_x, \qquad v = \phi_y \tag{1}$$

where

$$\phi_{xx} + \phi_{yy} = 0$$

The x-momentum equation is

$$-\frac{p_x}{\rho} = (U_1 + \phi_x)\phi_{xx} + (V_1 + \phi_y)\phi_{xy} + \phi_{xt} \tag{2}$$

where p is the disturbance pressure and ρ the density. Equation (2) may be integrated in x from far upstream to the cascade inlet (station 1, $x = 0$).

$$-\frac{p_1}{\rho} = U_1\phi_{x1} + \frac{{\phi_{x1}}^2}{2} + V_1\phi_{y1} + \frac{{\phi_{y1}}^2}{2} + \phi_{t1} \tag{3}$$

If any one of the variables, u_1, v_1, p_1, or most conveniently ϕ_1, is known as a function of position along the cascade inlet y and time t, the entire upstream flow is known. Observe that the disturbance velocities are not required to be small in these equations.

The downstream field disturbances cannot be defined by a potential since they contain vorticity shed by the cascade airfoils as their lift changes. This vorticity is convected downstream with the fluid. The disturbance velocities u and v are not instantaneously specified by values given at the cascade exit (station 2) but depend on the past history of the flow as carried by its vorticity. The same is true of the pressure. If the downstream disturbance is postulated to be small compared to the mean velocity and equations of motion are linearized, it turns out that the pressure (but not the velocities) is then specified at each instant by velocity values given at station 2. The pressure itself is, in this case, a potential function.

The only attempts at nonlinear downstream solutions are those of Kriebel [16, 20] who uses a vortex-shedding model and computes a velocity of stall propagation, and Fabri [15] who views the stall zone as a wake of "dead fluid" and obtains, in addition to a propagation velocity, the ratio of stalled to unstalled blades and the pressure amplitude of the disturbance. In both cases the flow has been assumed to be steady in a co-ordinate system moving with the stall cells. For reasons to be given, this assumed steady motion makes it inherently impossible to predict the number of stall cells. Since it is extremely difficult to describe the downstream field with equations which are both nonlinear and nonsteady, and since it appears to the authors that much new, useful information is still to be gained from the linearized downstream field, this linearization will be adopted. In this we follow many previous authors [14, 15, 17, 18, 19].

The linearized momentum equations for the downstream field are

$$-\frac{p_x}{\rho} = U_2u_x + V_2u_y + u_t \tag{4a}$$

$$-\frac{p_y}{\rho} = U_2v_x + V_2v_y + v_t \tag{4b}$$

Continuity requires

$$u_x + v_y = 0 \tag{5}$$

and by direct differentiation of (4a) and (4b), using (5), we find

$$p_{xx} + p_{yy} = 0 \tag{6}$$

If we use a superscript * to denote the harmonic conjugate function, defined by

$$p_y = p_x^*, \qquad p_x = -p_y^* \tag{7}$$

we may rewrite (4a) as

$$\frac{p_y^*}{\rho} = -U_2v_y + V_2u_y + u_t \tag{8}$$

This equation applies everywhere in the field, and in particular at $x = 0$ (station 2). Integrating (8) along $x = 0$ from $y = 0$ gives

$$\frac{p_2^*}{\rho} = -U_2v_2 + V_2u_2 + \int_0^y u_{t2}dy - C(t) \tag{9}$$

C is an arbitrary function of time. The conjugate of equation (9) is

$$-\frac{p_2}{\rho} = -U_2v_2^* + V_2u_2^* + \int_0^y u_{t2}^*dy - C'(t) \tag{10}$$

Here the conjugates of the functions $u_2(y)$ and $v_2(y)$ are themselves specified only along the line $x = 0$ (station 2),[11] and C' is another arbitrary function of time. Equation (10) determines p everywhere at station 2 when the velocity components there (u_2, v_2, and u_{t2}) are known. Therefore, using equation (6) we could proceed to find p everywhere in the downstream field. The conjugate functions, u_2^*, v_2^*, and u_{t2}^*, are taken to have by definition zero average value (averaged in y) and therefore $C'(t)$ is the average value of p_2/ρ. If p were to vanish as $x \to \infty$, as is often assumed, $C'(t)$ would be zero. However, the disturbance pressure, p, need not vanish as $x \to \infty$; we can only require that it be uniform in y. Since the cascade characteristics are not necessarily linear, a change in stall configuration at constant mass flow (constant U_1), in general, would result in a change in the over-all pressure rise. Thus $C'(t)$ cannot be zero; it must be free to change with a change in stall configuration.

[11] The definition of the harmonic conjugate for a field function, equation (7), is exact. The harmonic conjugate of a function specified only along a line is defined only when the line is part of a region. We take the region to be $x \geq 0$ for exit functions (e.g., u_2 and v_2) and $x \leq 0$ for inlet functions (e.g., u_1 and v_1). Care must be taken when transforming across the cascade (e.g., $u_1 = u_2$ implies $u_1^* = -u_2^*$).

In a test compressor operating at constant rpm, and fixed throttle, a transient change in stall configuration will change the downstream pressure which, in turn, will result in the change in mass flow appropriate to the particular throttle characteristic. In formulating a time-dependent stall theory we have multiple choices; for example, we can hold the mean axial velocity constant implying a throttle with infinite impedance, or we can make the throttle "elastic" to simulate the effect of a compressible fluid in a large receiver. If we use either a finite impedance throttle or an elastic throttle, we must admit time-dependent mass flow and therefore must change the boundary conditions on u at ∞ shown in Fig. 5. It is obviously simpler to hold mean axial velocity constant; this we shall do. A theory of true surge of course would have to grapple with the alternatives.

We now have u_1, v_1, and p_1 expressed in terms of a single variable, ϕ, and a single relation coupling u_2, v_2, and p_2, equation (10). At this point the cascade characteristics enter. Three characteristics are needed to determine three independent variables (one upstream and two downstream). Different theories have introduced different assumptions to fix these variables. Two papers [11, 13] eliminate the need to consider the downstream field by assuming $p_2 = \text{const}$, an assumption of questionable validity in view of more recent data.

With the exception of the two papers just mentioned (where the question does not arise) all authors assume continuity across the cascade in the form

$$u_1(y, t) = u_2(y, t) \tag{11}$$

which we accept here. Since $u_1 = \phi_{x1}$ and $u_1^* = \phi_{x1}^* = \phi_{y1}$ equation (10) becomes

$$-\frac{p_1}{\rho} = -U_1 v_2^* - V_2 \phi_{y1} - \phi_{t1} - C'(t) \tag{12}$$

The second characteristic commonly used is a geometric one—a relation for the exit flow angle. Emmons [11], Stenning [13], Marble [18], Sears [19] (in his channel theory), and Fabri [15] take the exit angle to be fixed. This is experimentally a fairly good assumption. Sears [19] in his airfoil theory takes airfoil circulation to be linear in incidence angle with a phase lag similar to that used in flutter theory. This is indirectly equivalent to making exit flow angle a linear function of incidence, with a phase lag. It appears to the authors that for the bulk of stall-propagation data the exit-flow-angle changes are sufficiently small that either the exit angle should be taken constant, in which case

$$v_2^* = u_2^* \frac{V_2}{U_2} = -\phi_{y1} \frac{V_2}{U_2} \tag{13}$$

can be used to eliminate v_2^* from (12), or else v_2^* should differ from this value by a small amount which is linear in the inlet velocities ϕ_{x1} and ϕ_{y1}. A time lag or phase lag might be attached to this small difference.

The third cascade characteristic must be a momentum condition. In the papers by Emmons [11] and Stenning [13] this purpose is served indirectly by an area ratio which describes the contraction of the jets of high-energy fluid discharging from the passages between blades with varying thickness of wake. Area ratio is taken linear in the incidence, and a time delay is incorporated to describe boundary-layer-growth time. Marble [18] assumes a pressure rise which is discontinuous at a critical incidence angle—a normal rise through good flow blades and no rise across stalled blades. Fabri [15] uses two different linear relations between loss and incidence, one for stalled and one for unstalled blades, with a critical incidence angle demarking the two regions. These two theories involve no time lag. In his channel theory, Sears [19] takes loss coefficient proportional to incidence with phase lag. Sears' [19] airfoil theory is loss-free and, as remarked previously, incorporates a phase lag in the geometric condition. It is the opinion of the authors that the momentum condition can be expressed most conveniently in terms of a loss coefficient which is a function of incidence. This function should be strongly nonlinear to describe actual blade behavior, although the discontinuous (piecewise-linear) model of Fabri is quite extreme. A time delay in the change of the loss level seems important, for reasons which follow.

Combining the three cascade conditions with the two field relations (3) and (10) yields a single equation relating various derivatives of ϕ evaluated at $x = 0$ (station 1). This is essentially the form of all previous theories: A potential function in the region $x \leqslant 0$ defined by a differential boundary equation at $x = 0$. The theories can be classified according to whether or not the boundary equation is nonsteady (involves time derivatives of ϕ) and/or nonlinear.[12] The two theories of Sears [19] are both linear and steady (written in the co-ordinate system moving at stall speed), those of Emmons [11] and Stenning [13] are linear and nonsteady, and those of Marble [18] and Fabri [15] are steady and nonlinear (through the discontinuous cascade-momentum condition). The boundary condition formulated in this paper is both nonlinear and nonsteady. The ability of the theories to predict the various features of stall propagation depends on the foregoing classification.

If the general nonlinear, nonsteady boundary equation given previously is linearized in the customary way, we obtain a system whose solution may be expressed as an integral (superposition) of simple waves of the type $a_0 \exp(kx + jky + \omega t)$ where a_0 is the initial wave amplitude and k is the wave number (k is real and $\geqslant 0$). The quantity ω is complex; the real part of ω is the rate of growth or decay for the wave and the imaginary part the frequency. The ratio of the imaginary part of ω to k is the negative of the propagation velocity, V_p. Inserting this simple wave into the linearized boundary equation gives a polynomial in k and ω the roots of which determine ω for a given k. (There can be multiple solutions.) In general there will be ranges of k for which the waves decay in time (stable regions) and ranges of k for which the waves will grow (unstable regions). For the linearized system there is no process to limit the growth and it is not possible to say which of the unstable waves the actual, nonlinear system will finally select. Under certain critical conditions there may be only one wave number which will grow [13] but this is not significant since the rate of growth of such a wave is vanishingly small. A linear, steady theory can be shown to be a special case of this linear, nonsteady theory, equivalent to constraining ω to be purely imaginary. Thus the linear, steady theory will yield the pair of values (k, ω) which mark the boundary points between stable and unstable waves. It would seem that these neutrally stable waves are not as significant as the waves which possess high growth rates.

In contrast to the foregoing linear analysis, we can form a nonlinear, steady theory from the general, nonlinear, nonsteady theory by replacing every partial time derivative in the boundary equation by V_p times the partial derivative in y. Thus for ϕ_t, ϕ_{xt}, ϕ_{tt}, and so on, we write $V_p\phi_y$, $V_p\phi_{xy}$, $V_p^2\phi_{yy}$, and so forth, respectively. The analysis of nonlinear equations is not as well developed as that for linear equations, but it is well understood that relatively simple equations (the Van der Pol equation for example) possess finite oscillatory solutions which the system approaches asymptotically. We expect that if our mathematical description of stall is reasonably accurate the steady, nonlinear, boundary equation will possess as a solution a finite disturbance, periodic in the y-co-ordinate which is one of the asymptotic solutions of the nonsteady equations. The wave length, wave shape,

[12] The Laplace field equation for ϕ applies at each instant and is inherently linear.

and amplitude of the steady solution are all determined by the selection of V_p. The relative stability of the asymptotic situation obtained compared with that of other possible solutions cannot be determined. In general there will be ranges of V_p for which such solutions can be found, and ranges of V_p for which they will be excluded (only a zero amplitude solution is permitted). We are once again confronted with the question of which V_p and which solution the system ultimately will achieve. The two published theories of this type [15, 18] are rather special cases of this general description. In both cases the range of V_p is predicted unequivocally. Wave shape (fraction of stalled blades) is also uniquely determined. However, wave length is completely unspecified in these theories.

From these considerations the authors conclude that an adequate prediction of stall propagation can be achieved only through a theory which is both nonlinear and nonsteady. The nonlinearity is required to provide a growth-limiting mechanism for unstable waves and the nonsteady description is required to permit a stability analysis of steady solutions, thereby giving a criterion for selection between them. This is the point of view taken in a companion paper by Kronauer [21].

Even a nonlinear, nonsteady analysis is not, in itself, sufficiently general to guarantee prediction of a wave number. To illustrate this let us suppose that the cascade characteristics were so chosen that the final boundary equation contained only ϕ_x, ϕ_y, and ϕ_t in various nonlinear combinations. Since ϕ_x and ϕ_y have the units of a velocity, ϕ must have the units of a length squared divided by a time, and ϕ_t then has the units of velocity squared. The boundary equation, regardless of its degree of nonlinearity, can only involve a ratio of velocities; it cannot give a length. This case is not an unusual one; it follows from the model developed in the foregoing if exit flow angle and loss coefficient are both taken to be instantaneous functions of incidence. The theories of Marble [18] and Fabri [15] are both (steady) examples.

Because of the difficulties inherent in a nonlinear, nonsteady analysis, Kronauer's work is restricted to systems where the wave shape may be approximated by a sinusoid. Admittedly, this is not particularly accurate for the wave forms observed in stall propagation, except possibly in the case of weak multicell stall. One significant result of his analysis is the prediction that when an existing stall-cell pattern becomes unstable (through a change in throttle setting) the instability will manifest itself as a slowly growing phase modulation of the pattern, the wave length of the modulation being the longest permitted by the system (circumference length). This prediction is confirmed by data of a new kind presented in another companion paper by Rockett [10]. Here, long-time records of stall propagation show clearly this type of phase modulation[13] and give an unusual insight into the subsequent process of cell-number change. From the modulation data, it is also possible to separate the influences of throttle setting (mass flow) and cell number on propagation velocity. Previous data always have associated a particular cell number with a particular mass flow; thus the influence of the two variables could not be separated.

Conclusions

From both experiment and theory we find that the stability mechanism determining wave length in the multicell regime is weak. Very small changes in system parameters can make significant changes in cell number.[14] Moreover, the circumference length plays a vital role in determining cell number. This explains why a stator located several stall wave lengths downstream of a rotor, remote inlet guide vanes, or even relatively small casing-support spiders can influence the number of cells. Blade rows are "widely spaced" only when the spacing is of the order of the circumference length.

The general theoretical considerations given here show that a complete description of stall propagation can be provided only by a model which is both nonlinear and nonsteady. Further, though these are necessary conditions, they are not sufficient. In addition, the cascade characteristics must be such that the final boundary condition will contain terms of enough dimensional variety to permit the extraction of both stall velocity and wave length. Characteristics which depend directly on only the inlet velocities and pressure result in a boundary condition involving only ϕ_x, ϕ_y, and ϕ_t which, as we have seen, is not sufficient. Stenning's inclusion of the inertia of the fluid in the cascade in the momentum condition [13] adds ϕ_{xt} to the set. Viewed dimensionally, this term makes a wave-length prediction possible, but in his (linear) theory this does not happen. The analysis simply shifts the boundary of the upstream momentum-field chord length; it does not introduce length in a significant way.

A more promising dimensional diversity is afforded by the idea of a time delay or phase lag in the response of the cascade to inlet conditions. Of the two, time delay seems preferable since phase lag implies a sinusoidal disturbance shape. Stenning's experience shows that under appropriate conditions the inclusion of a time delay predicts a band of unstable wave numbers. The band width shrinks to zero at the flow corresponding to stall inception. It follows from our previous remarks that a nonlinear, nonsteady theory incorporating a time delay has all of the requisite features for a complete prediction of rotating stall behavior. Whether the predicted results will agree with experiment is still an open question. An alternative to the time-delay hypothesis would make the cascade characteristics depend on spatial gradients of the inlet velocities as well as on the velocities themselves.

Regarding the appropriate manner of including nonlinear effects, it is well known that cascade-loss coefficients (time average) rise quite abruptly at the stall point. This is support for the piecewise-linear assumption of Marble [18] and Fabri [15]. Indeed, except for the inability to predict wave length, these studies give a remarkably accurate picture of stall propagation at high flows; narrow, widely spaced stall regions; a high axial velocity as the blades enter the stall cell; the fraction of annulus occupied by stall cells increasing linearly with decreasing flow from the stall-inception flow. A quasilinear analysis, e.g., Kronauer [21], is fundamentally unable to describe these "spiky" stall cells. With suitable modification to include both transients and a time delay in cascade response, the piecewise-linear treatment seems a most attractive way to handle the complexities of a nonlinear system.

[13] The experimental and analytic discovery of phase modulation were completely independent and virtually simultaneous, December, 1956.

[14] This is supported by the audio hot-wire data of Sovran [8].

References

1 H. P. Grant, data notebooks at the Harvard-Pratt and Whitney Project and unpublished internal reports.

2 T. Iura and W. D. Rannie, "Observations of Propagating Stall in Axial Flow Compressors," California Institute of Technology, Mechanical Engineering Laboratory Report No. 4, April 1953.

3 M. Huppert and W. Benser, "Some Stall and Surge Phenomena in Axial Flow Compressors," *Journal of the Aeronautical Sciences*, vol. 20, 1953, pp. 835–845.

4 S. R. Montgomery and J. J. Brum, "An Investigation of Rotating Stall in a Single Stage Axial Compressor," Massachusetts Institute of Technology, Gas Turbine Laboratory Report No. 29, May, 1955.

5 E. Costilow and M. Huppert, "Rotating Stall Characteristics of a Rotor With High Hub-Tip Radius Ratio," NACA TN 3518, August, 1955.

6 J. Valensi, "Experimental Investigation of the Rotating Stall in a Single Stage Axial Compressor," Institute of the Aeronautical Sciences Twenty-Fifth Annual Meeting, 1957, preprint No. 700 and *Journal of the Aeronautical Sciences*, vol. 25, 1958, pp. 1–10, 72.

7 J. A. Rockett, "Stall Propagation in Axial Flow Compressors," PhD thesis, Harvard University, Division of Engineering and Applied Physics, 1958.

8 G. Sovran, "The Measured and Visualized Behavior of Rotating Stall in an Axial-Flow Compressor and in a Two-Dimensional Cascade," TRANS. ASME, series A, *Journal of Engineering for Power*, vol. 81, 1959, pp. 24–34.

9 A. H. Stenning, B. S. Seidel, and Y. Senoo, "Stall Propagation in a Cascade of Airfoils," Massachusetts Institute of Technology, Gas Turbine Laboratory Report No. 41, August, 1957.

10 J. A. Rockett, "Modulation Phenomena in Stall Propagation," published in this issue, pp. 417–425.

11 H. W. Emmons, C. E. Pearson, and H. P. Grant, "Compressor Surge and Stall Propagation," TRANS. ASME, vol. 77, 1955, pp. 455–469.

12 C. E. Pearson, "A Study of Surge in Compressors and Jet Engines," *Journal of the Aeronautical Sciences*, vol. 22, 1955, pp. 10–16.

13 A. H. Stenning, "Stall Propagation in Axial Compressors," Massachusetts Institute of Technology, Gas Turbine Laboratory Report No. 28, April, 1955.

14 W. D. Rannie and F. E. Marble, "Unsteady Flows in Axial Turbomachines," *Communication aux Journées Internationales de Sciences Aeronautiques*, Paris, France, 1957.

15 J. Fabri and R. Siestrunck, "Rotating Stall in Axial Flow Compressors," *Journal of the Aeronautical Sciences*, vol. 24, 1957, pp. 805–812, 820.

16 A. R. Kriebel and B. S. Seidel, "Stall Propagation in a Cascade of Airfoils," NACA TN 4134, June, 1958.

17 W. R. Sears, "On Asymmetric Flow in an Axial Flow Compressor Stage," *Journal of Applied Mechanics*, vol. 20, TRANS. ASME, vol. 75, 1953, pp. 57–62.

18 F. E. Marble, "Propagation of Stall in a Compressor Blade Row," *Journal of the Aeronautical Sciences*, vol. 22, 1955, pp. 541–554.

19 W. R. Sears, "Rotating Stall in Axial Compressors," *Journal of Applied Mathematics and Physics*, vol. 6, 1955, pp. 429–455.

20 A. R. Kriebel, "Stall Propagation in a Cascade of Airfoils," *Journal of the Aeronautical Sciences*, vol. 23, 1956, p. 897.

21 R. E. Kronauer, "Propagation and Stability of Nonlinear Waves With Application to Cascade Stall," submitted to the ASME for publication.

DISCUSSION

A. H. Stenning[15]

This elusive and fascinating problem has remained unsolved for several years, and many of us have given up for want of fresh ideas. The authors are to be congratulated for their persistence and their ingenious analytical and experimental work. One must agree with their conclusions about the ingredients required for an adequate theory. At M.I.T., we had originally hoped that the inclusion of a time lag and the inertia of the fluid in the cascade would supply these ingredients, but the resulting theory did not give the right wave patterns. It appears that a satisfactory theory must include a characteristic dimension of the cascade (to fix the cell width) and that we still lack some part of the physical picture of cascade stall which would enable us to introduce the characteristic dimension properly. Perhaps, the fundamental work now being done on unsteady boundary layers will lead us to a better understanding of the phenomenon.

References [4] and [13] are now out of print in their original form, but are available as NACA TN 3823 and NACA TN 3580, respectively.

[15] Assistant Professor of Nuclear Engineering, Massachusetts Institute of Technology, Cambridge, Mass.

Modulation Phenomena in Stall Propagation

JOHN A. ROCKETT[1]

Assistant Project Engineer,
Pratt and Whitney
Aircraft, E. Hartford, Conn.

Recent experimental work on stall propagation in a single-stage research compressor is described. At certain fixed operating points, several different stall patterns were found to exist. Transitions from one pattern to the other occurred spontaneously, reversibly, and fairly frequently. These transitions were studied in detail. A regular modulation of the stall-propagation velocity is associated with the transition process. The modulation is used to determine stall frequency as a function of both wave number and mass flow. Stall-cell size measurements, static-pressure surveys, and a study of the region downstream of the stall-propagating rotor are described.

Compressor instability has been studied at Harvard for a number of years. Stall propagation, in particular, has been explored intensively. In a companion paper [1][2] we review the experimental work which has been done on stall propagation both at Harvard and elsewhere; in this paper we will present the most recent experimental findings on stall propagation in the Harvard single-stage axial compressor.

The general layout of the single-stage axial compressor, designated HX-1, is shown in Fig. 1. The rotor is 14 in. diam, has a hub-tip ratio of 0.572, and, in the configuration tested, is fitted with 34 NACA-409 airfoils tapered, cambered, and twisted to give approximately "free-vortex" flow at the design point. The HX-1 is a particularly fortunate design as it has no inlet guide vanes, struts, or other obstructions permanently fitted in or near the inlet. Further, the stator can be located at various positions from close behind the rotor to six chords downstream or removed completely. All the tests reported here were run with the stator at the extreme downstream position, six chords, and no inlet guide vanes. The HX-1 is driven by a 600-hp induction dynamometer. Compressor rpm is controlled by manually varying the resistance in the motor-armature circuit. Very precise speed control is not possible with this system, especially at low power, fluctuations of 1 to 2 per cent being common. However, as shown in Fig. 2, the dimensionless compressor performance is quite independent of rpm and it is, therefore, hoped that these small rpm fluctuations are not important. The diffuser is a long smooth horn and the exhaust throttle a movable plug rather like a trumpet mute. When running stalled the machine is sensitive to throttle position. It has been necessary to reproduce the throttle setting to 1/10 per cent in area in order to reproduce the various stall phenomena. A 25 per cent decrease in throttle area from the peak pressure-rise setting covers most of the interesting stall operation.

The principal instrument for the investigation of rotating stall has always been the hot-wire anemometer. The Harvard Project has six identical frequency-compensated, constant-current anemometers. They are reliable and easy to use. These particular units have limited low-frequency response (down 3 db in amplitude at 10 cps) giving some wave-form distortion in certain of the stall configurations recorded. However, a constant-resistance, hot-wire anemometer and an additional constant-current unit, both with response to 0 cps have been used to check the interpretation of these records. For the tests reported here the outputs of the hot-wire anemometers were fed either to a DuMont Type 322-A dual-beam oscilloscope or, through compensating power amplifiers, to a Westinghouse Type PA seven-channel recording oscillograph. With the compensation provided by the power amplifiers the string galvanometers of the PA recorder could resolve the individual compressor-blade wakes quite well. Owing to the large amount of frequency compensation introduced by the hot-wire amplifier, power-amplifier-system noise pickup was a serious problem. To obtain clear records required care in every detail of the instrumentation and was a test of patience.

The only camera available to us for use with the PA oscillo-

[1] Formerly, post-doctoral Research Assistant, Harvard University, Cambridge, Mass.

[2] Numbers in brackets designate References at end of paper.

Contributed by the Fluid Mechanics Subcommittee of the Hydraulics Division and presented at the Annual Meeting, New York, N. Y., November 30–December 5, 1958, of The American Society of Mechanical Engineers.

Note: Statements and opinions advanced in papers are to be understood as individual expressions of their authors and not those of the Society. Manuscript received at ASME Headquarters, September 11, 1958. Paper No. 58—A-152.

Nomenclature

A = stall-perturbation amplitude

B = stall amplitude

C_p = $\dfrac{\text{total pressure rise across compressor}}{\text{dynamic pressure corresponding to mean rotor speed}}$

C_w = $\dfrac{\text{mass flow through compressor}}{\text{mass flow when mean axial velocity equals mean rotor speed}}$

D = function of mass flow in the stall frequency-wave number correlation

E = constant in stall frequency-wave number correlation

g = acceleration of gravity

h = blade height

k = integer

L = linear distance between stall cells

l = width of stall cells

m = integer

N = number of stall cells

n = integer

R = mean rotor radius

t = time

u = axial velocity

V_r = tangential velocity of rotor = $R\Omega_r$

w = mass flow

y = linear co-ordinate measured along mean rotor circumference

θ = angle relative to compressor casing measured in plane of rotor

Λ = stall-wave number

λ = stall-perturbation-wave number

ρ = fluid density

σ = stall-perturbation-growth rate

ϕ = phase angle

Ω_r = rotor angular velocity

Ω_s = stall angular velocity

ω_c = $\omega_c = \Omega_s \pm \omega_s$

ω_s = stall-perturbation angular velocity

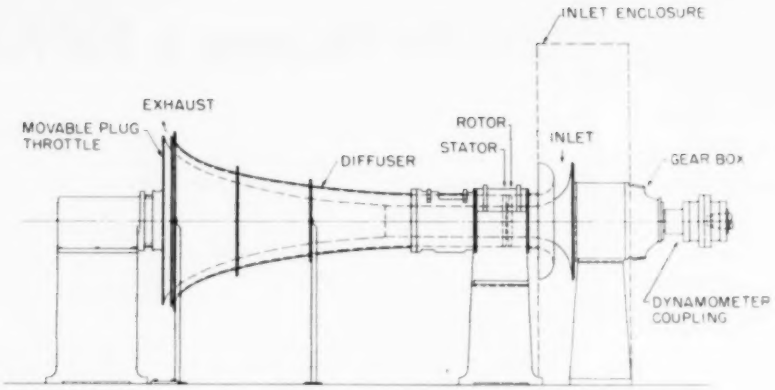

Fig. 1 General arrangement of HX-1 test stand

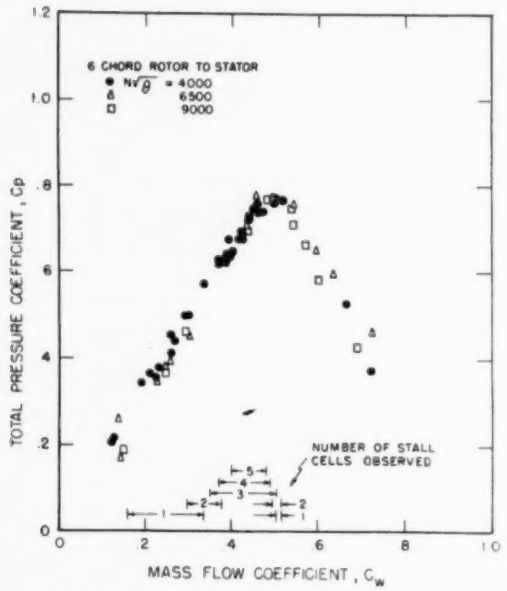

Fig. 2 Single-stage compressor; over-all performance

graph exposes a 12-in. film strip at virtually any film speed desired. Most of our data have been obtained with the compressor turning at 4000 rpm and a film speed of 28 to 30 ips.[3] Thus each record covers about 30 revolutions of the compressors. A film speed below 20 ips is impractical owing to the limited optical resolution of the oscillograph. By using film rather than paper we have largely escaped the problem of record shrinkage during processing. However, some correction has had to be made on some of the records for changes in camera speed during the exposure.

Phase Modulation of Stall Spots

The number of stall spots and the stall-propagation velocity associated with a given flow condition are relatively easy quantities to measure and are of basic importance. They have been measured by numerous investigators. At Harvard most of the past work has been done by photographing cathode-ray oscillograph traces. The author has taken numerous records by this method. While doing this, a low-frequency oscillation of the cell spacing was frequently noticed; it was sufficiently large in amplitude to interfere with accurate stall-velocity measurements. This oscillation was a transient condition, usually lasting only a few seconds, but would recur at frequent intervals. Although the oscillation of the stall spots could be observed using the cathode-ray oscilloscope, the PA oscillograph provided a more convenient means of recording it. The PA records although of limited length contained sufficient information to permit quantitative analysis of the transient oscillation of the stall-cell spacing. Such an analysis was necessary if accurate stall-propagation measurements were to be made.

If the stall spots were uniformly spaced, and propagated with uniform velocity, the angular position of the nth spot relative to the casing would be given by

$$\theta_n = \left(\theta_0 + 2\pi \frac{n}{N}\right) + \Omega_s t$$

and the propagation velocity by

$$R \frac{d\theta_n}{dt} = R\Omega_s$$

where

θ = angular position, radians
N = total number of spots on wheel
Ω_s = propagation velocity, radians per sec
t = time, sec
R = radius at probe

If the propagation velocity varied periodically with time, the foregoing suggests that an appropriate expression for the velocity would be

$$R \frac{d\theta_n}{dt} = R[\Omega_s + \omega_s A \cos(\omega_s t + \phi)]$$

and

$$\theta_n = \left(\theta_0 + 2\pi \frac{n}{N}\right) + \Omega_s t + A \sin(\omega_s t + \phi) \qquad (1)$$

where

ω_s = frequency of perturbation, radians per sec
A = amplitude of velocity perturbation, radians
ϕ = phase angle. We will assume a specific form for this,

[3] When studying the flow downstream of the rotor and for certain other special purposes, film speeds of 50 to 120 ips were used.

showing later that the assumption is justified; i.e.,

$$\phi = \phi_0 + 2\pi \frac{n}{N}$$

Then, if the kth probe is mounted at an angle θ_k, the mth passage of the nth stall cell will be recorded by the probe at a time $t_{m,n,k}$ given by

$$\theta_k + 2\pi m = \theta_n = \left(\theta_0 + 2\pi \frac{n}{N}\right) + \Omega_s t_{m,n,k} + A \sin(\omega_s t_{m,n,k} + \phi) \quad (2)$$

Rearranging this equation gives

$$A \sin\left[\omega_s t_{m,n,k} + \left(\phi_0 + 2\pi \frac{n}{N}\right)\right] = \theta_k - \theta_0 + 2\pi\left(m - \frac{n}{N}\right) - \Omega_s t_{m,n,k} \quad (3)$$

Note that, in this equation, $t_{m,n,k}$ is a discrete, not a continuous variable. Thus, if θ_0 and Ω_s are known, a plot of the right-hand side of (3) against $t_{m,n,k}$ should reveal the amplitude and frequency of a periodicity of this type.

θ_0 and Ω_s can be determined quite easily by fitting a straight line to the observed $t_{m,n,k}$ using the method of least squares. To do this the total time interval recorded must be long compared with the period of the oscillation, and the correct numbering of the stall cells, n, must be determined. With only two probes it is not certain that the correct numbering can always be done; in practice the data have been such that no difficulty has arisen. With the numbering fixed and θ_0 and Ω_s determined, the number of stall cells and their mean propagation velocity are known. These are the quantities we originally set out to measure.

Observations of Stall-Cell Number and Velocity

The stall behavior of the single-stage compressor has been studied carefully using the foregoing method of data analysis. It has been found that the rotor stalls initially with a three-cell pattern.[4] Opening the throttle slightly after stall has been established produces a stable two-cell pattern. Further opening of the throttle results in a single stall cell. The single-cell pattern persists over long periods of time and is a stable stall configuration, but it is associated with a very narrow range of throttle settings—about 1 per cent of the throttle area at stall. In the absence of stall the machine will run indefinitely at these same throttle settings without stalling. Still further opening of the throttle restores the machine to the unstalled condition. Phase modulation of the stall pattern as described in the foregoing, i.e., periodic oscillation of the propagation velocity, has been observed with both the two and one-cell patterns. The amplitude of the modulation is small, usually less than 2 per cent of the cell spacing. This modulation was recorded on films obtained with the camera drive motor off. Thus the possibility of periodic film-speed oscillations induced by the motor governor was eliminated. The records were corrected carefully for "coast," the camera slowing down about 10 per cent during the exposure.

Closing the throttle after one-cell stall has been established, causes reversion to the two and three-cell patterns. Further closing of the throttle produces a four-cell pattern. This is almost invariably phase modulated, often with large amplitude. A portion of one of the more spectacular records of modulation is shown in Fig 3. On this record a practiced eye can pick out the

[4] An initial two-cell pattern is also found. The range of throttle settings between the stall margin, throttle closing, and that where the three-cell pattern is the more stable is so narrow that a special throttle control was needed to establish this.

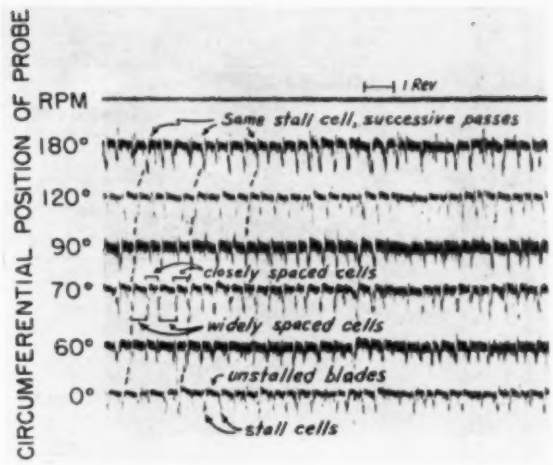

Fig. 3 Part of an oscillograph record of phase-modulated stall propagation

modulation. Note that the cell spacing alternates between widely spaced cells and closely spaced ones. Fig. 4 presents the plot of the right side of equation (3) for each of the four stall spots. The modulation is decreasing in amplitude.[5] The phase relation just assumed would give, with $n = 0, 1, 2, 3$:

Cell No. 1	$n = 0$	$A \sin(\omega_s t + \phi_0)$
Cell No. 2	$n = 1$	$A \cos(\omega_s t + \phi_0)$
Cell No. 3	$n = 2$	$-A \sin(\omega_s t + \phi_0)$
Cell No. 4	$n = 3$	$-A \cos(\omega_s t + \phi_0)$

Thus the plots for cells 1 and 3 should be 180 deg out of phase, the plots for cells 2 and 4 also 180 deg out of phase and shifted 90 deg with respect to the 1, 3 plot. This is indeed the case. Modulated 1, 2, 3 and 4 cell records have been obtained, all of which verify the assumed phase relation $\phi_n = \phi_0 + 2\pi n/N$. Throughout the range of throttle settings where four-cell patterns are observed three-cell pattern also are found, some modulated, some unmodulated. With the throttle fairly well closed several records have been obtained which show five stall cells. The five-cell pattern was not stable, lasting, in one case, only $4\frac{1}{2}$ revolutions of the rotor. Again, plotting the data referred to a uniformly rotating co-ordinate system, we are able to follow the history of the extra cell, Fig. 5. This extra cell might be considered as an aberration of the basic four-cell pattern. However, such aberrations are fairly common. Upon closing the throttle still further a large two-cell pattern is formed, and eventually a large one-cell pattern. The large stall cells involve strong reverse flow.

In addition to the phase modulation there appears to be some amplitude modulation of the pattern. In this case the cells seem to be smallest when they are farthest apart. The cell width is somewhat more difficult to determine than its position since the trailing edge of the cell does not produce quite as sharp a signal as the leading edge. To date no consistent amplitude modulation has been proved.

The regular periodic cell movement shown in Fig 4 is by no means universally observed. Fig. 5, for example, while indicating

[5] Iura and Rannie [2] reported considerable error in the phase difference measured for a single cell. Grant and others at Harvard [3] including the author, have found a similar scatter in individual phase-difference measurements. A possible source of this scatter is clear from Fig. 4. Due to the large amplitude phase modulation, individual phase-difference measurements using a single pair of probes and a short record could produce a wide variety of results quite apart from the random scatter inherent in all data.

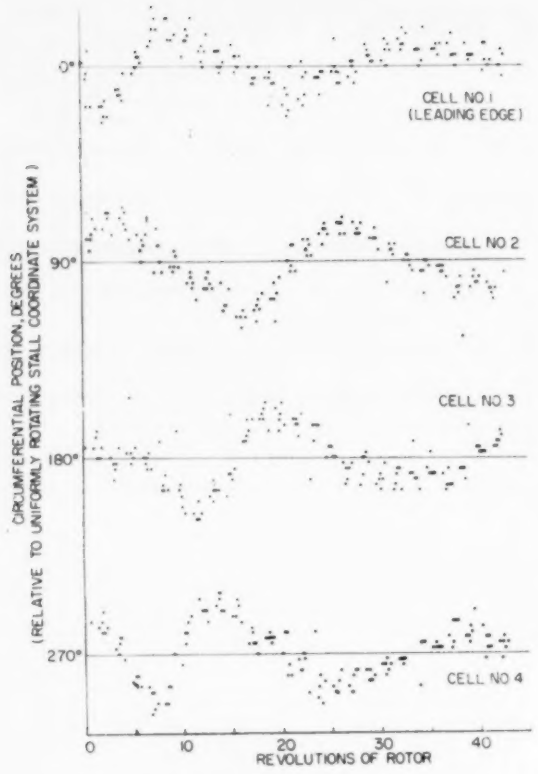

Fig. 4 Stall modulation

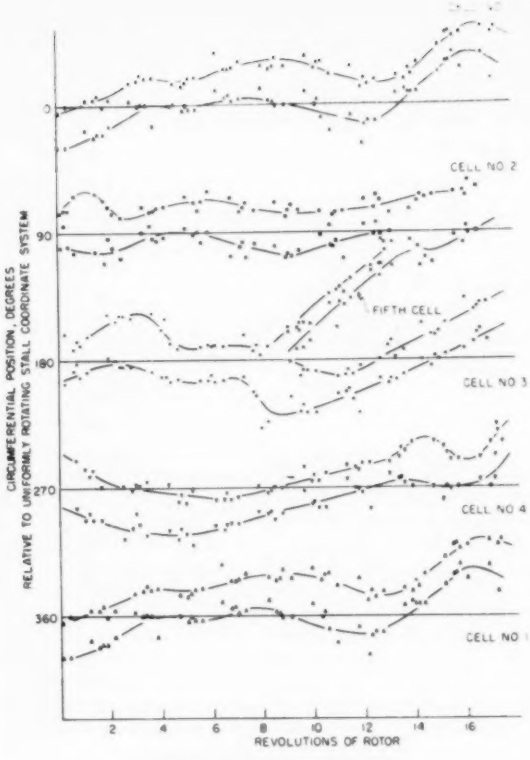

Fig. 5 4–5 cell stall patterns

perturbations in cell position up to 30 per cent of the mean spacing, shows no regular trend. Vigorous nonperiodic perturbations also are found when there is no evidence on the record of a change in the number of cells. As our records are all short, 12 in. being the film length available, it is not possible to show the complete development of the modulation pattern. Visual observation of the CR oscilloscope indicates that the modulation becomes irregular just prior to a change in the number of stall cells, regaining a regular form shortly after the new pattern is established. Thus the record of Fig. 4 was possibly but not necessarily obtained shortly after a change from three to four cells had occurred.

While the foregoing experiments were being performed, Professor Kronauer was developing, independently, a quite general theory of stall behavior. He assumed that a homogeneous, quasi-linear, partial differential operator on the cascade-inlet velocities could be obtained from the equations of the upstream and downstream flow fields and the cascade characteristics. Kronauer, however, did not attempt to derive an explicit operator. Rather, making use of the general theory of quasi-linear processes, he drew several conclusions about the kind of stall behavior to be expected. These conclusions are discussed in detail in a companion paper [4]. Kronauer's model predicted the phase modulation observed by the author.[6] He gave it the following interpretation: Let us suppose that, at a certain mass flow, a particular stall pattern, for example, three cells, is stable and propagates at a steady velocity. Further, suppose that by changing the mass flow a small amount this pattern becomes unstable. At the new operating point, the theory indicates that both two-cell and four-cell patterns can grow, provided they appear simultaneously and grow, initially, at the same rate. Considering the three stall patterns to be represented by three cosine waves, a phase-modulated superposition wave would be produced if the three cosines are related by

$$B\cos(\Lambda y - \Omega_s t) + Ae^{\sigma t}\{\cos[(\Lambda + \lambda)y - (\Omega_s + \omega_s)t] - \cos[(\Lambda - \lambda)y - (\Omega_s - \omega_s)t]\}$$

where σ is the initial growth rate of the perturbation stall pattern, Λ the wave number, and Ω_s the frequency. Λ is proportional to the number of stall cells. This representation will satisfy the linear part of the partial differential equation only if the three (Λ, Ω_s) pairs are close together and lie on the tangent to the $\Omega_s(\Lambda)$ curve at the point (Λ, Ω_s). Accepting this interpretation, the records of modulated stall become especially valuable. From each record of steady stall propagation, a single (Λ, Ω_s) pair may be obtained; this gives one point on the $\Omega_s(\Lambda)$ curve. But, from each record of modulated stall propagation, three (Λ, Ω_s) pairs may be obtained; these determine a short segment of the $\Omega_s(\Lambda)$ curve. If we know this curve, we know at least something about the form of the associated quasi-linear operator.

A large number of stall records has been obtained and analyzed. Considering only those records which showed steady stall patterns, or periodic, modulated patterns, and disregarding those which were nonperiodic or which showed the actual stall-cell-number change, three quantities were measured: The number of cells N, the fundamental propagation frequency Ω_s, and the modulation frequency ω_s. The observed stall-propagation frequencies were plotted versus mass flow as follows:

[6] The first quantitative experimental data were obtained in November, 1955. Kronauer did not see these until after his theory had been developed. The author had been taking modulation data about 6 months when he first learned of Kronauer's study.

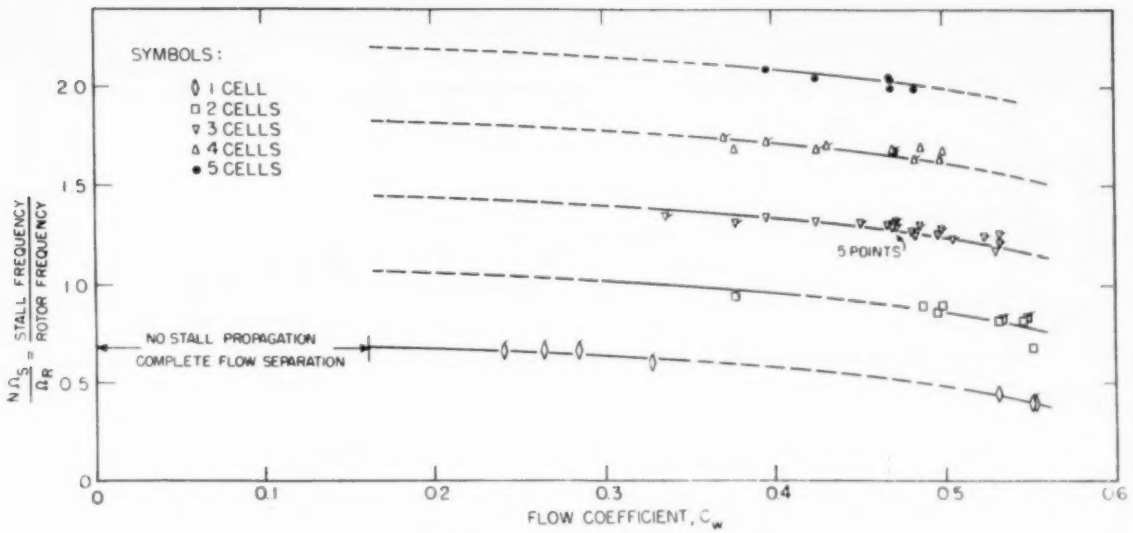

Fig. 6 Stall-propagation frequency versus mass flow

1 A characteristic symbol was used for each N-value.

2 For steady propagating stall, a single point corresponding to the observed frequency was entered at the appropriate mass flow. A flag was attached to the symbol.

3 For periodic modulated-stall propagation, three points were plotted. One, corresponding to the mean observed frequency Ω_s, was entered at the appropriate mass flow and the symbol flagged. Two additional points were entered at the same mass flow and frequencies corresponding to the upper and lower side bands, $\omega_s = \Omega_s \pm \omega_s$; the symbols had no flags. For one-cell modulated patterns only the upper side band was used.

This plot is reproduced in Fig. 6. It revealed that the large-amplitude disturbances propagated at the same frequency as the small-amplitude perturbations with the same N and mass flow. The plot also showed a small, but definite dependence of stall frequency on mass flow. This mass-flow dependence of stall frequency could be separated from the cell-number dependence in a simple way. It was observed that a curve, faired through the data for one wave number, could be fitted to the data for another wave number by a simple translation parallel to the ω axis; the translation required was proportional to N. From these faired curves, values of ω for fixed mass flow were read. Fig. 7 is a cross plot prepared in this way. It is the frequency-wave number curve corresponding to a flow coefficient, $C_w = 0.489$. The five data points are very nearly on a straight line.

$$\frac{\Omega_s}{\Omega_r} = D + EN \tag{4}$$

where D is a function of mass flow and $E = 0.380$ is a constant independent of mass flow. The dependence of D on mass flow can be determined by translating the data in Fig. 6 by an amount $-EN$, Fig. 8.

$$D(C_w) = \Lambda(N, C_w) - EN \tag{5}$$

Note that this separation of effects is not possible with the data obtained by earlier experimenters, since, if the separation is to be accurate, the data for different numbers of cells must overlap This overlap is achieved by using the additional information provided by the modulation frequency. The separation is essential in determining the frequency-wave number relation.

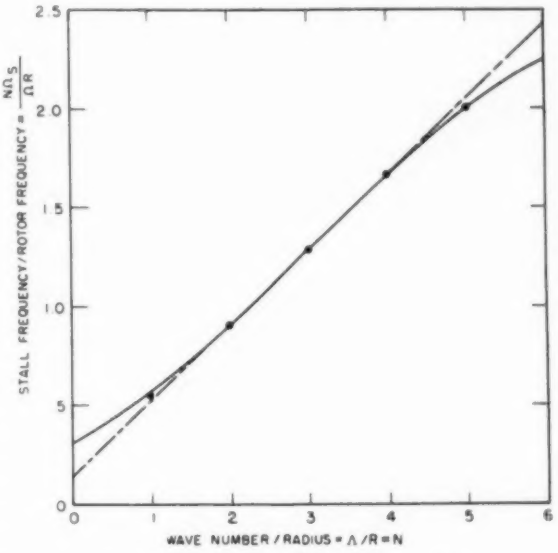

Fig. 7 Stall frequency versus wave number

For our compressor the stall-propagation velocity is given, with considerable accuracy, by

$$V_s = V_r\left(\frac{D}{N} + E\right) \tag{6}$$

where V_r is the rotor velocity, E a constant, N the number of stall cells, and D, as we have shown, a slowly varying function of mass flow. None of the existing stall theories obtains an expression of this form.

Observations of Stall-Cell Size

The size of an individual stall cell varies with time. Generally, however, the average width of all the stall cells on the rotor is

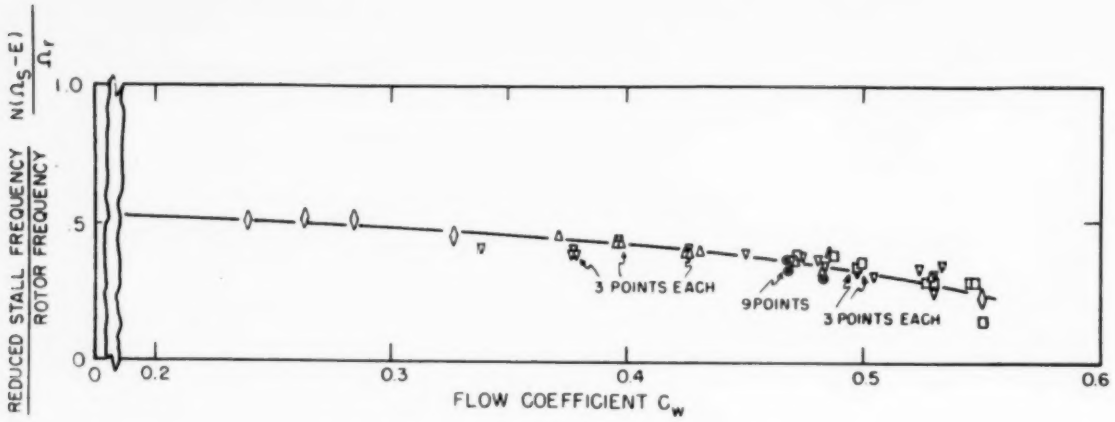

Fig. 8 Stall propagation; frequency dependence on mass flow

nearly constant. By averaging the widths of all the stall cells for a series of measurements made at different times a fairly reproducible measure of the stall-cell size may be obtained. With our compressor the stall cells grow steadily as the machine is throttled.

Fig. 9 shows the per cent of the annulus blocked by stall versus mass flow. Even with the averaging used, there is considerable data scatter. At the highest mass flow at which stall is observed (throttle opening) a single stall cell is found; the cell width indicates that $1^1/_2$ blade gaps are blocked by stall. Closing the throttle slightly produces a two-cell pattern, each cell being the same size as the single-cell pattern observed previously, the total amount of the annulus block is doubled. Further throttling produces either three cells similar in size to the initial single cell, or two slightly larger cells each of which extends over two blade gaps. A four-cell pattern with cells as narrow as those observed with 1, 2, and 3 cells has not been recorded as yet. The narrowest four-cell pattern measured shows 23 per cent of the annulus stalled which, since the rotor has 34 blades, means an average of two stalled blades per cell. Once a three-cell pattern is established the stall cells grow in size as the throttle is closed. When the throttling has progressed to the point where each cell covers four to five blades, patterns with one or two large cells become more stable than the smaller three or four-cell configurations but the total stalled area seems to be independent of the number of cells. At low mass flows a single large cell is found which may embrace more than half the blades.

For all the stall patterns a single approximate rule seems to hold; the stall width varies linearly with mass flow,

$$\frac{l}{L} = \left(1 - \frac{C_w}{C_{w0}}\right) \tag{7}$$

where

l = stall-cell width
L = stall-cell spacing $= 2\pi R/N$
C_w = mass-flow coefficient
C_{w0} = a reference mass-flow coefficient

A similar relation was noted by Fabri [5]. Marble's theory gives a relation equivalent to (7). His argument is similar to the one given later if we transpose static pressure and velocity.

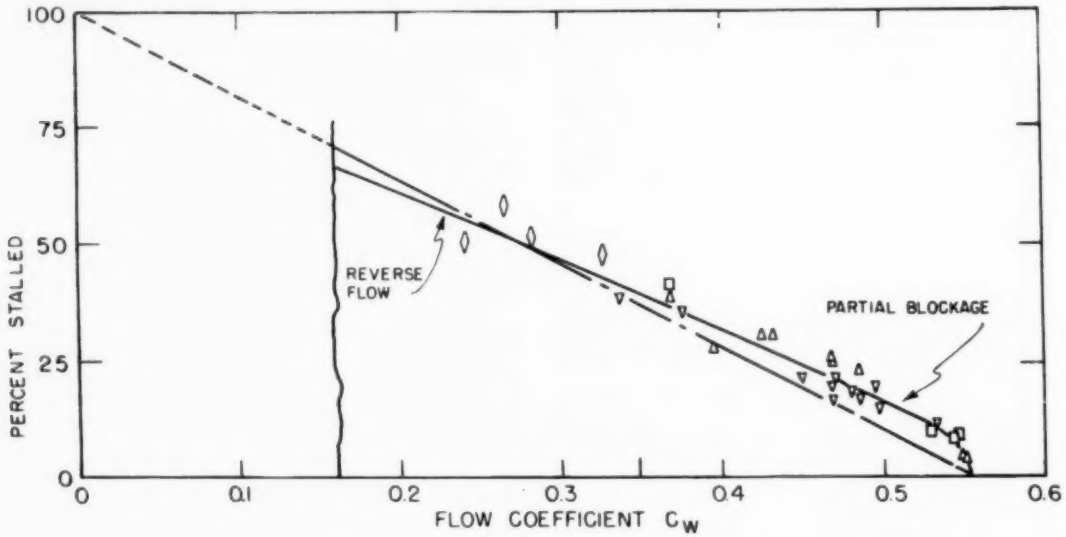

Fig. 9 Per cent of rotor annulus stalled versus mass flow

Iura and Rannie [2] found that, in their compressor, cell size increased as mass flow decreased but not in a linear fashion, the increase being more rapid at low flows.

Equation (7) may be given a simple interpretation. Assume that the axial velocity through the unstalled blades is a constant, u_0, for all mass flows and that the average axial velocity through the stalled blades is u_s, then the average mass flow per unit length is given by

$$w = \frac{\rho g h}{L} [(L - l)u_0 + l u_s]$$

Rearranging, this gives

$$\frac{l}{L} = \left(1 - \frac{w}{w_0}\right) \Big/ \left(1 - \frac{u_s}{u_0}\right)$$

where

h = blade height
$w_0 = \rho g h L u_0$ = a reference mass flow

But the experimental line gives $l/L = 1$ when $w = 0$; therefore $u_s = 0$ is indicated. Thus the linear relation between cell size and mass flow with complete blockage at zero flow suggests that no net flow is passed through the stall cell regardless of cell size and a constant axial velocity is associated with the unstalled blades for all values of mass flow at which rotating stall is found. There are several difficulties with this simple model. There is evidence (discussed later) that there are local regions of strong reverse flow in the large single-stall cells. Thus u_s, the average axial velocity through the stall cell, could be negative at low enough mass flows. Further, the weak stall cells observed at high mass flows do not seem to cause the same degree of flow blockage as the large cells observed at low mass flows. Emmons [3] observed that the stall cells found at high mass flows were narrower near the blade roots than at the tips. Iura [2] also reported tapered stall cells. Our high mass-flow stall records (obtained from the same compressor configuration tested by Emmons) suggest uniform-width cells of decreasing intensity between the blade tip and root. This is a slightly different conclusion from Emmons' but the result is the same; u_s, the average flow through the stalled blades could be positive at high enough mass flows. If the assumption of constant axial velocity past the unstalled blades is retained (we are developing instrumentation to check this) then the variation of u_s with mass flow would require a curve lying above the line at high mass flows and below the line at low mass flows. Such a curve may be fitted to our data, see Fig. 9.

Pressure Measurements

A few qualitative measurements of the static pressure rise across the stalled rotor have been attempted. The pressure transducer used was a constant-temperature hot wire mounted across the diameter of a small tube. To measure the static pressure rise across the rotor, one end of the tube was connected to an OD static tap close ahead of the rotor, the other to an OD static tap one chord downstream of the rotor.[7] A hot-wire probe was mounted close behind the rotor to record the axial velocity at the mid-span point in the azimuth plane of the static taps; thus a rough check on the pressure-transducer response was possible. The operation of this pressure instrument requires that the flow through the short tube be proportional to the static pressure difference across it. No pressure calibration of the instrument was attempted. Theoretically, the signal should be a nonlinear function of pressure.[8]

[7] These tests were to check the frequency response and phase shift of the transducer. Measurements close behind the rotor are possible.

[8] For a discussion of the instrument see [7].

Tests were run with varying length connecting tubes to check the phase shift and attenuation characteristics of the transducer. For the length connector normally used between the upstream static tap and the hot wire, less than 5 deg phase lag was found when the other end of the transducer was left open to the atmosphere. If a length of tube was then connected to the open end and a sharp pressure pulse applied at the static tap (rotor stall) not only the pulse but also an echo was recorded. As the open-end tube was shortened, the echo moved toward the exciting pulse and decreased in amplitude; the interval between the initial pulse and its echo corresponded to the "organ pipe" frequency of the open-ended tube. For the length tube used between the transducer and the downstream static tap a small echo remained and is visible on some of the records. It is not large enough to alter significantly the pressure wave forms associated with stall.

Fig. 10 shows the pressure-transducer wave form and the associated hot-wire, axial-velocity trace for a relatively high mass-flow stall. The velocity trace is inverted, a velocity decrease producing an upward displacement of the trace. The average vertical position of the velocity trace is arbitrary. The pressure trace is deflected downward by a decrease in velocity through the tube; zero velocity, i.e., zero pressure difference, corresponds to a scale reading of 45. Thus the record shows that there is a decrease in static pressure rise across the rotor during stall, but a significant residual pressure rise is found in the stall portion of the cycle. The maximum pressure rise recorded is the same as the steady pressure rise associated with unstalled operation at the surge limit.

Fig. 11 shows the same pair of signals at a relatively low mass flow. The pressure signal drops to 45 at two points near the center of the record and to 48 at a nearby point. Between the two 45 points the flow past the transducer wire probably has reversed direction, indicating a higher static pressure upstream of the rotor than downstream. Comparing a number of simultaneous records of static pressure across the rotor and axial velocity close behind the rotor suggests that reverse flow through the rotor might occur at those blades where the upstream static pressure exceeds that downstream.

The existence of reverse flow during the rotating stall has been conclusively demonstrated by Professor Kronauer. He inserted an absorbent probe moistened with lead acetate upstream of the rotor. Then with the machine throttled to give a large single rotating-stall cell, hydrogen sulfide was admitted downstream of the stator (at a point more than six chords downstream of the rotor). Immediately after admitting the gas the leaded probe was removed. It was found to be blackened, indicating that an appreciable amount of the sulfide had been convected upstream. The hydrogen-sulfide tests were useful but not popular, and have not been repeated by the author.

The pressure measurements illustrate several additional features of rotating stall:

1 The records reproduced in Figs. 10 and 11 both indicate a decrease in static pressure rise with time during the unstalled portion of the stall cycle. This is quite characteristic although only a few records have been obtained in which the fall-off is as pronounced as in Fig. 11. The concomitant decrease in axial velocity is not as large as indicated on this record due to the low-frequency phase distortion introduced by the anemometer amplifier; there apparently is some velocity decrease.

2 The maximum pressure rise, attained just prior to blade stall, is the same for all stall configurations and equal to that associated with unstalled operation at $C_w = 0.552$. (Note that, due to the relative motion of the blades with respect to the stall cell, the blade-stalling edge of the cell is the right edge on the record.)

3 The pressure records of large, single-cell stall frequently,

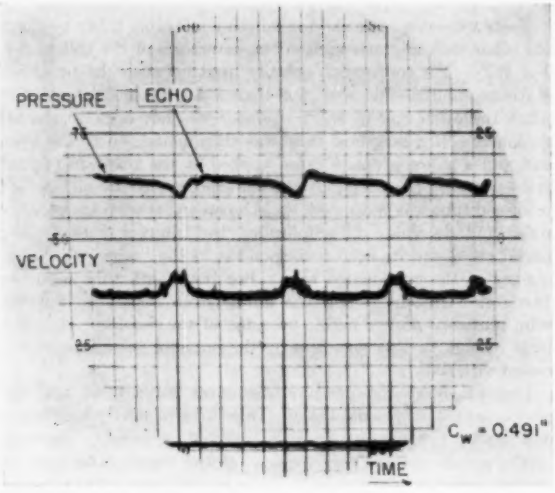

Fig. 10 Pressure fluctuations during high flow stall propagation

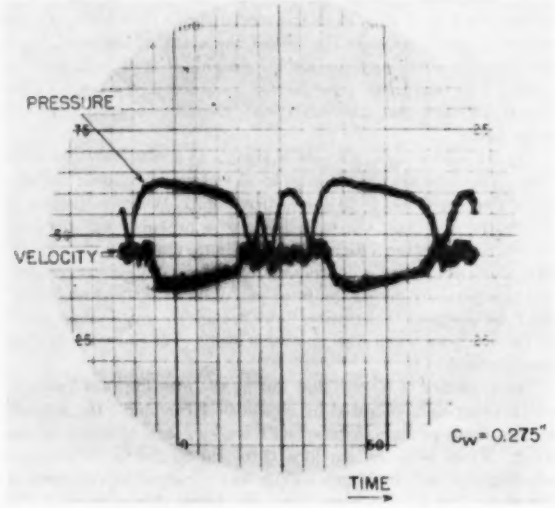

Fig. 11 Pressure fluctuations during low flow stall propagation

but not always, show an extra pulse at the left edge of the stall. The stall cell at the center of Fig. 11 shows such a pulse; the pressure drops to 48, rises to 55, and then drops to 45. After noting this pressure behavior the multichannel hot-wire records were examined in search of an explanation. The only clue to the double pressure pulse given by the hot wires is a frequently occurring double velocity pulse. Between these pulses it may be that stall is much less severe. These double pulses may represent a latent tendency for the cell to split. While investigating this it was discovered that many of the large stall cells showed a small cell just to the left (destalling side) of the main stall. This fraying of the left edge of a stall cell is caused by certain unco-operative blades which do not recover from stall as promptly as they should.

4 Although the absolute static pressure measured one chord downstream of the rotor is quite constant during small multicell-stall propagation (the fluctuation is an order of magnitude less than that measured across the rotor), the static pressure fluctuates violently during large single-cell stall. This is not surprising in view of the reverse flow associated with the large stall cells.

Changes in Number of Stall Cells

The process by which a stall cell is lost or added to the pattern on the stall-propagating rotor has been observed frequently by the author. Short but detailed records of various parts of this process have been obtained with the PA oscillograph. By supplementing these with a familiarity with the hot-wire traces as they develop and change on the cathode-ray oscilloscope face, the entire transition may be followed. Three phases of the process may be distinguished: Beginning with steady stall, the pattern first becomes modulated. This is quickly followed by a period, which may last as much as half a second, of cell splitting and recombination. Finally the new pattern emerges with large-amplitude phase modulation; the modulation slowly decays leaving the new steady pattern. A complete transition sequence takes roughly 4 to 5 sec.

To date no records which can be identified positively as showing the premodulation have been obtained. Thus if there is any regular, periodic, increasing-amplitude phase modulation at this stage, we cannot demonstrate it. Visual observation indicates that it is possible for a periodic modulation to grow to quite large amplitude and then decay without any change in the number of cells occurring.

Fig. 12 shows the first stages of splitting and recombination for an unstable three-cell pattern. Here the three-cell pattern propagates at 43.7 per cent rotor speed during the first 8 revolutions of the rotor. This propagation frequency is plotted in Fig. 6 (furthest three-cell point to the left) and falls close to the faired curve. Beginning with the twelfth revolution, cell No. 2 slows down relative to the rotor to 40.3 per cent rotor speed and is overtaken and absorbed by cell No. 1. Shortly thereafter a new cell erupts from the other side of No. 1 just as though No. 2 had moved steadily through it. The behavior shown on this record has a characteristic appearance when watched on the cathode-ray oscilloscope. It reminds the author of the interweav-

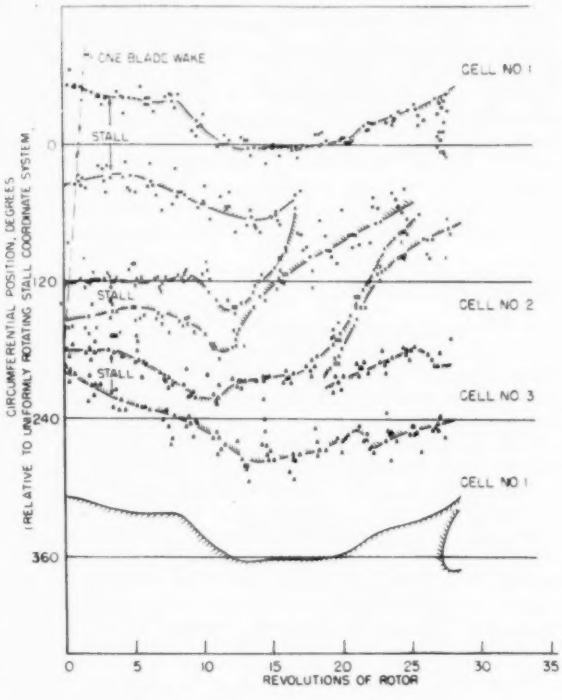

Fig. 12 Stall-cell-number change

ing pattern of railroad tracks viewed from the window of a fast-moving train; the apparent motion of one stall cell through several others resembles the track pattern as one passes a pair of interlocking switches.

The small stall cell which separates from cell No. 3 in. Fig. 12 at the 18th revolution might survive, crossing cell No. 1 just beyond the edge of the record. Details such as this cannot be picked out readily on the swiftly changing oscilloscope stall pattern (this cell needed only 1/8 sec to separate from No. 3, move across the intervening blades and be absorbed in No. 1); nevertheless, on occasion we have seen what appeared to be two small cells moving in unison across three larger cells. The portion of the transition recorded on the short film strip used by the PA oscillograph camera is a matter of chance. So far, although many records have been obtained, none has shown the end of the splitting and recombination phase.

Oscilloscope watching seems to indicate that either the splitting stops, leaving a pattern with one less cell, or the small, slow-moving cell grows with successive collisions (and probably speeds up also). Eventually it turns away from an approaching cell leaving a pattern with one more stall cell. In either case the new pattern, once established, evens out through a decaying phase modulation such as that shown in Fig. 4. The total number of stall cells need not change as a result of the transition sequence. The final number of cells depends on the net number of cell divisions and recombinations. Variants of the sequence described previously have been observed. Thus a cell may split and the slow moving piece be absorbed by the succeeding cell without further splitting or any significant modulation, Fig. 5. On other occasions, the piece may turn away from the succeeding cell establishing immediately a pattern with one more cell. Cells are sometimes added by nucleating an extra cell between existing cells, and cells are sometimes lost by decay (without amalgamation). In both these cases there seems to be a regular modulation in the process of equalizing the cell spacing after the change in number of cells.

An exponential decay fitted to the phase modulation shown in Fig. 4 is attenuated 50 per cent in 24 revolutions. This is a much slower growth rate than would be associated with the initiation of stall from the unstalled condition. The initial multicell stall appears virtually instantaneously and, using a different test configuration single-cell stall over 35 per cent of the rotor can develop in only 12 revolutions. However, the disappearance of stall with increasing flow is quite gradual, requiring 1/2 to 1 sec for the stall pattern to disappear from the oscilloscope. The agreement between this and the decay rate observed in Fig. 4 may be a coincidence, but it is interesting.

Wake Studies

The six hot wires also have been used to study the flow downstream of the stall-propagating rotor. For these tests two probes were mounted directly behind the rotor so that the stall-cell number and propagation velocity could be determined; the remaining probes were distributed along the axis of the machine ahead of and behind the rotor. It was found that, for the small, multicell-stall patterns observed at relatively high flows, the rotor stall was not synchronized with the stator stall. In fact, the stator carried three cells while the rotor carried two, and the propagation velocities relative to the casing were different. Close behind the stall-propagating rotor was found a series of high-velocity jets separated by "dead" fluid. In the region of the stall cells the dead wakes occupied nearly all the interblade passage. Downstream of the rotor mixing were slow, individual blade wakes maintaining their character well downstream; an especially prominent stall wake or an especially narrow one could often be followed through the entire rotor-stator gap. While mixing was slow, static-pressure equalization was rapid. For small stall cells, the static pressure one chord downstream was essentially constant, although there was a considerable pressure fluctuation close upstream of the rotor.[9] The pressure fluctuations decay roughly exponentially with distance from the rotor.

Conclusions

The most significant experimental result is the discovery and analysis of the oscillation of the stall-cell velocity. From this we have been able to deduce the stall frequency-wave number characteristic of the machine and to separate the stall-frequency expression into two parts, one dependent solely on the number of stall cells, the other dependent solely on mass flow. Of secondary importance are the wake study and the information we have gathered about the stall-number transition process. The wake study seems to justify the assumption of inviscid flow downstream of the stalled rotor since no appreciable mixing was discovered in the region where static-pressure equalization was occurring.

A number of features of stall propagation have still to be clarified. The cell-number transition process can be studied by the data-handling technique developed for the phase-modulation analysis. For this, an oscillograph camera capable of recording, with good detail, the flow pattern over a period of at least 1000 revolutions of the rotor will be needed. The reduction and plotting of the data on such a film is an awe-inspiring task but, at the moment, we see no short cut which will yield the same amount of detailed information. Tedious though this will be, it is perhaps the most valuable test that can be made.

A "constant-resistance-ratio hot-wire anemometer" has been developed recently. This instrument automatically compensates for instantaneous temperature fluctuations in the main stream giving an output which is related to the fluid velocity only. With such an instrument it should be possible to make the quantitative measurements needed to establish the operating point of the unstalled blades. This will require patience. Grant, prior to 1950, attempted, with only limited success, to make similar quantitative velocity measurements on the unstalled compressor. At that time the hot wire had not been developed to its present form, but the calibration difficulties he encountered should not be underrated. Ultimately these quantitative measurements might be recorded on the long films with the qualitative, time-phase data from the constant-current anemometers, to give a more complete description of the flow.

References

1 H. W. Emmons, R. E. Kronauer, and J. A. Rockett, "A Survey of Stall Propagation—Experiment and Theory," published in this issue, pp. 409–416.

2 T. Iura and W. D. Rannie, "Observations of Propagating Stall in Axial Flow Compressors," California Institute of Technology Mechanical Engineering Laboratory, Report No. 4, April, 1953.

3 H. W. Emmons, C. E. Pearson, and H. P. Grant, "Compressor Surge and Stall Propagation," TRANS. ASME, vol. 77, 1955, pp. 455–469.

4 R. E. Kronauer, "Propagation and Stability of Nonlinear Waves With Application to Cascade Stall," submitted to THE AMERICAN SOCIETY OF MECHANICAL ENGINEERS for publication.

5 J. Fabri and R. Siestrunck "Rotating Stall in Axial Flow Compressors," *Journal of the Aeronautical Sciences*, vol. 24, 1957, pp. 805–812.

6 F. E. Marble, "Propagation of Stall in a Compressor Blade Row," *Journal of the Aeronautical Sciences*, vol. 22, 1955, pp. 541–544.

7 R. E. Kronauer and H. P. Grant, "Pressure Probe Response in Fluctuating Flow," Second U. S. National Congress of Applied Mechanics, University of Michigan, Ann Arbor, Mich., June 14–18, 1954.

[9] No pressure fluctuation has been detected either upstream or downstream of this particular stator when it is stall-propagating. No velocity fluctuations upstream have been found either. This is puzzling.

HAROLD J. HOGE
SUZANNE S. EICHACKER
DAVID L. FISKE
Quartermaster Research and Engineering Center, Natick, Mass.

Studies of Jet Compression—I

Apparatus and Methods. Results With Air at Room Temperature

An experimental jet compressor (ejector) employing gases at subatmospheric pressures is described and data are presented showing efficiencies obtained with air used as both the driving and the driven fluid. A technique is described by means of which efficiency may be determined as a function of outlet pressure and entrainment ratio. Curves are presented showing that efficiency passes through a maximum as outlet pressure is increased. The compression ratio of the driven fluid likewise passes through a maximum as the outlet pressure is increased, but the maximum of efficiency occurs at a slightly higher pressure than the maximum of compression ratio. The highest efficiency achieved was 20.6 per cent, at an entrainment ratio of 1.3 and a compression ratio of 1.14. The ratio of pressure of driven stream to pressure of driving stream at time of contact has been determined. The value of this pressure ratio corresponding to maximum efficiency was found to increase linearly with entrainment ratio, over most of the range of the measurements.

Introduction

THE SIMPLICITY of jet compression makes it attractive for many applications from an engineering standpoint. In spite of the low efficiencies ordinarily achieved, jet compression has been rather widely employed in steam-jet refrigeration, in air ejectors, in mine and tunnel ventilation, in mercury diffusion pumps, etc. If higher efficiencies could be achieved, a number of practical uses for jet compression would be opened up, particularly in applications to refrigerators, heat pumps, and fluid circulators. The present paper is the first report on a program to determine to what extent the limitations on efficiency are fundamental, and to what extent efficiency can be improved by proper geometrical design and by proper choice of operating conditions.

Experimental studies of jet compression have been made by Keenan, Neumann, and Lustwerk [1],[1] by Keenan and Neumann [2], by Kastner and Spooner [3], by Royds and Johnson [4], and by others. The results have been analyzed with the aid of basic thermodynamics and fluid mechanics, using the equations of energy, continuity, momentum, and state. Flügel [5] appears to have been the first to develop this type of analysis. These analyses contain simplifying assumptions such as "constant pressure mixing" or "constant area mixing," which have complicated the problem of comparing theory with experiment. The picture of the mixing process is not very clear, and in spite of the rather extensive published investigations of various sizes and shapes of nozzles, mixing throats, and diffusers, the design of jet pumps remains on a primarily empirical basis.

The present paper contains a description of our apparatus and of the method of taking and analyzing the data. It also contains the experimental results obtained with room-temperature air

Contributed by the Hydraulic Division and presented at the Semi-Annual Meeting, Detroit, Mich., June 15–19, 1958, of THE AMERICAN SOCIETY OF MECHANICAL ENGINEERS.

NOTE: Statements and opinions advanced in papers are to be understood as individual expressions of their authors and not those of the Society. Manuscript received at ASME Headquarters, February 28, 1958. Paper No. 58—SA-13.

[1] Numbers in brackets designate references at end of paper.

Nomenclature and Dimensions

η = efficiency of the jet compressor, defined by equation (1)
η_{MAX} = maximum efficiency attained for a fixed value of m/M
m = flow of driven gas, lb per hr
M = flow of driving gas, lb per hr
P = pressure, mm Hg
T = temperature, deg F abs
h = enthalpy, Btu per lb
s = entropy, Btu per lb deg F
u = velocity, ft per sec
c_p = specific heat at constant pressure, Btu per lb deg F
G = flow per unit area, lb per hr ft^2
A = cross section area, ft^2
R = gas constant, 0.068549 Btu per lb air deg F abs

Superscripts:

* = state at sonic velocity

Subscripts:

1 = initial state of driving fluid
2 = state corresponding to isentropic expansion of driving fluid to pressure at state 5
3 = initial state of driven fluid
5 = state of driving fluid at beginning of mixing
6 = state of driven fluid at beginning of mixing
7 = state at completion of mixing
8 = final state, at compressor exit
9 = state corresponding to isentropic compression of driven fluid to pressure at final state 8
10 = state corresponding to isentropic expansion of driving fluid to pressure at final state 8
a, b, . . . i = taps for pressure measurement; refer to Fig. 2 for locations

The following dimensions refer to the apparatus used in the present experiments:
Driving-fluid nozzle No. 2 (the only nozzle used):

(*Continued on next page*)

utilized as both the driving and the driven fluid. Only one driving-fluid nozzle (No. 2) was employed. The observed inlet and outlet pressures, together with the corresponding temperatures, have been used to compute the over-all efficiency of the jet compressor as influenced by the conditions of operation.

Apparatus and Procedure

A diagram of the apparatus is given in Fig. 1. Ordinary atmospheric air supplied both the driving and driven streams. The pressure difference motivating the jet is obtained by means of a large vacuum pump (15 cfm capacity) attached to the jet-compressor outlet. The use of lowered, as against elevated pressures, offers the advantage that all pressures are readily measured by mercury manometers. Reduced pressure offers also the advantage of reduced density, making possible a nozzle diameter of convenient size without excessive quantity of flow. Such a system makes it possible to use much higher pressure ratios than could be conveniently reached in a system in which atmospheric pressure is the low, rather than the high, limit.

The driving and driven streams are measured at atmospheric temperature and pressure by two ordinary (dry) gas meters. The two lines connecting the meters to the jet compressor each contain a simple needle valve (V_1, V_2) to control the flow rate. The pressure drops across these two valves were always more than sufficient to produce sonic flow. Hence a valve could be adjusted to give a particular flow rate, which would remain constant except for the small changes due to variations in room temperature and barometric pressure. The nondependence of flow rate on downstream conditions proved to be a great convenience in taking data. The lines from the meters to the jet compressor passed through thermostated heating baths designed to control the stream temperatures. Thus far these baths have not been used.

Three thermocouples are placed inside the jet compressor, to measure, respectively, the inlet temperature of the driving and the driven streams, and the outlet temperature of the mixed stream. Temperature measurements were made with these couples on a few occasions, to see whether there was any net heat transfer from the apparatus to the gas flowing through it. In one case (run 70) the outlet temperature was about 2.5 deg F higher than the weighted average of the inlet temperatures, but mostly the changes were less than 1 deg F and are considered small enough to be neglected in the present paper.

The pressure at the outlet of the jet compressor is controlled by valve V_3 in the line leading to the vacuum pump. This valve consisted of a length of heavy-wall rubber tubing (5/8 inch ID) clamped between two boards that could be drawn together by screwing down on a hand wheel. Adjustment of the outlet pressure to any desired value required only a few seconds.

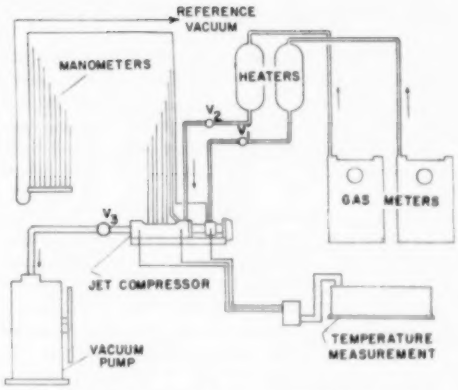

Fig. 1 Flow diagram of experimental equipment

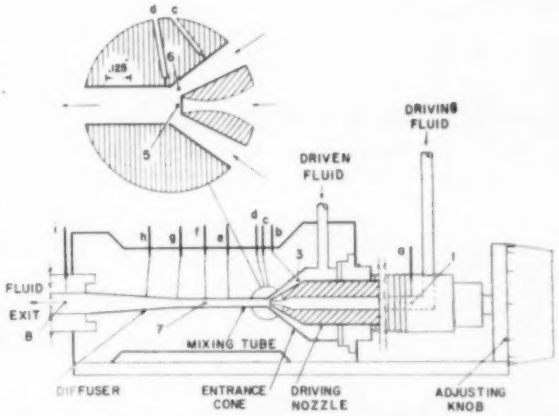

Fig. 2 Cross section of jet compressor with enlarged view of entrance to mixing tube

The central element of the experimental equipment is shown in Fig. 2. It is an assembly of brass parts composing an ejector system. The major part, indicated as "jet compressor" in Fig. 1, consists of entrance cone, mixing tube, and diffuser. The driving-fluid nozzle may be moved axially with respect to the rest of the apparatus. It is the function of the bellows to permit movement of the nozzle without loss of gas by leakage past the gland. Nozzle position is controlled by rotation of the adjusting knob, one

Nomenclature and Dimensions

throat diameter = 0.0595 in.
exit diameter = 0.0710 in.
throat-to-exit distance = 0.122 in.
angle of outer conical surface with axis = 25 deg

Entrance cone for driven fluid:

diameter at upstream end = 1.25 in.
angle of wall with axis = 35 deg

Mixing tube:

diameter = 0.1875 in.
length = 1.67 in.
length ÷ diameter = 8.9

Diffuser:

diameter at tap g = 0.1891 in.
diameter at tap h = 0.2544 in.
diameter at outlet = 0.3755 in.
length = 1.80 in.
angle of wall with axis = 3.0 deg

Distance of planes of pressure-tap openings, etc., from junction of entrance cone and mixing tube, measured along axis of flow, with distances increasing in direction of flow:

beginning of entrance cone = −0.76 in.
tap b = −0.48 in.
tap c = −0.18 in.
junction of entrance cone and mixing tube = 0 in.
tap d = +0.03 in.
tap e = 0.65 in.
tap f = 1.15 in.
junction of mixing tube and diffuser = 1.67 in.
tap g = 1.69 in.
tap h = 2.31 in.
end of diffuser = 3.47 in.

graduation of which corresponds to a nozzle movement of 0.001 inch.

Provision is made for pressure measurements at 9 different points within the jet apparatus. The various pressure taps are lettered a, b, ... i in the diagrams, and each is connected to an arm of a mercury manometer. Two mercury manometers are used, each with a reference arm in which a vacuum is maintained by a mercury-diffusion pump. The pressure readings are thus absolute.

When the flow of driven fluid is equal to or greater than the flow of driving fluid, the amount of compression produced is small. That is, the compression ratio is only slightly greater than unity. Under these conditions changes in pressure within the jet compressor could not be measured with sufficient accuracy with the mercury manometers. An oil manometer was therefore added, and was connected in parallel with the mercury manometer, to all taps except tap a, at which the pressures were too high to be read on the oil manometer. The oil manometer can be used either as a differential or as an absolute manometer. The ratio of the densities of mercury and oil, as determined by a comparison of column heights when both were relatively large, is 14.813. The use of the oil manometer appears to have increased the accuracy of the data at least tenfold in the regions where the mercury manometer was unsatisfactory.

Definition of Efficiency of Jet Compressor

The jet compressor receives two streams of fluid, one at a relatively high pressure and the other at a relatively low pressure, and delivers them as a single stream at some intermediate pressure. Useful work is done in compressing the low-pressure stream, and the source of this work is the expansion of the high-pressure stream. The process may be conveniently followed by reference to the enthalpy-entropy diagram of Fig. 3. This is an actual representation of some of the experimental data plotted to scale, but our present concern is only with the qualitative aspects of the diagram. Point 1 represents the initial state of the driving fluid, and the condition line 1-5 represents states that are passed through during expansion and acceleration in the driving-fluid nozzle. The positions within the apparatus at which the various states are reached are shown in Fig. 2 by a series of points numbered to correspond to the points in Fig. 3. The points numbered 3 represent initial states of the driven fluid. For definiteness, consider only the one referring to observation 79k. The condition line 3-6 represents states along the path of expansion and acceleration of the driven fluid before it meets the driving fluid. The point 6 is enclosed in parentheses because, unlike the other points on the diagram, it is not plotted to scale. The mixing process cannot be represented on the diagram, but after mixing, the moving stream is in some state 7. The condition lines 7-8 represent states along the path of final deceleration and compression to the outlet pressure P_8.

In the jet compression process, driving fluid has decreased in pressure from state 1 to the outlet pressure P_8. If such a process were to occur in a lossless turbine the maximum work that could be performed by unit mass of driving fluid is equal to the isentropic enthalpy drop $h_1 - h_{10}$. We will accept the same definition

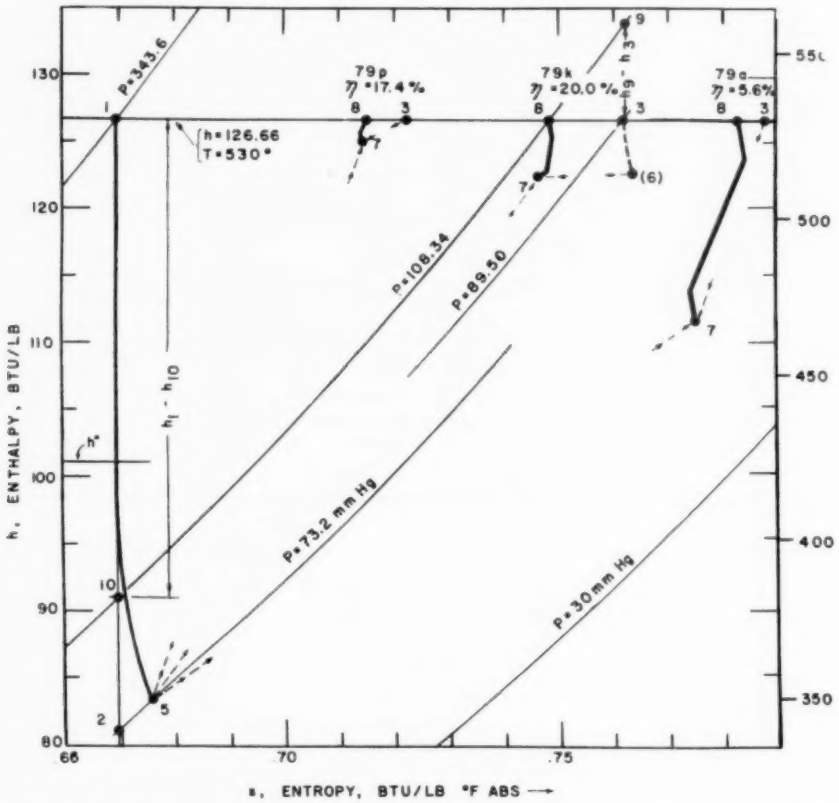

Fig. 3 Enthalpy-entropy diagram showing condition lines for observations 79a, 79k, and 79p. Drawn to scale except for point 6 which is schematic.

for the maximum work that could be done by unit mass of driving fluid in passing through a hypothetical lossless jet compressor. If we similarly imagine a lossless compressor compressing driven fluid from state 3 to the outlet pressure P_8, the minimum work required per unit mass is equal to the isentropic enthalpy rise $h_9 - h_3$. We will accept $h_9 - h_3$ as the amount of work done when unit mass of driven fluid passes through the jet compressor. Let m be the rate of flow of driven fluid in pounds per hour, and let M be the corresponding rate of flow of the driving fluid. Then the work actually done within the apparatus in one second is $m(h_9 - h_3)$ and the maximum work that could be done in a lossless process is $M(h_1 - h_{10})$. The efficiency η is defined as the ratio of these quantities or

$$\eta = \frac{m}{M}\,\frac{h_9 - h_3}{h_1 - h_{10}} \qquad (1)$$

In the actual jet-compression process the two streams are mixed and delivered in state 8, whereas in the idealized process used for comparison the turbine exhaust is in state 10 and the blower output is in state 9. It is recognized that states 9 and 10 are not in general "dead states." If point 8 represents the dead state, the temperature differences $T_9 - T_8$, and $T_8 - T_{10}$ could be used to operate Carnot engines and perform work as the fluids were brought from states 9 and 10 to state 8. It is customary to disregard such quantities of work in defining the efficiency of a steam turbine [6], and it appears desirable to follow the same practice for jet compression, even though the quantities of work disregarded may be relatively more important in the jet compressor. If we were to include these quantities of work in the computation we would obtain a quantity based on changes in available energy that Keenan [6, p. 297] has called the effectiveness, to distinguish it from the conventional efficiency.

Having defined the efficiency η in the conventional manner, one must keep in mind that η refers to only one step in the complete process in which thermal energy is used to do useful work of compression. To obtain high over-all thermodynamic efficiency, we must first learn how to design a jet compressor giving a high value of η. Then such a compressor must be incorporated into a system that is thermodynamically efficient in the over-all sense. That is, heat must be absorbed at the highest practical temperature and rejected at the lowest practical temperature. All irreversible processes must be reduced in importance. The last condition requires that T_8, T_9, and T_{10} should not be widely different, and in part establishes the optimum location of state 1 relative to states 3 and 8.

Experimental Results

In a typical run, the mass rates of flow m and M were set to the desired values and held constant throughout the run. The outlet pressure P_8 was set at some desired value and the 9 pressures were read and recorded. Then P_8 was set at another value and the process repeated until the run was completed. In all the data now being reported, the position of the driving-fluid nozzle was held constant. The nozzle was advanced until it touched the entrance to the combining tube. It was then backed off 0.175 in. at which position the tip was 0.05 in. upstream from the entrance to the mixing tube. The circular insert in Fig. 2 is a scale drawing of the nozzle in operating position. All measurements reported here were taken with this setting. In several preliminary measurements, efficiency was measured as a function of nozzle position. These measurements indicated that, so long as extreme settings were avoided, the effect of nozzle position on efficiency was not large. The accepted setting is an intermediate one that is believed to be reasonably suitable for all the data reported. The observed volume rates of flow were converted to mass rates of flow on the assumption that the air passed through the gas meters at 70 deg F and 760 mm Hg, under which conditions a flow rate of 1 liter per min is equivalent to 0.1587 lb per hr.

Table 1 Experimental data for three typical runs

Observation	Pressures, mm Hg, at various taps: a (P_1)	b (P_3)	c	d (P_6)	e	f (P_7)	g	h	i (P_8)	η
	Run 84, m/M = 0.0744				M = 1.57 lb per hr					
a	341.5	13.8	13.80	13.53	13.39	15.02	12.65	12.28	20.75	1.66
m	339.5	13.5	13.47	13.10	15.02	18.16	21.80	33.62	37.67	5.43
p	339.2	14.2	14.17	13.73	21.36	31.68	34.38	46.02	42.66	6.16
n	341.5	16.0	16.00	15.66	28.12	37.60	38.79	43.85	46.11	6.02
o	341.3	22.7	22.70	22.36	36.94	48.45	49.16	52.94	54.73	5.23
g	341.0	34.0	34.00	33.80	48.99	61.34	62.22	65.19	66.61	4.22
l	343.2	62.7	62.70	62.56	85.25	91.59	91.05	81.09	93.99	2.96
k	342.0	140.0	140.00	139.53	161.60	164.10	163.29	164.64	165.21	1.92
	Run 47, m/M = 0.421				M = 1.57 lb per hr					
a	344.5	30.9	30.44	25.10	28.22	26.52	20.39	18.15	30.64	0.11
k	343.8	30.5	30.43	25.30	25.71	28.34	27.09	34.99	42.68	9.36
o	342.0	35.7	35.63	31.99	34.55	40.22	42.99	50.96	55.88	14.14
j	344.2	44.9	44.83	42.47	45.37	52.39	59.08	66.30	69.61	15.38
n	344.1	52.1	52.00	50.08	58.48	71.85	73.31	75.96	78.19	14.79
d	345.1	75.2	75.17	73.95	86.68	96.87	96.97	100.31	101.93	12.98
i	344.2	108.6	108.57	107.72	128.11	130.71	129.76	132.23	133.68	10.79
h	345.3	153.1	153.07	152.53	170.15	172.98	172.31	174.20	175.14	9.43
g	344.5	180.0	179.66	179.53	196.20	197.96	197.35	198.97	199.85	8.26
	Run 79, m/M = 1.00				M = 1.58 lb per hr					
a	342.2	61.2	60.80	50.06	47.50	47.56	52.15	59.11	65.79	5.58
b	342.6	65.6	65.26	58.01	54.60	56.96	61.36	68.16	74.44	10.40
w	338.3	69.5	69.16	60.93	60.25	65.86	69.64	76.39	81.99	14.56
d	337.2	72.5	72.16	64.39	64.40	71.22	74.73	81.95	87.08	16.81
n	343.7	76.7	76.43	66.87	67.54	75.51	78.68	86.01	90.67	18.03
v	343.4	76.4	76.10	68.84	69.79	78.70	81.40	88.69	93.01	18.58
r	344.2	79.8	79.46	72.58	74.74	84.26	86.14	93.30	97.28	19.17
g	344.8	84.0	83.66	77.18	80.29	89.91	91.53	98.45	102.19	19.60
h	344.6	84.7	84.39	77.95	81.22	90.88	92.40	99.35	102.96	19.67
r	342.0	87.0	86.66	80.55	85.39	95.17	95.44	102.12	105.90	19.79
k	344.5	89.5	89.23	83.26	89.50	99.09	98.44	105.09	108.34	19.99
l	344.3	92.8	92.53	86.79	95.57	103.60	102.15	108.56	111.44	19.71
n	344.3	101.6	101.36	96.23	109.33	113.85	111.89	117.84	120.64	19.54
o	344.4	132.0	131.86	128.09	138.55	144.66	143.85	148.47	150.67	18.27
p	344.2	158.7	158.56	155.60	165.99	171.32	170.62	174.43	176.32	17.43

Having defined the efficiency η corresponding to each setting of the outlet pressure P_8 was computed from equation (1), using enthalpies obtained from the gas tables of Keenan and Kaye [7]. The enthalpies h_1 and h_3 remain constant at 126.66 Btu per lb in consequence of the assumption that the inlet air was always at 530 F abs. Data selected from three typical runs are given in Table 1, and in Fig. 4 the efficiencies found in these runs are plotted against the outlet pressure P_8. About half the experimental data have been omitted from Table 1, but the plotted points in Fig. 4 represent all the data taken in the three runs. As the outlet pressure P_8 is increased, the efficiency first rises, then passes through a maximum, and finally decreases. The height of the maximum and the general shape of the curve clearly depend on the entrainment ratio. In a run such as those shown in Fig. 4, a change in P_8 is accompanied, in general, by changes in all the other observed pressures except P_1. Since the flow at the throat of the driving-fluid nozzle is sonic, changes in conditions downstream from the

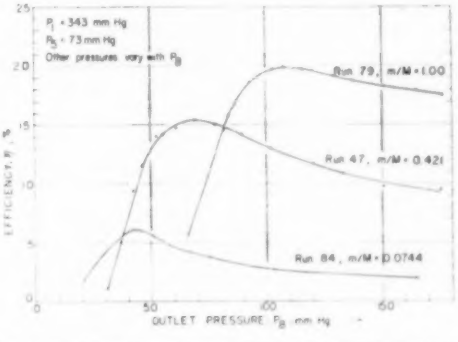

Fig. 4 Efficiency versus outlet pressure for three typical runs

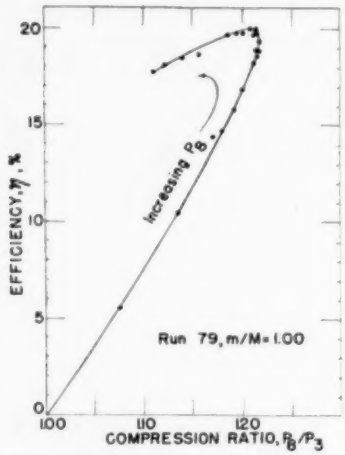

Fig. 5 Efficiency versus compression ratio for a typical run

Table 2 Conditions at efficiency maxima

The values of η max were determined from the curves of Fig. 4 and from similar plotted curves for all the other runs. Data in the table refer to conditions at these maxima.

Run	P_1 mm Hg	P_3 mm Hg	P_8 mm Hg	P_8/P_1	P_8/P_3	M lb/hr	m/M	η max %	P_6/P_5
59	344.0	17.0	48.0	0.1395	2.820	1.59	0.0559	4.50	0.23
84	340.0	15.4	45.0	0.1324	2.915	1.57	0.0764	6.15	0.21
58	346.8	17.0	46.0	0.1326	2.700	1.59	0.0851	6.40	0.22
52	342.5	16.4	44.0	0.1285	2.680	1.56	0.106	7.61	0.23
57	346.7	18.0	47.5	0.1370	2.638	1.59	0.115	8.60	0.24
63	342.0	19.7	47.0	0.1374	2.385	1.58	0.161	10.60	0.28
56	347.0	25.2	55.0	0.1585	2.180	1.59	0.190	11.60	0.33
62	346.0	28.1	48.0	0.1387	1.995	1.59	0.241	12.30	0.31
45	346.5	32.8	60.0	0.1732	1.828	1.57	0.296	14.05	0.41
46	346.0	38.5	64.0	0.1850	1.662	1.58	0.361	14.80	0.50
47	343.8	43.8	68.0	0.1978	1.553	1.57	0.421	15.30	0.56
48	344.8	50.7	76.0	0.2204	1.498	1.58	0.495	17.30	0.65
87	343.1	53.3	77.0	0.2244	1.445	1.58	0.553	17.77	0.68
50	342.5	58.0	81.0	0.2365	1.397	1.57	0.630	18.40	0.76
78	345.2	71.5	92.0	0.2665	1.287	1.58	0.806	19.10	0.90
79	344.5	89.2	108.0	0.3135	1.211	1.58	1.00	19.90	1.13
80	336.9	105.3	122.0	0.3621	1.159	1.58	1.20	20.50	1.36
86	333.0	106.9	122.0	0.3664	1.141	1.56	1.32	20.50	1.40
85	337.0	106.5	121.0	0.3590	1.136	1.56	1.40	20.55	1.39
83	336.9	111.0	124.0	0.3681	1.117	1.57	1.52	19.60	1.39
82	345.2	114.9	126.0	0.3392	1.079	1.58	1.83	15.80	1.34
69	515.8	15.5	56.5	0.1095	3.645	2.38	0	0	0.15
68	402.8	32.9	64.0	0.1589	1.943	1.84	0.277	14.20	0.35
72	346.5	49.5	74.0	0.2136	1.495	1.59	0.485	16.65	0.62
73	304.0	58.7	78.0	0.2566	1.328	1.40	0.681	17.90	0.85
77	255.8	68.8	81.5	0.3186	1.185	1.18	1.01	18.00	1.17

throat cannot affect P_1, which remains substantially constant throughout a run.

Many investigators have analyzed their data using the compression ratio, P_8/P_3, as an independent variable where we have used the outlet pressure P_8. Fig. 5 shows how one of the curves (run 79) of Fig. 4 is transformed when compression ratio is used as the abscissa instead of outlet pressure. The high-pressure arm of the original curve is folded over and lies above the low-pressure arm. Hence there are in general two different modes of operation corresponding to the same compression ratio, and the mode in which both P_8 and P_3 are larger gives the higher efficiency. It has sometimes been assumed that, for a given entrainment ratio, maximum efficiency is synonymous with maximum compression ratio. A look at equation (1) shows that this is only approximately true. The maximum value of $h_9 - h_3$ will occur when P_8/P_3 is maximum and if, changes in the denominator of equation (1) are negligible, maximum efficiency will coincide with maximum compression ratio. However, changes in the denominator cannot be entirely neglected. As P_8 increases, h_{10} increases and the denominator decreases. This displaces the point of maximum efficiency to a higher value of P_8 than that corresponding to maximum compression ratio. For example, in run 79 the maximum compression ratio (P_8/P_3) occurred at P_8 = 97 mm Hg whereas the maximum efficiency occurred at P_8 = 108.0 mm Hg.

To find the relation between entrainment ratio and efficiency, a large number of runs was made and the results plotted in the manner of Fig. 4. The maximum efficiency was then read from each curve and recorded. The maximum efficiencies thus found are given in Table 2, together with the values of P_8 and other important parameters that correspond to the maximum value of η.

For most of the data in Table 2, M is approximately equal to 1.587 lb per hr (10 l per min). All the data for which M has this value are represented in Fig. 6, in which maximum efficiency is plotted against entrainment ratio. Starting at zero with zero entrainment, the curve rises to a maximum efficiency of 20.6 per cent at an entrainment ratio of about 1.3 and then starts to fall. The last part of the curve is dotted, to indicate a rapid decrease in accuracy above an entrainment ratio of about 1.35.

Efficiency curves such as those shown in Fig. 4 sometimes showed irregularities, which often took the form of sharp drops in efficiency covering a range in P_8 of 5 to 10 mm Hg. These irregularities were at first attributed to experimental error, but later it was found that in many cases they were highly reproducible.

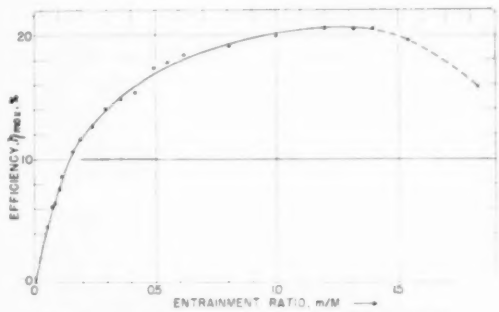

Fig. 6 Maximum efficiency versus entrainment ratio

Further study will be required to establish their cause. It is believed that the accuracy of Fig. 6 is not seriously affected by the existence of these irregularities.

The relationship between the pressures of the driving and the driven streams as they come in contact is a matter of considerable interest. If the driving fluid has a higher pressure than the driven stream it is said to be underexpanded. Conversely, the condition in which the driving stream has the lower pressure is referred to as overexpansion. Royds and Johnson [4] suggest that an air ejector should be operated with a moderate amount of underexpansion. In the discussion on their paper, and elsewhere in the literature, a number of opinions on this question are expressed. Our data give an experimental answer to this problem. The pressure P_5 of the driving fluid as it leaves the driving-fluid nozzle cannot be directly measured in our apparatus. However, if a reasonable value of nozzle efficiency is accepted, this pressure can be calculated with an error that probably does not exceed 10 per cent. Such a calculation has been made, using methods described later in this paper, where the plotting of points on the h-s diagram is described. The pressure P_6 is the pressure of the driven fluid when it first comes in contact with the driving fluid. Contact occurs at a point somewhere between the two pressure taps c and d, Fig. 2. The pressure P_d at tap d, the first tap on the mixing tube, was taken to be P_8. This procedure requires some justification. Reference to Table 1 shows that P_d was always somewhat lower than P_c. The percentage difference in the neighborhood of maximum efficiency was 3.4 for run 84, 5.3 for

run 47, and 6.7 for run 79. Hence within an error of 10 per cent or less, the pressure at either tap can be taken to represent P_8. It is not considered possible that a pressure widely different from P_c or P_d could exist between the two taps because the flow of driven fluid was always subsonic in this region.

For each point of maximum efficiency in Table 2, the pressure ratio P_6/P_5 has been computed and included in the table. When this ratio is plotted against the entrainment ratio m/M, the curve of Fig. 7 is obtained. The value of P_6/P_5 at maximum efficiency increases with m/M. Within the experimental error the relation is linear up to $m/M = 1.0$. In this region P_6/P_5 appears to rise slightly above the straight line. Near $m/M = 1.2$ the curve levels out and appears to diminish slightly at the highest entrainment ratios investigated. The linear portion of the graph in Fig. 7 does not pass through the origin but it comes rather near it. Now a straight line passing through the origin of Fig. 7 corresponds to a simple variation of conditions inside the jet compressor. With P_5 and M held constant (this was the case with Fig. 7) a straight line through the origin corresponds to the acceptance of a constant volume-rate of flow of driven fluid. Under such circumstances, when the entrainment ratio is increased both the pressure and the density of the driven fluid increase in proportion, and there is no change in the velocity of the driven fluid. This picture does not exactly correspond to the situation shown in Fig. 7 but it is not a bad approximation for a considerable range of m/M.

At an entrainment ratio of approximately 0.88, P_6/P_5 reaches the value 1. For all lower entrainment ratios, maximum efficiency requires the driving fluid to be underexpanded ($P_6/P_5 < 1$). Conversely, if the entrainment ratio is greater than 0.88, overexpansion of the driving fluid ($P_6/P_5 > 1$) is required for maximum efficiency. These results refer, of course, only to the apparatus used in the present experiments. One would expect that, if another apparatus were used, a curve of the same general shape as Fig. 6 would be obtained, but it would not necessarily pass through the same numerical values. It must also be borne in mind that both P_6 and P_5 are uncertain by perhaps 10 per cent, so that the ordinates in Fig. 7 are uncertain by 15 or 20 per cent. The internal consistency is much better than this figure, of course.

In the theory of constant-pressure mixing, the driving and driven streams are assumed to be at the same constant pressure from the moment of contact until mixing is complete. In Fig. 7, constant-pressure mixing is probably approximated most closely when $P_6/P_5 = 1$, since in this case the assumed conditions are at least satisfied as mixing begins. The efficiency maxima of runs 84, 47, and 79 were compared with Fig. 11 of Keenan, Neumann, and Lustwerk [1], which is based on the theory of constant pressure mixing. Using the experimentally observed abscissa (our P_1/P_2) and the curve corresponding to our area-ratio (=9.93) the ordinate (P_8/P_2 in our notation) can be obtained and compared with the experimentally observed value.

The results of the comparison are as follows:

Run	84	47	79
m/M	0.0744	0.421	1.00
A_7/A^*	9.93	9.93	9.93
P_1/P_2	22.021	7.851	3.863
P_8/P_2	2.915	1.553	1.211
(P_8/P_2) calc from KNL's Fig. 11	3.7	1.9	1.3
(P_8/P_2) obs/(P_8/P_2) calc	0.79	0.82	0.93
P_6/P_5	0.21	0.56	1.13

The agreement is slightly better near $P_6/P_5 = 1$ than elsewhere. If, instead of using the area-ratio curve of Fig. 11 of Keenan, et al., we ignore it and use the entrainment-ratio curves corresponding to experiment, the agreement between observed and calculated values of P_8/P_2 is much worse than that shown in the table above. Since our data were not taken under conditions that would provide an optimum test of either constant-pressure or constant-area mixing, a full-scale comparison with these theories has not been included in this paper.

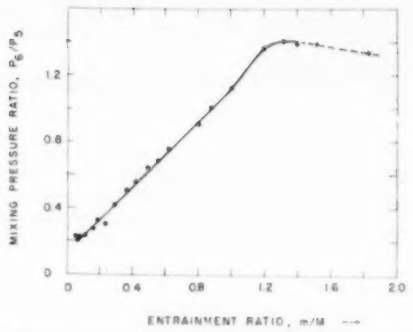

Fig. 7 Mixing pressure ratio at maximum efficiency versus entrainment ratio

Plotting Experimental Data on the *h-s* Diagram

A few typical sets of observations from the experimental data have been plotted to scale in the *h-s* diagram of Fig. 3. The condition lines are helpful in visualizing various parts of the compression process, and the increases in entropy indicate where the major losses occur. The data plotted in Fig. 3 are observations 79a, 79k, and 79p, all from Table 1. Referring to Fig. 4, one observation corresponds to a point near the maximum of the efficiency curve, and the other two correspond to points near the two ends. The condition line 1-5 represents passage of the driving fluid through its nozzle and is the same for all the observations. The mixing process cannot be represented in the diagram. Three arrows point from state 5 to the three states 7, indicating that after mixing is complete the mixed stream is in state 7. The points 7 correspond to pressure tap f. The three states 3 represent the initial condition of the driven fluid. Arrows indicate that during the mixing process the driven fluid is transferred to the appropriate state 7. A part of the path from 3 to 7 (3-6) can be plotted if the necessary data (pressures and cross-section areas) are available. The paths 3-6 have not been plotted to scale in Fig. 3 but for one observation (79k) the path is shown schematically. The three lines 7-8 represent states along the path of deceleration and compression of the mixed stream between the last tap on the mixing tube and the outlet. These lines all show a small over-all increase of entropy in the direction of flow, as they should. The fact that the curves exhibit a few *decreases* of entropy between successive experimental points must be attributed to the cumulation of errors in the flow rates, cross section, and observed pressures. Fig. 3 shows clearly that the large entropy increases, and hence the large losses, are associated with the mixing process. This conclusion comes as no surprise, of course.

The method by which points on the condition lines may be located on the *h-s* diagram will be briefly described. There is, of course, no trouble with the points 1, 3, and 8. In these states the fluid is at rest, and measurements of pressure and temperature permit the enthalpy and entropy to be determined from the Gas Tables [7]. The pressures of these states were measured and the temperatures were assumed always to be 530 F abs (70 F). Hence $h_1 = h_3 = h_8 = 126.66$ Btu per lb. The assumption that T_3 is the same as T_1 and T_2 is easily justified by the law of conservation of energy, provided heat transfer to or from the gas within the apparatus is negligible, and provided it is permissible to treat h as a function of temperature only. These conditions were adequately satisfied in the present experiments.

The points representing states in which the fluids are in motion may be located with the aid of Fanno lines. Using the equations

of energy and continuity, the ideal gas law, and the approximation $h_1 - h = c_p(T_1 - T)$, the equation of a Fanno line may be put in the form

$$T = \frac{c_p P^2}{G^2 R^2}\left[-1 + \left(1 + 2T_1\frac{G^2R^2}{c_pP^2}\right)^{1/2}\right] \qquad (2)$$

where G is the mass flow rate per unit of cross section area and T_1 is the temperature of the fluid when at rest. Since the mass flow rates m and M are known G can be computed for any point at which the cross section has been measured (cf table of dimensions). Substituting observed values of P into equation (2), T is obtained. All other thermodynamic properties may then be obtained from the Gas Tables [7].

This procedure was used for the points on the condition lines 7-8 using $T_1 = T_3 = 530$ F abs. Unfortunately it could not be used for the point 5. The pressure at point 5 (driving-nozzle exit) is of particular interest because it is at this point that the driving and driven streams first come in contact. The nature of the apparatus did not permit P_5 to be experimentally observed, so it was necessary to compute P_5 on the basis of some reasonable assumption regarding losses. The losses were assumed to be negligible in the subsonic part of the nozzle and to be 10 per cent in the supersonic part. By trial it was found that a temperature drop from 530 to 441.5 F abs was sufficient to impart sonic velocity to air at the lower temperature. The temperature and enthalpy at the throat are $T^* = 441.5$ F abs and $h^* = 105.47$ Btu per lb. The velocity of sound at this temperature [8] is 1030 ft per sec and the pressure $P^* = 0.528P_1$ with the assumption of no losses. Referring to Fig. 3, the assumption of 90 per cent efficiency in the supersonic region of the nozzle requires that point 5 should satisfy the condition $h^* - h_5 = 0.90\ (h^* - h_2)$ where point 2 lies on the isentropic through point 1 and the constant-pressure line through point 5. Using equation (2) it was found by trial that the condition was satisfied when $T_5 = 350.3$ F abs, $h_5 = 83.64$ Btu per lb, and $P_5/P_1 = 0.213$. These values are independent of P_1 under the assumed conditions and to the accuracy of the gas tables used. The velocity at point 5 is found from the enthalpy drop to be 1468 ft per sec. The velocity of sound in air at $T_5 = 350.3$ F abs is 918 ft per sec [8]. Hence the Mach number is 1.60 if the assumed losses are correct.

Conclusions

The results presented in the present paper show how the condition of maximum operating efficiency of a jet compressor may be found, when entrainment ratio and outlet pressure are varied. The changes in these two variables automatically introduce changes in many other variables, including the initial pressure of the driven fluid and the compression ratio. However, some of the important parameters could not be varied because of the nature of the apparatus, and others that could have been varied have so far been held constant by choice. The variables that we have thus far not fully investigated include the expansion ratio of the driving fluid, the position of the driving-fluid nozzle, the temperatures of the input streams, the geometry of the inlet, diffuser, and other parts of the apparatus, and the molecular-weight ratio of the driving and driven fluids. These facts leave plenty of reason to hope that efficiencies substantially above 20.6 per cent (which is the highest value now being reported) are not out of the question. Present plans call for systematic study of the variables thus far not investigated.

Acknowledgment

The authors wish to acknowledge valuable consultations with Prof. Joseph Kaye of the Massachusetts Institute of Technology during the course of this research.

References

1 J. H. Keenan, E. P. Neumann, and F. Lustwerk, "An Investigation of Ejector Design by Analysis and Experiment," *Journal of Applied Mechanics*, vol. 17, TRANS. ASME, vol. 72, 1950, pp. 299–309.

2 J. H. Keenan and E. P. Neumann, "A Simple Air Ejector," *Journal of Applied Mechanics*, vol. 9, TRANS. ASME, vol. 64, 1942, pp. A-75–81.

3 L. J. Kastner and J. R. Spooner, "An Investigation of the Performance and Design of the Air Ejector Employing Low-Pressure Air as the Driving Fluid," *Proceedings of the Institution of Mechanical Engineers*, vol. 162, 1950, pp. 149–159. Discussion, ibid., pp. 160–166.

4 R. Royds and E. Johnson, "The Fundamental Principles of the Steam Ejector," *Proceedings of the Institution of Mechanical Engineers*, vol. 145, 1941, pp. 193–209. Discussion, ibid., vol. 146, 1942, pp. 223–235.

5 G. Flügel, "The Design of Jet Pumps," National Advisory Committee for Aeronautics, TM 982, 1941, translated from VDI Forschungsheft 395, 1939.

6 J. H. Keenan, "Thermodynamics," John Wiley & Sons, New York, N. Y., 1941, p. 155.

7 J. H. Keenan and J. Kaye, "Gas Tables," John Wiley & Sons, New York, N. Y., 1948. Table 1 of this collection was used.

8 J. Hilsenrath, et al., "Tables of Thermal Properties of Gases," National Bureau of Standards Circular 564, 1955, p. 63.

Journal of BASIC ENGINEERING

Information for Authors

• Manuscripts should be submitted in final form to the Editor. Each manuscript must be accompanied by a statement that it has not been published elsewhere nor has it been submitted for publication elsewhere. A paper which would occupy more than 8 pages of the Journal may be returned to the author for abridgment.

• The author should state his business connection, the title of his position, and his mailing address. A short abstract (50 to 100 words) should be included on the first page immediately preceding the introductory paragraph of the paper.

Three copies of the manuscript are required. One of these must be a carefully prepared printer's copy, typed in double spacing, on one side of the page only, with wide margins, on $8^1/_2$ by 11-in. opaque white paper. Mimeographed manuscripts, if prepared with exceptional care, can be accepted provided they are completely edited.

• As far as possible, all mathematical expressions should be typewritten. Greek letters and other symbols not available on the typewriter should be carefully inserted in ink. Care should be taken to distinguish between capital and lowercase letter, between zero (0) and the letter (*O*), between the numeral (1) and the letter (*l*), etc. A letter representing a vector cannot be printed with an arrow above or below it. The letter should be underscored with a single wavy line, wherever it appears in the text, to designate boldface type.

• A list of symbols carefully marked for the use of the editor (thus: κ, Greek l.c. kappa), if it has not been included in the body of the paper, should accompany the manuscript on a separate page.

• Before preparing a manuscript the author should study printed articles in the Journal, with special attention to the form and style of mathematical expressions, tables, footnotes, references, and abstract. Numbers that identify mathematical expressions should be enclosed in parentheses. Numbers that identify references at the end of the paper should be enclosed in brackets. Care should be taken to arrange all tables and mathematical expressions in such a way that they will fit into a single column when set in type. Equations that might extend beyond the width of one column (fractions that should not be broken or long expressions enclosed in parentheses) should be rephrased to go on two or more lines within column width. Fractional powers are preferred to root signs and should always be used in more elaborate formulas. The solidus should be used instead of the horizontal line for fractions wherever possible.

• A normal paper should not exceed 8 pages in the Journal. It is about 8000 words or 20 double-spaced typewritten pages exclusive of drawings. A Technical Brief should not exceed 750 words or about one page in the Journal inclusive of drawings.

• Originals and two copies of figures must accompany the manuscript. Line drawings should not be larger than $8^1/_2 \times 11$ in. and should be planned for reduction to column width. Lettering should be large enough to be clearly legible when the illustration is reduced. The originals of line drawings must be in India ink on white or pale blue tracing paper or tracing cloth. Photographs of equipment or test specimens must be glossy prints and should be used sparingly. Captions for figures should be typed double-spaced and included as the last page of the manuscript. The figure number and author's name should be written in the margin or on the back of each illustration.

• Titles of papers should be brief.

• Authors can obtain copies of the ASME Manual MS-4, "An ASME Paper," from the Editor and are urged to do so before drafting their papers in final form.

• Papers published in Journals of the Transactions of the ASME must be presented at a Meeting, either in person or by title.

• An author is entitled to 25 preprints free of charge (in the case of two authors, 15 each; three or more authors, 10 each). Larger quantities of preprints or reprints can be ordered from Editorial Department, The American Society of Mechanical Engineers, 29 West 39th Street, New York 18, N. Y. Quotations will be sent on request.

Please address all communications to:

Editor, ASME,

29 West 39th Street,

New York 18, N. Y.

ASME Publications Committee